Magnetogalvanic effects in ferromagnets of reduced dimensions

Dissertation

zur Erlangung des Doktorgrades

des Department Physik

der Universität Hamburg

vorgelegt von

André Kobs
aus Hamburg

Hamburg
Januar 2013

Gutachter der Dissertation:	Prof. Dr. Hans Peter Oepen *Universität Hamburg, Germany* Prof. Dr. Bernard Dieny *SPINTEC, CEA-INAC, Grenoble, France* Prof. Dr. Alexander Gerber *Tel Aviv University, Israel*
Gutachter der Disputation:	Prof. Dr. Hans Peter Oepen *Universität Hamburg, Germany* Prof. Dr. Kornelius Nielsch *Universität Hamburg, Germany*
Datum der Disputation:	17. Mai 2013
Vorsitzender des Prüfungsausschusses:	PD Dr. Alexander Chudnovskiy
Vorsitzender des Promotionsausschusses:	Prof. Dr. Peter Hauschildt
Dekan der Fakultät für Mathematik, Informatik und Naturwissenschaften:	Prof. Dr. Heinrich Graener

Abstract

This thesis deals with three topics in the field of research of magnetogalvanic effects in ferromagnets of reduced dimensions.
The first subject concerns the magnetic microstructure of domain walls located at the bend of soft magnetic V-shaped nanowires. Three different types of domain walls were observed by means of scanning electron microscopy with polarization analysis (SEMPA) and obtained from micromagnetic simulations, namely, the symmetric and asymmetric transverse domain wall as well as the vortex domain wall, that are well known from a straight wire geometry. The implementation of a symmetry breaking bend affects the spatial potential landscape while the details of the pinning behavior of the domain walls at the bend derive from the topology of their microstructures. The dependence of the preponderant domain wall type on bending angle reveals that, besides the wire's dimensions, the bending angle is a further parameter to adjust the wall type on purpose. Concerning vortex domain walls it is shown that the sense of magnetization rotation around the vortex core, which was found to be inherently linked to the position of the core with respect to the wire's bisection, is tunable via magnetic seeding fields that are slightly tilted out of the symmetry axis of the wire. The possibility to intentionally control the vortex wall properties gives a high flexibility for future concepts of vortex-based memory devices.
The second project of this thesis introduces a method that enables the investigation of the magnetization reversal of individual nanomagnets with lateral dimensions of $\gtrsim 100$ nm by means of magnetotransport. The method consists of the preparation of micro-circuits including the creation of the nanomagnet from a laterally homogeneous metallic stack by means of focused ion beam (FIB) technique and allows the subsequent *in situ* magnetoresistance (MR) investigation utilizing a micromanipulator under ultra-high vacuum conditions. The top-down creation of the nanomagnet is based on rendering the surrounding metal paramagnetically by means of ion beam-induced mixing of the material layers of the stack. Importantly, as the paramagnetic material constitutes the input leads it has to maintain a good electrical conductance to guarantee a high sensitivity for the magnetogalvanic effects of the nanomagnet. In order to find adequate stacks an *in situ* MR method for characterizing the influence of ion-bombardment on the electrical and magnetic properties was developed. This method was applied for different stacks containing a 20 nm thick soft magnetic permalloy layer. The best suited stack was used to demonstrate the potential and sensitivity of the MR investigations of individual nanomagnets in the case of rectangular prisms (rectangles) with lateral dimensions of 600×300 nm^2, 800×400 nm^2, and 1000×500 nm^2. The remagnetization behavior of the two generic cases with the magnetic field applied perpendicularly (hard axis) and in parallel (easy axis) to the long axis of the rectangles obtained from single field cycles is analyzed by utilizing the anisotropic MR (AMR). Reversible and irreversible remagnetization processes are quantified and unambiguously assigned to the involved micromagnetic states. The main result is that the energy density of the micromagnetic Landau state can be obtained from the hard axis remagnetization behavior, in accordance with domain theoretical considerations and micromagnetic simulations.
The third subject of this thesis deals with comprehensive investigations of the MR of

Co/Pt layered structures performed for current in-plane (CIP) geometry in the temperature range of 4.2 K $\leq T \leq$ 295 K. The MR investigations are accompanied by the determination of the magnetic and structural properties of the samples prepared by sputtering techniques in order to enable and ensure a reasonable interpretation of the MR results. The key result was the discovery that the longitudinal resistivity ρ_{xx} depends on the magnetization orientation within the plane perpendicular to the current direction. The fingerprint of the discovered MR effect is that ρ_{xx} shows a symmetry adapted $\cos^2$ dependence on the angle that the magnetization $\mathbf{M}$ includes with the surface normal and is largest for $\mathbf{M}$ oriented along the latter. By varying the Co layer thickness (0.8 nm $\leq t_{\mathrm{Co}} \leq$ 50 nm) of Pt/Co/Pt sandwiches a $1/t_{\mathrm{Co}}$ dependence of the effect was found providing strong evidence that it originates at the Co/Pt interfaces. Thus, the effect was named anisotropic interface magnetoresistance (AIMR). The thickness dependence of the AIMR can be phenomenologically described by the Fuchs-Sondheimer model by assuming that the scattering probability of the electrons at the Co/Pt interfaces is enhanced by 3% when changing the magnetization from any desired in-plane direction to the out-of-plane direction. In the thickness regime where sandwiches and Co/Pt multilayers exhibit a perpendicular magnetic anisotropy the AIMR is in the same order of magnitude as the AMR. This finding is important in the light of recent efforts to study domain wall resistance in the framework of spintronics as the AIMR is inherently included in the detected domain wall resistance as an extrinsic contribution. The existence of the AIMR is also demonstrated theoretically in terms of a fully relativistic spin-polarized *ab initio*-type approach by using layer-resolved resistivities in particular confirming that the effect mainly originates in the vicinity of the Co/Pt interfaces. In addition to the discovery of the AIMR the experimental results for the sandwiches further show that the various MR effects existing in the Co material, i.e., the AMR, spin-disorder MR, as well as the anomalous and normal Hall effect, are significantly affected by the finite size of the Co layer thickness. In the case of the anomalous Hall effect it is additionally observed that the scattering processes of the electrons at the Co/Pt interfaces provide a significant contribution to this particular effect.

Kurzzusammenfassung

Diese Dissertation befasst sich mit drei Themen aus dem Forschungsgebiet magnetogalvanischer Effekte in Ferromagneten mit reduzierten Dimensionen.
Der erste Themenabschnitt behandelt die magnetische Mikrostruktur von Domänenwänden, die sich am Knick von weichmagnetischen V-förmigen Nanodrähten befinden. Drei verschiedene Typen von Domänenwänden wurden mittels Rasterelektronenmikroskopie mit Polarisationsanalyse (SEMPA) beobachtet sowie aus mikromagnetischen Simulationen erlangt. Dies sind die von der geraden Drahtgeometrie bekannte symmetrische und asymmetrische Transverswand sowie die Vortexwand. Die Implementierung des symmetriebrechenden Knicks ändert die räumliche Potentiallandschaft, wobei die Details des Pinningverhaltens der Domänenwände am Knick aus der Topologie ihrer Mikrostrukturen folgen. Die Abhängigkeit des vorherrschenden Domänenwandtyps vom Knickwinkel zeigt, dass dieser neben den Drahtabmessungen ein weiterer Parameter ist, um den Domänenwandtyp gezielt einzustellen. Im Falle von Vortexwänden lässt sich der Drehsinn der Magnetisierung um den Vortexkern, welcher inhärent mit der Position des Kerns bezüglich der Spiegelachse des Drahtes verbunden ist, mittels externer magnetischer Felder steuern. Die Möglichkeit, die Eigenschaften der Vortexwand nach Belieben einzustellen, eröffnet zukünftigen Konzepten vortex-basierter Speichermedien eine hohe Flexibilität.
Im zweiten Themenabschnitt dieser Arbeit wird eine Methode vorgestellt, welche die Untersuchung einzelner Nanomagneten mit lateralen Abmessungen $\gtrsim 100$ nm mittels Magnetotransport ermöglicht. Das Verfahren besteht aus der Präparation von Mikrostromkreisen einschließlich der Erzeugung des Nanomagneten aus einem lateral homogenen metallischen Schichtsystem mittels fokussierter Ionenstrahl (FIB)-Technik. Dieses erlaubt zudem die anschließende *in situ* Magnetowiderstands (MR)-Untersuchung mittels eines Mikromanipulators im Ultrahochvakuum. Die "top-down" Herstellung des Nanomagneten basiert auf der Überführung des ihn umgebenden Materials in die paramagnetische Phase unter Ausnutzung der Ionenbeschuss-induzierten Durchmischung der metallischen Schichten. Das so hergestellte paramagnetische Material bildet gleichzeitig die elektrischen Zuleitungen, deren gute Leitfähigkeit somit unabdingbar ist, um eine hohe Empfindlichkeit auf die magnetogalvanischen Effekte des Nanomagneten zu gewährleisten. Auf der Suche nach geeigneten Schichtsystemen wurde ein *in situ* MR-Verfahren entwickelt, das die Charakterisierung des Einflusses des Ionen-Beschusses auf die elektrischen und magnetischen Eigenschaften ermöglicht. Diese Methode wurde auf unterschiedliche Schichtsysteme angewendet, die jeweils einen 20 nm dicken weichmagnetischen Permalloy-Film enthalten. Sodann wurde das am besten geeignete Schichtsystem verwendet, um das Potential und die Empfindlichkeit der MR-Untersuchungsmethode von einzelnen Nanomagneten anhand von rechteckigen Prismen (Rechtecken) mit lateralen Abmessungen von 600×300 nm^2, 800×400 nm^2, und 1000×500 nm^2 zu demonstrieren. Das Ummagnetisierungsverhalten wurde im Falle eines angelegten Magnetfeldes senkrecht (harte Richtung) bzw. parallel (leichte Richtung) zur langen Achse der Rechtecke in einzelnen Felddurchläufen unter Ausnutzung des anisotropen MR (AMR) analysiert. Es konnten reversible und irreversible Ummagnetisierungsprozesse quantifiziert und eindeutig den beteiligten mikromagnetischen Zuständen zugeordnet werden.

Als Hauptergebnis ergab sich dabei, dass die Energiedichte des mikromagnetischen Landau-Zustands aus der Ummagnetisierung in harter Richtung bestimmt werden kann, was in Übereinstimmung mit domänentheoretischen Überlegungen und durchgeführten mikromagnetischen Simulationen steht.
Das dritte Thema dieser Arbeit befasst sich mit umfassenden Untersuchungen des MR von Co/Pt-Schichtsystemen, die im Temperaturbereich von $4.2\ \mathrm{K} \leq T \leq 295\ \mathrm{K}$ durchgeführt wurden, wobei der Strom entlang der Schichtebenen eingeprägt ist. Diese Untersuchungen werden durch eine Bestimmung der strukturellen und magnetischen Eigenschaften der mittels Sputtertechniken hergestellten Proben ergänzt. Dadurch wird eine fundierte Interpretation der MR-Ergebnisse sichergestellt. Das Schlüsselergebnis war hierbei die Entdeckung, dass der Längswiderstand ρ_{xx} von der Orientierung der Magnetisierung innerhalb der Ebene senkrecht zur Stromrichtung abhängt. Das Wesen dieses MR-Effekts ist es, dass ρ_{xx} ein symmetrieadaptiertes $\cos^2$ Verhalten vom Winkel zeigt, den die Magnetisierung $\mathbf{M}$ mit der Oberflächennormalen einschließt und am größten für eine Ausrichtung von $\mathbf{M}$ entlang der Normalen ist. Bei der Variation der Co-Schichtdicke ($0.8\ \mathrm{nm} \leq t_{\mathrm{Co}} \leq 50\ \mathrm{nm}$) von Pt/Co/Pt-Sandwichstrukturen zeigt der entdeckte Effekt eine $1/t_{\mathrm{Co}}$-Abhängigkeit, welche eindeutig belegt, dass dieser Effekt an den Co/Pt-Grenzflächen entsteht. Daher wurde der Effekt als anisotroper Grenzflächenmagnetowiderstand (AIMR[1]) bezeichnet. Die Dickenabhängigkeit des AIMR kann phänomenologisch mit dem Fuchs-Sondheimer-Modell unter der Annahme beschrieben werden, dass sich die Streuwahrscheinlichkeit der Elektronen an den Grenzflächen um 3% erhöht, wenn die Magnetisierung von einer beliebigen Richtung in der Ebene parallel zur Oberflächennormalen reorientiert wird. In dem Dickenbereich, in dem die Sandwichstrukturen und Co/Pt-Multilagen eine senkrechte magnetische Anisotropie aufweisen, ist der AIMR von gleicher Größenordnung wie der AMR. Dieser Befund ist im Hinblick auf die jüngsten Erkenntnisse über den Domänenwandwiderstand im Forschungsgebiet der Spintronik wichtig, da der AIMR inhärent als extrinsischer Beitrag im gemessenen Domänenwandwiderstand enthalten ist. Die Existenz des AIMR wurde zudem theoretisch in einer vollständig-relativistischen, spin-polarisierten *ab initio*-Studie unter Verwendung von schichtaufgelösten Widerständen nachgewiesen. Diese bestätigt, dass der Effekt hauptsächlich an den Co/Pt-Grenzflächen entsteht. Neben der Entdeckung des AIMR zeigen die experimentellen Ergebnisse für die Sandwichstrukturen, dass die weiteren MR-Effekte, die im Co-Material existieren (AMR, Spinwellen-MR sowie der anomale und normale Hall Effekt), deutlich von den reduzierten Abmessungen der Co-Schichtdicke beeinflusst sind. Beim anomalen Hall Effekt konnte zudem beobachtet werden, dass die Streuprozesse der Elektronen an den Co/Pt-Grenzflächen einen signifikanten Beitrag zu diesem Effekt leisten.

[1] engl. anisotropic interface magnetoresistance

Contents

1 Introduction **1**

2 Basics of Micromagnetism **5**
2.1 Magnetic energy contributions 6
2.1.1 Exchange interaction 6
2.1.2 Magnetostatic energy 7
2.1.3 Magnetocrystalline and surface anisotropy 11
2.1.4 Experimental determination of anisotropies 12
2.1.5 Influence of roughness, interdiffusion, and strain on anisotropy 15
2.2 Magnetic domain walls in thin films 17
2.3 Micromagnetic Simulations and Exchange Lengths 20

3 Domain walls in V-shaped soft magnetic nanostrips **23**
3.1 Experimental procedure 26
3.1.1 Investigation method - Scanning electron microscopy with polarization analysis (SEMPA) 26
3.1.2 Preparation of V-shaped wires via focused ion beam (FIB) . . 27
3.1.3 Preparation and properties of $Co_{39}Fe_{54}Si_7$ film 28
3.1.4 Parameters for micromagnetic simulations 29
3.1.5 Seeding of domain walls at the bend of the wires 30
3.2 Magnetic microstructure of domain wall types 31
3.2.1 Symmetric transverse domain wall 32
3.2.2 Vortex domain wall 35
3.2.3 Asymmetric transverse domain wall 38
3.3 Influence of width and bending angle on the domain wall type 40
3.3.1 Width variation 40
3.3.2 Bending angle variation 41
3.4 Controlling the properties of vortex domain walls via external seeding fields 43
3.4.1 Modification of the sample layout 44
3.4.2 Results of the SEMPA investigations and OOMMF simulations 45
3.4.3 Discussion of the relaxation process 47
3.5 Conclusion and outlook 50

4 Magnetization reversal and magnetic energy of individual submicron rectangles investigated via anisotropic magnetoresistance **53**
4.1 Magnetic microstructure of submicron softmagnetic rectangles 56
4.1.1 Flux-closure states 56
4.1.2 High remanence states 58

4.1.3 Phase diagram . . . 58
4.2 Experimental setup . . . 60
4.2.1 UHV-dualbeam chamber . . . 60
4.2.2 *In situ* magnetoresistance setup . . . 61
4.3 MR measurement scheme . . . 63
4.4 Preliminary considerations and investigations . . . 65
4.4.1 Anisotropic magnetoresistance of multi-domain particles . . . 65
4.4.2 Realization of paramagnetic leads . . . 68
4.4.3 Properties of the 10 nm Cr/ 20 nm Py/ 2.5 nm Pt stack . . . 76
4.4.4 FIB procedure for preparing micro-circuits . . . 83
4.4.5 Proof of principle . . . 84
4.5 SEMPA investigations of the remanence state of submicron rectangles 84
4.5.1 Remanence state after pretreatment in easy axis fields . . . 86
4.5.2 Remanence state after pretreatment in hard axis fields . . . 86
4.6 Magnetization reversal and magnetic energy of single submicron permalloy rectangles . . . 87
4.6.1 Easy axis magnetization behavior of single rectangles . . . 87
4.6.2 Energy density of single rectangles obtained from hard axis magnetization behavior . . . 91
4.7 Conclusion and outlook . . . 104

5 Magnetogalvanic effects of Co/Pt layered structures - Anisotropic Interface Magnetoresistance 109
5.1 Fundamentals of the magnetotransport of ferromagnetic transition metal films . . . 113
5.1.1 Basics of electrical resistivity - Ohm's law, Boltzmann equation, Matthiesen's rule, and Bloch-Grüneisen formula . . . 113
5.1.2 Resistivity of thin films - Fuchs-Sondheimer model . . . 120
5.1.3 Resistivity of ferromagnetic transition metals . . . 125
5.1.4 Magnetoresistance effects . . . 132
5.2 Preparation of Co/Pt layered structures . . . 149
5.2.1 Deposition of Co and Pt layers via sputter techniques . . . 149
5.2.2 Construction of the Co/Pt samples . . . 151
5.2.3 MR sample layout and electrical contacting . . . 152
5.2.4 MR sample series . . . 154
5.3 Structural and magnetic properties of Co/Pt layered structures . . . 154
5.3.1 Structural properties . . . 154
5.3.2 Magnetic properties . . . 180
5.4 Magnetoresistance measurements . . . 195
5.4.1 MR measurement setup . . . 195
5.4.2 MR measurement scheme . . . 195
5.5 Magnetoresistance of Pt/Co/Pt sandwiches - Anisotropic Interface Magnetoresistance (AIMR) . . . 198
5.5.1 Magnetoresistance of Pt/Co/Pt sandwiches grown on SiO_2 . . . 198
5.5.2 Phenomenological description of sandwich resistance . . . 209

5.5.3 Comparison of AMR and AIMR for Pt/Co/Pt sandwiches grown on SiO_2 and Si_3N_4 . . . 221
5.6 Temperature dependence of $\rho(\mathbf{M}, \mathbf{H})$ in Pt/Co/Pt sandwiches . . . 223
5.6.1 Temperature dependence of zero-field resistivity . . . 224
5.6.2 Dependence of resistivity on applied field and magnetization orientation below room temperature . . . 230
5.6.3 Temperature dependence of anisotropy constants . . . 232
5.6.4 Temperature dependence of magnetoresistance effects . . . 234
5.7 Anisotropic Interface Magnetoresistance (AIMR) of Co/Pt multilayers 239
5.7.1 Influence of magnetic microstructure on resistivity & domain wall resistance . . . 239
5.7.2 Dependence of AIMR on Pt interlayer thickness and bilayer repetition . . . 244
5.8 Conclusion and outlook . . . 250

Bibliography **263**

Publications **333**
Publication List and Conference Contributions . . . 333
Publication related to chapter 3 . . . 339
Publication related to chapter 4 . . . 340
Publications related to chapter 5 . . . 341

Acknowledgement **342**

1 Introduction

In 1831, Michael Faraday made the groundbreaking discovery of the phenomenon of electromagnetic induction [1], i.e., the creation of an electrical field due to a changing magnetic flux, which is one of the cornerstones of the theory of electromagnetism formulated by James Clark Maxwell at the beginning of the 1860s [2, 3]. At roughly the same time the first observations were made that the electrical resistivity of metals is influenced by magnetic fields. William Thomson later known as Lord Kelvin discovered magnetogalvanic effects in the longitudinal resistivity (1860-1861) [4], while Edwin Herbert Hall observed the existence of a field-dependent transversal component of resistivity (1879-1881) [5, 6, 7, 8]. In both cases it was found that, in addition to the *normal* magnetogalvanic effects also occurring in non-ferromagnetic metals, in ferromagnets further magnetogalvanic phenomena exist, which can be solely related to the spontaneous magnetization, i.e., the so-called anisotropic magnetoresistance (AMR) and anomalous Hall effect (AHE), respectively.
From today's technological point of view, however, both magnetoresistance effects play only a minor role: Although the AHE can be several orders of magnitude larger than the normal Hall effect in ferromagnets it is not established in magnetic field sensor devices since the size of the normal Hall effect in semiconducting materials can easily compete with the size of the AHE [9, 10, 11, 12]. Despite of a systematic research of the AMR starting in the 1950s the magnetoresistance ratio of the AMR, i.e., the maximum change of the resistivity compared to the resistivity, does not exceed a few percent at room temperature, which is connected with the fact that the AMR is a consequence of the relatively weak spin-orbit interaction [13]. Nevertheless, this magnitude was acceptable in order to guarantee a continued exponential growth of storage density in hard disk drives (HDDs), so that the AMR entered the market of information technology as a sensor in read heads superseding inductive-based read heads in 1991 [14].
Coincidentally, shortly before the first AMR read head launched the market the working groups of Peter Grünberg and Albert Fert independently discovered a new kind of magnetoresistance effect in ferromagnetic/non-ferromagnetic metallic layered structures in 1988 [15, 16], which was awarded with the Noble price for physics in 2007 [17, 18]. They observed a *giant* change of the resistivity when the relative orientation of magnetization of the individual layers changes from parallel to antiparallel alignment. The discovery of the giant MR (GMR) is based on the invention of new techniques enabling the preparation of thin layers of a few atomic monolayers with high purity as well as high quality of the interfaces [19, 20]. The magnitude of the GMR ratio, which can reach around hundred percent at room temperature, was the reason to replace the AMR by GMR read heads already within less than ten years after its discovery leading to an accelerated exponential growth of the storage density in HDD [14].

The discovery of the GMR initiated the development of the interdisciplinary field of intense research of "spin-electronics" or "spintronics", which deals with the investigation of the role of the electron's magnetic moment (or spin) on the electrical transport in order to push the technological progress in information technology. In the last almost 25 years ongoing improvements of preparation techniques have led to the discovery of new fascinating phenomena, which inspired the invention and implementation of new functional concepts for data processing as well as memory and logic devices[1].

One cornerstone was the discovery of tunneling magnetoresistance (TMR) in layered structures at room temperature in 1995 [33], where the ferromagnetic layers are separated by a nanometer thick insulating non-ferromagnetic spacer layer. Analogue to the GMR, in this so-called magnetic tunnel junction (MTJ) the electron flow from one ferromagnetic layer to the other depends on the relative orientation of magnetization of the layers [34]. The improvement of the TMR ratio of up to several 100% was one of the reasons to interchange the GMR by the TMR in HDDs in 2005 [14]. Moreover, MTJs are promising candidates for realizing logic gates of non-volatile magnetic random access memory (MRAM) devices [35, 36, 37, 34, 38]. One route to enhance the memory density of such devices is to use ferromagnetic layers/electrodes with perpendicular magnetic anisotropy (PMA) [39]. In order to overcome the shape anisotropy, which favours an in-plane orientation of the magnetization, a resulting PMA can be achieved by a high magnetocrystalline anisotropy like in CoCrPt alloys, which were succesfully utilized as a material for the first perpendicular recording HDDs in 2005 [40]. An alternative to realize PMA is the usage of a sufficiently high interface ansiotropy contribution [41], which is a phenomenon that i.a. occurs in Co/Pt layered structures important in this thesis. For MTJs equipped with Co/Pt electrodes that exhibit PMA TMR ratios of up to 19% could be achieved until now [39, 42, 43, 44, 45]. As it is also possible to implement a unidirectional anisotropy in Co/Pt stacks via the exchange-bias effect [46, 47, 48, 49, 50] they fulfill the necessary prerequisites for the application in future MTJ related devices. Interestingly, rather large spin-orbit interaction based phenomena were observed in Co/Pt based MTJs with only one ferromagnetic electrode. In (Co/Pt)/AlO_x/Pt the so-called tunneling anisotropic MR (TAMR) was found at low temperatures with a ratio of about 15% [51], which means that the tunneling probability varies by this value when changing the magnetization from any desired in-plane orientation to out-of-plane direction. Furthermore, in oxide/Co/Pt trilayers moderate in-plane current densities can be used to switch the Co magnetization orientation between the single-domain up and down state, as a consequence of the so-called spin-orbit torque (SOT) effect [52, 31, 53].

Another important branch in the field of spintronic emerged with the advent of preparation techniques in the end of the 1990s, which enable the creation of laterally confined magnetic structures with dimensions in the submicron regime [54]. In these nanomagnets the static and dynamic properties are strongly affected by their size and shape, so that they can be tuned on purpose to meet the requirements for spintronic applications. A lot of attention attracted soft magnetic nanowires

[1] For details the reader is referred to the following review articles dealing with the field of spintronics [21, 22, 23, 24, 25, 26, 27, 14, 28, 29, 30, 31, 32]

that contain domain walls separating homogeneously magnetized regions from each other [55]. The existence of the so-called spin-transfer torque (STT) effect, which was predicted in 1996 [56, 57, 58] and experimentally discovered two years later [59], particularly enables the possibility to induce a controlled domain wall movement by utilizing spin-polarized currents [60]. This observation inspired the development of future memory concepts like the race-track memory [61] and provides a further tool for domain wall-logic devices [62, 63]. One type of domain wall of particular interest is the so-called vortex domain wall. According to its name the microstructure contains a vortex, which is composed of a curling magnetization (clockwise or counterclockwise) around a sharp core, where the magnetization is forced out-of-plane pointing either up or down denoting the polarity. Concepts for using the polarity and sense of rotation of the vortex in future memory devices were recently proposed [64, 65].

This thesis covers three different aspects in the field of "Magnetogalvanic effects in ferromagnets of reduced dimensions", which are separately introduced and presented in the chapters 3 to 5. Chapter 3 deals with the magnetic microstructure of domain walls in V-shaped soft magnetic nanostrips, which is a geometry frequently utilized to reliably create and trap domain walls at the kink. The investigation performed by means of scanning electron microscopy with polarization analysis (SEMPA) provides a detailed knowledge of the magnetic microstructure, which is indispensable for a reasonable interpretation of any kind of transport experiment. Concerning vortex domain walls it is shown that the sense of magnetization rotation around the vortex core can be tuned intentionally via magnetic seeding fields, which provides high flexibility for future concepts of vortex-based memory devices.
While wires are frequently investigated the quantification of the magnetic properties of nanostructures, where all dimensions are minimized to the submicron regime, is lagging behind due to the missing sensitivity of conventional characterization techniques. A characterization is mandatory to pave the way for future technological applications of nanomagnets in logic devices based on inter-particle magnetostatic interactions (quantum cellular automata) [66] or in bit patterned storage media [67]. In chapter 4 a method is presented that enables *in situ* magnetotransport investigations of individual nanomagnets with lateral dimensions of $\gtrsim 100$ nm. The nanomagnets are prepared by focused ion beam (FIB) technique, which provides high flexibility to vary the size, shape, and magnetic environment of the nanostructure, which opens the way to systematically study corresponding dependencies of the magnetic properties on purpose. The potential and sensitivity of the *in situ* MR method is demonstrated by investigating the magnetization reversal of submicron soft magnetic rectangular prisms (rectangles) by utilizing the AMR as a probe. The main result is that the size-dependent energy density of the micromagnetic Landau state can be obtained from the hard axis remagnetization behavior. The feasibility of the *in situ* MR method to address individual nanomagnets that are arranged in arrays is also proofed.
The main topic of this thesis presented in chapter 5 deals with comprehensive investigations of magnetogalvanic effects of Co/Pt layered structures, which are frequently used components in recent spintronic research as mentioned above. In the

framework of this thesis a new kind of magnetoresistance effect was discovered in the current in-plane (CIP) geometry. The fingerprint of this MR effect is that the longitudinal resistivity shows a symmetry adapted $\cos^2$ dependence on the angle that the magnetization includes with the surface normal and is largest for the magnetization oriented along the latter. The investigations clearly point out that the mechanism behind this effect originates at the Co/Pt interfaces. Therefore, it was named anisotropic interface magnetoresistance (AIMR). The AIMR is also proven theoretically by means of a fully relativistic spin-polarized ab initio-type study. In addition to the discovery of the AIMR the experimental results further show that the various MR effects existing in the Co material, i.e., the AMR, spin-disorder MR, AHE, as well as the normal Hall effect, are significantly affected by the finite size of the Co layer thickness. An interface scattering contribution to the AHE is also reported.
Before presenting the three topics the following chapter 2 briefly introduces the basics of micromagnetism relevant for this thesis.

2 Basics of Micromagnetism

Generally, describing solid state phenomena on a microscopic scale is demanding as one is confronted with a many-body problem. The key for the understanding of ferromagnetism is the electronic structure under consideration of the electron spin [68]. Within the framework of quantum theory of solid states tremendous progress in the description of the itinerant ferromagnetism has been made by the development of density functional theory (DFT), which enables the *ab initio* calculation of bulk material parameters from the electronic structure [69, 70, 71]. For these calculations the (infinite) bulk is regarded to consist of a repetition of identical elementary cells, so that for the description it is sufficient to consider one cell only by assuming periodic boundary conditions. This strategy, however, fails for the description of samples of finite size or complex magnetic domain structures. To describe these "inhomogeneities" on a purely electronic level, even for structures which are only 100 nm in size, the calculation power of existing supercomputers is not sufficient [68]. In addition, for micro- and nanostructures the magnetostatic energy has to be considered, which is generally not included in the *ab initio* description.
The first section of this chapter (section 2.1) deals with the magnetic energy contributions. The route from the electron theory to the so-called micromagnetic approximation ("micromagnetism"), which is commonly suitable for the description of magnetic nanostructures with dimensions in the range of a few 10 nm to several microns [68], is exemplarily sketched there for the exchange energy[1].
The second section 2.2 deals with one consequence of the minimization of total energy, i.e., magnetic domain walls, which separate homogeneously magnetized regions ("magnetic domains") from each other.
The chapter closes with an introduction about the commonly used ansatz in order to find local minima of the energy landscape for a particular ferromagnetic sample by means of numerical calculations ("micromagnetic simulations").
It is worth mentioning that the domain theory is a good approximation on a further larger length scale [68]. Similar to micromagnetism, the ferromagnet is considered to be subdivided into domains with domain walls in between. However, details of the domain walls and other objects, for example magnetic vortices, are neglected and regarded to have infinitesimal small extensions. By assigning them an area or line energy density their contribution to the total energy is then simply considered by a corresponding integration. The domain theoretical approximation is a crude simplification but often gives a good impression about the domain pattern and the physics behind it. Nevertheless, for the quantitative comparison with experimental

[1] Note that the relevant length scales for magnetic inhomogeneities are in the nanometer range, so that the name nanomagnetism would be more appropriate. But nowadays this term is generally used for the description of magnetism within the atomistic approximation.

results a more detailed knowledge about the magnetic microstructure is mandatory. This requires the use of numerical calculations.

2.1 Magnetic energy contributions

In a ferromagnetic material the following four energy terms have to be considered, which sum up to the total magnetic energy E: The exchange energy E_{xc} which favors a parallel orientation of adjacent spins, the magnetocrystalline anisotropy E_{mca} which connects the spins with the crystal lattice, the Zeeman energy E_{Z} which forces the spins in the direction of an external magnetic field, and the stray field or demagnetization energy E_{d} which is connected with the existence of magnetic poles:

$$E = E_{\mathrm{xc}} + E_{\mathrm{mca}} + E_{\mathrm{Z}} + E_{\mathrm{d}} \tag{2.1}$$

Like every physical system, in equilibrium a magnetic system adopts a state for which the total energy is at a global or local minimum.
In the following, the above terms are discussed separately in detail, however, E_{d} and E_{Z} are combined to the term magnetostatic energy E_{ms} for the sake of convenience.

2.1.1 Exchange interaction

The fundamental microscopic mechanism of long range magnetic order phenomena in condensed matter is the exchange interaction between the electrons [72, 73]. This interaction is quantum mechanical in origin and relies on the repulsive Coulomb-interaction $H_{\mathrm{Coulomb}} = \frac{1}{2}\sum_{i\neq j}\frac{e^2}{4\pi\epsilon_0 r_{ij}}$ between the electrons under consideration of the Pauli exclusion principle. This principle is a consequence of the fermionic character of the electrons, which claims that the total wave function of the electron system has to be antisymmetric on interchange of any two (indistinguishable) electrons. The wave function can be expressed as a product of space Ψ and spin wave function χ, so that the symmetry of Ψ has to be the opposite of the symmetry of χ. The energy difference [72]

$$J \propto <\Psi_{\mathrm{symmetric}}|H_{\mathrm{Coulomb}}|\Psi_{\mathrm{symmetric}}> - <\Psi_{\mathrm{antisymmetric}}|H_{\mathrm{Coulomb}}|\Psi_{\mathrm{antisymmetric}}> \tag{2.2}$$

is the so-called exchange integral. For $J \neq 0$ a collective spin arrangement is preferred, which is either ferromagnetic (parallel orientation of the electron spins) in the case of an antisymmetric spacial wave function being energetically favorable ($J > 0$), or antiferromagnetic in the case of $J < 0$. In order to obtain the strength of J the complete electronic structure of the sample has to be considered in the calculation, which is not possible even for micro- and nanomagnets as discussed in the introduction of this chapter.
In a first step on the way to get a convenient expression of the exchange interaction, that can be handled in the micromagnetic length scale, the electron spins $\mathbf{S}$ are regarded as to be localized at the lattice points i, so that the exchange interaction

can be expressed as an effective spin-spin interaction of the form [72]:

$$H_{\mathrm{xc}} = -\sum_{i \neq j} J_{ij} \mathbf{S}_i \cdot \mathbf{S}_j \quad , \tag{2.3}$$

which is today known as Heisenberg Hamiltonian (atomistic approximation) [73]. J_{ij} is the so-called exchange constant. As the exchange interaction is only short-range in nature, in a further assumption only nearest neighbor interaction is considered.
The transition to the micromagnetic approximation is a transition to continuous variables neglecting the discrete atomistic nature of the bulk [68]. For instance, summations are replaced by integrals and the spin (magnetic moment) is replaced by an average quantity, i.e., the saturation magnetization M_{S} (averaged density of magnetic moments).
Due to the strength of the exchange interaction on small length scales only small angle deviations between adjacent spins can occur. Thus, the scalar product in Eq. 2.3 can be expanded into a Taylor series, which can be terminated after the first term. Finally, in micromagnetism the exchange energy of a sample of volume V is given by [68]:

$$E_{\mathrm{xc}} = A \int_V \left((\nabla m_x)^2 + (\nabla m_y)^2 + (\nabla m_z)^2 \right) dV \quad , \tag{2.4}$$

where A is a material specific constant, the so-called exchange stiffness and $m_i = M_i / M_{\mathrm{S}}$ is the normalized magnetization component along i.
For instance, regarding Permalloy, which is used in chapter 4, the exchange stiffness is $A = 13$ pJ/m [74]. For a parallel alignment of the spins the exchange energy is minimal while for an antiferromagnetic alignment the energy is maximum. The energy density difference between both states is in the range of GJ/m^3 (0.1 eV/atom) reflecting the high strength of the exchange interaction [75].

2.1.2 Magnetostatic energy

The magnetostatic energy E_{ms} is the sum of the Zeeman energy caused by the interaction of the magnetization $\mathbf{M}$ with an external field $\mathbf{H}_{\mathrm{a}}$ and of the stray field energy [76]. The latter is a self-energy that is generated by the magnetization itself as a consequence of the second Maxwell equation $\mathrm{div}\mathbf{B} = \mu_0 \mathrm{div}(\mathbf{M} + \mathbf{H}_{\mathrm{d}}) = 0$. $\mathbf{H}_{\mathrm{d}}$ is the so-called demagnetization field, which arises if sinks and sources (poles) of the magnetization ($\mathrm{div}\mathbf{M} \neq 0$) are generated. For a ferromagnetic sample of arbitrary shape the magnetostatic energy in an applied field is [72]:

$$E_{\mathrm{ms}} = -\frac{\mu_0}{2} \int_V \mathbf{M} \cdot \mathbf{H}_{\mathrm{d}} \, \mathrm{d}V \; - \; \mu_0 \int_V \mathbf{M} \cdot \mathbf{H}_{\mathrm{a}} \, \mathrm{d}V \tag{2.5}$$

In mathematical terms, the stray field energy (first integral) resembles the Zeeman energy (second integral), i.e., the stray field energy is caused by the interaction of $\mathbf{M}$ with $\mathbf{H}_{\mathrm{d}}$. Notice, as $\mathbf{M}$ vanishes outside the ferromagnet both integrals must be taken only over the volume V of the ferromagnet. Nevertheless, the stray field

energy implicitly includes the energy, which is associated with $\mathbf{H}_\mathrm{d}$ outside the ferromagnet[2].
The stray field energy is always positive semi-definite, so that the existence of $\mathbf{H}_\mathrm{d}$ always enhances the total energy of a ferromagnet. Therefore, the stray field energy term always tries to achieve magnetic patterns with as little volume charges $\rho_m = -\mathrm{div}\mathbf{M}$ and surface charges $\sigma = \mathbf{M} \cdot \mathbf{n}$ as possible (Brown's pole avoidance principle) [76, 77].

2.1.2.1 Demagnetization field and demagnetization factors

In general, the determination of the stray field energy is rather complicated as the volume integral in Eq. 2.5 contains the demagnetization field, which also has to be evaluated by the following integration about the volume and the surface of the ferromagnet [68]:

$$\mathbf{H}_\mathrm{d}(\mathbf{r}) = \frac{1}{4\pi}\int_V \frac{(\mathbf{r}-\mathbf{r}')\mathrm{div}\mathbf{M}(\mathbf{r}')}{|\mathbf{r}-\mathbf{r}'|^3}dV' + \frac{1}{4\pi}\oint_{\delta V} \frac{(\mathbf{r}-\mathbf{r}')\mathbf{M}(\mathbf{r}')\cdot\mathbf{n}}{|\mathbf{r}-\mathbf{r}'|^3}dS' \tag{2.6}$$

These integrations can only be carried out analytically in a few cases. An exceptional case are ellipsoids that are homogeneously magnetized. Then, the demagnetization field is uniform and linearly related to its origin, i.e., the magnetization, by the demagnetization factor $\overleftrightarrow{N}$, which is a tensor of second rank (matrix) [77]:

$$\mathbf{H}_\mathrm{d} = -\overleftrightarrow{N} \cdot \mathbf{M} \tag{2.7}$$

If the coordinate system is in accordance with the main axes (a, b, c) of the ellipsoid, $\overleftrightarrow{N}$ can be diagonalized. The trace of $\overleftrightarrow{N}$ is always unity. The derivation of $\overleftrightarrow{N}$ is extensive and has been carried out by J. A. Osborn for a variety of ellipsoids [78]. Due to symmetry considerations for simple geometries as spheres ($a = b = c$), cylindrical wires ($a \to \infty$, $b = c \ll a$), and thin films ($a = b \to \infty$, $c \ll a$), the demagnetization factors are:

$$\overleftrightarrow{N}_\mathrm{sphere} = \begin{pmatrix} \frac{1}{3} & 0 & 0 \\ 0 & \frac{1}{3} & 0 \\ 0 & 0 & \frac{1}{3} \end{pmatrix}, \quad \overleftrightarrow{N}_\mathrm{wire} = \begin{pmatrix} 0 & 0 & 0 \\ 0 & \frac{1}{2} & 0 \\ 0 & 0 & \frac{1}{2} \end{pmatrix}, \quad \overleftrightarrow{N}_\mathrm{film} = \begin{pmatrix} 0 & 0 & 0 \\ 0 & 0 & 0 \\ 0 & 0 & 1 \end{pmatrix} \tag{2.8}$$

For wires with finite length and rectangular-shaped cross-section with dimensions $a \gg b \gg c$, where a is the wire length, b is the wire width, and c is the thickness, investigated in this thesis (see chapter 3) it is adequate to use an ellipsoidal approximation for the determination of the demagnetization factor [73, 79, 80, 81]. The diagonal demagnetization factor terms are then simply given by:

$$N_x = 0, \quad N_y \approx \frac{c}{b}, \quad N_z \approx 1 - N_y \tag{2.9}$$

[2]It should be mentioned that the terms demagnetization field and stray field are equivalent. It is common use to call $\mathbf{H}_\mathrm{d}$ inside the ferromagnet demagnetization field and outside the ferromagnet stray field.

For non-ellipsoidal bodies $\mathbf{H}_\mathrm{d}(\mathbf{r})$ is not uniform but is a function of the spatial coordinates $\mathbf{r}$. In order to determine the demagnetization energy for non-ellipsoidal bodies, so-called magnetometric demagnetization factors $\overleftrightarrow{N}^{\mathrm{eff}}$ have been deduced. They are defined in such a manner that the demagnetization energy density can be calculated according to

$$(E/V)_\mathrm{d} = -\frac{\mu_0}{2}\mathbf{H}_\mathrm{d}\cdot\mathbf{M} = \frac{\mu_0}{2}(\overleftrightarrow{N}^{\mathrm{eff}}\cdot\mathbf{M})\cdot\mathbf{M} \quad , \tag{2.10}$$

while $\overleftrightarrow{N}^{\mathrm{eff}}$ does not depend on the spatial coordinates as it is the case for ellipsoids. Even for right rectangular prisms (=right cuboids or just "rectangles"), which is another geometry of interest within this thesis (see chapter 4), the analytical derivation and the results for the terms of the tensor $\overleftrightarrow{N}^{\mathrm{eff}}$ are rather complex [82]. Utilizing Eq. (1) in Ref. [82] the following magnetometric demagnetization factors have been calculated for the dimensions of the rectangles investigated in chapter 4.

$$\begin{aligned}
\overleftrightarrow{N}^{\mathrm{eff}}_{1000\times500\times20\ \mathrm{nm}^3} &= \begin{pmatrix} 0.0266 & 0 & 0 \\ 0 & 0.0546 & 0 \\ 0 & 0 & 0.9188 \end{pmatrix} \\
\overleftrightarrow{N}^{\mathrm{eff}}_{800\times400\times20\ \mathrm{nm}^3} &= \begin{pmatrix} 0.0315 & 0 & 0 \\ 0 & 0.0647 & 0 \\ 0 & 0 & 0.9038 \end{pmatrix} \\
\overleftrightarrow{N}^{\mathrm{eff}}_{600\times300\times20\ \mathrm{nm}^3} &= \begin{pmatrix} 0.039 & 0 & 0 \\ 0 & 0.0802 & 0 \\ 0 & 0 & 0.8808 \end{pmatrix}
\end{aligned} \tag{2.11}$$

It should be explicitly emphasized that the demagnetization factors only depend on the aspect ratios of the rectangle and are independent of the actual size of the ferromagnet. This means in particular that in the case of performing a scaling of the film thickness, that keeps the aspect ratios constant, identical demagnetization factors for the rectangles are obtained.

2.1.2.2 Shape anisotropy

As can be clearly seen from Eq. 2.10 under consideration of the (magnetometric) demagnetization factors of Eq. 2.8 and Eq. 2.11, the stray field energy depends on the orientation of magnetization, except for the case of a sphere. In general, a dependence of the energy on the orientation of magnetization is called anisotropy [73]. For the orientation dependence of the stray field energy it is called shape anisotropy. According to Eq. 2.8 for thin films the stray field energy density is:

$$(E/V)_{\mathrm{d,\ film}} = \frac{\mu_0}{2}(\overleftrightarrow{N}_{\mathrm{film}}\cdot\mathbf{M})\cdot\mathbf{M} = \frac{\mu_0}{2}M_z^2 = \frac{\mu_0}{2}M_\mathrm{S}^2\cos^2\Theta \quad , \tag{2.12}$$

where Θ is the angle between the film normal and the magnetization. The stray field energy density is at its maximum $\frac{\mu_0}{2}M_\mathrm{S}^2$ for $\Theta = 0°$ and is at its minmum (zero) if the magnetization lies in the film plane ($\Theta = 90°$). The energy density difference between these directions of easiest and hardest magnetizability resembles the shape

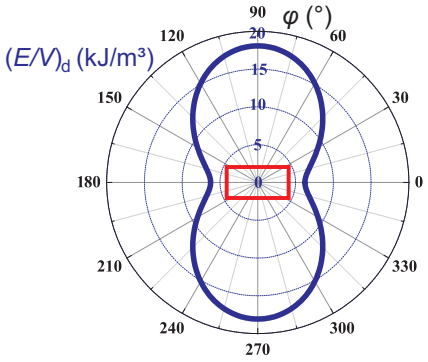

Figure 2.1: Stray field energy density $(E/V)_\mathrm{d}$ of a $1000 \times 500 \times 20$ nm^3 homogeneously magnetized cuboid in dependence of the angle φ between magnetization and the long axis given as a polar plot. For permalloy ($M_\mathrm{S} = 820$ kA/m) the energy density difference between the directions of easiest and hardest magnetizability, i.e., the anisotropy constant, is $K_{\mathrm{d,\ rectangle}} = 11.8$ kJ/m^3.

anisotropy constant K_d:

$$K_{\mathrm{d,\ film}} = \frac{\mu_0}{2} M_\mathrm{S}^2 \tag{2.13}$$

For the Co films, utilized in chapter 5, by using the saturation magnetization at room temperature of $M_\mathrm{S} = 1.4$ MA/m [83], $K_{\mathrm{d,\ Co\ film}} = 1.23$ MJ/m^3 is obtained. As the trace of $\overleftrightarrow{N}$ is always unity there is no other geometrical shape which can exhibit a larger shape anisotropy than a thin film. The size of the shape anisotropy is three orders of magnitudes smaller than the exchange interaction.
In the absence of a magnetic field for wires and rectangles with $N_z \gg N_x, N_y$, investigated in the chapters 3 and 4, similar to thin films, the magnetization lies in the xy plane to minimize stray field energy. For these investigations only in-plane fields are applied, thus $M_z = 0$. If φ is the angle between the magnetization and the length of the long axis (x axis, $N_x < N_y$), the stray field energy density of the rectangles (and wires) is:

$$\begin{aligned}(E/V)_{\mathrm{d,\ rectangle/wire}} &= \frac{\mu_0}{2}(N_x M_x^2 + N_y M_y^2) = \frac{\mu_0}{2} N_x M_\mathrm{S}^2 \cos^2\varphi + \frac{\mu_0}{2} N_y M_\mathrm{S}^2 \sin^2\varphi \\ &= \frac{\mu_0}{2} M_\mathrm{S}^2 (N_y - N_x) \sin^2\varphi + \underbrace{\frac{\mu_0}{2} M_\mathrm{S}^2 N_x}_{\text{constant}}\end{aligned} \tag{2.14}$$

Consequently, the (in-plane) shape anisotropy constant $K_{\mathrm{d,\ rectangle}}$ for rectangles (and wires) is:

$$K_{\mathrm{d,\ rectangle}} = \frac{\mu_0}{2} M_\mathrm{S}^2 (N_y - N_x) \tag{2.15}$$

In Fig. 2.1 the stray field energy density of a rectangle with dimensions of $1000 \times 500 \times 20$ nm^3 in dependence of the in-plane orientation of $\mathbf{M}$ is given as a polar plot.

2.1.3 Magnetocrystalline and surface anisotropy

For the Co/Pt(111) layered structures, which are the topic of chapter 5, further significant anisotropy contributions arise from their crystalline structure. In this section the magnetocrystalline volume and surface anisotropy are briefly introduced. The influence of particular structural properties on both anisotropy contributions is not addressed until section 2.1.5 for the sake of convenience. In contrast to the Co/Pt films, the permalloy and CoFeSi films used in chapters 3 and 4 are soft magnetic. This means that the above mentioned anisotropy contributions can be neglected as they are by several orders of magnitude smaller than the shape anisotropy.

2.1.3.1 Magnetocrystalline volume anisotropy

The magnetocrystalline volume anisotropy is a consequence of the spin-orbit interaction (SOI), which can be expressed by the Hamiltonian $H_{\mathrm{SOI}} = A\mathbf{L}\cdot\mathbf{S}$, where A is a constant reflecting the strength of the interaction [77]. The orbital momentum $\mathbf{L}$ is firmly linked to the crystal lattice and due to the SOI the corresponding energy density depends on the orientation of the spins $\mathbf{S}$ with respect to the crystal lattice. For hexagonal crystals this energy density is only a function of the angle θ between the c-axis and the orientation of magnetization [84], so that the corresponding anisotropy is generally referred to as being *uniaxial*. The uniaxial energy density can be expanded into a power series of the form [73]

$$(E/V)_{\mathrm{mca},\,V} = K_{1V}\sin^2\theta + K_{2V}\sin^4\theta + \mathcal{O}(\sin^6\theta) \tag{2.16}$$

and can normally be terminated after the second order as $K_{iV} \ll K_{jV}$ for $i > j$ [73]. The coefficients K_{1V} and K_{2V} are the uniaxial anisotropy constants of first and second order, respectively. For hexagonal Co the c-axis is the easy axis of magnetizability. In literature, values in the range of $K_{1V} = 400 - 560$ kJ/m^3 and $K_{2V} = 100 - 150$ kJ/m^3 were experimentally found at room temperature [85, 73]. Thus, the magnetocrystalline anisotropy in hcp Co is almost half the size of the shape anisotropy of a thin Co film (see text in connection with Eq. 2.13: $K_{\mathrm{d,\,Co\,film}} = 1.23$ MJ/m^3). With decreasing temperature the K_1 value grows continuously to $K_{1V} = 690 - 840$ kJ/m^3 at liquid helium temperature (4.2 K) while K_2 only shows a slight dependence on temperature below 300 K [85].
For fcc Co the easy axes of magnetization are the $< 111 >$ directions [86]. However, the magnetocrystalline anisotropy is one order of magnitude smaller than for hcp Co due to the higher symmetry of cubic lattices, so that it can be neglected compared to the shape anisotropy in a good approximation [87, 86, 85, 73].
Without going into detail here, the Co/Pt(111) films investigated in this work are polycrystalline but exhibit a pronounced out-of-plane texture. That signifies that in every crystallite one specific lattice axis is predominantly oriented in stacking direction while the other axes are randomly oriented. As a result, the out-of-plane direction is outstanding, so that depending on the kind and degree of out-of-plane texture a corresponding net uniaxial magnetocrystalline anisotropy is expected.
As for Co the magnetocrystalline anisotropy is always lower than the shape anisotropy it cannot be sufficient by itself to create a perpendicular easy axis of magnetization.

2.1.3.2 Surface and interface anisotropy

Surfaces and interfaces interrupt the translational symmetry of a crystal lattice. In 1954, L. Néel suggested a magnetic anisotropy contribution K_S which arises due to this symmetry breaking as the atoms at surfaces (or interfaces) have less nearest neighbors of the same element compared to atoms in bulk (Néel's pair interaction model) [88, 89]:

$$(E/V)_{\mathrm{mca},\,S} = \frac{2K_S \sin^2\theta}{t} \quad , \tag{2.17}$$

where θ is the angle between film normal and magnetization, t is the film thickness, and the prefactor of two accounts for the two surfaces. In 1968, a surface contribution to the anisotropy has been experimentally observed for the first time by U. Gradmann and J. Müller in thin epitaxial NiFe films on Cu(111) [90]. For these films the authors found an easy axis of magnetization perpendicular to the film surface (perpendicular magnetic anisotropy (PMA)) for films with a thickness of 1.8 monolayers. Furthermore, it was analyzed that the anisotropy scales with the inverse thickness in accordance with the prediction of Néel (Eq. 2.17) [91]. This result in particular shows that the surface anisotropy can overcome the volume contributions of anisotropy in ultrathin films in order to attain an effective PMA [92]. Regarding multilayers a PMA was first observed by Carcia et al. for Co/Pd systems in 1985 [93] and later for Co/Pt in 1988 [94]. Furthermore, Co based multilayers with PMA were found for Co/Au, Co/Ru, and Co/Ir systems [95, 41]. Generally, in these studies an almost inverse thickness dependence of the anisotropy in agreement with Eq. 2.17 was found. Deviations and possible reasons are noted in section 2.1.5. Besides Co based multilayers, interface anisotropies of Fe based multilayers often favor a PMA, whereas for Ni based multilayers usually a negative K_S was found [41]. For Co/Pt(111) films typical values for the interface anisotropy were experimentally found to be in the range of $K_S = 0.27 - 1.29$ mJ/m^2 [41, 96], which is in the order of 1 meV per interface atom. Although Néel's pair interaction model predicts the correct order of magnitude for K_S it fails to supply exact numbers and even the sign [92]. For the theoretical derivation of the anisotropy constants K_S as well as K_V *ab initio* calculations must be performed, which is a challenge in particular for the volume part K_V due to its small value in the range of μeV per atom [97, 98, 99, 100].

2.1.4 Experimental determination of anisotropies

In the first part of this section it is shown how the different anisotropy contributions can be disentangled experimentally while the second part gives the answer about how the anisotropy constants can be determined experimentally from the hard axis remagnetization curves.

2.1.4.1 Effective magnetic anisotropy

In general, a superposition of the various existing anisotropies of a sample is measured. As for the polycrystalline Co/Pt(111) films the shape, interface, as well as magnetocrystalline volume anisotropy terms are uniaxial with respect to the stacking direction they simply sum up to the total or so-called effective anisotropy. With

the legitimate redefinition of the zero value in the stray field energy of a thin film (Eq. 2.12): $(E/V)_{\mathrm{d,\ film}} = \frac{\mu_0}{2} M_\mathrm{S}^2 \cos^2\Theta = -\frac{\mu_0}{2} M_\mathrm{S}^2 \sin^2\Theta + \mathrm{const.}$ [101] for the first order effective anisotropy constant $K_{1,\mathrm{eff}}$ the following expression is obtained:

$$K_{1,\mathrm{eff}} = \underbrace{K_{1V} - \frac{\mu_0}{2} M_\mathrm{S}^2}_{K_{1V,\mathrm{eff}}} + \frac{2K_{1S}}{t} \tag{2.18}$$

As there exist no higher orders for the shape anisotropy and as K_{2S} was experimentally found to be almost zero for Co/Pt layered structures [102, 103] the second order anisotropy constant is basically determined by magnetocrystalline volume anisotropy. For Co/Pt samples values for K_{2V} similar to that of bulk Co were found (see section 2.1.3) [104].
The surface term $2K_{1S}$ can be disentangled from $K_{1,\mathrm{eff}}$ via thickness t variation of the ferromagnetic layer. It is common use to plot $K_{1,\mathrm{eff}} \cdot t$ versus t:

$$t \cdot K_{1,\mathrm{eff}}(t) = K_{1V,\mathrm{eff}} \cdot t + 2K_{1S} \tag{2.19}$$

From the linear characteristic the intersection with the ordinate yields $2K_{1S}$, while the slope reflects $K_{1V,\mathrm{eff}}$. The slope is negative as the shape anisotropy of Co is always stronger than the magnetocrystalline anisotropy. K_{1V} can be determined simply from $K_{1V} = K_{1V,\mathrm{eff}} + \frac{\mu_0}{2} M_\mathrm{S}^2$ in a good approximation as also for ultrathin Co layers in Co/Pt layered structures M_S was found to depend only slightly on thickness and resembles the bulk value of Co [105, 106, 107].
As for Co/Pt layered structures $K_2 > 0$ always applies, this means that $K_{1,\mathrm{eff}} \geq 0$ yields a perpendicular easy axis of magnetization [101, 108]. By increasing the magnetic layer thickness $K_{1,\mathrm{eff}}$ decreases and becomes negative above a certain thickness, so that a gradual spin-reorientation transition (SRT) to easy plane behavior occurs via the so-called region of canted magnetization ($K_2 > 0, -2K_2 < K_{1,\mathrm{eff}} < 0$). In this region the directions of easiest magnetizability include the canting angle

$$\Theta_\mathrm{C} = \arcsin \sqrt{\frac{-K_{1,\mathrm{eff}}}{2K_2}} \tag{2.20}$$

with the film normal [109, 110, 111, 112, 103]. This condition represents magnetization orientations lying on two cones with the same opening angle Θ_C, so that the region of canted magnetization is also frequently called cone state region. Typically the cone state region corresponds to a narrow thickness range of 0.1 nm. In general, the SRT for Co based multilayers is in the region of $t \lesssim 2$ nm [92], while the actual value depends on the nonmagnetic metal and structural properties [41]. For Fe based multilayers the SRT was found to be at smaller thicknesses despite similar values for K_S. This is due to the stronger shape anisotropy contribution and the absence of significant PMA supporting K_V contributions [41]. In addition to the variation of the magnetic layer thickness the SRT can be driven by changing the temperature [113, 104] and thickness of the non-ferromagnetic interlayers [109, 103].
It is worth mentioning that instead of the canted phase in the case of $K_2 < 0$ the SRT proceeds for $0 < K_{1,\mathrm{eff}} < 2|K_2|$ via the phase of coexisting in-plane and per-

pendicularly magnetized domains [101, 114, 108] as e.g. discovered experimentally for Co on Au(111) [115, 116, 117].

2.1.4.2 Anisotropy versus Zeeman energy

When applying external fields the Zeeman energy has to be also considered in the minimization of the total free energy (see Eq. 2.1). This term favors the orientation of the magnetization along the field direction, as $(E/V)_{\mathrm{Z}} = -\mu_0 \mathbf{M} \cdot \mathbf{H} = -\mu_0 M_{\mathrm{S}} H \cos\Phi$, where Φ is the angle between $\mathbf{M}$ and $\mathbf{H}$.
In principle, there are two independent mechanisms how the magnetization orientation changes with field: The magnetization can rotate coherently from the easy axis of magnetization into the field direction and magnetic domains can be nucleated with subsequent movement of domain walls and domain annihilation. Up to now only systems with homogeneous magnetization were considered; domain walls are introduced in the next section 2.2. However, the method to determine the anisotropy constants from the coherent rotation processes that occur during the hard axis remagnetization presented in the following is not restricted to single-domain systems. A necessary prerequisite is that the creation and annihilation of a multi-domain state as well as the movement of domain walls is virtually invisible in the hard axis remagnetization $M(H)$ curve, so that only coherent rotation processes are detected. This is generally fulfilled for the out-of-plane (in-plane) remagnetization for thin films with perpendicular hard (easy) axis as the projection of the magnetization along the field direction is the same in each domain for arbitrary field strengths. From the coherent rotation processes within the domains it is then possible to determine the anisotropy that counterbalances the Zeeman torque. By using the definition of the uniaxial anisotropy constants of Eq. 2.18 the free energy density in second order approximation is given by:

$$E/V = K_{1,\mathrm{eff}} \sin^2\Theta + K_2 \sin^4\Theta - \mu_0 H M_{\mathrm{S}} \cos\Phi \quad , \tag{2.21}$$

where the latter term is the Zeeman energy density. If the film normal is the easy axis of magnetization a field has to be applied in any in-plane direction, thus $\Phi + \Theta = 90°$, as Θ is the angle between film normal and $\mathbf{M}$. Then, the equilibrium zero-torque condition $\partial(E/V)/\partial\Theta = 0$ yields:

$$\begin{aligned} 2K_{1,\mathrm{eff}} \sin\Theta + 4K_2 \sin^3\Theta &= \mu_0 H M_{\mathrm{S}} \quad , \\ \frac{2K_{1,\mathrm{eff}}}{M_{\mathrm{S}}} m_{||} + \frac{4K_2}{M_{\mathrm{S}}} m_{||}^3 &= \mu_0 H(m_{||}) \quad , \end{aligned} \tag{2.22}$$

with $m_{||} = M_{||}/M_{\mathrm{S}} = \sin\Theta$ the (parallel to field) in-plane component of magnetization. This means that cubic fitting of the dependence of the external field $\mu_0 H(m_{||})$ on $m_{||}$, i.e., the inverse characteristics of the measured curve, provides the anisotropy constants.
If the film normal is the hard axis (easy plane behavior) the derivation is similar. But in this case a field has to be applied along the film normal, thus $\Phi = \Theta$;

$\partial(E/V)/\partial\Theta = 0$ then yields:

$$\begin{aligned} 2K_{1,\text{eff}}\cos\Theta + 4K_2\cos\Theta\sin^2\Theta &= -\mu_0 H M_\text{S} \quad , \\ -\left(\frac{2K_{1,\text{eff}}}{M_\text{S}} + \frac{4K_2}{M_\text{S}}\right) m_\perp + \frac{4K_2}{M_\text{S}} m_\perp^3 &= \mu_0 H(m_\perp) \quad , \end{aligned} \tag{2.23}$$

with $m_\perp = M_\perp/M_\text{S} = \cos\Theta$ the out-of-plane component of magnetization (parallel to field). It must be emphasized that both (inverse) magnetization curves $H(m) \propto m + m^3$ are qualitatively the same for perpendicular easy axis and easy plane. However, the meaning of the anisotropy constants on the quantitative evaluation of the magnetization with field changes (compare prefactors in Eqs. 2.22 and 2.23).

In the case of soft magnetic wires and rectangles the determination of the anisotropy constant is easier as there is no surface anisotropy and a negligibly small magnetocrystalline volume anisotropy. The only effective anisotropy is due to the shape: $K_{1,\text{eff}} = K_{\text{d, rectangle}}$, $K_2 = 0$. For applying an in-plane field into the hard axis the free energy is:

$$E/V = K_{\text{d, rectangle}}\sin^2\Theta - \mu_0 H M_\text{S}\cos\Phi, \quad \Theta + \Phi = 90° \quad , \tag{2.24}$$

where it should be remembered that in this context Θ is the angle between the long axis of the rectangle and the magnetization. The zero torque condition yields:

$$\begin{aligned} \partial(E/V)/\partial\Theta = &2K_{\text{d, rectangle}}\sin\Theta - \mu_0 H M_\text{S} = 0 \quad , \\ m_\perp(H) = &\frac{\mu_0 H M_\text{S}}{2K_{\text{d, rectangle}}} \end{aligned} \tag{2.25}$$

with $m_\perp = M_\perp/M_\text{S} = \sin\Theta$. This means that the component of the magnetization $M_\perp$ aligned in parallel to the field increases linearly with the external field $\mu_0 H$.

2.1.5 Influence of roughness, interdiffusion, and strain on anisotropy

The following section briefly discusses the influence of roughness, interdiffusion, and strain on magnetic anisotropy.
For the sake of convenience up to now the individual layers in multilayer systems were considered to have ideal flat surfaces and sharply defined interfaces on the atomic level. Experimentally, films cannot be grown in such a perfect manner [118, 20]. In contrast, "real" surface/interface regions show a roughness, i.e., the vertical position of the surface/interface exhibits a certain degree of variation. In addition, at the interfaces between two layers of different materials there is a region of interdiffusion, i.e., in the vertical direction there is a gradual transition from one material to the other. Both ingredients can have strong impact on the magnetic anisotropy [41]. In the case of roughness, due to symmetry reasons the atoms located at steps reduce the overall interface anisotropy of crystalline origin (reducing

PMA for Co/Pt(111)) [119], while the demagnetization fields connected with the edges of terraces reduce the shape anisotropy (favoring PMA) [120]. However, the "shape interface" contribution is estimated to be negligibly small for typical roughnesses found experimentally [41].
The existence of interdiffusion, on the one hand, might decrease the (magnetocrystalline) interface anisotropy as it causes a randomness in the ferromagnetic-nonferromagnetic interatomic bonds [121, 122]. On the other hand, it is frequently argued in literature that the interdiffusion zone might contribute to or even enhance the perpendicular magnetic anisotropy for Co/Pt(111) layered structures [94, 123, 124, 125] as CoPt(111) alloy films exhibit a magnetic anisotropy with the easy axis oriented along the [111] direction [126, 127, 128]. Fostered by the finding of a relatively large perpendicular magnetic anisotropy for CoPt(111) films of up to $K_{1V,\mathrm{eff}} = +0.3$ MJ/m^3 [129, 123] the dependence of the anisotropy on composition and chemical order have been extensively studied up to now (see e.g. Refs. [130, 131, 132, 133, 134, 135, 136] and references therein).
Moreover, for simplicity it was neglected up to now that lattice strain can occur in multilayered systems that is initiated by the mismatch of the lattice parameters between the adjacent layers of different materials [137, 138, 139]. For instance, for Co on Pt(111) the lattice mismatch is $\approx 11\%$ with respect to the lattice parameter of bulk Co. The strain alters the overlap of the atomic wave functions and therefore the spin-orbit-interaction so that changes in the magnetocrystalline anisotropy occur (magneto-elastic anisotropy) [140, 141, 138]. If the strain, which is linearly related to the magnetoelastic anisotropy constant K_{me} in a first order approximation, does not change with magnetic layer thickness K_{me} provides a contribution to the anisotropy constant $K_{1V,\mathrm{eff}}$. However, it is often assumed that strain relaxes proportional to the inverse layer thickness so that the bulk-like magnetoelastic anisotropy contribution K_{mea} can be misinterpreted in terms of a surface anisotropy [142, 95, 138].
Besides the strain, the degree of roughness and/or interdiffusion can be dependent on layer thickness as well, e.g. due to changes between 2D and 3D growth modes with thickness. In the limit of small layer thicknesses of a few atomic layers the magnetic layer can be laterally discontinuous, so that it is split into islands. Then, a lower K_S occurs compared to a continuous layer, as the discontinuous layer has less interface regions in stacking direction [143, 144, 41]. Moreover, the interdiffusion zone changes when the nominal layer thickness falls below the thickness of the interdiffusion zone. The latter scenarios provide some of the many proposed explanations for the often found shortfall of $K_{1,\mathrm{eff}} \cdot t$ from the linear t dependence at small layer thicknesses.
In conclusion, the often phenomenologically justified separation of the anisotropy in an interface and volume term according to Eq. 2.19 is rather artificial as details about the roughness and interdiffusion of the interfaces as well as about the strain are not explicitly considered. As these properties strongly depend on the preparation method and growth conditions it is not astonishing that a rather wide spread of K_S and K_V values, e.g. for Co/Pt(111) multilayers, is documented in literature. As already stated above for Co/Pt(111) $K_S = 0.27 - 1.29$ mJ/m^2 was found, while the range for the effective volume anisotropy is reported to $-K_{1V,\mathrm{eff}} = 0.28 - 1.15$ MJ/m^3 [145, 146, 41]. Consequently, for a reasonable interpretation of

the values the various structural influences on the anisotropy contributions have to be estimated, which in turn means that an accurate investigation of the structural properties is mandatory.
Comprehensive reviews about the magnetic anisotropy in multilayered systems containing transition metals are Refs. [147, 91, 141, 148, 19, 138, 92, 139].

2.2 Magnetic domain walls in thin films

Up to now only a homogeneous magnetization was considered. But in general the magnetization of a ferromagnet is by no means homogeneous. The reason for this is the pole avoidance principle as with a homogeneously magnetized body a large amount of surface charges and thus stray field energy is connected. At the expense of a small increase of exchange energy this energy term and thus the total free energy of a ferromagnet (see Eq. 2.1) can be significantly reduced by the formation of ferromagnetic domains [83]. Inside a domain the magnetization orientation is almost homogeneous in order to reduce the exchange energy between adjacent spins but the orientation of magnetization between adjacent domains can be arbitrary. The transition region between adjacent domains is called α-domain wall, where α is the angle between both magnetization orientations. There is no discontinuous transition between two domains (infinitesimal small domain wall width) as the exchange energy, which is connected with a domain wall, can be minimized at the expense of stray field energy if the magnetization rotation from one domain to the other is divided on several atomic lattice planes.
The alignment of a domain wall between adjacent domains with given magnetization orientations is not arbitrary due to energy reasons: To avoid global magnetic charges, which would be otherwise connected with the domain wall ("charged walls"), on both sides of the wall the magnetization component perpendicular to the domain wall has to be the same (continuity of the normal component of $\mathbf{M}$) [76, 149]. This means that the wall has to include the same angle $\alpha/2$ with the magnetization on both sides of the wall.
On a larger scale, the interplay in the minimization of the mentioned energy associated with a domain wall and of the overall stray field energy of the sample determines the characteristic domain size. For more details the reader is referred to Refs. [150, 151, 152, 153] and references therein as this topic will not be addressed here.
In brief, the properties of domain walls in soft magnetic thin films and films with perpendicular easy axis are discussed separately in the following. Thereby, it is considered that the magnetization is homogeneous over the whole thickness (z-direction) of the film also in the region of the domain wall. This assumption is generally made as a first approximation; the possibility of an additional z dependence of the magnetization inside a domain wall is e.g. discussed in Refs. [154, 155, 77].

Soft magnetic thin films: Generally, there are two fundamental possibilities concerning the rotation of magnetization inside a domain wall: The magnetization can rotate either in the plane of the wall (Bloch-wall, see Fig. 2.2(a)) or perpendicularly

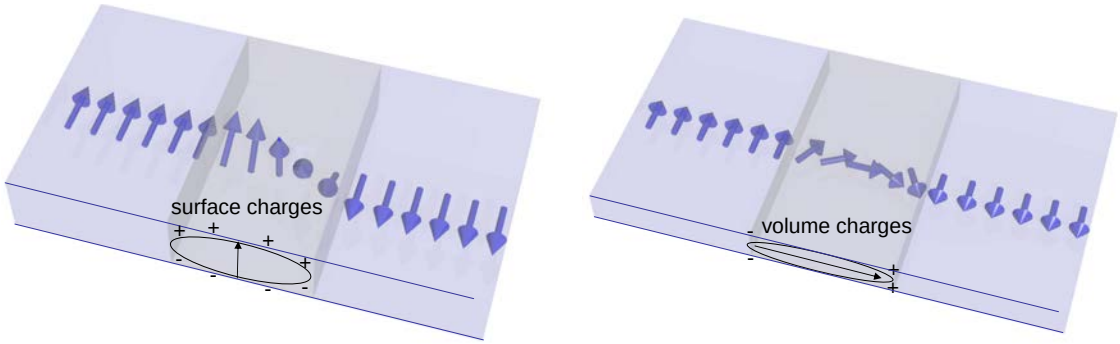

Figure 2.2: (a) 180° Bloch wall and (b) 180° Néel wall in a soft magnetic thin film. The local magnetic charges $(+, -)$ connected with the walls are drawn. In the case of the Bloch wall surface charges are generated in the region of the domain wall while in the case of the Néel wall volume charges in the region of the wall are present.

to the plane of the wall (Néel-Wall, see Fig. 2.2(b)). In bulk materials the Bloch wall is energetically favored as in the wall region only a negligibly small amount of surface charges exists, while no volume charges between the wall planes are generated (see Fig. 2.2(a)) [156, 76]. For thin films, where the domain wall width is in the range of the film thickness, L. Néel stated that a lower stray field energy can be achieved if the magnetization rotates in the film plane [157, 158, 159, 76]. This wall type, named after him Néel wall, possesses volume charges between the side planes of the wall, while the film surface, which is relatively large compared to the volume in the region of the domain wall, remains charge-free (see Fig. 2.2(b)). For permalloy the transition from Bloch to Néel wall was experimentally found in the range of about 50 nm, whereas the transition is not abrupt [77, 76]. Instead, a third domain wall type, which has been named cross-tie wall, occurs in a relatively small span of thicknesses around 50 nm announcing the transition [160, 161, 162]. The complex microstructure of a cross-tie wall will not be addressed here. However, for the thin soft magnetic films with thicknesses of $18 - 20$ nm used in this thesis Néel walls can be expected.
A variety of rather complex models exist yielding similar results for the dependence of the energy per area related with Néel and Bloch walls on film thickness (see Refs. [77, 76, 73] and references therein). These models qualitatively resemble the experimental results, like the dependence of the domain wall width δ on film thickness or the transition thickness between Bloch and Néel walls[3] [165, 77].
The result of a calculation for 180° walls in permalloy can be exemplarily seen in Fig. 2.3(a). Without going into detail, the properties of a 180° Néel wall for the borderline cases of small and large film thicknesses are briefly discussed in the fol-

[3]The models also provide spatial profiles of the walls. For the Néel wall structure important in this work details are not completely understood [163, 77]. But as a fact it is unquestionable, that in the center of the wall cross-section the rotation of the magnetization is strongest while there is a region of low rotation at the borderlines ("tails"), where the wall merges with the domains. Typically, δ is denoted as the intersection of a slope with the spin rotation in the center of the wall with the horizontal straight lines, which corresponds to the magnetization orientation within the domains [164].

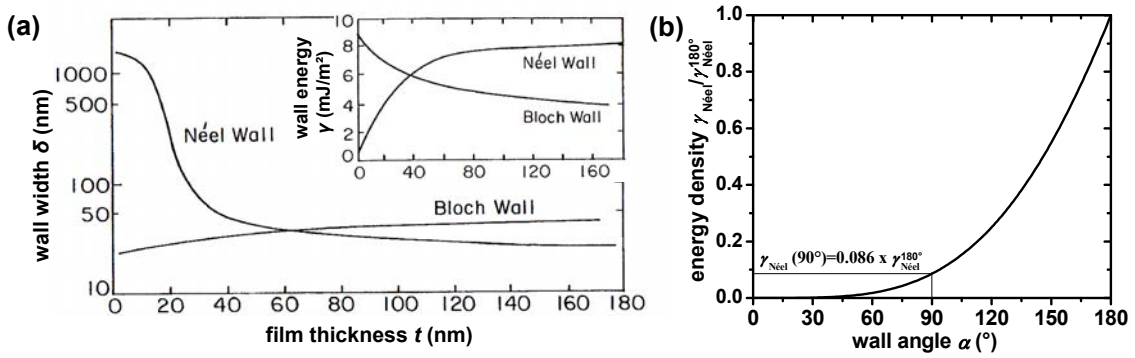

Figure 2.3: (a) Domain wall thickness and energy per unit area (inset) of a Bloch and a Néel wall in dependence of the film thickness. The parameters of the calculation are $A = 1 \cdot 10^{-11}$ J/m, $\mu_0 M_S = 1$ T, and $K = 100$ J/m^3, which are similar to the properties of permalloy. From Ref. [73]. (b) Néel wall energy density per unit area as a function of wall angle.

lowing: The energy per area of the wall decreases with film thickness (see inset in Fig. 2.3(a)) as the stray field energy decreases caused by the changing aspect ratio of the wall cross-section [164], which in turn enables a broadening of the wall to minimize exchange energy. At ultrathin film thicknesses $t \ll \delta_{\text{Néel}}$ the energy density per area $\gamma_{\text{Néel}}$ and the thickness of the wall are given by [73]:

$$\gamma_{\text{Néel}} \approx \pi t M_S^2, \qquad \delta_{\text{Néel}} \approx \pi \sqrt{\frac{2A}{K}} \tag{2.26}$$

Note that the energy of the wall is solely determined by magnetostatic energy times thickness, while the width is thickness-independent and only governed by the interplay between the exchange interaction with the magnetocrystalline anisotropy K. The latter has been neglected up to now as per definition the term soft magnetic means that K is several orders of magnitude lower than the shape anisotropy (see section 2.1.3). Eq. 2.26 holds for a uniaxial anisotropy in the case of negligible K_2, where the easy axis is assumed to be parallel (perpendicular) to the magnetization within the domains (domain wall). For typical K, which are in the range of a few 100 J/m^3, the domain wall width is in the range of several 100 nm (see Fig. 2.3(a)). Otherwise, for large $t \gg \delta_{\text{Néel}}$ ($K \ll \frac{\mu_0 M_S^2}{2}$) the properties of a Néel wall are [164]:

$$\gamma_{\text{Néel}} \approx 4\sqrt{\frac{A\mu_0 M_S^2}{2}}, \qquad \delta_{\text{Néel}}^{180} \approx \pi \sqrt{\frac{2A}{\mu_0 M_S^2}} \tag{2.27}$$

Comparison with the corresponding counterpart in Eq. 2.26 shows that the equations for δ are the same if K is substituted by $\mu_0 M_S^2$, so that also in this borderline case δ does not depend on film thickness. The energy per area is thickness-independent and depends also on the exchange stiffness A in contrast to Eq. 2.26. For the material parameters of permalloy the wall width can be estimated to about 30 nm at film thicknesses above 100 nm. Note that the results of Eq. 2.27 are only justified at thicknesses, where the Néel wall structure is not the global minimum and Bloch

walls are favored (see inset of Fig. 2.3(a)).
The permalloy thickness of 20 nm utilized in this thesis lies between both borderline cases, where no convenient expressions for δ and $\gamma_{\text{Néel}}$ exist[4]. The values can be estimated from the curves in Fig. 2.3(a) to $\delta_{\text{Néel}} \approx 200$ nm, $\gamma_{\text{Néel}} \approx 4$ mJ/m^2. The latter is equivalent to $\gamma'_{\text{Néel}} = 0.8 \cdot 10^{-16}$ J/μm in a 20 nm thick film.
Up to now only the energy related with 180° Néel walls was considered. Certainly, domain walls exist between domains whose magnetization orientations are not necessarily antiparallel to each other. Néel showed that the energy density connected with a Néel wall strongly depends on the wall angle α [157]:

$$\gamma_{\text{Néel}}(\alpha) = \gamma^{180}_{\text{Néel}} \cdot \left(1 - \cos\left(\frac{\alpha}{2}\right)\right)^2, \tag{2.28}$$

as can be seen in Fig. 2.3(b). This result has been verified by micromagnetic simulations [74].

Films with perpendicular easy axis: Attention should be paid to the fact that for systems with perpendicular easy axis, as Co/Pt layered structures investigated in chapter 5, Bloch walls occur although the ferromagnetic layer is ultrathin. This is no contradiction to the statements made above as a Néel and a Bloch wall would rotate within the film plane due to geometrical reasons. Therefore, for both wall types surface charges are avoided [84]. However, while with a Néel wall a large amount of volume charges would be connected this is not the case for a Bloch wall. The energy per area and width of a Bloch wall in first order approximation of the effective anisotropy $K_{1,\text{eff}}$ is given by [164]:

$$\gamma^{180}_{\text{Bloch}} \approx 4\sqrt{AK_{1,\text{eff}}} \quad , \quad \delta^{180}_{\text{Bloch}} \approx \pi\sqrt{\frac{A}{K_{1,\text{eff}}}} \tag{2.29}$$

2.3 Micromagnetic Simulations and Exchange Lengths

For a given magnetic microstructure $\mathbf{M}(\mathbf{r})$ the various energy terms of Eq. 2.1 can be calculated with more or less effort. Stationary states $\mathbf{M}_{\text{stat}}(\mathbf{r})$ correspond to minima in the energy landscape. The difficulty is to find these minima. Certainly, for any domain configuration the total energy can be calculated in order to find the one which has the lowest energy [77]. But the risk is to ignore further configurations and to ignore the history of the applied field. To get rid of these risks Brown developed a variational principle with the idea that $\mathbf{M}_{\text{stat}}(\mathbf{r})$ must be the result of the calculation without the necessity to guess it beforehand. The results of the variational principle are the so-called Brown's differential equations, which are in vector notation [166, 77]:

$$\mathbf{N}_{\text{eff}} = \mathbf{M}_{\text{stat}}(\mathbf{r}) \times \mathbf{H}_{\text{eff}} = 0 \tag{2.30}$$

[4]Expressions are e.g. given in the textbook of A. Aharoni [77].

$\mathbf{H}_{\text{eff}}$ is the so-called effective field, which is related to the total energy (density) of Eq. 2.1 as follows [166, 68]:

$$\mathbf{H}_{\text{eff}} = -\frac{1}{\mu_0}\nabla_{\mathbf{M}} E = \frac{2A}{\mu_0 M_{\text{S}}^2}\nabla^2\mathbf{M} - \frac{1}{\mu_0}\frac{\partial(E/V)_{\text{mca}}}{\partial\mathbf{M}} + \mathbf{H}_{\text{a}} + \mathbf{H}_{\text{d}} \tag{2.31}$$

Brown's equations show that for an energy minimum there is no effective torque $\mathbf{N}_{\text{eff}}$ acting on the magnetization so that the magnetization is oriented in parallel to the effective field.
In order to describe the dynamical evolution of the magnetization the so-called Landau-Lifschitz-Gilbert (LLG) equation is often used [167]:

$$\frac{d\mathbf{M}}{dt} = \gamma\mathbf{M}\times\mathbf{H}_{\text{eff}} + \frac{\alpha}{M_{\text{S}}}\mathbf{M}\times\frac{d\mathbf{M}}{dt} = -\frac{\gamma}{1+\alpha^2}\mathbf{M}\times\left(\mathbf{H}_{\text{eff}} + \frac{\alpha}{M_{\text{S}}}\mathbf{M}\times\mathbf{H}_{\text{eff}}\right) \tag{2.32}$$

The second terms correspond to the phenomenological damping term, where α is the damping parameter. γ is the gyromagnetic ratio $\gamma = g\mu_B/\hbar$, where g denotes the Landé factor, $\hbar$ is the Planck constant and μ_B is the Bohr magneton.
Micromagnetic simulations, like the object oriented micromagnetic framework (OOMMF) utilized in this work, solve the LLG numerically by dividing the ferromagnetic sample with volume V in small portions, in which the magnetization is assumed to be homogeneous [168]. In OOMMF a cuboid mesh is used. The critical parameter in this discretization are the dimensions (l_1, l_2, l_3) of the cuboids (cell size): On the one hand, if the size is chosen too small the calculation would last endlessly as the number of cuboids n corresponds to $V/(l_1 l_2 l_3)$ and the time of the calculation is proportional to n^2. On the other hand, the discretization must be fine enough to calculate the magnetic microstructure and the associated free energy terms of objects as e.g. domain walls or vortices in a good approximation. The length scale below the magnetization of such objects can be regarded as spatially homogeneous defines the so-called exchange length [68]

$$\delta_{\text{ms}} = \sqrt{\frac{2A}{\mu_0 M_{\text{S}}^2}} \quad \text{or} \quad \delta_{\text{mca}} = \sqrt{\frac{A}{K}} \tag{2.33}$$

depending on the dominating energy term which competes with the exchange energy [169, 170, 171, 172]. δ_{ms} is the magnetostatic exchange length and δ_{mca} the magnetocrystalline exchange length[5]. The exchange length indicates the transition from an exchange interaction governed length scale to a stray field or magnetocrystalline anisotropy dominated length scale. Thus, realistic results of the calculations that mimics the actual pattern and energy of a microstructure can be expected only for cell sizes with $l_i \leq \delta_{\text{ms}}$ (or $l_i \leq \delta_{\text{mca}}$).
Starting from an arbitrary configuration $\mathbf{M}(\mathbf{r})$ OOMMF solves the LLG equation iteratively until the angle between $\mathbf{H}_{\text{eff}}(\mathbf{r})$ and $\mathbf{M}(\mathbf{r})$ everywhere in the sample is typically below 10^{-5} rad. The obtained magnetic microstructure $\mathbf{M}_{\text{stat}}(\mathbf{r})$ corresponds

[5] δ_{ms} and δ_{mca} differ from the width of a Néel wall $\delta_{\text{Néel}}$ in the borderline cases of small and large film thicknesses only by a factor of π and $\sqrt{2}\pi$, respectively (see Eq. 2.26 and Eq. 2.27).

to a minimum in the energy landscape.
In this thesis the basic package of OOMMF was used, where influences of finite temperatures are not taken into account.
More information and critical remarks about the state of the art of micromagnetic simulations can be found in the comprehensive reviews [173, 174, 175] and the references therein.

3 Domain walls in V-shaped soft magnetic nanostrips

In general, when the dimensions of a physical system are shrinked to the order of magnitude of characteristic length scales the related physical properties are strongly influenced by the sample geometry, besides their dependencies on intrinsic material properties [54, 24]. An example for drastic changes in the magnetic microstructure is the film thickness-driven transition from a Bloch to a Néel domain wall when the thickness reaches the dimension of the exchange length as shown in section 2.2. Nowadays, fabrication techniques are available, which enable the preparation of magnetic elements, in which besides the thickness, also the lateral dimensions can be minimized to the nanoscale. Overviews of the various fabrication methods can be found e.g. in the review articles Refs. [176, 54, 177, 178, 179, 67, 180, 181].
One geometry of particular interest in recent research is the nanowire. This is the class of elements where two dimensions are laterally confined and where the length of the wire is much larger [55]. This chapter deals with soft magnetic nanowires which have a rectangular cross section (nanostrips) with a large aspect ratio, i.e., the strips typically exhibit a width w of a few 100 nm, while their thickness t is in the range of a few 10 nm ($t < w \ll$wire length).
In such nanowires[1] in remanence the magnetization aligns along the long axis of the wire in order to minimize the stray field energy. The configuration of lowest energy is the quasi single-domain state as sketched in Fig. 3.1(a). Worth looking at are magnetic configurations, in which the nanowire contains two or more domains. As the magnetization within the domains aligns in parallel to the edges only 180° head-to-head or tail-to-tail configurations occur. In a nanostrip such configurations are always connected with a fixed amount of "global" magnetic charges of $2M_{\mathrm{S}}tw$ located at the transition region between both domains (see sketch in Fig. 3.1(b)) [182]. In extended thin films a zig-zag course of the domain wall is developed in the case that two domains meet head-on in order to reduce the charge density as a straight wall like the one depicted in Fig. 3.1(b) would exhibit the highest charge concentration [76]. The internal structure of a zig-zag pattern can be seen in Fig. 3.1(c). The magnetic charges are distributed in the space between the spikes, while the walls themselves are basically conventional uncharged side-by-side 180° Néel walls [76, 55]. In a nanostrip, however, the zig-zag strategy fails due to the small width of the wire and the question is what happens in the transition region from one domain to the other. The most simple configuration to imagine would be a charged 180° Néel wall as sketched in Fig. 3.1(b) but this configuration is not even a local energy minimum[2].

[1] In the following the generic term nanowire is used as a synonym for nanostrip.

[2] It should be mentioned here for clarity that in a nanowire the width of a Néel wall is also determined by the width of the wire, as a wide domain wall would exhibit a lot of surface

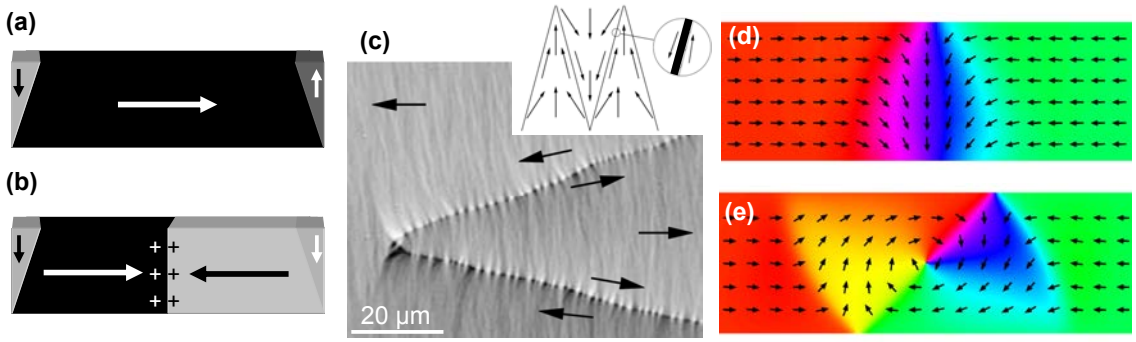

Figure 3.1: (a) Sketch of a quasi single-domain state in a nanostrip, which is the state of lowest energy. (b) 180° head-to-head domain configuration (arrow head points on arrow head) with a 180° positive (+) charged Néel wall in between. This configuration is not a local energy minimum. (c) shows a *zig* course of a domain wall in a 42 nm thick Co film, which separates two oppositely oriented domains that meet tail-on. The inset sketches the magnetization orientation of a zig-zag course in particular revealing that it is connected with the formation of uncharged 180° Néel walls. From Ref. [76]. (d) and (e) display the results of micromagnetic simulations, i.e., the microstructure of a transverse domain wall and of a vortex domain wall, respectively.

In a nanostrip the minimization of the sum of exchange and stray field energy leads to complex, mesoscopic spin structures in the transition region between the domains. In analogy to the transition regions in thin films or bulk these structures are also commonly called domain walls. The two most preponderant types were predicted by micromagnetic simulations by R. D. McMichael and M. J. Donahue in 1997: The so-called transverse domain wall (Fig. 3.1(d)), which is the global energy minimum for thin films and narrow wires and the vortex domain wall (Fig. 3.1(e)), which is the global energy minimum for large film thicknesses and broad wires. The details of the spin structures are explained in detail in section 3.2. Subsequently, these spin structures became the focus of research due to the following reason: They behave like quasi-particles [184], which can be manipulated on purpose by external magnetic fields [185, 186, 187] as well as electrical currents due to the spin-transfer torque (current induced domain wall movement) [56, 188, 60, 189, 190, 34, 191, 31, 192, 193]. At the same time, electrical currents are also affected by the domain wall yielding a domain wall resistance (DWR), which enables the electrical detection of the walls[3] [194, 195]. Based on this fundamental interactions, concepts for application of domain walls in logic and storage devices were proposed and are now under development [62, 61, 196, 197, 198].
A common strategy to modify the potential landscape for the domain walls concentrates on the introduction of geometrical elements which enable the reliable nucleation or pinning of domain walls. Typical pinning-sites are notches or anti-notches

charges at the edge. The Néel wall width of an uncharged 180° wall can be estimated by Eq. 2.26 utilizing the (in-plane) shape anisotropy constant of a wire (Eqs. 2.9, 2.15): $K \approx \frac{t}{w} M_S^2$ [183] and is therefore much smaller than in an extended ultrathin film (see section 2.2).

[3] In the complex microstructure of the walls the intrinsic DWR is generally overcompensated by the anisotropic magnetoresistance; more details about the DWR, see section 5.1.4.3.

in straight- or curved wires [199, 194, 200, 201, 202, 203, 204]. Alternatively, zigzag wires are used, in which domain walls can be easily created via in-plane seeding fields. It is noticeable that in spite of the frequent use of bent wires [205, 206, 207, 208, 209, 210, 211, 183, 212, 213, 214, 215, 216, 217, 218, 198, 219] the influence of the bent on the details of the wall microstructures and on the energy landscape has not been investigated yet. The knowledge of the exact magnetic fine structure, however, is necessary for a precise analysis and interpretation of the experimental results concerning spin-torque [220], domain wall resistance [200] and magnetization reversal [221, 204].
The influence of the bending angle α on the preponderant domain wall type pinned at the bend is therefore an important aspect which forms one focus of the present study addressed in section 3.3 of this chapter.
Beforehand, in section 3.2 the details of the magnetic fine-structure of the different wall types are discussed, which have been mapped with high resolution by means of scanning electron microscopy with polarization analysis (SEMPA). Besides the vortex and the transverse domain wall, asymmetric transverse domain walls have been found to be the third micromagnetic configuration [222, 55].
The SEMPA technique and the sample preparation of the V-shaped wires from homogeneous film via focused ion beam (FIB) milling is described in the following section 3.1. This section also includes a comprehensive characterization of the properties of the used non-standard $Co_{39}Fe_{54}Si_7$ film.
Section 3.4 deals with the seeding of vortex domain walls via external magnetic fields. The investigation demonstrates that the exact orientation of the seeding field controls the vortex wall properties which enables their tuning on purpose. Their reproducible manipulation is a necessary prerequisite for storage concepts based on vortex walls in combination with current induced domain wall movement, like in the race-track memory device [61].
Throughout this chapter the experimental results are compared to one another and complemented with micromagnetic simulations using OOMMF [169].
The chapter closes with a conclusion and outlook in section 3.5.

3.1 Experimental procedure

3.1.1 Investigation method - Scanning electron microscopy with polarization analysis (SEMPA)

Within this thesis scanning electron microscopy with polarization analysis (SEMPA or spin-SEM) was utilized in order to image the domain pattern of soft magnetic nanostructures (V-shaped wires, this chapter; rectangles, see chapter 4). The SEMPA apparatus enables the observation of two in-plane components of the magnetization which reveal the magnetization pattern with an angle resolution of $\pm 4^\circ$ down to a lateral resolution of about 15 nm, more details see Refs. [223, 224][4].
The following part gives a brief introduction about the working principle of SEMPA; a comprehensive review can be found e.g. in Refs. [225, 226]. When the focused beam of a scanning electron microscope (SEM) illuminates a ferromagnetic sample secondary electrons are generated at that position. The secondary electrons are spin-polarized, with a polarization (magnetic moment) that is antiparallel (parallel) to the magnetization orientation of the hit area of the sample. The reason for the spin polarization is the spin-dependent inelastic scattering of the secondary electrons with electrons of the sample involving electron-hole-pair creation (Stoner excitation). For more details about the origin of the spin polarization of the secondary electrons, see Refs. [227, 228, 229]. In order to analyze the spin polarization the secondary electrons are forced via electron optics into the spin-detector. Three different kinds of detectors have been established [223], i.e., the Mott detector, the low energy diffusive scattering (LEDS) detector, and the low electron energy diffraction (LEED) detector applied in this utilized SEMPA apparatus. The principle of polarization analysis of the LEED detector is based on the spin-dependent diffraction of the electrons at the surface of a W(100) single crystal. The spin-dependent diffraction results in an asymmetry in the intensity of opposite (2,0) diffraction peaks.
The probing depth of the spin polarization of the secondary electrons is only $3 - 8$ atomic layers depending on the material and energy of the secondary electrons indicating that SEMPA is a very surface sensitive technique [230, 231, 232]. Cap layers, oxide layers, or adsorbates in the range of only a few monolayers drastically degrade the spin polarization so that they have to be removed for SEMPA investigation [233, 234, 235]. Within this work, in order to obtain "clean" ferromagnetic surfaces the samples were soft sputtered by 600 eV Ar^+ ions. In order to maintain adsorbate-free surfaces over an adequate time span of several hours ultra-high vacuum (UHV) conditions with a base pressure of $\leq 1 \cdot 10^{-10}$ mbar were provided in the UHV-SEMPA chamber.
Besides SEMPA, various further techniques have been established in order to map the magnetic microstructure, e.g. Kerr-microscopy, which is used within this thesis to image the domain pattern of Co/Pt multilayers (see section 5.3.2.1). A comprehensive review about the different magnetic imaging techniques can be found in Ref. [225].

[4] A corresponding tilting of the sample with respect to the spin detector also enables the measurement of out-of-plane components of magnetization as demonstrated in Refs. [111, 112].

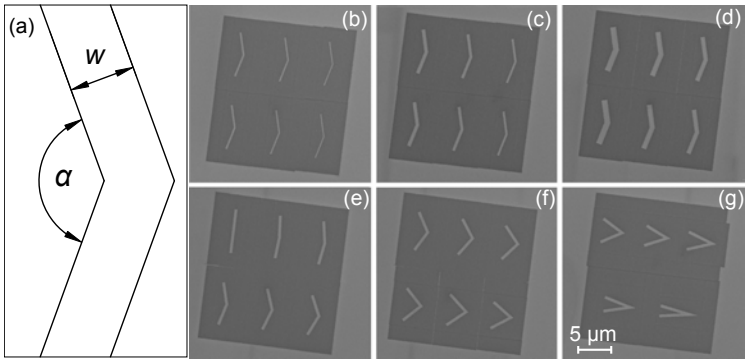

Figure 3.2: (a) Sketch of wire with definition of geometrical parameters. (b)-(g) SEM micrographs of the wires that have been investigated. Bright areas indicate magnetic material; in each sub-image, an array of six wires is present with magnetic material in the direct vicinity removed (dark). On a larger scale, fabricated structures are surrounded by the pristine magnetic film. In (b)-(d) the width w while in (e)-(g) the angle α was varied.

3.1.2 Preparation of V-shaped wires via focused ion beam (FIB)

Nanowires with varying width w and bending angle α were carved from a homogeneous film by means of focused ion beam (FIB) milling using 30 keV Ga^+ ions (see Fig. 3.2(a)). The magnetic film was a $Co_{39}Fe_{54}Si_7$ (at%) alloy with a thickness of 18 nm (see section 3.1.3). A dose of 20,000 $\mu C/cm^2$ was applied in order to remove the film completely[5]. The removal was checked by atomic force microscopy (AFM)[6]. Two sets of wire samples with the following parameters were prepared:

- variation of w in nine steps from 100 nm to 800 nm at constant $\alpha = 150°$, see Fig. 3.2(b)-(d).

- variation of α in 17 steps from 20° to 180° (straight wire) at constant $w =$ 400 nm, see Fig. 3.2(e)-(g).

For each pair (w, α) at least two wires were produced.
In order to obtain the best quality for the wires the following FIB procedure for the preparation of an array each containing six wires (see subimages (b)-(g) in Fig. 3.2) was used: The individual wires were prepared consecutively to minimize the influence of thermal drift. This was also the reason why for each wire the first step concentrated on removing the film on a large scale. After this time-consuming step, the second step focused on the precise material removal in the immediate vicinity of the evolving wire. In the array layouts special attention was given to the fact that the distances between the wires and to the pristine film were large enough to avoid significant magnetostatic interactions among each other [81, 180].

[5]The UHV chamber equipped with the FIB and further FIB parameters used for the sample preparation are described in section 4.2.1.
[6]For details about AFM or other scanning probe techniques, see e.g. Ref. [236].

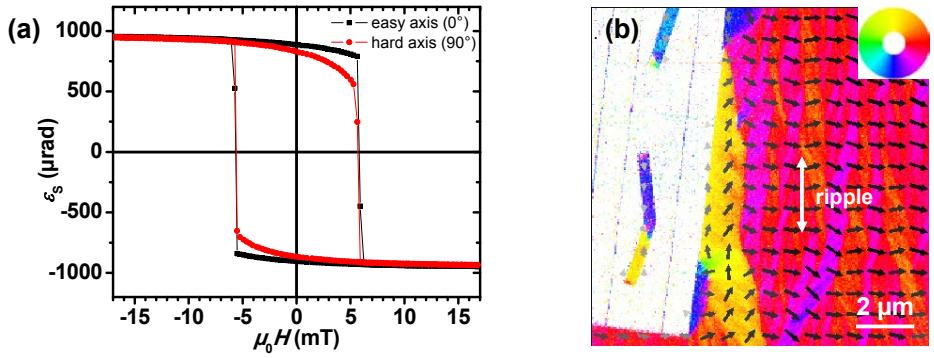

Figure 3.3: (a) Magnetization reversal of the pristine film for in-plane fields along two perpendicular directions with highest and lowest remanence. The curves were obtained by utilizing the longitudinal magnetooptical Kerr effect. (b) SEMPA image of a nanowire and of the adjacent magnetic film. The magnetization orientation is color coded according to the given color wheel as well as indicated by arrows. In the white area no magnetic signal was obtained, i.e., the area where the magnetic film was milled by FIB.

3.1.3 Preparation and properties of $Co_{39}Fe_{54}Si_7$ film

Permalloy ($Ni_{81}Fe_{19}$) is one of the standard soft magnetic materials. The reason for using another alloy for the investigation was that Ni has a relatively low spin polarization of the secondary electrons. Thus, permalloy which consists mainly of Ni, yields only a small contrast in the SEMPA investigation of about 6% (asymmetry of 3%). In contrast, the elements Fe and Co and its alloys exhibit high spin polarization of the secondary electrons yielding contrasts $> 10\%$ [237, 225]. However, these materials generally show a relatively strong magnetocrystalline anisotropy [238]. After some testing it was found out that a FeCo alloy with a small amount of Si fulfills the requirements of a low magnetocrystalline anisotropy and a high spin polarization of the secondary electrons, which is presented in the following after the preparation of the film is described [239].

The film with a thickness of 18 nm was grown onto naturally oxidized Si(100) via electron-beam evaporation from a single source with a mass composition of 0.3 g Co, 0.12 g Fe, and 0.12 g Si at a base pressure of $2 \cdot 10^{-8}$ mbar. The deposition rate (0.5 Å/s) was controlled by a thickness monitor (quartz crystal microbalance technique) and the thickness was cross-checked by AFM. The stoichiometry of the film was determined by energy dispersive x-ray spectroscopy (EDX)[7] to $Co_{39}Fe_{54}Si_7$ (at %). The difference between the stoichiometry of the melt and the film was caused by the difference in the vapor pressures of the individual elements.

The crystallinity of the sample was checked via high resolution SEM measurements with the result that the film is polycrystalline with a grain size of $\lesssim 10$ nm.

The magnetic properties of the $Co_{39}Fe_{54}Si_7$ film were studied by means of magnetooptical Kerr effect (MOKE), SEMPA and ferromagnetic resonance (FMR)[8]. Fig. 3.3(a) shows the hysteresis curves for two in-plane directions which are perpendicular to each other. In the two directions the highest and lowest value of the

[7] For details about EDX, see e.g. Ref. [240].
[8] For details about MOKE and FMR, see section 5.3.2

remanence was found with a difference of only 7% compared to the highest remanence. As the magnetization reversal is always dominated by irreversible domain wall movement at the coercive field of $\mu_0 H_c = (5.6 \pm 0.2)$ mT, which can be assumed to be initiated by local film inhomogeneities as e.g. defects at the film edges, a value for the strength of the anisotropy cannot be calculated. However, the almost isotropic behavior qualitatively shows that the film exhibits a vanishingly small uniaxial magnetocrystalline anisotropy, which can be definitely neglected compared to the shape anisotropy of the wires[9]. The reason why Si reduces the otherwise relatively strong magnetocrystalline anisotropy of the CoFe alloy was not further investigated within this thesis.
Fig. 3.3(b) is a SEMPA image, which shows the magnetic microstructure of a nanowire and the remaining film prior to any field treatment. The achieved polarization contrast is 11.2% and remains stable for hours after sputter cleaning, so that the film is very suitable for SEMPA investigation. In the vicinity of the FIB milled region, where the film has been removed, the magnetization is aligned in parallel to the edges in order to minimize stray field energy. Within the magnetic film, a so-called longitudinal ripple domain structure is visible, which means that locally the magnetization sligthly wiggles around an average direction [77]. This behavior was first found in polycrystalline permalloy films [241]. The explanation of the ripple formation is provided by the interplay of a random local anisotropy of each crystallite with an overall small uniaxial anisotropy and exchange interaction [242, 243]. The two latter terms are trying to keep the magnetic moments parallel to each other into a certain direction. At the same time, the random local anisotropy tries to tilt the moments of each crystallite into different directions yielding a characteristic ripple pattern. The presence of a ripple pattern impedes a full remanence, which is in accordance with the macroscopic remagnetization behavior (see Fig. 3.3(a)). More information about the ripple phenomena can be found in Ref. [243] and references therein.
The saturation magnetization of the film of $\mu_0 M_S = 1.8$ T was determined by means of FMR measurements performed by J. Topp, Institute of Applied Physics, University of Hamburg.

3.1.4 Parameters for micromagnetic simulations

Besides the saturation magnetization $M_S = 1.8$ T and the magnetocrystalline anisotropy $K \approx 0$ the exchange stiffness has to be known in order to perform micromagnetic simulations. For a $Co_{47}Fe_{53}$ alloy Liu et al. determined an exchange stiffness of $A = 35$ pJ/m, which is used in the following as approximation for the $Co_{39}Fe_{54}Si_7$ alloy [244]. If not otherwise stated a cell-size of 5 nm $\times$ 5 nm $\times$ thickness and a damping constant of $\alpha = 0.5$ is used for the simulations.

[9] The overall uniaxial magnetocrystalline anisotropy is assumed to be caused by the presence of external fields during film deposition; up to now, the reason for this phenomenon is not fully understood [77].

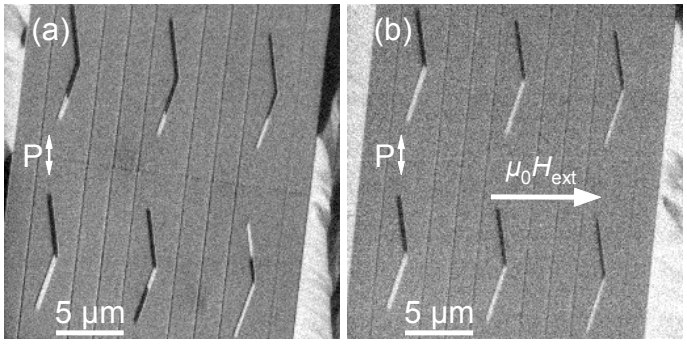

Figure 3.4: SEMPA micrographs of six wires obtained with one polarization sensitive axis of the polarization analyzer. (a) displays the magnetic microstructure in the "as fabricated" state, while the micrograph in (b) gives the domain pattern after applying an external field of $\mu_0 H_{\text{ext}} = 60$ mT along the direction indicated by the white arrow. The polarization sensitive axis (indicated by P) is parallel to the vertical edge of the SEMPA micrographs.

3.1.5 Seeding of domain walls at the bend of the wires

The SEMPA micrograph in Fig. 3.4(a) shows the magnetic microstructure of six wires as fabricated, i.e., before application of any magnetic fields. The black/white contrast reveals the magnetization component parallel to the vertical. Overall, the wires are predominantly (75%) in a multi-domain state, containing one or more domain walls. A straight forward explanation for the multi-domain configuration as virgin state is the ripple domain pattern observed in the unstructured film (see Fig. 3.4(a)). During the ion milling of the nanowires stray fields are generated due to poles at the upcoming edges. Consequently, the ripple pattern gets deformed as the magnetization starts to align along the wire arms. As the magnetization orientation locally varies the upcoming torque acting on the magnetization also varies locally so that a multi domain state can evolve[10].
In order to create domain walls at the bend of the wires an electromagnet was used, which is incorporated in the UHV-SEMPA chamber and provides *in situ* magnetic fields of up to ±60 mT. A magnetic field pulse ($\mu_0 H_{\text{ext}} = B_{\text{ext}} = 60$ mT, duration = 1 s) was applied along the direction indicated by the arrow in Fig. 3.4(b), i.e., an angle of 10° downwards with respect to the symmetry axis of the wires. The accuracy of the field direction was estimated to be ±2°.
The domain wall creation procedure followed a well established method (see e.g. Ref. [194]): While the field was applied the magnetization within the wires was tilted towards the direction of the external field. As the field strength was in the order of magnitude of the demagnetization field[11], it was expected to be sufficient to reorientate the magnetization within the wire arms. After field application the magnetization within the wire arms aligned along the wire edges in order to minimize

[10] A simple way to check this assumption of evolution of the initial domain state is to investigate samples, in which the applied Ga^+ dose, i.e. the material removal, in the vicinity of the wires is gradually varied. This has not been done yet.
[11] Utilizing Eqs. 2.7 and 2.9 with $w \geq 150$ nm: $\mu_0 H_{\text{d}} = \frac{t}{w} \cdot \mu_0 M_{\text{S}} \leq 210$ mT

stray field energy. Thereby, the torque acting on the magnetization was opposite in both arms. Hence, two domain states with a domain wall localized at the bends evolved, as can be exemplarily seen in Fig. 3.4(b)[12]. In order to check the reliability of the domain wall creation the micromagnetic states were imaged after several *in situ* remagnetization processes. Certainly, by reversing the direction of the field pulse tail-to-tail instead of head-to-head domain arrangements occurred. Altogether, the success rate to introduce a domain wall at the bend was 90%, whereas the wires with bending angles $\geq 160^\circ$ were not considered. All these wires exhibit a single-domain state with magnetization pointing upwards as the projection of the field on both wire arms is the same due to the field orientation of about 10° with respect to the wires' bisection. Consequently, this finding confirms the actual orientation of the external field.
The following sections focus on the arrangement of the magnetization in the small transition area between the black and the white domain.

3.2 Magnetic microstructure of domain wall types

This section concentrates on the magnetic microstructure of domain walls pinned at the bend of the nanowires. Before presenting the fine-structure separately for each wall type some definitions for their description are introduced. Recently, the magnetic microstructure of domain walls was described from a topological point of view [245, 182, 171]. The topology in the limit of preponderant magnetostatic energy[13] gives the key to a good understanding of details of the wall structures in nanostrips. The authors show that the domain walls are composite objects containing two or more topological defects. In general, topological defects are distortions from a spatially homogeneous configuration consisting of some core region, where order is destroyed and a far field region, where an elastic variable, here the magnetization, changes slowly in space [246]. An important fact is that topological defects cannot disappear by continuous deformation of the magnetization, so that they are stable objects from the topological point of view. Their physical stability, however, depends on the details of the energy landscape. To classify such defects the definition of the so-called winding number k by the following line integral is useful [246]:

$$\oint d\mathbf{\Theta} = \oint_{\Gamma} \frac{d\mathbf{\Theta}}{d\mathbf{s}} d\mathbf{s} = 2\pi k \tag{3.1}$$

where Γ is a closed loop in real space, here, onto the magnetization profile and $d\mathbf{\Theta}$ denotes the angular change in magnetization orientation on the infinitesimal element $d\mathbf{s}$. Fig. 3.5 illustrates particular cases of topological defects in two dimensional (2D) space, which are members of the classes with winding number $k = +1$ (vortex, (a)-(c)) and $k = -1$ (antivortex, (d)), that are important for this study. In an infinite 2D plane topological defects with finite extensions exhibit always integer winding numbers $k \in \mathbb{Z}$. For infinite half-spaces topological defects can also be located at the edges. These so-called edge defects have half integers of winding numbers when they

[12] The relaxation process is described in detail in section 3.4.3.
[13] domain theoretical treatment, see introduction of chapter 2

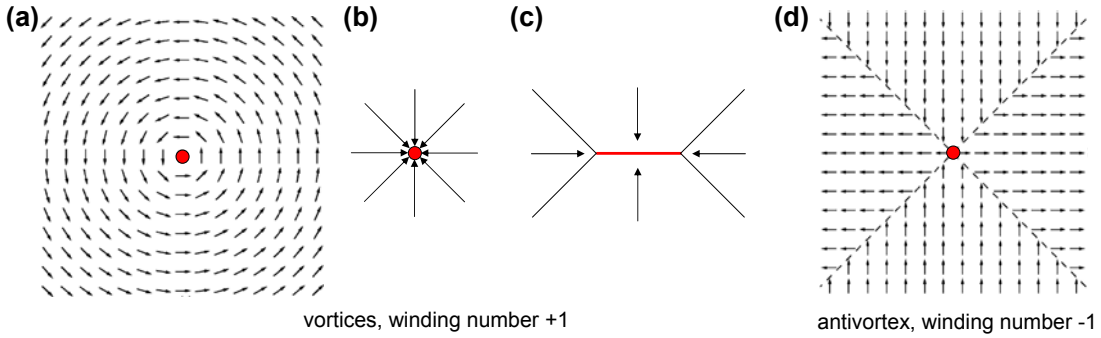

Figure 3.5: Magnetization orientation (black arrows) in the vicinity of particular two-dimensional topographical point or line defects (red dots or lines) with winding number ((a)−(c)) $k = +1$ and (d) $k = -1$ within the domain theoretical approximation. Objects with $k = +1$ ($k = -1$) are generally labeled as vortices (anti-vortices). (a) and (d) from Ref. [171].

are of finite size. This can be comprehended if only one half of the patterns displayed in Fig. 3.5 is considered in the evaluation of the line integral of Eq. 3.1. A stable domain wall microstructure in a straight wire segment always contains topological defects with half integer (integer) winding numbers located at the edges (within the nanostrip) due to symmetry reasons as described in Ref. [171]. Furthermore, it is shown that the total winding number $k = \sum_i k_i$ including all topological defects i of a domain wall must be zero and that the wall contains at least one edge defect at each side of the wire.
In the following the domain walls with the smallest number of defects are presented, which correspond to the structures observed in the experiments and the simulations. In the first part the symmetric transverse wall is described, the second part deals with the vortex wall structure, and the section is closed with a discussion of the asymmetric transverse wall. For more details about topological defects, the reader is referred to Refs. [246, 245].

3.2.1 Symmetric transverse domain wall

Fig. 3.6(a) shows a typical SEMPA image of a transverse head-to-head domain wall in a bent wire. Comparing the SEMPA image with the corresponding result of the micromagnetic simulation (see Fig. 3.6(b)), it is evident that both patterns give the same general features of the wall fine structure. As mentioned in the introduction of this chapter a head-to-head (tail-to-tail) domain arrangement is connected with a fixed amount of global magnetic charge that is stored in the volume $\mathrm{div}\mathbf{M} \neq 0$ or at the surface $\mathbf{M} \cdot \mathbf{n} \neq 0$, or most likely at both [182]. The local magnetic charge distribution of the simulated domain pattern can be seen in Fig. 3.6(c), where the divergence of $\mathbf{M}$ is displayed.
For the sake of simplicity, before discussing the fine-structure in the case of a bent wire, it is described for a straight wire geometry. Fig. 3.6(d) (and Fig. 3.1(d)) shows the corresponding result of a micromagnetic simulation. Basically, the transverse wall has a triangular shape with the wall magnetization pointing along the short

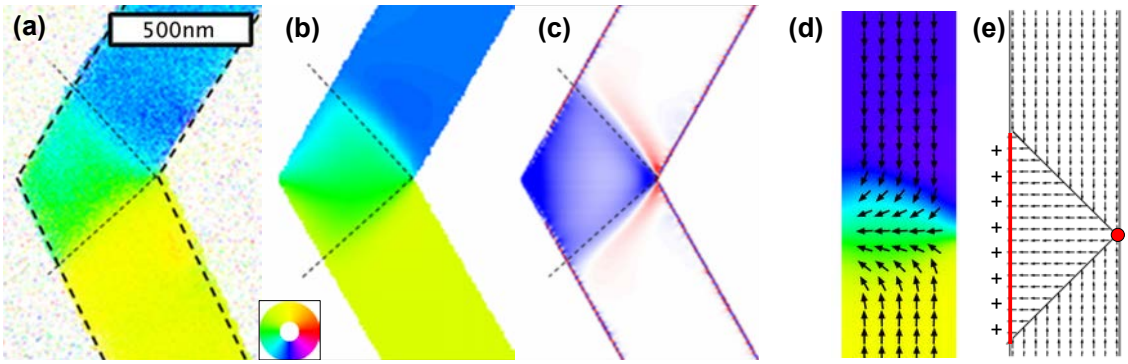

Figure 3.6: Magnetic microstructure of transverse domain walls. (a) is a SEMPA micrograph of a wire with $w = 400$ nm and $\alpha = 120°$, while (b) is the result of a micromagnetic simulation for the same geometrical set of parameters. The magnetization orientation is color coded according to the given color wheel. (c) displays the divergence of $\mathbf{M}$ of the pattern shown in (b). Red denotes positive values, blue negative values, and white is equal to zero. The dashed lines in (a)-(c) are guide to the eyes. The domain pattern in (d) is the result of a simulation for a straight wire ($w = 100$ nm), while (e) sketches this structure in domain theoretical approximation that is free of volume charges containing two edge defects that are highlighted in red. The positive magnetic surface charges are indicated by + symbols. (e) from Ref. [182].

axis of the wire. In the case of the domain theoretical treatment the transverse wall can be simplified to the structure depicted in Fig. 3.6(e). The wall magnetization is separated from the magnetization within the wire arms by two 90° Néel walls that run diagonally across the wire and merge at the edge on the right-hand side of the wire. This formation avoids charged walls in contrast to the pattern with a 180° Néel wall displayed in Fig. 3.1(b) as both 90° Néel walls include the same angle with the magnetization on both sides of the walls[14]. Consequently, the complete microstructure is free of volume charges, so that the total charge $2M_S tw$ is stored at one of the edges (left edge in Fig. 3.6(e)). The point where the two Néel walls merge corresponds to a topological point defect located at the edge. By comparison with the antivortex structure shown in Fig. 3.5(d) it is evident that the edge defect is equivalent to the left half part of the antivortex. As a result, according to Eq. 3.1, the defect exhibits a winding number of $-1/2$. A corresponding comparison with Fig. 3.5(c) reveals that the charged edge region corresponds to a rather extended line edge defect with a length of $2w$ and a winding number of $+1/2$ [182].
There are four possible formations of a transverse wall in a straight wire. First, the location of the $\pm 1/2$ edge defects can be interchanged, which changes the orientation of the rectangular wall region and of the wall magnetization by 180°. These two e.g. head-to-head walls can be mapped into their tail-to-tail counterparts by means of a time-inversion ($\mathbf{M} \rightarrow -\mathbf{M}$) operation. Summarizing the topological treatment, the transverse wall is a composite object containing two edge defects which exhibit two opposite winding numbers of $\pm 1/2$. This is the smallest number of defects a domain wall in a nanostrip may contain as the total topological charge of the wall has to be

[14] Besides, the two 90° walls exhibit a much lower energy than the (uncharged) 180° wall, as the wall energy density is reduced by more than 90% (see Fig. 2.3(b)).

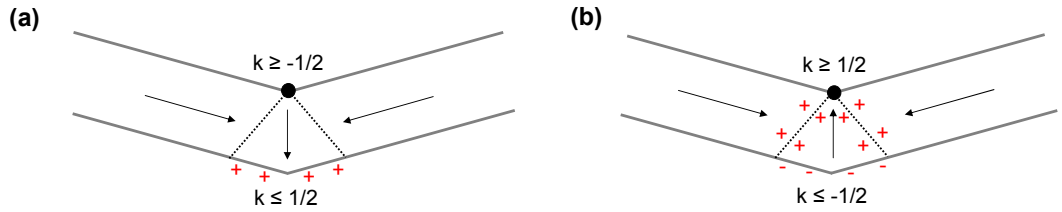

Figure 3.7: Sketch of the magnetization orientation of head-to-head transverse domain walls with the fractional antivortex located at the (a) inner and (b) outer kink, respectively. The magnetic surface and volume charges are indicated by + and − symbols.

zero and two edge defects have to appear (see above).
The transition from the domain theoretical treatment to the actual domain pattern (Fig. 3.6(d)) can be comprehended by considering the fact that the 90° Néel walls acquire a finite width as the exchange interaction has to be taken into account, which in particular results in a broadening of the $-1/2$ edge defect. Furthermore, to minimize the total magnetostatic energy the angle between the magnetization orientation and the edge is gradually reduced on the way to the edge as a consequence of the spatial dependence of the demagnetization factor[15]. Hereby, surface charges are reduced at the expense of volume charges (see Fig. 3.6(c)). Consequently, the extent of the $+1/2$ edge defect is less than $2w$.
The consequences of the implementation of a bend on the wall microstructure and energy are discussed in the following. The comparison of Fig. 3.6(d)) with Figs. 3.6(a),(b) reveals that the transverse wall located at the bend is connatural to the wall located in a straight wire segment. The wall magnetization is located at the bend while retaining the axial symmetry of the microstructure with respect to the short wire axis crossing the fractional antivortex edge defect. In the experiment and in the simulation only transverse walls were found where the fractional antivortex edge defect is located at the inner kink. In this case the magnetization rotation within the two Néel walls is in each case $\alpha/2$, so that according to Eq. 2.28 the Néel wall energy and thus the overall energy of the transverse wall is efficiently reduced compared to a wall position in a straight wire segment. Furthermore, the surface charges are significantly reduced as, roughly speaking, the wall magnetization includes the angle $\alpha/2$ with the edge instead of 90°. As a result, the bend acts as an attractive potential for the transverse wall.
The reason why the configuration with a fractional antivortex edge defect located at the outer kink is no stable configuration can be comprehended by taking a look at Fig. 3.7, where the magnetization orientation for the two kinds of head-to-head configurations in a bend wire is sketched. Obviously, in the case of the fractional antivortex edge defect settled at the outer (inner) kink, the total rotation angle of the magnetization is enhanced (reduced) by $180° - \alpha$ compared to a straight wire segment. This is equivalent to an enhancement (reduction) of the absolute value in topological winding number of the edge defects. Therefore, the energy stored in the Néel walls is correspondingly enhanced (reduced). The energetic unfavorable

[15]The spatial dependence of the demagnetization factor of a rectangle magnetized along the hard axis is shown in Fig. 4.31.

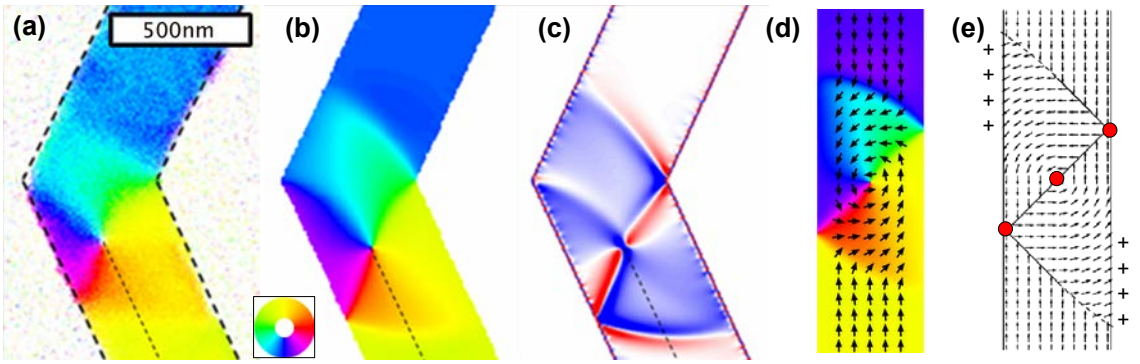

Figure 3.8: Magnetic microstructure of vortex domain walls. (a) is a SEMPA micrograph of a wire with $w = 400$ nm and $\alpha = 130°$, while (b) is the result of a micromagnetic simulation for the same geometrical set of parameters. The magnetization orientation is color coded according to the given color wheel. (c) displays the divergence of $\mathbf{M}$ of the pattern shown in (b). Red denotes positive values, blue negative values, and white is equal to zero. The dashed lines in (a)-(c) are guide to the eyes. The domain pattern in (d) is the result of a simulation for a straight wire ($w = 400$ nm), while (e) sketches this structure in domain theoretical approximation that is free of volume charges containing two edge and one volume defect that are highlighted in red. The positive magnetic surface charges are indicated by + symbols. (e) from Ref. [182].

case is additionally connected with charged Néel walls, so that altogether such a configuration would get expelled from the bend.
In conclusion, the implementation of the bend lifts the energetic degeneration of the two head-to-head (tail-to-tail) transverse domain wall configurations and excludes the existence of one configuration located at the bend.
In the following section the findings for the vortex domain wall are described.

3.2.2 Vortex domain wall

The SEMPA micrograph of Fig. 3.8(a) exemplarily displays the magnetic fine-structure of a vortex domain wall located at the bend ($w = 400$ nm, $\alpha = 130°$). Obviously, the microstructure is more complex than for a transverse domain wall. Similar to the findings for the transverse wall the microstructure obtained from simulations (see Fig. 3.8(b)) show the same characteristic features as the experimental finding. Again, the microstructure in the case of a straight wire is initially discussed for the sake of convenience. Based on the simulated microstructure of a straight wire (see Fig. 3.8(d)) Fig. 3.8(e) displays the domain theoretical model of a vortex domain wall in a straight wire that is free of magnetic volume charges [182]. The vortex domain wall can be regarded to consist of two $-1/2$ edge defects and a vortex (core) with winding number $+1$. According to the prerequisites mentioned above, after the transverse wall the vortex domain wall is the state with the lowest number of topological defects[16]. All these defects lie on a line that runs diagonally across the wire. This line, in the following called center wall, consists of two 90° Néel walls in

[16] A composite domain wall microstructure containing two $+1/2$ edge defects and an antivortex $k = -1$ is not stable, see Ref. [171].

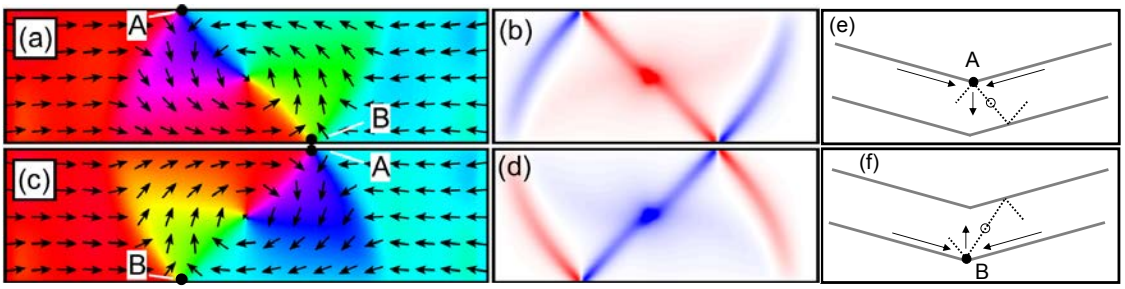

Figure 3.9: Possible configurations of a head-to-head vortex wall. In (a) and (b) the counterclockwise and clockwise configuration obtained via OOMMF is displayed, respectively. The direction of magnetization is color coded and indicated by black arrows. In (c) and (d) the z component of the curl of the vector fields of (a) and (b) is shown, red denotes positive values, blue negative values, and white is equal to zero. In (e) and (f) sketches of the magnetization orientation around the edge defects are shown for one defect located at the inner and outer kink, respectively.

series with the same sense of rotation connected at the core and terminated by edge defects. Additionally, starting at the edge defects, a kind of 90° Néel wall is built on either side of the center wall acting as borderline to the adjacent domains. The magnetization rotation across the latter borderlines decreases when moving from the edge defect towards the opposite side of the wire. For the sake of clarity the borderlines to the adjacent domains are called transition lines. The center wall is tilted against the main axis of the straight wire in order to allow the transition lines to start under 90° to the center wall at the edge defects. Around the edge defects the magnetization at the edge is perfectly aligned in parallel to the edge of the wire preventing any stray field.
As discussed in detail for the transverse wall the transition from the simplified domain theoretical model to the actual domain pattern is connected with a reduction of surface magnetic charges on the cost of volume charges (divergence of $\mathbf{M}$, see Fig. 3.8(c)) and with an exchange energy driven broadening of the Néel wall widths. Furthermore, in the vicinity of the (topological) vortex core the magnetization is forced out-of-plane to reduce exchange energy pointing either up or down. In general, the magnetization orientation of the core is defined as polarity. In patterned soft magnetic nanoelements the vortex core radius is in the order of the magnetostatic exchange length, i.e., in the range of 10 nm (see e.g. Ref. [247] and references therein).
In the following, the rotation of the magnetization around the vortex core is discussed. The domain structure depicted above clearly reveals the fact that in nanostrips the rotation of the vortex is not continuous as it is inherently conjectured from drawing a parallel to vortices in nanodisks. In literature, the experimental studies and simulations concerning vortex domain walls in nanostrips show this fact with more or less accuracy [200, 248, 184, 249]. Aforementioned Néel-wall-like fragments of the vortex wall are very well resolved in Lorentz microscopy studies, as the 90° walls appear as bright or dark stripes in the images [210, 250, 251, 217]. As the two 90° walls building the center wall give the same contrast in the Lorentz micrographs the center wall is usually labeled as 180° wall (see Fig. 3.9(c),(d)). An

important feature of the vortex walls in nanowires is the correlation between the tilting direction of the center wall and the sense of magnetization rotation, that can either rotate clockwise or counterclockwise[17]. In literature not considered so far is the fact, that the symmetry of the magnetic structure fixes the location of the edge defects with respect to the magnetization rotation around the central topological defect (vortex core). This originates from the edge defect that separates magnetic structures that are oriented antiparallel to each other and decomposes into two 90° domain walls at the very position of the edge defect. Changing the sense of rotation of the vortex has the immediate consequence that the center wall reverses its angle with respect to the wire axis and the edge defects appear on the opposite sides. No further combination of sense of rotation and center wall tilt is possible as other combinations enforce the creation of two 180° domain walls as transition lines to the adjacent domains. The two possible configurations for head-to-head walls in straight wires are shown in Fig. 3.9(a),(b). They can be transferred into each other by a mirror operation at the plane through the vortex core perpendicular to the plane of drawing and parallel/perpendicular to the wire axis, respectively. Applying the same argumentation for tail-to-tail walls, the two possible combinations of sense of rotation and wall tilt are opposite to the case of head-to-head walls (time inversion). The depicted special symmetry of head-to-head (tail-to-tail) walls is responsible for effects found in magnetotransport measurements that have been appointed to the sense of rotation [200, 217]. As the sense of rotation and the tilt of the center wall lifts the high symmetry of the domain wall structure, any symmetry-breaking element (e.g., notches, kinks) in a wire causes different pinning of the vortex wall and different properties for clockwise and counterclockwise sense of rotation.
In the following, the consequence of the implementation of a bend on the vortex wall microstructure is discussed. The comparison of Fig. 3.8(d) with Figs. 3.8(a),(b) reveals that the vortex wall located at the bend is connatural to the wall located in a straight wire segment. In contrast to transverse walls, which are centered with respect to the symmetry axis, the vortex walls are slightly shifted out of the symmetry axis. This fact is typically observed for bend wires or wires with notches [210, 184]. Furthermore, only head-to-head walls with a clockwise (counterclockwise) sense of rotation located in the upper (lower) arm of the wire were found in the experiment and simulation (see Fig. 3.15 below)[18]. For tail-to-tail walls the opposite dependence of sense of rotation on wall location was found. The reason for the connection between wall position and sense of rotation is discussed in the following.
The exact position of the vortex walls in a bent wire is suchlike that one of the fractional antivortex edge defects is located at the inner kink. The reason for this behavior is analogous to the pinning of the transverse wall at the bend described above: The magnetization rotation within the two Néel walls merging in the edge defect that is located at the bend is reduced in each case to $\alpha/2$ (compared to a wall position in a straight wire segment) and thus their energy is efficiently reduced. Consequently, the vortex wall microstructure is in a local energy minimum and therefore pinned at the bend. The reason why the microstructure with a fractional antivortex

[17] The sense of rotation is often referred to as chirality in literature.
[18] This statement applies when looking upon the wire with the tip pointing to the left and has to be correspondingly inverted when changing the view by 180°.

located at the outer kink is no stable configuration can be made obvious by the following arguments. Imagine the two possible head-to-head vortex wall configurations in a straight wire shown in Fig. 3.9(a) and (b) that are forced into an upward bent wire with the edge defect settled at the inner (A) or outer (B) kink. For both cases a sketch of the orientation of the magnetization around the edge defects is shown in Fig. 3.9(e) and (f), respectively. Obviously, in the case of settling the edge defect at the outer (inner) kink the total rotation angle of the magnetization in the vicinity of the edge is enhanced (reduced) by $180^\circ - \alpha$ as the magnetization is aligned in parallel to the edge in the wire arms. This is equivalent to an increase (decrease) of the absolute value in topological winding number of the edge defect so that the energy stored in both Néel walls is correspondingly enhanced (reduced). The energetically unfavorable case is additionally connected with charged Néel walls, so that altogether such a configuration is no (local) energy minimum.
In conclusion, the spatial symmetry of the magnetic microstructure of the vortex wall links the sense of rotation with the position of the vortex wall in a bent wire. In section 3.4 it is shown that the exact orientation of the external magnetic seeding field is the control to tune the sense of rotation (position of the wall) in the evolving state of remanence.
In the following section, the microstructure of the asymmetric transverse wall is briefly described, which was found to be the third (metastable) state. The description reveals in particular the close relationship between the three types of domain walls.

3.2.3 Asymmetric transverse domain wall

In the SEMPA investigation a few configurations that are similar to the one exemplarily shown in Fig. 3.10(a) were mapped as remanence state. In the micromagnetic simulation suchlike configurations were also found as local minima as can be seen in Fig. 3.10(b), whereas, however, these microstructures are no global energy minimum for any set of geometrical parameters used in the experiment. Comparing the microstructure of Figs. 3.10(a) and (b) with the respective counterparts found for the transverse wall (see Figs. 3.6(a) and (b)) it is obvious that they are asymmetric mutations of this wall type. Accordingly, in literature, the asymmetric configuration is called asymmetric transverse wall, which was first predicted in 2005 by micromagnetic simulations as third stable state in straight wires [222, 55] and that was experimentally first observed in wires with notches in 2007 [252]. From the simulation, for material parameters that mimic permalloy, the asymmetric transverse wall was found to be the global energy minimum in a very small wire parameter regime, where the vortex and the symmetric transverse wall are nearly equal in energy, under the constraint that the wire thickness is $t < 10$ nm.
The micromagnetic structure of the asymmetric transverse wall was also discussed from a topological point of view in Ref. [182]. Fig. 3.10(d) is the result of a micromagnetic simulation for a straight wire. According to O. Tchernyshyov and co-workers the domain pattern of the asymmetric transverse wall resembles a mutated vortex wall (domain theoretical simplification, see Fig. 3.10(e)), where the vortex core is shifted on the center wall towards one of the edge defects so that the core is almost

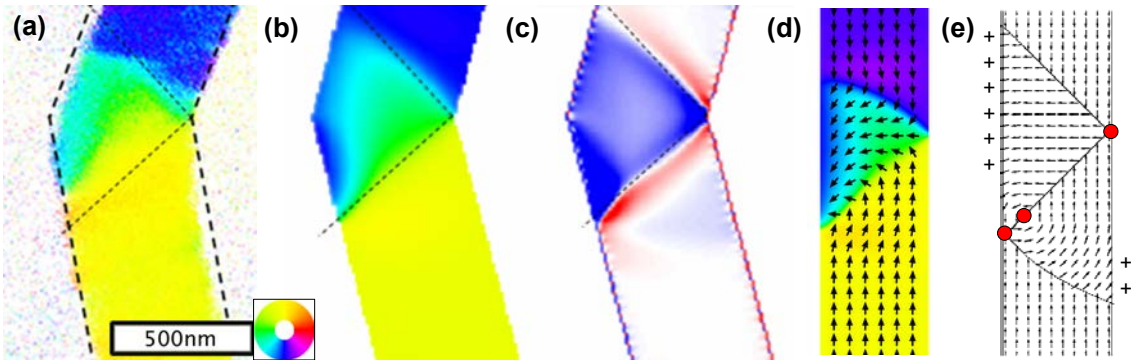

Figure 3.10: Magnetic microstructure of asymmetric transverse domain walls. (a) is a SEMPA micrograph of a wire with $w = 400$ nm and $\alpha = 150°$, while (b) is the result of a micromagnetic simulation for the same geometrical set of parameters. The magnetization orientation is color coded according to the given color wheel. (c) displays the divergence of $\mathbf{M}$ of the pattern shown in (b). Red denotes positive values, blue negative values, and white is equal to zero. The dashed lines in (a)-(c) are guide to the eyes. The domain pattern in (d) is the result of a simulation for a straight wire ($w = 400$ nm), while (e) sketches this structure in domain theoretical approximation that is free of volume charges containing two edge and one volume defect that are highlighted in red. The positive magnetic surface charges are indicated by + symbols. (e) from Ref. [182].

located at the edge. It is worth mentioning that if the vortex core with $k = +1$ reaches the edge it would annihilate with the $k = -1/2$ edge defect to an edge defect with $k = +1/2$ [182]. This structure is then equivalent to the (symmetric) transverse domain wall (see Fig. 3.6(e)). That, in fact, the asymmetric transverse wall exhibits properties of the vortex wall can be best seen in Fig. 3.10(c), where the magnetic charge distribution obtained from the simulation for the wall located at the bend of the wire is shown. At the position where the Néel wall, that is located in the lower wire arm, touches the outer edge it merges with a weak transition line. This feature suggests that the asymmetric transverse wall is probably a metastable state, where the vortex core has failed to nucleate during the relaxation process. A further hint for this assumption is the fact that the asymmetric transverse wall was only experimentally found for the set of parameters, where the vortex wall is the global energy minimum. Moreover, in the experiment only states were found, where the transition line-like feature starts at the outer bend. As the region of highest magnetization rotation is located there it is evident to assume that the vortex core nucleates at the outer bend of the wire. This finding is confirmed in section 3.4.3, where the remagnetization process that results in a vortex domain wall as remanence state is presented.

Similar to vortex and transverse walls only asymmetric domain walls were found as remanence state in the experiment and the simulation, where the fractional antivortex is located at the inner kink. The explanation is an adaption of the corresponding passages given in section 3.2.1 and 3.2.2, so that it can be omitted here. It is worth to note, however, that in a straight wire there are eight energetically degenerated asymmetric transverse wall configurations, instead of four as it is the case for the

transverse and the vortex wall[19]. This is due to the lower symmetry of this microstructure. For four of them the bend provides an attractive (repulsive) potential.

In conclusion, the implementation of the symmetry breaking bend alters the spatial potential landscape for each wall type suchlike that the energetic degeneration for the possible wall configurations is lifted. For instance, the bend region acts as an attractive (repulsive) potential for the domain walls, if the wall enters the bend region in such a way that a fractional antivortex edge defect would locate at the inner (outer) kink.
In the following sections only the vortex and the transverse wall are considered as the simulations suggest that the asymmetric transverse wall is no global minimum for any set of parameters used in the experiments. Furthermore, no systematic dependence of its occurrence on geometrical or experimental parameters has been ascertained out so far.
In the next section, the influence of the variation in geometrical wire parameters on the preponderant type of domain wall, i.e., whether the transverse or the vortex wall is favored, is presented.

3.3 Influence of width and bending angle on the domain wall type

The energy associated with the transverse and the vortex wall comes predominantly from the stray field energy [169]. However, the relative part in stray field energy is larger for the transverse wall. Therefore, for particular geometrical parameter regimes the gain in the stray field energy can be larger than the cost in exchange energy by forming the vortex domain wall.
This section is subdivided into two parts. Section 3.3.1 demonstrates the influence of the width for a fixed bending angle of $\alpha = 150°$, while section 3.3.2 presents the influence of the bending angle (fixed width of $w = 400$ nm) on the evolving domain wall type.

3.3.1 Width variation

In Fig. 3.11(a)-(c) SEMPA images of three nanowires with different wire widths are displayed. For narrow wires $w \leq 200$ nm symmetric transverse walls were found (Fig. 3.11(a)), while for broad wires $w \geq 150$ nm vortex walls (Fig. 3.11(b),(c)) were observed. Wires with widths of 150 nm and 200 nm contained both type of domain walls. It is worth mentioning that for wires with $w \geq 400$ nm in a few cases a zig-zag-like domain wall structure was observed, which resembles the mesoscopic 180° head-to-head domain wall structure that is present in extended thin films (see Fig. 3.1(c)) announcing the transition region from wire-like to film-like behavior.
The wire width driven transition from the transverse to the vortex wall was also investigated via OOMMF. For that purpose the total energy for both wall types

[19] By considering also the polarity of the vortex core, there exist eight degenerated vortex wall configurations.

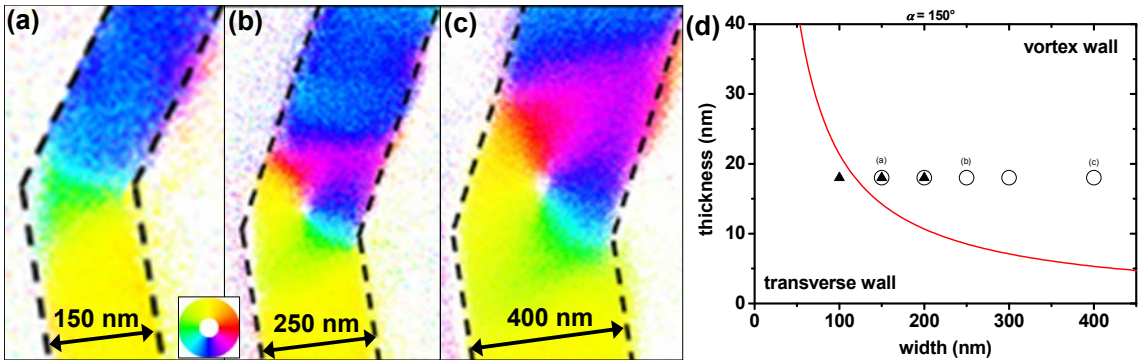

Figure 3.11: (a)-(c) display SEMPA micrographs of the domain walls for three different widths as labeled in the images ($\alpha = 150°$). (d) Phase diagram $t(w)$ for nanowires with a bending angle of $\alpha = 150°$. The calculated line of equal energy is shown along with experimental results, where ◯ and ▲ indicate vortex and transverse walls, respectively. For $w = 150$ nm and 200 nm both domain wall types were experimentally observed.

in dependence on the wire width as well as on film thickness was calculated. In Fig. 3.11(d) the evaluated line of equal energy for the transverse and the vortex wall is displayed. In this commonly called "phase diagram" also the experimental results are plotted. It is obvious that the simulations basically reproduce the experimental findings, predicting a transition from the transverse to the vortex wall as global minimum at a width of about 120 nm (at $t = 18$ nm).
The experimental and simulated results are in accordance with the findings for straight wires, which means that the transverse wall is the global energy minimum for thin and narrow wires while the vortex wall is the domain wall with lowest energy for thick and broad wires [169, 184]. Furthermore, the calculated line of equal energy fulfills the term $w \cdot t = \text{const.}$ as determined for straight wires [169, 184]. McMichael and Donahue did not only predict the vortex and transverse wall via simulations as well as calculated the line of equal energy in the phase diagram, but they also analytically estimated the energy difference between both domain wall types in straight wires [169]. For the difference in stray field energy they estimated that it is basically the stray field energy of the wall magnetization of the transverse wall that is oriented perpendicularly to the main wire axis: $\Delta E_{\text{stray field}} \propto -\mu_0 M_S^2 t^2 w$. The difference in exchange energy is estimated to be mainly given by the vortex present for the vortex wall, that yields: $\Delta E_{\text{exchange}} \propto tA$, where A is the exchange constant [169, 184]. In the region where both wall energies are identical the sum of the energy difference is zero, yielding $w \cdot t = \text{const.}$ as observed in the experiment and simulation.
In conclusion, the phase diagram obtained for bent wires is qualitatively connatural to the one obtained for straight wires.

3.3.2 Bending angle variation

This section discusses the influence of the bending angle on the preponderant domain wall type. In Fig. 3.12 SEMPA images of the domain walls found in nanowires with different bending angles are displayed ($w = 400$ nm). Micrographs of wires with

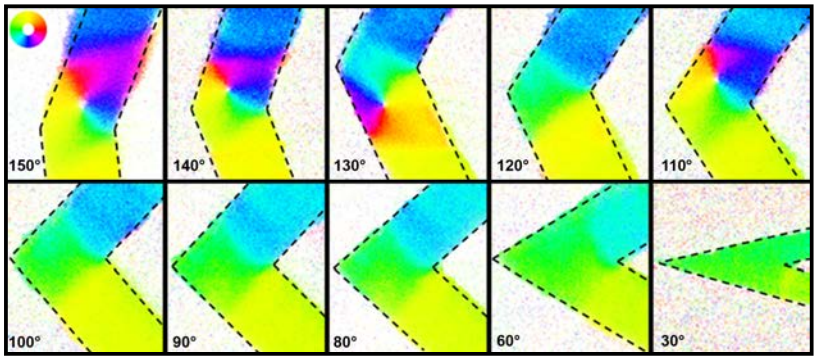

Figure 3.12: Series of SEMPA images of nanowires with varying bending angle α as labeled in the images ($w = 400$ nm). The orientation of magnetization is given according to the color wheel.

bending angles $\alpha \geq 160°$ are not shown as they do not contain any domain wall as already discussed in section 3.1.5. Concerning bending angles $\alpha \geq 110°$ vortex walls were found, while for $\alpha \leq 120°$ transverse walls were observed. This finding implies that for $\alpha = 110°$ and 120° both types of domain walls were detected. The total energy of both wall types in dependence of wire width and bending angle at a fixed thickness of 18 nm was calculated via OOMMF. In Fig. 3.13(a) the evaluated line of equal energy can be seen in the $w(\alpha)$ phase diagram together with the experimental results. While the experimental results indicate a transition from the transverse to the vortex wall at an angle range of $110° \leq \alpha \leq 120°$, the calculation reveals a transition at a slightly lower bending angle of about 93°. The difference can be explained by the following argumentation. For $93° \leq \alpha \leq 120°$ the vortex wall is the lowest energy configuration but the transverse wall constitutes a local energy minimum that can be entered during the relaxation process [253]. This explanation can also account for the slight difference between the experimentally found and calculated transition between both wall types observed for the width variation presented in the previous section (see Fig. 3.11(d)).
By additionally varying the thickness of the wire a three dimensional phase diagram that displays the "plane" of equal energy in dependence of the three geometrical parameters is obtained. The results of the simulation are shown in the conventional $t(w)$ phase diagram of Fig. 3.13(b), in which the lines of equal energy are plotted for different bending angles $\alpha \geq 90°$. Generally, when lowering the bending angle the parameter region grows where the transverse wall is the global minimum. This is in accordance with the findings for the particular set of parameters investigated experimentally (fixed thickness and width) as presented above.
For each bending angle the calculated line of equal energy $t(w)$ is a hyperbola ($w \cdot t = \text{const.}$), which was already shown for straight wires [169] and for the particular angle of $\alpha = 150°$ as discussed in section 3.3.1. Currently, the development of a phenomenological description concerning the dependence of the line of equal energy on bending angle is under progress [E13]. The model will help to understand the transition between both wall types in analogy to the analytical estimation of the transition undertaken in Ref. [169] for straight wires. Qualitatively, the bending angle dependence of the line of equal energy is certainly governed by the reduction

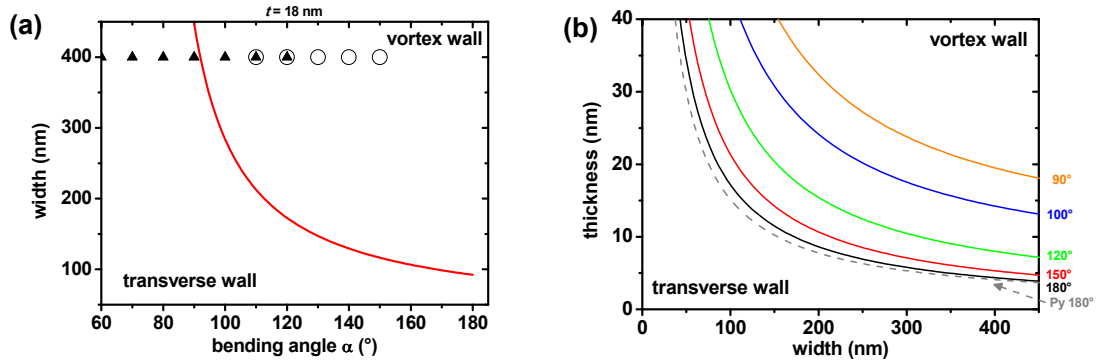

Figure 3.13: Phase diagrams for bent nanowires. (a) $w(\alpha)$ phase diagram for a constant thickness of $t = 18$ nm. The calculated line of equal energy is shown along with experimental results, ◯ and ▲ indicate vortex and transverse walls, respectively. For $\alpha = 110°$ and 120° both domain wall types were experimentally observed. (b) $t(w, \alpha)$ phase diagram. For particular bending angles α the calculated lines of equal energy are displayed. For comparison the diagram also includes the result for straight Py wires taken from Ref. [222].

in stray field energy with decreasing the bending angle as the relative part in stray field energy to the total energy is larger for the transverse wall compared to the vortex wall. Thus, by lowering α the total energy of the transverse wall is more efficiently reduced and the area in the (t, w) space expands where the transverse wall is the global minimum.
In conclusion, the results reveal that besides wire width and thickness the bending angle is a further parameter to tune the domain wall type in the state of remanence on purpose. It is worth mentioning that the plane of equal energy in the three-dimensional (t, w, α) space is almost identical regarding the intrinsic material parameters of the CoFeSi alloy and permalloy as can be exemplarily seen in Fig. 3.13(b) for a bending angle of 180° (straight wire). This is due to the fact that the magnetostatic exchange length for both materials is nearly identical. Therefore, the presented results for the CoFeSi alloy are also quantitatively valid for permalloy in a good approximation.
The following section deals with the tuning of the vortex wall properties by means of external magnetic fields.

3.4 Controlling the properties of vortex domain walls via external seeding fields

The strategy used in this work to introduce the domain walls at the bend by applying an external seeding field that is approximately oriented along the wire's bisection was utilized in various studies [206]. Depending on the direction of the external seeding field, a head-to-head or tail-to-tail domain configuration evolves, while the geometrical parameters of the wire decide if a vortex or a transverse wall is created between the domains, as presented in the previous section. While the influence of the seeding field on the magnetization orientation within the domains can be easily understood (see section 3.1.5), it is still an open question what determines the

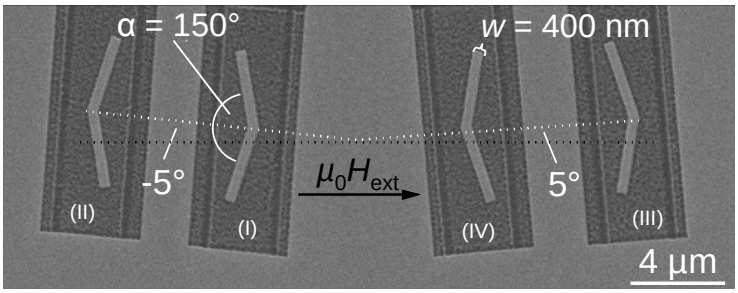

Figure 3.14: SEM image of the modified sample layout showing four V-shaped wires of 400 nm width. The symmetry axis (bisection) is indicated by the white dotted line. The black arrow gives the direction of the external field used for seeding the domain walls.

vortex wall properties, i.e. the sense of rotation and the position of the core with respect to the symmetry axis. Both properties are inherently linked to each other as explained above in section 3.2.2.
In the SEMPA investigation head-to-head vortex walls were observed where the vortex core was predominantly placed in the upper arm of the wire (see e.g. Fig. 3.12). A straight-forward explanation for this observation would be the exact orientation of the external seeding field, which was slightly tilted by about 10° with respect to the wire's bisection (see section 3.1.5). In order to experimentally prove this hypothesis in a strictly scientific manner a further study was performed, which is presented in this chapter. In the first part 3.4.1 the modified sample layout is presented. In the second section 3.4.2 the results are given, which confirmed the assumption that the exact orientation of the seeding field is the control that determines the sense of rotation and location of the vortex walls. Based on the considerations about the vortex wall properties in bend wires, discussed in section 3.2.2, micromagnetic simulations of the relaxation process provide an explanation for this behavior. The results of this investigation were published in the Physical Review B [E4]. The letter can be found in the attachments.

3.4.1 Modification of the sample layout

The direction of the magnetic field and the orientation of the sample with respect to the field cannot be manipulated *in situ*, so that before the inward transfer into the SEMPA chamber the sample has to be mounted correspondingly to the sample holder. Thus, in order to investigate the influence of the orientation of the magnetic field on the vortex wall properties wires have been created by FIB with tilt angles of ±5° ((I), (III)) and ±175° ((II), (IV) in Fig. 3.14), while the sample is mounted in such a way that the magnetic field direction is along 0° (see black arrow in Fig. 3.14). Such an arrangement of wires allows to investigate all four generic cases of field orientation simultaneously. To make sure that the emerging domain wall is predominantly a vortex domain wall a wire width of $w = 400$ nm and a bending angle of $\alpha = 150°$ was used as for this set of parameters the vortex wall is definitely the global energy minimum (see Fig. 3.13(a)).

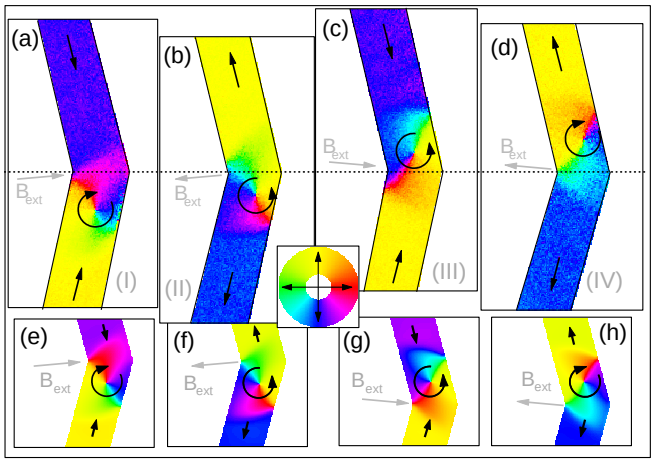

Figure 3.15: (a)-(d) SEMPA images of vortex domain walls in V-shaped wires after field application in the indicated directions (gray arrows). The labels (I)-(IV) refer to the four arrangements in Fig. 3.14. The orientation of the magnetization is indicated by the black arrows and color coded according to the given color wheel. The images have been rotated so that the bisections of the wires are aligned with the black dotted line. In the images only the signal of the wire, i.e., within the black solid lines, is displayed. (e)-(h) Micromagnetic simulations of the corresponding geometries from (a)-(d) after pretreatment in an external field of $B_{\mathrm{ext}} = 60$ mT that is oriented along the directions indicated by the gray arrows.

3.4.2 Results of the SEMPA investigations and OOMMF simulations

After the application of the seeding field of $B_{\mathrm{ext}} = 60$ mT the domain patterns of several wires were imaged. SEMPA micrographs of the predominant vortex wall structures for the four different orientations are shown in Figs. 3.15(a)-(d). It has to be noted that no other vortex domain configuration besides the four shown in Figs. 3.15(a)-(d) has been found in the experiments in accordance with the symmetry considerations made in section 3.2.2. Head-to-head and tail-to-tail vortex walls are seeded depending on the direction of the magnetic field (see section 3.1.5). The position and sense of rotation of the walls, however, depends on the exact orientation of the magnetic field. In Fig. 3.15(a) ($B_{\mathrm{ext}} = +60$ mT at -5°) the vortex core of the head-to-head wall is moved into the lower arm and the sense of rotation is clockwise. Reversing the direction of the seeding field creates a tail-to-tail wall in remanence. The vortex core is again placed in the lower arm while the sense of rotation is switched from clockwise to counterclockwise (see Fig. 3.15(b)). In Fig. 3.15(c) and Fig. 3.15(d) the orientation of the seeding field ($B_{\mathrm{ext}} = \pm 60$ mT) was applied at +5° with respect to the symmetry axis. The remanent configuration shows again a head-to-head/tail-to-tail wall, respectively. The vortex, however, nucleates in the upper part of the wire for both field directions. The sense of rotation again depends on the sign of the applied field, a counterclockwise/clockwise orientation was found for the two cases (see Fig. 3.15(c) and Fig. 3.15(d)). To summarize the experimental results: both the orientation of the external seeding field with respect to the symmetry axis and the sign determine which of the four micromagnetic configurations

in Fig. 3.15 occurs. The four states can be transferred into each other by symmetry operations. A mirroring at the dashed line transfers state (a) into state (c) and (b) into (d) respectively. The states (a) and (b) can be mapped onto each other by means of a time-inversion ($\mathbf{M} \rightarrow -\mathbf{M}$, $\mathbf{H} \rightarrow -\mathbf{H}$) operation, equally (c) and (d).
The results were strictly proven experimentally by measuring overall 47 independent domain arrangements (three in situ remagnetization processes). A 64% majority of all examined magnetization processes gave vortex patterns that agree with the proposition for the four different vortex configurations. This is a reasonable success rate compared to similar statistics on vortex wall behavior [252, 254]. A wrong vortex configuration was found with a probability of 11%, i.e., when state (a)/(b) was found instead of (c)/(d) and vice versa. Besides vortex walls, transverse walls (14%) were found and 11% of the magnetization processes did not show a domain wall at all. Considering only the cases when vortex walls were generated the proposed structures appeared with a probability of 86%.
To emphasize the experimental results, micromagnetic simulations were performed using OOMMF. The microstructure in remanence was simulated after switching off a magnetic field of $B_{\text{ext}} = \pm 60$ mT, tilted $\pm 5^\circ$ out of the symmetry axis, corresponding to the four situations in the experiments. The micromagnetic configurations are plotted in Figs. 3.15(e)-(h). For the simulation the following geometrical parameters were used: wire width 400 nm, thickness 45 nm, bending angle 150° (further parameters of the simulation, see section 3.1.4)[20]. Comparing the SEMPA images (Figs. 3.15(a)-(d)) with the results of the micromagnetic simulation (Figs. 3.15(e)-(h)), it is evident that the experiments and simulations gave the same magnetic structures, i.e., the sense of rotation and position of the vortex core.
Due to the high spatial resolution of the measurements, the position of the vortex core could be determined experimentally with a high accuracy and therefore enables a reasonable comparison with the results of the micromagnetic simulations. The simulation gave a distance of the core to the symmetry axis of 212 nm and a lateral shift toward the outer edge of 20 nm, respectively. In the SEMPA images slightly varying core positions were found. On average, the SEMPA images revealed a distance of the core to the symmetry axis of (215 ± 50) nm and a lateral shift of (33 ± 30) nm. Within the experimental uncertainty, both values are in very good agreement with the simulations. Thus, it can be concluded that the input parameters used for the numerical simulation represent the experimentally studied system quite well. Consequently, it appeared justified to use the simulation to understand the relaxation into the zero-field magnetic configurations in order to reveal the mechanisms that determine the position of the core and therefore the sense of rotation of the vortex wall.

[20] Compared with the experiment a system with higher thickness was simulated. The reason for this approach was to overcome the well-known problem that simulations at $T = 0$ K do not necessarily find the global energy minimum (vortex wall), as long as there exists an energy barrier to the local energy minimum for the transverse wall [253, 184].

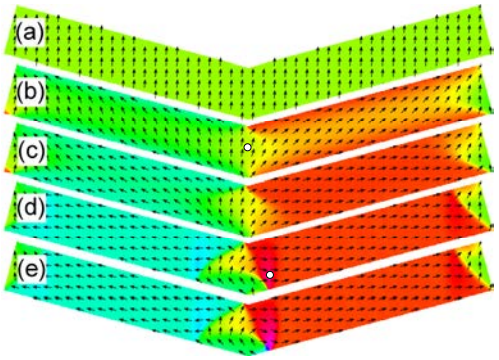

Figure 3.16: Details of the simulation of the relaxation starting from the fully saturated state (a) with a high damping constant of $\alpha = 0.5$. The field is aligned 5° toward the right-hand side of the symmetry axis. The relaxation steps shown are: (b) 50 steps, (c) 80 steps, (d) 300 steps, and (e) 400 steps. The simulation converges after 11647 steps, yielding the configuration of Fig. 3.15(h). The white dots are marker points, which are discussed in the text.

3.4.3 Discussion of the relaxation process

The simulation of the relaxation process presented in the following only deals with one experimental geometry (see (IV) in Figs. 3.14, 3.15) as the other arrangements can be directly traced back to the described situation via symmetry considerations, as discussed above. In order to reproduce the experimental situation, where the magnetic field was reduced slowly compared to the intrinsic magnetodynamic time scale in the simulations, the field has to be reduced in several steps to zero using a realistic damping constant. Otherwise, unrealistic dynamical effects could influence the results. An alternative is to choose a high damping constant and switching off the field in a single step. Both procedures were performed obtaining similar results, in particular, the evolving remanent domain configuration was the same. As the first method is very time consuming, the relaxation steps are presented using the second method, where a large damping constant of $\alpha = 0.5$ was utilized. To demonstrate that the determination of the sense of rotation is caused by the symmetry violation of the seeding field the results for the starting configuration with perfectly field aligned moments are presented. The special steps of the relaxation process are displayed in Fig. 3.16. Fig. 3.16(a) gives the start situation, where all moments are aligned 5° toward the right-hand side with respect to the symmetry axis (vertical direction). The relaxation is driven by the shape anisotropy, which is most effectively reduced by rotating the moments into the direction parallel to the edges. The torques acting in the two arms are oppositely oriented as the angles between the moments and the edges are opposite one another in the field-aligned state. The rotation into the directions along the wire axis initially appears in the vicinity of the edges (see Fig. 3.16(b)). The magnetization within the arm of the wire that has the smaller angle to the field direction (right-hand side) relaxes first, while in the arm on the opposite side the relaxation has just started at the edges. The configuration in Fig. 3.16(b) is quite similar to the simulated microstructure achieved in a static field of $B_{\mathrm{ext}} = 60$ mT, which is used in the experiments. In the

bend region the magnetization is preferentially oriented in the former field direction with a continuous transition to the magnetization in the arms of the wire. A slight asymmetry appears as the relaxation on the right-hand side is stronger than on the left-hand side, which pushes the transition region slightly into the left arm. Consequently, the magnetization around the symmetry axis is tilted farther to the right (see white dot in Fig. 3.16(b)), which is the first indication of a certain sense of rotation that is induced by the relaxation and the initial asymmetric field orientation. In the next phase after 80 steps (Fig. 3.16(c)), the magnetization in the interior of the two arms has further relaxed toward the wire axes. This relaxation step defines the transition lines and drives them closer into the bend region, which causes a stronger rotation here. The sense of rotation is determined by the tendency to keep the magnetization parallel to the edges while around the symmetry axis nearly no shape-induced torque is effective. Here, the magnetization rotates to establish the continuous transition between the oppositely magnetized arms while the former sense of rotation is maintained and the asymmetry is even enhanced. In the next phase after 300 steps (Fig. 3.16(d)), the transition line on the right-hand side continues to move into the bend region while the magnetization rotation appears also across the transition line (see white dot in Fig. 3.16(d)). At this step, the sense of rotation of the vortex is clearly visible and the first structure that tags the center wall is established. As the sense of rotation and the tilting of the center wall are strongly correlated (see section 3.2.2), the center wall has to move into the right arm, as the edge defect has to settle at the inner kink. Next (Fig. 3.16(e)), a combined vortex core/edge defect is created at the end of the sharp transition line on the right-hand side, thus generating all structures needed for the center wall. Finally, vortex core and edge defect separate and the center wall is pushed further away from the bend region in order to allow the second 90° segment at the edge defect to develop, acting as transition line to the domain in the arm on the right-hand side (resulting remanence state, see Fig. 3.15(h)). In contrast, the transition line on the left-hand side is almost unchanged during relaxation after the step shown in Fig. 3.16(c).

In brief, the driving force of the relaxation process stems from the shape anisotropy that acts first on the moments at the edges. Inside the bend region the net torque is vanishingly small or the opposite torques on both sides compensate each other, which lets the moments stay almost in the field-aligned orientation, e.g., toward the right-hand side. The shape aligned moments along the edges and the former field aligned moments in the bend region then define the sense of rotation of the vortex. As the sense of rotation and the tilt of the center wall are linked, the vortex core settles in the arm that is closer to the seeding field direction.

The core nucleation process (Fig. 3.16(e)) was predicted for the reversed case in Ref. [182], the annihilation of the vortex core with the edge defect (see also section 3.2.3). A further hint for the proposed nucleation process concerns the findings for the asymmetric transverse wall presented in section 3.2.3. Experimentally, only configurations were found, where the transition-line like feature started at the outer edge. This is the point of the asymmetric transverse wall where the magnetization rotates strongest (see Figs. 3.10(b),(d)) so that it can be assumed that a combined vortex core/edge defect might be created there. Furthermore, in the experiment

the transition line-like feature was predominantly found in the arm that is closer to the seeding field direction in accordance with the simulations (see Fig. 3.16(e)). Therefore, the asymmetric transverse wall can be regarded as a metastable state, where the vortex core has failed to nucleate. In turn, the microstructure basically provides a snapshot of features of a frozen intermediate state before the vortex core is nucleated.
The results presented here are not limited to the discussed geometry. They can be seen as a more universal behavior for the seeding of vortex walls in bent nanowires in a particular span of geometries. Certainly, it has to be considered that vortex walls must be energetically more favorable than transverse walls, which depends on the wire dimensions as well as on the bending angle as shown in section 3.3. The limitations regarding the tilting angle of the seeding field Θ with respect to the symmetry axis are: The lower bound is given by the fact that the symmetry has to be broken, i.e., $\Theta > 0°$. The upper bound is determined by the torques in the arms, which have to be oriented oppositely, i.e., $\Theta < 90° - \frac{\alpha}{2}$ (with bending angle α). For larger Θ domain walls cannot be nucleated.

3.5 Conclusion and outlook

The magnetic microstructure of domain walls in bent nanowires in the state of remanence was investigated by means of SEMPA technique with a high spatial and angular resolution of about 15 nm and of ±4°, respectively, and was complemented with micromagnetic simulations. For the SEMPA investigations wires with different width w and bending angle α ranging from 150 nm $\leq w \leq$ 800 nm ($\alpha = 150°$ fixed) and $20° \leq \alpha \leq 180°$ ($w = 400$ nm fixed) were carved from a soft magnetic, 18 nm thick $Co_{39}Fe_{54}Si_7$ alloy by means of FIB technique. After the application of a seeding field that was slightly tilted with respect to the wires' bisection three different types of domain walls located at the bend were observed. The magnetic microstructures are connatural to the microstructures of domain walls in a straight wire segment, namely, the symmetric and asymmetric transverse domain wall as well as the vortex domain wall. According to O. Tchernyshyov and co-workers [245, 171, 182] the mesoscopic, complex microstructures of the domain wall types can be seen as composite objects consisting of two or three topological defects. The lateral arrangement of the topological defects gives a good access to the important features and the correlations between the magnetic microstructures of the domain wall types including their spatial symmetries. The asymmetric transverse wall exhibits micromagnetic features of the vortex and symmetric transverse walls and can be regarded as a metastable intermediate state, where the vortex core virtually failed to nucleate. Only a few asymmetric transverse walls were experimentally observed, while no systematic dependence of its occurrence could be identified. For head-to-head (tail-to-tail) domain walls in a straight wire the spatial symmetries allow two generic configurations each for vortex and symmetric transverse walls, while for asymmetric transverse walls four energetically degenerated configurations exist. The implementation of the symmetry breaking bend alters the spatial potential landscape for each domain wall type, so that the region of the bend provides an attractive (repulsive) potential when the fractional antivortex edge defect is located at the inner (outer) kink. In the case of the symmetric (asymmetric) transverse wall this fact excludes the existence of one (two) generic configuration located at the bend. In the case of the vortex wall this fact implies that both generic configurations can be attractively pinned at the bend. However, as the opposite sense of rotation of the magnetization around the vortex core between both configurations is inherently connected to an opposite tilting angle of the center wall with respect to the wire axis the position of the vortex core is firmly linked to the sense of rotation. For instance, for head-to-head walls in a downward bend wire a clockwise (counterclockwise) sense of rotation is always connected to a vortex core located in the right (left) wire arm.
The results concerning the influence of the bending angle on the predominant domain wall type clearly reveal that besides the wire width and thickness the bending angle is a further parameter to tune the domain wall type on purpose. For large bending angles vortex walls were experimentally observed while for small bending angles symmetric transverse walls were found. Micromagnetic simulations reveal that for the set of parameters investigated experimentally only vortex and symmetric transverse walls are global energy minima. Furthermore, the simulations are in good accordance with the experimentally found bending angle driven tran-

sition from a vortex to a (symmetric) transverse wall. By additionally varying the thickness the simulations reveal that for arbitrary fixed bending angles the line of equal energy between both states is a hyperbola ($w \cdot t = \text{const.}$) as it is the case for straight wires, while the constant monotonically increases with α. The phenomenological description of the dependence of the line of equal energy on bending angle, which is currently under development, will help to understand the underlying mechanism [E13]. However, the fact that by lowering α the area in the (t, w) phase diagram expands, where the transverse wall is the global minimum, already reveals that the reduction in stray field energy is the driving force as the relative part in stray field energy to the total energy is larger for the transverse wall compared to the vortex wall.
Nowadays, the investigation of the influence of the bending angle for different widths and film thicknesses (10 nm and 30 nm) is under progress in order to verify the three-dimensional (t, w, α) phase diagram in a rigorous manner [E13]. Thereby, it will be interesting to see if a systematic occurrence of the asymmetric transverse wall can be observed as micromagnetic simulations suggest that at small thicknesses this wall type even constitutes a global energy minimum in a narrow region in the phase diagram [222].
Concerning vortex walls it is unambiguously shown in this chapter that the sense of magnetization rotation around the vortex core/ position of the vortex core can be tuned on purpose via magnetic fields that are slightly tilted out of the symmetry axis of the wire [E4]. The core is always located in the wire arm, which includes a smaller angle with the direction of the magnetic seeding field. Micromagnetic simulations allow the understanding of the relaxation process which reveals that the shape anisotropy-induced relaxation in the arms and the field alignment in the bend region fix the sense of rotation in the beginning of the relaxation process. At the moment, the remagnetization process of bend wires is under investigation by means of magnetoresistance measurements as explicitly shown in the outlook of chapter 4 in order to experimentally comprehend the relaxation. The possibility to purposely control the sense of rotation and the polarity of a vortex domain wall, the latter via slight out-of-plane field components, gives more flexibility in future concepts of vortex-based memory devices [64, 65]. For instance, a bend injection wire can be used to define a certain vortex configuration which acts as a four-state bit element and can be moved into a memory array utilizing the spin transfer torque effect, in analogy to the working principle of the racetrack memory [61].

4 Magnetization reversal and magnetic energy of individual submicron rectangles investigated via anisotropic magnetoresistance

The knowledge about the magnetization reversal process gives a direct access to the understanding about the evolving micromagnetic remanence state as presented in connection with the seeding of vortex domain walls in the previous chapter (section 3.4). Only the remanence state was obtained directly from the experiment there, while the remagnetization process was modeled via micromagnetic simulations. Therefore, the task is to experimentally detect the remagnetization as well. For nanowires, as they are predestined for resistance measurements due to their shape, the anisotropic magnetoresistance (AMR) is frequently used as an integrative probe for the magnetization orientation during magnetization reversal [80, 255, 256, 257, 258, 26, 259, 260, 261, 262, 263]. For instance, for straight wires, which are in a single-domain state, the resistance versus field curves particularly enable the determination of the easy axis switching field and of the shape anisotropy, the latter from the hard axis curve (see section 2.1.4.2). While the magnetic properties of wires are frequently investigated, the quantitative study of artificial[1] nanostructures is rare, where all three dimensions are shrinked to the nanoscale [269, 270, 271, 272], and most often performed with the help of nanostructure arrays [273, 274, 54, 177, 179, 275, 276, 277, 278, 180]. The reason for this is that the addressing of individual nanostructures is very demanding due to the missing sensitivity of conventional characterization techniques. In order to study e.g. the size and shape dependence of magnetic properties of single nanostructures, new methods have to be developed. The route to achieve the required sensitivity for measuring magnetic properties of single nanostructures is via miniaturized probes, i.e. the whole measuring device has to be scaled down, which are combined with conventional macroscopic measurement tools. The pioneering experiment in this field was the successful measurement of magnetic-flux density via micro-superconducting quantum interference device (micro-SQUID) by W. Wernsdorfer et al. in 1995 [279, 280, 281].
However, most of the studies concerning artificial nanostructures deal with nanostructure arrays which typically consist of hundreds to thousands of structures. Cer-

[1] It is worth to emphasize that tremendous progress in the characterization and quantification of the magnetic properties of single atoms and self-assembled nanostructures as clusters and nanoislands grown on top of perfect substrates were made within the last years, which was enabled by the improvements of scanning probe techniques [264, 265, 266, 267, 268].

tainly, the averaging over such a large number of structures would yield reasonable results in the case of perfectly identical structures. But due to small unavoidable variations in shape and structure size, which are inherently connected with any kind of preparation technique, the single structure behavior is masked by the averaging. Furthermore, magnetostatic interactions between the particles within the array are difficult to take into account [282, 283].
In this chapter, an approach for the investigation of the magnetization reversal of individual nanomagnets with lateral dimensions down to some 100 nm via AMR is presented. The sample preparation by means of Focused Ion Beam (FIB) milling of a laterally homogeneous stack and the MR investigation including the electrical contacting via a micromanipulator were performed at the very same position in an ultra-high vacuum (UHV) chamber. As time-consuming sample exchange was avoided highest efficiency was achieved. Furthermore, the uninterrupted vacuum conditions reduced the danger of sample degradation due to oxygen exposition, which can have a drastic impact on the properties of nanostructures as they exhibit a large surface to volume ratio. The high flexibility of the direct top-down structuring via FIB technique enables the possibility to vary parameters of the nanostructure, such as size and shape as well as magnetic environment on purpose. As numerous structures can be made from the very same film this opens the way to systematically study dependencies on particular parameters, while highest possible comparability is achieved.
The UHV chamber containing FIB and *in situ* MR setup is presented in detail in section 4.2.
Afterwards, the MR measurement scheme is introduced in section 4.3.
The core regarding the investigation of the magnetization reversal of individual nanomagnets via AMR is the FIB preparation of a micro-sized circuit including the nanomagnet to be measured. The preparation process via FIB contains the creation of the nanomagnet by rendering the surrounding film material paramagnetically by means of ion beam-induced mixing of the material layers of the stack and the carving of the path, which forces the current through the nanomagnet during the MR measurement. Section 4.4 contains a detailed description of the FIB preparation of the micro-circuit. Importantly, as the paramagnetically rendered material serves as input leads for the MR investigation it has to maintain a good conductance. In order to find adequate layered film systems a powerful *in situ* MR method for characterizing the influence of ion-bombardment on the electrical and magnetic properties was developed, which is also described in section 4.4. This method was applied for different stacks containing a 20 nm thick softmagnetic permalloy layer. For the superior stack the magnetic properties as well as the influence of ion bombardment on the structural properties and on the chemical composition are presented in section 4.4 as well.
The superior stack was used to demonstrate the potential and sensitivity of the MR investigations of single nanomagnets in the case of rectangular prisms (rectangles) with lateral sizes below one micron and a lateral aspect ratio of 2:1. Three different lateral sizes were investigated: 600×300 nm^2, 800×400 nm^2, and 1000×500 nm^2. The chosen thickness of 20 nm and the aspect ratio of the softmagnetic rectangles correspond to the parameters of the so-called standard problem No. 1 (SP1) [284].

The standard problems were defined by the Micromagnetics Modeling Activity Group of the National Institute of Standards and Technology (NIST) in 1997. The aim is to check the reliability of new codes by comparing the results with reference solutions of typical micromagnetic problems[2]. Subsequently, similar parameters are often used in theoretical/ computational [285, 74, 286, 287] as well as experimental work [288, 289, 290, 291, 292]. From these studies it is known that for this class of elements a variety of micromagnetic states are local energy minima. Consequently, this fact stresses the need for the investigation of individual structures as integrative measurements of the magnetization reversal averaging over several hundreds of structures, that might be in several different micromagnetic states, provides only minor qualitative information about the single structure behavior.
In the first part of this chapter (section 4.1) the domain patterns that correspond to stable micromagnetic states in submicron softmagnetic rectangles are introduced.
The MR investigations of the rectangles are complemented by domain structure investigations of the remanence state via scanning electron microscopy with polarization analysis (SEMPA). The SEMPA results are presented in section 4.5.
The resistance versus field curves for magnetic fields applied along the short (magnetic hard) and long (magnetic easy) axis are separately presented and discussed in section 4.6. The MR curves were obtained in a single field cycle, so that any kind of averaging can be excluded which might mask the single remagnetization behavior. From the MR curves in combination with the knowledge about the remanence state the easy axis and hard axis remagnetization behavior of the rectangles could be clearly deduced. In particular, the hard axis loops enable the quantification of the size-dependent magnetic energy of the micromagnetic Landau domain pattern.
The chapter closes in section 4.7 with a conclusion and an outlook, where in particular the feasibility of the *in situ* MR method to address individual nanomagnets arranged in an array is demonstrated.

[2]A critical remark on SP1 of A. Aharoni can be found in Ref. [174].

4.1 Magnetic microstructure of submicron softmagnetic rectangles

This section gives an overview of the domain patterns, which are stable states in rectangular shaped nanostructures made of softmagnetic thin films. Although these states are a result of the complex interplay between the stray field and exchange energy in the minimizing of the total energy (Eq. 2.1) the patterns can be understood qualitatively by simple considerations. The patterns can be subdivided into two groups according to their net-magnetization in remanence [74]: One group contains the so-called flux-closure states with (almost) zero net-magnetization in remanence while the other group contains the so-called high remanence states.

4.1.1 Flux-closure states

In order to reduce the stray field energy, surface charges have to be avoided. As already discussed in section 2.1.2 surface charges at the large upper and lower side are circumvented when the magnetization is oriented in the film plane. Accordingly, the stray field energy is further reduced if the magnetization is also oriented along the other edges which cannot be achieved with a homogeneous magnetization within a finite element. Consequently, a multi-domain state has to evolve. As discussed in section 2.2, "charged" domain walls are energetically unfavorable and avoided if the domain wall includes the same angle with the magnetization on both sides of the wall. There are only a few fundamental domain patterns which fulfill these requirements. For the construction of such demagnetized states a simple graphical method exists, which was developed by H. A. M. van den Berg [293, 294, 295]. The simpleness of the method, which is briefly described in the following, is astonishing as it is based on complicated mathematics [68]. For arbitrary shaped softmagnetic two-dimensional elements ($M_z = 0$) the method consists in drawing circles, which tangents the edges of the element at least twice. The connections of the central points of these circles specify the location of the domain walls, which are regarded as infinitesimal narrow[3]. The direction of the magnetization within the domains is perpendicular to the radius vectors, which connect the central points of the circles with the element edges. The result of the van den Berg method is not unique, so that several domain patterns can be constructed. The direction of the magnetization can be rotated by 180°. Moreover, it is possible to divide the element before the construction into several parts and to apply the construction separately to each part. Three results of the van den Berg construction in the case of rectangular structures with an aspect ratio of 2:1 can be seen in Fig. 4.1: the so-called Landau state (a), diamond state (b), and cross-tie state (c). The agreement with the corresponding demagnetized states obtained from micromagnetic simulation and observed experimentally via SEMPA in $1000 \times 500 \times 20$ nm^3 elements is quite obvious in Fig. 4.1. In the following, the states experimentally observed in this study, i.e., the Landau state and the diamond state, are briefly introduced separately.

[3] domain theoretical treatment, see introduction of chapter 2

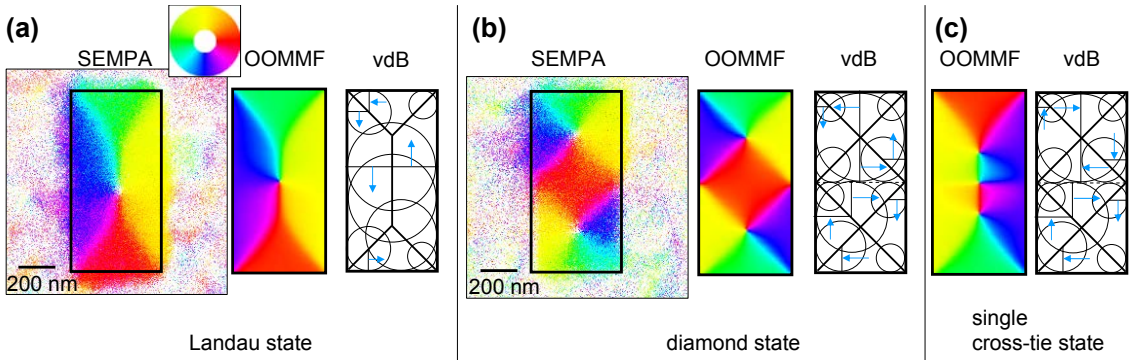

Figure 4.1: Domain patterns of flux-closure states. (a) Landau state, (b) diamond state, and (c) cross-tie state. In (a) and (b), besides the pattern obtained from micromagnetic simulations using OOMMF and the constructions via the van den Berg (vdB) method, a SEMPA micrograph of a $1000 \times 500 \times 20$ nm^3 permalloy structure is given as well. In the SEMPA and OOMMF images the magnetization orientation is color coded according to the given color wheel, while in the vdB construction it is given by blue arrows. Prior to the construction for the diamond and cross-tie state the rectangle is subdivided into two squares along the dashed line. While the diamond state exhibits mirror symmetry with respect to the direction of the short axis, the Landau and the cross-tie states are point symmetric with respect to the center of the rectangle.

Landau state

The Landau state consists of four domains and exhibits point symmetry with respect to the rectangle center (see vdB construction in Fig. 4.1(a)). The magnetization within the two large and small domains is oriented in an antiparallel manner to each other, respectively. The small domains close the magnetic flux of the large domains so that surface charges are avoided. The microstructure of the "real" Landau state, however, deviates from the depicted "ideal" Landau state. This is due to the reason that the energy of a Néel wall is significantly reduced if the wall angle is lowered as presented in section 2.2 (see Eq. 2.28 and Fig. 2.3(b)). Accordingly, in order to minimize the overall energy of the domain pattern the wall angle between the two large domains is smaller than 180°, while it is 180° in the case for the ideal Landau pattern obtained from the van den Berg construction. This strategy, however, is accompanied by the appearance of charged domains [74]. In the case of an ideal rectangle with dimensions of $2000 \times 1000 \times 20$ nm^3 the total energy is minimized for a wall angle between the two large domains of 145° instead of 180° [74, 292]. For this wall angle the wall energy density is reduced by about 50% (see Fig. 2.3(b)). As point symmetry has to be preserved in the real Landau pattern both large domains split into two sub-domains with a low angle domain wall in-between (see Fig. 4.1(a)). In the center of the rectangle a vortex-like structure evolves. The magnetization in each subdomain includes a relatively large angle of 17.5° with the long axis of the rectangle. In order to reduce stray field energy the angle is gradually reduced on the way to the outer edges to minimize surface charges at the expense of volume charges as a consequence of the spatial dependence of the demagnetization factor (see Fig. 4.31 in the results of section 4.6.2), so that the stated angle tilt has to

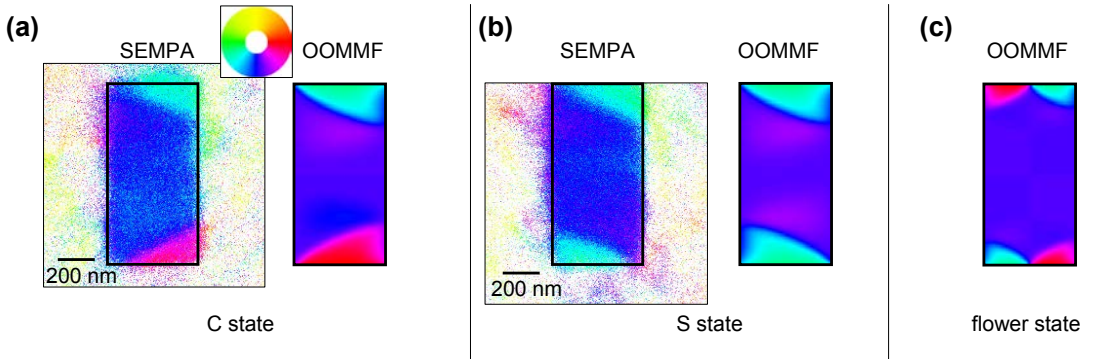

Figure 4.2: Domain patterns of high remanence states. (a) C state, (b) S state, and (c) flower state. The magnetization is color coded according to the given color wheel. In (a) and (b), besides the pattern obtained from micromagnetic simulations using OOMMF, a SEMPA micrograph of a $1000 \times 500 \times 20$ nm^3 permalloy structure is given as well.

be understood as a mean value. In the experiments the degree of wall angle tilt depends on the quality of the structure edges [292, 296].

Diamond state

The diamond state consists of seven domains and exhibits mirror symmetry with respect to the short axis of the rectangle (see Fig. 4.1(b)). Basically, the main difference to the Landau state is the center domain, which is oriented in parallel to the short axis. The other six domains, which are of the same size as the small domains for the ideal Landau pattern, can be regarded as flux-closure domains. In contrast to the ideal Landau state the ideal diamond state only exhibits 90° walls. As recently shown via micromagnetic simulations the closure domains of a real diamond state split as well in order to reduce the total energy of the structure [287].

4.1.2 High remanence states

Besides the flux-closure states the other class of domain patterns in submicron rectangles are the high remanence states. Also for these states the magnetization is oriented in the film plane but it is nearly oriented homogeneously along the long axis as it is the case for straight wires as shown in Fig. 3.1(a). In order to reduce the magnetostatic energy characteristic inhomogeneities near the short edges of the elements develop (more details, see Ref. [74]). Three different high remanence states exist in rectangular structures that are named after the course of the magnetization within the structure: In Fig. 4.2 the (a) C state, (b) S state, (c) flower state can be seen.

4.1.3 Phase diagram

Except for the cross-tie and the flower state all introduced domain patterns were experimentally observed in the rectangles fabricated for the MR investigations reflecting the fact that they correspond to local minima in the energy landscape. In

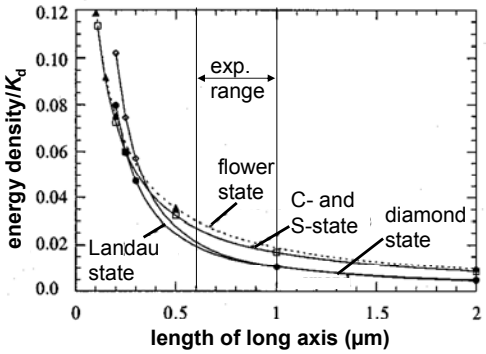

Figure 4.3: Total energy density in units of $K_\mathrm{d} = \frac{\mu_0}{2} M_\mathrm{S}^2$ for the various micromagnetic states in 20 nm thick rectangles with a lateral aspect ratio of 2:1 in dependence of the length of the long axis. In order to mimic permalloy the parameters of the calculations are $A = 1.3 \cdot 10^{-11}$ J/m, $M_\mathrm{S} = 800$ kA/m, and $K = 500$ J/m^3. From Ref. [74]

Fig. 4.3 the calculated energy density of the different states are given as a function of the length of the long rectangle axis in the case of 20 nm thick permalloy. Below 100 nm length the flower state is the global minimum. Above, the C and S state, which are nearly similar in energy, are the energetically favorable configurations[4]. The transition from the flower state to the C or S state with increasing length is caused by a reduction in stray field energy as in the flower state the two domains at each edge (instead of one in the case of the C or S state) occupy each only half of the width and therefore extending only half as wide into the element [74]. Consequently, the flower state exhibits a higher remanence. Replacing the C and S state the first flux-closure state that becomes global energy minimum at a length of 250 nm is the Landau state. This state is favored compared to the diamond state at relatively small lengths as it consists only of four domains in contrast to seven, so that the total wall length is smaller. However, the reason why the Landau state is replaced by the diamond state at about a length of 1.1 μm is due to the fact that in contrast to the (ideal) Landau state the (ideal) diamond state only possesses 90° Néel walls, that are about ten times lower in energy than a 180° Néel wall (see Fig. 2.3(b)). At a large length of about 4.3 μm the cross-tie structure is the global minimum, which achieves a further reduction in energy by reducing the total length of the 90° walls [74].
In the range of 600 nm to 1000 nm investigated in this thesis the Landau state is the global energy minimum but at least the C, S, and diamond state are local minima. The occurrence of a particular state in remanence depends on the magnetic history as shown in section 4.5.

[4]Strictly speaking, in remanence the C state is slightly lower in energy. But already in the presence of small external fields that are not aligned in parallel along the long axis the S state is favored due to the Zeeman energy term.

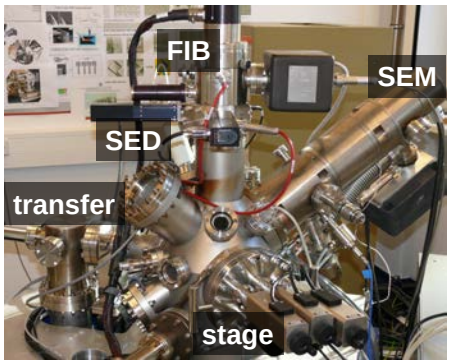

Figure 4.4: Exterior view of the UHV-dualbeam chamber, which also contains the *in situ* MR setup. The main components are tagged.

4.2 Experimental setup

The preparation of the microcircuits including the submicron rectangles as well as of the V-shaped wires, which are the topic in chapter 3, were performed with focused ion beam (FIB) technique. An exterior view of the used ultra-high vacuum (UHV) dualbeam chamber can be seen Fig. 4.4. The term dualbeam is commonly referred to as a combination of FIB and scanning electron microscope (SEM). Besides the sample preparation, the investigation of the rectangles via magnetotransport was performed in the very same UHV chamber. For that purpose the chamber is equipped with further components, which are presented in detail in part 4.2.2. Beforehand, in the following section 4.2.1 an overview about the basic instrumentation of the UHV chamber and their importance concerning the preparation and MR investigations is given.
The possibility for a direct structuring of micro- and nanostructures and its subsequent investigation via magnetotransport in the very same UHV chamber was realized with this setup for the first time. The setup is presented in detail in Ref. [E1].

4.2.1 UHV-dualbeam chamber

Besides the *in situ* MR setup for the investigation of nanostructures, the UHV-dualbeam chamber is equipped with the three basic components: the FIB column, the SEM, and the stage. The FIB column[5] operated with a gallium liquid metal ion source is mounted in the vertical position to provide highest stability. The ion beam can be focused up to a full width at half maximum intensity of about 10 nm. For the FIB operation a base pressure of $< 10^{-8}$ mbar is required, which is fulfilled as the typical base pressure of the chamber is $< 5 \cdot 10^{-10}$ mbar. The working principle of the FIB technique is not addressed here so that the interested reader is referred to Refs. [297, 298, 299]. The interaction of high energetic ions with matter is briefly described in section 4.4.1. Unless otherwise stated the typical specifications of the FIB preparation are: energy of the Ga^+ ions 30 keV, probe current $20 - 40$ pA, and step size of the scanning 5 nm. In order to obtain a homogeneous material removal,

[5] Canion 31-Plus, Orsay Physics

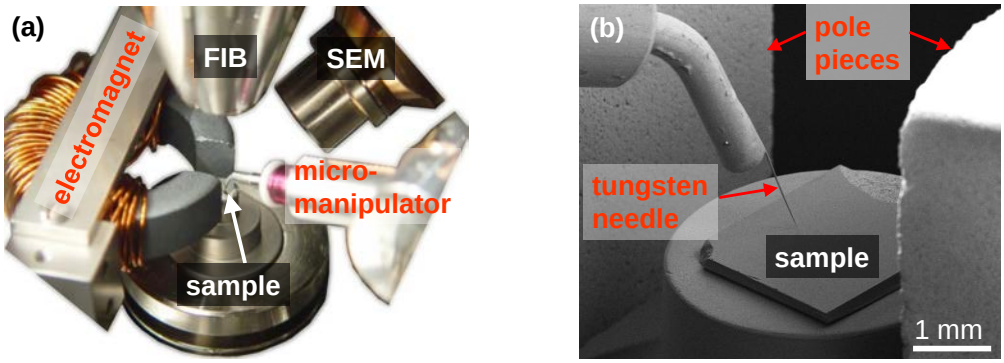

Figure 4.5: (a) Photograph and (b) SEM image showing the arrangement of the main components within the UHV-dualbeam chamber.

i.e., to avoid edge and redeposition effects, the dose is applied in several cycles with a maximum area (line) dose per cycle of 200 μC/cm^2 (1000 pC/cm). For the used films within this thesis these dose values typically correspond to a material removal of less than 0.5 nm per cycle.
The SEM column[6] is mounted at 58° with respect to the vertical direction and has a lateral resolution of about 25 nm. The SEM is used as a non-destructive method to monitor the FIB preparation as well as the electrical contacting via the micromanipulator.
The five axis stage[7] enables the manipulation of the sample position in all three directions with an accuracy in the micron range manually or by means of a motor control unit. Furthermore, the sample can be rotated by 360° and tilted by 30°. The latter degree of freedom was not used within this thesis so that the sample surface was always oriented horizontally. After the inward transfer of the specimen into the chamber the height of the sample was aligned in such a way that the electron and the ion beam hit the sample in the same small area. After FIB preparation the MR investigations could be performed immediately at the very same sample position.

4.2.2 *In situ* magnetoresistance setup

In this section, the *in situ* MR setup for the investigation of nanostructures is presented. In Fig. 4.5(a) the interior of the dualbeam chamber can be seen, in particular the components for the MR investigation. Basically, it consists of two components: An electromagnet and a micromanipulator which is utilized for the electrical contacting of the structures. In the following, the two components are briefly described. The upgrade of the setup performed within the scope of this thesis is presented in section 4.7.

Electromagnet

The electromagnet consists of a softmagnetic ferrite toroid which is wrapped with approximately 250 turns of a capton-covered copper wire of 0.5 mm diameter acting

[6] JAMP-30, JEOL Ltd.
[7] AP-81030, JEOL Ltd.

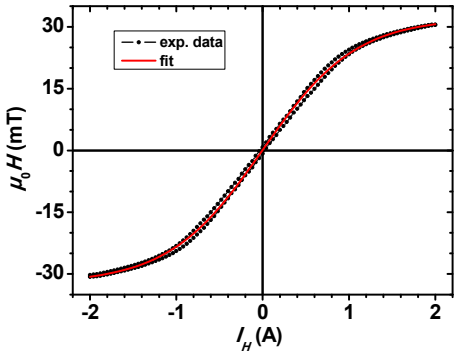

Figure 4.6: Dependence of the magnetic field $\mu_0 H$ generated in the gap of the toroid on current I_H. The calibration curve was phenomenologically fitted by a Boltzmann equation.

as coil. The toroid exhibits a gap of about 6 mm for the sample to be placed in between (see Fig. 4.5(b)). The magnet is attached to a linear feedthrough via a titanium holder, which allows a movement of the magnet in one direction and a rotation around the axis of the feedthrough. This enables the precise centering of the sample between the pole pieces for the MR measurements and the retraction of the magnet from measuring position to clear the way for sample exchange.
Before the magnet was incorporated in the chamber the magnetic field $\mu_0 H$ that is produced in the gap of the toroid in dependence of the current through the coil I_H was measured by means of a Hall probe. As the side planes of the pole pieces are much larger than the sample, the magnetic field can be considered as homogeneous within the gap. The corresponding calibration curve is displayed in Fig. 4.6. The magnet has only a small remanence and exhibits a linear current to field behavior up to currents of about 0.8 A, which corresponds to fields of about 19.5 mT. At the maximum current of ± 2 A the magnet is almost saturated producing a field of about 30.6 mT. The resistance of the coil is about 0.7 Ω, so that also for the maximum current of ± 2 A only a small power of 2.8 W is produced. The associated Joule heating for continuous operation at 2 A results in a temperature increase at the coil up to 40 °C, however, no temperature increase within the gap of the toroid was detected. This shows that the heat is predominantly transported to the titanium holder via thermal contact. Thus, the thermal stability at the sample position is maintained. Furthermore, the temperature at the coil is sufficiently low in order to avoid parasitic outgassing of the capton coverage which would disturb the ultra-high vacuum conditions.

Micromanipulator

Generally, the electrical contacting even for structures with lateral dimensions above one micron is challenging. For instance, utilizing electron-beam lithography (EBL), which is frequently used for nanostructuring, one additional EBL process with several time consuming steps is required for the contacting [300, 270, 290, 301]. Here a very time-saving method was used. In order to contact the nanostructures electrically a tungsten needle with a sharp tip of a few 100 nm in diameter attached to a

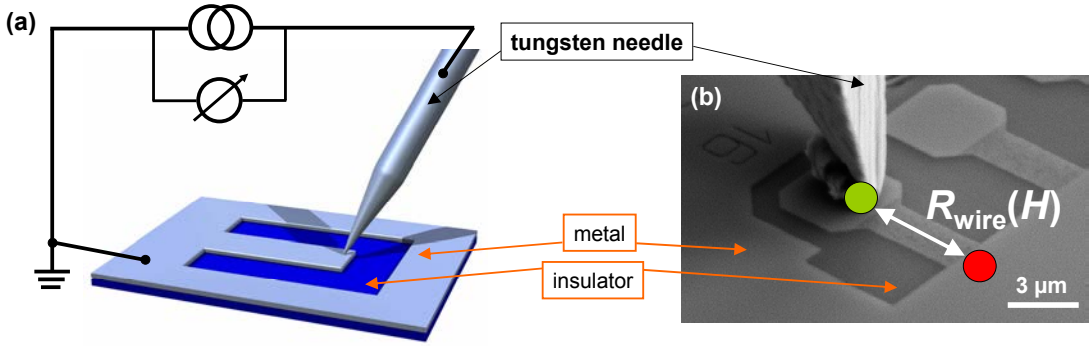

Figure 4.7: (a) Scheme of the *in situ* MR measurement principle. The nanowire, which is connected to the grounded film at one side, is milled from a laterally homogeneous ferromagnetic film by using FIB. The resistance of the wire can be measured when the tungsten needle attached to a micromanipulator contacts the end of the wire. The approaching process of the tip of the needle is monitored via SEM. (b) SEM micrograph of a nanowire with the needle in MR measuring position (green dot). The red dot marks the position of the needle for measuring the film in front of the wire. The difference of both MR measurements basically corresponds to the resistance $R_{\mathrm{wire}}(H)$ of the wire.

micromanipulator[8] is utilized (see Fig. 4.5(b)). The micromanipulator is mounted at the stage and enables the positioning of the needle and thus the electrical contacting of any point of the sample with an accuracy in the nanometer range.

4.3 MR measurement scheme

The micromanipulator enables to perform two-point probe measurements as the sample holder serves as second electrode. A sketch of the resistance measurement principle of nanostructures is given in Fig. 4.7(a). The FIB is utilized to remove the film material down to the electric insulating substrate to create any kind of structure, which is connected to the film at one side. The tungsten tip contacts the other side of the structure and a current is driven through the structure via the needle to the film and the voltage drop is measured. The disadvantage of this method (two-point probe measurement) is that the voltage drop (resistance) of the whole circuit is measured, including in particular contributions of the tungsten needle and of the ferromagnetic film. Generally, these undesired contributions are small. They can be quantified and eliminated to a certain amount by performing quasi-three point measurements, i.e., the tip is additionally positioned in front of the structure on the film as demonstrated in Fig. 4.7(b). By subtracting the resulting MR curve from the MR curve, where the needle contacts the structure, the MR curve of the mere structure is obtained in a good approximation. The magnetization reversal of softmagnetic thin films for fields applied in the film plane generally is a stochastic process, so that the subtraction cannot eliminate all features in the MR curve induced by the film. However, in the case of the MR measurements of the rectangles the undesired MR contributions of the film are even smaller than the resolution of

[8]MM3A-EM UHV, Kleindiek Nanotechnik GmbH

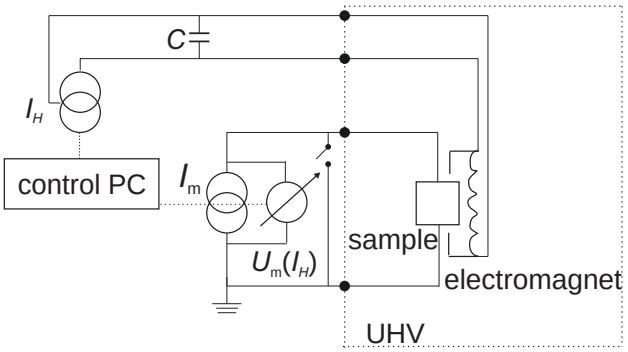

Figure 4.8: Circuit diagram of the *in situ* MR setup.

the measurement as shown in section 4.4.4. Furthermore, as there can be different contact resistances between tip and film in successively contactings the above mentioned procedure might yield an error in the determination of the overall resistance of the structure.
Prior to the MR investigations of a sample series the tip of the tungsten needle was typically sharpened to a diameter of a few 100 nm utilizing the FIB. This procedure enables to cut e.g. a nagged or damaged tip *in situ* so that no tip exchange is necessary which would be connected with a time-consuming venting and bake-out of the UHV chamber.
The typical MR measurement procedure of a microstructure was performed as follows: First, the sample was correspondingly rotated to reorient the sample with respect to the direction of the magnetic field. Then, the magnet was positioned around the sample. The following approaching process of the tip to contact the micro-circuit was monitored via SEM. In the meantime the electrical loop was grounded to prevent any discharging that would damage the structure. When the tip came in mechanical contact with the structure, a slight bending of the tip was observed. Then, the movement of the tip was stopped, the grounding was removed, and a resistance measurement was performed. Generally, the resistance was found to drift over time probably caused by further sliding of the tip across the structure due to the strain that was created during tip bending. To get rid of the drift the tip was slightly lifted in the lowest mode (steps of 5 nm) until the resistance remained constant over time. Finally, the MR measurement was started.
For the resistance measurements a programmable current source and nanovoltmeter were used[9]. The pulse delta mode was chosen, which has the advantages compared to the direct current mode that the average power fed into the sample is reduced and that a higher signal to noise (S/N) ratio can be attained. The S/N ratio is 10^5 when synchronization with the frequency of mains is made.
For the MR measurement the direct current through the coil of the electromagnet I_H was typically swept in 200 steps from $+I_{H,\max}$ to $-I_{H,\max}$ and then reversed by utilizing a programmable bipolar current source[10]. Both current sources and the nanovoltmeter were addressed by a control PC for the automatic recording of

[9]Keithley Model 6221 AC and DC current source; Keithley Model 2182A Nanovoltmeter
[10]Kepco Bipolar Operational Power Supply 20-5M

the MR measurement curve (see Fig. 4.8). At each magnetic field step I_H the voltage drop $U_{\mathrm{m}}(I_H)$ was measured utilizing a rectangular current pulse with an amplitude of $I_{\mathrm{m}} = 300\ \mu$A and a duration of $t = 10$ ms (duty cycle of 10%). For the rectangle structures this current corresponds to maximum current densities of $5 \cdot 10^{10}$ A/m^2. In the current range of $0.1 - 0.5$ mA no deviations from Ohm's law were detected revealing that the used current density did not cause any detectable heating of the submicron samples. Furthermore, this current density is about two orders of magnitude lower than required to move domain walls in permalloy via the spin-transfer-torque [60]. Consequently, the probing current can be regarded to be non-invasive.

4.4 Preliminary considerations and investigations

As presented above the *in situ* MR setup enables the investigation of structures which have an electrical connection at one side to the magnetic film (see Fig. 4.7). In order to investigate single nanostructures that are magnetically decoupled from the film the approach has to be modified as schematically shown in Fig. 4.9. Again, the micro-circuit is contacted at one side with the tungsten needle. The current is driven from the needle to the film which serves as second electrode crossing the ferromagnetic particle in between. In contrary to the approach presented above in the environment of the ferromagnetic particle the long range magnetic order of the film material is destroyed due to Ga^+ ion bombardment. Importantly, as the bombarded film material serves as electrical input leads for the MR investigation it has to maintain a low resistance in order to keep the sensitivity for magnetogalvanic effects high.
The following section 4.4.1 briefly introduces the anisotropic magnetoresistance (AMR) which is used as a probe for the magnetization orientation of the rectangles. Section 4.4.2 deals with the experimental principle and the investigations, which were performed to find a film system that can be rendered paramagnetically by means of FIB while a good conductance is guaranteed. The magnetic properties and the influence of the ion bombardment on the structural and chemical properties of the superior film system used for the MR investigation of the rectangles are presented in the subsequent section 4.4.3. The details of the micro-circuit including the ferromagnetic rectangle as well as the FIB procedure of its preparation are described in section 4.4.4. The section closes with a proof of principle of the MR investigation method (section 4.4.5).

4.4.1 Anisotropic magnetoresistance of multi-domain particles

As a probe for the magnetization orientation the anisotropic magnetoresistance (AMR) was utilized, which is the dominating MR effect in permalloy thin films. The AMR is presented in detail in section 5.1.4. For the investigations conducted in this chapter it is sufficient to know the dependence of the resistance on magnetization orientation $\mathbf{M}$ with respect to the current direction $\mathbf{j}$ as a consequence of the

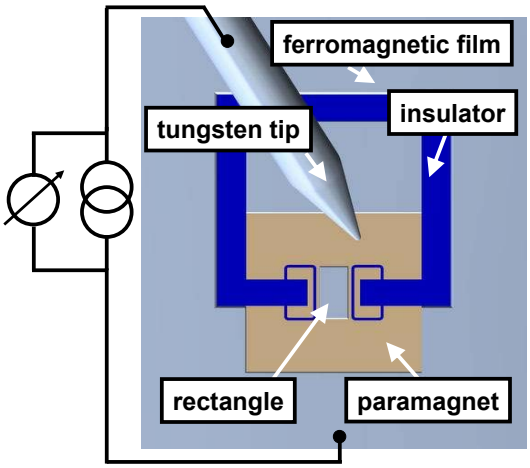

Figure 4.9: Sketch of the layout of the micro-circuit and the *in situ* MR measurement principle to investigate magnetically decoupled nanostructures. The tungsten tip contacts the circuit within the blue yoke-shaped frame. In the frame region the ferromagnetic film is totally removed by FIB milling, so that the current, which flows from the tip to the film, has to pass the small ferromagnetic rectangle within the gap of the yoke-shaped frame. The environment of the rectangle is rendered paramagnetically by FIB irradiation while a good conductance is maintained.

presence of the AMR:

$$R(\varphi) = R_{||} - \underbrace{(R_{||} - R_{\perp})}_{\Delta R>0} \cdot \sin^2\varphi = R_{||} - \Delta R \cdot \frac{M_{\perp}^2}{M_{\mathrm{S}}^2} \quad , \tag{4.1}$$

where φ is the angle between $\mathbf{M}$ and $\mathbf{j}$. From the equation it becomes apparent that the resistance is smallest (highest) when $\mathbf{M}$ and $\mathbf{j}$ are oriented perpendicularly (in parallel) to each other. $\Delta R/R_{\perp}$ defines the AMR-ratio.
Eq. 4.1 is valid for a homogeneous magnetization orientation. In the following it is explained how the overall resistance is composed of the contribution of the individual domains in the case of a multi-domain pattern. The AMR is a π-periodic effect. Thus, two domains of the same dimensions both exhibit the same resistance, when the magnetization is oriented in an antiparallel manner to each other. As the overall magnetization averages out, this special case clearly points out that for the calculation of the overall resistance by means of Eq. 4.1 no average magnetization $\frac{M_{\perp}}{M_{\mathrm{S}}}$ may be assumed (macrospin model). Instead, the resistance of each domain has to be calculated individually via Eq. 4.1, while its relative contribution to the overall resistance depends on its area filling. This ansatz implies that the current density is homogeneous within the ferromagnetic particle although the conductivity of the individual domains is different due to the AMR. This so-called uniform current model [290] is justified in a good approximation, as shown in the following by simple considerations, because the AMR-ratio is typically only a few percent.
Imagine a hypothetical particle consisting of two domains A and B, where the domain wall is oriented perpendicularly to the current direction (see Fig. 4.10(a)). The domain wall is regarded as infinitesimal small and its contribution to the resistance

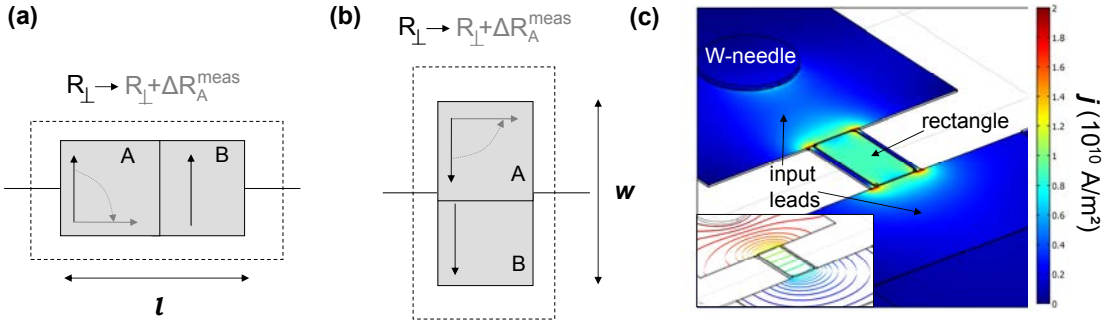

Figure 4.10: (a) and (b) are circuit diagrams for two domains that are connected in series and in parallel, respectively. While the magnetization of domain A switches from perpendicularly to in parallel oriented with respect to the current direction the resistance increases by $\Delta R_{\mathrm{A}}^{\mathrm{meas}}$. (c) Simulated current density distribution within a rectangle with dimensions of 1000×500 nm^2 for a current of $I = 0.15$ mA. The inset shows the lines of equal potential. For the simulation the resistivity and dimensions of the rectangle and of the input leads were used that were determined from the experimental results of section 4.4.3 for the Cr/Py/Pt stack.

is neglected. The position of the domain wall and therefore the relative length of the domains $l_i = a_i \cdot l$, $i = \mathrm{A}, \mathrm{B}$, is arbitrary ($l = l_{\mathrm{A}} + l_{\mathrm{B}} = (a_{\mathrm{A}} + a_{\mathrm{B}})l = \text{const.} \Rightarrow a_{\mathrm{A}} + a_{\mathrm{B}} = 1$). As generally $R = \rho l/wt$ applies, where t is the thickness, w the width of the particle, and ρ the resistivity, the resistance is the same as for two independent particles that are connected in series. The overall resistance $R_\perp$ and the overall maximum resistance change due to the AMR, i.e., ΔR, are simply subdivided on both domains according to their lengths (areas):

$$R_{\perp,i} = R_\perp \cdot a_i, \quad \Delta R_i = \Delta R \cdot a_i, \quad i = \mathrm{A}, \mathrm{B} \tag{4.2}$$

If only the magnetization of domain A switches from perpendicularly to in parallel oriented to the current (domain A in Fig. 4.10(a)), while the other orientation of magnetization is fixed, the measured resistance change $\Delta R_{\mathrm{A}}^{\mathrm{meas}}$ is just proportional to the area of the former domain (A) in accordance with the uniform current model:

$$\Delta R_{\mathrm{A}}^{\mathrm{meas}} = (R_{\perp,\mathrm{A}} + \Delta R_{\mathrm{A}} + R_{\perp,\mathrm{B}}) - R_\perp = \Delta R \cdot a_{\mathrm{A}} \tag{4.3}$$

More complex is the situation if a hypothetical particle is considered, where the domain wall is oriented in parallel to the current direction (see Fig. 4.10(b)). In the case of an arbitrary domain wall position $w_i = a_i \cdot w$, $i = \mathrm{A}, \mathrm{B}$, ($w = w_{\mathrm{A}} + w_{\mathrm{B}} = (b_{\mathrm{A}} + b_{\mathrm{B}})w = \text{const.} \Rightarrow b_{\mathrm{A}} + b_{\mathrm{B}} = 1$) the situation is equivalent to two homogeneously magnetized particles that are connected in parallel (as $R = \rho l/wt$ applies). Thus, $R_\perp$ and ΔR are subdivided on both domains according to the reciprocal of their widths (areas):

$$R_{\perp,i} = R_\perp / b_i, \quad \Delta R_i = \Delta R / b_i, \quad i = \mathrm{A}, \mathrm{B} \tag{4.4}$$

If now, again, only the magnetization of domain A switches from perpendicularly to in parallel oriented with respect to the current direction the measured resistance

change is:

$$\Delta R_{\mathrm{A}}^{\mathrm{meas}} = \frac{R_{\perp,\mathrm{B}} \cdot (R_{\perp,\mathrm{A}} + \Delta R_{\mathrm{A}})}{R_{\perp,\mathrm{A}} + \Delta R_{\mathrm{A}} + R_{\perp,\mathrm{B}}} - R_{\perp} \tag{4.5}$$

Utilizing the expressions of Eq. 4.4 yields:

$$\Delta R_{\mathrm{A}}^{\mathrm{meas}} = \Delta R \cdot b_{\mathrm{A}} \cdot \left(1 + b_{\mathrm{B}} \frac{\Delta R}{R_{\perp}} + b_{\mathrm{B}}^2 \left(\frac{\Delta R}{R_{\perp}}\right)^2 + ...\right) \approx \Delta R \cdot b_{\mathrm{A}} \text{ for } \Delta R \ll R_{\perp} \tag{4.6}$$

In this case the measured resistance change is only proportional to the area of domain A in a first approximation. However, as the AMR-ratio is typically $\Delta R/R_{\perp} \approx 1\%$ the deviation of the measured value $\Delta R_{\mathrm{A}}^{\mathrm{meas}}/R_{\perp}$ from $b_{\mathrm{A}}\Delta R/R_{\perp}$ is proportional to $(\Delta R/R_{\perp})^2$ and therefore two orders of magnitude smaller than the measured quantity. As the sketched situation considers the extremal case, where the resistance difference between both domains is maximum, the made statement is valid for arbitrary orientations of magnetization of both domains. Furthermore, it remains valid for any domain pattern as any domain pattern can be described by a combination of an arbitrary number of parallel and serial circuits.
Besides the influence of the magnetization on the current density also the current path may provide an inhomogeneous lateral current density profile within the particle. For the layout used for the MR investigations of the rectangles the lateral current density distribution was simulated (for $\mathbf{M} = 0$)[11]. The result is displayed in Fig. 4.10(c) revealing that the current density can be regarded as laterally homogeneous within the rectangle in a good approximation.
In conclusion, in the analysis of the experimental MR curves of the rectangles the assumption of a homogeneous current density is justified, so that the resistance contribution of the individual domains depends only on their area filling and magnetization orientation.

4.4.2 Realization of paramagnetic leads

In order to find an adequate film system, which enables the FIB creation of paramagnetic leads with a commensurate electrical conductance for the suggested MR investigation of magnetically decoupled nanostructures (see Fig. 4.9) first the interaction of solids with energetic 30 keV Ga^+ ions provided by the FIB has to be understood. This process is briefly described in the next section 4.4.2.1. Comprehensive overviews about this topic are e.g. given in Ref. [299, 302]. In section 4.4.2.2 the composition of the used layered film systems and their preparation are given. Section 4.4.2.3 introduces the principle, which was developed and applied to investigate the effects of Ga^+ ion irradiation on the magnetic and electrical properties of the films. Finally, the results of this investigation for the different film systems are presented and discussed.

[11] Software Comsol multiphysics, www.comsol.com

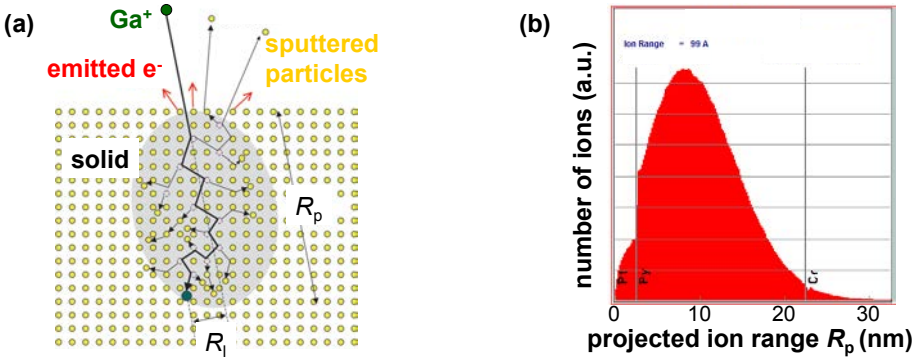

Figure 4.11: (a) Scheme of the incidence of an energetic Ga^+ ion hitting a crystal lattice. Due to elastic scattering processes with the target atoms a widely ramified collision cascade is produced. From Ref. [302]. (b) Transport of Ions in Matter (TRIM) simulation [303] of the projected ion range distribution of 30 keV Ga^+ ions in a 10 nm Cr/ 20 nm Py/ 2.5 nm Pt stack.

4.4.2.1 Ga^+ ion bombardment of solid states

If an energetic ion hits a solid state (target) the kinetic energy of the ion is transferred to the target atoms due to elastic and inelastic interactions [302]. In the actual case under consideration of 30 keV Ga^+ ions hitting targets with similar atomic mass the passage of an ion can be described by the so-called linear cascade model [299]. In this regime the momentum of the ions is sufficient, so that elastically strucked target atoms can contribute to a further branch of the cascade, as schematically shown in Fig. 4.11(a). As the main part of the elastic energy transfer yields the production of phonons, the number of atoms kicked from their former lattice points within the volume of the cascade is relatively low. Thus, the assumption that predominantly independent two-body collisions occur is justified[12]. If a cascade takes place in the vicinity of the surface target atoms can be sputtered. This means that the energy transfer to surface atoms is sufficient to overcome the surface binding energy of the target material. After $\approx 10^{-11}$ s the kinetic energy of the ion is completely transferred to the target and the ion gets implanted. As can be seen in Fig. 4.11(b) for low doses, where sputtering is negligible, the projected ion range and thus the Ga concentration within the target material is almost normally distributed[13]. For 30 keV Ga^+ ions the mean projected range is about $10 - 100$ nm depending on the target material and atomic structure [299].
In the cascade volume plenty of lattice defects are generated yielding a subsequent amorphization with dose [305]. As the ion gets implanted also the chemical composition of the target changes [306]. In the case of multilayers intermixing of the atoms of both layers can occur, if the cascade volume reaches to the interface. Multilayer systems whose magnetic properties depend strongly on the quality of the stacking

[12]This assumption is only justified if collision cascades that are produced by different ions do not temporally overlap. This is the case if the ion density of the beam is smaller than 10^4 A/cm^3 [304]; this is justified in our experiment and for the FIB technique in general, with $< 10^3$ A/cm^3.
[13]Note that in the TRIM simulation the target is assumed to be amorphous. Furthermore, ion implantation and sputtering is neglected.

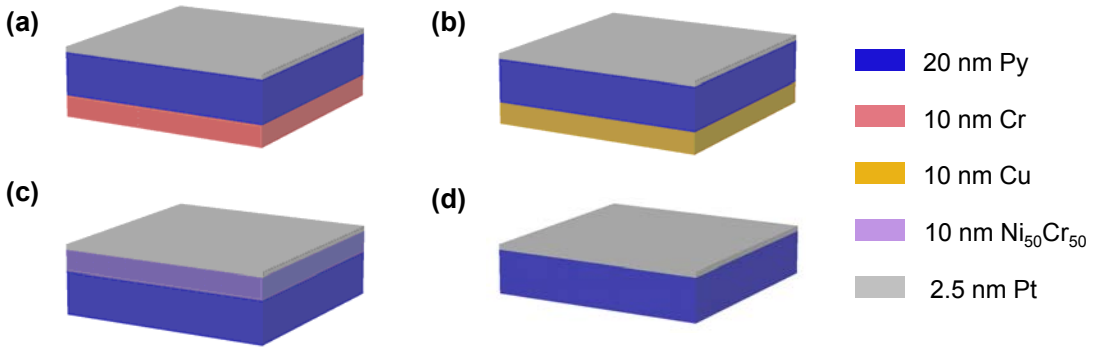

Figure 4.12: Schemes of the fabricated stacks: (a) Cr/Py/Pt, (b) Cu/Py/Pt, (c) Py/NiCr/Pt, (d) Py/Pt.

and interfaces are very sensitive to ion bombardment. Examples are the interface anisotropy of Co/Pt multilayers, which are the topic of chapter 5 [307, 308, 309, 153], or the giant magnetoresistance (GMR) effect [310, 311]. The first time it was shown that ion bombardment can be a versatile tool to tune the corresponding magnetic properties on purpose was demonstrated by C. Chappert et al. utilizing Co/Pt multilayers in 1998 [312]. In general, the required dose is so small that sputtering is negligible and hence a "pure magnetic modification" is possible. For more details about the influence of ion irradiation on the magnetic and structural properties of various multilayer systems the reader is referred to the comprehensive review articles of J. Fassbender et. al. [313, 314].

4.4.2.2 Film preparation and used film systems

The layered films are prepared by means of electron-beam evaporation at a base pressure of 10^{-8} mbar at room temperature. In the chamber up to three different materials can be evaporated from different melting pots. Depending on the material the deposition rate was in the range of $0.2 - 1$ Å/s and was controlled via a thickness monitor (quartz crystal microbalance technique). As substrate material electric insulating Si_3N_4 was used.
An overview about the prepared stacks is given in Fig. 4.12. The stacks are described and motivated in the following. As ferromagnetic layer permalloy ($Ni_{81}Fe_{19}$) was used for all stacks. Permalloy is a softmagnetic standard material, which exhibits a relatively high anisotropic magnetoresistance (AMR) [13]. This is desirable as the AMR was the probe for the investigation of the magnetization reversal of the rectangles. The thickness was chosen to be 20 nm which corresponds to the thickness of the standard problem No. 1 (see introduction of this chapter).
In literature it was demonstrated that relatively high doses are required to render permalloy paramagnetically due to Ga^+ ion implantation [315, 306, 316] as approximately 20 at% of Ga in permalloy are necessary to produce a paramagnetic alloy. For the 20 nm thick film this high concentration cannot be obtained before the whole film is sputtered. Generally, seed and cap layers are used to improve the adhesion of the magnetic films and to prevent it from oxidation, respectively [317, 314]. As pure Ga implantation is not sufficient enough, these layers should also contribute

to render the permalloy layer paramagnetically at a relatively low ion dose due to ion beam-induced mixing, so that for the MR investigation of the rectangles paramagnetic input leads with a good conductance can be created (see Fig. 4.9). Coincidentally, for the typical seed layer materials Cr and Ta it is known that already a small amount of these metals in permalloy destroys the long range magnetic order ($\approx$ 8 at% Cr [318, 319, 320], $\approx$ 10 at% Ta [305, 320]). As the vapor pressure of Ta is low it was not possible to prepare Ta with the used setup so that only Cr was applicable as seed layer (see Fig. 4.12(a)). From literature it is known that Cr can be efficiently ion-beam mixed with permalloy [321, 322].
Similar to Cr a small amount of Cu in permalloy yields a paramagnetic alloy [318]. Thus, a stack with Cu as seed layer was also fabricated (see Fig. 4.12(b)). For both metals a seed layer thickness of 10 nm was used. This thickness was a compromise as on the one hand, the thickness should be as small as possible in order to avoid significant current shunt through the seed layer to keep the sensitivity for galvanomagnetic effects high. On the other hand, the thickness was not chosen smaller as the paramagnetic regime should be achieved, while the ion beam-induced mixing of the stack with the electric insulating substrate is as small as possible as it degrades the conductivity of the leads.
A third stack was prepared by using a 10 nm thick paramagnetic $Ni_{50}Cr_{50}$ alloy on top of the Py layer (without a seed layer) following a work performed by Kaminsky et al. [323] (see Fig. 4.12(c)). They demonstrated that a 15.5 nm Py/ 9 nm $Ni_{50}Cr_{50}$ stack is already rendered paramagnetically due to 30 keV Ga^+ ion beam-induced mixing of the layers before the whole NiCr layer is sputtered. Another reason to use such a stack was that according to TRIM simulations the mean range of the 30 keV Ga^+ ions was estimated to be about 10 nm (see Fig. 4.11(b)). As the interface between Py and NiCr is located at that distance a more efficient intermixing was expected already for the very first incoming ions in comparison to the films with the Py layer on top, where the interface is located at a distance of 22.5 nm to the surface.
As a reference also a pure 20 nm Py film was prepared (see Fig. 4.12(d)).
The used materials oxidize under ambient conditions, so that all samples were capped with a Pt thickness of 2.5 nm[14]. It was expected that the intermixing of Py with Pt has only minor influence on the degeneration of the long range magnetic order as R. E. Parra and J. W. Cable showed that the saturation magnetization of NiPt alloys only slightly depends on the Pt concentration up to a Pt fraction of 50 at% [325, 326, 320, 327]. However, at higher Pt concentrations a strong decrease was found, so that at a Pt fraction of 58 at% the alloy is already paramagnetic. As a consequence of the ion beam-induced mixing these high Pt concentrations were only expected at rather low doses in the vicinity of the former Py/Pt interface region, while at high doses most of the Pt was sputtered. This statement is confirmed by the results presented in section 4.4.3.

[14]The oxidation of the films should be avoided as the insulating Ni- and Fe-oxides drastically change the electrical and magnetic properties [324].

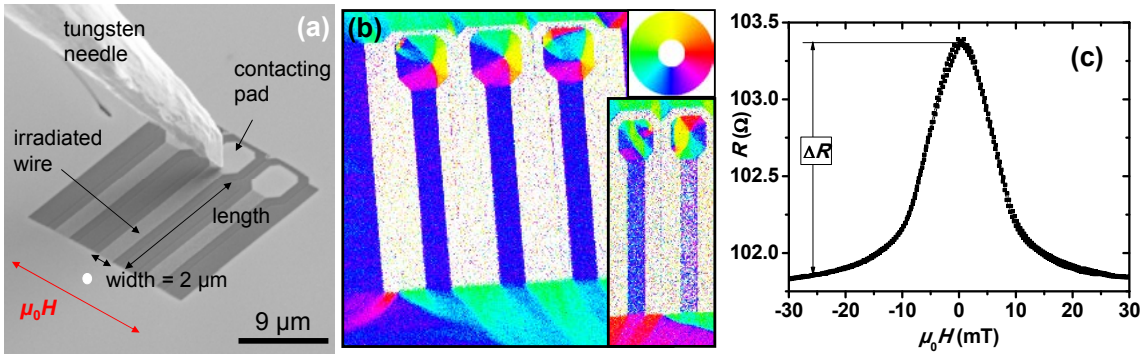

Figure 4.13: (a) SEM image of three wires carved from Cr/Py/Pt film with the tungsten tip in measuring position. Note that the wire regions appear darker than the pristine film as a consequence of the Ga^+ ion irradiation. White dot, see text. (b) SEMPA image of the remanence state of three unirradiated wires (left) and of two wires where an area dose of 160 and 1,600 $\mu C/cm^2$ was applied, respectively (lower right). The magnetization in the wire regions is single-domain with a magnetization pointing downwards as indicated by the color wheel. (c) MR measurement of one of the unirradiated wires shown in (b) with the field oriented along the short wire axis (see red arrow in (a)).

4.4.2.3 Influence of ion bombardment on resistance and AMR

Investigation principle: This paragraph deals with the principle to investigate the influence of the Ga^+ ion irradiation on the electrical and magnetotransport properties of the stacks. The principle is based on the preparation of Ga^+ ion irradiated, micron-sized wires by means of FIB technique and their subsequent characterization via *in situ* magnetoresistance measurements. Three wires can be exemplarily seen in Fig. 4.13(a). In the dark regions the film material was completely removed by FIB milling. For that purpose an area dose of 20,000 $\mu C/cm^2$ was used, which is sufficient for all stacks. The wires consist of a contacting pad, where the samples were contacted with the tungsten needle, and of a wire region, where a particular area dose was applied. Various wires with varying area dose in the range of 0 (control), $160 - 16{,}000$ $\mu C/cm^2$ were prepared. The wire shape supplies a well-defined current path and thus enables a precise determination of the conductivity of the (irradiated) film material. As a probe for the degeneration of the long range magnetic order with dose the strength of the AMR-ratio can be utilized [318]. This quantity can be easily determined from MR measurements of the wires which is explained in the following. In the SEMPA images of Fig. 4.13(b) it can be seen that in remanence the magnetization is oriented along the long wire axis due to the shape anisotropy. According to the equation for the AMR (Eq. 4.1) the resistance is then at its maximum. As shown in Fig. 4.13(c) by applying a field in the direction of the short wire axis (transverse MR geometry) a reversible parabolic reduction of the resistance with field was found. According to Eq. 4.1 this behavior can be attributed to a coherent rotation of the magnetization into the field direction. The resistance decreases until the magnetization is oriented along the short wire axis. In a good approximation this is the case at the maximum field of 30 mT as the almost saturated MR curve indicates. Thus, the maximum resistance change in transverse

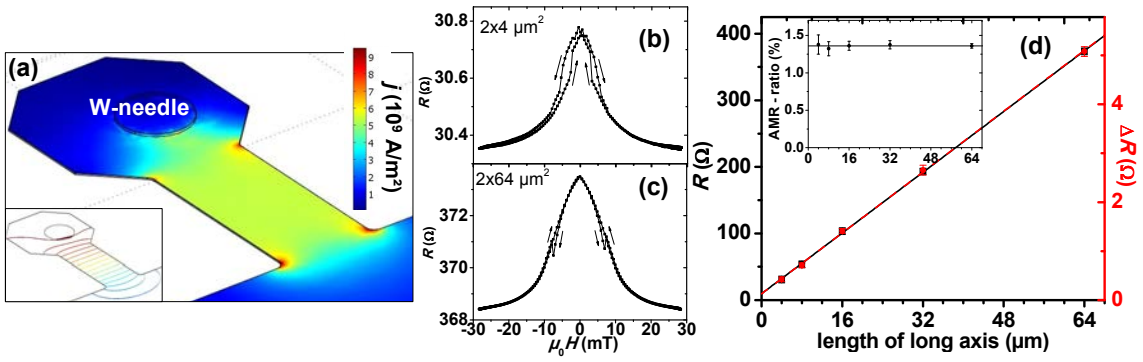

Figure 4.14: (a) Simulated lateral current density distribution of a wire sample ($w = 2$ μm, $t = 30$ nm) for a current of $I = 0.3$ mA. The inset shows the lines of equal potential. (b) and (c) displays transverse MR curves of rectangles with $s = 2$ and $s = 32$, respectively. (d) shows the dependence of the resistance $R(0)$ (■) and ΔR (●) as a function of the length of the long wire axis, while the inset gives $\Delta R/R(0)$, i.e., the AMR-ratio. The lines are linear fits.

MR geometry resembles ΔR in Eq. 4.1.
The SEMPA investigations reveal the presence of single-domain states in remanence for aspect ratios s of the wire region of $s = 2 - 32$ (wire width 2 μm). The reason why also for $s = 2$ a single-domain state is present, while it resembles the aspect ratio of the rectangles investigated in this work, can be explained by the fact that the magnetic wire is in direct exchange contact to the adjacent magnetic film and contacting pad. Consequently, no magnetic poles are created at the wire ends so that besides the exchange energy also the stray field energy in the wire region is reduced. Hence, the demagnetization field H_D is the same as for an infinite long wire, so that H_D can be estimated by $|H_\mathrm{D}| \approx M_\mathrm{S} t/w \approx 10$ mT (Eqs. 2.7, 2.9). As the available maximum field in the experiment is 30 mT a width of 2 μm was chosen in order to have the possibility to reorientate the magnetization along the short wire axis, which is the case as shown in Fig. 4.13(c). It should be recalled that Fig. 4.13(c) is a difference measurement, where the MR measurement of the film was subtracted (tungsten needle located at the position indicated by the white dot in Fig. 4.13(a)). The MR measurement of the film only shows small changes of the resistance with field of $\lesssim 0.05$ Ω revealing that the rest of the circuit in the MR measurements of the wires basically provides a field independent off-set of about $10 - 20$ Ω depending on the film system.
Besides the wire region, in the transition regions to the film and to the contacting pad the current density is relatively high. This can be seen in Fig. 4.14(a), where the simulated current density distribution is displayed[15]. Consequently, the transition regions provide significant contributions to the MR signal despite the accomplishment of difference measurements. In order to examine their contributions transverse MR curves of unirradiated Cr/Py/Pt wires with different lengths (aspect ratios s) were measured. This enables a quantification as the contributions of the wire regions increase linearly with wire length while the contributions of the transition

[15]Software Comsol multiphysics, www.comsol.com

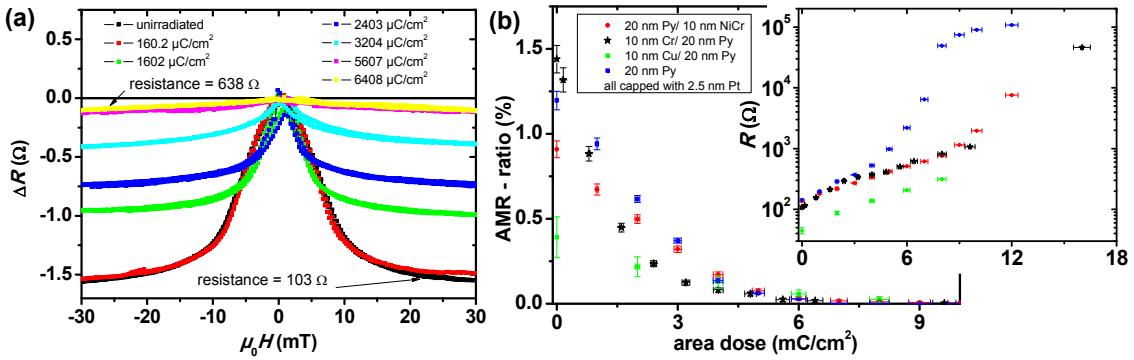

Figure 4.15: (a) Array of transverse MR curves $\Delta R(\mu_0 H) = R(0) - R(\mu_0 H)$ of Ga^+ irradiated Cr/Py/Pt wires. (b) AMR-ratio and resistance $R(0)$ (inset) as a function of area dose for the four film systems.

regions remain constant. Fig. 4.14(b) and (c) show the difference measurements for $s = 2$ and $s = 32$, respectively. From the curves the resistance in remanence $R(0)$[16] and $\Delta R = R(0) - R(\mu_0|H| = 30\ \text{mT})$ were evaluated. The results are plotted in Fig. 4.14(d) in dependence of the length of the long wire axis. Both values lie on linear slopes as expected from $R = \rho \cdot l/(w \cdot t)$. The slopes intersect with the ordinate at $R = (10 \pm 3)\ \Omega$ and $\Delta R = (0.13 \pm 0.03)\ \Omega$. These constant (length independent) fractions can be attributed to the transition regions and becomes particularly noticeable in the MR curve for the shortest wire in deviations from the parabolic shape at low fields (see Fig. 4.14(b)). The relative contribution of the transition regions to the total signal is significantly reduced for $s = 8$ (see Fig. 4.13(c)) and is not observable in the MR curve for $s = 32$ (see Fig. 4.14(c)). Nevertheless, the obtained MR-ratio $\Delta R/R(0)$ does not depend on wire length, so that this quantity is already well estimated for $s = 2$ (see inset of Fig. 4.14(d)).

Results and discussion: For the investigations of the influence of the Ga^+ irradiation an aspect ratio of $s = 8$ was used for all film systems. This is a compromise between the minimization of the influence of the transition regions and of the duration of the FIB preparation of a single wire sample. Besides saving time the latter should be kept as small as possible to minimize thermal drift that destroys the quality of the structure. Fig. 4.15(a) exemplarily shows transverse MR curves of differently Ga^+ ion irradiated Cr/Py/Pt wires. From the curves the MR-ratio $\Delta R_{AMR}/R(0)$ in saturation ($\mu_0|H| = 30\ mT$) was determined. The dose dependence of the MR-ratio for the four stacks is displayed in Fig. 4.15(b). For all films the MR-ratio decreases monotonically with dose. As the AMR is only present in ferromagnetic materials a vanishing of the effect indicates the loss of ferromagnetism. For the Cr/Py/Pt stack the decrease of the AMR-ratio with dose is strongest (black stars), so that the paramagnetic regime (vanishingly small AMR-ratio) is achieved with the lowest dose of all films. In addition, the pristine Cr/Py/Pt stack exhibits the largest MR-ratio of (1.44±0.05)%, which makes it the best candidate for the MR

[16]The specification of the micromagnetic state is only of minor importance as in this study the AMR-ratio is $\lesssim 1.5\%$.

investigation of the ferromagnetic rectangles. Despite the current shunt through the Cr the MR-ratio is even larger than for the pure Py film with $(1.20 \pm 0.05)\%$. Such a behavior has also been found by Lee et al. for permalloy films by using NiCr alloys as seed layers [317]. The authors attribute the enhancement of the AMR-ratio to both the decrease in the resistivity and the increase in $\Delta\rho$ triggered by a larger grain size and a pronounced (111) texture. The question if these structural differences are also the reason for the enhanced AMR-ratio in the Cr/Py/Pt was not subject of this thesis.
The AMR-ratio for the stack with Cu as seed layer is more than three times lower than for using Cr. This behavior can be mainly attributed to a larger current shunt through the Cu as indicated by the much smaller resistivity of the pristine stack compared to all other stacks (see inset of Fig. 4.15(b)). This finding was qualitatively expected from the (room temperature bulk) conductivity of Cu ($\sigma_{Cu} = 58.8\ (\mu\Omega\text{cm})^{-1}$ [83]), which is much higher than for Cr ($\sigma_{Cr} = 7.8\ (\mu\Omega\text{cm})^{-1}$ [83]).
For the stack with the NiCr layer a slightly higher dose is required to render it paramagnetically compared to the stack with Cr as seed layer. This result shows that the possibly improved intermixing, as it was expected prior to the investigation (see previous section), is overcompensated by the less amount of Cr in the NiCr layer. Compared with the investigation of Kaminsky et al. a more than three times higher paramagnetic dose is required [323], which can be explained to some extent by the usage of a 4.5 nm thicker permalloy layer.
In conclusion, the results of the dose dependence of the AMR-ratio strongly favor the Cr/Py/Pt stack for the investigation of the magnetoresistance of the rectangles. However, to be suited for the investigation the dose dependence of the resistance should be preferably small. At the dose of 5,600 μC/cm^2, where the AMR-ratio is reduced to about 1% of the value of the pristine stack, the remaining metallic material can be regarded as being paramagnetic. For such a dose the resistance is only about five times larger than for the unirradiated wire (see inset of Fig. 4.15(b)), so that the stack is very well suited and therefore chosen for the MR investigation of the rectangles. In contrast to the Cr/Py/Pt stack, for the Py/Pt sample it was observed that the vanishing of the AMR-ratio occuring at a higher dose of 7,000 μC/cm^2, is connected with a strong increase of the resistance by a factor of 80 compared to the unirradiated stack. This high value in resistance indicates that at the paramagnetic dose already a large amount of the metallic material is sputtered. Furthermore, it reveals that the Ga implantation in combination with the ion beam-induced mixing with the substrate material is not sufficient to create a paramagnetic alloy that is still a good conductor.
For the preparation of the micro-circuits from the Cr/Py/Pt stack a safety margin for rendering the leads paramagnetically was considered, so that a slightly higher dose of 6,000 μC/cm^2 was utilized. For such leads the total resistance of the micro-circuits is only $80 - 190\ \Omega$ as shown in section 4.6. The actual value depends on the rectangle size and its orientation. With the resolution of the MR setup of $\Delta R/R \approx 1 \cdot 10^{-5}$ (see section 4.3) this enables the detection of resistance changes down to $\approx 1 - 2$ mΩ.
It may well be assumed that a more efficient intermixing can be obtained by utilizing a Cr/Py/Cr sandwich system. But as for the Cr/Py/Pt stack the paramagnetic

regime is already reached when the remaining metallic material has still a conductance that is comparable with the pristine stack it was decided to abstain from using a sandwich due to the following reasons. First, it should be possible to easily perform SEMPA investigations of the remanence state of the rectangles. Due to the short probing depth of SEMPA (see section 3.1.1) the material on top of the permalloy layer have to be removed by soft Ar^+ ion sputtering before SEMPA investigation [232]. For thick cap layers this process step is time-consuming and it is a challenge to tune the Ar^+ ion sputtering process to the desired remaining film thickness. This means in particular, that the Py/NiCr/Pt stack would have exhibited outstanding advantages, if it was to be used instead of the Cr/Py/Pt stack. Second, a Cr/Py/Cr sandwich would conceal the danger that the ion beam-induced intermixing could be too effective so that the magnetic properties are altered already on low ion dose application as it is the case e.g. for Co/Pt multilayers mentioned in section 4.4.2.1. The reason to avoid such a high level of sensitivity on dose is connected with the characteristic radial beam profile of a FIB [328]. It consists of an intensive center, which can be described by a Gaussian distribution with a FWHM of ≈ 10 nm and a long tail whose intensity decays exponentially. At a distance of 100 nm from the center the Ga^+ intensity is about 1% of the center intensity. This means that at this distance from the paramagnetic regions a dose of ≈ 60 μC/cm^2 is applied, which would alter the magnetic properties if the stack is too sensitive. From Fig. 4.15(b) it becomes evident that for the Cr/Py/Pt stack for the lowest dose of 160 μC/cm^2, where a small material removal of about 0.2 nm can be detected via AFM (see section 4.4.2), the AMR-ratio (resistance) is only slightly reduced (enhanced). This finding shows that the long tail of the ion beam does not alter the magnetic properties of the mere rectangular structure and reveals that significant gradual material modifications only take place at the structure edges with an edge width considerably smaller than 100 nm.
More details about the influence of the ion bombardment on topography and chemical composition of the Cr/Py/Pt stack are given in the following section. Beforehand, this section deals with the results of the comprehensive characterization of the magnetic and electrical properties of the Cr/Py/Pt stack used for the MR investigation of the rectangles.

4.4.3 Properties of the 10 nm Cr/ 20 nm Py/ 2.5 nm Pt stack

In a first step the remagnetization of the stack was determined by performing MOKE measurements for various in-plane orientations of the magnetic field. Fig. 4.16 shows the remagnetization curves for the direction with highest and lowest remanence, respectively, which are oriented 90° to each other. The curve with highest remanence (easy axis curve) is rectangular with almost complete remanence. At the coercive field of (0.7 ± 0.2) mT the remagnetization abruptly occurs via nucleation of domains, that are oriented in parallel to the field, and subsequent domain wall motion. The hard axis curve also shows a small hysteresis revealing that besides a coherent rotation of the magnetization domain wall movement contributes to the signal as well. Due to the presence of the latter it is only possible to estimate from the curve an upper bound for the uniaxial magnetocrystalline anisotropy constant K. For that

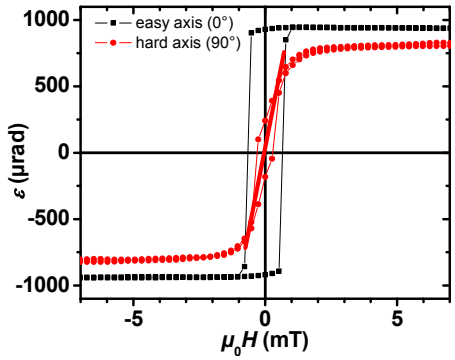

Figure 4.16: Magnetization reversal of the Cr/Py/Pt stack for in-plane fields along two perpendicular directions with highest and lowest remanence. The curves were obtained by utilizing the longitudinal magnetooptical Kerr effect. The thick red line is a linear fit to the hard axis curve for the estimation of the uniaxial in-plane anisotropy constant of the Py layer.

purpose a linear curve is fitted to the curve which runs through the points where the curve starts to open (see thick red line in Fig. 4.16). According to Eq. 2.25 (first order approximation) it is $\frac{\epsilon}{\epsilon_S} = \frac{M_\perp}{M_S} = \frac{\mu_0 H M_S}{2K}$, where ϵ_s is the ellipticity in saturation. Utilizing the slope of the curve $s = \epsilon/(\mu_0 H)$ and the saturation magnetization of permalloy (see below) the anisotropy can be obtained via $K = \frac{M_S}{2}\frac{\epsilon_S}{s}$ to $K = (360 \pm 30)$ J/m^3. This value is two orders of magnitudes lower than the shape anisotropy of the rectangles (see Fig. 2.1), so that it can be neglected in the considerations of section 4.6.2, where the magnetic energies of the rectangles are presented.

For a precise analysis of the MR curves of the rectangles the magnetoresistance properties of the stack have to be examined. The magnetoresistance was characterized by four-point-probe measurements utilizing a macroscopic wire sample. The wire was prepared simultaneously with the laterally homogeneous sample used for the *in situ* investigations utilizing a shadow-mask technique, which is explained in detail in section 5.2.3. The dimensions of the wire are $l' = 6$ mm and $w = 0.5$ mm. The current is driven through the wire while the voltage drop along $l = 4$ mm is measured. The dependence of the resistance on magnetic fields up to ± 6 T is shown in Fig. 4.17(a). The two curves show the resistance for in-plane fields that are oriented in parallel and perpendicularly to the current direction, respectively. As can be seen in particular in the inset the anisotropic MR dominates the resistance change at small fields as the magnetization can easily be field aligned. In both geometries a linear decrease in resistance was found which dominates the resistance change at high fields. The slope is almost identical in both geometries and of about $1 \cdot 10^{-6}$/mT. This behavior is often referred to as annihilation of spin-waves with field. Details about the so-called spin-disorder MR are given in section 5.1.4. As the magnetic fields in the *in situ* measurements are relatively small (≤ 30 mT), the spin-disorder contribution of $\lesssim 2\ m\Omega$ is comparable to the measurement resolution, so that it can be neglected compared to the AMR contribution.

For a quantitative discussion of the MR curves of the rectangles the strength of the AMR of the film has to be evaluated. From the field sweep measurements of the

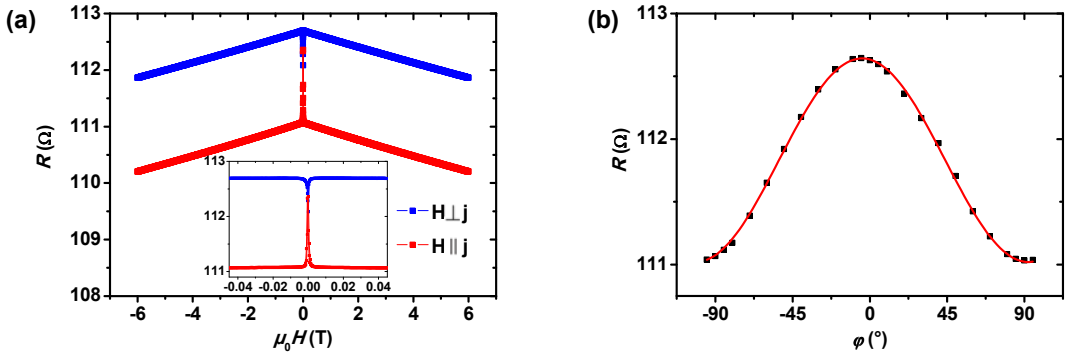

Figure 4.17: Magnetoresistance behavior of the 10 nm Cr/ 20 nm Py/ 2.5 nm Pt stack. For the MR measurements a macroscopic wire sample with dimensions of $l' = 6$ mm, $w = 0.5$ mm is used, while the voltage drop is measured along a length of $l = 4$ mm. (a) $R(\mu_0 H)$ curves for **H** applied in parallel (blue) and perpendicularly (red) to the current direction, respectively. The inset is a zoom revealing the curves for small fields. (b) R as a function of φ, where φ is the angle between current and magnetization **M**, while the latter is also oriented in the film plane. A magnetic field strength of $\mu_0 H = 50$ mT was used forcing **M** always parallel to **H**. The red solid line is a fit according to Eq. 4.1.

macroscopic wire sample the resistivity change due to the AMR $\Delta\rho = \Delta R \cdot \frac{w \cdot t_{\mathrm{Py}}}{l}$ was determined to

$$\Delta\rho_{\text{ex situ}} = (0.39 \pm 0.02)\ \mu\Omega\text{cm} \quad , \tag{4.7}$$

where t_{Py} is the thickness of the permalloy layer. This value was cross-checked by rotating the sample in an in-plane saturation field of 50 mT (see Fig. 4.17(b)). As the spin-disorder MR is isotropic this enables a precise determination of $\Delta\rho$.
$\Delta\rho$ was also determined from the *in situ* MR measurement of the unirradiated wire sample to $\Delta\rho_{\text{in situ}} = (0.37 \pm 0.02)\ \mu\Omega$cm (see Fig. 4.13(c)). It should be noted that the *in situ* and *ex situ* wires have the same aspect ratio so that the extrinsic quantities R and ΔR can be directly compared with each other. From both investigation methods similar values were found, in particular, the AMR-ratios are in accordance within the experimental error margins: $\Delta R/R_{\text{in situ}} = (1.44 \pm 0.05)\%$, $\Delta R/R_{\text{ex situ}} = (1.52 \pm 0.03)\%$. The good correspondence between the results of both investigation methods demonstrates the suitability of the *in situ* MR investigation procedure for the wire samples for the characterization of the resistivity and the AMR of the films.
Besides the precise knowledge of $\Delta\rho$ for the quantification of the anisotropy of the rectangles, it is essential to know the saturation magnetization. The saturation magnetization of the stack was determined via superconducting interference device (SQUID)[17] and cross-checked via ferromagnetic resonance (FMR)[18] to

$$M_{\mathrm{S}} = (820 \pm 40)\ \text{kA/m} \tag{4.8}$$

The SQUID and FMR measurements were performed by O. Albrecht and F. Balhorn, respectively, both from Institute of Applied Physics, University of Hamburg.

[17] For details about SQUID, see Ref. [329].
[18] For details about FMR, see section 5.3.2.2

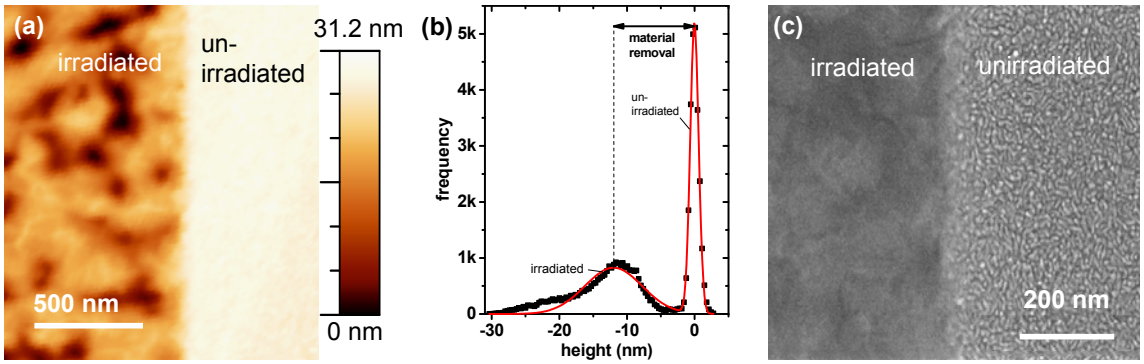

Figure 4.18: Detail of (a) AFM and (c) SEM image of the transition region between film and irradiated area, where the paramagnetic dose of 6,000 μC/cm^2 was applied. (b) is the histogram of the height profile of the AFM image.

Influence of the ion bombardment on the topography and composition

This section briefly discusses the influences of ion irradiation on film topography and chemical composition. For the former atomic force microscopy (AFM)[19] and high resolution scanning electron microscopy (SEM) were utilized. In order to quantify the material removal height profiles were taken from the transition regions between the FIB irradiated wires and the pristine film via AFM (see Fig. 4.18(a)). In each case the histograms of the height profiles $z(x, y)$ show two Gaussian profiles which can be attributed to the unperturbed film and to the irradiated area, respectively (see Fig. 4.18(b)). The distance between both accumulation points in the histograms corresponds to the averaged material removal. For the whole area dose range up to 20,000 μC/cm^2, where the whole film is sputtered, a linear dependence of material removal with dose was found. The slope corresponds to a sputter rate of $Y_r = (0.20 \pm 0.05)$ μm^3/nC. The investigation in particular reveals the remarkable result that after the application of the paramagnetic dose of 6,000 μC/cm^2 in the average only 12 nm of the film material is removed. This means that for the input leads nearly 2/3 of the metallic film is still available for the electrical conductance. The relatively large error in Y_r is not caused by an inaccuracy in dose application or AFM measurement but is a consequence of the upcoming surface roughness with dose (see irradiated area in Fig. 4.18(a),(c)). As indicated by the scale bar in Fig. 4.18(a) the maximum height difference of 31.2 nm nearly corresponds to the total thickness of the Cr/Py/Pt stack of 32.5 nm revealing that for the paramagnetic dose the complete film is almost locally removed. For higher doses no closed film coverage exists anymore and islands of film material develop.
The roughness is not caused by a spatial inhomogeneous dose application - the step size of the scanning of the FIB is 5 nm - but can be explained with a different orientation of the crystal lattice of the crystallites with respect to the direction of ion incidence, which is explained in the following. If a crystal lattice has a high symmetry with respect to the direction of ion incidence an ion can penetrate more deeply into the crystal using the "channels" between neighboring atomic lattice planes before it hits a target atom (channeling effect) [330, 331, 332]. Thus, the collision

[19]For details about AFM or other scanning probe techniques, see e.g. Ref. [236].

cascade starts in a deeper region so that the energy transfer to surface atoms and consequently the sputter rate is reduced. Accordingly, in a polycrystalline sample with a random orientation of the crystallites the sputter rate locally varies resulting in a strong roughening of the surface. A standard measure for the roughness of the film is the root mean square (RMS) roughness, i.e., the standard deviation of the height profile $z(x, y)$ from the mean value of the height $\overline{z}$:

$$\sigma_{\mathrm{RMS}} = \sqrt{\frac{1}{M \cdot N} \sum_{n,m=1}^{M,N} (z(x_m, y_n) - \overline{z})^2} \tag{4.9}$$

After the application of the paramagnetic dose the RMS roughness was increased to 6 nm, while the pristine film has only a value of $\sigma_{\mathrm{RMS}} = 0.6$ nm. Further dose application again reduced the roughness (see e.g. the insulating regions in Fig. 4.20). This can be explained with the absence of the channeling effect for the amorphous Si_3N_4 substrate in combination with the so-called edge effect [302]: At an edge a larger area of the collision cascade takes place in the vicinity of the surface so that the sputter rate at edges is enhanced. More explicitly, the higher the gradient in the height profile the larger the sputter rate so that the surface roughness decreases with increasing dose.
Besides the roughening, a growth of the grain size with dose was found. While the unirradiated film has a grain size of $\lesssim 10$ nm as determined via high resolution SEM images (see Fig. 4.18(c)) for the paramagnetic dose the irregular island-like grains have a large size distribution with diameters of about 50 nm to 200 nm (see Fig. 4.18(a),(c)). An ion beam induced grain growth was often found for polycrystals and can be attributed to the energy transfer from the ions to the target atoms [333, 315].
From Fig. 4.18(c) it can be seen that a transition region of finite size exists between the paramagnetic area and the ferromagnetic film with a width of $\lesssim 40$ nm. In this region an intermediate grain size of about $20 - 30$ nm can be estimated that determines the roughness of the (rectangle) edges due to the channeling effect. The magnetic edge, however, is probably smoother than the topographic edge as it is reasonable to assume that predominantly the applied dose determines the magnetic properties of the film.

In order to investigate the dose dependence of the chemical composition of the film energy dispersive x-ray spectroscopy (EDX) was performed[20]. For the investigation 18 squared areas with an edge length of 10 μm were FIB irradiated with different area doses in the range of $160 - 19{,}200$ μC/cm^2. For each area the middle part with dimensions of about 3×3 μm^2 was scanned with a SEM beam and the originating x-ray spectrum was recorded via an EDX-detector. By scanning such a large area possible influences of the laterally inhomogeneous material removal on the spectra are averaged out. To obtain quantitative results from the analysis of the spectra the measurement time for each irradiated area was the same (1,500 s) and all experimental parameters were held constant during investigation with around 1,300 detected

[20]For details about EDX, see e.g. Ref. [240].

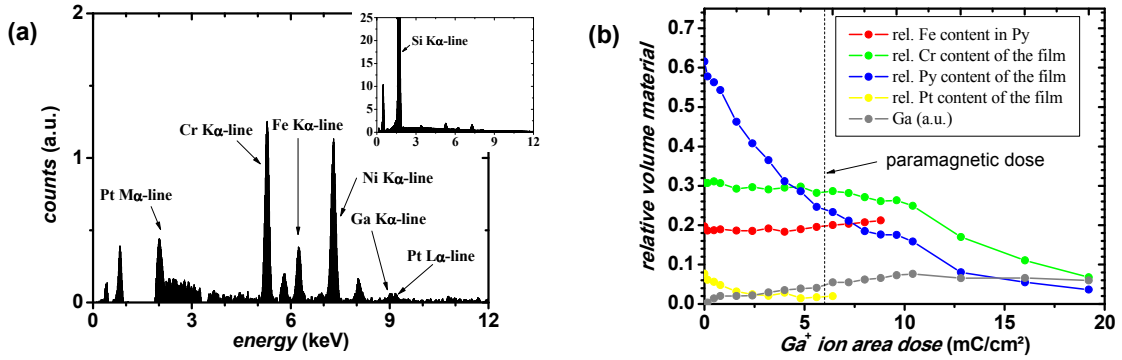

Figure 4.19: (a) X-ray spectrum of the stack, where a dose of 1,600 μC/cm^2 was applied. This spectrum was obtained from the raw spectrum (see inset) by subtracting the spectrum of the mere Si_3N_4 substrate. Note that the dominating Si Kα line has a peak value of about 200 counts revealing that only about 1 of 100 characteristic x-rays originates from the film material. (b) Dose dependence of the film composition.

x-rays per second. The energy of the e$^-$-beam was chosen to $E_0 = 20$ keV, which is sufficient to push the inner shell electrons of all film elements as well as Ga out of the atoms to generate characteristic x-rays. The disadvantage of such a high energy is that the penetration depth d of the electrons is $d \approx 2$ μm according to the following empirical equation $d = \frac{0.1E_0^{1.5}}{\rho}$, $[d] = \mu$m, $[E_0] =$ keV, and $[\rho] =$ g/cm^3 [240]. Consequently, the x-ray spectra are dominated by the characteristic Kα line of the Si substrate, which is beneath the 200 nm thick electric insulating Si_3N_4 layer, as can be exemplarily seen in the inset of Fig. 4.19(a). Nonetheless, the characteristic x-ray peaks of the film elements and Ga are clearly distinguishable from the bremsstrahlung's background. For the quantitative analysis of the film composition the contributions of the Si Kα line and of the bremsstrahlung have to be eliminated. For that purpose a spectrum of the mere Si_3N_4 covered Si substrate without film was recorded as well. Afterwards, this spectrum was subtracted from the spectra of the (FIB irradiated) film areas. Before the subtraction the Si Kα peak height of the substrate spectrum was correspondingly normalized to the Si Kα peak height in the particular measurements. As can be exemplarily seen in Fig. 4.19(a) the difference spectra basically reveal the fractions of the Ga$^+$ ion bombarded film. For the quantification of the dose-dependent film composition the Kα lines of the implanted Ga and of the film elements Cr, Fe, and Ni, as well as the Lα line of the Pt were used. For each line the intensity within the half width at half maximum of each line peak was integrated. The (integrated) intensities of each line were normalized to the corresponding line intensity obtained from the (difference) spectrum of the unirradiated film. For each film element this quantity is a measure for the remaining amount of material. To get direct access to the dose dependence of the film composition the normalized line intensities were weighted according to the known volume material composition of the unirradiated film: Py : Cr : Pt = 8 : 4 : 1. This calibration is necessary as the cross-sections for the generation of the characteristic x-rays for the particular elements are different.
The so determined film composition in dependence of Ga$^+$ dose is displayed in Fig. 4.19(b). There was no calibration standard for Ga so that only a qualitative

trend for the amount of implanted Ga can be extracted from the Ga Kα line intensity (gray curve). The amount of implanted Ga increases up to a dose of about 10 mC/cm^2, while it is nearly constant at higher doses. This behavior can be explained by the fact that at high doses the Ga implantation is overcompensated by the sputtering of the former implanted Ga. This stationary state is reached, when a film thickness is sputtered which corresponds to the averaged range of the Ga^+ ions [299]. In contrary to low doses, where the Ga depth distribution within the target material follows a Gaussian curve (see Fig. 4.11(b)), the maximum Ga concentration is expected to be near the surface [302]. Park et al. investigated the Ga implantation depth profile of the stationary state after the sputtering of Py with 50 keV Ga^+ ions by means of Auger electron spectroscopy (AES) in combination with gradual soft Ar^+ ion sputtering [316]. They found a maximum in the Ga concentration of $15 - 20$ at.% in the range of $0 - 20$ nm from the surface and a subsequent exponential decrease with depth, suchlike that in 100 nm depth the Ga concentration was ≈ 4 at.%. Compared to this thesis the energy of the Ga^+ ions was higher (larger projected ion range) and the sputter rate was about half the size, so that the mentioned Ga concentrations can be seen as upper bounds. More importantly, Park et al. also determined the Ga implantation depth profile in the lateral direction [316]. This profile follows an exponential law with a maximum of 50 at.% Ga at the surface and a lifetime of only about 3 nm, so that at a depth of 10 nm Ga was not detected. This finding shows that undesired Ga implantation in the lateral direction, which might significantly alter the magnetic properties, is restricted to the direct vicinity of the structured edges.
Coming back to the dose dependence of the film composition, the amount of volume material of Ni and Fe (blue line) can be phenomenologically described by an exponential decay with a lifetime of (6.4 ± 0.4) mC/cm^2. As indicated by the red line the ratio of the Fe to Ni material is independent on dose, so that a preferential sputtering of one of the Py constituents can be ruled out.
At low doses the Cr sputtering is basically hindered by the overlaying Py and Pt layers, so that up to a dose of about 10 mC/cm^2 the amount of Cr is unchanged and then decays exponentially with a lifetime of (8 ± 2) mC/cm^2 (green curve).
The dose dependence of the Pt material can also be well-described by an exponential decay with a lifetime of (1.2 ± 0.2) mC/cm^2.
In order to interpret the exponential behavior it should be recalled that the AFM investigation reveals that in the average the volume material removal is linear with dose. Thus, at the first glance the exponential decays might indicate that drastic ion beam-induced mixing of the layers among each other and at high doses also with the substrate material occur. But this conclusion is hazy as the sputter yield locally varies due to the channeling effect, so that in particular for area doses slightly higher than the paramagnetic dose of 6,000 μC/cm^2 the film is locally removed as mentioned above. As a consequence, not every ion contribute to the removal of the film material anymore, so that only an effective dose acts yielding to deviations from the linear film material removal with dose.
However, in conclusion it is unquestionable that i.a. for the paramagnetic dose the Ga bombardment creates a NiFePtGa alloy whose stoichiometry exhibits a heterogeneous depth profile. In order to get a better understanding about the chemical

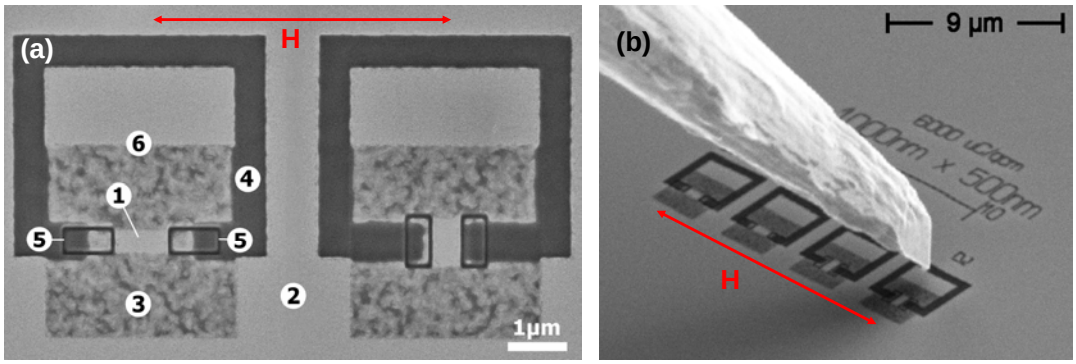

Figure 4.20: (a) SEM micrograph of two micro-sized circuits with different orientations of the ferromagnetic rectangles (1) with respect to the field direction (see red arrow). The rectangles of a size of 800 × 400 nm^2 are surrounded by paramagnetic material (3) which was created by Ga^+ ion bombardment out of the ferromagnetic film (2). The dark gray parts (4,5), where the metal was totally removed by sputtering, are electrically insulating. (b) SEM image of four micro-circuits with 1000 × 500 nm^2 sized rectangles. The tip is positioned a few microns above one of the structures.

composition after Ga^+ ion bombardment, AES in combination with soft sputtering or scanning ion mass spectroscopy (SIMS) would be appropriate. Furthermore, a visual impression about the intermixing might be provided by cross-sectional transmission electron microscopy.

4.4.4 FIB procedure for preparing micro-circuits

SEM images of two micro-circuits for the MR investigation of the rectangles can be seen in Fig. 4.20(a). The FIB preparation was performed in three steps: in the first step a yoke-shaped structure (4) was milled with a Ga^+ area dose of 20,000 μC/cm^2, which insulates the framed region from the film (2) except for the small part in the gap of the yoke. In the second step the rectangle (1) in the gap of the yoke was created. For that purpose, the area around the rectangle was irradiated with a Ga^+ area dose of 6,000 μC/cm^2 (3) in order to destroy the long-range magnetic order while conductance is maintained (see above). Narrow isolation lines (5) were prepared in the third step close to the rectangle (nominal distance of 75 nm) so that almost the whole current has to pass through the rectangle and any bypassing current is kept negligibly small (see Fig. 4.10(c)). This layout creates the highest current density of the whole electrical circuit in the region of the rectangle, which enhances the sensitivity for the ferromagnetic structure. This preparation procedure guarantees the most precise geometry of the rectangle as any distortion due to thermal drift is minimized. The second micro-sized circuit on the right-hand side of Fig. 4.20(a) has a different orientation of the rectangle with respect to the magnetic field and current direction. This arrangement enables the investigation of both generic geometries (hard and easy axis) without rotating the sample. Fig. 4.20(b) shows a SEM image of four micro-circuits (two for each rectangle orientation) that are successively prepared by FIB with the tungsten tip positioned a few microns above one of the structures.

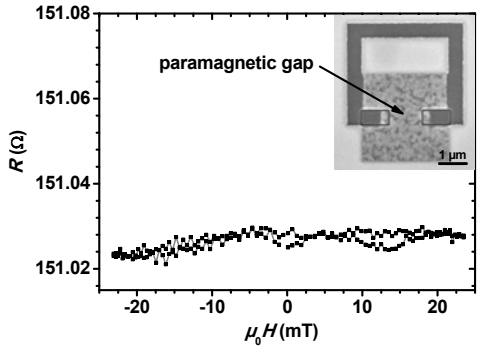

Figure 4.21: MR measurement of a paramagnetic gap. An SEM micrograph of the micro-sized circuit is shown as inset.

For the two different measurement geometries the maximum resistance change of the rectangles due to AMR was calculated using the value $\Delta\rho_{\text{ex situ}}$ obtained from the *ex situ* measurement of a macroscopic wire (see Eq. 4.7) via $\Delta R = \Delta\rho \cdot \frac{l}{w \cdot t_{\text{Py}}}$. When the current runs along the short and the long axis the maximum resistance change due to AMR is

$$\Delta R_{\text{ea}} = (0.10 \pm 0.01)\ \Omega \quad \text{and} \quad \Delta R_{\text{ha}} = (0.39 \pm 0.04)\ \Omega \quad , \tag{4.10}$$

respectively.

4.4.5 Proof of principle

As a proof of principle it was examined if parasitic contributions to the resistance due to magnetogalvanic effects in the whole electrical circuit including the ferromagnetic film occur. For that purpose micro-circuits with identical layout were created with FIB while the rectangles have also been rendered paramagnetically via ion bombardment applying the above mentioned Ga^+ ion dose of 6,000 $\mu C/cm^2$ (see inset of Fig. 4.21) The resistance versus magnetic field curve of one of these circuits is shown in Fig. 4.21. Within the resolution of the experiment ($\Delta R/R = 1 \cdot 10^{-5}$) no dependence on the magnetic field was found. This result clearly demonstrates that the applied ion dose is sufficient to destroy ferromagnetism. In addition, it reveals that any magnetoresistance signal arising from the ferromagnetic film is negligibly small, which in turn proves the high sensitivity for the ferromagnetic nanostructures.

4.5 SEMPA investigations of the remanence state of submicron rectangles

As presented in section 4.1 for the dimensions of the rectangles used in this work a lot of different micromagnetic configurations exist that are local energy minima and similar in energy. Therefore, it is quite possible that the resulting remanence state is affected by differences in magnetic history, so that not necessarily the global

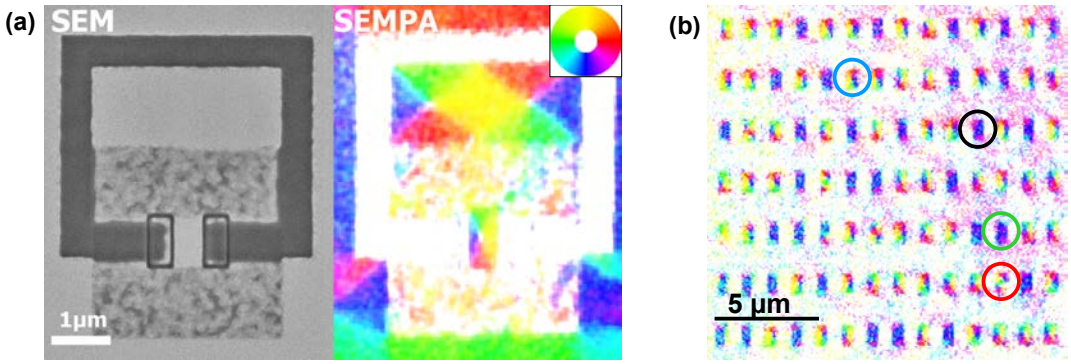

Figure 4.22: (a) SEM and SEMPA image of a micro-circuit with a 800×400 nm^2 sized rectangle for investigating the hard axis remagnetization behavior via AMR. After pretreatment in a corresponding magnetic field the rectangle is in a Landau state as can be seen according to the given color wheel. (b) SEMPA image of an array of 98 rectangles with dimensions of 1000×500 nm^2 after the very same pretreatment in a magnetic field oriented along the short axis. Most of the rectangles are in the Landau state (blue circle), some are in a C or S state (green and black circle, respectively), while only a few are in the diamond state (red circle).

minimum, i.e., the Landau state, should be found [334]. As the MR measurements provide an integrative signal of the whole structure and as the AMR depends quadratically on the magnetization orientation with respect to the current direction it is not necessarily easy to identify the involved micromagnetic configurations from the characteristics of the MR curves. Therefore, for a firm interpretation of the MR curves it is mandatory to know e.g. the remanence state, which can be used as a starting point for the interpretation.
For the investigation of the magnetic microstructure of the rectangles SEMPA is used by utilizing the UHV system, which is introduced in section 3.1.1. After the MR measurements of the rectangles the remanence state of the very same structures was imaged after the very same magnetic field pretreatment with an amplitude of 23 mT (see Fig. 4.22(a)). In order to examine if the MR samples are in the corresponding typical remanence state, for each size and both generic orientations of the rectangle with respect to the magnetic field direction arrays of 98 magnetically decoupled rectangles were investigated as well (see Fig. 4.22(b)). These six different kind of arrays were correspondingly prepared by FIB using the above mentioned paramagnetic dose.
Before presenting the results, the pretreatment of the sample for the SEMPA investigations is briefly described. At first, the cap layer was removed by soft 600 eV Ar^+ ion sputtering. Secondly, as Py predominantly consists of Ni, which has a relatively low spin polarization of the secondary electrons (see section 3.1.3), for contrast enhancement the sample was dusted with a few monolayers of Fe as Fe has the highest spin polarization of the secondary electrons of the ferromagnetic $3d$ elements [234, 162, 225, 335]. The thickness of the dusting layer is a crucial parameter as, on the one hand, the SEMPA contrast should to be significantly enhanced. For that purpose the thickness of the Fe dusting layer should be comparable to or thicker than the probing depth of about 8 monolayers [231]. On the other hand,

the dusting layer has to be thin enough to be noninvasive, i.e., that it does not significantly alter the total free energy of the system and subsequently the domain pattern. My colleague Dr. S. Hankemeier showed in his PhD thesis that the used Fe thickness of about 1.3 nm fulfill both requirements [239].
Qualitatively, the following micromagnetic configurations were found: the high remanence C and S state and the flux closure Landau and diamond state. From high resolution SEMPA images of these particular states (see Figs. 4.1, 4.2) the area filling of the domains oriented in parallel to the short axis are graphically determined. For the high remanence C and S state a fraction of $(27 \pm 5)\%$ was obtained, while for the Landau state and for the diamond state the investigations resulted in fractions of $(25 \pm 6)\%$ and $(50 \pm 6)\%$, respectively. These values are necessary for the quantitative analysis of the MR curves (see below).
In the following the results of the remanence states are presented separately for pretreatments in a magnetic field applied along the easy axis and hard axis, respectively.

4.5.1 Remanence state after pretreatment in easy axis fields

Independent of the size of the rectangles the very same rectangles used for the MR investigation are in a C or S state. In the arrays 75 (95/98) out of 98 of the largest (intermediate/smallest) rectangles are in a C or S state after the very same pretreatment in magnetic fields. The remaining rectangles exhibit a flux-closure structure, like the Landau or diamond state. In nearly all the C or S states the magnetization within the large domain is oriented along the former field direction. The statistical investigation clearly reveals that the C or S state is the preponderant remanence state after applying a field along the easy axis for the used dimensions.

4.5.2 Remanence state after pretreatment in hard axis fields

Fig. 4.22(a) shows a SEMPA image of a micro-circuit for the largest rectangle revealing that the rectangle is in a Landau state. This remanence state has also been found for the intermediate and smallest rectangles. For the arrays the Landau state is also the predominant state. After the very same pretreatment in magnetic fields 58 (88/97) out of 98 rectangles exhibit the Landau state in the case of the largest (intermediate/smallest) size. The remaining rectangles show C or S states with the exception of five diamond states for the largest size.
The statistical investigation shows that the Landau state is the preponderant remanence state after pretreatment in a field oriented along the hard axis. The reason why just for the largest rectangles many C and S states were found, although the energy density difference of the C and S states to the Landau state is larger than for the smaller sizes (see section 4.1), can only be explained by anticipating a result of the MR investigation: For small fields the MR measurements indicate that the Landau state is only reversibly deformed. For the intermediate and smallest rectangle the maximum field of 23 mT is not sufficient to cause an irreversible transition from the Landau state to a C or S state. For the largest rectangle structures, however, this transition was always observed in every field cycle in the region of the maximum

field. Thus, the relative high fraction of C or S states in remanence can be explained by the fact that the irreversible transition back into the Landau state is a statistical process which partially occurs not until small reversed fields are applied.

4.6 Magnetization reversal and magnetic energy of single submicron permalloy rectangles

In this section the MR measurements of the rectangles are presented and discussed. The first section 4.6.1 deals with the remagnetization behavior with field applied along the short axis of the rectangles (easy axis). Subsequently the hard axis remagnetization behavior is presented in section 4.6.2, which in particular enables the determination of the magnetic energy of the involved micromagnetic states.
The results of this investigation are published in compact form in the Physical Review B [E2]. The Letter can be found in the attachments.

4.6.1 Easy axis magnetization behavior of single rectangles

Typical MR measurements of the rectangles for magnetic fields applied in parallel to the long axis are shown in Fig. 4.23. The curves were obtained in one single field cycle. For all three sizes of the rectangles similar curves were found which demonstrates almost identical magnetization behavior. Starting at ± 23 mT the resistance increases continuously towards zero field with a change in resistance of $16 - 20$ mΩ. This value corresponds to $(18 \pm 4)\%$ of the value of $\Delta R_{\mathrm{ea}} = (0.10 \pm 0.01)\ \Omega$, which corresponds to the maximum resistance change due to the AMR in this MR geometry (see Eq. 4.10). At a small opposite field the resistance jumps by a value of about $19 - 23$ mΩ corresponding to $(21 \pm 4)\%$ of ΔR_{ea}. Further increase of the opposite field up to a value of $4 - 9$ mT causes only slight variations in the resistance. Then, a resistance drop with similar height as for the jump was found. While the posistive jump appears at almost the same field, the field value at which the resistance drop appears, varies slightly from cycle to cycle. This stochastic behavior can be exemplarily seen in Fig. 4.23(a), where $R(H)$ curves for two field cycles are plotted.
From the MR curves of Fig. 4.23 the magnetization behavior of the rectangles can be deduced with the help of the SEMPA investigation. As presented in section 4.5.1 the SEMPA images reveal that the very same rectangles are either in the C or S state after sweeping the magnetic field along the long axis of the rectangles from ± 23 mT to zero. In this interval of the field cycle the MR curves are continuous which indicates that only reversible magnetization processes occur so that the micromagnetic structure is essentially the C or S state. Depending on the field strength the C or S state becomes distorted by the magnetic field. As in remanence the center domain is aligned along the field direction this is certainly the case for any applied field minimizing the Zeeman energy term. Thus, only the magnetic microstructure in the end domain regions as well as the borderline regions to the center domain might be affected due to the magnetic field. There are two possible scenarios which are in accordance with the resistance increase on field reduction. There can either be a reversible reduction of the magnetization tilting within the end domains towards the long axis

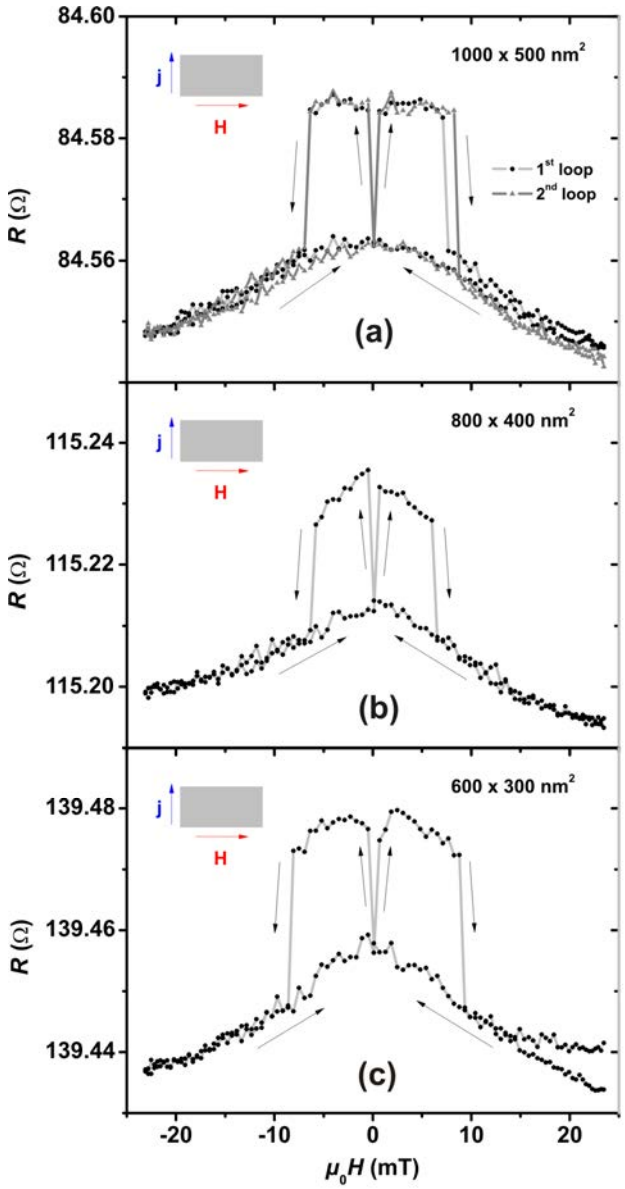

Figure 4.23: Resistance versus field curves for field applied in parallel to the long axis of the rectangles (easy axis loops). The arrows indicate the field sweep direction. The dimensions of the rectangles are (a) 1000×500 nm^2, (b) 800×400 nm^2, and (c) 600×300 nm^2.

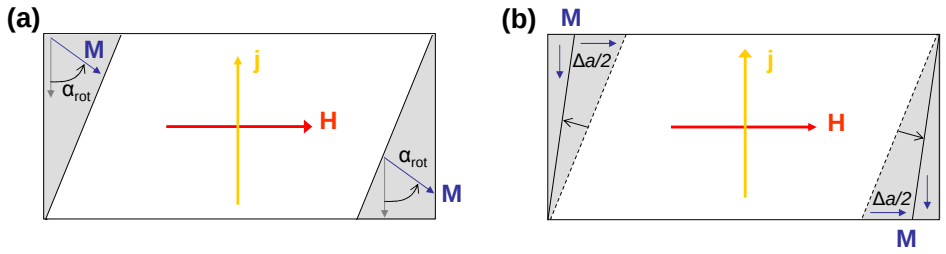

Figure 4.24: Sketch of the possible reversible processes, which might occur yielding a reduction of the resistance with increasing field. In (a) the magnetization rotates in the closure domains, while in (b) the domain walls shift minimizing the size of the closure domains. The latter process is the more probable one, see text.

of the rectangle or a reversible domain wall shift that increases the area of the center domain (see Fig. 4.24). Both scenarios are discussed quantitatively in the following in the domain theoretical approximation. The area filling of the end domains of the C or S state in remanence is $(27 \pm 5)\%$. According to the uniform current model (see section 4.4.1) this means that a complete orientation of the end domains along the field/ perpendicular to the current direction would yield a resistance increase compared to the remanence state of $\Delta R_{ea}^{\mathrm{C/S}} = 0.27 \times \Delta R_{\mathrm{ea}} = 26\ \mathrm{m\Omega}$. This value has to be compared with the measured resistance increase of $\Delta R_{ea}^{\mathrm{reversible}} = (18 \pm 2)\ \mathrm{m\Omega}$ between 23 mT and zero field.
For a rotation of the magnetization in the end domains the angle α_{rot} which generates the measured value can be calculated utilizing the angle dependence of the AMR (Eq. 4.1):

$$\alpha_{\mathrm{rot}} = \arcsin\left(\sqrt{\frac{\Delta R_{\mathrm{ea}}^{\mathrm{reversible}}}{\Delta R_{\mathrm{ea}}^{\mathrm{C/S}}}}\right) = (56 \pm 4)^{\circ} \tag{4.11}$$

For the reversible domain wall movement which causes a shrinking of the end domains at the expense of a growth of the center domain the corresponding change in the area filling of the end domains/ center domain normalized to the rectangle area can be calculated from:

$$\Delta a_{\perp} = \frac{\Delta R_{\mathrm{ea}}^{\mathrm{reversible}}}{\Delta R_{\mathrm{ea}}} = (18 \pm 4)\% \tag{4.12}$$

This means that at a field of 23 mT the area filling of the end domain has to shrink to $(9 \pm 7)\%$.
However, the remagnetization process is certainly none of both idealized borderline cases. But the relatively high rotation angle of the first scenario would be accompanied by a considerable increase in stray field energy due to the generation of a large amount of surfaces charges. In contrary, in the second scenario the magnetization is oriented in parallel to the edges everywhere, so that it can be assumed that the domain wall displacement process is the dominating one. The latter process has already been observed in larger permalloy rectangles [334].
The irreversible jump at a small opposite field with a height of about $(21 \pm 4)\%$

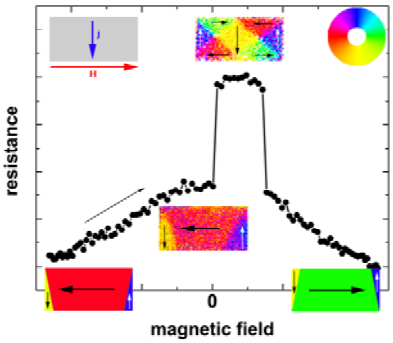

Figure 4.25: Cartoon of supposed magnetization behavior for fields applied along the easy axis. The domain structures at zero and small positive fields are SEMPA micrographs, while the two others are sketches. The magnetization orientation is color coded according to the given color wheel.

of ΔR_{ea} indicates that the resulting magnetic microstructure exhibits large supplemental domains with magnetization orientations along the current direction/ perpendicular to the field. It is reasonable to assume that the system jumps into a flux closure pattern because the Landau as well as the diamond state are lower in energy than the C or S state for the dimensions used here (see section 4.1.3). As the Landau and the C or S state have almost the same area filling of domains that are oriented in parallel to the current the Landau state would yield a similar resistance. In contrast, the difference in area filling (normalized to the rectangle area) $\Delta a_{||}$ between the diamond state $a_{||}^{\mathrm{diamond}}$ and the C or S state $a_{||}^{\mathrm{C/S}}$ fits well with the height of the jump $\Delta R_{\mathrm{ea}}^{\mathrm{jump}}/\Delta R_{\mathrm{ea}} = (21 \pm 4)\%$:

$$\Delta a_{||} = a_{||}^{\mathrm{diamond}} - a_{||}^{\mathrm{C/S}} = (23 \pm 11)\% \tag{4.13}$$

Consequently, it is reasonable to assume that the diamond state is created.
Small external opposite fields certainly reversibly disturb the structure of the diamond state until the irreversible drop in resistance occurs. As the height of the drop is similar to the height of the jump and as the state at 23 mT is a field distorted C or S state the drop can be attributed to the inverse switching process, namely that the diamond state is transformed into the C or S state.
In Fig. 4.25 the depicted easy axis magnetization behavior is graphically summarized. For the sake of completeness it is worth mentioning that deviations from this typical remagnetization behavior were sometimes observed for rectangles with the largest dimensions of 1000×500 nm^2. For some structures in $\lesssim 10\%$ of successive field cycles at irregular intervals the large irreversible resistance steps fail to appear in one sweep direction as exemplarily shown in Fig. 4.26 or in very rare cases in both sweep directions. The absence of the resistance jump at a small opposite field indicates either that there is a different intermediate state or that there is a direct transition from one C or S state to another with reversed magnetization orientation in the center domain. Instead of the diamond state the intermediate state is assumed to be the Landau state as the transition from the C or S state to the Landau state does not strongly affect the resistance due to a similar area filling of domains

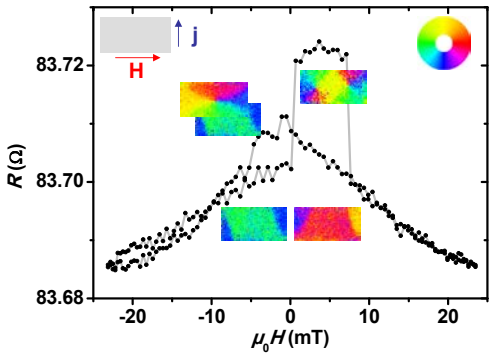

Figure 4.26: Easy axis loop for the largest rectangle (1000×500 nm^2), which was found for a few sweeps at irregular intervals. At a small negative opposite field the jump in resistance fails to appear. The domain structures are SEMPA micrographs.

oriented perpendicularly to the current direction (see section 4.5). This exception from the general remagnetization behavior reveals the competition of two different remagnetization paths so that in successive field cycles only a stochastic probability can be quoted on which path the remagnetization will develop. This stochastic behavior highlights the need for single field cycle measurements to avoid a masking of the single remagnetization behavior by the averaging over several cycles.
In conclusion, the easy axis remagnetization behavior of single submicron rectangles is extracted from the MR measurements in combination with the knowledge about the remanence state obtained from SEMPA investigations. The irreversible switching processes between the remanent C or S state and the diamond state is the dominating feature in the MR curve, which could be unambiguously identified by the quantitative analysis. This study clearly demonstrates the potential and sensitivity of the investigation method to obtain quantitative results.

4.6.2 Energy density of single rectangles obtained from hard axis magnetization behavior

The results of the MR measurements of the rectangles for magnetic fields applied in parallel to the short axis (hard axis of magnetization) are shown in Fig. 4.27. For the sake of better comparison the ordinate scales are identical in all plots. The curves were obtained in one single field cycle. Basically, similar to the easy axis curves, the shape of the curves does not change with rectangle size: For all three sizes the same type of parabolic resistance versus field curve was found as indicated by the parabolic fits in Fig. 4.27 (dashed red lines). Deviations from the parabolic dependence were found around zero field and for the largest rectangle additionally at high fields. Attention should be paid to the fact that the amount of the resistance change becomes drastically smaller with shrinking dimensions of the rectangles.
The SEMPA investigations (see section 4.5.2) show that in remanence the rectangles are predominantly in a Landau state after pretreatment in magnetic fields parallel to the short axis. From this finding the following magnetization procedure can be deduced (see Fig. 4.28): According to the dependence of the resistivity on magnetization orientation due to the AMR (see Eq. 4.1) the parabolic field dependence

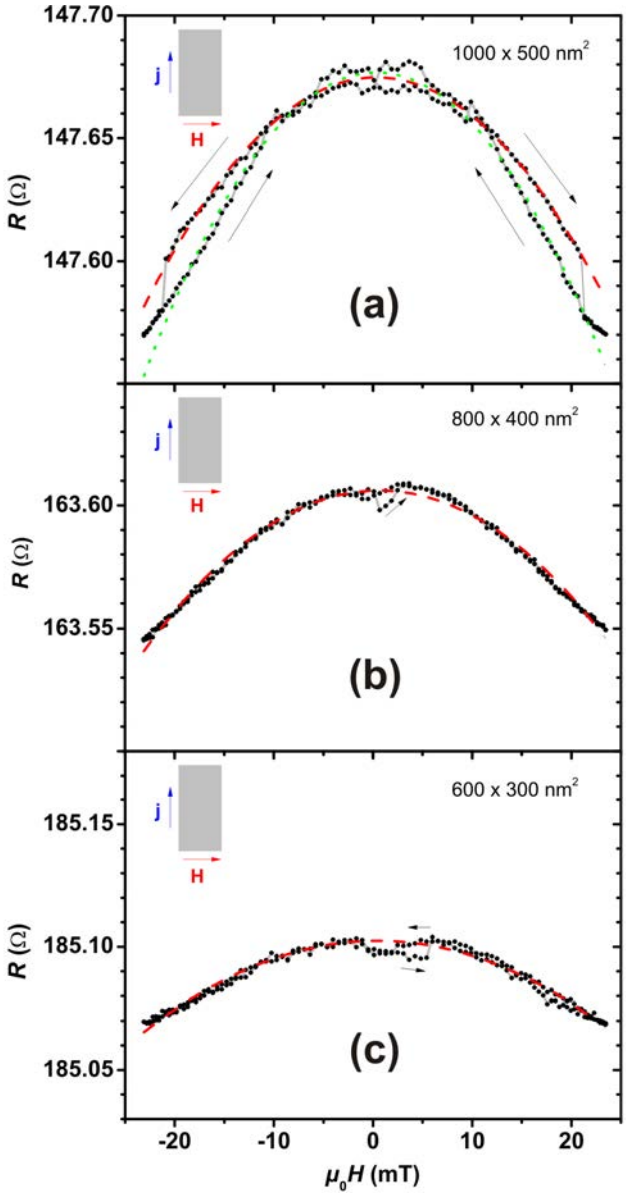

Figure 4.27: Resistance versus field curves for field applied in parallel to the short axis of the rectangles (hard axis loops). The arrows indicate the field sweep direction. The dimensions of the rectangles are (a) 1000×500 nm^2, (b) 800×400 nm^2, and (c) 600×300 nm^2. The dashed lines show parabolic fits which indicate (coherent) magnetization rotation during the reversal process.

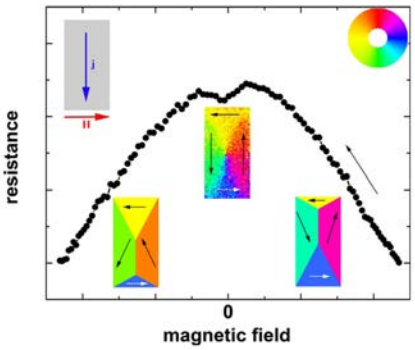

Figure 4.28: Cartoon of supposed magnetization behavior for fields applied along the hard axis. The domain structure at zero field is a SEMPA micrograph, while the two others are sketches. The magnetization orientation is color coded according to the given color wheel.

indicates that the magnetization component perpendicular to the current increases linearly with field. This behavior is typical for a coherent rotation of magnetization in the case of a uniaxial anisotropy (see Eq. 2.25). Under consideration that the remanent state is a Landau state the only mechanism that creates a parabolic MR signal is the rotation of the magnetization of the two large domains in the following called center domains. The reason for this assumption is twofold. At first, according to domain theoretical considerations (see section 4.6.2.2) and performed micromagnetic simulations (see section 4.6.2.3), the magnetization orientation of the two small closure domains is in the whole field range either parallel or antiparallel to field/ perpendicular to the current direction. Furthermore, as the area of both oppositely magnetized closure domains changes by almost the same amount while the one shrinks and the other grows and as both magnetization orientations exhibit the same resistivity, the resistance is not affected within the error margins of the experiment. This means that the closure domains are virtually invisible in the MR curve, so that the field-dependent signal is only created by the coherent rotation of magnetization in the center domains. The second reason is that the real Landau state creates stray fields that are caused by a slight tilting of the magnetization in the large domains out of the direction parallel to the long axis (see section 4.1). External fields along the short axis can easily affect this pre-existing tilting and increase the angle of tilt even at small fields. Hence, a magnetization tilting in the center domains of the Landau state occurs.
For the largest structure irreversible changes in the resistance can be seen at large fields. The hysteretic behavior is appointed to a sudden change in domain structure after the rotation has become so large that a low-angle domain wall can easily be moved and a field distorted C or S state is created.
In the following section the anisotropy is quantified from the MR curves.

4.6.2.1 Determination of the anisotropy from MR measurements

In the case that the coherent rotation of the magnetization within the large domains of the Landau structure dominates the MR curve the magnetic anisotropy that counterbalances the Zeeman torque can be calculated (see section 2.1.4.2). The

equilibrium magnetization orientation in dependence of the external field $m_\perp(H)$, i.e., Eq. 2.25, can be put into the equation of the AMR (Eq. 4.1):

$$R(\mu_0 H) = R_{||} - \Delta R_{\mathrm{ha}}^{\mathrm{L}} \cdot \left(\frac{\mu_0 H M_{\mathrm{S}}}{2K^{\mathrm{exp}}} \right)^2 \quad , \tag{4.14}$$

where K^{exp} is the anisotropy constant and M_{S} is the saturation magnetization of the permalloy film (see Eq. 4.8). $\Delta R_{\mathrm{ha}}^{\mathrm{L}}$ is the maximum resistance change of the Landau state that can be caused by the coherent rotation of the center domains in hard axis geometry. If the total size and orientation of the closure domains with respect to the current direction do not change with field, $\Delta R_{\mathrm{ha}}^{\mathrm{L}}$ is a constant and determined by the area filling of the center domains. From SEMPA micrographs it is deduced that they occupy (75±6)% of the rectangle area (see section 4.5). In a good approximation the magnetization of the center domains is oriented in parallel to the current direction in remanence and oriented perpendicularly to the current direction at sufficiently high fields, so that a maximum resistance change of $\Delta R_{\mathrm{ha}}^{\mathrm{L}} = 0.75 \times \Delta R_{\mathrm{ha}} = (0.29 \pm 0.04)\ \Omega$ can be expected. Thereby, ΔR_{ha} corresponds to the maximum resistance change due to the AMR in this MR geometry (see Eq. 4.10).
K^{exp} was determined by fitting the hard axis curves utilizing

$$R(\mu_0 H) = R_{||} - a(\mu_0 H)^2 \quad , \tag{4.15}$$

where a is the fitting parameter. The corresponding fits can be seen as red dashed lines in Fig. 4.27. Comparison of the coefficient of Eqs. 4.14 and 4.15 yields:

$$K^{\mathrm{exp}} = \frac{M_{\mathrm{S}}}{2} \cdot \sqrt{\frac{\Delta R_{\mathrm{ha}}^{\mathrm{L}}}{a}} \tag{4.16}$$

Before presenting the calculated values for K^{exp} the rotation angles are presented at certain field values in order to get a better impression of the magnitude of the coherent rotation of magnetization. The largest structure exhibits a reversible resistance change of about 25% of $\Delta R_{\mathrm{ha}}^{\mathrm{L}}$ when sweeping the field from 0 to 21 mT, i.e., up to the field at which the irreversible jump occurs. This value corresponds to a magnetization rotation of $\alpha = \arcsin(\sqrt{0.25}) = 30°$ in the direction of the external field. In the case of the smaller structures, the rotation angle at maximum field is 26° (19°) for the intermediate (smallest) rectangle. The smaller rotation indicates a stronger magnetic anisotropy that competes with the Zeeman energy.
Finally, the anisotropy constants K^{exp} determined from the hard axis curves for the three sizes of rectangles are listed in Tab. 4.1. The results for the anisotropy constants should be comparable to the shape anisotropy constants because the magnetocrystalline anisotropy of the film is very small ($\approx 360\ \mathrm{J/m^3}$, see section 4.4.3) and the only effective anisotropy is due to the shape. In its strict definition the latter is the difference between the energy of the saturated states along the hard and the easy axis. The shape anisotropy constants $K_{\mathrm{d}}^{\mathrm{theo}}$ were calculated in section 2.1.2 utilizing the magnetometric demagnetization factors and cross-checked via micromagnetic

dimensions (nm^3)	K_d^{theo}	K_d^{sim}	K^{exp}
$1000 \times 500 \times 20$	11.8	11.8	17 ± 2
$800 \times 400 \times 20$	14.0	14.0	21 ± 2
$600 \times 300 \times 20$	17.4	17.4	27 ± 3

Table 4.1: Anisotropy constants of cuboids from calculation, micromagnetic simulation, and experiment (in kJ/m^3).

simulations (K_d^{sim})[21]. In Tab. 4.1 K_d^{theo} and K_d^{sim} are also listed. It is obvious that the experimental values do not fit the simulated and the theoretical values that are identical as expected. The experimental results are systematically larger, meaning that either there do exist some further contributions to the anisotropy or the properties of the nanostructures diverge considerably from the assumptions. The properties, such as saturation magnetization and size, were cross-checked. As they were identical with the values used for the analysis additional contributions to the anisotropy have to be considered.
The values for the shape anisotropy constants were calculated for homogeneously magnetized rectangles, so that the experimental results reveal that the magnetic microstructure of the Landau state affects the anisotropy. In order to explore the meaning of the obtained anisotropy values first a domain theoretical description of the remagnetization of the Landau state is given in the next section 4.6.2.2, followed by the results of micromagnetic simulations presented in section 4.6.2.3.

4.6.2.2 Domain theoretical description of the remagnetization of the Landau pattern

In this section the influence of an external field oriented in parallel to the short axis on the ideal Landau state is described domain-theoretically, i.e., domain walls are regarded as infinitesimal narrow. As already discussed above the field acts as a torque on the magnetization in the center domains yielding a magnetization rotation into the field direction. There is no torque on the closure domains and their orientations do not change with field. However, their sizes change as the former 90° Néel walls between center and closure domains shift with field. The position of the domain walls are determined by the continuity conditions of the normal components of magnetization across the walls to avoid magnetic charged domain walls (see section 2.2) [149]. This boundary condition implies that the sizes of the closure domains only depend on the magnetization tilting α within the center domains (see Fig. 4.29(a)). The total area of both closure domains normalized to the area of the rectangle $A_{closure}$ as a function of α is:

$$A_{closure} = A_1 + A_2 = \frac{1}{8}\left(\tan\left(\frac{\frac{\pi}{2}+\alpha}{2}\right) + \tan\left(\frac{\frac{\pi}{2}-\alpha}{2}\right)\right) \tag{4.17}$$

[21] In the simulation a strong magnetic field is used to saturate the magnetization along the hard and easy axis, respectively. The difference in stray field energy between both states corresponds to the shape anisotropy constant.

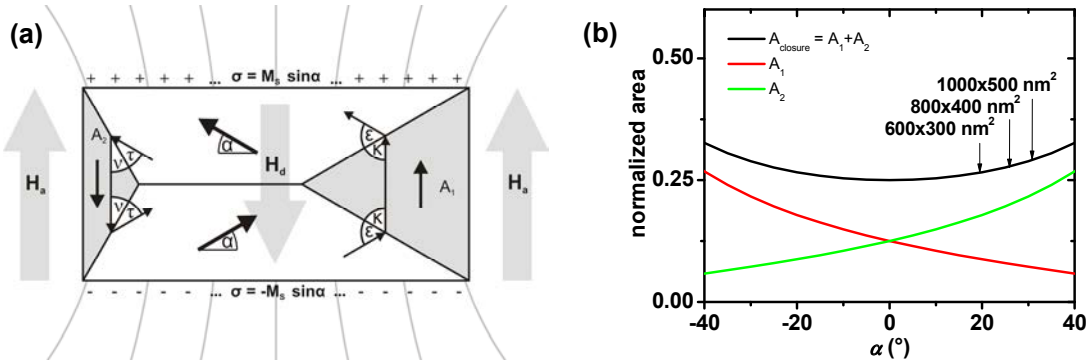

Figure 4.29: (a) Magnetic microstructure of the Landau state distorted by an external field $\mathbf{H}_\mathrm{a}$. The position of the domain walls and thus the area of the closure domains A_1 and A_2 is determined by the angle relations $\epsilon = \kappa$, $\kappa = \frac{\pi/2+\alpha}{2}$, and $\tau = \nu$, $\nu = \frac{\pi/2-\alpha}{2}$. Otherwise, the domain walls would possess magnetic charges. The surface charge density $\sigma = M_\mathrm{S} \sin\alpha$ provides the existence of the demagnetization field $\mathbf{H}_\mathrm{d}$ inside the rectangle. (b) Relative part of the area of the closure domains A_1, A_2, and $A_\mathrm{closure} = A_1 + A_2$ in dependence of α. The arrows indicate the maximum rotation angle for each size observed in the experiments. As can be seen A_closure changes only up to 3.8% (3.0%, 1.4%) in the case of the largest (intermediate, smallest) rectangle.

As can be seen in Fig. 4.29(b) A_closure is nearly constant within the angle range $\alpha \leq 30°$ observed in the experiments. For the largest structure a transition from a Landau to a C or S state at $\alpha = 30°$ is observed. This means that there exists no higher rotation angle at which the Landau state is a local energy minimum. As for the smaller dimensions the maximum rotation angles are even smaller the assumption of a constant A_closure seems to be justified in the determination of the anisotropy from the experimental curves (see above). The following paragraphs separately deal with the magnetostatic energy and the domain wall energy, respectively.

Magnetostatic energy: The magnetostatic energy (Zeeman energy and stray field energy) of the field distorted Landau state is determined in order to get an explicit dependence between the tilting angle α and the external magnetic field H_a, starting with the Zeeman term. According to Eq. 2.5 the Zeeman energy density of the center domains $(E/V)_{\mathrm{Z,\ center}}$ is simply:

$$(E/V)_{\mathrm{Z,\ center}} = -\mu_0 M_\mathrm{S} H_\mathrm{a} \sin\alpha \tag{4.18}$$

The Zeeman energy density of the closure domains diverge from $(E/V)_{\mathrm{Z,\ center}}$, in particular the Zeeman energy densities of both closure domains are different in sign. In the calculation it has to be considered that with increasing field the size of the in parallel to field oriented closure domain grows while the other shrinks:

$$(E/V)_{\mathrm{Z,\ closure}} = -\mu_0 M_\mathrm{S} H_\mathrm{a} \cdot \frac{A_1 - A_2}{A_1 + A_2} \quad , \tag{4.19}$$

where A_1 and A_2 are the areas of the closure domains normalized to the rectangle area (see Fig. 4.29(a)). Using equation Eq. 4.17 yields:

$$\begin{aligned}(E/V)_{\text{Z, closure}} &= -\mu_0 M_\text{S} H_\text{a} \cdot \underbrace{\left(\frac{\tan\left(\frac{\frac{\pi}{2}+\alpha}{2}\right) - \tan\left(\frac{\frac{\pi}{2}-\alpha}{2}\right)}{\tan\left(\frac{\frac{\pi}{2}+\alpha}{2}\right) + \tan\left(\frac{\frac{\pi}{2}-\alpha}{2}\right)} \right)}_{\sin\alpha} \\ &= -\mu_0 M_\text{S} H_\text{a} \sin\alpha = (E/V)_{\text{Z, center}}\end{aligned} \tag{4.20}$$

This means that the combined averaged Zeeman energy density of both closure domains resembles the Zeeman energy density of the center domains.
The determination of the stray field energy density of the field distorted Landau state is more complicated. The reason for this is that even for a single-domain state in a rectangle there does not exist a homogeneous demagnetization field, so that the simple dependence $\mathbf{H}_\text{d} = -\overleftrightarrow{N}\mathbf{M}$ is not valid (see section 2.1.2). Though the demagnetization energy of single-domain states can be calculated by utilizing magnetometric demagnetization factors it fails in the case of a multi-domain pattern, where the exact spatial shape of $\mathbf{H}_\text{d}(\mathbf{r})$ has to be known. In the following the approximation is to deal with a homogeneous demagnetization field $\mathbf{H}_\text{d}(\mathbf{r}) = \mathbf{H}_\text{d}$. The validity of this approximation is discussed further below.
The stray field is caused by the surface charges generated at the long edge of the rectangle. The surface charge density is $\sigma = \mathbf{M} \cdot \mathbf{n} = M_\text{S} \sin\alpha$. Assuming that there is a homogeneously magnetized cuboid with the same surface charge density $\sigma = M_\text{S} \sin\alpha$. As the demagnetization field is determined solely by the surface and volume charges this hypothetical cuboid exhibits the same stray field as the field distorted Landau state. Thus, the demagnetization field $\mathbf{H}_\text{d}$ is simply $\mathbf{H}_\text{d} = -N_y\mathbf{M} = -N_y\mathbf{M}_S \sin\alpha$, which is assumed to be constant within the whole rectangle as discussed above and N_y is the y component of the magnetometric demagnetization factor (see Eq. 2.11). Consequently, the stray field density within the center domains of the field distorted Landau state then is:

$$\begin{aligned}(E/V)_{\text{d, center}} &= -\frac{\mu_0}{2}\mathbf{H}_\text{d} \cdot \mathbf{M} = \frac{\mu_0}{2} N_y M_\text{S} \sin\alpha \cdot M_\text{S} \sin\alpha \\ &= \underbrace{\frac{\mu_0}{2} M_\text{S}^2 N_y}_{K_\text{d}^\text{L}} \sin^2\alpha\end{aligned} \tag{4.21}$$

Similar to the Zeeman energy density, the demagnetization energy density within the individual closure domains is different to $(E/V)_{\text{d, center}}$ but the combined average stray field density of the closure domains resembles $(E/V)_{\text{d, center}}$:

$$\begin{aligned}(E/V)_{\text{d, closure}} &= \frac{\mu_0}{2} H_\text{d} M_\text{S} \underbrace{\frac{A_1 - A_2}{A_1 + A_2}}_{\sin\alpha} \\ &= \underbrace{\frac{\mu_0}{2} N_y M_\text{S}^2}_{K_\text{d}^\text{L}} \sin^2\alpha = (E/V)_{\text{d, center}}\end{aligned} \tag{4.22}$$

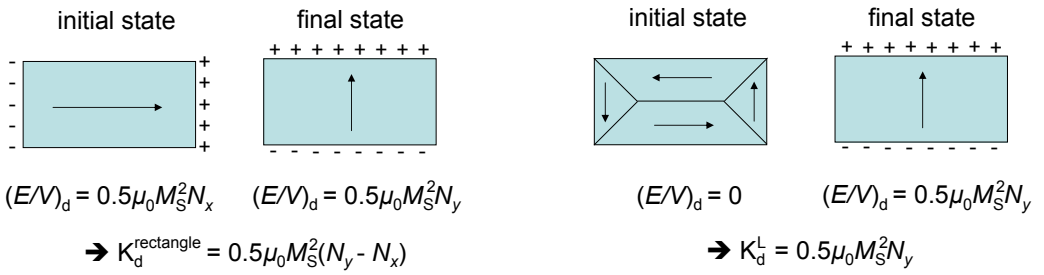

Figure 4.30: Visualization of the difference in stray field energy between (a) homogeneously magnetized particles and (b) the ideal Landau and the hard axis magnetized state.

Thus, the total magnetostatic energy density of the field distorted Landau state under the assumption of a spatially homogeneous demagnetization field is:

$$(E/V)_{\text{ms, Landau}} = K_{\text{d}}^{\text{L}} \sin^2 \alpha - \mu_0 M_{\text{S}} H_{\text{a}} \sin \alpha \tag{4.23}$$

This expression equals the total magnetostatic energy of homogeneously magnetized rectangles (see Eq. 2.24) with the exception that the uniaxial anisotropy constant is

$$K_{\text{d}}^{\text{L}} = \frac{\mu_0}{2} M_{\text{S}}^2 N_y \quad , \tag{4.24}$$

instead of $K_{\text{d, rectangle}} = \frac{\mu_0}{2} M_{\text{S}}^2 (N_y - N_x)$. It is worth mentioning that K_{d}^{L} exactly corresponds to the stray field energy difference between the ideal Landau state in remanence and the hard axis magnetized state (see Fig. 4.30(b)). The demagnetization energy of the Landau state is zero as no volume or surface charges exist while the energy of the hard axis magnetized state is per definition given by the magnetometric demagnetization factor to $(E/V)_{\text{d},y} = \frac{\mu_0}{2} M_{\text{S}}^2 N_y$ (see section 2.1.2.1). In Tab. 4.2 the calculated anisotropy constants K_{d}^{L} are given together with the shape anisotropy constants and the experimental values. The shape anisotropy is lower than K_{d}^{L}, as the former is the energy difference between the single-domain states depicted in Fig. 4.30(a), revealing the vanishing stray field energy for the Landau state. Nevertheless, it is obvious that the measured values are systematically lower than K_{d}^{L}. One reason could be the domain wall energy of the Landau state, which lowers the energy density difference to the hard axis magnetized state. Before the domain wall energy is estimated domain-theoretically the restrictions of the considerations made above are briefly discussed.
In contrast to a single-domain particle Eq. 4.23 is not valid for arbitrary α. One reason is that there does not exist a continuous transition between the two involved states as in topological terms the topological line defect (180° domain wall) cannot disappear solely by coherent rotation (see section 3.2). Second, if there would be a reversible remagnetization behavior up to $\alpha \geq 60°$ then Eq. 4.17 and therefore Eq. 4.23 is not valid anymore as the two closure domains would overlap each other to maintain the continuity conditions of the normal components of magnetization across the walls. At even higher angles the closure domains would literally spread above the borders of the rectangle. However, this high angle regime is not entered experimentally. The irreversible jump in resistance found for the largest rectangle

dimensions (nm^3)	K_d^{theo}	K_d^L	$-K^{*L}_{DW}$	K_{total}^L	K^{exp}
$1000 \times 500 \times 20$	11.8	23.1	2.0	21.1	17 ± 2
$800 \times 400 \times 20$	14.0	27.3	2.5	24.8	21 ± 2
$600 \times 300 \times 20$	17.4	33.9	3.3	30.6	27 ± 3

Table 4.2: Energy densities of cuboids from experiment K^{exp} and domain theoretical considerations (in kJ/m^3). Definitions of the latter, see text.

(see Fig. 4.27(a)) happens at a field that corresponds to an angle of $\alpha = 30°$, where it is assumed that the perpendicularly to field oriented and therefore energetically unfavorable closure domain is abandoned. The resulting quasi single-domain state exhibits a completely different magnetostatic energy so that Eq. 4.23 loses its validity. Furthermore, except for the initial and final state depicted in Fig. 4.30(b), the spatial dependence of the demagnetization field has to be taken into account, which is assumed to be homogeneous across the rectangle in the derivation of Eq. 4.23. The actual shape of $\mathbf{H}_d$ should be briefly discussed.
Recently, A. Aharoni analytically derived spatially resolved expressions of the demagnetization factors for rectangular prisms with semi-axes (a, b, c), which are homogeneously magnetized along one of the edges (y-direction) [336]. As stated above the demagnetization field for the field distorted ideal Landau state resembles the one for a homogeneously magnetized state with a surface charge density of $\sigma = M_S \sin\alpha$ (see Fig. 4.29(a)). Aharoni suggested two types of demagnetization factors [336]. One of them is given by an averaging over the x and z directions at any value of y, in the following called $N'_y(y)$ ("generalized ballistic" demagnetization factor). Here exists a certain averaging, while for the other proposed factor there is no averaging at all: Aharoni calculated this factor for the line that runs through the center of the prism (with coordinates (0,0,0)) parallel to y, so that it is again only a function of y, and called it "local" demagnetization factor $N^*_y(y)$. He showed that for thin film elements $a \ll b, c$ both $N^*_y(y)$ and $N'_y(y)$ are nearly the same. This means that the dependence of the demagnetization factors on the x and z coordinates can be neglected in a good approximation so that the actual demagnetization field is basically only a function of y. $N^*_y(y)$ was calculated by using Eq. (5) in Ref. [336] for the three dimensions used in this work. The results can be seen in Fig. 4.31. Also shown as dashed horizontal lines are the corresponding values of the magnetometric demagnetization factors N_y from Eq. 2.11, which correspond to the average of $N^*_y(y)$. $N^*_y(y)$ and therefore $\mathbf{H}_d \approx N^*_y(y) M_S \cdot \mathbf{e}_y$ gradually increases with increasing $|y|$. Therefore, for arbitrary H_a, in order to reduce the total energy of the domain pattern, the angle between the magnetization and the edge is correspondingly reduced on the way to the edge, so that surface charges are minimized at the expense of volume charges and exchange energy. The actual shape of $\mathbf{H}_d$ reveals the limits of the validity of the domain theoretical treatment of the Landau state and demonstrates the need for a more sophisticated approach, i.e., micromagnetic simulations. The results of micromagnetic simulations are presented after the estimation of the domain wall energy in domain theoretical approximation is given.

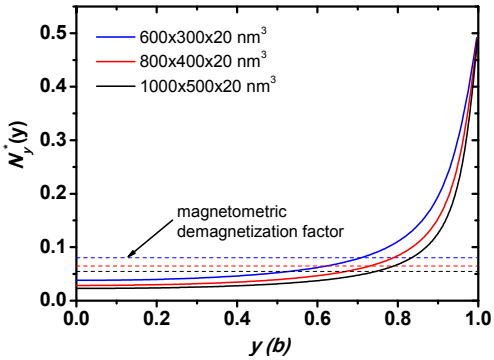

Figure 4.31: Local demagnetization factor $N_y^*(y)$ for the three rectangle sizes ($y = 0$: center, $y = b$: edge). The dashed horizontal lines are the results for the magnetometric demagnetization factors N_y.

Domain wall energy: In order to estimate the domain wall energy of the Landau state a line energy density of $\gamma_{180°} = 8 \cdot 10^{-15}$ J/μm was considered for a 180° Néel wall in a 20 nm thick permalloy film (see section 2.2). According to Eq. 2.28 most of the domain wall energy is stored in the 180° wall that separates the two center domains. As the angle α varies only by $\leq 30°$ in the experiment the energy change of the other walls that are 90° Néel walls in remanence can be neglected compared to the energy change for the 180° wall. The length of the wall

$$l_{\text{center wall}} = w\left(2 - \frac{1}{2}\left(\tan\left(\frac{\frac{\pi}{2} - \alpha}{2}\right) + \tan\left(\frac{\frac{\pi}{2} + \alpha}{2}\right)\right)\right) \tag{4.25}$$

is $l_{\text{center wall}} \approx w$ for $\alpha \leq 30°$ in a good approximation (w: length of the short rectangle axis), so that the wall energy density (per rectangle volume V) can be estimated by utilizing Eq. 2.28 and a line energy density of the wall of $\gamma'_{180°} = 0.8 \cdot 10^{-16}$ J/μm (see page 20) to:

$$(E/V)^{\text{L}}_{\text{DW}} \approx \gamma'(\alpha) \cdot \frac{w}{V} = \underbrace{\frac{w}{V} \cdot \gamma'_{180°}}_{-K^{*}{}^{180°}_{\text{DW}}} (1 - \sin\alpha)^2 \tag{4.26}$$

This term has to be considered in the minimization of the energy in Eq. 4.23. As $(E/V)^{\text{L}}_{\text{DW}}$ varies by $(1 - \sin\alpha)^2$ instead of $-\sin^2\alpha$ a deviation from a pure uniaxial behavior occurs. A minimization of the total energy is resigned here due to the following reason. In the derivation of Eq. 4.26 an ideal Landau state is assumed, whereby $(E/V)^{\text{L}}_{\text{DW}}$ is drastically overestimated. As presented in section 4.1 the real Landau state exhibits a wall angle of about 145° ($\alpha \approx 17.5°$) instead of 180° ($\alpha = 0°$) in remanence, so that the wall energy is reduced by about 50%. Therefore, the domain wall energy density in remanence $(E/V)^{\text{L}}_{\text{DW}}$, i.e., the difference in domain wall energy between the hard axis magnetized state and the Landau state, is roughly estimated by:

$$-K^{*\text{L}}{}_{\text{DW}} \approx \frac{w}{V}\gamma'(145°) \tag{4.27}$$

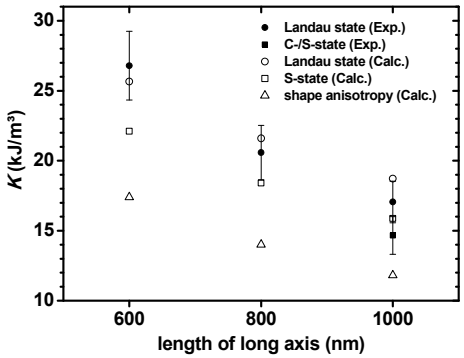

Figure 4.32: Energy density differences K for different sizes of Py rectangles. The open symbols represent the calculated shape anisotropy and calculated energy density differences between the hard axis saturated state and certain domain structures given as labels in the plot. The filled symbols were obtained by fitting a uniaxial behavior to the hard axis MR curves of Fig. 4.27.

The calculated values are given in Tab. 4.2. It is obvious that they are considerably smaller than the constants $K_{\mathrm{d}}^{\mathrm{L}}$. Consequently, the change in domain wall energy with field results only in small deviations from the uniaxially anisotropic behavior (deviations from the parabolic $R(\mu_0 H)$ curve), which is caused by the interplay between stray field and Zeeman energy (see Eq. 4.23). As the domain wall energy density $(E/V)_{\mathrm{DW}}^{\mathrm{L}}$ enhances the energy density of the Landau state compared to the hard axis magnetized state it contributes to a stronger decrease of the resistivity with field and therefore to a larger curvature. In fact, the combined energy density of the stray field and the domain wall, i.e., $K_{\mathrm{total}}^{\mathrm{L}}$, only deviates by less than 25% compared to the experimental value K^{exp} for all three rectangle sizes (see Tab. 4.2). In conclusion, the domain theoretical description basically predicts a parabolic $R(\mu_0 H)$ behavior for small $\alpha \leq 30°$. In a good approximation it indicates that the measured anisotropy constant K^{exp} corresponds to the magnetic energy density of the Landau state. This is surprising because for the estimation of the domain wall energy as well as for the magnetostatic energy partially crude simplifications were made.
As already discussed above, micromagnetic simulations are necessary to get a more precise access to the involved energy terms.

4.6.2.3 Comparison of experimental results with micromagnetic simulations

The intrinsic material parameters for the OOMMF simulations correspond to the experimentally determined values ($M_{\mathrm{S}} = 820$ kA/m, $K \approx 0$) and the literature value of the exchange stiffness of permalloy $A = 13$ pJ/m [74]. Further parameters are: cell size 5 nm × 5 nm × thickness of 20 nm, and damping constant $\alpha = 0.5$.
In a first step the energy density of the micromagnetic states that were found in the SEMPA investigations were calculated via OOMMF. The calculated energy density differences between the hard axis magnetized state and the domain patterns, i.e., the S state (□) and the Landau configuration (○), are shown in Fig. 4.32 in combination with the experimental values (●) versus long axis size. The shape anisotropy

dimensions (nm^3)	K_d^{theo}	$K_d^{L,\,sim}$	$-K_{xc}^{L,\,sim}$	$K_{total}^{L,\,sim}$	$K_{fit}^{L,\,sim}$	K^{exp}
$1000 \times 500 \times 20$	11.8	20.3	1.6	18.7	19 ± 1	17 ± 2
$800 \times 400 \times 20$	14.0	23.8	2.2	21.6	23 ± 1	21 ± 2
$600 \times 300 \times 20$	17.4	30.3	4.7	25.6	31 ± 2	27 ± 3

Table 4.3: Energy densities of cuboids from experiment K^{exp} and OOMMF calculations (in kJ/m^3). Definitions of the latter, see text.

constants are also shown for comparison (△). It is evident that the calculated energy density differences fit the experimental results quite well. For the small and intermediate rectangles the experimental values are very close to the calculated values of the most probable domain configuration, i.e., the Landau state. In particular, it turns out that the anisotropy can be used to distinguish between different domain configurations. One direct proof becomes evident from the magnetization behavior of the largest rectangle, where at a field of about 21 mT the irreversible change from the Landau to the C or S state was found (see jump in Fig. 4.27(a)). Here, the energetically unfavorable closure domain of the Landau state is abruptly abandoned and a quasi single-domain state with closure domains at the long edges evolves. As there is an energy barrier between the high remanence state and the Landau configuration the inverse transition back into the Landau state does not take place until the field is reduced to small values. As can be seen in Fig. 4.27(a) also the part of the MR curve when a high remanence state is present exhibits a parabolic behavior as indicated by the green dashed line which is a quadratic fit. The curvature of the parabola differs from the curvature for the Landau state revealing that the magnetization rotation in the two states is counterbalanced by different torques, yielding different anisotropies (• and ■ in Fig. 4.32). For the calculation of the anisotropy utilizing Eq. 4.16, $\Delta R_{ha}^{C/S} = 0.73 \times \Delta R_{ha} = (0.29 \pm 0.04)\ \Omega$ is used for the down scan, yielding $K = (15 \pm 2)\ kJ/m^3$. The anisotropy of the C or S state, i.e., the energy density difference to the hard axis saturated state, is therefore smaller than for the Landau state, which means that the C/S state is higher in energy as predicted from micromagnetic simulations (see section 4.1). Quantitatively, the energy density difference between the C/S state and the Landau state can be obtained from the experiments, yielding $(2.4 \pm 0.7)\ kJ/m^3$, which fits well the value of $2.8\ kJ/m^3$ from the calculations (see difference between □ and ○ in Fig. 4.32). This finding must be treated with some restraint as in contrast to the Landau state the area filling of the closure domains vary in a complex manner with the external field strength and contribute to the MR signal.

Similar to the domain theoretical considerations the calculated values from the OOMMF simulations reveal the astonishing fact that the magnetic energy of the Landau state is measured. For the sake of completeness the calculated energy density difference between the hard axis magnetized state and the Landau state $K_{total}^{L,\,sim}$ is listed in Tab. 4.3 and divided in stray field $K_{total}^{L,\,sim}$ and exchange energy density $K_{xc}^{L,\,sim}$.

A further route to prove the experimental results is to simulate the remagnetization of the Landau state via OOMMF and to model the MR curve. For that purpose

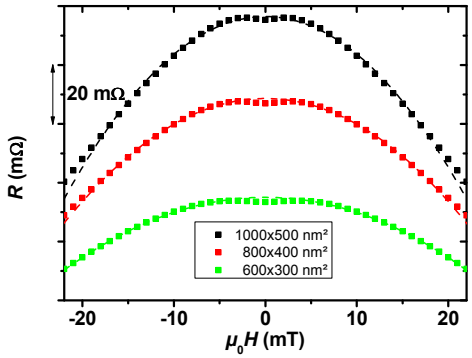

Figure 4.33: Hard axis MR curves calculated from the simulated remagnetization behavior of the Landau state for the three rectangle sizes. The dashed lines are parabolic fits revealing that coherent rotation processes of the magnetization dominates the reversal as also found experimentally (see Fig. 4.27). In contrast to the experiment for the largest structure the drop in resistance indicating the irreversible transition from the field distorted Landau to the high remanence state was found at a slightly higher field of 29 mT (not shown).

the Landau state was exposed to external fields in the range of -23 mT to 23 mT, that were applied at an angle of 3° with respect to the short axis of the rectangle to avoid metastable steady state configurations that might occur for 0° due to the high symmetry. For each field step the evolving result of the simulation was used to compute the AMR separately for each cell. According to the uniform current model the overall resistance of the rectangle is then simply given by the summation of the resistances of each cell (see section 4.4.1). The resulting MR curves for the three rectangle sizes can be seen in Fig. 4.33. Evidently, similar to the experimental results the simulated curves also show an almost perfect parabolic behavior with a decrease of the curvature on decreasing the size[22]. Quantitatively, the anisotropies $K_{\mathrm{fit}}^{\mathrm{L,\,sim}}$ determined according to Eq. 4.16 by using the curvatures obtained from a parabolic fitting of the simulated MR curves are in good accordance with the experimental results K^{exp} as well as the calculated values $K_{\mathrm{total}}^{\mathrm{L,\,sim}}$ as can be seen in Tab. 4.3. Again, the simulation indicates that in fact the energy density of the micromagnetic Landau pattern can be obtained from the hard axis remagnetization curve.

It is worth mentioning that for the simulations perfect cuboids were considered whose edges are perfect planes. In contrast, the edges of the FIB prepared rectangles deviate from this ideal concept due to the finite profile of the ion beam and the polycrystallinity of the film (see section 4.4.3). The former results in tilted edges while the latter induces edge roughness. Both deviations from an ideal structure reduce the shape anisotropy [337, 338, 296]. In order to investigate their influence on the energy density of the Landau state experimentally the edge properties of the rectangles can be varied on purpose with the high flexibility of the FIB technique.

[22] The simulations reveal that the combined size of both closure domains does not significantly change with field in the span up to ±23 mT in accordance with the domain theoretical considerations (see Fig. 4.29(b)).

4.7 Conclusion and outlook

In this chapter a method is presented, which enables the preparation of micro-circuits from laterally homogeneous metallic stacks by means of focused Ga^+ ion beam (FIB) technique including the creation of an individual nanomagnet with lateral dimensions of $\gtrsim 100$ nm. The method further allows its subsequent investigation by means of magnetotransport in the very same UHV chamber utilizing a micromanipulator [E2]. The top-down creation of the nanomagnet is based on 30 keV Ga^+ ion beam-induced mixing of the metallic layers within the stack in order to destroy the long range magnetic order in the environment of the upcoming nanomagnet. The paramagnetically rendered metallic material constitutes the input leads for the magnetoresistance investigations, so that it has to maintain a good electrical conductance to guarantee a high sensitivity for the magnetogalvanic effects of the nanomagnet. In order to create a well-defined current path that forces the current from the micromanipulator through the nanomagnet to the adjacent pristine film, which serves as second electrode, the paramagnetic material is tailored to a micro-circuit by means of FIB milling of the whole metallic material down to the electric insulating substrate.
For the purpose of finding stacks that are suited for studying the remagnetization of thin soft magnetic nanomagnets a necessary preliminary work was the development of an *in situ* MR method, which enables the characterization of the influence of the ion-bombardment on the electrical and magnetic properties. The method consists of carving micron-sized wires via FIB, which are subsequently irradiated by Ga^+ ions gradually varying the applied dose from wire to wire. From the transverse MR curves of the wires the overall resistance and the magnitude of the anisotropic magnetoresistance (AMR) in dependence of dose can be determined. The vanishing of the AMR above a specific dose (paramagnetic dose) reveals the loss in ferromagnetic order. This *in situ* MR method was applied to different stacks including a 20 nm thick permalloy layer. As a result it was found out that a 10 nm Cr/ 20 nm Py/ 2.5 nm Pt stack is very well suited for the MR investigation of single nanomagnets as it fulfills all necessary prerequisites: At first, it has a relatively high AMR ratio of about 1.5%, so that the AMR can be used as the probe for the magnetization orientation of the nanomagnets. Secondly, it can be rendered paramagnetically with a relatively low paramagnetic dose of 6,000 $\mu C/cm^2$, where only about half the thickness of the Py layer is sputtered. For the paramagnetic dose the resistance of the material is only enhanced by a factor of five, so that a high signal to noise ratio during the MR measurements of the nanomagnets is possible. Thirdly, the stack is insensitive on low ion dose applications, so that significant influences of the tail of the FIB beam on the magnetic properties of the nanostructures can be ruled out. The magnetic properties of the pristine stack, namely the saturation magnetization, uniaxial (in-plane) anisotropy constant, and AMR, were determined to $M_S = (820 \pm 40)$ kA/m, $K \approx 0.4$ kJ/m^3, and $\Delta\rho_{AMR} = (0.39 \pm 0.02)$ $\mu\Omega$cm, respectively.
By utilizing the above mentioned stack (10 nm Cr/ 20 nm Py/ 2.5 nm Pt) and paramagnetic dose (6,000 $\mu C/cm^2$) the feasibility of the method for the FIB preparation and subsequent *in situ* MR measurement of single nanomagnets was successfully

demonstrated for the investigation of the remagnetization behavior of individual submicron rectangles with lateral dimensions of 600×300 nm^2, 800×400 nm^2, and 1000×500 nm^2. The MR curves were obtained in single field cycles, so that any kind of averaging which might mask the single remagnetization behavior is excluded. The two generic cases with the magnetic field oriented perpendicularly and in parallel to the long axis of the rectangles were investigated. The used micro-circuit layouts ensure a well-defined homogeneous current density within the nanomagnets, so that without expense a quantitative analysis of the MR curves is possible. Due to the knowledge about the magnetic properties of the stack and the remanence states obtained by SEMPA investigations reversible and irreversible remagnetization processes could be quantified and unambiguously assigned to the involved micromagnetic states. In the case of the magnetic field applied in parallel to the long axis, the dominating feature is the switching between the quasi single-domain C/S state and the diamond state. In the case of the magnetic field applied perpendicularly to the long axis, the parabolic resistance versus field behavior can be attributed to a coherent rotation of the magnetization within the large domains of the Landau state. The coherent rotation curves were used to determine the anisotropy constant of the individual rectangles. Importantly, the anisotropy significantly deviates from pure shape anisotropy. The good correspondence with domain theoretical considerations and micromagnetic simulations provides strong evidence that the energy density difference between the Landau state and the hard axis magnetized single-domain state is measured, which amounts to $K^{\mathrm{exp}} = (17 \pm 2)$ kJ/m^3 ((21 ± 2) kJ/m^3/ (27 ± 3) kJ/m^3) for the largest (intermediate/ smallest) rectangle. These results clearly demonstrate that the magnetization rotation is not only affected by the shape of the sample but is also influenced by the actual domain configuration.

Within the framework of this thesis systematic investigations were started to quantify the magnetostatic interaction between nanomagnets. The knowledge about the inter-particle interactions is indispensable on the way to high density storage and new interaction-based logic devices, so that corresponding investigations are nowadays one focus of intense research in the field of magnetism of reduced dimensions [339, 340, 341, 342, 343, 344, 345, 346, 347, 348, 349, 350, 351, 352]. The implemented method for the FIB preparation and subsequent *in situ* MR measurement of individual nanomagnets is very well suited for such investigations due to the following reasons. In addition to the variation of the shape and size of the nanomagnet the high flexibility of the FIB technique enables the magnetic structuring of its environment on purpose, so that in particular any desired arrangement of nanomagnets can be realized. Furthermore, the subsequent carving of a micro-circuit allows the exclusive electrical addressing of the nanomagnet of interest in order to exclude contributions of the magnetic environment to the MR signal that would otherwise make the interpretation of the single particle behavior more difficult or even impossible. The first initiated project for *locally* studying the magnetostatic interaction of a nanomagnet with a well-defined magnetic environment briefly introduced in the following deals with the well-characterized submicron rectangles that are arranged in a linear array with the long axes oriented side by side to each other [296, 353, 354, 355, 356, 357, 358]. By utilizing the same stack, paramagnetic

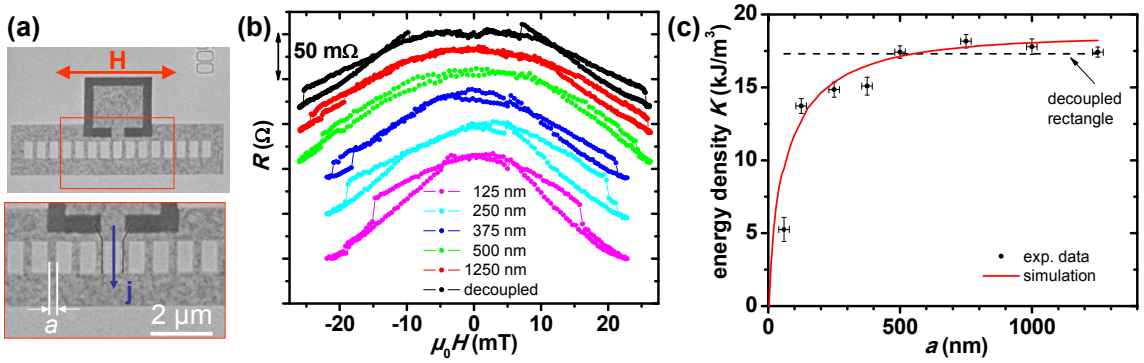

Figure 4.34: Magnetostatic interaction between permalloy rectangles arranged in a linear array with dimensions of 1000 × 500 × 20 nm^3. (a) SEM micrographs of a micro-sized circuit. The rectangles are surrounded by paramagnetic material that was created by Ga^+ ion bombardment out of the ferromagnetic film. The distance between the rectangles is $a = 250$ nm. The dark gray parts, where the metal was totally removed by sputtering, are electrically insulating, so that the current **j** can only pass through the rectangle in the middle of the array. (b) Resistance versus field curves for field applied in parallel to the short axis of the rectangles (hard axis loops) for different distances a as labeled in the graph. (c) Energy density difference in dependence of distance a obtained from the experimental curves and micromagnetic simulations.

dose, and sizes for the rectangles as used for the study of single magnetically decoupled rectangles presented in this thesis the distance a between the rectangles was varied from several hundreds of nanometers down to 60 nm. SEM images of one sample can be exemplarily seen in Fig. 4.34(a). It is obvious that the layout of the micro-circuit is a corresponding adaption of the layout used for the MR investigation of the decoupled rectangles (see Fig. 4.20(a)). For the MR measurements the micromanipulator has to contact the interior of the insulating yoke-shaped frame, so that the current is driven from the micromanipulator to the film by crossing only the rectangle in the lateral middle of the array. This is guaranteed by thin isolation lines that were prepared close to this nanomagnet (see lower image in Fig. 4.34(a)). The measurement of only one rectangle avoids any averaging over the ensemble which would otherwise mask the single particle behavior and, in addition, the transition lines again provide a well-defined homogeneous current density within the rectangle, a necessary prerequisite to obtain easily quantitative results. Fig. 4.34(b) shows the hard axis MR curves for different distances a. In each case a parabolic behavior was measured, however, the curvature was found to increase with decreasing the distance a between the rectangles accompanied by a decrease of the switching field, where the irreversible transition from the Landau to the quasi single-domain state occurs. From the curvature obtained from the parabolic fitting of the MR curves the anisotropy was calculated according to Eq. 4.16. The anisotropy in dependence of distance a can be seen in Fig. 4.34(c). In addition, the results of micromagnetic simulations using OOMMF are shown, which were obtained by using periodic boundary conditions (infinite long interaction chain of rectangles [359, 168]) and corresponds to the energy density difference of the Landau state to the hard axis magnetized single-domain state. Obviously a good accordance between experiment

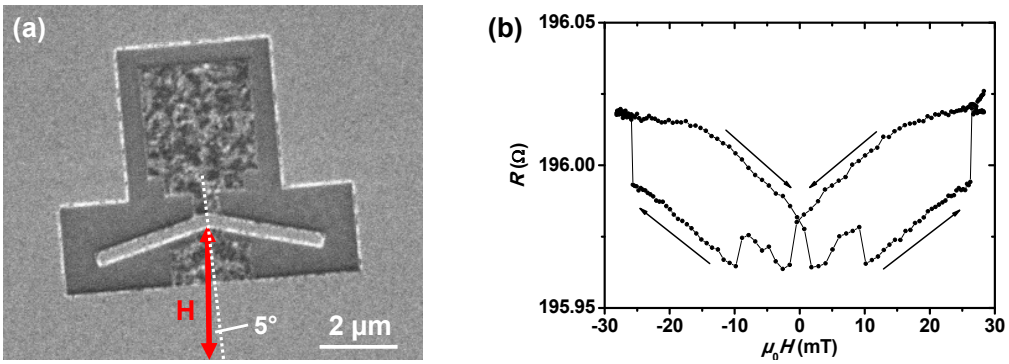

Figure 4.35: (a) Scanning ion microscopy (SIM) image of a micro-circuit for measuring the magnetization reversal of the bend region of a V-shaped Cr/Py/Pt nanowire with a width of 400 nm and a bending angle of 150°. In the speckled regions the metallic material is paramagnetic and was created by Ga^+ ion bombardment out of the ferromagnetic film (6,000 $\mu C/cm^2$) serving as input leads for the MR measurements. In the smooth dark gray regions the metal stack was completely removed. (b) Resistance versus field curve for a field direction (red arrow in (a)) that is tilted by 5° with respect to the wire's bisection/ current direction (dotted line in (a)). The black arrows indicate the field sweep direction.

and simulation was found in particular revealing a strong magnetostatic interaction between the rectangles below $a \approx 100$ nm. At the moment an analytical model is under development to quantitatively understand the interaction of the multi-domain particles being in the Landau state [E14].
In addition to the investigation of magnetostatic interactions the developed method of the FIB preparation and subsequent *in situ* MR investigation of individual nanomagnets easily allows the lateral selection of parts of a nanomagnet as can be exemplarily seen in Fig. 4.35(a) for the special case of a bend wire geometry covered in the previous chapter 3. The current is impressed from the contacting pad along the bisection of the wire, while the width of the leads is 500 nm, so that the current only passes through the bend region of the wire. The lateral selection provides the possibility to focus on the area of interest as e.g. in nanowires the complex remagnetization of the whole structure is generally hard to extract from integrative MR measurements [360]. By varying the position and width of the input leads a certain kind of lateral resolution with the AMR probe can be obtained. Fig. 4.35(b) displays preliminary results of the MR measurements of the wire shown in Fig. 4.35(a) when sweeping the field whose direction is tilted by 5° with respect to the bisection mimicking the field geometry for the seeding of vortex walls with defined sense of rotation introduced in section 3.4. A hysteretic behavior was found whereby the drops and jumps of the resistance are probably connected with the creation and annihilation of the vortex core, respectively. In future it is planned to create MR structures, where the leads are gradually shifted with respect to the bisection in order to experimentally verify the remagnetization behavior for the seeding of vortex walls proposed in section 3.4.3 by means of micromagnetic simulations. However, the MR measurement in Fig. 4.35(b) is a minor loop as the accessible maximum field strength of ±30 mT is too low to align the magnetization with field in a good approximation. As discussed in section 3.1.5 a field strength of about ±60 mT is

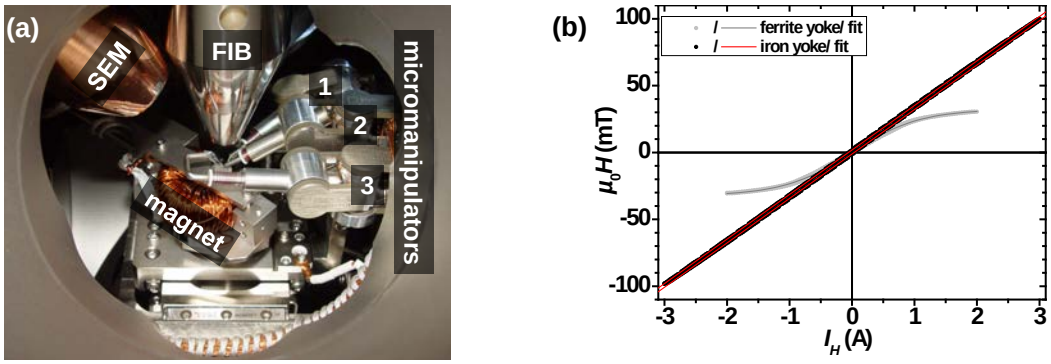

Figure 4.36: (a) Interior view of the UHV-dualbeam chamber showing the arrangement of the main components after the upgrade, i.e., the implementation of two additional micromanipulators and the interchange of the ferrite toroid of the electromagnet by an iron toroid. (b) Dependence of the magnetic field $\mu_0 H$ generated in the gap of the toroid consisting of ferrite and iron, respectively, on current I_H driven through the coil. The calibration curves were phenomenologically fitted by straight lines and a Boltzmann equation, respectively.

necessary to reorientate the magnetization within the wire arms.
In order to have the possibility to apply higher field strengths for future investigations the *in situ* MR setup was equipped with a soft-annealed Fe yoke replacing the ferrite yoke. The calibration curve of the electromagnet with the Fe yoke can be seen in Fig. 4.36(b) revealing an almost linear behavior of the generated field within the gap of the yoke on the current through the coil I_H with a small hysteretic behavior (remanence ≈ 1 mT) and a field of about 66 mT at $I_H = 2$ A, where the Joule heating can still be regarded to be negligibly small (see section 4.2.2). In addition to the enhancement of the maximum accessible field strength two additional micromanipulators were recently incorporated in the UHV-dualbeam chamber as can be seen in Fig. 4.36(a). These micromanipulators extend the scope of possible investigations as they enable the performance of four-point measurements, the simultaneously measuring of magnetostatically interacting nanomagnets, or the detection of the anomalous Hall effect (AHE). The latter can particularly be used to detect the polarity and even the sense of rotation of vortex cores [361] e.g. in the case of the bend wire geometry.
Finally, it is worth to emphasize that the implemented method of FIB preparation and subsequent *in situ* MR investigation of individual nanomagnets is not restricted to soft magnetic structures and the utilization of the AMR (or the AHE) as a probe. By using a protection layer that shields the Ga^+ ions of the tail of the FIB beam nanostructures can be carved out of stacks whose magnetic properties strongly depend on the quality of the stacking and interfaces. For instance, nanostructures made of Co/Pt multilayers (investigated in the following chapter 5) or consisting of spin-valves [362, 363] can be created, so that in the case of the latter their remagnetization can be electrically detected by utilizing the giant magnetoresistance (GMR) effect [364, 177, 365, 366].

5 Magnetogalvanic effects of Co/Pt layered structures - Anisotropic Interface Magnetoresistance

The chapter begins with the explanation why the magnetogalvanic effects of Co/Pt layered structures were systematically investigated within this thesis, which led to the discovery of the so-called Anisotropic Interface Magnetoresistance (AIMR) effect. Since the work of P. F. Carcia et al. in 1988 [94] it is known that contrary to soft magnetic thin films Co layers with a thickness of a few atomic monolayers sandwiched by Pt(111) layers exhibit a perpendicular magnetic anisotropy (PMA), i.e., an easy axis of magnetization parallel to the film normal (see section 2.1.3). In our working group an expertise in fabricating Co/Pt(111) multilayers with sputter-techniques was acquired over the past years [367, 112, 103, 368]. The standard methods for the investigation of the in-plane and out-of-plane remagnetization of the multilayers are the longitudinal and the polar magnetooptical Kerr effect (MOKE) [369, 370]. As an alternative and extension for measuring the remagnetization the idea was to utilize magnetoresistance (MR) effects as well. In addition, as it is possible to study individual nanostructures by downscaling the size of the electrical circuit, as particularly shown for soft magnetic submicron rectangles in the previous chapter, the aim was to investigate the magnetic properties of single Co/Pt nanodots with PMA and diameters $\lesssim 30$ nm produced in a well-established top-down preparation process [371, 372, 373]. In particular, for the investigation of nanodots with PMA the so-called anomalous Hall effect (AHE) is known to be very appropriate as a probe [374, 375, 376, 377, 378, 379].
Initially, in order to proof the feasibility of the MR effects to investigate Co/Pt layered structures the MR properties of several multilayers with PMA were characterized. For that purpose the samples were grown on insulating glass substrate and electrically contacted by means of standard ultrasound bonding technique. Two bonds were used to impress the current and to measure the longitudinal resistance in a two point measurement geometry. An additional pair of bonds served as voltage probes for measuring the Hall effects. The resistance in dependence of the magnetic field, which was swept from +800 mT to −800 mT and then reversed, was measured for the three principle field directions with respect to the current direction and stacking (see Fig. 5.1(a)). While the field dependent Hall resistance was in qualitative accordance with the expectation (not shown) the behavior of the longitudinal resistance, which can exemplarily be seen for a representative sample in Fig. 5.1(b), was surprising as described in the following. In order to understand the shape of the MR curves they are compared with the remagnetization of the films detected by MOKE. The longitudinal MOKE measurement displays a hard axis be-

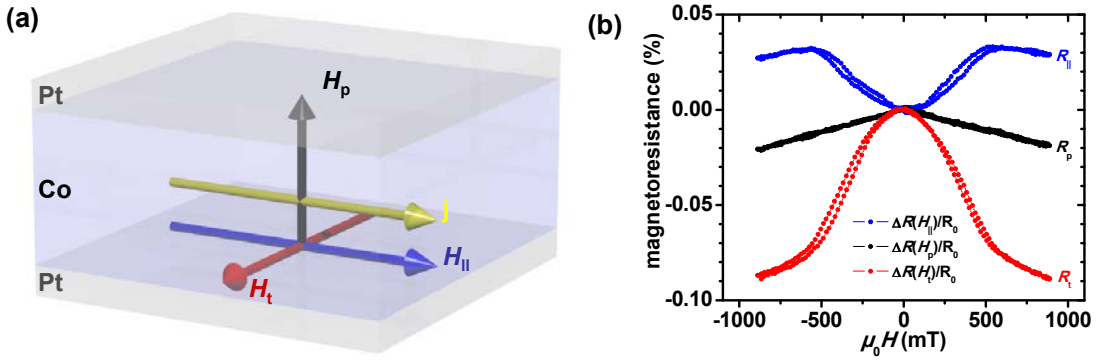

Figure 5.1: (a) Sketch of a Pt/Co/Pt sandwich, where the current **j** flows in the plane. The three generic directions of the magnetic field **H** with respect to the current direction and layer stacking are drawn, i.e., the so-called longitudinal (||), transverse (t), and polar (p) geometry. In (b) the corresponding magnetoresistance curves of a 5 nm Pt/ (0.8 nm Co/ 2 nm Pt)$_4$/ 1 nm Pt multilayer deposited on glass substrate are shown. The magnetic field $\mu_0 H$ was swept between ±800 mT while the magnetoresistance curves $(R(\mu_0 H) - R(\mu_0 H = 0))/R(\mu_0 H = 0)$ were recorded. Note that above technical saturation the transverse resistance R_t is lower than the polar resistance R_p. This difference in resistance is in the same order of magnitude as the difference between the longitudinal resistance $R_{||}$ and the transverse resistance R_t, i.e., the AMR.

havior and reveals that for any desired in-plane direction the sample is magnetically saturated by a field of about ±600 mT. Up to this field strength a relatively strong parabolic change of the resistance with field occurs (blue and red MR curve). When the magnetization is oriented along the field direction only a slight linear decrease of the resistance with field remains. The resistance for sweeping a field oriented along the magnetically easy axis only shows a slight field dependence, namely for both field directions a linear decrease in resistance with increasing the field strength (black MR curve). The corresponding polar MOKE measurement shows a rectangular hysteresis with a coercive field of about 20 mT revealing that the orientation of the magnetization with respect to the current direction does not virtually change during the whole field sweep.

Above technical saturation ($M_S||H$) the magnitude of the linear slope in the magnetoresistance curves is basically the same for all three generic field orientations. As already stated in connection with the MR curves of the permalloy film in section 4.4.3 this isotropic high-field behavior can be attributed to the annihilation of spin waves with increasing field (spin-disorder MR). The (field independent) difference in resistance between the two in-plane curves above technical saturation corresponds to the expected behavior, namely $R_{||} > R_t$. This difference in resistance is the consequence of the anisotropic magnetoresistance (AMR), which was used as a probe for the magnetization orientation of the rectangles in the previous chapter (see section 4.4.1), as the angle between current and magnetization direction is different by 90°, while the orientation of the magnetization with respect to the stacking and polycrystalline structure is the same in both geometries.

Before the first MR measurements of the Co/Pt samples were conducted it was naively expected that above technical saturation the resistance is identical in the

polar and transverse MR geometry. The reason for this was that in both cases the magnetization is oriented perpendicularly to the current direction, so that the action of the AMR effect is the same. Against this expectation the results showed a significant difference, namely $R_\mathrm{p} > R_\mathrm{t}$, as can be clearly seen in Fig. 5.1(b). In literature an effect was already described which results in a difference between the polar and transverse resistance in thin polycrystalline films consisting of ferromagnetic transition metals. This so-called geometrical size effect (GSE) is caused by the texture of the films (further details see section 5.1.4) and results in the fact that the polar resistance is smaller than the transverse resistance. In contrast to the signature of the GSE, however, for Co/Pt layered structures the opposite behavior was found. To stress the point, the depicted characteristic $R_\mathrm{p} > R_\mathrm{t}$ have not been reported for thin polycrystalline layers of ferromagnetic transition metals until now, so that within this thesis investigations have been started with the main objective to reveal the origin of the discovered MR effect.
In order to measure the resistance quantitatively, i.e., to determine the resistivity of the samples, a wire shaped sample design was used, which supplies a well-defined current path with laterally homogeneous current density. The design of the macroscopic wire samples that allows the detection of the Hall voltage and longitudinal resistivity in four-point probe geometry as well as the preparation of the Co/Pt layered structures with sputter techniques is presented in section 5.2.
The results of the structural and magnetic characterization of the samples is discussed in section 5.3. The crystallinity as well as the structural properties of the interfaces were investigated by means of x-ray techniques as both play a crucial role for the magnetic properties of Co/Pt layered structures (see section 2.1.5). Vice versa, the magnetic anisotropy of the samples determined via MOKE and AHE was used as a sensitive probe to reflect small changes in the structural properties. Besides the anisotropy the saturation magnetization was measured by ferromagnetic resonance measurements. The determination of the material properties in dependence of particular sample parameters provides a good foundation in order to give a reasonable interpretation of the results of the magnetoresistance investigations.
The experimental MR measurement setup of the room temperature investigations and the MR measurement scheme are presented in section 5.4.
From section 5.5 to 5.7 the results of the MR investigations of Co/Pt layered structures are presented and discussed. The topic of section 5.5 are the results of the MR investigations of Pt/Co/Pt sandwiches, which in particular demonstrates that the discovered $R_\mathrm{p} > R_\mathrm{t}$ effect originates at the Co/Pt interfaces. Thus, the effect was named anisotropic interface magnetoresistance (AIMR). The AIMR is also proven theoretically by means of an *ab initio* study whose results are presented in connection with the experimental findings. In addition to the discovery of the AIMR the experimental investigations further show that the various MR effects existing in the Co material, i.e., the AMR, spin-disorder MR, AHE, as well as the and normal Hall effect, are significantly affected by the finite size of the Co layer. An interface scattering contribution to the AHE was also observed.
The preliminary results of the temperature dependence of the AIMR and the other MR effects are presented in section 5.6, especially revealing the existence of the AIMR effect down to 4.2 K.

Section 5.7 deals with the AIMR of Co/Pt multilayers, where it is shown that the AIMR is generally in the same order of magnitude as the AMR for Co/Pt multilayers with PMA (see exemplarily Fig. 5.1(b)). In connection with this result the corresponding important implications concerning recent efforts for studying the intrinsic domain wall resistance are discussed. In particular, this finding shows that when investigating the magnetoresistance it is mandatory to be aware of the various effects which can probably take place in order to avoid misinterpretation of the experimental data. Therefore, the following section 5.1 deals with the experimental and theoretical background concerning the resistivity and magnetoresistance effects of thin films consisting of ferromagnetic transition metals.
The chapter is closed with a conclusion and an outlook in section 5.8.

5.1 Fundamentals of the magnetotransport of ferromagnetic transition metal films

This section gives an overview of the electrical resistivity of thin films consisting of ferromagnetic transition metals. In section 5.1.1 the basics of the semi-classical description of the electrical transport in solid state physics are introduced. The second section 5.1.2 deals with the Fuchs-Sondheimer model, which phenomenologically describes the influence of the scattering of electrons at surfaces on resistivity. Section 5.1.3 concerns the characteristics of the resistivity of ferromagnetic transition metals, which is quite complex in comparison to alkali or noble metals with filled d-orbitals[1]. Finally, in section 5.1.4 the various effects that are caused by the influence of external as well as internal magnetic fields on the resistivity are presented.

5.1.1 Basics of electrical resistivity - Ohm's law, Boltzmann equation, Matthiesen's rule, and Bloch-Grüneisen formula

In section 5.1.1.1 the symmetry properties of the resistivity tensor in the presence of magnetic fields is discussed. Section 5.1.1.2 deals with the sources of resistivity in the absence of magnetic fields and gives a description of electrical resistivity within the framework of the semi-classical Boltzmann equation. The subsequent part 5.1.1.3 introduces Matthiessen's rule, which attests that the different resistivity contributions simply add to an overall resistivity. The section is closed with the temperature dependence of the resistivity of alkali and noble metals (section 5.1.1.4).

5.1.1.1 Ohm's law in the presence of magnetic fields - symmetry considerations

The current density $\mathbf{j}$ produced by an applied electric field $\mathbf{E}$ is related to it through Ohm's law, which is in its general case in the absence of any thermal gradients [380, 381]:

$$\mathbf{j} = \overleftrightarrow{\sigma} \cdot \mathbf{E} \tag{5.1}$$

Here $\overleftrightarrow{\sigma}$ is the electrical conductivity, which is a tensor of second rank (matrix). In the experiment the current density $\mathbf{j}$ is generally controlled rather than the electric field $\mathbf{E}$, i.e., a voltage produced by a given primary current is measured. Therefore, it is more convenient to formulate the inverse relationship of Eq. 5.1 as the current (density) is the independent variable:

$$\mathbf{E} = \overleftrightarrow{\rho} \cdot \mathbf{j} \quad , \tag{5.2}$$

where $\overleftrightarrow{\rho} = \overleftrightarrow{\sigma}^{-1}$ is the electrical resistivity tensor. As the topic of interest is the influence of magnetic fields on the electric resistivity a more generalized form of Ohm's law is needed which includes the expression of magnetic fields [381]. This

[1] Within this thesis the term noble metal is restricted to noble metals with filled d-orbitals.

is achieved by writing the resistivity tensor as a general function of the magnetic fields [382]:

$$\mathbf{E} = \overleftrightarrow{\rho}(\mathbf{M}, \mathbf{H}) \cdot \mathbf{j} \tag{5.3}$$

In the following it is only dealt with an external field $\mathbf{H}$ for the sake of clarity, as the corresponding results for the magnetization $\mathbf{M}$ can be obtained by a substitution of the variable $\mathbf{H}$ by $\mathbf{M}$. Expanding each component of $\overleftrightarrow{\rho}(\mathbf{H})$ in a Taylor series yields

$$\rho_{ik}(\mathbf{H}) = \rho_{ik}^{(0)} + R_{ikp}^{(1)} H_p + R_{ikpq}^{(2)} H_p H_q + ... \quad , \tag{5.4}$$

where $\rho_{ik}^{(0)}$, $R_{ikp}^{(1)}$, $R_{ikpq}^{(2)}$ are the taylor coefficients. Note, that Einstein's summation convention is used, which implies the summation over all possible values of the indices p and q. Generally, the Taylor series can be terminated after the quadratic term. Expectations are discussed in Ref. [382]. The Taylor coefficients underlie restrictions arising from the so-called Onsager principle of microscopic 'reversibility' [383, 384] as well as from the symmetries (crystal, stacking) of the sample. Onsager's principle is universally valid as it applies for all transport phenomena and does not depend on details of a distinct transport process. In particular, for the electrical conductivity the Onsager principle states that if the velocities of the electrons are reversed simultaneously the electrons will retrace their former paths, i.e., $\rho_{ik} = \rho_{ki}$. This is equivalent to the statement that the equation of motion is invariant under time transformation $t \mapsto -t$. In the presence of a magnetic field there is no reversibility for the path of an electron unless the velocity (current density) as well as the magnetic field is reversed, which yields:

$$\rho_{ik}(\mathbf{H}) = \rho_{ki}(-\mathbf{H}) \tag{5.5}$$

For more details concerning the Onsager principle, see Refs. [383, 384, 385]. Applying the theorem to each component of $\overleftrightarrow{\rho}$ leads to the fact that the diagonal part has to consist of even powers of H_p only. In addition, the coefficients are functionally related to each other leading to a further reduction in the number of independent variables:

$$\rho_{ik}^{(0)} = \rho_{ki}^{(0)}, \quad R_{ikp}^{(1)} = -R_{kip}^{(1)}, \quad R_{ikpq}^{(2)} = R_{kipq}^{(2)}, \tag{5.6}$$

the latter for all permutations of p and q. Besides the Onsager principle, restrictions for the coefficients arise from the particular crystal symmetry of the sample [386]. This work does not deal with perfect epitaxial single crystals but with polycrystalline films that are out-of-plane textured (definition, see section 2.1.3.1). As the grain size is in the nanometer range and significantly smaller than the macroscopic sample, influences of the crystallinity average out for any in-plane (x and y) direction and only the out-of-plane (z) direction is outstanding. In addition, the translational symmetry in the out-of-plane direction is broken, which is caused by the Co/Pt stacking with a sequence at the nanoscale.

The in-plane isotropy results in the fact that ρ_{ii} is the same for any in-plane (xy-plane) direction of the electric field. Furthermore, in the absence of a magnetic field, which perturbs the isotropy, there can be no component of the electric field along the y direction when the current runs along x, so that $\rho_{xy}^{(0)}$ and $\rho_{yx}^{(0)}$ must be

zero [381].
Taking all these considerations into account leads to the following resistivity tensor for Co/Pt layered structures (only the leading terms in **H** are considered):

$$\overleftrightarrow{\rho}(\mathbf{H}) = \begin{pmatrix} \rho_{xx}^{(0)} + R_{xxpq}^{(2)} H_p H_q & R_{xyp}^{(1)} H_p & \rho_{xz}^{(0)} + R_{xzp}^{(1)} H_p \\ -R_{xyp}^{(1)} H_p & \rho_{xx}^{(0)} + R_{xxpq}^{(2)} H_p H_q & \rho_{xz}^{(0)} + R_{xzp}^{(1)} H_p \\ \rho_{xz}^{(0)} - R_{xzp}^{(1)} H_p & \rho_{xz}^{(0)} - R_{xzp}^{(1)} H_p & \rho_{zz}^{(0)} + R_{zzpq}^{(2)} H_p H_q \end{pmatrix} \tag{5.7}$$

In conclusion, for out-of-plane textured Co/Pt layered systems four functionally independent components of the resistivity tensor exist, namely ρ_{xx}, ρ_{xy}, ρ_{zz}, and ρ_{xz}. The other components can be traced back from these components.
In the experiment (see section 5.2.3) a wire shape sample geometry was used impressing the current in-plane (CIP) in a particular, say in the x direction, while the voltage drops along the x and the y direction were measured, which enables the determination of the components ρ_{xx} and ρ_{xy}. The two other components of the resistivity tensor are not accessible in CIP geometry. To determine ρ_{zz} a current perpendicular plane (CPP) geometry must be utilized (see section 5.8).
Subsequently, as the symmetry considerations are completed, which supply a framework of the symmetry of the effects to be expected, the physical causes of the electrical resistivity are discussed starting with the field independent terms $\rho_{ii}^{(0)}$.

5.1.1.2 Sources of electrical resistivity and Boltzmann-equation

The electrical conductivity of solid materials is caused by the movement of electrical charges. In metals (conductors) electrons of the conduction bands perform the charge transport. As a good approximation the electrons can be regarded as a free electron gas, i.e., the dispersion relation $E = \frac{\hbar^2 \mathbf{k}^2}{2m^*(\mathbf{k})}$ is valid [83]. Here, m^* is the effective mass of the electrons of a distinct band and **k** vector, which depends on the bending of the band structure:

$$\frac{1}{(m^*(\mathbf{k}))_{ij}} = \frac{1}{\hbar^2} \frac{d^2 E}{dk_i dk_j} \tag{5.8}$$

This means that the effect of the periodic lattice potential is fully included in m^*. In thermal equilibrium, in the field free case the electrons occupy the states according to the Fermi distribution function [387]:

$$f_0(E,T) = \frac{1}{\exp\left(\frac{E-E_\mathrm{F}}{k_\mathrm{B}T}\right) + 1} \quad , \tag{5.9}$$

where E_F is the Fermi energy, which is typically about $1-3$ eV and therefore two orders of magnitude larger than the thermal energy at room temperature of $k_\mathrm{B}T = 25$ meV. Accordingly, at room temperature the deviations of $f_0(E,T)$ from the Heavyside step function at $T = 0$ are only small and can be neglected in a good approximation.
Applying an electric voltage results in an electric field **E**, which exerts a force

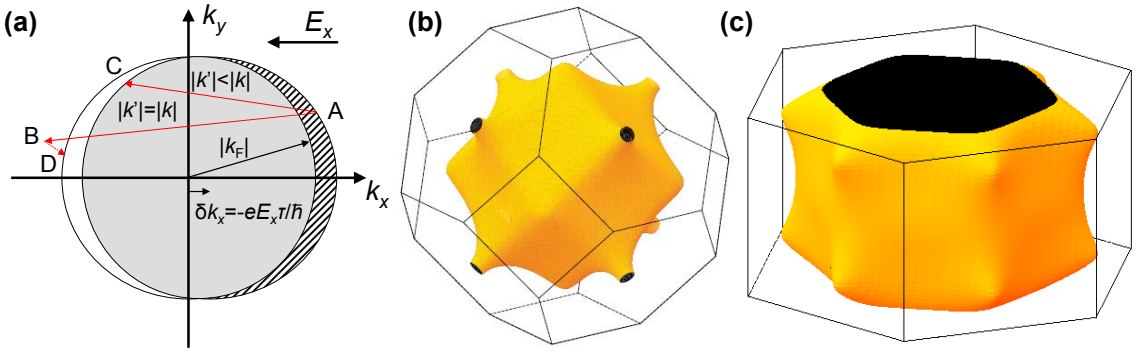

Figure 5.2: (a) sketches a two-dimensional section through the Fermi sphere of a free electron gas. In equilibrium the gray and white regions up to the Fermi energy are occupied with $\sum_{\mathbf{k}_{\mathrm{occ.}}} \mathbf{k} = 0$. Under the influence of a time-independent electric field E_x the interplay between the influence of E_x and scattering processes yields a constant shift of each state by $\delta k = -eE_x\tau/\hbar$, so that the Fermi sphere is elongated (gray and dashed region). Elastic (A$\longrightarrow$B) and inelastic scattering processes (A$\longrightarrow$C, B$\longrightarrow$D) are indicated by red arrows. (b) Calculated Fermi surface of the majority electrons of the 6$^{\mathrm{th}}$ band of fcc Co. From Ref. [391]. (c) Calculated Fermi surface of the majority electrons of the 11$^{\mathrm{th}}$ band of hcp Co. From Ref. [392].

$\hbar\dot{\mathbf{k}} = -e\mathbf{E}$ on the electrons yielding an elongation of the Fermi sphere [387]. This means that every electron, which occupies a state with wave vector $\mathbf{k}$ at the time t was located at $t - \mathrm{d}t$ at $\hbar\mathbf{k} - (-e)\mathbf{E}\mathrm{d}t$. Thus, in the case of an ideal crystal the application of a time-independent field yields a uniform elongation of the Fermi sphere with time. This is equivalent to a vanishing resistivity as the current density rises steadily: $\dot{\mathbf{j}} = -\frac{2e\hbar}{Vm^*}\sum_{\mathbf{k}_{\mathrm{occ.}}} \dot{\mathbf{k}} = ne^2\mathbf{E}/m^*$, where V is the crystal volume and n is the electron density [388, 389]. The reason for this behavior is that the electrons occupy eigenstates of the periodic potential of the crystal (or a superposition of them), the so-called Bloch-states, which are stationary solutions of the time-independent Schrödinger equation [390]. In order to obtain a finite conductivity this means that deviations from the perfect periodicity of the crystal lattice have to exist which perturb the propagation of the stationary states. Deviations can either be static (lattice defects in single crystals, i.e., dislocations, vacancies, interstitials, stacking faults, impurities; grain boundaries in polycrystalline samples; surfaces/interfaces, which are important for thin films/ multilayers) or dynamic like phonons or magnons. The latter are the quasi-particles of the collective thermal excitation of the spin system that are important in the case of the resistivity of ferromagnetic metals, which is the subject of section 5.1.3, and not considered until then. At the deviations the electron waves can be scattered from one edge of the Fermi surface to the other as schematically shown in Fig. 5.2(a), which yields a constant elongation of the Fermi surface in the case of a constant (time-independent) electric field. To sum up, the electrical transport is an interplay between the acceleration caused by electric fields acting uniformly on every electron and scattering processes, which are random events forcing the electrons back to their equilibrium positions in $\mathbf{k}$-space. In mathematical terms, the ultimate goal is to determine the non-equilibrium Fermi distribution function. With the considerations made above, the Fermi-distribution

at a given time t can be traced back from the Fermi-distribution at a time $t - \mathrm{d}t$ by $f(\mathbf{k}, t) = f(\mathbf{k} + \mathbf{E}\mathrm{d}t/\hbar, t - \mathrm{d}t) + \left(\frac{\mathrm{d}f}{\mathrm{d}t}\right)_{\mathrm{scat}} \mathrm{d}t$, where the first term describes the influence of the electric field and $\left(\frac{\mathrm{d}f}{\mathrm{d}t}\right)_{\mathrm{scat}}$ the influence of the scattering [387]. For time-independent electric fields there is a dynamical balance between scattering and influence of the field so that the distribution function does not change with time: $\mathrm{d}f/\mathrm{d}t = 0$. A Taylor series expansion up to the linear terms in t leads to [387]:

$$-\frac{e}{\hbar}\mathbf{E} \cdot \nabla_{\mathbf{k}} f = \left(\frac{\mathrm{d}f}{\mathrm{d}t}\right)_{\mathrm{scat}} \tag{5.10}$$

This is the so-called Boltzmann-equation for the steady state condition, which describes how the distribution function is altered under the influence of a constant external field and the presence of scattering of the electrons.
In the scattering term $\left(\frac{\mathrm{d}f}{\mathrm{d}t}\right)_{\mathrm{scat}}$ the various scattering mechanisms are included. The important quantity for the description of any scattering process is the transition rate from one Bloch state $\Phi(\mathbf{k})$ to any other Bloch state $\Phi(\mathbf{k}')$ under the influence of a distinct scattering potential V. A way to calculate the transition rate $\Gamma_{\mathbf{k},\mathbf{k}'}$ is known as Fermi's golden rule (time-dependent perturbation theory), which is [393, 394]:

$$\Gamma_{\mathbf{k},\mathbf{k}'} = \frac{2\pi}{\hbar} | < \Phi(\mathbf{k}')|V|\Phi(\mathbf{k}) > |^2 D(E') \quad , \tag{5.11}$$

where $D(E')$ is the density of states at the energy E' of the final state. The total scattering rate is then proportional to the summation over all possible combinations of $\mathbf{k}$ and $\mathbf{k}'$.
To abandon the microscopic nature of any scattering process the so-called relaxation time approximation is frequently used. This approximation assumes that the temporal rate for the Fermi surface to be forced back to its equilibrium position f_0 is the stronger the larger the elongation of f is, so that [387]:

$$\left(\frac{\mathrm{d}f}{\mathrm{d}t}\right)_{\mathrm{scat}} = -\frac{f(\mathbf{k}) - f_0(\mathbf{k})}{\tau} \tag{5.12}$$

This assumption implies in particular that there exists a characteristic relaxation time τ so that $f(\mathbf{k})$ relaxes exponentially back to $f_0(\mathbf{k})$ when the external field is switched off.
A solution of the Boltzmann equation $f(\mathbf{k})$ in the relaxation time approximation is given in the next section for the special case of thin films. With a given solution the conductivity $\sigma = \frac{\mathbf{j}}{\mathbf{E}}$ can be calculated by summing up the velocities of the occupied states [387]:

$$\mathbf{j} = -\frac{e}{8\pi^3} \int \mathrm{d}\mathbf{k}\ \mathbf{v}(\mathbf{k}) f(\mathbf{k}) \tag{5.13}$$

In the case of cubic symmetry, i.e., fcc, bcc, and sc lattices, the resistivity $\rho^{(0)}$ is intrinsically isotropic, so that it is a scalar quantity. The reason for this is that because of symmetry reasons the electrons find equivalent conditions whatever their direction of impressed motion in the crystal lattice is [381]. Under the assumption of a quasi free electron gas, where the parabolic dispersion relation is valid for

all **k** (**k**-independent m^*) for the conductivity the famous classical Drude result is obtained [395]:

$$\sigma \approx \frac{e^2 n}{m^*}\tau \ , \quad n = \frac{k_\mathrm{F}^3}{3\pi^2} \quad , \tag{5.14}$$

if the electron mass m is substituted by the effective mass m^*. n is the electron density and k_F the Fermi wave vector.
In contrast to cubic lattices (see Fig. 5.2(b)), for non-cubic crystal lattices like e.g. hcp (see Fig. 5.2(c)), the area of the Fermi surface projected along certain directions is different, which results in a resistivity anisotropy , i.e., that the resistivity $\rho^{(0)}$ is a tensor (see Eq. 5.7). Qualitatively, if the relaxation time can be assumed to be isotropic then the anisotropy is purely geometrical in origin and can be estimated from the ratio of the projected areas of the Fermi surface along certain directions [381]. The resistivity anisotropy is most pronounced in crystalline hcp Co, where at room temperature the resistivity along the c-axis is $\rho^0_{[0001]} = 10.280\ \mu\Omega$cm, while the resistivity in the basal plane is $\rho^0_{[10\bar{1}0]} = 5.544\ \mu\Omega$cm [396]. More details about the resistivity anisotropy in crystals can be found in Ref. [381] and references therein.
In order to comprehend the relative elongation of the Fermi surface utilizing typical electric fields of a few V/cm a qualitative comparison of the Fermi wave vector $k_\mathrm{F} \approx 1 \cdot 10^8$ cm^{-1} ($n \approx 3 \cdot 10^{22}$ cm^{-3}) with the elongation δk_x is given. For typical resistivities of metals at room temperature of $\rho = 1 - 10\ \mu\Omega$ cm [83] typical relaxation times of about $\tau = 0.1 - 0.01$ ps are obtained via Eq. 5.14 by using the free electron mass. This value corresponds to an elongation of $\delta k_x = eE\tau/\hbar = 10^{-2}$ cm^{-1}, so that the electric field causes only an infinitesimal displacement of the Fermi sphere in comparison to the radius of about $\delta k_x / k_\mathrm{F} = 10^{-10}$ [393]. Thus, only the conduction electrons in the direct vicinity of the Fermi surface contribute to the electrical transport. It is therefore appropriate to define as the mean free path λ, i.e., the average distance an electron travels between two collisions:

$$\lambda = v_\mathrm{F}\tau \quad , \tag{5.15}$$

where $v_F = \hbar k_\mathrm{F}/m^* \approx 10^8$ cm/s is the Fermi velocity. λ is typically in the range of $10 - 100$ nm at room temperature.

5.1.1.3 Matthiessen's rule - Separating different scattering contributions

As stated above, electrons can be scattered at static deviations from the perfect crystal lattice and at dynamic deviations like phonons. In the case of low static defect concentrations the phonon spectrum is not altered with the concentration, so that the electron-phonon scattering rate is only affected by temperature, i.e., the phonon concentration. In contrast, normally the scattering rate at static lattice defects is just proportional to the defect density x_i of a distinct kind of defect i (as long as the band structure of the material is not significantly affected by the impurities) [393] but does not change with temperature. Thus, it can be assumed in a good approximation that the scattering processes of the electrons caused by different types of lattice deviations are simply additive and do not influence each

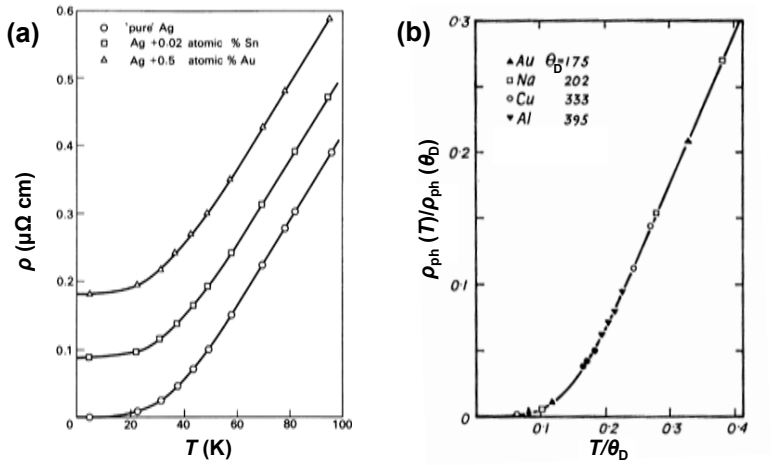

Figure 5.3: (a) Temperature dependence of the resistivity of pure Ag and of Ag with a small amount of Sn and Au, respectively. The Sn and Au impurities do not alter the shape of the $\rho(T)$ curve, however, they affect the residual resistivity $\rho(T = 0)$, so that a temperature-independent offset between the three curves exist. Thus, Matthiessen's rule (Eq. 5.17) is fulfilled. From Ref. [393]. (b) Reduced resistivity $\rho_{\mathrm{ph}}(T)/\rho_{\mathrm{ph}}(T = \Theta_{\mathrm{D}})$ for various alkali and noble metals as a function of reduced temperature T/Θ_{D}. Θ_{D} is the Debye temperature. The solid line is a fit according to Eq. 5.18 reflecting the universal temperature dependence of the resistivity. From Ref. [404].

other [397, 393]. As the scattering rate is inversely proportional to the characteristic time τ between two collisions the total relaxation time τ is then given by [387]:

$$\frac{1}{\tau} = \frac{1}{\tau_{\mathrm{st}}} + \frac{1}{\tau_{\mathrm{ph}}(T)} + \ldots \quad , \tag{5.16}$$

where τ_{ph} and $\tau_{\mathrm{st}} = (\sum_i \frac{1}{\tau_{i,\mathrm{st}}(x_i)})^{-1}$ are the scattering times for the scattering at phonons and static lattice defects. The "..." represent further scattering processes like e.g. the scattering at magnons which is discussed in section 5.1.3. This implies for the resistivity [393]:

$$\rho = \rho_{\mathrm{st}} + \rho_{\mathrm{ph}}(T) + \ldots \tag{5.17}$$

This simple additive relation is known as Matthiessen's rule, which A. Matthiessen discovered experimentally by performing elaborate studies about the temperature dependence of the resistivity of metals and alloys already in the time span of 1860−64 [398, 399, 400, 401] and which is even valid for nano-sized polycrystalline samples in a good approximation [402, 403][2]. The validity of the rule can exemplarily be seen in Fig. 5.3(a). Deviations from Matthiessen's rule are discussed in Refs. [397, 405, 406, 407, 408].

[2] At Matthiessen's time, certainly, there did not exist a realistic imagination about the atomistic structure of solids. Two of the findings of his studies were that the difference in resistivity between 0°C and 100°C is basically independent of the degree of purity of the sample and that the purer the samples the lower the resistivity is. The modern, general form of these two findings is Eq. 5.17, which came to be known as Matthiessen's rule.

5.1.1.4 Bloch-Grüneisen formula - temperature dependence of resistivity

As stated above, the temperature dependence of the resistivity is connected with the phonon concentration. Phonons freeze out at low temperatures and get excited at elevated temperatures. According to the Debye law the phonon density is proportional to T^3 at low temperatures [397]. But the number of large angle electron-phonon scattering from one point of the Fermi-surface to the other (see Fig. 5.2(a)) is limited by energy and momentum conservation leading to a further factor of T^2, so that $\rho_{\mathrm{ph}}(T) \propto T^5$ for $T < \Theta_{\mathrm{D}}$, where Θ_{D} is the Debye temperature. At high temperatures the electron-phonon scattering probability is proportional to the phonon concentration, thus $\rho_{\mathrm{ph}}(T) \propto T$. The two borderline cases are included in the so-called Bloch-Grüneisen formula [409, 410], which describes the temperature dependence of resistivity of alkali and noble metals within the whole span of temperature [397][3]:

$$\rho_{\mathrm{ph}}(T) = A_{\text{el-ph}} \left(\frac{T}{\Theta_{\mathrm{D}}}\right)^n \int_0^{\Theta_{\mathrm{D}}/T} \frac{x^n dx}{(e^x - 1)(1 - e^{-x})}, \quad n = 5 \quad , \tag{5.18}$$

where $A_{\text{el-ph}}$ is a material specific constant, while $A_{\mathrm{D}} = \frac{A_{\text{el-ph}}}{\rho_{\mathrm{ph}}(T=\Theta_{\mathrm{D}})} = 4.225$. Consequently, the reduced resistivity $\rho_{\mathrm{ph}}/\rho_{\mathrm{ph}}(T = \Theta_{\mathrm{D}})(T)$ only depends on Θ_{D}, so that the temperature dependence of the reduced resistivity of alkali and noble metals might lie on a universal curve when plotted against T/Θ_{D}. In Fig. 5.3(b) the temperature dependence of the resistivity of various metals is shown. The solid line is a fit according to Eq. 5.18, which shows a good description of the data and thus demonstrates the universal validity of the Bloch-Grüneisen formula under consideration of Matthiessen's rule (Eq. 5.17). Experimentally, as there is only a vanishingly small number of electron-phonon collisions at liquid Helium temperature (see Fig. 5.3(b)), $\rho_{T=4.2K}$ provides the residual resistivity ρ_{st} in a good approximation. The so-called residual resistivity ratio

$$RRR = \frac{\rho_{T=295\ \mathrm{K}}}{\rho_{T=4.2\ \mathrm{K}}} \tag{5.19}$$

states, which scattering process dominates at room temperature and is a measure for the structural disorder of the sample [389].

5.1.2 Resistivity of thin films - Fuchs-Sondheimer model

Surfaces and interfaces perturb the translational symmetry of a crystal. Thus, it has to be assumed that they act as scattering elements for the electrons. Already before a realistic theoretical model of solid states was proposed it was known that the electrical resistivity of thin films ρ' is larger than the corresponding bulk value ρ and that the ratio ρ'/ρ increases when the film thickness decreases. The first such experimental observations were made by Isabelle Stone by using silver "films" with thicknesses down to 13 nm in 1898 [411]. Three years later, J. J. Thomson, who discovered experimentally the existence of electrons shortly before (1897), proposed

[3] The temperature dependence of transition metals is discussed in section 5.1.3

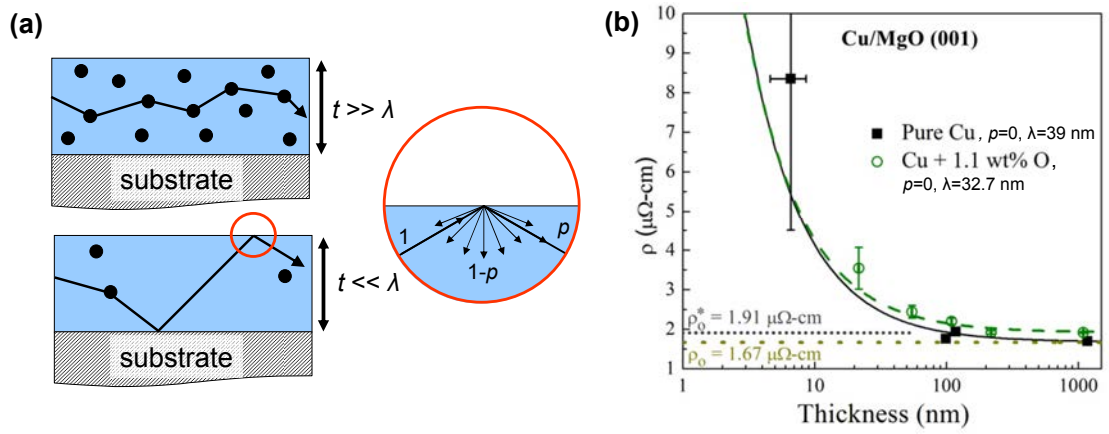

Figure 5.4: (a) Sketch of scattering processes of an electron in a thin film, with $t \gg \lambda$ (top) and $t \ll \lambda$ (down). Within the Fuchs-Sondheimer model a part p of the scattering processes of the electrons at the surfaces is assumed to be specular, while the remainder $(1-p)$ is assumed to be diffusive. (b) Resistivity ρ of epitaxial Cu and CuO films grown on electric insulating MgO(001) in dependence of film thickness. The curves were fitted according to Eq. 5.27 (solid and dashed lines) indicating fully diffusive scattering ($p = 0$). For $p = 1$ the resistivity would not depend on thickness (dotted lines). From Ref. [413].

a free electron gas model with the result that surface scattering significantly enhances the resistivity by decreasing the film thickness t when t is in the order of magnitude of the mean free path of the electrons (see Fig. 5.4(a)) [412]. When more realistic models of the inner structure of atoms and solids were proposed and quantum mechanics succeeded to describe the electrical transport [390, 409], K. Fuchs adapted Thomson's model in 1938 [414] by treating the surface scattering in the framework of the (semiclassical) description of the electrical transport utilizing the Boltzmann-equation. E. H. Sondheimer gave a comprehensive review about this topic in 1952 [415][4]. Since then this description is known as Fuchs-Sondheimer (FS) model, which is presented in the following.
In the derivation of the Boltzmann equation described in the previous section an infinite system is considered so that the distribution function has no spatial dependence. In thin films the reduced dimensionality leads to the fact that the Fermi distribution function f also depends on the spatial coordinates of the electrons: $f = f(\mathbf{r}, \mathbf{k}, t)$. Thus, a further term in the Boltzmann equation appears [414, 415, 408]:

$$\mathbf{v} \cdot \nabla_{\mathbf{r}} f - \frac{e}{\hbar} \mathbf{E} \cdot \nabla_{\mathbf{k}} f = -\frac{f(\mathbf{k}) - f_0(\mathbf{k})}{\tau} \tag{5.20}$$

As in thin films the translational symmetry is only broken in one direction, say the z direction, the problem can be traced back to a one-dimensional problem. In the following, the notation of the distribution function $f = f_0(E) + g(z, \mathbf{k})$ is used, where f is the equilibrium distribution function which is valid in the absence of an

[4]The article of Sondheimer was the first article to appear in Advances in Physics. In 10/2001 it was reprinted, see Ref. [416]. Until then it was cited more than 1000 times and was ranked 5^{th} with respect to the most cited articles of this famous journal.

applied field and g is the deviation in the presence of an applied field. Assuming a constant electric field in any in-plane, say the x direction, the Boltzmann equation in relaxation-time approximation is [408]:

$$v_z \frac{\delta g}{\delta z} + v_x e E_x \frac{df_0}{dE} = -\frac{g}{\tau} \quad , \tag{5.21}$$

which has the solution:

$$g(z, \mathbf{k}) = v_x e E \frac{df_0}{dE} \left(1 + \underbrace{F(\mathbf{k}) \exp\left(-\frac{m^* z}{\hbar \tau k_z} \right)}_{G(z,\mathbf{k})} \right) \quad , \tag{5.22}$$

where $F(\mathbf{k})$ is an arbitrary function. To determine $G(z, \mathbf{k})$ boundary conditions have to be introduced for the Fermi distribution function at the surfaces of the film. A general ansatz of Fuchs and Sondheimer was to assume that a fraction p of the electrons is scattered specularly at the surfaces meaning that for these electrons there is no loss in forward momentum when scattered at the surfaces, while the velocity component v_z is reversed. The other fraction, namely $1 - p$ is assumed to be scattered diffusively with complete loss in forward momentum[5]. The parameter p is called specularity parameter. Thus, the distribution function at the surfaces located at $z = 0$ and $z = t$ (t is the thickness of the film), respectively, for electrons moving away from the surfaces ($v_z \gtrless 0$) are [416]:

$$\begin{aligned} f_0 + g^+(v_z, z = 0) &= p(f_0 + g^-(-v_z, z = 0)) + (1 - p) f_0 \\ &\Longleftrightarrow g^+(v_z, z = 0) = p g^-(-v_z, z = 0) \\ f_0 + g^-(v_z, z = t) &= p(f_0 + g^+(-v_z, z = t)) + (1 - p) f_0 \\ &\Longleftrightarrow g^-(v_z, z = t) = p g^+(-v_z, z = t) \end{aligned} \tag{5.23}$$

With these boundary conditions $G^{\pm}(v_z)$ is obtained to:

$$\begin{aligned} G^+(z, v_z) &= -\frac{1 - p}{1 - p \exp(-t/\tau v_z)} \exp\left(-\frac{z}{\tau v_z} \right) \quad , \\ G^-(z, v_z) &= -\frac{1 - p}{1 - p \exp(t/\tau v_z)} \exp\left(\frac{t - z}{\tau v_z} \right) \end{aligned} \tag{5.24}$$

To calculate the current density/conductivity the results for the distribution functions (Eqs 5.22, 5.24) have to be put in the integral for the current density of Eq. 5.13. The process concerning the question of how to deal with the integral to get a convenient expression is described in detail in Ref. [416]. The result is the

[5]The artificiality of this ansatz was already critically remarked by Sondheimer in Ref. [415].

famous Fuchs-Sondheimer solution:

$$\sigma_{\mathrm{FS}}(t,p,\lambda,\sigma_{\mathrm{bulk}}) = \sigma_{\mathrm{bulk}}\left(1-\frac{3}{2}\frac{\lambda}{t}(1-p)\int_1^\infty \frac{\left(\frac{1}{x^3}-\frac{1}{x^5}\right)\left(1-\exp(-\frac{t}{\lambda}x)\right)}{1-p\exp(-\frac{t}{\lambda}x)}dx\right) \tag{5.25}$$

σ_{bulk} is the bulk value of the conductivity, which corresponds to Eq. 5.14, i.e., the Drude result of the Boltzmann equation. λ is the bulk mean free path[6], which is functionally related to σ_{bulk} (compare Eq. 5.14 and Eq. 5.15) as charge conservation has to be maintained [417]:

$$\frac{\sigma_{\mathrm{bulk}}}{\lambda} = \left(\frac{8\pi}{3}\right)^{1/3}\frac{e^2}{h}n^{2/3} \tag{5.26}$$

In order to get an imagination about the dependence of the resistivity on film thickness the limiting expression of Eq. 5.25 is given, which is valid for large film thicknesses $t \gg \lambda$:

$$\rho_{\mathrm{FS}} = \rho_{\mathrm{bulk}}\left(1+\frac{3\lambda(1-p)}{8t}\right) \tag{5.27}$$

As can be seen the model predicts that the resistivity should show a $1/t$ dependence except for the case of $p = 1$, where ρ_{FS} always equals ρ_{bulk}.
In Fig. 5.4(b) the thickness dependence of the resistivity of epitaxial Cu and Cu with a small amount of oxygen is shown. The solid lines represent fits according to the Fuchs-Sondheimer model, which are obviously in good agreement with the experimental data. The obtained specularity parameter is $p = 0$ (fully diffuse surface scattering), which the authors attributed to the high density of surface steps with a period of less than 1 nm [413].

5.1.2.1 Improvements of the Fuchs-Sondheimer model

Since the development of the FS-model there has been a variety of publications which deal with extensions and refinements of the theory, including the treatment of e.g. surface roughness, polycrystallinity, interface scattering in the case of multilayers, and lateral confined systems. In the following a short overview of the most important concepts is given. A comprehensive overview is provided by M. A. Angadi [418].
In 1950 the results of K. Fuchs were extended to model the resistivity of square [419] and circular [420, 421] wires, which was also reviewed in Sondheimer's famous review two years later [415]. Recently, the models could be applied to describe the resistivity of thin wires as a function of the wire dimensions [422, 423, 424, 425, 426, 427, 428, 429].
However, for the depiction of the resistivity of the wires, which are in the majority polycrystalline, grain boundary scattering has to be considered as well. The description of the scattering of electrons at grain boundaries in the framework of

[6]It should be noted that in the FS-model all scattering mechanisms except surface scattering are expressed in terms of a relaxation time/mean free path.

the Boltzmann-equation was deduced by A. F. Mayadas and M. Shatzkes in the late 1960s [430, 431] who attributed the enhanced resistivity of thin polycrystalline films to grain boundary scattering, which is superimposed on surface scattering. Until then, it was common believe that grain boundaries have only minor impact on the resistivity [397]. The importance of the so-called Mayadas and Shatzkes model (MS-model) relies on the observation that for thin polycrystalline films a variation of grain size with film thickness is often found. The general rule is that the thinner the films the smaller the grains are. Consequently, in addition to the surface scattering the grain boundary scattering contribution changes with film thickness. The MS-model predicts that similar to surface scattering, which is an important contribution to the resistivity if $t \lesssim \lambda$, the grain boundary scattering has to be taken into account if the average grain size $r \lesssim \lambda$. They found that the resistivity for metals with grain boundaries is larger than for boundary free material according to [431]

$$\sigma_{\mathrm{gr}} = \sigma_{\text{single crystal}} \cdot \left(1 - \frac{3\alpha}{2} + 3\alpha^2 - 3\alpha^3 \ln(1 + 1/\alpha)\right), \quad \alpha = \frac{\lambda}{r} \cdot \frac{R}{1-R} \quad , \quad (5.28)$$

where R is the reflection probability of the electrons at the grain boundary. In analogy to the phenomenological surface specularity parameter p of the FS-model, $R = 0$ means that the grain boundaries are transparent and do not affect the resistivity while $R \longrightarrow 1$ implies total reflection of the electrons.
Recently, the direct evidence was offered that grain boundaries provide a source of resistivity. By using the tips of a four-probe scanning tunneling microscope the resistivity of single grain boundaries could be measured [432, 433].
Nowadays, it is common use to describe the resistivity of thin films by utilizing both models, i.e., the FS- and the MS-model [434, 435, 436, 437, 438, 425, 439]. In the case of thickness-independent grain sizes the contribution of the grain boundary scattering to the resistivity is only an offset and the thickness dependence of the resistivity can be well-described by the FS-model [425].
Real film surfaces are by no means flat. Thus, several descriptions to deal explicitly with the influence of the surface topography on the resistivity were introduced [440]. S. B. Soffer included the (microscopic) surface (root mean square) roughness σ_{RMS} (see Eq. 4.9) in the phenomenological specularity parameter p. Furthermore, he deduced that p depends on the angle of incidence of the electrons at the surface θ, which is neglected in the FS-model. For a vanishing roughness correlation length p is related to σ_{RMS} and θ by [440, 441]:

$$p(\cos\theta) = \exp\left(-\left(\frac{4\pi\sigma_{\mathrm{RMS}}}{\lambda_{\mathrm{F}}}\right)^2 \cos^2\theta\right) \quad (5.29)$$

Thereby, $\cos\theta = x$ is the integration variable in Eq. 5.25, and $\lambda_{\mathrm{F}} = 2\pi/k_{\mathrm{F}}$ is the Fermi wave length, which is about a few Angstroms in metals [442]. This extension allows to substitute the fit-parameter p in Eq. 5.25 by Eq. 5.29 if the surface roughness is known [443, 403].
For very rough (macroscopic modulated) film surfaces it is often found that the resistivity increases much stronger when decreasing the film thickness than the

FS- or Soffer-model predict [417, 443, 444, 445]. To model the surface scattering at such "island-like" films Y. Namba considered a geometrical heterogeneous film cross-section by introducing a local thickness $t(x)$ [446, 447]. To handle the macroscopic roughness mathematically he assumes a sinusoidal corrugated surface topography [447].
M. S. P. Lucas extended the FS-model to the more general case in which the top and bottom film surface have different scattering properties by considering different specularity parameters at each surface [448]. In particular, this treatment seems to be traceable when no or different materials for the seed and cap layers are used [449, 439, 450, 429].
Multilayers can be treated within the FS-model by assuming different distribution functions f_0^i as well as g^i according to Eq. 5.22 for each layer i [451, 452, 453, 454]. The functions $F^i(v)$ are then determined by corresponding boundary conditions at each interface. In general, the assumption is that a fraction R of the electrons is reflected specularly at the interface while a fraction T is transmitted with no loss in forward momentum. Then, the remainder $1-(R+T)$ is assumed to be scattered diffusively at the interface. In the context of the discovery of giant magnetoresistance (GMR) in 1989 this kind of boundary conditions under consideration of the spin degree of freedom ($\uparrow$,$\downarrow$) of each layer ($g^i = g^i_\uparrow + g^i_\downarrow$) was successfully used as a starting point to model the GMR [452, 455, 456, 457, 458, 459].
The given overview shows that there might be a variety of film properties that affect the electron scattering in thin films. Thus, as critically remarked by J. R. Sambles [460] a detailed knowledge of the film morphology is mandatory for a reasonable interpretation of the experimental data.
Besides the semi-classical description within the framework of the Boltzmann equation, many other theoretical approaches to describe the resistivity of thin films and multilayers were proposed. Overviews and comparisons of the approaches are e.g. given in Refs. [453, 461, 462] and references therein.

5.1.3 Resistivity of ferromagnetic transition metals

In this section an overview of the resistivity of ferromagnetic transition metals is presented in conjunction with concepts for their description. In contrast to alkali and noble metals[7] they exhibit a rather complex behavior. Basically, the concepts can be divided into two main approaches depending on whether the d electrons are regarded as localized at the lattice points or as delocalized in a band-structure (itinerant models). The respective most prominent concepts of both approaches are presented starting with the itinerant model in section 5.1.3.1. After presentation of the localized model in section 5.1.3.2 further contributions to the resistivity that might be present at low temperatures are introduced in section 5.1.3.3.

5.1.3.1 s-d scattering and Mott's two-current model

Especially striking is the fact that in transition metals with s, p as well as d partly occupied bands at the Fermi energy the resistivity is in the order of magnitude of 10

[7] Note that within this work the term noble metal is restricted to noble metals with filled d-orbitals.

$\mu\Omega$ cm at the Debye temperature Θ_D [73]. This is much larger than the resistivity of alkali and noble metals, where only s and p bands intersect the Fermi energy (in the order of magnitude of 1 $\mu\Omega$ cm at Θ_D [73]). At the first glance it seems to be contradictable that the adding of d electrons enhances the resistivity of a metal as the electron density n is increased (see Eq. 5.14) [463]. But contrary to free-electron-like s bands the d bands are rather narrow, so that according to Eq. 5.8 the terms of the effective mass m^* tensor are large reflecting the more localized character of the d electrons. As a consequence, according to Eq. 5.14 $\sigma_d \ll \sigma_s$ applies, so that in transition metals like in alkali and noble metals, the current flow is predominantly performed by the s electrons and the contribution σ_d can be neglected.
In order to explain the relatively high resistivity of transition metals Sir Nevil V. Mott considered in 1935 the possibility of transitions of the electrons from one band to another (interband scattering) during electron-phonon scattering besides intraband scattering processes [464, 465, 397, 466][8]. Due to the presence of the d states at the Fermi energy the contribution of the s-s interband scattering to the resistivity is not altered. However, the partly filled d bands provide further scattering processes of the s electrons as the s electrons can be scattered into the more localized d states [464, 397, 466]. According to Fermi's golden rule (see Eq. 5.11) the probability for this so-called s-d scattering is higher than for s-s scattering due to the high density of states of the d bands at the Fermi energy (see Fig. 5.6(a)), which is connected with their high effective mass. Thus, the s-d scattering processes dominate the resistivity in transition metals yielding higher resistivities in comparison to noble and alkali metals, where only s-s scattering is possible.
The d electrons interact with each other via exchange forces causing the itinerant ferromagnetism in transition metals. Therefore, it would be not surprising that connections between resistivity and magnetism exist if the fact is correct that the d states significantly affect the resistivity [73, 459]. This can be seen e.g. by taking a closer look at the temperature dependence of the resistivity. Nonmagnetic transition metals exhibit a linear increase in resistivity above the Debye temperature as described in the last section. This behavior is also found for ferromagnetic transition metals above the Curie temperature as can be seen in Fig. 5.5(a). In contrast, below the Curie temperature T_C the resistivity increases much stronger. From that it can be concluded that the electrons are additionally scattered by mechanisms that depend significantly on the magnetic state of the material. In particular, as the extrapolation of the linear behavior above T_C would yield an anomalous high residual resistivity, it suggests that the scattering probability of the electrons is significantly enhanced in the paramagnetic state. As this scattering contribution is present for ferromagnetic materials above T_C it could be also expected to find this scattering contribution in paramagnetic transition metals due to the close relationship in electronic structure [405]. For example Ir and Rh are isoeletronic to Co as it is in the same column of the periodic table; the same holds for Ni, Pd, and Pt.
While the temperature-dependent part of the resistivity of alkali and noble metals, i.e., the intraband s-s electron-phonon scattering, can be well-described by the

[8] Due to the overlap of the bands the differentiation between s, p and d electrons is rather artificial as hybridization takes place. But hybridization has only minor influence on the resistivity and can be neglected in a first approximation [73].

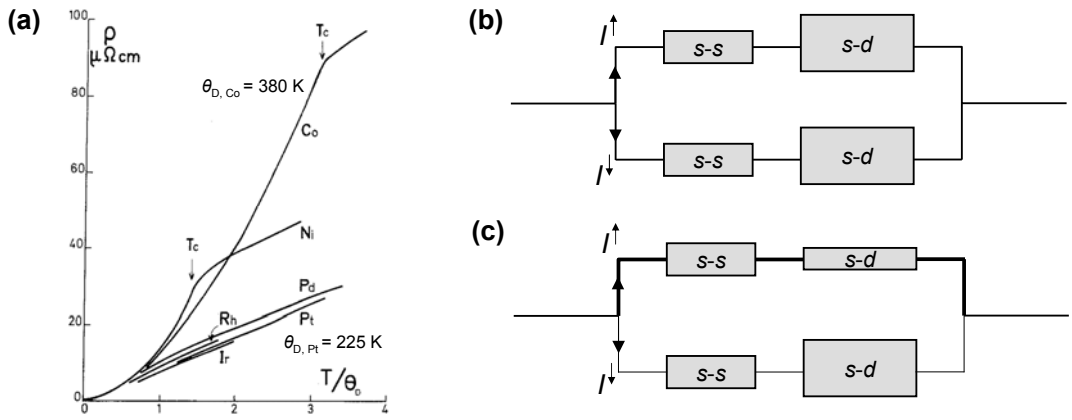

Figure 5.5: (a) Temperature dependence of the resistivity in dependence of the reduced temperature T/Θ_D for several transition metals. From [467]; Θ_D for Co and Pt from [468]. (b) and (c) are schemes of the resistivity network according to Mott's two current model that mimic the resistivity of paramagentic and ferromagnetic transition metals, respectively. The model assumes that the majority (↑) and minority (↓) electrons contribute independently to the resistivity and that contributions of *s*-*s* and *s*-*d* scattering are simply additive.

Bloch-Grüneisen formula within the whole temperature range (see Eq. 5.18 and Fig. 5.3(b)) the temperature dependence also of paramagnetic transition metals below Θ_D is more complex as additionally electron-phonon *s*-*d* scattering takes place. A. H. Wilson showed under consideration of momentum conservation that this resistivity term varies with T^3 at low temperatures instead of T^5 as it is the case for *s*-*s* scattering [469]. Within the whole temperature range the electron-phonon *s*-*d* scattering can be described by the so-called Bloch-Wilson equation, which is equivalent to the Bloch-Grüneisen equation if $n = 3$ is chosen [469, 470]:

$$\rho_{s-d\ \mathrm{scat.}}(T) = A_{\mathrm{el\text{-}ph},\ s-d\ \mathrm{scat.}} \left(\frac{T}{\Theta_\mathrm{D}}\right)^n \int_0^{\Theta_\mathrm{D}/T} \frac{x^n dx}{(e^x-1)(1-e^{-x})}, \quad n=3 \quad , \tag{5.30}$$

where $A_{\mathrm{D},s-d\ \mathrm{scat.}} = \frac{A_{\mathrm{el\text{-}ph},\ s-d\ \mathrm{scat.}}}{\rho_{s-d\ \mathrm{scat.}}(T=\Theta_\mathrm{D})} = 2.084$ [468]. The Bloch-Wilson equation does not describe the anomalous behavior of the resistivity around T_C which is connected with a stronger decrease of the resistivity below T_C. To explain this behavior Mott further assumed that the spin-degree of freedom is conserved during the vast majority of scattering processes [466]. Thus, the resistivity can be described by an electrical circuit, where two independent channels exist in parallel: One channel for the majority electrons (↑) and one channel for the minority electrons (↓) (see Fig. 5.5(b)) [466, 73]:

$$\rho = \left(\frac{1}{\rho_\uparrow} + \frac{1}{\rho_\downarrow}\right)^{-1} \tag{5.31}$$

From that so-called Mott's two-current model the difference in resistivity between the paramagnetic and ferromagnetic state can be understood by looking at the corresponding density of states, which are schematically shown in Fig. 5.6. The subbands for majority and minority electrons are plotted separately. In the paramagnetic state

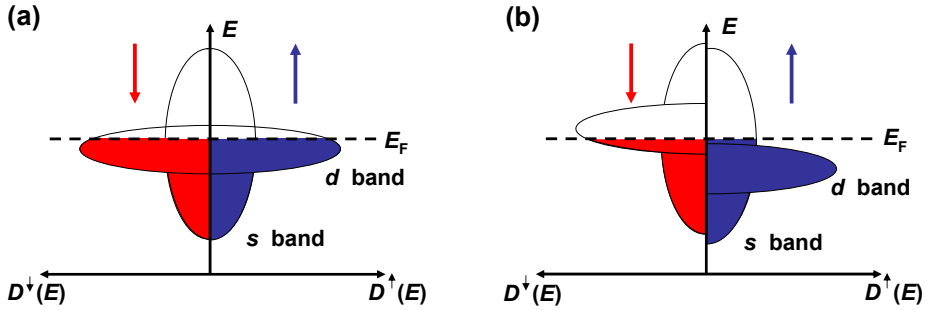

Figure 5.6: Schematics to visualize the density of states of (a) paramagnetic transition metals and of (b) strong ferromagnets like Co and Ni well below T_C.

there is no difference in the band structure of the two sub-bands (see Fig. 5.6(a)). In the ferromagnetic state the two sub-bands are split in energy as a consequence of the exchange interaction so that the number of majority electrons $N^{\uparrow}$ differs from $N^{\downarrow}$ providing a spontaneous magnetization. Fig. 5.6(b) shows the splitting for a so-called strong ferromagnet like Ni or Co at low temperatures, where the $d^{\uparrow}$ sub-band is fully depressed below the Fermi energy. As there are no $d^{\uparrow}$ states at the Fermi energy and as the spin is conserved $s^{\uparrow}$ electrons cannot be scattered into d states (see Fig. 5.5(c)). As a consequence of the disappearance of the predominant s-d scattering for the majority spins the resistivity is strongly reduced compared to the paramagnetic case, where all s electrons can be scattered into the d band (compare circuits of 5.5(b) and (c)). In the ferromagnetic case the ratio α of the spin-down and spin-up resistivities

$$\alpha = \frac{\rho_{\downarrow}}{\rho_{\uparrow}} \tag{5.32}$$

is $\alpha \gg 1$ so that the current is predominantly carried by the majority electrons [471, 73].

By increasing the temperature the exchange splitting is reduced so that the $d^{\uparrow}$ band intersects the Fermi energy and s-d scattering processes also for majority-electrons become possible. By considering that the top of the d band is parabolic the density of states at the Fermi energy and thus, according to Eq. 5.11, the $s^{\uparrow}$-$d^{\uparrow}$ scattering probability should be proportional to $\left(1 - \frac{M_S(T)}{M_S(0)}\right)^{1/3}$ [465]. This term qualitatively reproduces the experimentally found difference between isoelectronic Ni and Pd [472, 473, 397], in particular the anomalous behavior of the resistivity of Ni around T_C (see Fig. 5.5(a)). More details about the high temperature behavior of the resistivity of Fe, Co, and Ni and their alloys can be found e.g. in the Refs. [474, 475, 476, 477, 478] and the references therein.

In the temperature range between 4.2 K and 295 K investigated in this work M_S of Co is nearly constant with $M_S(T) \approx M_S(0)$, so that the density of states can be regarded as temperature-independent. Thus, the temperature dependence of the dominant s-d scattering should solely be described by the Bloch-Wilson equation (Eq. 5.30). In fact, G. K. White and S. B. Woods, who investigated the resistivity of various transition metals up to 300 K and collected older results prior to 1959 found

that the resistivity can be described by a term such as Eq. 5.30 for $T \gtrsim 10$ K [468]. For Fe, Co, and Ni the best fit is obtained for $n = 3.3$, 3.3, and 3.1, respectively. The deviation to a slightly higher value than $n = 3$ can be attributed to a commensurate small s-s scattering contribution for which, according to the Bloch-Grüneisen's formula (Eq. 5.18), $n = 5$ is expected. For Pt they found a higher value of $n = 3.7$, which reflects the general trend, that paramagnetic transition metals exhibit values around $n = 4$. For ferromagnetic as well as paramagnetic transition metals for $T \lesssim 10$ K ($T \lesssim \Theta_D/20$) the resistivity was found to vary with T^2. This behavior was experimentally observed for the first time for Pt in 1933 [479]. Possible reasons are discussed in the next paragraphs.
Since the development of the two current model, it was further extended and often used to explain the resistivity in transition metals and its alloys (see e.g. Refs. [480, 391, 26] and the references therein). As shown in section 5.1.4.1, the model provides a good basis for the understanding of the anisotropic magnetoresistance effect.
The end of this paragraph deals with the foundation of the two-current model, which is the assumption that the spin is conserved during the majority of scattering processes. In general, the dominating spin-flip mechanism is the scattering of the electrons by magnons, which was neglected until now. During an electron-magnon scattering process a majority electron is transformed to a minority electron under annihilation of a magnon and vice versa. In particular, as the electron-magnon scattering provides $s^{\uparrow}$-$d^{\downarrow}$ scattering processes the resistivity of the majority channel and thus, according to Eq. 5.31, the overall resistivity is enhanced. As shown in the next paragraph 5.1.3.2 in comparison to the electron-phonon scattering the scattering of electrons at magnons has minor impact on the overall resistivity in the temperature range investigated in this work [481], thus Mott's two-current model is legitimate in a good approximation[9].

5.1.3.2 s-d interaction and "spin-disorder" resistivity

In spite of the success of the two-current model, however, Mott himself recognized that the electron-phonon s-d scattering is not sufficient by itself to fully explain the electrical resistivity of (ferromagnetic) transition metals [482]. One reason is that the resistivity of Fe also shows a similar temperature dependence as Ni and Co, although it is not a strong ferromagnet. This means that for Fe also at low temperatures the majority d band intersects the Fermi energy, so that $s^{\uparrow}$-$d^{\uparrow}$ scattering is not suppressed. Besides this discrepancy, the d electrons of Fe are stronger localized than for Ni or Co [475]. Hence, it is questionable if they can still be regarded as itinerant or rather as localized at the lattice points. More importantly, also the ferromagnetic rare earths show a similar temperature dependence of the resistivity as the ferromagnetic transition metals. In the rare earths the f-electrons provide the ferromagnetism but they do not constitute a collective band as they are strongly localized at the atoms [483]. Thus, neither the two-current model nor the underlying electron-phonon interband scattering can be applied to describe the resistivity.

[9] The interested reader is referred to the improvement of Mott's two-current model including spin-flip scattering processes, which is given by I. A. Campbell and A. Fert in Ref. [480].

Based on these circumstances scattering mechanisms were proposed, where the d (or f) electrons are regarded as well-localized, while the s electrons are again regarded as quasi-free. The most prominent mechanism is the so-called s-d (s-f) interaction presented in the following.
In the 1950s authors on both sides of the Iron Curtain recognized independently that the exchange interaction between the spins **S** of the conduction s electrons and the spins **J** of the localized magnetic d- or f-electrons should provide an additional contribution to the resistivity [470]. In the "West", at first T. Kasuya considered the exchange interaction in the scattering potential in terms of $\Gamma \mathbf{S} \cdot \mathbf{J}$ [483, 467], where Γ is a constant reflecting the strength of the interaction. He deduced the following temperature-dependent contribution to the resistivity [467]:

$$\rho_{s-d \text{ interaction}}(T) = \rho_{\mathrm{PM}} \frac{(J - | < J > |)(J + 1 + | < J > |)}{J(J+1)} \tag{5.33}$$

Above T_{C} the spins of the d electrons are oriented randomly as no long-range magnetic order exists, so that $| < J > | = M_{\mathrm{S}} = 0$. Then, $\rho_{s-d \text{ interaction}}$ equals the temperature-independent term, here called paramagnetic (PM) resistivity ρ_{PM}. Below T_{C} with decreasing temperature $| < J > |$ monotonically increases so that $\rho_{s-d \text{ interaction}}$ decreases correspondingly. At $T = 0$ K, when all spin fluctuations die out, $| < J > | = J$ yielding $\rho_{s-d \text{ interaction}} = 0$. Qualitatively, the depicted temperature dependence of $\rho_{s-d \text{ interaction}}$ resembles the main features of the experimental curves (see Fig. 5.5(a)). As the size of $\rho_{s-d \text{ interaction}}$ depends on the degree of spin-disorder it is often referred to as "spin-disorder" resistivity. Thereby, it is differentiated between two types of spin-disorder: The disorder in the spin-orientation and as the spins of the d electrons are regarded as well-localized the disorder in their spatial location [484]. Thus, the former type of disorder can be attributed to spin-waves (below T_{C}) and the latter to phonons. The theoretical difficulty is to determine the size of both contributions in $\rho_{s-d \text{ interaction}}$ as well as their explicit dependences on temperature. In accordance with other authors Kasuya deduced an expression for the spin-wave part showing that for low temperatures below about 10 K

$$\rho_{s-d \text{ interaction}}(T) = \alpha T^2 \tag{5.34}$$

providing a significant contribution to the resistivity as α is in the order of magnitude of 10^{-5} $\mu\Omega\mathrm{cmK}^{-2}$ [485, 484, 470]. For this low temperature region I. Mannari found that the phonon contribution of the spin-disorder resistivity is negligibly small [484]. The theoretical values of α for Co, Fe, and Ni are in good agreement with the experimental results of White and Woods ($\alpha_{\mathrm{exp}} = 1.3 - 1.6 \cdot 10^{-5}$ $\mu\Omega\mathrm{cmK}^{-2}$) [468], who observed a T^2-like deviation of the resistivity from the Bloch-Wilson equation below 10 K as already mentioned in the previous section 5.1.3.1.
For $T > 10$ K the theoretical values $\rho_{s-d \text{ interaction}}$ are too small to account for significant contributions of electron-magnon scattering to the overall resistivity. Therefore, D. A. Goodings extended Kasuya's theory by assuming that the $3d$ electrons are not only localized but also itinerant in character [470]. He artificially supposed that there is a localized $3d$ electronic part which provides the s-d interaction while, besides the s band, the itinerant $3d$ electronic part is regarded to constitute a further

conduction band. The latter enables electron-magnon scattering processes caused by the *s*-*d* interaction involving interband $s^{\uparrow,\downarrow}$-$d^{\downarrow,\uparrow}$ transitions besides intraband $s^{\uparrow,\downarrow}$-$s^{\downarrow,\uparrow}$ transitions only considered by Kasuya. With the combination of *s*-*d* interaction and interband transitions proposed by Mott (see above), Goodings qualitatively showed that a relatively large $\rho_{s-d\text{ interaction}}$ results above ≈ 10 K which arises almost entirely from electron-magnon $s^{\uparrow,\downarrow}$-$d^{\downarrow,\uparrow}$ scattering processes. Below ≈ 10 K the electron-magnon $s^{\uparrow,\downarrow}$-$d^{\downarrow,\uparrow}$ scattering is negligibly small and $\rho_{s-d\text{ interaction}}$ is primarily governed by $s^{\uparrow,\downarrow}$-$s^{\downarrow,\uparrow}$ scattering and proportional to T^2 in accordance with the results of Kasuya.
Recently, Raquet et al. refined Gooding's description for the high temperature regime up to $T = T_C/2$ and extended it for high magnetic fields $\lesssim 100$ T [481][10]. The consideration of the latter provides a description of the so-called spin-disorder magnetoresistance (SMR) as shown in the next section. For Co the authors predict that $\rho_{s-d\text{ interaction}}$ depends quadratically on temperature up to $T \approx 250$ K, while for higher temperatures a stronger dependence than αT^2 is expected as a consequence of the magnon mass renormalization (temperature dependence of the magnon mass/ magnon dispersion relation) [481]. Utilizing the experimental results from the SMR measurements α_{Co} is determined to $\alpha_{Co} \approx 2.1 \cdot 10^{-5}$ $\mu\Omega\text{cmK}^{-2}$, which is coincidently similar to the value obtained by the low temperature experiments of White and Woods. Raquet et al. compared the calculated $\rho_{\text{sd, spin-disorder}}(T)$ with the experimentally determined temperature-dependent part of the resistivity of Co films and came to the conclusion that the spin-flip scattering via magnons is responsible for 18% of the temperature-dependent part of the resistivity for Co at room temperature. Similar results are obtained for Ni and Fe.
Nowadays, a combination of the T^2 law and the Bloch-Wilson formula is frequently used to fit the temperature dependence of the resistivity of ferromagnetic transition metal films in the range of up to $\gtrsim 300$ K [486, 487, 488, 489, 490][11].
The section is closed with a brief overview of the various resistivity contributions existing at low temperatures $\lesssim 10$ K.

5.1.3.3 Further resistivity contributions at low temperatures $\lesssim 10$ K

The experimentally found dependence of $\rho = \alpha T^2$ for transition metals at low temperatures $\lesssim 10$ K was often attributed to *s*-*d* electron-electron scattering processes [492, 468, 493, 494, 467] besides electron-magnon scattering. One reason to doubt the hypothesis of electron-magnon scattering to be responsible for this behavior is that besides ferromagnets also non-ferromagnetic transition metals exhibit a T^2 dependence of ρ in the same order of magnitude, while for paramagnets according to Eq. 5.33 $\rho_{s-d\text{ interaction}} = \rho_{PM}$ should be temperature-independent. In particular, for Co and Pt similar values of $\alpha_{exp} = 1 - 1.8 \cdot 10^{-5}$ $\mu\Omega\text{cmK}^{-2}$ are experimentally found (see for Pt and Co Refs. [479, 468, 495, 496, 497] and Refs. [468, 493, 498], respectively, and references therein).

[10] For details the reader is referred to the original publication Ref. [481].
[11] Recently, the first *ab initio* type description of the temperature dependence of the magnetic part of the resistivity was presented in Ref. [491], where a qualitative agreement with the experiments for bulk Co and Fe were obtained.

The famous $\rho_{ee} = \alpha T^2$ law was theoretically determined by W. G. Baber in 1937 by considering collisions of s electrons with itinerant d electrons under momentum and energy conservation [492]. For systems of lower dimensionality a different temperature dependence was theoretically predicted [499]: For two (one) dimensions, it is $\rho_{\mathrm{ee,2D}} \propto T^2 \ln(E_\mathrm{F}/k_\mathrm{B}T)$ ($\rho_{\mathrm{ee,1D}} \propto T$). The 2D behavior was experimentally confirmed for thin films consisting of ferromagnetic transition metals [500, 501, 502], while for narrow nanowires a transition from 2D to 1D behavior was found [503, 502, 504, 260] clearly indicating the existence of a significant electron-electron scattering contribution at low temperatures. For further details about the electron-electron scattering mechanism the reader is referred to Refs. [492, 397, 505, 506, 507, 499] and references therein. Besides, Ref. [507] also includes an overview of further proposed electron-magnon scattering mechanisms.
In addition to electron-electron scattering in two dimensional systems a resistance minimum and subsequent logarithmic increase with decreasing temperature can also be a consequence of the weak electron localization effect (WEL) [500]. The WEL is essentially caused by quantum interference of the conduction electrons at defects in (weak) structural disordered systems (more details see Ref. [499, 508, 509]). As the phase coherence of the electrons gets partially destroyed already in the presence of small external fields, while electron-electron scattering is hardly affected, both effects can be disentangled experimentally [510, 501, 504].
For the sake of completeness it is mentioned that the so-called Kondo effect, which is caused by spin-flip scattering processes of the electrons at magnetic impurities in non-ferromagnetic metals, also manifests in a logarithmic increase of the resistivity with decreasing temperature [511, 512, 513].

5.1.4 Magnetoresistance effects

The generic terms galvanomagnetic effects, magnetotransport or magnetoresistance (MR) stand for the influence of magnetic fields on the electrical resistivity [73]. In the following an overview of the various MR effects is given, which have been observed in thin films of polycrystalline ferromagnetic transition metals and its alloys until now. It is common use to refer to an effect as normal or ordinary effect, when it arises (also) from the flux density of an external field. These effects are present in all metallic materials, i.e., the ordinary Lorentz MR and the normal Hall effect. In ferromagnetic materials additional MR effects are present, which can be attributed solely to the (spontaneous) magnetization $\mathbf{M}$. These effects are often labeled as extraordinary or anomalous as generally they are significantly larger than the normal MR effects.
In the first section 5.1.4.1 the effects that do not only occur in thin films but also in bulk materials are presented, which affect the diagonal terms of the resistivity tensor.
In the second section 5.1.4.2 the effects are discussed, which yield the presence of off-diagonal terms. These effects are known as Hall effects.
Since fabrication methods were developed, which enable the preparation of thin films with high purity as well as high quality of the interfaces, further MR effects were discovered for film thicknesses that are in the range or smaller than the electron mean

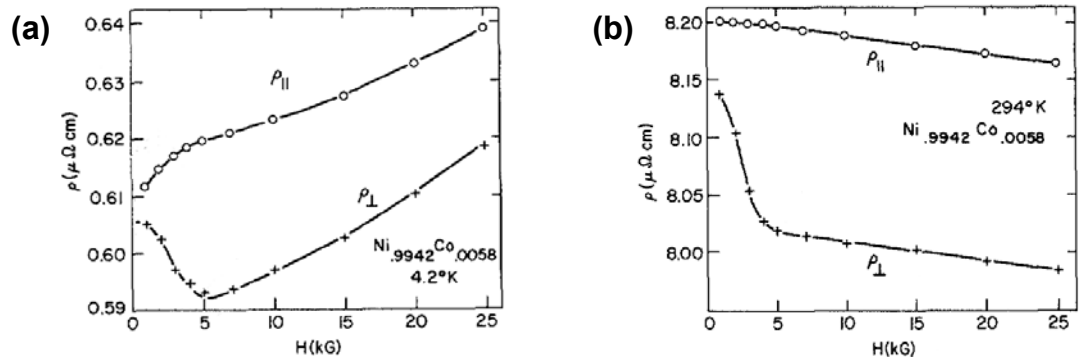

Figure 5.7: Resisitivity ρ of a NiCo alloy as a function of magnetic field H oriented perpendicularly ($\perp$) and in parallel ($||$) to the current direction at (a) 4.2 K and (b) room temperature. Above $H = 5$ kG technical saturation ($H||M_S$) is ensured. From Ref. [13].

free path. The most prominent effect is the giant MR (GMR) [15, 16], which was allocated by the Noble Price in physics in 2007 [17, 18]. The GMR and the related tunneling MR (TMR) effect [33] occur in multilayers when the relative orientation of the magnetization of the individual layers changes from parallel to antiparallel alignment. For details about GMR and TMR the reader is referred to the review articles Refs. [514, 461, 459, 515, 17, 516] and references therein as these effects will not be addressed here. In addition to these prominent effects, further effects appear that are also present in single ferromagnetic layers like the geometrical size effect (GSE) and the *intrinsic* domain wall resistance (iDWR). These effects of finite size are the topic of the third section 5.1.4.3. In recent times, for the investigation of the interactions between spin-polarized currents and magnetic domain walls, which involves the iDWR and the spin-transfer torque effect, Co/Pt layered structures were frequently utilized.

5.1.4.1 Magnetoresistance effects of polycrystalline bulk materials

This section deals with the effects which influence the diagonal terms of the resistivity tensor of Eq. 5.7. As a consequence of the Onsager principle (see section 5.1.1.1) these resistivity terms are even functions of $\mathbf{M}$ or $\mathbf{H}$. Generally, three fundamental magnetoresistance effects take place in polycrystalline ferromagnetic transition metals, which can be seen in Fig. 5.7. There, the resistivity of a NiCo alloy is shown for two different temperatures as a function of applied field for the two generic orientations between magnetic field and current direction. Generally, the resistivity change below technical saturation ($M_S||H$) is dominated by the anisotropic MR (AMR). The two other effects, the spin-disorder MR (see Fig. 5.7(b)) as well as the Lorentz MR (see Fig. 5.7(a)) might only be significantly apparent at large fields above technical saturation. In the following, the effects are presented separately in detail starting with the AMR.

Anisotropic Magnetoresistance (AMR): Because of the AMR[12] the resistivity depends on the magnetization orientation with respect to the current direction. From the resistivity versus field curves of Fig. 5.7 the AMR contribution can be determined by extrapolating the high-field behavior of the resistivity above technical saturation to zero field. As can be seen the resistivity is smaller (larger) when magnetization and current are oriented perpendicularly (in parallel) to each other. The difference in resistivity [13]

$$\Delta\rho_{\mathrm{AMR}} = \rho_{||} - \rho_{\perp} \tag{5.35}$$

divided by the resistivity $\rho_{\perp}$ defines the *AMR-ratio*

$$AMR\text{-}ratio = \frac{\Delta\rho_{\mathrm{AMR}}}{\rho_{\perp}} \tag{5.36}$$

AMR-ratios of polycrystalline bulk materials of Fe, Co, and Ni are in the range of a few percent and only exhibit a slight temperature dependence, namely, they decrease with increasing temperature [517, 518, 519].
Generally, for thin films it was experimentally found that $\Delta\rho_{\mathrm{AMR}}$ is basically independent of film thickness, so that the *AMR-ratio* is only affected by the thickness dependence of ρ [520, 13, 521, 522]. The actual value of $\Delta\rho_{\mathrm{AMR}}$, however, strongly depends on the sample preparation process, i.e., the sample properties, as it was e.g. shown in the case of Co thin films [523].
If the resistivity behaves isotropically at high external magnetic fields as e.g. shown in Fig. 5.7(b) then $\Delta\rho_{\mathrm{AMR}}$ can also be determined by rotating the sample in a sufficiently high saturation field forcing **M** parallel to **H**. At room temperature this is the case for the 20 nm thick permalloy layer used for the investigations of chapter 4 as can be seen in Fig. 4.17(a). The rotation of the magnetization of the Py layer reveals that the resistivity exhibits a $\cos^2$ dependence on the angle φ between magnetization and current direction due to the AMR (see Fig. 4.17(b)) [524, 386]:

$$\rho(\varphi) = \rho_{\perp} + \Delta\rho_{\mathrm{AMR}} \cos^2\varphi \tag{5.37}$$

Although the AMR was discovered by W. Thomson [4] - later known as Lord Kelvin - already in 1856 no simple model of this effect exists until now which enables a quantitative description. As shown at the end of this paragraph a fully relativistic *ab initio* theoretical description of the AMR for certain alloys shows a good quantitative agreement with experimental results. It took almost 100 years from discovery until qualitative descriptions of the underlying mechanism were proposed by several authors (see Ref. [525] and references therein). Similar to the description of the resistivity (see section 5.1.3) the mechanisms are essentially based on the *s-d* exchange interaction (localized spins [526, 164]) or Mott's two current model (itinerant spins). Based on the latter, from today's view the most prominent model for transition metals was proposed by J. Smit, which is described in the following [518, 13].

[12]The name anisotropic magnetoresistance is widely accepted today. In older publications there exist different names for the AMR, for example: extraordinary MR, ferromagnetic resistivity anisotropy, orientation effect or spontaneous resistance anisotropy.

Smit was stimulated by former experimental studies carried out for NiFe and NiCo alloys [527, 528] to perform a comprehensive investigation of the AMR of binary alloys consisting of Ni and different amounts of Fe, Co, and Cu, respectively. For these alloys relatively large *AMR-ratios* compared to single element samples were found of up to 20% at low temperatures and of up to 6% at room temperature. An important finding was that the *AMR-ratio* strongly depends on the stochiometry of the alloys. In NiFe alloys the maximum *AMR-ratio* is observed at a portion of 90% of Ni, which is nearby the permalloy ($Ni_{81}Fe_{19}$) composition. J. L. Snoek stressed the point that the maximum in the *AMR-ratio* of the binary alloys is correlated with an integer number of Bohr magneton per atom of the magnetization [529]. In fact, Smit could unambiguously show that the *AMR-ratio* of NiFe, NiCo, and NiCu alloys in dependence on Bohr magneton number lie on an universal curve with the maximum at $\approx 1\mu_B$. Former results suggested that there might be simple correlations between the maximum in AMR and "singularities" of other magnetic properties as magnetostriction and magnetocrystalline anisotropy [529]. As these phenomena are caused by the spin-orbit interaction (SOI) (see section 2.1.3) Smit concluded that the AMR is also caused by SOI. His description of the AMR based on Mott's two-current model (see section 5.1.3.1) considers the spin-orbit scattering potential [73]

$$V_{\mathrm{S0I}} = A\mathbf{L}\cdot\mathbf{S} = A(L_zS_z + \frac{1}{2}(L^-S^+ + L^+S^-)) \quad , \tag{5.38}$$

as a small perturbation, where A is a positive constant depending only on the radial part of the wave functions, $P^{\pm} = P_x \pm iP_y, P = L, S$ is the creation/annihilation operator, and z is the quantization axis, thus the direction of M. To explain the mechanism of the AMR Smit only considered the last term $A(L^+S^-)$ in the scattering potential, which lowers the spin quantum number, i.e., transfers a majority electron to a minority electronic state (spin-flip), while it raises the angular momentum component along z. This shows, that besides the electron-magnon scattering the SOI terms L^-S^+ and L^+S^- provide further scattering paths which result in a mixing of spin-up and spin-down channels. In particular, the $A(L^+S^-)$ term enables the possibility of $s^{\uparrow}$ electrons to be scattered to $d^{\downarrow}$ states. According to Mott's two-current model the scattering of $s^{\uparrow}$ electrons to d states dominates the overall resistivity, so that the occurrence of additional $s^{\uparrow}$-$d^{\downarrow}$ scattering contributions might have a significant impact [73].
Smit explained the occurrence of a scattering anisotropy with the fact that the operator L^+ is not symmetrical with respect to the coordinates x,y,z. Based on the five exchange- and crystal-field-split atomic $3d$ wave functions, he illustrated that the transition probability of a free $s^{\uparrow}$ electron (infinite plane wave) to the perturbed atomic $3d^{\downarrow}$ wave functions is largest for electrons traveling parallel to z, i.e., the direction of magnetization. This is equivalent to the experimental finding, namely $\rho_{||} > \rho_{\perp}$.
Furthermore, he showed that for the scattering of the electrons at a non-spherical potential as it is the case e.g. for scattering at grain boundaries or at phonons the scattering anisotropy is lower than for the scattering at a spherical impurity potential [13]. The latter results in an increase of the *AMR-ratio* with decreasing

temperature as experimentally observed.
As shown by I. A. Campbell a further consequence of Smit's model is that the *AMR-ratio* is predicted to vary as $(\alpha - 1)$, where α is defined in Eq. 5.32 as a measure for the disparity in the *s-d* scattering of the two spin species [530, 73]. The larger α the stronger is the impact on the overall resistivity when an increase in $\rho^{\uparrow}$ occurs. This prediction could be confirmed for Ni based alloys quite well [531, 467].
In brief, some alternative explanations of the AMR are outlined. In contrast to Smit's description L. Berger explained the AMR by the action of the $L_z S_z$ term [532]. He showed that in the case where two $3d^{\downarrow}$ states intersect (in **k**-space) the spin-orbit interaction splits the degenerate states at the intersection into two mixed states, which have a strong anisotropic electron distribution connected with the direction of magnetization. Consequently, if the intersection is close to the Fermi energy a resistivity anisotropy results from *s-d* scattering of the electrons with minority spins and not with majority spins as Smit's model suggests. With this model Berger could explain qualitatively the experimental results, i.e., $\rho_{||} > \rho_{\perp}$ as well as the universal curve of the *AMR-ratio* versus Bohr magneton in Ni based alloys as it was found by Smit (see above).
Under consideration of the total spin-orbit operator the calculations of R. I. Potter support the hypothesis of Berger that the AMR ($\rho_{||} > \rho_{\perp}$) is caused by the anisotropic scattering of the minority electrons to $AL_z S_z$ mixed $3d^{\downarrow}$ states [533]. Furthermore, he found out that an inverted AMR ($\rho_{||} < \rho_{\perp}$) should occur if the anisotropic *s-d* scattering of majority spins to $(L^- S^+ + L^+ S^-)$ mixed $3d^{\downarrow}$ states would dominate [533]. The latter result provides an explanation for the experimental finding of an inverted AMR in a NiCr alloy [534], MIr alloys, M=(Ni, Co, Fe) [535], and half-metallic ferromagnets (see Ref. [519] and references therein).
Recently, fully relativistic *ab initio* calculations based on density functional theory of the resistivity became possible, which inherently avoids the treatment of spin-orbit interaction in perturbation theory. Comprehensive reviews about these formalisms and methods are given in Refs. [462, 536]. In particular, it could be confirmed that the AMR is caused by spin-orbit coupling [537]. For the Ni based alloys NiFe and NiCo [538, 539, 540, 541] as well as for CoPd and CoPt alloys [542] an acceptable quantitative agreement with experimental results is obtained. Moreover, the results show that the applicability of the two-current model to quantitatively describe the AMR in CoPd and CoPt is suitable while it is not the case for the Ni based alloys [543].
Finally, it is worth mentioning that in single crystals, even for cubic lattices, the resistivity strongly depends on both the orientation of the magnetization and the current with respect to the crystal axes in a complex manner [544, 386, 545, 381, 467, 546, 547]. Only in ideal polycrystals, where the crystal lattices of the individual grains are completely randomly oriented so that on a large scale any local anisotropy is averaged out, a complete vanishing of these crystallinity induced AMR contributions can be expected and Eq. 5.37 applies. Thus, it is not astonishing that in the presence of a texture, which provides an axial perturbation of the isotropy, besides the presented polycrystalline AMR a further anisotropy in the magnetoresistance occurs. This topic is further discussed in connection with the geometrical size effect (GSE) in section 5.1.4.3.

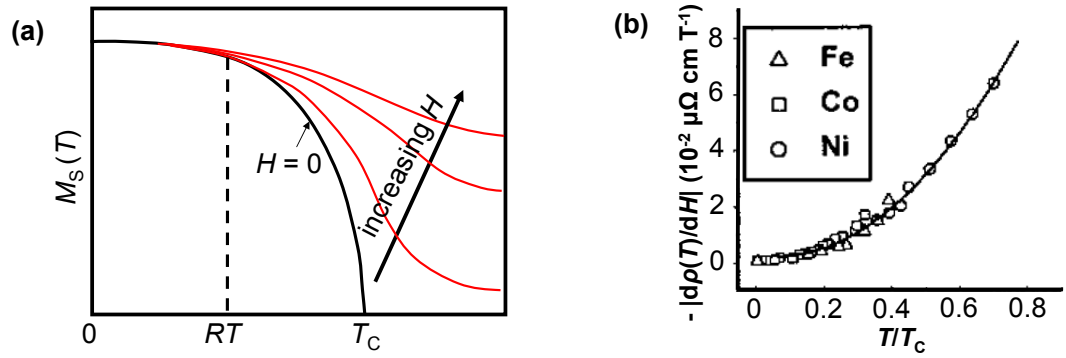

Figure 5.8: (a) Saturation magnetization M_S in dependence of temperature. At finite temperatures for a magnetic field **H** applied in parallel to **M** the absolute value of the latter is enhanced over the spontaneous value at $\mathbf{H} = 0$. According to Ref. [72]. (b) High field linear slopes $-|\mathrm{d}\rho/\mathrm{d}H|$ versus T/T_C for Co, Ni, and Fe films. From Ref. [481].

Spin-disorder Magnetoresistance (SMR): At elevated temperatures T not only the magnetization orientation is altered by the application of external magnetic fields but also its magnitude [72]. If **M** and **H** are oriented in parallel to each other then $|\mathbf{M}|$ is increased with increasing field over the spontaneous value $M_S(T)$ (see Fig. 5.8(a)), which is given by Bloch's famous $T^{3/2}$ law [548]

$$M_S(T) = M_S(0)(1 - BT^{3/2}) \quad , \tag{5.39}$$

where $B = 3.3 \cdot 10^{-6}$ K$^{-3/2}$ for bulk Co [549]. The field-induced increasing of **M** is equivalent to the annihilation of spin-waves. Correspondingly, the reduced magnon density becomes noticeable in a reduced spin-flip electron-magnon scattering contribution yielding an almost linear reduction of the overall resistivity with applied field (see Fig. 5.7(b))[13] [550]. This effect known as spin-disorder magnetoresistance (SMR) or negative MR is isotropic as the annihilation of spin-waves does not depend on a particular field orientation.
Recently, Raquet et al. systematically investigated the SMR for several Fe, Co, and Ni films within the temperature range of 1.8 K to 500 K and magnetic fields of up to 40 T [551, 552, 481]. Above technical saturation ($H||M_S$) within the whole field range they revealed that the negative slope of the resistivity with field ($-|\mathrm{d}\rho/\mathrm{d}H|$) is almost linear and that its magnitude depends on temperature. As can be seen in Fig. 5.8(b) the linear slopes $-|\mathrm{d}\rho/\mathrm{d}H|$ lie on a universal curve when plotted as a function of normalized temperature T/T_C providing strong evidence that the SMR is of magnetic origin. The increase of the SMR with increasing temperature can be qualitatively understood by the fact that the magnon population and therefore the annihilation of magnons with field is the larger the closer the temperature is to T_C (see Fig. 5.8(a)). In the investigations of Raquet et al. no thickness dependence of the SMR was observed in the range of 7 nm to 1 μm [481]. Thereby, the authors stated that the structural quality of the films only slightly influences the SMR attesting its intrinsic origin. For Co at room temperature the slope was found to be around -0.008 $\mu\Omega$cm/T.

[13] The effect was first observed by P. Kapitza for Ni in 1929 [550].

In order to describe the SMR theoretically the authors developed a model, which is based on the *s-d* interaction including intraband as well as interband scattering processes as already mentioned in section 5.1.3.2 [481]. They assumed that the external field mainly affects spin-flip scattering processes, i.e., the electron-magnon scattering part of the spin-disorder resistivity $\rho_{s-d\text{ interaction}}$ (see Eq. 5.34), while electron-phonon and electron-impurity scattering contributions are supposed to depend on the applied field in a negligibly small manner. In the following, only the results of the model should be addressed. For details of the derivation and made assumptions the reader is referred to the publication [481].
The model predicts the following temperature dependence of the linear resistivity versus field slopes:

$$-\left|\frac{\mathrm{d}\rho_{s-d\text{ interaction}}}{\mathrm{d}H}\right|_{M_\mathrm{S}||H} \propto T(1+2d_1T^2)\ln\frac{T}{T_0} \quad , \tag{5.40}$$

where T_0 is a temperature-independent constant. The parameter d_1 accounts for the magnon mass renormalization (temperature dependence of the spin-wave mass/ dispersion relation), which is in first order approximation: $D(T) \approx D_0(1-d_1T^2)$; D_0 is the zero-temperature magnon mass. As indicated by the solid line in Fig. 5.8(b) Eq. 5.40 fits the data quite well. For Co films the coefficient d_1 obtained from the fit was found to be in the range of $1.5-3\cdot10^{-6}$ K^{-2} [481, 553] and is in good agreement with theoretical calculations [554].
For $\mu_\mathrm{B}\mu_0H \gtrsim k_\mathrm{B}T$, i.e., at low T or high fields the model predicts deviations of the SMR from the linear response of ρ on H as

$$\Delta\rho_{s-d\text{ interaction}}(T,H) = \rho(T,H)-\rho(T,0) \propto \frac{\mu_0HT}{D(T)^2}\ln\left(\frac{\mu_\mathrm{B}\mu_0H}{k_\mathrm{B}T}\right) \quad , \tag{5.41}$$

which is in accordance with the experimental results [555].
Finally, the model enables the estimation of the electron-magnon scattering contribution $\rho_{s-d\text{ interaction}}$ to the total zero-field resistivity as already presented in section 5.1.3.2.
Recently, the SMR was studied in FePt films [555] and nanowires with high perpendicular magnetocrystalline anisotropy as well as in soft magnetic NiFe nanowires [556, 557] when magnetization and field are aligned in an antiparallel manner to each other. In this case the field increases the magnon population yielding a linear increase of the resistivity with field with the same slope as found for a parallel orientation[14]. In particular, it is shown that the SMR effect can be used to detect the position of a single domain wall in a FePt nanowire: The actual position of the wall pinned at a structural defect was traced back from the slope of the resistivity versus field curve, which is the superposition of the negative and positive slopes weighted according to the size of the in parallel and antiparallel to field oriented domains [556].

[14] In the early 1990s this behavior was also found by R. A. Hajjar and co-workers for Co/Pt layered structures with perpendicular easy axis of magnetization by using macroscopically sized samples [558, 559, 560, 561].

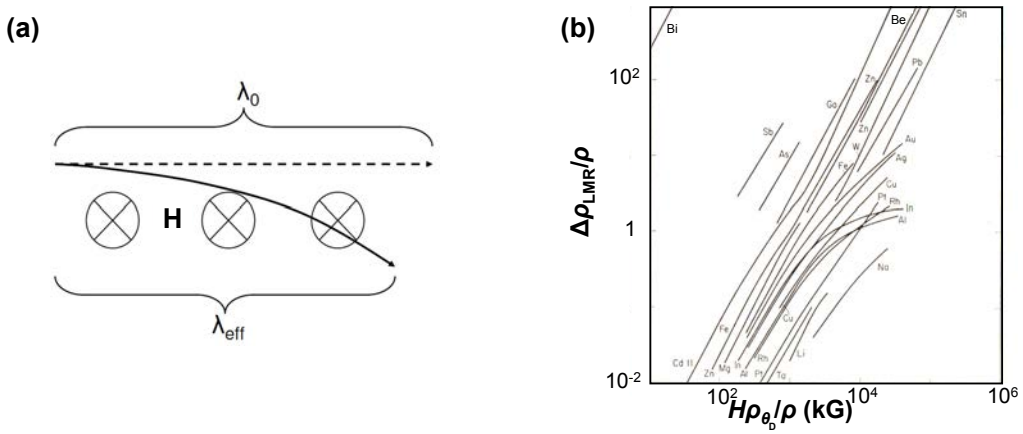

Figure 5.9: (a) Sketch to visualize the Lorentz MR. The solid (dashed) line corresponds to the mean free path λ_{eff} ($\lambda_0 > \lambda_{\text{eff}}$) of the elctrons in the presence (absence) of an applied field. (b) Transverse LMR of polycrystalline metals shown in the reduced Kohler diagram, i.e., $\Delta\rho_{\text{LMR}}/\rho$ is plotted versus $H\rho_{\Theta_{\text{D}}}/\rho$. From Ref. [562].

Lorentz Magnetoresistance (LMR): In Fig. 5.7(a) the so-called ordinary or Lorentz MR (LMR) is responsible for the anisotropic increase of the resistance above technical saturation. The LMR is present in all conductors, always positive, and caused by magnetic fields, which give rise to a Lorentz force F_{L} acting on the electrons [381][15]:

$$\mathbf{F}_{\text{L}} = -e(\mathbf{E} + \mathbf{v} \times \mu_0 \mathbf{H}) \tag{5.42}$$

The LMR can be qualitatively comprehended as the magnetic field forces the electrons on helical orbits, so that the effective mean free path in the direction of the electrical field $\mathbf{E}$ is reduced (see Fig. 5.9(a)) [562]. As the deflection of the electrons by the magnetic field is perturbed by the scattering of the electrons, the relative strength of the LMR depends on the ratio of the magnetic field and the disorder of the system, i.e., the resistivity. In fact, M. Kohler showed under theoretical considerations that the increase in resistivity $\Delta\rho_{\text{LMR}}$ above the zero field resistivity ρ obeys such a relation [562]

$$\frac{\Delta\rho_{\text{LMR}}}{\rho} = f(H/\rho) \quad , \tag{5.43}$$

where f is an element specific characteristic function that does not explicitly depend on temperature and the kind of scatterer [563, 564]. Eq. 5.43 is known as Kohler's rule, which is experimentally found to be generally obeyed. Fig. 5.9(b) shows the so-called reduced Kohler diagram, where the measured transverse $\Delta\rho_{\text{LMR}}/\rho$ is shown double logarithmically as a function of $H\rho_{\Theta_{\text{D}}}/\rho$ for various elements, where Θ_{D} is the Debye temperature. The use of the reduced resistivity $\rho_{\Theta_{\text{D}}}/\rho$ is convenient as it enables the presentation of the LMR of various conductors in a single diagram. For most of the elements a linear behavior with a slope of two is observed. This means that $\Delta\rho_{\text{LMR}}/\rho$ varies with H^2, which is theoretically expected for free electrons [564]. The statements made until now are valid for the transverse LMR but the LMR also occurs in longitudinal geometry, where $\mathbf{H}$ and $\mathbf{v}$ are parallel to each other and the

[15]Note that in ferromagnets $\mu_0 H$ has to be substituted by $B = \mu_0(H + M)$.

Lorentz force virtually vanishes (see Eq. 5.42). To understand the impact of the field on the longitudinal resistivity each point of the Fermi surface has to be taken into account. The longitudinal LMR arises basically because the external field shifts the electrons on the Fermi surface into a more vulnerable position from the scattering point of view in comparison to the field free case [381]. This effect also contributes to the transverse LMR, so that the overall transverse LMR is generally larger than the longitudinal LMR (see Fig. 5.7(a)). For more details about the LMR the reader is referred to Refs. [565, 381, 389, 566].
From the reduced Kohler diagram the strength of the LMR can be estimated, which is done in the following for the Co/Pt samples. In a rough approximation it is $\rho_{\Theta_D}/\rho \approx \rho_{295\ K}/\rho$ as the Debye temperature of Co and Pt is nearby room temperature (see Fig. 5.5(a)). The maximum LMR is obtained at low temperatures as $\rho_{295\ K}/\rho \leq \rho_{295\ K}/\rho_{4.2\ K}$, where the latter term is the residual resistivity ratio (RRR, see Eq. 5.19). As for the Co/Pt samples $1.28 < RRR < 1.50$ were found (see section 5.6.1) and maximum fields of 6 T are used in the experiment a maximum value of $\frac{\Delta\rho_{\mathrm{LMR,\ 6\ T}}}{\rho} \lesssim 1 \cdot 10^{-3}$ can be estimated from the reduced Kohler diagram utilizing the graph for Pt as an approximation for Co/Pt. As the resistivity of the films is about $25 - 40\ \mu\Omega$cm (see section 5.5.2) this yields a resistivity change of $\Delta\rho_{\mathrm{LMR,\ 6\ T}} \approx 0.025 - 0.04\ \mu\Omega$cm, which is similar to the spin-disorder MR expected for Co at 6 T (see previous paragraph).
However, in MR studies of polycrystalline Co films for similar thicknesses, RRR, and magnetic fields no LMR effects were found within the uncertainty of the experiment of $\Delta\rho/\rho < 1 \cdot 10^{-5}$ [553, 567]. Even for epitaxial Co films with a much larger $RRR = 27$ and fields of up to 40 T a vanishingly small LMR contribution was only detected at low temperatures (1.6 K). These findings indicate that the LMR in thin films is significantly reduced compared to the bulk case [568, 569]. In conclusion, it is expected that the LMR is negligibly small for the Co/Pt samples.
It is mentioned for the sake of completeness that for high fields (or very pure samples), namely $\omega_c\tau \gg 1$, where $\omega_c = e\mu_0 H/m^*$ is the cyclotron frequency and τ is the relaxation time, the resistivity may reach a saturation value or may increase indefinitely with field [570, 571, 572]. The particular characteristic of the $\rho(H)$ curve then provides information about the topography of the Fermi surface in the case of single crystals [573, 570, 571, 574, 575, 389]. Furthermore, in single crystals at low temperatures quantum oscillations (Shubnikov-de Haas oscillations) in the $\rho(H)$ curve occurs yielding further information of the Fermi surface [576, 572]. Regarding confined systems, size effects are present, for instance, in a thin film with high purity by applying a high field along the transverse direction so-called Sondheimer oscillations in $\rho(H)$ appear [416, 577, 572, 578].
In the next paragraph the MR effects are introduced, which affect the off-diagonal elements of the resistivity tensor. In contrast to the diagonal elements these so-called Hall effects are odd functions of $\mathbf{H}$ and $\mathbf{M}$.

5.1.4.2 Normal and Anomalous Hall effect

When a current-carrying material is placed in a magnetic field $\mu_0 H_z$ that is oriented perpendicularly to the current direction j_x an electric field E_y originates in the direction that is perpendicular to the current as well as perpendicular to the field. The first observation of this effect was made by E. H. Hall by using gold leaf in 1879 [5, 6]. This effect was named after him and is known as the normal Hall effect. It is present in all materials and can be attributed to the Lorentz force (see Eq. 5.42), which deflects the electrons to one side of the conductor. The corresponding transverse or Hall voltage U_y between the side planes is given by

$$U_y = R_0 \frac{I_x \mu_0 H_z}{t} \quad , \tag{5.44}$$

where t is the thickness of the sample in z-direction and R_0 is the so-called normal Hall constant. The knowledge about the latter enables the determination of the "effective" charge carrier density n^* and the kind of charge carrier q (electrons $q = -e$ or holes $q = e$) as [579][16]

$$R_0 = \frac{1}{q n^*} \tag{5.45}$$

Analogous to the conventional resistance the Hall resistance is defined as $R_{xy} = U_y / I_x$.
Only one year after the discovery of the normal Hall effect Hall made the observation that compared to Au a ten times larger effect in Fe, Co, and Ni occurs [6, 8]. The stronger effect, which is only present in ferromagnetic materials, was named spontaneous, extraordinary, or anomalous Hall effect (AHE) [580]. There, the following empirical relation was found [581, 582]:

$$U_y = (R_0 H_z + R_S M_z) \frac{\mu_0 I_x}{t} \tag{5.46}$$

Thereby, R_S is the so-called anomalous Hall constant, which can be much larger than R_0 reflecting the strength of the AHE with respect to the normal Hall effect. While the normal Hall effect can be easily understood as a consequence of the Lorentz force, it is nowadays accepted that the AHE is a consequence of the spin-orbit interaction (SOI) [580]. Based on the SOI several intrinsic and extrinsic scattering mechanisms that yield AHE contributions were proposed [583, 584, 585, 586], whereas the extrinsic mechanisms more or less depend in a complex manner on material parameters [587, 582]. Nevertheless, the theoretical models as well as the experimental results concerning bulk materials suggest the following correlation between R_S and the longitudinal resistivity ρ_{xx} [588]:

$$R_S = a \rho_{xx} + b \rho_{xx}^2 \quad , \tag{5.47}$$

[16] Note that n^* is the analogue to the effective mass m^* (see Eq. 5.8). Only for free electrons ($m = m^*$) n^* resembles the electron density n.

where a and b are material constants. However, in particular for thin metallic multilayers strong deviations from this dependency are frequently found, e.g. S. N. Song et al. found $R_S \propto \rho^{2.6}$ [589], so that the existing theories fail to describe the experiments [590, 591]. For details about the AHE the reader is referred to the comprehensive articles Refs. [579, 592, 593, 594, 582]. A brief overview of the experimental findings regarding the AHE in thin films and multilayers is given in connection with the results in section 5.5.1.4.
Literature values for the Hall constants for polycrystalline Co films at room temperature are [595, 596, 579, 597, 580]: $-R_0^{\mathrm{Co}} = 1.1 - 1.3 \cdot 10^{-10}$ m^3/C, $R_S^{\mathrm{Co}} = 0.6 - 3 \cdot 10^{-9}$ m^3/C. For pure single hcp Co crystals R_S was found to be anisotropic and up to three orders of magnitude lower than the above mentioned value, while R_0 is only slightly affected [598, 579, 571, 599, 580, 600]. These findings reveal the strong dependence of R_S on structural properties. Furthermore, while R_0 is nearly temperature-independent R_S^{Co} might strongly vary with temperature [579, 597, 580]. For polycrystalline Pt films R_0 was found to be one order of magnitude smaller than for Co: $-R_0^{\mathrm{Pt}} = 1.5 - 2.4 \cdot 10^{-11}$ m^3/C [380, 601, 579].

A further MR effect, which also appears in the off-diagonal elements of the resistivity tensor and also bears the name Hall, is the so-called planar Hall effect (PHE) discovered in 1954 in germanium [602]. The PHE is a manifestation of any magnetoresistance effect that produces an effective anisotropy in the resistivity ρ_{xx} as a consequence of the tensor characteristic of the resistivity [381]. For polycrystalline ferromagnetic films a PHE effect appears in ρ_{xy}, x is the current direction, when the magnetization direction is changed within the xy-plane as a further consequence of the anisotropic MR (AMR) [603, 380, 604, 605]. When α is the angle between current and magnetization the PHE exhibits the following angle dependence

$$\rho_{xy}(\alpha) = \underbrace{(\rho_{||} - \rho_{\perp})}_{\Delta\rho_{\mathrm{AMR}}} \sin\alpha\cos\alpha \quad , \tag{5.48}$$

so that a transverse resistivity ρ_{xy} (transverse voltage E_y) arises whenever the magnetization is neither perpendicular nor parallel to the current[17]. As the PHE is not addressed within this thesis for more information the reader is referred to the publications given above as well as to recent publications about this effect (see e.g. Refs. [606, 607, 608, 609, 610]).

[17] Note that in Eq. 5.7 only the leading terms of the taylor series expansion in $\mathbf{H}$ (and $\mathbf{M}$) are considered in the off-diagonal elements. As the planar Hall effect is a consequence of the AMR it is in contrast to the normal and anomalous Hall effect an effect of second order. The PHE and AMR can be composed to a generalized AMR: $\rho^{(2)}_{ik,\mathrm{AMR}} \propto M_k(\mathbf{e}_i \cdot \mathbf{M})$. Moreover, if the Lorentz MR is non-vanishingly small this effect also shows up as a planar Hall effect due to its anisotropic nature, which is neglected here for the sake of convenience [381].

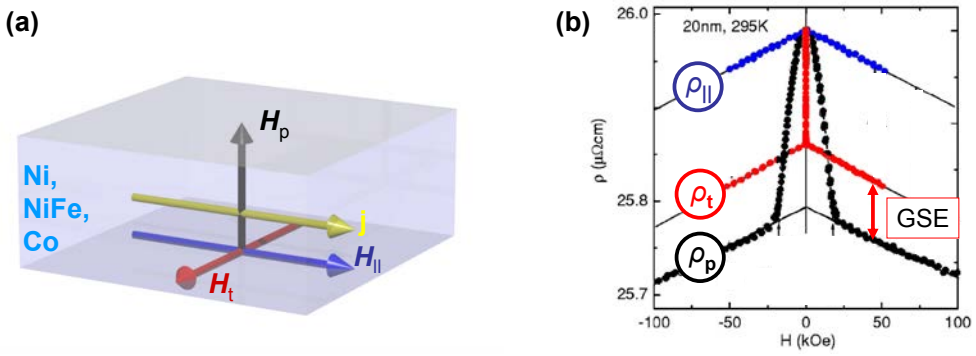

Figure 5.10: (a) Sketch of a magnetic film, where the current **j** flows in the plane. The three generic directions of the magnetic field **H**, i.e., the so-called longitudinal ($||$), transverse (t), and polar (p) geometry, are drawn. (b) displays the room temperature resistivity ρ versus applied field behavior for the three generic directions of a 20 nm thick Co film deposited on naturally oxidized Si(100) and capped with 3 nm Al. Above technical saturation, where the resistivity isotropically decreases with field due to the SMR, it is $\rho_t > \rho_p$ reflecting the presence of the GSE. This hierarchy of the saturation resistivities is in contrast to the findings for Co/Pt layered structures at small Co thicknesses as can be seen in Fig. 5.1(b). From Ref. [553].

5.1.4.3 Magnetoresistance effects of finite size

In this section the focus is on MR effects which are (also) present in metallic systems with a single ferromagnetic layer. In the first part the deceptively called geometrical size effect (GSE) is presented, which is caused by the texture in polycrystalline films. In the second part the resistivity, which is intrinsically connected with a domain wall, is briefly discussed.

Geometrical size effect (GSE): As discussed in section 5.1.2, in thin films, where the translational symmetry along the direction of the stacking is broken, the scattering at the surface/interface significantly contributes to the resistivity. For ferromagnetic systems the same symmetry consideration leads to the question if a change of the electrical resistivity appears when the magnetization is rotated from any in-plane to out-of-plane orientation. Actually, such considerations led to first investigations in 1972 [611]. By using a 107.5 nm thick polycrystalline Ni film T. T. Chen and V. A. Marsocci reported on variations in the resistivity depending on the orientation of the magnetization in the plane perpendicular to the current direction. The main result of Chen and Marsocci was that for the investigated temperature range of 4.2 K $\leq T \leq$ 300 K above technical saturation ($H||M_S$) different values of the resistivity for the magnetization oriented in-plane (ρ_t: transverse resistivity, see Fig. 5.10(a)) and perpendicular to the film plane (ρ_p: polar resistivity) were found with $\rho_t > \rho_p$ (see Fig. 5.10(b)). Moreover, it was observed that the resistivity exhibits a $\cos^2$ dependence on the angle θ between magnetization and film normal [611]:

$$\rho(\theta) = \rho_t + \underbrace{(\rho_p - \rho_t)}_{\Delta\rho_{GSE}<0} \cos^2\theta \quad , \tag{5.49}$$

The magnetization is always oriented perpendicularly to the current direction, so that the conventional AMR can be ruled out as the reason for this effect. As a systematic thickness variation was not performed by Chen and Marsocci and effects of the crystallinity dominated the findings the authors failed to give a conclusive interpretation of their results. The effect was called geometrical size effect (GSE), which reflects the original idea behind the investigation.
Similar investigations with the same finding $\rho_t > \rho_p$ were performed some decades later by T. G. S. M. Rijks and co-workers by using polycrystalline permalloy films with thicknesses of 4.5 nm $\leq t \leq$ 100 nm at $T = 5$ K [612]. Two different sets of samples were prepared utilizing different substrates, which strongly differ in the degree of fcc (111) out-of-plane texture[18] as checked via x-ray diffraction. The conclusion was that a strong correlation of the $\rho_t > \rho_p$ effect on the degree of texture of the films was predominant. Besides, the authors claimed to find some hints of a finite size effect correlated with $\rho_t > \rho_p$, which they theoretically predicted in an earlier publication [613]. However, they could not unambiguously disconnect it from effects due to texture.
Recently, W. Gil et al. demonstrated in a very systematic and conclusive study that the $\rho_t > \rho_p$ phenomenon is attributed to the texture of the films [553]. For the investigations they used polycrystalline Co films with a hcp (0001) out-of-plane texture. The authors defined the following ratio as a measure for the size of the GSE:

$$\frac{\Delta\rho_p}{\Delta\rho_t} = \frac{\rho_{||} - \rho_p}{\rho_{||} - \rho_t} \quad , \tag{5.50}$$

whereas the denominator is the conventional AMR as influences of texture or interfaces might be the same in both geometries because of symmetry reasons. For instance, if $\frac{\Delta\rho_p}{\Delta\rho_t} = 1$ applies, means that the "out-of-plane" AMR $\Delta\rho_p$ and the (conventional) "in-plane" AMR are the same and the GSE is zero. In this study it was demonstrated that the size of the GSE is independent of film thickness (10 nm $\leq t \leq$ 188 nm) and temperature (70 K $\leq T \leq$ 350 K) as long as the degree of texture does not change.
The explanation of the GSE by Gil et al. is based on Potter's description of the AMR (see section 5.1.4.1). They assumed that the anisotropic scattering of the minority electrons to the L_zS_z mixed $3d_\downarrow$ states is different for in-plane and out-of-plane directions of the magnetization due to the axial perturbation caused by the out-of-plane texture. Their adaptation of Potter's model in particular explains the experimentally found upper limit of $\frac{\Delta\rho_p}{\Delta\rho_t} = 2$ for permalloy [612] and Co films. Furthermore, it is in accordance with the essential features of the experimental findings, i.e., the temperature and thickness independence of the GSE.
Finally, it is explicitly mentioned that the GSE also occurs in textured thin ferromagnetic nanowires [259].

[18] This means that the textured permalloy films consist of grains with a fcc lattice, where the {111} direction is predominantly oriented perpendicularly to the film plane, while the (111) plane, which is consequently almost oriented in parallel to the film plane, is randomly oriented.

Intrinsic domain wall resistance (iDWR): Apart from a few exceptions only influences of a homogeneous magnetization on the resistivity were discussed until now. One exception is given in connection with the introduction of the SMR. There it was stated that in the case of a two domain state in a nanowire the overall SMR provides information about the position of the domain wall within the wire (see section 5.1.4.1). Furthermore, the composition of the overall resistance of multidomain patterns under consideration of the AMR effect is estimated in section 4.4.1. This treatment was successfully applied to deduce the magnetization reversal and magnetic energy of the submicron rectangles investigated in chapter 4. In both exceptional cases, however, the contributions of the domain walls to the resistance are not considered. Inside a domain wall the resistivity locally varies due to the presence of the addressed AMR/ SMR effects when the projection of the magnetization with respect to the direction of the current/ applied field changes there. This is generally the case, however, the corresponding complex contributions of domain walls to the overall resistance can be neglected in a first order approximation as their area filling is normally rather small. Besides these extrinsic contributions of a domain wall to the overall resistance it was suspected since the 1960s that further effects on the resistivity might exist that are intrinsically related to a domain wall meaning that a domain wall itself is a source of resistivity [26]. Without going into detail here, some features of the MR investigations of pure bulk crystals at low temperatures suggested that they might be consequences of scattering processes of the electrons at domain walls (see e.g. Refs. [614, 615] and references therein). These indirect hints led to first theoretical descriptions about the influence of a locally varying magnetization orientation on the resistivity [616, 617, 618]. The proposed mechanisms could be applied to explain the intrinsic domain wall resistance (iDWR) in the case of pure samples and low temperatures (for details, see Refs. [616, 617, 618, 619, 26]).
It was not until 1996 that the first direct evidence of iDWR was provided by Gregg et al. by using a 100 nm thick epitaxial Co film with a stripe domain pattern at room temperature, which the authors explained in analogy to the giant magnetoresistance effect [620][19]. Subsequently, iDWR was observed for a variety of material systems even for rather "impure" samples, while the investigation and quantification of iDWR was fostered by the development and application of more and more innovative experimental approaches [619, 621, 622, 623, 624, 625, 626, 627, 628, 629, 630, 631]. As a consequence of the experimental findings several theoretical descriptions of iDWR were proposed and refined [632, 619, 633, 634, 635, 636, 637]. For instance, P. M. Levy and S. F. Zhang solved the Boltzmann equation under consideration of the electron-spin and showed that in the case of a non-adiabaticity of the electron-spins during the propagation through the wall a mixing of both spin-channels occurs, so that according to Mott's two-current model (see section 5.1.3.1) the resistivity is enhanced [619, 26]. Importantly, also *negative* iDWR mechanisms were theoretically predicted meaning that due to the presence of a domain wall the resistivity decreases [638, 639, 637]. In fact, negative iDWR was frequently observed experimentally [640, 641, 205, 642, 643, 644]. A complete overview of the investigations and proposed mechanisms regarding iDWR would go beyond the scope of this thesis

[19] From today's view the measured MR signal is rather a consequence of the AMR effect originating from the flux closing Néel caps than caused by intrinsic domain wall resistance [26].

and in the following it is focused on the studies dealing with Co/Pt layered structures. Thereby, the reason is given why this system was frequently used for studying iDWR. For more details the interested reader is referred to the comprehensive review given by C. Marrows in 2005, where the historical perspective, recent experimental results, and the existing theories concerning iDWR are introduced [26].
Regarding the experimental studies of iDWR some of the controversies, even about the overall sign of this effect, seem to rely on the fact that the effect is relatively small and generally masked by the extrinsic resistance contributions that are associated with the micromagnetic configuration of the wall. Generally, in nanowires with in-plane magnetic anisotropy it is difficult to describe the AMR contribution of the domain walls correctly [205, 195, 645] because of their micromagnetic complexity that is explicitly discussed in detail in section 3.2. A similar situation applies to thick epitaxial films with an out-of-plane magnetocrystalline anisotropy, since at the surface flux closure structures are generated [620, 646, 642, 647]. In order to prevent this kind of problems, ultrathin systems with a high perpendicular magnetic anisotropy (PMA) have been frequently investigated [648, 649, 650, 651, 652]. In such systems simple Bloch walls occur in which the magnetization rotates within the wall plane (see section 2.2). Furthermore, they exhibit comparably small domain wall widths in the order of 10 nm, while the actual value depends on the anisotropy constant according to Eq. 2.29. As the iDWR is the larger the smaller the domain wall widths are a relatively large iDWR is expected. Moreover, various approaches, as e.g. the application of moderate Ga^+ irradiation to locally modify the anisotropy (see section 4.4.2.1), can be used to ensure the creation of a well-defined number of domain walls, so that in particular the influence of a single domain wall on the resistance can be investigated [650, 652, 653, 654]. A further advantage is that in the case of a current perpendicular wall (CPW) geometry as sketched in Fig. 5.11(a) no extrinsic AMR or Lorentz MR contributions exist that are superimposed on the iDWR as the magnetization is perpendicularly oriented with respect to the current direction everywhere within the sample with and without domain walls. Thus, the only effect that might give rise to a resistance change when a domain wall is generated or annihilated is due to the iDWR. This seemingly straightforward approach to measure the iDWR directly without the need for eliminating extrinsic MR contributions afterwards relies on the assumption that besides the AMR no other MR effects exist. However, this assumption is questionable as Co/Pt multilayers have distinct geometrical features like out-of-plane texture and alterations of materials in the stacking direction, both of which might cause further MR effects. In fact, as shown in the previous paragraph the presence of texture leads to the GSE effect, which can be of similar size as the AMR, so that the resistivity might significantly depend on the magnetization orientation with respect to the texture axis, i.e., the film normal. As the magnetization orientation with respect to the texture axis changes within a Bloch wall an extrinsic GSE contribution to the measured domain wall resistance might exist. Furthermore, as shown in the results presented in sections 5.5−5.7 the Co/Pt interfaces provide a further MR effect, which is also in the same order of magnitude as the AMR for Co/Pt layered structures with PMA, that also affects the resistance when the magnetization orientation changes from out-of-plane to any in-plane direction. Thus, the same argumentation as for the GSE applies and a

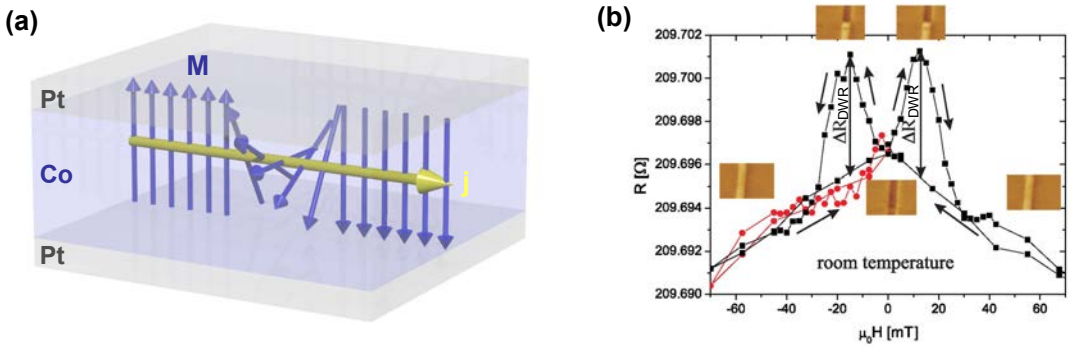

Figure 5.11: (a) Sketch of a Bloch wall in a Co layer with perpendicular magnetic anisotropy sandwiched by Pt, where a current runs through the wall (current perpendicular wall (CPW) geometry). (b) shows the resistance of a 5 nm Pt/(0.25 nm Co/0.95 nm Pt)$_7$/1 nm Pt nanowire with dimensions of $w = 415$ nm and $l = 2.6$ μm versus applied polar field averaged over four measurement cycles. The insets show magnetic force microscopy images of the corresponding domain arrangements within the wire. In the presence of a single domain wall, which resembles the CPW situation sketched in (a), the resistivity is enhanced by ΔR_{DWR} compared to the single-domain state. (b) from Ref. [650].

further extrinsic contribution to the measured DWR exists. The implications of the discovered anisotropic interface MR effect on the investigations concerning iDWR of Co/Pt layered structures are critically discussed in section 5.7.

In 2006, C. Hassel et al. for the first time ever measured the resistance change that appears in a ultrathin system with PMA when a single domain wall is generated or annihilated [650]. In this study a nanowire consisting of a Co/Pt multilayer was used and the domain wall was arranged suchlike that the CPW geometry applies. Thereby, the position of the domain wall within the wire was controlled via an out-of-plane magnetic field. Fig. 5.11(b) shows the MR measurement performed at room temperature in combination with images of the corresponding micromagnetic arrangements revealing that the resistance is enhanced by ΔR_{DWR} compared to a single-domain state when a single domain wall is located in the nanowire. By normalizing the effect to the region of the domain wall the authors estimated a positive domain wall resistance of about 1.8% with respect to the Co resistivity ρ_{Co} and they demonstrated that the value is in good agreement with the model of Levy and Zhang. This value is within the span of $\Delta\rho_{\mathrm{DWR}}/\rho_{\mathrm{Co}} \approx 0.1-2\%$ ($\Delta\rho_{\mathrm{DWR}} = 0.02-0.8$ $\mu\Omega$cm) reported for Co/Pt layered structures in CPW geometry [652, 654]. However, as critically remarked above, in the investigations concerning iDWR of ultrathin systems with PMA a determination of possible extrinsic contributions to the measured domain wall resistance was not given, so that the reported values for iDWR might be correspondingly superimposed by extrinsic MR effects.

It is worth mentioning that in connection with the presence of domain walls the so-called antisymmetric MR was frequently detected for systems with PMA [655, 656, 657, 658, 659, 660]. According to its name the effect yields an antisymmetric change of the resistivity when the magnetization of a multi-domain pattern is inverted: $\Delta\rho(\mathbf{M}) = -\Delta\rho(-\mathbf{M})$. According to current knowledge this effect seems to be no manifestation of a violation of the fundamental principle of Onsager (see

Eq. 5.6), instead, several conventional explanations for the underlying physics of this effect were proposed [657, 661, 658]. However, the actual mechanism is still under debate. For details about the antisymmetric MR the reader is referred to the given publications.
For the sake of completeness it should be stated that in the case of domain walls located at constrictions of atomic size a huge *ballistic* magnetoresistance was sometimes found. For a critical review about this topic, see Ref. [662].
Besides the investigation of intrinsic domain wall resistance Co/Pt multilayers were frequently used to study a further consequence of the interaction between domain walls and spin-polarized currents, i.e., the spin-transfer torque (STT) effect that leads to current-induced domain wall movement as already stated in the introduction of chapter 3 [663, 664, 653, 665, 666, 667, 668]. The reasons why this system is frequently used are similar as for studying iDWR, namely Co/Pt multilayers exhibit relatively narrow walls, so that a large STT can be expected [669], and the walls are Bloch walls with a rather low complexity, so that simple models for their description can be applied[20]. For details about the STT, which is one focus of recent research in the field of magnetism in reduced dimensions, the reader is referred to the review articles Refs. [670, 31].

[20] In connection with this thesis it was found out that the nucleation field of Co/Pt multilayer nanowires can be considerably tuned by using wire ends designed as a tip, suchlike that the sharper the tip the lower the nucleation field is. The nucleation of an oppositely oriented domain and the associated injection of a domain wall at relatively low fields is a prerequisite for the preparation of domain walls at comparably weak pinning sites. The latter are of interest in connection with current driven depinning of domain walls via STT since high current densities, which are otherwise required, can modify or even destroy the sample. The nanowires were prepared via electron beam lithography, so that the reduction of nucleation field can be attributed to a local reduction of the PMA caused by shadowing effects initiated by the resist mask during sputter deposition of the multilayer. For details, see Ref. [E11]

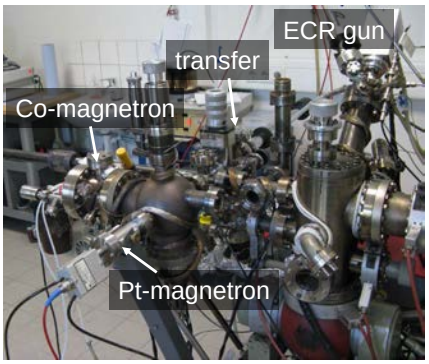

Figure 5.12: Exterior view of the UHV sputter chamber. The main components are tagged.

5.2 Preparation of Co/Pt layered structures

This section deals with the preparation of the Co/Pt samples, which were used for the MR investigations. In section 5.2.1 the deposition of the Co and Pt layers via sputter-techniques are introduced. The general construction of the samples and an overview of the sample series prepared for the systematic MR studies are presented in section 5.2.2. and 5.2.4, respectively, while in section 5.2.3 the MR sample layout and the electrical contacting is described.

5.2.1 Deposition of Co and Pt layers via sputter techniques

The Co/Pt films were grown at room temperature by sputter techniques in a UHV chamber, whose exterior view can be seen in Fig. 5.12. The base pressure was $< 2 \cdot 10^{-9}$ mbar. Based on the work of my former colleague Dr. H. Stillrich, two different sputter techniques were combined [671, 368]: The electron-cyclotron resonance (ECR) and the direct current (DC) magnetron sputtering. One of the results of his thesis is that the perpendicular magnetic anisotropy, which is a combination of magnetocrystalline volume anisotropy and interface anisotropy (see section 2.1.3), can be enhanced if first a seed layer of Pt is deposited via ECR and the following Co and Pt layers are prepared by DC magnetron sputtering [671, 368]. This can be qualitatively comprehended if the working principles of both sputter techniques are understood, which are briefly described in the following.
The ECR sputter technique is based on the creation of a noble gas plasma via electron cyclotron resonance and the subsequent acceleration of the positive charged ions to the spatially separated target. For that purpose a magnetron creates microwaves, which are injected via an antenna into the plasma chamber, where a noble gas is inserted via a dosing valve (see Fig. 5.13(a)). In the plasma chamber permanent magnets are mounted so that the electrons, which are e.g. initially created by collisions between noble gas atoms, are forced on helical paths due to the Lorentz force with the cyclotron frequency $\omega = eB/m$. If there is a match in the cyclotron-frequency with the frequency of the microwave, the energy of the wave is resonantly transferred to the electrons, which in turn are able to ionize further noble gas atoms. The ions are accelerated via high voltage from the plasma chamber to the target,

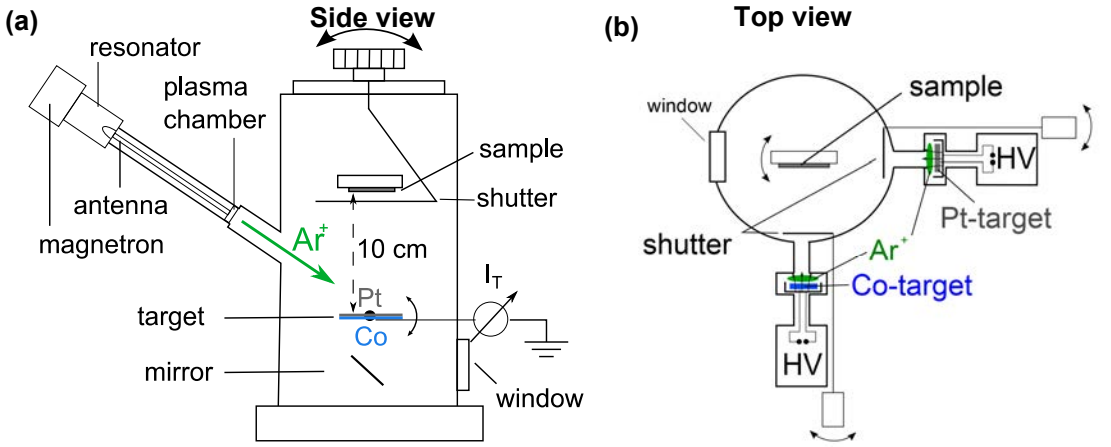

Figure 5.13: Schemes of (a) ECR and (b) magnetron chamber. In the case of ECR technique the Ar^+ ions are produced in a separated plasma chamber and subsequently accelerated to the target, while in the case of magnetron sputtering the plasma is directly created in front of the target. The manipulation of the orientation of the sample and of the target, the latter in the case of the ECR technique, are monitored visually through windows. The duration of layer preparation is manually controlled by shutters.

where they sputter the target material. The sputtered target atoms are deposited i. a. on the sample substrate which is placed face to face to the target in a distance of 10 cm [367]. Details of the ECR principle and of the ECR gun are given in Refs. [672, 367].
In this work Ar was used as noble gas with a working pressure of $2 \cdot 10^{-4}$ mbar. The acceleration voltage of the Ar^+ ions was adjusted to 1.2 keV, which provides a deposition rate of Pt of about 0.07 nm/s at the sample position. The deposition rate was calibrated by means of x-ray reflectometry (XRR, see section 5.3.1.2) and cross-checked via AFM and EDX. For the latter a reference sample with known thickness was used as calibration standard. The Pt target is a quadratic plate of 5 cm × 5 cm that is large enough, so that the whole Ar^+ ion beam hits the plate. During preparation the sputtering of the Pt target can be monitored via the sputter current I_t (see Fig. 5.13(a)).
In the case of the magnetron sputter technique the noble gas plasma is directly created in front of the target material (see Fig. 5.13(b)). Below the target permanent magnets are mounted which force the electrons on helical paths so that in front of the target the probability of the ionization of the noble gas is enhanced. For DC magnetron-sputtering utilized in this work the target is put on a negative potential, so that the created noble gas ions are accelerated to the target, where they sputter the target material. The strength of the potential and thus the energy of the noble gas ions defines the ion current at the target at a given working pressure. Further details of the working principle of magnetron sputtering can be e.g. found in Ref. [673, 674].
For the preparation of the Co and Pt layers an Ar working pressure of $3.3 \cdot 10^{-3}$ mbar was used. During magnetron-operation the ion current at the target was held constant at 30 mA for Pt and 50 mA for Co. Depending on the abrasion of the tar-

gets for these parameters the energy of the Ar^+ ions is $450 - 600$ eV for Pt and $290 - 310$ eV for Co. This corresponds to deposition rates of about $0.06 - 0.08$ nm/s for Pt (0.03 nm/s for Co) at the sample position, which is located at a distance of 10 cm to the targets. The same calibration procedure for the deposition rates as for ECR Pt was used. Both targets are cylindrical with an initial thickness of 3 mm. For Pt the diameter is 1" (2.54 cm) and for Co the diameter is twice as large. The reason for this circumstance is that the ferromagnetic Co shields the magnetic field of the permanent magnets to a certain amount. For the utilized 1" magnetrons[21] there is no corresponding magnet configuration available, which would allow the operation with such a thick ferromagnetic target. The thickest possible Co target for 1" magnetrons is 0.5 mm, which has the disadvantage that the Co is already dissipated after a small operation time of about 4 hours. The utilized 2" magnetron[22] equipped with Co has superseded the former 1" magnetron so that nowadays the operation time is enhanced to > 100 hours.
The main difference between the ECR and magnetron sputter technique affecting the film properties are the energy of the sputtering Ar^+ ions and the working pressure [368]. According to TRIM simulations [303] the first-mentioned difference results in an energy of the sputtered target atoms of about 30 eV for ECR and about 20 eV for magnetron sputtering. This energy difference of the sputtered atoms is further enhanced at the position of the substrate due to the different working pressures. While for the ECR the mean free path within the residual gas is about 40 cm and therefore six times as large as the distance between sample and target, the mean free path for the magnetron sputtering is only about 2 cm [20]. Thus, the magnetron sputtered Co and Pt atoms are significantly moderated on the way to the target by collisions with the Ar gas atoms. Compared to magnetron sputtering the higher energy (mobility) of the ECR sputtered atoms results in a more pronounced texture of the layer but in a stronger interdiffusion at the interfaces. In simplified terms the combination of an ECR seed layer, which initiates a pronounced textured film growth and the subsequent preparation of Co and Pt layers with magnetron sputtering, which causes low interdiffusion, enhances the overall perpendicular magnetic anisotropy [368]. A more detailed discussion about the structural properties and their consequences on anisotropy are given in section 5.3 and 5.4, respectively.
For the sake of completeness it is mentioned that besides the energy of the sputtered atoms the energy of the Ar^+ ions reflected at the target influences the kinetic of the film growth [674]. As their energy is significantly higher than the energy of the sputtered atoms by hitting the sample the Ar^+ ions can redistribute the deposited atoms. Details about the influence of various preparation parameters on sample quality can be e.g. found in Refs. [675, 676, 677, 678, 679, 680, 681, 674].

5.2.2 Construction of the Co/Pt samples

Generally, if not otherwise stated, the Co/Pt samples are built up as follows (see Fig. 5.14). The lower part of the Pt seed layer was prepared by ECR, while all other layers were prepared by DC magnetron sputtering. The thickness of the ECR

[21] A 310-XP, aja international, Inc.
[22] A 320-XP, aja international, Inc.

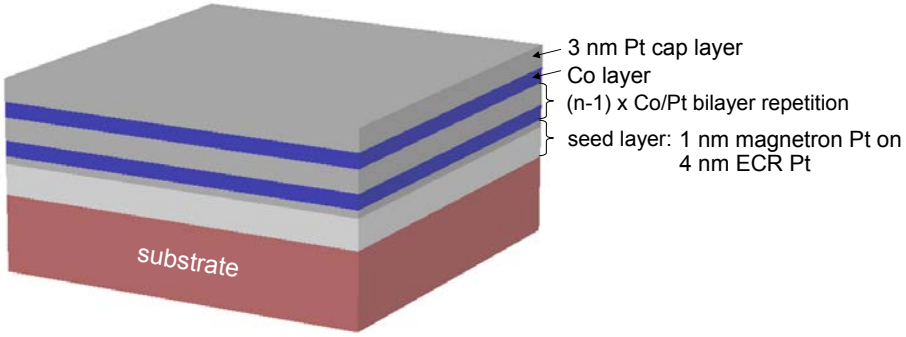

Figure 5.14: Scheme of the general layer construction of the $(Co/Pt)_n$ samples.

layer was chosen as small as possible in order to reduce the current shunt through the Pt material but as high as necessary to achieve the best possible quality in crystallinity and interfaces. Regarding the latter, Stillrich showed that an ECR seed layer thickness of 4 nm is sufficient as checked by determining the anisotropy constants of Co/Pt samples with different seed layer thicknesses grown on naturally oxidized Si [671]. This finding was approved within the framework of this thesis and, furthermore, it was found out that it is also valid for films grown on 300 nm thick SiO_2 (thermally oxidized Si) and 200 nm thick Si_3N_4 substrates. Importantly, the results reveal that the anisotropy constants of the films grown simultaneously on the three different kind of substrates depend on the particular substrate (see section 5.4) reflecting differences in the structural properties (see section 5.3).
After the deposition of the ECR seed layer a 1 nm thick Pt layer was grown via DC magnetron sputtering in order to avoid possible distortions of the growth of the subsequent Co and Pt layers caused by adsorbates, which could emerge during the transfer from the ECR sub-chamber to the magnetron sub-chamber [671].
All samples were capped by a 3 nm thick magnetron sputtered Pt layer in order to prevent Co from oxidation under ambient conditions. It was checked that the properties of the samples do not alter within two years after sample preparation.

5.2.3 MR sample layout and electrical contacting

In order to have the possibility to extract the resistivity ρ_{xx} from the resistance R_{xx} in the most simple and accurate way, it is useful to have a wire shape sample geometry. Then the simple relation

$$R_{xx} = \rho_{xx} \cdot \frac{l}{w \cdot t} \tag{5.51}$$

can be utilized, where l, w, and t are the length, width, and thickness of the wire. To achieve the wire shape a shadow mask was mounted on the substrate during Co/Pt preparation via a manipulator (see Fig. 5.15(a)). The shadow mask was made from a 100 μm thick aluminum plate by utilizing a focused laser beam cutting technique (laser spot diameter ≈ 10 μm)[23]. The dimensions of the wire are $w = 0.5$ mm and

[23] multiflex GmbH

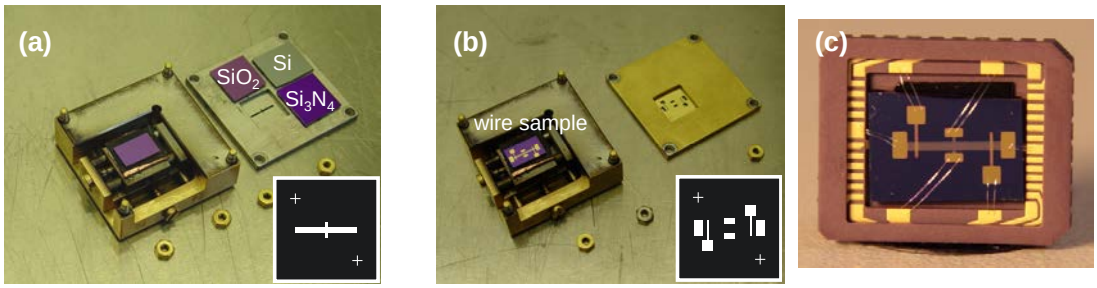

Figure 5.15: On the left hand side in (a) and (b) the sample holder equipped with a SiO_2 substrate is shown before and after the sample preparation, respectively. During Co/Pt preparation further substrates were attached to the mask frame (right hand side in (a)) in order to simultaneously obtain laterally homogeneous Co/Pt samples as well. The insets in the lower right schematically show the mask layouts for the preparation of the Co/Pt wire and the Cr/Au contact pads, respectively. (c) shows a wire sample attached to a chip carrier. The Cr/Au pads were electrically contacted to the chip carrier by means of 25 μm thick Al wires utilizing ultrasonic bonding technique.

$l' = 6$ mm. The small cross in the middle (see inset of Fig. 5.15(a)) is for measuring the off-diagonal element of the resistivity tensor ρ_{xy}. After the Co/Pt deposition a second mask served to prepare pads for the electrical contacting (see Fig. 5.15(b)). The contact pads of 20 nm Cr/ 100 nm Au were made by sputtering technique. The resulting sample geometry can best be seen in Fig. 5.15(c). The diagonal element ρ_{xx} was also measured in four-point-probe geometry as the current was impressed by the two outer gold contacts, while the voltage drop along a distance of $l = 4$ mm was measured by means of the two inner contacts crossing the ferromagnetic wire. For the MR measurements the samples were mounted to chip carriers and the corresponding electrical contacting between both was performed via ultrasonic bonding technique (see Fig. 5.15(c)).
Pieces of substrates were attached to the mask frame during Co/Pt preparation (see Fig. 5.15(a)). The resulting laterally homogeneous Co/Pt samples were used within this thesis in order to investigate the properties of the Co/Pt layered structures via x-ray techniques, MOKE, and FMR. As it was found out that the film properties depend on the kind of substrate, mentioned in the previous section, naturally oxidized Si(001), thermally oxidized Si(001) with a SiO_2 thickness of 300 nm, and Si(001) with a coverage of 200 nm thick Si_3N_4 were generally used as substrates. The two latter substrates are electrically insulating. In contrast, MR measurements of Co/Pt samples grown on naturally oxidized Si reveal a significant current shunt through the semi-conducting Si material, so that this substrate is unsuitable and therefore not used for the systematic MR investigations.

5.2.4 MR sample series

Within this thesis the following Co/Pt sample series were prepared for the MR investigations:

- sandwiches on 300 nm thick SiO_2: 5 nm Pt/ t_{Co}/ 3nm Pt
- sandwiches on 200 nm thick Si_3N_4: 5 nm Pt/ t_{Co}/ 3nm Pt
- multilayers on 300 nm thick SiO_2:
  5 nm Pt/ (0.8 nm Co/ t_{Pt})$_{n-1}$/ 0.8 nm Co/ 3 nm Pt, $n = 4$

For the sandwiches the Co thickness t_{Co} was varied between 0.8 nm and 50 nm. For the multilayers the Co thickness was held constant (at 0.8 nm), while the Pt interlayer thickness t_{Pt} was varied from 0.25 nm to 5 nm.
Besides these main sample series further multilayers with a different number n of bilayer repetitions were prepared.

5.3 Structural and magnetic properties of Co/Pt layered structures

Besides the magnetoresistance the structural (section 5.3.1) and magnetic properties (section 5.3.2) of the samples were investigated. For the former x-ray reflectometry and diffraction were applied, while for the latter magneto-optical Kerr effect and ferromagnetic resonance were utilized. Each method is briefly introduced before the results of the corresponding investigation are presented.

5.3.1 Structural properties

As mentioned in connection with the magnetic anisotropy in section 2.1.5 and with the resistivity of thin films in section 5.1.2 the structural characterization of the Co/Pt samples is essential for a reasonable interpretation of the experimental results, i.e., to trace back the features in the magnetic properties to the structure of the samples. The structural properties of the Co/Pt samples were investigated by means of x-ray diffraction (XRD) and x-ray reflectometry (XRR). For both investigation methods a commercial x-ray diffractometer[24] was used. The x-rays were generated by using Cu as anode material, where the Cu Kα line with a wave length of $\lambda = 1.5406$ Å was utilized. The investigations were performed in co-operation with the working group of Prof. Dr. Andreas Schreyer from the Helmholtz-Zentrum Geesthacht, Germany, under supervision of Dr. Dieter Lott within the scope of the Landesexzellenzinitiative (LEXI) Hamburg. In the following the functionality and the results of the XRD and XRR investigations are presented separately starting with XRD in section 5.3.1.1. At suitable positions the x-ray investigations are complemented by high resolution SEM investigations and preliminary results obtained via cross-sectional high resolution transmission electron microscopy (TEM). The

[24]Bruker AXS-D8 Advance Röntgendiffraktometer

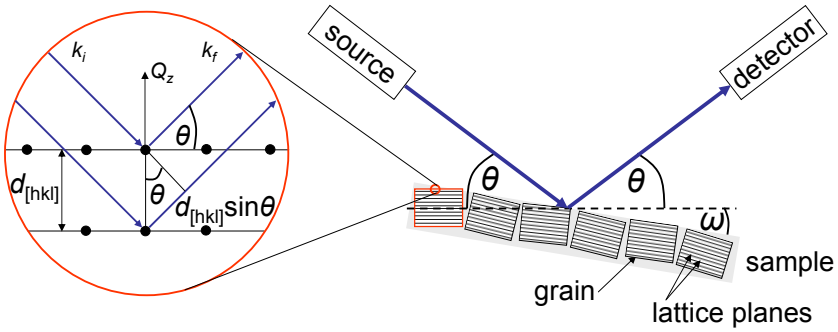

Figure 5.16: Schematic representation of the XRD measurement geometry. The zoom into the red crystallite reveals that the two specularly reflected beams from adjacent lattice planes constructively interfere when their path difference $2d_{[hkl]} \sin\theta$ corresponds to integer multiples of the wave length (Bragg's law). Besides θ the angle ω is varied experimentally, which enables the fulfillment of Bragg's law also for crystallites, where the crystal lattice planes are not oriented in parallel to the sample surface. $\omega = 0$ means that the bisecting line of incoming and diffracted light is parallel to the surface normal.

latter investigations were performed in co-operation with Dr. A. Chuvilin from CIC nanoGUNE, San Sebastian (Spain). For details about TEM the reader is referred to Ref. [682]. After presenting the XRR results in section 5.3.1.2, a summary with discussion is given in section 5.3.1.3.

5.3.1.1 Crystallographic properties investigated via x-ray diffraction

As the wave lengths of x-rays are in the order of magnitude of the interatomic distances x-ray diffraction is a suitable method to reveal information about the crystal structure. For that purpose the sample has to be irradiated with a collimated x-ray beam and the intensity of the small part of the beam, which is specularly reflected at the lattice points, has to be detected. For distinct incidence angles θ, where θ is the angle between the beam direction and sample surface, the specular reflections from different lattice planes interfere constructively with each other leading to characteristic diffraction peaks. The constructive interference condition is known as Bragg's law (see scheme on left hand side in Fig. 5.16) [83]:

$$2d_{[hkl]} \sin\theta = n\lambda \quad , \tag{5.52}$$

where $d_{[hkl]}$ is the distance between two lattice planes (interplanar spacing) and n is the order of diffraction. $[hkl]$ labels distinct directions of the crystal structure, which are perpendicular to a respective lattice plane (hkl). Thus, for a given wave length λ measuring the angle dependence of the diffraction peaks reveals information about the kind of lattice including its orientation and lattice parameter.
The lattice of bulk platinum is face-centered cubic (fcc) with a lattice spacing of the conventional cell of $a_{\mathrm{Pt,\ fcc}} = 0.392$ nm [85]. For this lattice only diffraction peaks with complete even or odd Miller indices h, k, l do not vanish because of symmetry reasons [83]. The lattice of bulk cobalt is hexagonal closed packed (hcp) at room temperature but changes instantly at about 400°C to fcc [683, 684]. The length of

fcc Pt	hcp Co	fcc Co
(111): 39.8°	(1000): 41.51°	(111): 44.42°
(200): 46.28°	(0002): 44.48°	(200): 51.75°
	(1001): 47.37°	

Table 5.1: Diffraction angles 2θ of the lowest non-vanishing Miller indices for the Co and Pt crystal lattices utilizing the $K\alpha$ wave length of Cu.

the conventional cell for hcp Co and fcc Co is $a_{\text{Co, hcp}} = 0.251$ nm, $c_{\text{Co, hcp}} = 0.407$ nm and $a_{\text{Co, fcc}} = 0.353$ nm, respectively [85]. For the hcp lattice only diffraction peaks that correspond to odd multiples of the [0001] direction are suppressed as the symmetry of the hcp lattice is lower than for a fcc lattice[25].
The expected angles 2θ for the diffraction peaks of bulk Co and Pt for the lowest non-vanishing Miller indices were calculated according to Eq. 5.52 and are listed in Tab. 5.1. Thereby, the corresponding interplanar distances were deduced from the given lattice parameters[26]. As can be seen in Tab. 5.1 the expected angles for the hcp Co(0002) and fcc Co(111) reflexes are practically the same reflecting an almost identical lattice spacing for $d_{\text{fcc, [111]}}$ and $d_{\text{hcp, [0002]}}$. The difference is within the resolution of the measurements of $\pm 0.03°$. Furthermore, it cannot be excluded that the Co grows slightly strained. Therefore, a differentiation between hcp Co(0001) and fcc Co(111) growth on Pt(111), which basically differ only in the stacking sequence (fcc (ABCABC...) vs. hcp (ABAB...)) [232], is not possible with the used reflection geometry.
The intensity I integrated in 2θ of a distinct Bragg peak is given by [686]

$$I \propto \frac{VF^2}{V_a^2}\left(\frac{1+\cos^2 2\theta}{2\sin 2\theta}\right) \quad , \tag{5.53}$$

where V and V_a is the volume of the crystal and of the conventional unit cell[27], respectively, while $F^2 = FF^*$ is the square of the structure factor. The term within the brackets is known as Lorentz-polarization factor[28]. For the fcc(111) and hcp(0002) reflexes it is $F_{111} = 4f$ and $F_{0002} = 2f$ [686], respectively, where f is the atomic scattering factor which is a measure for the scattering strength of an atom. f depends on the scattering angle θ, wave length λ as well as on the number and distribution of the atomic electrons [83]. The calculated atomic scattering factors for a variety of elements are tabulated in Refs. [687, 688] in dependence of $\sin\theta/\lambda$. Within this work the atomic scattering factors for the Pt(111) peak and the Co(0002)/ Co(111) peaks are $f_{\text{Pt(111)}} = 64.7$ and $f_{\text{Co(0002)}} = f_{\text{Co(111)}} = 19.5$, respectively. With these values by utilizing Eq. 5.53 a ratio in the measured intensities of the Pt(111) and

[25] For hcp the overdetermined indexing is utilized, where the c-axis corresponds to the 4^{th} index.
[26] The distance between adjacent lattice planes $d_{[hkl]}$ can be obtained from the following equations [685]: cubic lattice: $\frac{1}{d_{[hkl]}{}^2} = \frac{h^2+k^2+l^2}{a^2}$; hcp lattice: $\frac{1}{d_{[hkl]}{}^2} = \frac{4}{3}\frac{h^2+hk+k^2}{a^2} + \frac{l^2}{c^2}$.
[27] $V_{a,fcc} = a^3$, $V_{a,hcp} = \sqrt{3}a^2c/2$
[28] Eq. 5.53 is valid as long as absorption is negligibly small, which is fulfilled for x-rays in thin films [686].

Co(0002)/ Co(111) peaks of

$$\frac{I_{Co(0002)}}{I_{Pt(111)}} = k\frac{t_{\mathrm{Co}}}{t_{\mathrm{Pt}}}, \quad k = 0.14 \tag{5.54}$$

was calculated, where t_{Co} and t_{Pt} are the (total) thicknesses of the Co and the Pt layers. The prefactor k on the right hand side of Eq. 5.54 is the same for fcc and hcp Co as the ratio $\frac{F^2}{V_a^2}$ is virtually identical for both stackings. Thus, a differentiation between fcc Co and hcp Co is not possible.
As the Co/Pt samples within this work are polycrystalline it is essential to know the size of the grains as well as the degree of texture. It should be recalled that the term texture stands for a preferred orientation of the crystallites (see section 2.1.3.1).
The average grain size d_{grain} in the direction perpendicular to the reflecting planes analogous to to the coherence length and can be determined from the width of the diffraction peaks utilizing the so-called Scherrer-equation [689, 686]

$$d_{\mathrm{grain}} = \frac{0.94\lambda}{B_{2\theta}\cos\theta} \quad , \tag{5.55}$$

where $B_{2\theta}$ is the full width of the peak in radians at half maximum intensity and θ the angular peak position. With shrinking grain size in each grain (crystallite) the number of atoms that contribute to the diffraction is decreased so that in analogy to the number of grid lines in an optical grating the width of the reflex $B_{2\theta}$ increases [671]. It is important to note that inhomogeneous lattice strain yields an additional broadening of the peaks as in this case several slightly different interplanar lattice spacings and therefore Bragg conditions exist [685]. Consequently, if strain contributions to $B_{2\theta}$ are dominant the Scherrer-equation only provides a lower bound for the grain size.
To determine the degree of texture of the samples so-called "rocking" or ω scans must be performed. This means that for fixed θ the sample is rotated by an angle ω around the axis which is perpendicular to the plane that is spanned by the incoming and reflected x-ray beams (see Fig. 5.16). For a polycrystalline sample at the position of a diffraction peak in θ at a distinct ω only selected grains with a respective lattice orientation satisfy Bragg's law (see red grain in Fig. 5.16) and thus contribute to the peak. Upon changing ω the contribution of these grains disappears, while another class of grains with a distinct tilt of their lattice give rise to a peak. For the special case of $\omega = 0°$ only the grains with lattice planes running in parallel to the sample surface contribute to the diffraction peak. If the crystallites in the sample have a random orientation the intensity does not depend on ω.
For a reasonable interpretation of the intensity profiles including the assignment of the peaks to the individual layers the distortion of the crystalline lattice has to be taken into account, which is caused by the Co/Pt layered structure [690]. In the so-called kinematic approximation[29] the specularly scattered amplitude from a layered

[29] Multiple scattering, interference between incident and scattered beams, and absorption are neglected, which is legitimate for metallic multilayers in a good approximation [232].

structure can be calculated by [232]

$$A(Q_z) = \sum_{j=1}^{M} f_j^{\text{layer}} e^{iQ_z r_j} \quad , \tag{5.56}$$

where the sum is over each of the M monolayer in the layered structure, f_j^{layer} is the layer scattering factor (atomic scattering factor times atom density), and r_j is the position of the jth monolayer. Q_z is the momentum transfer perpendicular to the layer planes (see scheme on left hand side in Fig. 5.16), which is for the specularly reflected part of the beam:

$$Q_z = k_{f,z} - k_{i,z} = 2k_{f,z} = \frac{4\pi}{\lambda} \sin\theta \tag{5.57}$$

The scattered intensity is given by $I(Q_z) =< A(Q_z)|A(Q_z)^* >$. The special impacts of the layered structure on the intensity profiles are discussed in detail in connection with the results.

The diffraction intensity of the samples was predominantly measured in the range of $36.5° < 2\theta < 48°$, where the fcc Pt and Co(111), (200), and hcp Co(0002), (1000), (1001) bulk peaks are located (see Tab. 5.1). During the measurement of some samples ω was not held constant at $\omega = 0$ but was varied additionally between about -20° and 20°. Note that the rocking scans are restricted to $|\omega| < \theta$ due to geometrical reasons.
The calibration of the setup was checked via the position of the Si(200) reflex of the substrates, whose position at $2\theta = (32.97 \pm 0.03)°$ corresponded to the expected value of 32.96° ($a_{\text{fcc Si[200]}} = 0.543$ nm) [691]. Fig. 5.17(a) exemplarily shows the result of a diffraction measurement of a Co/Pt multilayer, a so-called diffraction map, where for each pair of $(\omega, 2\theta)$ the diffraction intensity $I(\omega, 2\theta)$ is color coded according to the given color bar. In the diffraction map the meaning of the peak properties is indicated.
At first, the general XRD results, which were found for all Co/Pt samples are presented.

General results: Fig. 5.17(b) shows the integrated intensity $I(2\theta) = \sum_\omega I(\omega, 2\theta)$ of the diffraction map presented in Fig. 5.17(a). As indicated by the red line the peak at the Pt(111) bulk position can be fitted to a normal (or Gaussian) distribution, which is representative for all peaks observed in the experiment in a good approximation[30]. The number of peaks, their definite position in the 2θ-direction as well as their full width at half maximum $B_{2\theta}$ depends on the particular sample and are discussed in detail after this section.
The second peak in Fig. 5.17(b) at about 37.9° is no fundamental Bragg peak but can be identified as the so-called -1 satellite reflex, which was observed for multilayers. As satellite reflexes are a consequence of a periodic distortion of the crystal lattice

[30] In literature, there is a variety of complex functions which are theoretically suggested for fitting XRD intensity profiles $I(2\theta)$. An overview can be found in Refs. [692, 693]

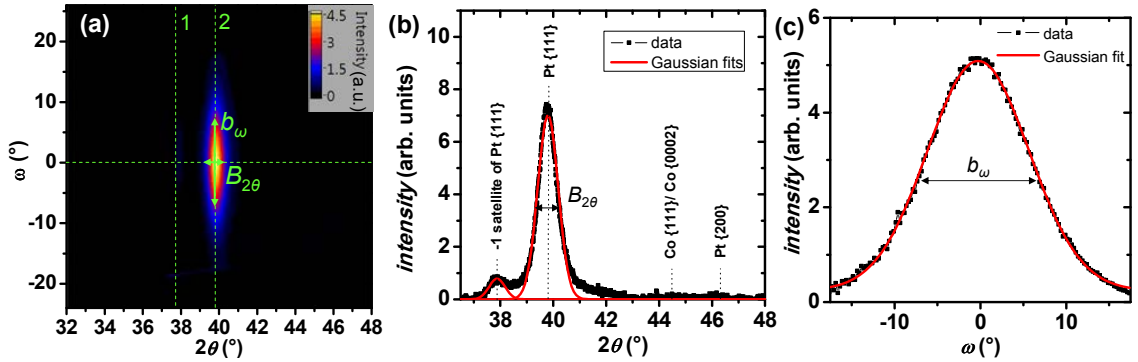

Figure 5.17: (a) Diffraction map $I(\omega, 2\theta)$ of a 5 nm Pt/ (0.8 nm Co/ 4 nm Pt)$_3$/ 0.8 nm Co/ 3 nm Pt multilayer grown on Si_3N_4. The intensity is color coded according to the given color bar. The positions of the -1 satellite reflex (1) and of the peak at the Pt(111) position (2) are indicated by vertical dashed lines. (b) shows the integrated intensity $I(2\theta) = \sum_\omega I(\omega, 2\theta)$ and (c) the cross-section $I(\omega)$ at the peak position $2\theta_{\text{fcc Pt(111)}} = 39.8°$. Both curves are fitted to a normal distribution (red lines) with a FWHM of $B_{2\theta}$ and b_ω, respectively.

their occurrence gives a first indication that the Co/Pt samples exhibit a well-defined variation in the chemical composition along the growth direction [694, 451, 232]. Quantitatively, the position of the satellite peaks in 2θ can be used to determine the Co/Pt bilayer thickness $t_{\text{Co/Pt}}$ via the diffraction condition [107]

$$2 \sin\theta = \lambda(1/d_{[111]} + n/t_{\text{Co/Pt}}) \quad , \tag{5.58}$$

where $d_{[111]}$ is determined from the position of the fundamental Bragg peak by using Bragg's law (Eq. 5.52) and n is the order of the satellite reflex. From the peak positions in Fig. 5.17(b) a bilayer thickness of $t_{\text{Co/Pt}} = (4.8 \pm 0.2)$ nm was obtained, which is in accordance with the nominal bilayer thickness of 4.8 nm. A possible reason why the +1 satellite peak has not been observed is discussed in the paragraph, where the results for the multilayers are presented. Moreover, further important implications of the periodicity of multilayers on the spectra are discussed there.
Similar to $I(2\theta)$ the cross-sections $I(\omega)$ of the diffraction maps at the peak positions in 2θ can be well fitted to normal distribution functions as can be exemplarily seen in Fig. 5.17(c). Thereby, the maximum of the peaks occurred around $\omega \approx 0$ within the error margins of the experiment. As stated above an ω scan reveals the angular distribution of the crystallite lattices with respect to the film normal, i.e., the film texture. For all samples peaks were always found in the vicinity of the calculated fcc Pt(111) bulk position $2\theta_{\text{fcc Pt(111)}} = 39.8°$ (see Fig. 5.17(a),(b)). As the maximum is at $\omega \approx 0$ the Pt layers within the crystallites are preferentially oriented with the (111) lattice planes running in parallel to the film plane. Thus, the Pt layers exhibit a pronounced out-of-plane (111) texture. The tilt of the crystallites with respect to the film normal is normally distributed as indicated by the fit in Fig. 5.17(c). Hence, a quantitative measure for the degree of texture is the full width at half maximum b_ω, which strongly depends on the substrate as shown below. A further evidence for the Pt(111) texture of the films is the absence of the Pt(200) peak at

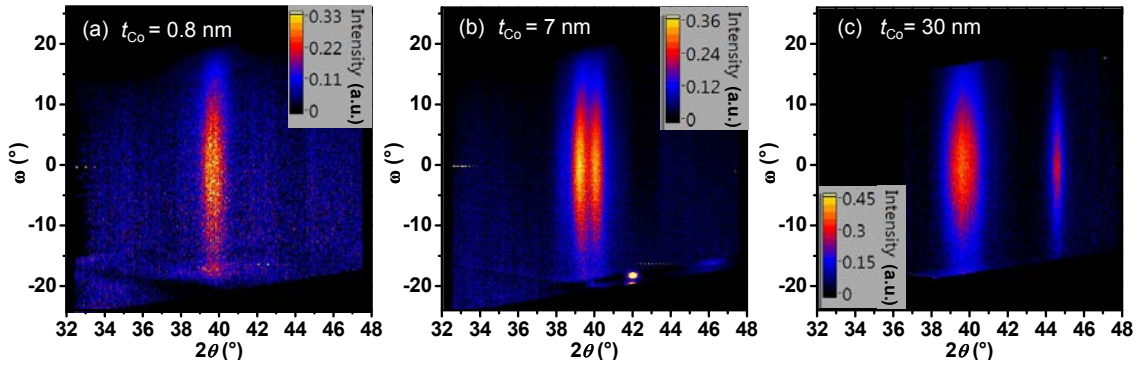

Figure 5.18: Diffraction maps $I(\omega, 2\theta)$ of Pt/Co/Pt sandwiches grown on SiO_2 with (a) $t_{Co} = 0.8$ nm, (b) $t_{Co} = 7$ nm, (c) $t_{Co} = 30$ nm. The intensity is color coded according to the given color bars. The lower signal to noise ratio in (a) can be attributed to a smaller sample size and lower duration of measurement.

$2\theta_{\text{fcc Pt(200)}} = 46.28°$ in the intensity profiles of all samples (see Fig. 5.17(a),(b)). For a random orientation of the crystallites it is expected that the intensities of the (200) and of the (111) peaks have a similar size [688].
On a Pt surface with (111) texture it can be assumed that Co grows with a fcc (111) or hcp (0001) texture. As can be seen in Fig. 5.17(a),(b) there is no peak visible at the expected fcc (111)/hcp (0002) Co peak position. One reason for this finding is that the expected intensity is about one order of magnitude lower compared to the intensity of the Pt(111) peak for the same amount of Co and Pt (see Eq. 5.54), so that the Co volume material was often too small to overcome the experimental detection limit.
In the following further results are discussed separately for Pt/Co/Pt sandwiches and Co/Pt multilayers grown on SiO_2, while the influence of the substrate on structural properties is discussed in the last part of this section.
If not otherwise stated, for a quantitative analysis the peaks in the intensity profiles $I(2\theta)$ (diffraction maps $I(2\theta, \omega)$) were fitted to 1D (2D) normal distribution functions. From these fits the position of the maximum of the peaks $I_{max}(2\theta_0)$ ($I_{max}(2\theta_0, \omega_0 \approx 0)$) and the full width at half maximum of the peaks $B_{2\theta}$ (and b_ω) was evaluated. The (2D) integrated intensity of the peaks depends on the exact sample size. Thus, only a comparison of the intensity of different peaks in the very same measurement is reasonable.

Results for Pt/Co/Pt sandwiches grown on SiO_2: At first the results for the Pt/Co/Pt sandwiches grown on SiO_2 are presented, where the Co thickness was varied between 0.8 and 50 nm (see section 5.2.4). In Fig. 5.18 selected diffraction maps for three different Co thicknesses are shown, which qualitatively reveal the signatures that are representative for the corresponding thickness regime. As can be seen the intensity profile $I(2\Theta)$ changes drastically with the Co thickness t_{Co}. For the samples with $t_{Co} = 0.8$ nm (see Fig. 5.18(a)) and $t_{Co} \geq 9$ nm (see Fig. 5.18(c)) one peak in the 2θ region of the Pt(111) bulk peak occurs, while for the samples with an intermediate Co thickness (1 nm $\leq t_{Co} \leq$ 7 nm) two peaks at that position are present (see Fig. 5.18(b)). In addition, in the vicinity of these peaks slight shoulders

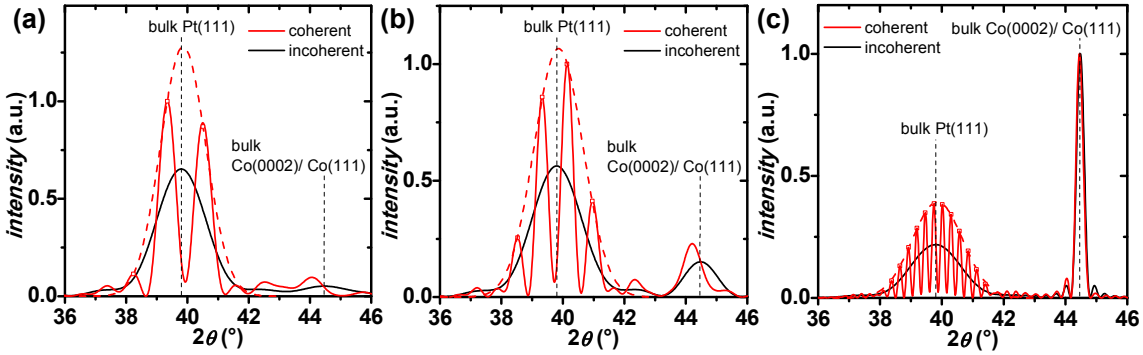

Figure 5.19: Modeled coherent (red) and incoherent (black) intensity profiles $I(2\theta)$ for (a) $N_{\mathrm{Co}} = 16$, (b) $N_{\mathrm{Co}} = 34$, and (c) $N_{\mathrm{Co}} = 147$. The red dashed lines are Gaussian fits to the maxima of the multiple peaks in the vicinity of the position of the Pt(111) bulk peak.

were frequently found as a further feature of the spectra. At the position of the fcc Co(111) and hcp Co(0002) bulk peaks a reflex was observed for $t_{\mathrm{Co}} \geq 12$ nm (see Fig. 5.18(c)).
For a comprehension of the experimental intensity profiles in order to extract information about the crystalline structure the spectra of the following simple step function model were calculated by utilizing Eq. 5.56:

$$A(Q_z, N_{\mathrm{Co}}) = \underbrace{f_{\mathrm{Pt}}^{\mathrm{layer}} \sum_{j=1}^{N_{\mathrm{seed}}} e^{iQ_z d_{\mathrm{seed}} j}}_{\text{Pt seed layer}} + \underbrace{f_{\mathrm{Co}}^{\mathrm{layer}} \sum_{j=1}^{N_{\mathrm{Co}}} e^{iQ_z (d_{\mathrm{Co}} j + d_{\mathrm{seed}} N_{\mathrm{seed}})}}_{\text{Co layer}} + \underbrace{f_{\mathrm{Pt}}^{\mathrm{layer}} \sum_{j=1}^{N_{\mathrm{cap}}} e^{iQ_z (d_{\mathrm{cap}} j + d_{\mathrm{Co}} N_{\mathrm{Co}} + d_{\mathrm{seed}} N_{\mathrm{seed}})}}_{\text{Pt cap layer}} , \tag{5.59}$$

where d_i are the interplanar spacings and N_i are the number of atomic monolayers (i = seed, Co, cap). By using the material parameters of bulk Co and Pt[31] and a thickness of the seed and cap layer that correspond to the values used in the experiment ($N_{\mathrm{seed}} = 22$ and $N_{\mathrm{cap}} = 13$), the model curves $I(Q_z, N_{\mathrm{Co}}) = < (A(Q_z, N_{\mathrm{Co}}) | A(Q_z, N_{\mathrm{Co}})^* >$ reveal a number of general features. Examples of spectra can be seen in Fig. 5.19. For comparison, the spectra for incoherent stacking between the three individual metal layers are also shown, which were obtained by calculating the intensity separately from the three sums in Eq. 5.59. The differences between coherent and incoherent stacking reveal that the coherent spectra are not only a result of a superposition of the independent signals of the individual layers. In the vicinity of the position of the Pt(111) bulk peak multiple peaks are present instead of one peak in the case of incoherent stacking. The thicker the Co layer

[31] $d_{\mathrm{Co,\ bulk}} = 2.035$ Å and $d_{\mathrm{Pt,\ bulk}} = 2.263$ Å. The layer scattering factors f_j^{layer} were calculated from the product between the atomic scattering factors ($f_{\mathrm{Pt}} = 64.7$ and $f_{\mathrm{Co}} = 19.5$) and the atomic density in the (111) plane, which is given by $4/(\sqrt{3}a_{fcc}^2)$ (Co: 0.185 atoms/Å^2, Pt: 0.150 atoms/Å^2), to $f_{\mathrm{Pt}}^{\mathrm{layer}} = 9.72$ and $f_{\mathrm{Co}}^{\mathrm{layer}} = 3.61$.

the higher the number of peaks is. For arbitrary N_{Co} the envelope of these peaks can be well-described by a Gaussian distribution as shown by the dashed lines in Fig. 5.19, whose maximum is located at the position expected according to Bragg's law (Eq. 5.52) for a Pt single crystal. Thus, this property can be used to determine the interplanar spacing of the Pt layers d_{Pt} from the spectra. The width of the envelope is independent of N_{Co} with a value of $B_{2\theta}^{\mathrm{Pt\ theo}} = (1.8 \pm 0.1)^{\circ}$, which resembles the widths of the Pt peak in the case of incoherent stacking. Utilizing the Scherrer equation (Eq. 5.55) $B_{2\theta}^{\mathrm{Pt,\ theo}}$ corresponds to the thickness of the Pt seed layer of (4.9 ± 0.3) nm. This fact points out the dominance of the seed layer material in the signal, which is a consequence of its larger thickness compared to the thickness of the cap layer. It is worth mentioning that the envelope function deviates from a pure Gaussian distribution at the flanks. In particular, slight differences in the interplanar spacing between seed and cap layer manifest in the characteristics of the flanks.

The position of the peak in the vicinity of the bulk Co(111)/(0002) peak depends on N_{Co}. By increasing N_{Co} the position of the peak in 2θ increases leveling for $t_{\mathrm{Co}} \gtrsim 20$ nm into the value expected according to Bragg's law for a Co single crystal. For these large Co thicknesses also the other properties of the peak are virtually indistinguishable from an individual Co crystal as can be seen in Fig. 5.19(c). Thus, in this thickness regime the width of the peak $B_{2\theta}^{\mathrm{Co,\ theo}}$ is solely determined by the thickness of the Co layer according to the Scherrer equation. For smaller t_{Co} the width of the peak is smaller than for an individual Co crystal of the same thickness. The ratio of the integrated intensity of the peak(s) in the vicinity of the Pt(111) bulk position and of the peak nearby the Co(111)/ Co(0002) bulk position normalized to the ratio of the total thickness of the Co and Pt layer was evaluated. They are identical for coherent and incoherent stacking with a value of about $k = 0.16$ that is independent of N_{Co}. This behavior clearly points out that also in the case of coherent stacking the integrated intensity at the Pt and Co bulk peak is basically caused by the Pt and Co layers, respectively[32].

In Fig. 5.20 selected (coherent) model spectra are compared with their experimental counterparts for three different Co layer thicknesses. In the experimental curves the integrated intensity of the Co peak compared to the integrated intensity of the Pt peak(s) is smaller than expected from the theoretical values, so that the Co peak emerged from the background not until a thickness of $t_{\mathrm{Co}} \geq 12$ nm. For $t_{\mathrm{Co}} \geq 20$ nm, where a Co peak can be clearly distinguished from the background, the k_{exp} value ranges from (0.04 ± 0.01) to (0.06 ± 0.01), while a systematic dependence on Co thickness was not found.

Between the experimental and modeled intensity profiles there is a good correspondence in the region of the Pt peaks in the range of 4 nm $\leq t_{\mathrm{Co}} \leq 7$ nm, as can be exemplarily seen in Fig. 5.20(a) and (b). In particular, the existence of multiple Pt peaks in the experimental intensity profiles indicates that the Pt/Co/Pt sandwich structure constitutes single crystalline phases along the growth direction in spite of the chemical modulation. For higher thicknesses the multiple peaks observed in the model spectra were not found experimentally (see Fig. 5.20(c)). Instead, a Gaus-

[32] The slight difference to the k-value given in Eq. 5.54 ($k = 0.14$) can be explained by the neglect of the Lorentz polarization factor considered in Eq. 5.53.

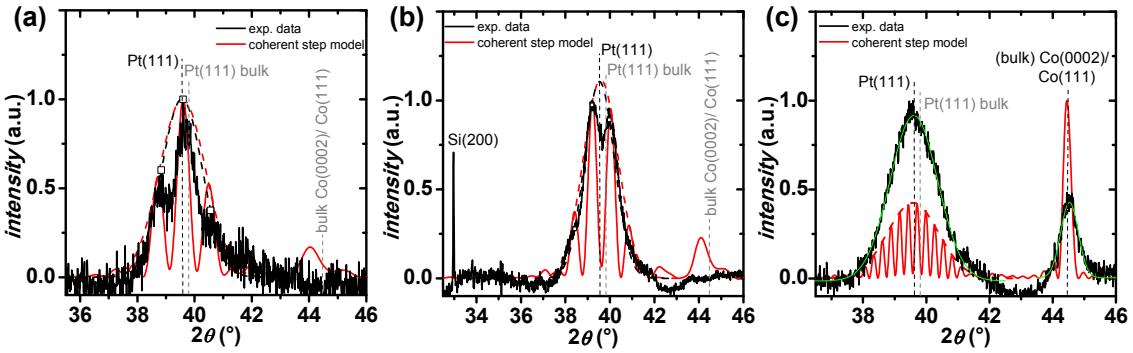

Figure 5.20: Experimental intensity profiles (black) and coherent model spectra (red) for (a) $t_{Co} = 6$ nm ($N_{Co} = 29$), (b) $t_{Co} = 7$ nm ($N_{Co} = 34$), and (c) $t_{Co} = 30$ nm ($N_{Co} = 147$). For the model spectra $d_{cap} = d_{seed} = 2.278$ Å ($d_{Co,\,bulk} = 2.035$ Å) is chosen in order to mimic the experimental data. The dashed lines are Gaussian fits to the maxima of the multiple peaks in the vicinity of the position of the Pt(111) bulk peak. The green lines in (c) are Gaussian fits.

sian distribution was detected as it was found in the modeled spectra in the case of incoherent stacking. Thus, these results indicate that a long-range crystalline order in films with large Co thicknesses is not maintained [695]. The loss in coherence becomes obvious in the spectra already for $t_{Co} \leq 7$ nm in terms of significant intensity between the multiple peaks (see Fig. 5.20(b)). For small Co thicknesses in the range of 1 nm $\leq t_{Co} \leq 3.2$ nm the envelope of the experimental peaks can be still described by a Gaussian distribution but the positions of the multiple peaks do not match between model and experiment (not shown). Furthermore, at $t_{Co} = 0.8$ nm only one peak remains (see Fig. 5.18(a)). These findings highlight the limitations of the simple step function model in the case of thin layer thicknesses. Here, the contributions from the Co/Pt interface regions are relatively high, where deviations from an ideal stacking can be expected (see section 2.1.5). Currently, a refined model is under development adapting the approach of E. Fullerton et al. [696], where the influence of interface roughness and interdiffusion as well as of lattice strain and strain relieving misfit dislocations on the spectra is taken into account (see also Refs. [697, 698, 699, 232]). Fitting the intensity profiles with such a model will help to extract this information about the crystalline structure. However, for such a detailed analysis a higher signal to noise ratio of the scattered intensity is desirable in order to e.g. detect the signal from the Co material over the whole thickness range or the details of the Pt peak(s). Therefore, high intensity XRD at synchrotron sources are planned (more details, see section 5.3.1.3). It should be recalled that within this thesis the roughness and interdiffusion at the interfaces was determined by XRR as shown in the next section 5.3.1.2.

In the following the results of the quantitative analysis of the experimental spectra concerning the crystallinity of the samples are presented. In Fig. 5.21(a) the position of the Co and of the Pt peak, i.e., the interplanar spacing of the lattice planes in growth direction, in dependence of the Co thickness can be seen as black symbols. Certainly, in the case of multiple Pt peaks, the maximum of the envelope Gaussian fit is presented (blue symbols).

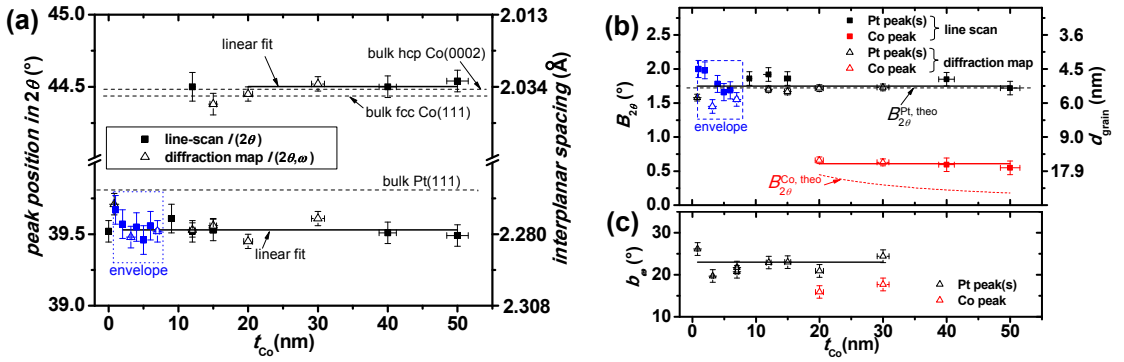

Figure 5.21: (a) displays the peak positions in 2θ/ interplanar spacing in dependence of the Co thickness. (b) and (c) show the full width at half maximum of the peaks in 2θ ($B_{2\theta}$/ d_{grain}) and in ω (b_ω), respectively. In (a) and (b), for 1 nm $\leq t_{\mathrm{Co}} \leq$ 7 nm, the properties of the envelope Gaussian fit are given in blue. The solid lines in (a)-(c) are horizontal fits. In (c) only the Pt values are fitted.

Except for small Co thicknesses $t_{\mathrm{Co}} \leq 1$ nm the position of the Pt peak does not change with thickness within the uncertainty of the experiment. For $t_{\mathrm{Co}} > 1$ nm a mean value of $2\theta_{\mathrm{Pt(111)}} = (39.53 \pm 0.04)°$ was found, which corresponds to an interplanar lattice spacing of $d_{\mathrm{Pt}} = (2.278 \pm 0.003)$ Å. This value is about 0.7% larger than the Pt bulk value ($d_{\mathrm{Pt,\ bulk}} = 2.263$ Å). The mean value resembles the lattice spacing that was found for the seed layer (zero thickness value, see Fig. 5.21(a)) revealing that already the Pt seed layer grows slightly tensely strained. To reveal possible slight differences in the lattice spacing between cap and seed layer, that become noticeable in the characteristics of the envelope function as mentioned above, high intensity XRD is required. It is worth mentioning that for a fcc lattice a peak shift can also be a consequence of deformation faults. Such stacking faults, however, always result in a shift of the (111) peak towards larger 2θ [686], so that they can be ruled out as the reason for the observed peak shift to lower 2θ.
Similar to Pt, the position of the Co peak does not change with thickness within the uncertainty of the experiment. It should be recalled that in the case of thickness-independent interplanar spacings d and coherent growth the position of the Co peak increases with the Co thickness. However, for $t_{\mathrm{Co}} \gtrsim 20$ nm, where a Co peak can be clearly distinguished from the background, the expected deviation from the bulk peak position is within the range of the error bars. For $t_{\mathrm{Co}} \geq 20$ nm the mean value of the peak position is determined to $2\theta_{\mathrm{Co}} = (44.50 \pm 0.03)°$. This corresponds to an interplanar spacing between adjacent lattice planes of $d_{\mathrm{Co}} = (2.034 \pm 0.004)$ Å, which is identical to the bulk values of fcc/hcp Co of $d_{\mathrm{Co,\ bulk}} = 2.038$ Å/2.035 Å. This result indicates that at least parts of the Co layer exhibit the bulk crystal lattice. Information about the interplanar spacing at small Co thicknesses are presented in the results for Co/Pt multilayers.
In Fig. 5.21(b) $B_{2\theta}$ is displayed as a function of t_{Co}. The width of the Pt peak (envelope of the multiple Pt peaks) is thickness-independent and similar to the theoretical value $B_{2\theta}^{\mathrm{Pt,\ theo}}$ (see black lines in Fig. 5.21(b)). This finding reveals that the Pt layers constitute single crystalline phases along the stacking direction.
For $t_{\mathrm{Co}} \geq 20$ nm, the signals of the Co peak were high enough to determine its width

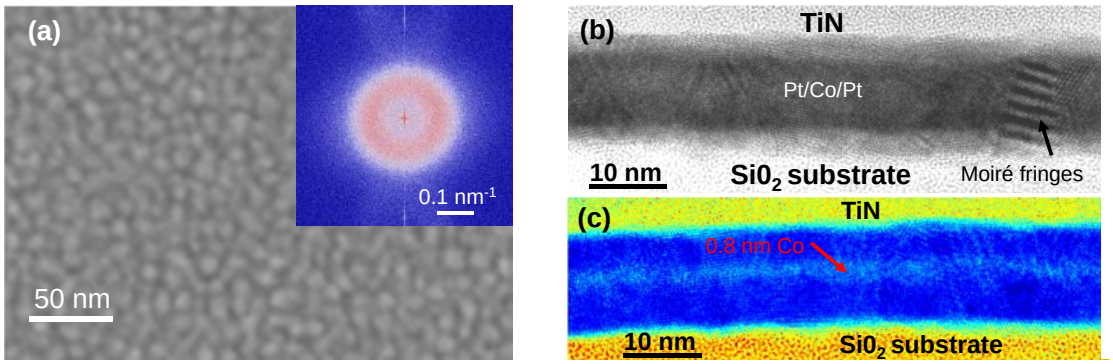

Figure 5.22: (a) Detail of a 23×15 μm^2 sized SEM image scanned with 0.74 nm/pixel obtained from a Pt/Co/Pt sandwich with a Co thickness of $t_{\mathrm{Co}} = 50$ nm. The inset is the Fourier transformation of the entire SEM image. (b) and (c) show cross-sectional TEM images of a Pt/Co/Pt sandwich with a Co thickness of $t_{\mathrm{Co}} = 0.8$ nm. In (c) the blue regions correspond to Pt-rich and the cyan regions in between to Co-rich regions, respectively. The TiN overlayer is not relevant here. For another study the TiN was prepared afterwards on top of the Co/Pt film, where it successfully served as a protection layer during FIB nanostructuring. As mentioned in section 4.4.2.1 the magnetic properties of the Co/Pt interfaces are very sensitive on irradiation already for low ion doses, so that the Ga^+ ions in the tail region of the FIB beam have to be shielded from there.

$B_{2\theta}^{\mathrm{Co}}$. In this thickness regime $B_{2\theta}^{\mathrm{Co}}$ was found to be thickness-independent within the error margins of the experiment (see red symbols in Fig. 5.21(b)) with a mean value of $B_{2\theta}^{\mathrm{Co}}$=$(0.61 \pm 0.03)^\circ$. According to the Scherrer equation (Eq. 5.55), which is applicable to the sandwich structure for $t_{\mathrm{Co}} \gtrsim 20$ nm (see above), a shrinking of $B_{2\theta}^{\mathrm{Co}}$ with t_{Co} was theoretically expected in the case of single crystalline Co phases along the out-of-plane direction (see red dashed line in Fig. 5.21(b)). Besides the loss in coherence due to structural disorder within the Co layer the Co peak might be additionally broadened by inhomogeneous strain or instrumental broadening. The latter can be ruled out as it was estimated to be $\approx 0.04^\circ$ [700]. Furthermore, a significant contribution of inhomogeneous strain is unlikely as the Co material contributing to the Co peak exhibits the bulk lattice parameter (see Fig. 5.21(a)), so that it can be regarded as relaxed. Hence, it is reasonable to assume that the behavior of $B_{2\theta}^{\mathrm{Co}}$ is basically caused by a loss in long-range crystalline order within the Co layer at large Co thicknesses. Utilizing the Scherrer equation and the mean value determined from the Co peak position ($2\theta_{\mathrm{Co}} = (44.50 \pm 0.03)^\circ$) a coherence length of $d_{\mathrm{Co,\,grain}} = (15 \pm 1)$ nm was determined. The thickness-independent coherence length indicates that the structural disorder is similar in all samples with $t_{\mathrm{Co}} \geq 20$ nm. High intensity XRD is required in order to verify that for $t_{\mathrm{Co}} \lesssim d_{\mathrm{Co,\,grain}}$ the Co layer basically constitutes single crystalline phases along the growth direction.
In order to determine the lateral grain size high resolution SEM was used. Fig. 5.22(a) exemplarily shows an SEM image of a sample with $t_{\mathrm{Co}} = 50$ nm. For samples with $t_{\mathrm{Co}} \geq 15$ nm the contrast is sufficient to determine the lateral grain size from the corresponding fourier transformation (see inset of Fig. 5.22(a)). A thickness-independent lateral grain size of $d_{\mathrm{grain}}^{\mathrm{lateral}} = (11 \pm 2)$ nm was found revealing that $d_{\mathrm{grain}}^{\mathrm{lateral}}$ is determined by the growth of the seed layer. This finding suggests that the

crystallites grow in a columnar structure during the subsequent magnetron sputtering of the Co and Pt layers, however, with a certain degree of structural disorder as the XRD measurements indicate.
The polycrystallinity was also observed in cross-sectional high resolution TEM images, which were made for the sample with the smallest Co thickness of $t_{\mathrm{Co}} = 0.8$ nm. For the TEM investigation vertical slices (cross-sections) with a thickness of about 25 nm were prepared from the sample by FIB. As can be seen in Fig. 5.22(b) atomic lattice planes with different orientation are clearly visible. The thickness of the cross-section is about twice as large as the lateral grain size. Thus, the pattern is a superposition from a few grains, so that it cannot be used for a quantitative determination of the lateral grain size or of the structural disorder. On the right hand side in Fig. 5.22(b) so-called Moiré fringes can be seen. They occur when the electron beam passes through adjacent crystallites, whose crystallographic axes only exhibit slightly different orientations with respect to each other [677]. This particular arrangement of adjacent crystallites is rather coincidental as over a large range no further fringes are observed. However, the formation of the fringes along the whole thickness of the sandwich qualitatively reveals a well-defined crystalline order along the stacking direction in accordance with the quantitative XRD results. While the crystal lattices of the grains are randomly oriented with regard to the directions parallel to the film surface the films exhibit a pronounced out-of-plane texture as already explained in the general results. It should be recalled that the tilt of the Pt(111) lattice planes of the crystallites with respect to the film surface is normally distributed. Fig. 5.21(c) shows the dependence of b_ω (FWHM of the intensity profile in ω) on t_{Co}. As can be seen b_ω is thickness-independent within the error margins of the experiment with a relatively large mean value of $(23 \pm 2)^\circ$ for the Pt peaks. The thickness independence reveals that the texture is initiated by the growth of the seed layer on the substrate, which is a further indication of a subsequent columnar growth of the Co and of the Pt cap layer on top of the seed layer.

Results for Co/Pt multilayers grown on SiO_2: In this part the results for Co/Pt multilayers grown on SiO_2 are presented, where the Pt interlayer thickness t_{Pt} was varied between 0.25 and 5 nm, while the Co thickness was held constant at 0.8 nm (see section 5.2.4). The degree of texture is independent of interlayer thickness t_{Pt} and basically the same as for the sandwiches (see next paragraph), so that it is reasonable to focus on the intensity profiles $I(2\theta)$ only. Fig. 5.23 shows selected intensity profiles for different Pt interlayer thicknesses. A peak at the expected fcc(111)/hcp(0002) Co bulk position was not observed for any multilayer (see e.g. Fig. 5.17), so that for a better comparison between the curves only the region of interest ($36.5^\circ \leq 2\theta \leq 44^\circ$) is shown. Similar to the Co thickness dependence found for the sandwiches a complex dependence of the intensity on Pt interlayer thickness t_{Pt} was observed nearby the position of the bulk Pt(111) peak. For $t_{\mathrm{Pt}} \geq 1.5$ nm only one fundamental diffraction peak occurs, whose position shifts to lower 2θ with increasing thickness revealing information about the interplanar spacing within the Co/Pt bilayers as shown below.
Contrary to Pt/Co/Pt sandwiches, there exist many publications dealing with XRD

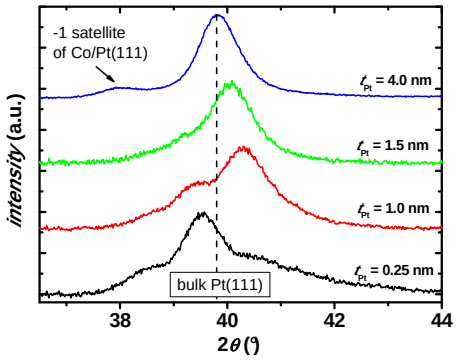

Figure 5.23: X-ray diffraction scans $I(2\theta)$ of Pt 5nm/(Co 0.8 nm/Pt $t_{\mathrm{Pt}})_3$/Co 0.8 nm/ Pt 3nm multilayers ($n = 4$) with varying Pt interlayer thickness t_{Pt}. The dashed line labels the peak position of bulk Pt(111).

investigation on Co/Pt multilayers. The main features of the XRD spectra found in these studies are briefly recapitulated as a starting point in order to interpret the measured $I(2\theta)$ curves correctly. In studies, where a rather thick Pt seed layer was used ($\geq$ 18 nm), besides satellite peaks, two fundamental Bragg peaks in the vicinity of the Pt(111) bulk peak were observed in the spectra [701, 702, 703, 704, 705, 706]. In these papers, one peak was always found very close to the position of the Pt(111) bulk value and was attributed to the relatively thick Pt seed layer. This interpretation is confirmed by the finding in Ref. [701], where it was shown that this peak vanished when the Pt seed layer was omitted. Furthermore, in investigations where no Pt seed layer or, with respect to the complete Co/Pt bilayer material, a relatively thin Pt seed layer was used only the "second" peak was observed [695, 707, 708, 701, 107, 709, 710, 711, 712]. This fundamental peak was always detected between the Pt(111) and fcc(111)/hcp (0002) Co bulk peak positions shifting to higher angles (lower angles) with increasing Co (Pt) content in the Co/Pt bilayers. To comprehend this behavior the influence of the Co/Pt superlattice structure, i.e., the periodic lattice distortion caused by the multilayered structure, on the x-ray diffraction spectrum is briefly discussed. Based on Eq. 5.56 a closed form for the scattering amplitude of an ideal superlattice with atomically sharp alternating layers of materials A and B was calculated by A. Segmüller and A. E. Blakeslee [694, 232]:

$$\begin{aligned} A(Q_z) = & \frac{\sin(Q_z d(N_A+N_B)n/2)}{\sin(Q_z d(N_A+N_B)/2)} \times \\ & \times \left(f_A^{\mathrm{layer}} \frac{\sin(Q_z N_A d_A/2)}{\sin(Q_z d_A/2)} + f_B^{\mathrm{layer}} e^{iQ_z d(N_A+N_B)/2} \frac{\sin(Q_z N_B d_B/2)}{\sin(Q_z d_B/2)} \right) \end{aligned} \quad , \tag{5.60}$$

where d_A and d_B are the interplanar lattice spacings, N_A and N_B the number of atomic layers, f_A^{layer} and f_B^{layer} the layer structure factors, and n the number of bilayers. Q_z is the wave vector as defined in Eq. 5.57 and d is the average lattice spacing [694]

$$d = \frac{N_A d_A + N_B d_B}{N_A + N_B} \tag{5.61}$$

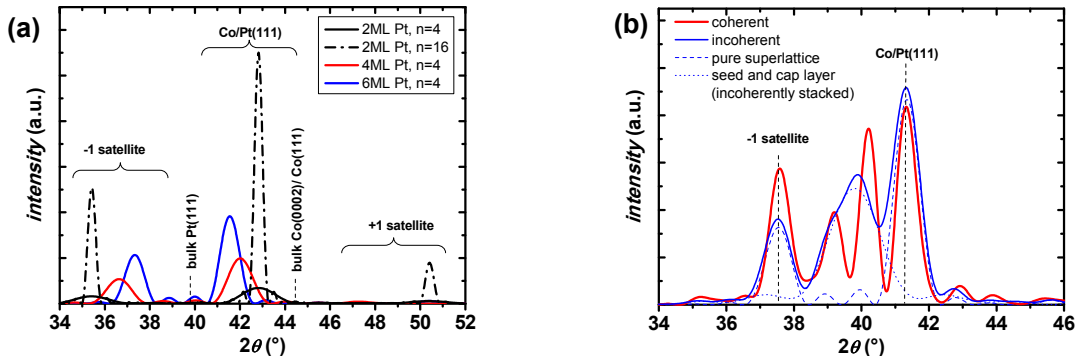

Figure 5.24: Step model scattering intensities. The model parameters are $N_{\mathrm{Co}} = 4$, $d_{\mathrm{Co,\,bulk}} = 2.035$ Å, $d_{\mathrm{Pt,\,bulk}} = 2.263$ Å, $f_{\mathrm{Pt}}^{\mathrm{layer}} = 9.72$ and $f_{\mathrm{Co}}^{\mathrm{layer}} = 3.61$. In (a) ideal superlattice spectra for different atomic monolayers (ML) N_{Pt} and number of bilayers n are shown. (b) displays in red (solid blue) the calculated spectrum of a Co/Pt superlattice for $N_{\mathrm{Pt}} = 7$ and $n = 4$, which is coherently (incoherently) sandwiched by a Pt seed and cap layer ($N_{\mathrm{seed}} = 22$, $N_{\mathrm{cap}} = 6$). The spectrum of the pure superlattice (dashed line) and of the cap and the seed layer (dotted line) are drawn for comparison.

The scattering intensity is $I(Q_z) =< A(Q_z)|A(Q_z)^* >$. By using the material parameters of Co and Pt (see caption of Fig. 5.24) and typical multilayer parameters ($N_A, N_B \leq 10$, $2 < n < 100$) the $I(Q_z)$ curves reveal a number of general features. Examples can be seen in Fig. 5.24(a). Instead of the Pt(111) and Co(0002)/ Co(111) bulk peaks the spectra consist of satellite peaks accompanying one fundamental Bragg peak, which is labeled as Co/Pt(111) peak in the following. The distance between the satellites and the Co/Pt(111) peak is determined by the bilayer thickness as discussed above (see Eq. 5.58). A further important consequence of the multilayered structure is that the position of the Co/Pt(111) peak corresponds to the average interplanar spacing d according to Bragg's law (Eq. 5.52). This explains the general trend found for multilayers as stated above, that the Co/Pt(111) peak position is basically dictated by the ratio of Co to Pt material in the bilayer. Consequently, evidence for strain are deviations from the calculated d-value utilizing the respective bulk lattice parameters.
As the nominal thickness of the individual Co and Pt layers are ultrathin significant deviations from the atomically sharp step function model were expected (section 2.1.5) and observed (section 5.3.1.2). However, the position of the Co/Pt(111) peak is insensitive on the exact nature of the periodic modulation in composition and lattice spacing [694]. In any case the position of the fundamental superlattice peak is determined by the average lattice spacing d according to Bragg's law, so that also in the case of strong interdiffusion, when the bilayer basically constitutes an inhomogeneous alloy whose stoichiometry varies in the vertical direction, d can be determined correspondingly[33].
By including a seed and a cap layer term according to Eq. 5.56 in the superlat-

[33] In the case of (111) textured, homogeneous $Co_{1-x}Pt_x$ alloys [129, 713, 136] the XRD spectra display one CoPt(111) diffraction peak revealing the interplanar spacing, whose position is dictated by the Co to Pt ratio. Certainly, due to the absence of periodic lattice distortion no satellites occur.

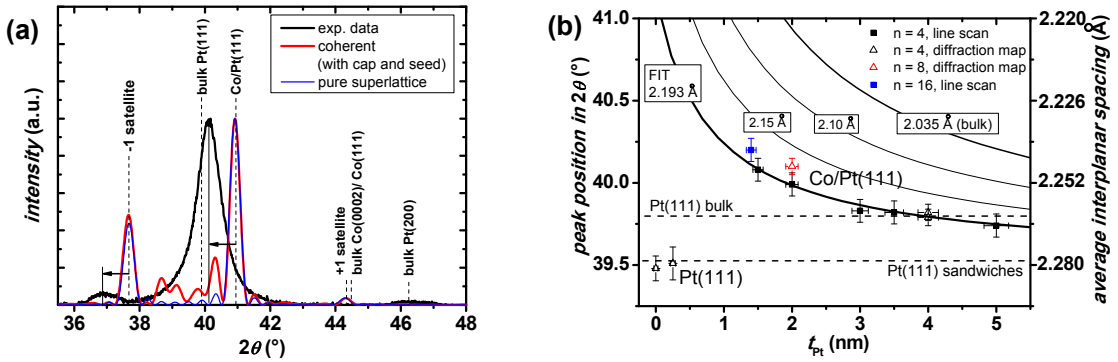

Figure 5.25: (a) Experimental intensity profile (black) of a 5 nm Pt/(0.8 nm Co/2 nm Pt)$_8$/1 nm Pt sample and coherent step model (thick red) with the model parameters: $N_{\mathrm{Pt}} = 9$, $N_{\mathrm{Co}} = 4$, $N_{\mathrm{cap}} = 4$, $N_{\mathrm{seed}} = 22$, $d_{\mathrm{Pt}} = 2.278$ Å, $d_{\mathrm{Co,\,bulk}} = 2.034$ Å, $n = 8$. The pure Co/Pt superlattice spectrum without cap and seed layer is shown for comparison (thin blue). From the positions of the experimental Co/Pt(111) and -1 satellite peak the bilayer thickness was determined to $t_{\mathrm{Co/Pt}} = (2.9 \pm 0.1)$ nm utilizing Eq. 5.58, which verifies the nominal bilayer thickness. (b) displays the peak positions in 2θ/ interplanar spacing in dependence of the Pt interlayer thickness. The solid line is a fit according to the step function model to the data for $n = 4$ and $t_{\mathrm{Pt}} \geq 1.5$ nm. The dotted lines are model curves calculated for different $d_{\mathrm{Co,\,ML}}$ as labeled in the graph ($d_{\mathrm{Pt,\,ML}} = 2.278$ Å).

tice model (Eq. 5.60) a further complex superstructure occurs in the $I(Q_z)$ spectra. However, for the thicknesses of the seed, cap, and Co layers ($t_{\mathrm{Co}} = 0.8$ nm) used in this work the positions of the Co/Pt(111) peak and of the satellites are basically unaffected and begin to dominate the calculated spectrum when the number of atomic layers in the Co/Pt superlattice is at least ≈ 1.5 times larger than the number of layers in the seed and cap layer[34]. For the main sample series with $n = 4$ this condition is satisfied for $t_{\mathrm{Pt}} \gtrsim 1.6$ nm (see Fig. 5.24(b)), so that in this thickness regime d can be directly determined from the maximum of the experimental spectra. For smaller t_{Pt} the rather complex multi-peak spectra (see Fig. 5.23) are dominated by the contributions of the seed and the cap layer masking the contributions of the bilayers.

In Fig. 5.25(a) the measured and calculated intensity profile for a 5 nm Pt/(0.8 nm Co/2 nm Pt)$_8$/1 nm Pt multilayer are shown, where the spectra are clearly dominated by the Co/Pt superlattice. In the calculation $d_{\mathrm{Pt}} = 2.278$ Å and $d_{\mathrm{Co}} = 2.034$ Å were used, which resemble the values found for the Pt/Co/Pt sandwiches at large t_{Co}. In this case the peak position of 40.93° corresponds to a lattice spacing of $d_{\mathrm{calc}} = 2.203$ Å as expected from Eq. 5.61. It is obvious that the experimental curve is significantly shifted to lower 2θ. The position of the experimental peak is about 0.8° smaller ($(40.10 \pm 0.05)°$) than the calculated value corresponding to $d_{\mathrm{exp}} = (2.247 \pm 0.003)$ Å. Thus, for this particular sample d_{exp} is about 2.0% larger than d_{calc} revealing that in the stacking direction the Co lattice is under stronger tensile strain than the Pt lattice is under compressive strain.

Fig. 5.25(b) displays the position of the Co/Pt(111) peak in dependence of the Pt

[34] In order to avoid double counting a fraction of the seed (or cap) layer was treated as a part of one of the bilayers.

interlayer thickness determined from the experimental spectra. Furthermore, for $t_{\mathrm{Pt}} = 0.25$ nm the interplanar spacing of the seed (and cap) layer was determined from the envelope of the multiple peaks, which is legitimate for such small t_{Pt}, resembling the value found for the sandwiches. The value at $t_{\mathrm{Pt}} = 0$ nm in Fig. 5.25(b) belongs to the sandwich with $t_{\mathrm{Co}} = 3.2$ nm, which is also shown for comparison.
The position of the Co/Pt(111) peak decreases (interplanar distance increases) with increasing t_{Pt} as qualitatively expected from Eq. 5.61 using the respective bulk lattice parameters. Quantitatively, in order to estimate the interplanar spacings $d_{\mathrm{Co,\,ML}}$ and $d_{\mathrm{Pt,\,ML}}$ the experimental data points of the samples of the main sample series ($n = 4$) were fitted by Bragg's law (Eq. 5.52) utilizing Eq. 5.61 under the conditions $N_i = t_i/d_i$ (i = Co,Pt). The black solid line in Fig. 5.25(b) is the resulting fit, which shows a good correspondence with the data yielding $d_{\mathrm{Pt,\,ML}} = (2.278 \pm 0.005)$ Å and $d_{\mathrm{Co,\,ML}} = (2.193 \pm 0.005)$ Å (independent of t_{Pt}). While $d_{\mathrm{Pt,\,ML}}$ resembles the value found for the seed (and cap) layer, $d_{\mathrm{Co,\,ML}}$ is by about 8% larger than the Co bulk value, which was obtained for the Co material within the sandwiches at large t_{Co}. Certainly, the determined d_{ML}-values are rather artificial as the XRR investigations, presented in the next section, reveal that for the used Co layer thickness the Co material is basically interdiffused with Pt. Furthermore, gradual changes in the interplanar spacing within the bilayers are likely to exist. Nevertheless, the good accordance between the fit and the data demonstrates that the average lattice spacing d is simply proportional to the Co to Pt ratio within the bilayers. Furthermore, the fit definitely reveals that the Co material incorporated in a Pt matrix is under strong tensile strain along the stacking direction, while the Pt material basically grows close to its natural interplanar lattice spacing.
Up to now, besides the samples of the main series ($n = 4$) two samples with $n = 8$ and 16 were investigated as well (see Fig. 5.25(b)). Both measurements indicate no significant dependence of d_{ML} on n. Further investigations of samples with different n particularly for $t_{\mathrm{Pt}} \leq 1.6$ nm might be helpful to disentangle the intensity contributions of the seed layer and Co/Pt bilayers in order to determine d in this thickness regime. For instance, deviations from the fit of the applied simple step function model would demonstrate that d is not simply proportional to the Co to Pt ratio.
In any case, the fitting of the intensity profiles with a refined model as discussed in connection with the results of the sandwiches, that e.g. explicitly includes the complex morphology of the Co/Pt interface, will help to gain a deeper insight into the interatomic arrangement (more discussion, see section 5.3.1.3).
It is worth mentioning that a clear evidence exists that the interplanar spacing of the Co (rich) phase is smaller than the spacing of the Pt (rich) phase. The observed asymmetry in the intensities of the satellite peaks with the same order $\pm n$ is a consequence of such a difference in the interplanar spacing [694, 232]. More explicitly, in XRD studies concerning Co/Pt multilayers the negative reflexes were always found to be larger than their positive counterparts, e.g. in the framework of this thesis only -1 reflexes but no $+1$ reflexes were observed (see Figs. 5.17, 5.23, 5.25). This behavior indicates that the heavier Pt element (larger layer scattering factor) has a larger interplanar spacing than the Co layers as expected from the respective bulk values. This feature of the superlattice spectra can be easily checked by interchang-

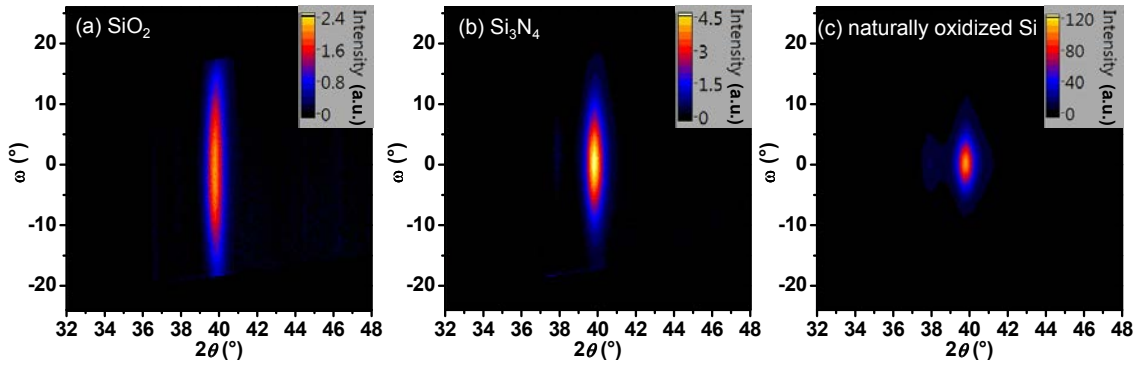

Figure 5.26: Diffraction maps $I(\omega, 2\theta)$ of a Co/Pt multilayer with $t_{\mathrm{Pt}} = 4$ nm simultaneously grown on (a) SiO_2, (b) Si_3N_4, and (c) naturally oxidized Si. The intensity is color coded according to the given color bar.

ing d_{Co} and d_{Pt} in the superlattice model [232].
It is important to note that a source of misinterpretation can be the non-consideration of a possible loss in crystallographic coherence due to structural disorder. In the XRD investigations of Refs. [695, 712], which also dealt with rather large individual layer thicknesses (t_{Co} and $t_{\mathrm{Pt}} \geq 2$ nm), the superlattice spectra started to be superimposed by additional Bragg peaks at bilayer thicknesses of ≈ 4 nm. The position of the additional peaks corresponded to the Pt(111) and hcp Co(0002)/ fcc Co(111) reflexes indicating that the long-range crystalline order in the multilayers with large periodicity was not maintained [695, 698, 696, 139]. In this work the loss in coherence is hard to observe as at high t_{Pt} the Co/Pt(111) peak is virtually located at the Pt(111) position and the incoherent Co signal is expected to be below the detection limit. Nevertheless, the literature values as well as the fact that in the case of the sandwiches the loss in coherence was observed at first at rather high thicknesses of the stack a significant impact on the multilayer spectra can be excluded.
For the sake of completeness it should be mentioned that SEM investigations of a multilayer with $t_{\mathrm{Pt}} = 5$ nm ($n = 4$) reveal a lateral grain size of about 12 nm, which is similar to the value determined for the sandwiches. Moreover, the texture is basically the same for multilayers and sandwiches grown on the same substrate. These findings attest that the grain size and the texture were initiated by the growth of the Pt seed layer in accordance with the assumed columnar growth of the Co/Pt bilayers on top of the seed layer.

Influence of the substrate on film texture: Fig. 5.26 exemplarily displays three diffraction maps of Co/Pt multilayers simultaneously grown on different substrates. Particularly striking is that b_ω strongly depends on the kind of substrate. The degree of texture is basically caused by the substrate, while it is independent on the distinct composition of the stack (compare e.g. Fig. 5.18 and Fig. 5.26(a)) in accordance with the assumed columnar growth (see above). The films grown on naturally oxidized Si exhibit the most pronounced texture with $b_{\omega,Si} = (7 \pm 1)^\circ$. For Si_3N_4 as substrate the angle spread is about twice as large as for Si with $b_{\omega,SiN} = (14 \pm 1)^\circ$, while the largest value was found for the films grown on SiO_2 with $(23 \pm 2)^\circ$ (see Fig. 5.21(c)). Besides the texture the investigations performed so far for selected samples indicate

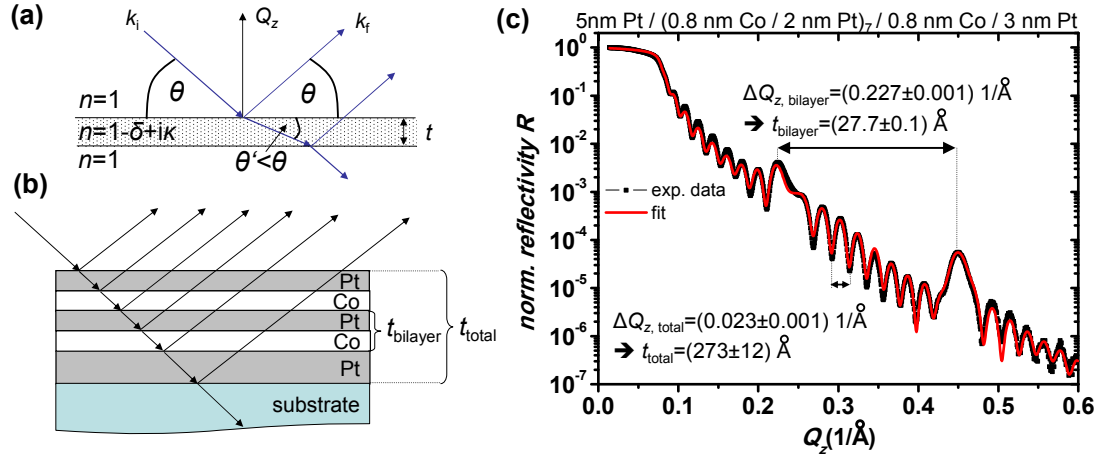

Figure 5.27: (a) Refraction and reflection of an x-ray beam hitting a thin layer with thickness t. The interference of the partial waves refracted from the two interfaces generates oscillations (Kiessig fringes) in the reflectivity profile $R(\theta)$. (b) In a periodically layered structure the interferences of the reflected partial waves additionally yield beating waves in $R(\theta)$. (c) Reflectivity R in dependence of the scattering vector Q_z for a multilayer with $n = 8$ and a Pt interlayer thickness of $t_{\mathrm{Pt}} = 2$ nm. From the oscillation and beating wave period the total thickness of the stacking and the bilayer thickness was verified utilizing Eq. 5.64 and Eq. 5.65, respectively. The red solid line is a fit utilizing the software PARRAT32 [715], which is used in particular to determine the thickness of the roughness/ interdiffusion regions.

no further drastic differences in the crystallinity of the very same films grown on the different substrates. For sandwiches and multilayers grown on Si_3N_4 the intensity profiles $I(2\theta)$, in particular the number of peaks, their position in 2θ, and their width $B_{2\theta}$ are similar to their counterparts grown on SiO_2. The same statement holds for multilayers grown on naturally oxidized Si substrate. If this is also the case for sandwiches grown on naturally oxidized Si substrate was not checked, yet. Moreover, for the sandwiches with $t_{\mathrm{Co}} = 50$ nm grown on the different substrates similar lateral grain sizes of about 11 nm were determined from high resolution SEM images.

5.3.1.2 Interfacial properties investigated via X-ray reflectometry

While the diffraction peaks occur at relatively high angles providing information about the crystal lattice, x-rays can also be used at small incidence angles with respect to the sample surface ($\theta < 10°$) to reveal information about the construction of multilayers [714].
Consider an incoming x-ray wave hitting the interface between two media which have different index of refraction $\widehat{n} = n + i\kappa$. As for any electromagnetic wave the wave splits into a reflected and refracted part (see Fig. 5.27(a)). The imaginary part considers that the beam is absorbed in the media (κ: absorption coefficient). The change in the direction of propagation of the refracted beam is described by Snell's law which is a consequence of the boundary conditions that the wave and its

derivation must be continuous at the interface [716]:

$$\widehat{n} \cdot \cos\theta = \widehat{n}' \cdot \cos\theta' \tag{5.62}$$

For x-rays in media the real part of the refraction index is $n = 1 - \delta < 1$, where the deviation from unity δ is typically in the order of 10^{-5}. Thus, the refracted part of a beam coming from vacuum ($\widehat{n} = n = 1$) penetrating in media is slightly refracted towards the sample surface (see Fig. 5.27(a)). Setting $\theta' = 0$ and using the expansion of cosines for low θ, $\cos\theta \approx 1 - \theta^2$, the critical angle of incidence of $\theta_c = \sqrt{2\delta} \approx 5$ mrad (0.3°) is obtained from Eq. 5.62, below which total external reflection occurs [716].
Beyond the critical angle of total reflection the specularly reflected and transmitted amplitude of the wave is given by the Fresnel equations, which are a further consequence of the boundary conditions of the continuity of the wave at the interface [716]. For low angles the expression for the amplitude of the specular reflectivity r is:

$$r(\theta) = \frac{\theta - \theta'}{\theta + \theta'} \tag{5.63}$$

The absolute square of r yields the quantity to be measured, i.e., the intensity of the reflectivity R.
Up to now only one interface is considered. For two interfaces (thin layer with thickness t, see Fig. 5.27(a)) the transmitted part of the wave at the top interface is again partially reflected and refracted at the bottom interface. The reflected waves from the top and the bottom interfaces interfere so that the intensity reflectivity spectrum $R(\theta)$ displays oscillations. These oscillations are known as Kiessig fringes named after H. Kiessig who discovered this phenomenon utilizing thin Ni "mirrors" in 1931 [717]. From the position of the peaks/dips of the spectrum, which corresponds to constructive/destructive interference of the waves, he derived the thickness of the Ni mirrors with high precision. The derivation of an exact result for $R(\theta)$ under consideration of multiple (infinite) reflection and refraction of the waves at both interfaces can be found e.g. in Ref. [716].
To get rid of the explicit dependence of the intensity reflectivity curve $R(\theta)$ on the wave length λ it is common use to plot R versus wave vector Q_z, where the latter is defined via Eq. 5.57. Then, there is a simple relation between the thickness of the layer t and the oscillation period (distance between two peaks/dips) ΔQ_z in the $R(Q_z)$ curve: $\Delta Q_z = \frac{2\pi}{t}$. A method to extend the exact result for a single layer (two interfaces) to the case of a multilayered system was derived by L. G. Parrat in 1954 [718, 716]. The $R(Q_z)$ curve again shows oscillations with a period of

$$\Delta Q_{z,\,\mathrm{total}} = \frac{2\pi}{t_{\mathrm{total}}} \quad , \tag{5.64}$$

where t_{total} is the thickness of the multilayer stack. In particular, for a periodic layered structure the oscillations are superimposed by beating waves with a period of

$$\Delta Q_{z,\,\mathrm{bilayer}} = \frac{2\pi}{t_{\mathrm{bilayer}}} \quad , \tag{5.65}$$

where t_{bilayer} is the thickness of the bilayers (see Fig. 5.27(b)). Fig. 5.27(c) exemplarily displays the $R(Q_z)$ curve of a Co/Pt multilayer sample. From both periods the nominal total thickness of the stack and the nominal bilayer thickness were obtained, which verify the used deposition rates for the sample preparation (see section 5.2.1). "Real" surfaces and interfaces are by no means sharp on the atomic level, so that roughness as well as interdiffusion at the interfaces is present (see section 2.1.5). As a consequence of both, the refractive indices do not change abruptly from one layer to the other. Besides the thickness of the layers this fact enables the determination of the width of the roughness/interdiffusion region from the specular reflectivity curve. To quantify them the measured specularity curves, which were generally performed up to $Q_z \approx 0.6$ Å^{-1}, were fitted utilizing the software PARRAT32 [715], which is based on Parrat's exact recursive method. To fit the data the so-called scattering length density ρ of Pt and Co has to be known, which is an imaginary quantity. This quantity depends on the atomic properties and on the wave length in a complex manner. For a particular wave length and element at the homepage of the center of x-ray optics[35] two constants β and δ can be calculated, which enables the determination of ρ via $\rho = \frac{2\pi}{\lambda^2}\delta + i\frac{2\pi}{\lambda^2}\beta$. For Co and Pt for the used wave length it is obtained: $\rho_{\mathrm{Co}} = 6.3 \cdot 10^{-5}\text{Å}^{-2} + i \cdot 9.1 \cdot 10^{-6}\text{Å}^{-2}$, $\rho_{\mathrm{Pt}} = 1.4 \cdot 10^{-4}\text{Å}^{-2} + i \cdot 1.3 \cdot 10^{-5}\text{Å}^{-2}$. Besides the thickness of the layers j the individual interfacial thicknesses σ_j are fitting parameters, which in particular enables the differentiation between an interfacial thickness for the Co growth on Pt σ_{Co} or vice versa σ_{Pt}. In the fitting procedure the σ_j correspond to the full-width at half maximum of the normal distribution of the scattering length density gradient at the given interface j [715].
A differentiation between roughness and interdiffusion from the specular reflectivity is not possible. In order to disentangle both interface properties rocking scans have to be performed to measure the off-specular reflectivity components caused by diffusive scattering processes (measurement geometry, see Fig. 5.16). While interdiffusion does not cause diffusive scattering this is the case for roughness [716]. For several samples rocking scans at some particular fixed values of Q_z were performed. To quantify the interface roughness from the rocking scans the TRDS_SL simulating software[36] was used. With this software it is possible to simulate rocking scans to compare them with the experimental results. TRDS_SL is based on the complex theoretical work of Sinha et al. [719], where a relation between the angular dependence of the rocking scan with the Fourier transformation of the roughness profile is formulated. To describe the roughness distribution of isotropic interfaces Sinha et al. proposed the following lateral correlation function $C(\mathbf{r} = (x, y)) = \sigma^2_{\mathrm{RMS}} e^{-|\mathbf{r}|^2/\xi^2}$, where σ_{RMS} is the rms roughness (see Eq. 4.9) and ξ is the in-plane correlation length. Within this work for the simulation the roughness of the individual interfaces is assumed to be not correlated with respect to each other (correlation in z direction). This is justified as only strong correlations significantly affect the off-specular reflectivity. For more details the reader is referred to the above mentioned homepage of the TRDS_SL simulating software, where also a variety of publications

[35] http://henke.lbl.gov/optical_constants/pert_form.html
[36] sergey.gmca.aps.anl.gov/TRDS_sl.html

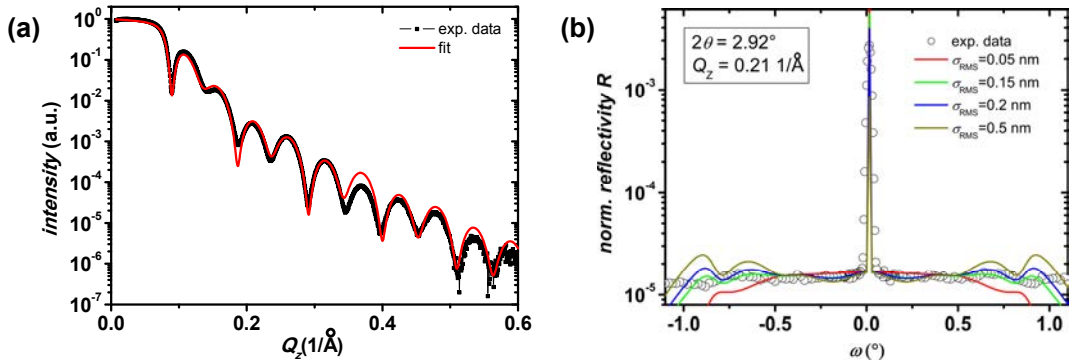

Figure 5.28: (a) (Specular) reflectivity R in dependence of the scattering vector Q_z for a Pt/Co/Pt sandwich with a Co thickness of $t_{\mathrm{Co}} = 3.2$ nm. The red solid line is a fit utilizing PARRAT32 [715]. (b) Rocking scan at $Q_z = 0.21$ Å^{-1} for the very same sample (off-specular reflectivity). The solid lines are simulated curves with different σ_{RMS}. The in-plane correlation length was set to $\xi = 20$ nm.

is given as reference.
In the following the XRR results are presented.

Results: Concerning the roughness and interdiffusion of the Co/Pt samples the quantitative analysis of the XRR measurements does not reveal any remarkable dependence on particular properties like t_{Co} for sandwiches, t_{Pt} for multilayers, or the kind of substrate. In the case of the latter the only difference that is worth mentioning is that the quality of the fits of the specular curves is inferior for the films that are grown on naturally oxidized Si. A possible explanation for this finding is the thin Si oxide layer that is not explicitly considered in the fitting procedure. Apart from that, the results quantitatively indicate that the interfacial properties are similar for all Co/Pt samples fabricated according to the preparation procedure presented in section 5.2.
As can be exemplarily seen in Fig. 5.27(c) and Fig. 5.28(a) the specular reflectivity curves $R(Q_z)$ can be quite well fitted with the PARRAT32 software. From the fits of the $R(Q_z)$ curves the nominal thickness of the individual layers were verified with high accuracy. Concerning the thickness of the interfacial roughness and interdiffusion region no significant differences between σ_{Co}, σ_{Pt}, and for the Pt growth on the substrates, were found. From the analysis of the measurements of several samples a mean value for the interfacial thickness of $\sigma = (7 \pm 2)$ Å was determined.
Fig. 5.28(b) exemplarily shows a rocking scan measured at $Q_z = 0.21$ Å^{-1} for the sandwich with $t_{\mathrm{Co}} = 3.2$ nm. Besides, several via TRDS_SL simulated curves for different σ_{RMS} ($\xi = 20$ nm) are shown as solid lines as well. ξ basically determines the slope of the curve, while σ_{RMS} accounts for the amplitude of the oscillations. The best correspondence with the experimental curve can be obtained for a rather small interface roughness of $\sigma_{\mathrm{RMS}} = 1.5$ Å. In particular, the complete absence of the so-called Yoneda wings in the diffusive scattering at about $\omega = \pm 0.9°$, that occur when the incident (or reflected) angle of the x-rays equals the critical angle for total external reflection, indicates a rather low interface roughness [720]. From the comparison between simulation and experimental curves of several samples and

roughness σ_{RMS}	interdiffusion σ_{diff}	lat. grain size $d_{\mathrm{grain}}^{\mathrm{lateral}}$	texture b_ω
(2 ± 1) Å	(5 ± 2) Å	(11 ± 2) nm	Si: $(7 \pm 1)^\circ$ Si_3N_4: $(14 \pm 1)^\circ$ SiO_2: $(23 \pm 2)^\circ$

Table 5.2: Structural properties of Co/Pt layered structures.

Q_z values a mean value of $\sigma_{\mathrm{RMS}} = (2 \pm 1)$ Å was estimated. This finding shows that the interfaces are very smooth with a roughness that corresponds to the thickness of only about one atomic layer.
As the total interfacial thickness corresponds to $\sigma = (7 \pm 2)$ Å this result additionally reveals that the region of interdiffusion at the Co/Pt interface exhibits a thickness of $\sigma_{\mathrm{diff}} = (5 \pm 2)$ Å.
A visual impression about the interfacial regions is provided by the TEM image shown in Fig. 5.22(c), where the electron diffraction contrast is color coded, which particularly enables the discrimination between Co and Pt material. Although the Co thickness is only 0.8 nm a distinct Co layer region can clearly be identified, which qualitatively confirms the XRR results. As the TEM image is a superposition from the diffraction of a few grains in a row a quantification of the interface properties from the image is not possible.
The surface roughness of the films was checked via AFM. For all films a RMS roughness of (3 ± 2) Å was found, which resembles the roughness of the used virginal substrates. The surface roughness is similar to the interface roughness found via XRR.
In the following part the structural results are summarized and discussed also with a view to the results of other studies concerning Co/Pt layered structures.

5.3.1.3 Summary and discussion of the structural results

Selected structural properties of the Co/Pt samples are listed in Tab. 5.2. The investigations reveal that they exhibit a well-defined layered structure with an interface roughness in the range of one monolayer (ML) and an interdiffusion region of about two to three MLs. No indications were found that both interface properties depend on the definite stacking sequence of the magnetron sputtered layers or on the thickness of the individual layers. In conclusion, for sufficiently large layer thicknesses $\gtrsim 0.7$ nm ($\gtrsim$ 3ML), where the individual layers can be regarded as laterally continuous, the degree of roughness and interdiffusion at the interfaces remain constant, so that their influence on the magnetic properties do not change with thickness. However, it is worth mentioning that possible variations in the lattice strain or in the chemically ordering of the interface atoms might alter the magnetic properties of the interface regions. As discussed in section 2.1.5 and 5.2.1 the sample properties strongly depend on the preparation method and growth conditions. Therefore, a quantitative comparison with other studies is rather complex and would go beyond the scope of this thesis. In any case, it can be stated that the obtained values for the interdiffusion and interface roughness are within the span of the results found in other studies concerning Co/Pt layered struc-

tures [721, 722, 676, 723, 724, 725, 680, 726, 727, 728, 729, 367, 730].
The crystal structure of the Co/Pt films is polycrystalline with a (111) out-of-plane texture and a lateral grain size of (11 ± 2) nm that was initiated during the growth of the Pt seed layer on the substrates. The rather large coherence lengths within the Co and Pt layers as well as the coherence between the Co and Pt layers suggest single crystalline phases along the stacking direction. However, the loss in coherence observed at large Co layer thicknesses reveals a certain degree of structural disorder. A columnar (111) growth of Co/Pt layered structures with a lateral grain size in the same order of magnitude was frequently observed [675, 731, 676, 145, 732, 677, 678, 733, 702, 734]. The texture of the films is pronounced in such a manner that with respect to the film surface the orientation of the (111) lattice planes of the crystallites are normally distributed. This behavior was already found for Co/Pt films before [723, 678, 702]. Within this study, however, it is ascertained that the full width at half maximum intensity of the normal distribution b_ω depends on the kind of substrate (see Tab. 5.2). That the degree of the texture is altered by the kind of underlayer was frequently shown in literature [701, 723, 677, 735]. The reason why the kind of substrate affects the texture was not investigated within this thesis.
The average spacing between the Pt(111) lattice planes is 0.7% larger than the bulk value. In particular, the Pt seed layer grows suchlike tensely strained on the substrates. Possible reasons are reviewed in Ref. [736] and will not be discussed here.
The limited experimental sensitivity for crystalline Co disables a statement about the interplanar Co-Co spacing for thin Co thicknesses t_{Co} in the case of the sandwiches. For $t_{\mathrm{Co}} \geq 12$ nm, where a Co peak can be observed, the properties of the Bragg peak indicate that the Co material contributing to the peak is basically unstrained exhibiting the bulk lattice of Co. However, the findings for the multilayers reveal that for a thin Co thickness ($t_{\mathrm{Co}} = 0.8$ nm), where the Co material is basically interdiffused with the Pt, the Co is significantly tensely strained in the growth direction. The average interplanar spacing of the Co (rich) phase seems to be closer to the bulk value of Pt than to the bulk value of Co. However, a pseudomorphic growth of Co on Pt can be excluded.
To gain a deeper insight into the interatomic arrangement within the Co/Pt samples the results of other studies are briefly discussed in the following. The overview is restricted to the results of Co/Pt growth at room temperature. The influence of heat treatment during or after sample preparation is briefly discussed in section 5.8.
Besides XRD diffraction, which is the standard characterization technique [139], the lattice parameters of Co/Pt(111) multilayers were frequently investigated by high resolution TEM and/ or selected area electron diffraction (SAED) [676, 723, 721, 732, 724, 737, 148, 702, 367]. Qualitatively, in-plane and out-of-plane strains in both Co and Pt layers due to the 11% mismatch between both lattice parameters (with respect to the Co lattice parameter) and the relaxation of the strains with increasing layer thicknesses was frequently observed. For instance, Zhang et al. measured plan-view SAED patterns of $(t_{\mathrm{Co}}/1.6 - 1.9\ \mathrm{nm\ Pt})_{15}$ multilayers ($t_{\mathrm{Co}} = 3 - 14$ Å, 50 Å) [724, 737] and determined the in-plane lattice parameters. For $t_{\mathrm{Co}} = 3$ Å the Co material is basically interdiffused with and virtually indistinguishable from the Pt layers, which is about 2.4% compressively strained [737]. At $t_{\mathrm{Co}} = 6$ Å Co starts

to develop its own lattice, which is tensely strained in the in-plane direction by about 2%. A compressive strain of similar amount was found for Pt at this Co thickness. Moreover, for $t_{\mathrm{Co}} \geq 9$ Å indications for strongly strained layers in the vicinity of the Co/Pt interfaces were observed. With further increasing t_{Co} the lattice of the interior of the Co and Pt layer gradually relaxes reaching the respective bulk values in the range of 12 Å $> t_{\mathrm{Co}} >$ 50 Å. A similar qualitative behavior regarding the thickness dependence of out-of-plane lattice strain of multilayers with similar composition was observed by Li et. al. using cross-sectional HRTEM and SAED [676, 732]. Certainly, the exact numbers of strain depend on the individual layer and bilayer thickness as well as on the preparation method and growth conditions. However, the described thickness dependence of the strain within the Co lattice is qualitatively in accordance with the observations of this study, i.e., a strongly tensely strained Co lattice at $t_{\mathrm{Co}} = 0.8$ nm and a relaxed one at $t_{\mathrm{Co}} \geq 12$ nm.
It is worth mentioning that the depicted three-dimensional tensile strain of the Co layer is in contradiction with the principle of elastic response, i.e., vanishing stress along the stacking direction [138, 139]. The mismatch between the crystal lattices of Co and Pt might result in tensile in-plane strain of the Co lattice as experimentally observed in Refs. [724, 737]. However, the elastic response then predicts a compressive out-of-plane strain in the Co layer as a result of the in-plane strain [738, 138]. Quantitatively, for instance regarding isotropic strain $\epsilon_1 = \epsilon_2 = \epsilon_0$ within the hcp(0001) and fcc(111) plane, respectively, the out-of-plane strain is given by [141]

$$\epsilon_3^{\mathrm{hcp}} = -2\frac{c_{13}^{\mathrm{hcp}}}{c_{33}^{\mathrm{hcp}}}\epsilon_0 \ , \quad \epsilon_3^{\mathrm{fcc}} = -2\frac{c_{11}^{\mathrm{fcc}} + 2c_{12}^{\mathrm{fcc}} - 2c_{44}^{\mathrm{fcc}}}{c_{11}^{\mathrm{fcc}} + 2c_{12}^{\mathrm{fcc}} + 4c_{44}^{\mathrm{fcc}}}\epsilon_0 \quad , \tag{5.66}$$

which yields for both crystal lattices almost identical values of $\epsilon_3^{\mathrm{hcp}} = -0.58\epsilon_0$ and $\epsilon_3^{\mathrm{fcc}} = -0.57\epsilon_0$ by using the elastic constants of hcp and fcc bulk Co of $c_{13}^{\mathrm{hcp}} = 103$ GPa, $c_{33}^{\mathrm{hcp}} = 358$ GPa, $c_{11}^{\mathrm{fcc}} = 242$ GPa, $c_{12}^{\mathrm{fcc}} = 160$ GPa, and $c_{44}^{\mathrm{fcc}} = 128$ GPa [141][37].
A possible explanation for the apparent tensile strain along the stacking direction found for nominal Co layer thicknesses of a few MLs refers to the interdiffusion with the Pt. For a homogeneous binary alloy $\mathrm{A}_x\mathrm{B}_{1-x}$ (x in at%), in a first approximation, the resulting lattice parameter is simply given by $\overline{a} = (a_{\mathrm{A}}x + a_{\mathrm{B}}(1-x))$, where a_{A}, a_{B} are the bulk lattice parameters of both constituents (Vegard's law) [741, 139, 136]. Consequently, the interdiffusion with the Pt particularly enhances the interplanar spacing of the Co (rich) phase compared to bulk Co.
Due to the complexity of a multilayer system to extract information about the interatomic arrangement it is convenient to study the initial growth of Co on Pt(111) and Pt on Co(0001), which was frequently done by using surface sensitive characterization tools (Co on Pt(111), Refs. [742, 743, 744, 745, 746, 747, 748, 749, 750, 751, 752, 124, 753, 754, 755], Pt on Co(0001), Refs. [756, 757, 758, 759, 760]). A complete summary would go beyond the scope of this thesis so that again only selected results are briefly discussed. Concerning Co deposits ($1 - 15$ MLs) on Pt(111) (at room temperature) an elaborate study was performed by E. Lundgren et. al. utiliz-

[37] Note, that experimental results as well as *ab initio* calculations for the elastic constants of Co/Pt multilayers indicate certain modifications of the elastic constants at the Co/Pt interfaces [710, 739, 711, 740, 139]

ing scanning tunneling microscopy (STM) [749]. They found that the first Co layer predominantly grows at the fcc Pt(111) lattice sites. The associated tensile strain within the Co layer is thereby reduced by a large number of defects, in particular by the formation of a dislocation network separating the predominant fcc regions from narrow hcp regions (see also Refs. [761, 762, 754]). The formation of the second ML of Co lifts the dislocations to a large extent and the in-plane lattice parameter is already rather close to that of bulk Co with a tensile strain of about 1.5% (with respect to the Pt lattice parameter). No further change in lattice parameter was observed up to 5 MLs, while for higher thicknesses no statement was possible. The exact number in lattice strain is in disagreement with Ref. [745], where for 2 MLs of Co a tensile strain of 3.4% was observed. Furthermore, relaxed Co was also reported for 2 MLs of Co [744, 746, 124]. It is worth mentioning that, in general, the rearrangement of several layers is nothing unusual when additional layers are deposited [749], so that in particular interdiffusion of Co and Pt might occur. Interdiffusion was not detected by Lundgren et. al. but due to the insensitivity of STM to the buried layers it could not be excluded[38].
Concerning the growth mode Lundgren et. al. observed a change from flat (2D) to island-like (3D) growth at 3.5 MLs. The authors stated that the 2D growth indicates interlayer diffusion across step edges whose numerousness is a further consequence of the lattice mismatch between Co and Pt. At higher coverages the number of step edges were minimized reflecting the reduced influence of the interface region and 3D growth established. A change from 2D to 3D growth mode was often reported for Co on Pt(111) at about ≥ 3 MLs [744, 745, 748].
A consequence of the 3D growth mode is that the Co layer exhibits a certain degree of surface roughness. By preparing a Pt layer on top of Pt(111)/Co, as done by Thiele et. al. for $5-6$ MLs of Co [744], the Pt atoms preferentially occupy the sites between the Co islands before establishing a homogeneous Pt layer on top. Thus, the Co/Pt interface was found to be less sharp than the interface between the single crystal Pt(111) and Co on top. This finding shows that the results of the initial growth studies of Co and Pt on flat, single crystal surfaces cannot be simply transferred one by one to the growth of Co/Pt multilayers. However, as Pt seems to grow relatively smooth on Co [756, 758, 759], with an island height that does not exceed 4 MLs before their coalescence [758], the presented results regarding the growth of Co on Pt(111) single crystal surfaces can be used as a starting point. Such a smooth growth of Pt is in accordance with the small surface roughness of (3 ± 2) Å found within this study.
Coming back to the work of Lundgren et. al. above 5 MLs of Co a fcc (111) stacking was predominantly found. Besides, a few hcp stacked islands as well as fcc twinning was observed (coexistence of stacking sequences (ABC...) and (CBA...) initiated by stacking faults in the lower layers). Although hcp is the stable phase for bulk Co below ≈ 400 °C [684] a (twinned) fcc stacking was also observed in other studies (see Refs. [764, 724, 743, 753]). In disagreement with these studies a hcp (0001) stacking

[38] The possibility of rearrangements within the buried layers also has to be considered in the interpretation of the results of Refs. [763, 137], where the evolution of the lattice parameter was detected for the topmost layer, inter alia, during the growth of a Co/Pt multilayer by means of reflection high-energy electron diffraction (RHEED).

on Pt(111) was demonstrated in Refs. [745, 746, 702], while a mixture of twinned fcc and hcp stacking was also reported [765, 748]. In particular, for the growth of a Co layer by means of ECR sputtering on top of an ECR prepared Pt(111) seed layer the coexistence of hcp and fcc stacking was shown [367]. Furthermore, Nakajima et. al. reveal evidence of a transition from fcc to hcp stacking above 8 MLs [766]. Hints for such a transition in the same thickness regime are also reported in Ref. [767].
The discussion clearly shows the difficulty of deducing general statements about the details of the growth of Co/Pt layered structures. This highlights the need for complementary structural investigations of the samples within this study in order to gain a more complete picture about the interatomic arrangement, i.e., lattice strain, Co stacking sequence, and the chemically formation at the alloyed Co/Pt interface region. For that purpose the started HRTEM investigations will be continued and improved [768]. Furthermore, it is planned to carry out resonant diffraction studies around the Co (K-edge at 7.7088 keV) and the Pt L-edges (L_3-edge at 11.562 keV, L_2-edge at 13.272 keV)[39]. By using photon energies slightly lower and higher than the absorption edges it is possible to gain an element specific contrast in the diffraction pattern and thus determine the individual contributions of Co and Pt to each of the observed diffraction peaks. Moreover, the high intensity of the synchrotron radiation is required to overcome the detection limit of the Co material experienced at the standard x-ray tubes for small Co layer thicknesses $t_{\mathrm{Co}} < 12$ nm.
It should be noted that the high intensity of the synchrotron radiation can be additionally used to investigate the so-called truncation rods (surface x-ray diffraction (SXRD)) [769, 765, 124]. The finite size of every crystal does not only cause a broadening of the Bragg peaks (see Scherrer equation, Eq. 5.55) but yields also to the fact that a small amount of the intensity is scattered far away from the Bragg peaks. The characteristics of the diffraction pattern between the Bragg peaks, i.e., the truncation rods, depends, among other things, on the degree of interdiffusion and roughness, so that the spectra can be used to cross-check the XRR results. Furthermore, SXRD measurements provide a possibility to determine the atomic stacking sequence of Co [767, 765, 753].
A complementary study already planned concentrates on extended X-ray absorption fine structure (EXAFS) investigations[40] to determine particularly the Co stacking sequence and the interatomic distances/ lattice strains [770, 746, 753, 716]. In general, EXAFS is a method to determine the chemical and physical state of a selected element from the fine-structure of the x-ray absorption probability versus x-ray energy in the range of about 300 eV around the absorption edge. This method is especially sensitive to the coordination chemistry, coordination number, distances, and species of the atoms surrounding the selected element.

5.3.2 Magnetic properties

Besides magnetotransport the magnetic properties of the Co/Pt films were investigated by means of magnetooptical Kerr effect (MOKE) and ferromagnetic reso-

[39]Beamline P09 (PETRA III) at DESY (Hamburg, Germany).
[40]Beamline PGM-3 (BESSY II) at BESSY (Berlin, Germany).

nance (FMR). The results of both methods are presented separately starting with MOKE in section 5.3.2.1, which was used to investigate the remagnetization and the anisotropy of the films. The MOKE investigations are supplemented by the measurements of the anomalous Hall effect (AHE). Finally, section 5.3.2.2 presents the FMR investigations, which were applied to determine the saturation magnetization.

5.3.2.1 Remagnetization and anisotropy obtained via MOKE and AHE

The magneto-optical Kerr effect (MOKE) occurs in the reflection of light hitting a ferromagnetic sample resulting in a change of the polarization of the light. MOKE originates from the dependence of the dielectricity tensor on the magnetization orientation, which is caused by the spin-orbit interaction. Due to the small penetration depth of optical light in metals of about a few tens of nanometers the MOKE is particularly suited to investigate thin films. More information about MOKE can be found in Refs. [771, 772] and references therein. The utilized experimental setup is described in Refs. [370, 671].
In contrast to the soft magnetic films used in chapter 3 and 4, besides the longitudinal MOKE, which is sensitive to the magnetization component parallel to the film surface and the plane of incidence, the polar MOKE was utilized as well. The latter is sensitive to the out-of-plane component of magnetization. In the case of the longitudinal (polar) MOKE the ellipticity (rotation) of the reflected wave was measured. Both measured quantities are proportional to the corresponding component of magnetization [369][41].

Pt/Co/Pt sandwiches: The electromagnet of the MOKE setup provides magnetic fields of up to ± 0.9 T. This field strength was not sufficient to align the magnetization along the out-of-plane direction for sandwiches with a Co thickness of $t_{\mathrm{Co}} \gtrsim 3.5$ nm. Consequently, for these films the anisotropy constants could not be determined from the polar MOKE curves. However, in contrast to the MOKE setup, the magnetoresistance setup (see section 5.4) provides magnetic fields of up to ± 11 T, which, certainly, is more than sufficient to fully align the magnetization along any field direction. The qualitative results of the $\rho_{xy}(H_{\mathrm{p}})$ measurements are anticipated here, as the anomalous Hall effect (AHE), which, as expected, dominates the $\rho_{xy}(H_{\mathrm{p}})$ curves below technical saturation, is proportional to the out-of-plane component of magnetization (see Eq. 5.46). Therefore, the AHE contribution in $\rho_{xy}(H_{\mathrm{p}})$ directly reflects the out-of-plane remagnetization of the films, so that it can particularly be used to determine the anisotropy constants of the films with easy plane behavior. Above technical saturation the $\rho_{xy}(H_{\mathrm{p}})$ curves generally exhibit a linear negative slope as a consequence of the normal Hall effect (see Eq. 5.46 and Fig. 5.39(b) below). Exceptions are discussed in section 5.5.1.1. In order to obtain

[41] In order to separate the longitudinal and polar Kerr effects from each other the experimental method proposed in Ref. [772] was applied in the case of the determination of the hard axis curve for films with perpendicular easy axis. The separation is mandatory as the polar Kerr effect is significantly larger than the longitudinal Kerr effect, so that the coherent rotation processes of the magnetization are generally superimposed by changes of the perpendicular component of the magnetization.

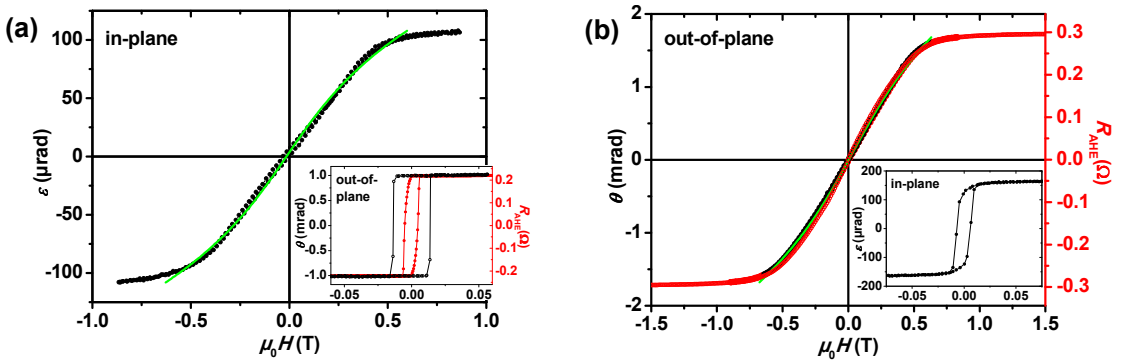

Figure 5.29: Magnetization reversal of Pt/Co/Pt sandwiches for (a) $t_{\mathrm{Co}} = 0.8$ nm and (b) $t_{\mathrm{Co}} = 2$ nm. The in-plane remagnetization is only measured by MOKE (black symbols), while the out-of-plane remagnetization is additionally measured by AHE (red symbols). The green lines are fits to the respective hard axis (or plane) curve (obtained by MOKE) in order to estimate the anisotropy constants of the films. The respective easy axis (or plane) curve is given as inset (lower right).

the pure $M_{\mathrm{p}}(H_{\mathrm{p}})$ dependence the high-field behavior was extrapolated to zero field and the extrapolated curve (usually a straight line) was subsequently subtracted from the $\rho_{xy}(H_{\mathrm{p}})$ measurement. Certainly, the subtraction is mandatory to determine the anisotropy constants correctly.

Fig. 5.29 exemplarily shows the remagnetization curves obtained for Pt/Co/Pt sandwiches with a perpendicular easy axis (Co thickness of $t_{\mathrm{Co}} = 0.8$ nm (a)) and with easy plane ($t_{\mathrm{Co}} = 2$ nm (b)), respectively. For the out-of-plane remagnetization the AHE contribution to the $\rho_{xy}(H_{\mathrm{p}})$ curve (AHE curve) is displayed together with the polar MOKE curve. In general, for the films with easy plane behavior the AHE curve is in very good accordance with the polar MOKE curve (see Fig. 5.29(b)) reflecting the tight correlation between AHE and M_{p}, so that both methods particularly yield the same anisotropy constants within the error margins of the experiments (see Fig. 5.30(b) below). However, for the samples with perpendicular easy axis differences between the shape of the polar curve and the AHE curve were found as can be exemplarily seen in the inset of Fig. 5.29(a). While both curves are almost rectangular with complete remanence, the coercive field in the MOKE measurement is generally larger compared to the AHE curve revealing that the remagnetization starts sooner in the AHE curves. In contrast to the AHE curves the MOKE curves were obtained from laterally homogeneous samples (see section 5.2.3). The reason why the remagnetization via domain wall movement is fostered in the wire shaped samples is assumed to be a consequence of the edges of the wires. The wire edges are not sharp but show a lateral thickness profile due to shadowing effects caused by the mask technique during sample preparation. As below a certain nominal Co layer thickness of $t_{\mathrm{Co}} \approx 0.5$ nm the anisotropy constant $K_{1,\mathrm{eff}}$ decreases with decreasing the Co layer thickness (see discussion below) a respective gradual decrease of the anisotropy constant should be present in the vicinity of the edges. Thus, the edge regions might act as nucleation sites for oppositely oriented domains yielding reduced coercive fields compared to a laterally homogeneous film. In fact, by performing Kerr-microscopy investigations of the wire samples it was observed that the

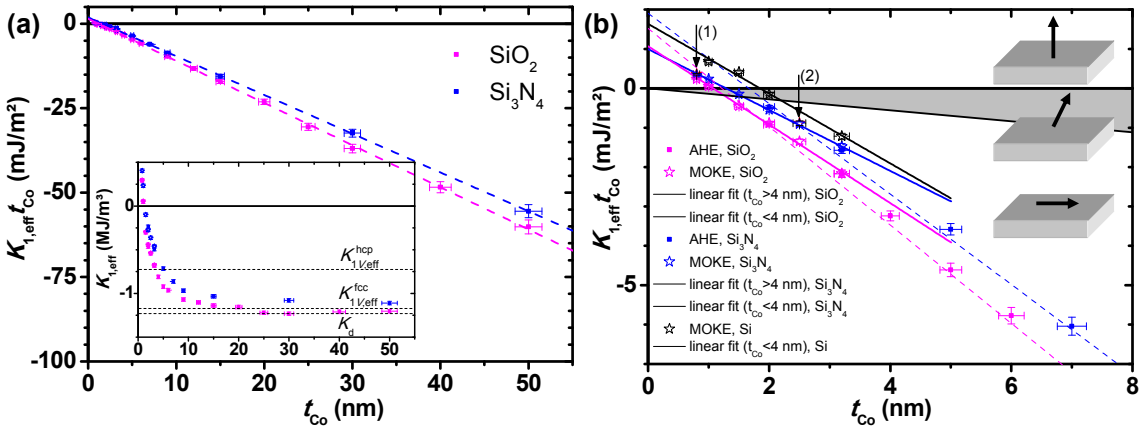

Figure 5.30: Co thickness dependence of the first order anisotropy constant $K_{1,\mathrm{eff}}$ of Pt/Co/Pt sandwiches. (b) is a zoom in (a) displaying $K_{1,\mathrm{eff}} \cdot t_{\mathrm{Co}}(t_{\mathrm{Co}})$ for $t_{\mathrm{Co}} \leq 7$ nm revealing two different linear regimes. The dashed and solid lines are linear fits to the data points for $t_{\mathrm{Co}} > 4$ nm and $t_{\mathrm{Co}} < 4$ nm, respectively. In (b) the sketches mark the different regions of easiest magnetizability, whereas the region of canted magnetization is additionally shaded in gray. The labeled arrows point to two data points obtained for Si as substrate, which deviate from the linear behavior (not considered in fitting procedure). In (a) $K_{1,\mathrm{eff}}$ versus t_{Co} is given as inset. The dashed horizontal lines mark the shape anisotropy $K_{\mathrm{d}} = -\frac{\mu_0}{2} M_{\mathrm{S}}^2 = -1.23\ \mathrm{MJ/m^3}$ and the effective first order anisotropy constants of fcc and hcp bulk Co of $K_{1V,\mathrm{eff}}^{\mathrm{fcc}} \approx -1.17\ \mathrm{MJ/m^3}$ and $K_{1V,\mathrm{eff}}^{\mathrm{hcp}} \approx -0.73\ \mathrm{MJ/m^3}$, respectively.

remagnetization generally starts at the wire edges.

The hard axis (or plane) curves of magnetizability display a reversible behavior revealing a coherent rotation of magnetization (see Fig. 5.29). In order to obtain the anisotropy constants in second order approximation the curves were fitted in the case of an easy axis and easy plane behavior to Eq. 2.22 and Eq. 2.23, respectively, by utilizing $\frac{\epsilon}{\epsilon_{\mathrm{S}}} = \frac{M_{||}}{M_{\mathrm{S}}}$ and $\frac{\theta}{\theta_{\mathrm{S}}} = \frac{R}{R_{\mathrm{S}}^*} = \frac{M_{\perp}}{M_{\mathrm{S}}}$. For ϵ_{S}, θ_{S}, and R_{S}^* the respective values above technical saturation and for the saturation magnetization the Co bulk value of $M_{\mathrm{S}}^{\text{bulk Co}} = 1.4\ \mathrm{MA/m}$ was used.

Starting with the results for the second order anisotropy constant K_2, independent of the kind of substrate and Co thickness, similar values of $(70 \pm 30)\ \mathrm{kJ/m^3}$ were found. This finding particularly reveals that K_2 is basically caused by the volume, i.e., $K_2 = K_{2V}$, while surface contributions are zero ($K_{2S} \approx 0$) in accordance with the findings in Refs. [773, 102]. The value of K_{2V} resembles the values found in other studies concerning Co/Pt layered structures [109, 104, 103].

Turning to the results of the first order anisotropy constant $K_{1,\mathrm{eff}}$, Fig. 5.30(a) shows $K_{1,\mathrm{eff}} \cdot t_{\mathrm{Co}}$ as a function of Co thickness for films grown on SiO_2 and Si_3N_4 substrate. On this large scale for both substrates the curves seem to lie on straight lines with negative slopes within the whole thickness range as indicated by the dashed lines in accordance with the simple phenomenological model, which separates the anisotropy in a surface and a volume term (see Eq. 2.19). The dashed lines are linear fits performed for Co thicknesses $t_{\mathrm{Co}} \geq 5$ nm. Obviously the negative slope is stronger for the films grown on SiO_2 compared to Si_3N_4. Fig. 5.30(b) is a zoom into Fig. 5.30(a), where $K_{1,\mathrm{eff}} \cdot t_{\mathrm{Co}}$ is displayed up to $t_{\mathrm{Co}} = 7$ nm. The linear fits for $t_{\mathrm{Co}} \geq 5$ nm are

	K_{1V} for $t_{\mathrm{Co}} < 4$ nm	K_{1V} for $t_{\mathrm{Co}} > 4$ nm	K_S for $t_{\mathrm{Co}} < 4$ nm	K_S for $t_{\mathrm{Co}} > 4$ nm
SiO_2	0.24 ± 0.03	-0.01 ± 0.03	0.54 ± 0.03	0.8 ± 0.2
Si_3N_4	0.47 ± 0.02	0.08 ± 0.02	0.50 ± 0.03	1.0 ± 0.2
Si	0.34 ± 0.06	-	0.82 ± 0.06	-

Table 5.3: Anisotropy constants K_{1V} (in MJ/m^3) and K_S (in mJ/m^2) of Pt/Co/Pt sandwiches grown on SiO_2, Si_3N_4, and naturally oxidized Si. For the latter the values are only valid for $t_{\mathrm{Co}} \gtrsim 1$ nm. K_2 was found to be independent of thickness and substrate material with a value of $K_{2V} = (70 \pm 30)$ kJ/m^3.

again shown as dashed lines for comparison. On this smaller scale it is evident that for small thicknesses $t_{\mathrm{Co}} < 4$ nm the $K_{1,\mathrm{eff}} \cdot t_{\mathrm{Co}}(t_{\mathrm{Co}})$ curves deviate from pure linear behavior. For both substrates an apparently abrupt transition occurs from the mentioned linear behavior found for large Co thicknesses ($t_{\mathrm{Co}} > 4$ nm) to another linear behavior with a smaller negative slope valid at small Co thicknesses ($t_{\mathrm{Co}} < 4$ nm). The latter is indicated by the solid lines in Fig. 5.30(b), which are linear fits for the region $t_{\mathrm{Co}} \leq 3.2$ nm. As the effective volume anisotropy $K_{1V,\,\mathrm{eff}}$ and the surface anisotropy K_S contributions correspond to the slope and to the half of the interception with the ordinate, respectively (see Eq. 2.19), the bend in the $K_{1,\mathrm{eff}} \cdot t_{\mathrm{Co}}(t_{\mathrm{Co}})$ characteristic reveals significant differences in these anisotropy constants for both thickness regimes.
In Fig. 5.30(b) also the evolution of the anisotropy constant in the thin thickness regime for the films grown on naturally oxidized Si substrate is shown (black symbols)[42]. For this sample series also a linear $K_{1,\mathrm{eff}} \cdot t_{\mathrm{Co}}(t_{\mathrm{Co}})$ behavior was observed, with the exception of the value at $t_{\mathrm{Co}} = 0.8$ nm, where the onset of a collapse occurs (see black arrow labeled as (1)). The anisotropy value at $t_{\mathrm{Co}} = 0.8$ nm could be reproduced for nominally identical samples, so that, in contrast to the alleged outlier at $t_{\mathrm{Co}} = 2.5$ nm (see black arrow labeled as (2)), the collapse reflects further changes in the volume and/ or surface anisotropy constants below $t_{\mathrm{Co}} \approx 1$ nm[43].
For the films grown on Si $K_{1,\mathrm{eff}}$ is systematically larger than for the films on top of the other substrates. Here, the spin reorientation transition (SRT) from out-of-plane easy axis to easy plane behavior via the canted phase (see section 2.1.4.1) was estimated to start at $t_{\mathrm{Co}} \approx 1.9$ nm. For SiO_2 and Si_3N_4 as substrate the SRT is initiated at $t_{\mathrm{Co}} \approx 1.1$ nm and $t_{\mathrm{Co}} \approx 1.3$ nm, respectively.
The first order volume anisotropy $K_{1V} = K_{1V,\,\mathrm{eff}} + \frac{\mu_0}{2} M_S^2$ and the surface anisotropy K_S obtained from the linear fits via Eq. 2.19 are listed in Tab. 5.3. The listed values are within the span of values reported in literature for Co/Pt(111) layered structures ($K_S = 0.27 - 1.29$ mJ/m^2, $K_{1V} = 0.08 - 0.95$ MJ/m^3 [145, 96, 146, 41], see

[42] It is recalled that MR investigations for films grown on naturally oxidized Si substrate were not performed due to the drastic current shunt through the Si, so that anisotropy constants for $t_{\mathrm{Co}} > 4$ nm could not be determined.

[43] Note that for SiO_2 (Si_3N_4) as substrate also a collapse in $K_{1,\mathrm{eff}} \cdot t_{\mathrm{Co}}(t_{\mathrm{Co}})$ was observed: For the sandwich with $t_{\mathrm{Co}} = 0.5$ nm a value of $K_{1,\mathrm{eff}} \cdot t_{\mathrm{Co}} \approx 440$ kJ/$m^3 \cdot 0.5$ nm (480 kJ/m$^3 \cdot 0.5$ nm) was found, while the sample with $t_{\mathrm{Co}} \approx 0.8$ nm exhibits a value is $K_{1,\mathrm{eff}} \cdot t_{\mathrm{Co}} \approx 290$ kJ/m$^3 \cdot 0.8$ nm (400 kJ/$m^3 \cdot 0.8$ nm).

section 2.1.5). In the following possible reasons for the changes in K_S and K_{1V} with Co thickness and their dependence on the kind of substrate are discussed. First, it is dealt with the collapse of anisotropy at $t_{\mathrm{Co}} \lesssim 1$ nm observed for the series grown on naturally oxidized Si. Such a behavior was often reported for Co/Pt(111) in this thickness regime [675, 708, 774, 701, 775, 776, 742, 145, 777, 146, 107, 102, 704, 125, 368, 778]. In these references it was frequently assumed that the collapse is a consequence of the fall of the nominal Co thickness below the thickness of the roughness and interdiffusion zone σ as discussed in detail in section 2.1.5 [41]. In this work, the size of $\sigma = (7 \pm 2)$ Å (see section 5.3.1.2) would fit to explain the collapse. However, σ was found to be basically independent of the kind of substrate. Consequently, changes in roughness and interdiffusion should have manifested independently from substrate in the anisotropy and can be ruled out to be the only reason for the collapse. In literature, another frequently proposed explanation for the collapse concerns the relaxation of the residual strain within the Co material with increasing Co thickness. For instance, considering elastic as well as dislocation energies (van der Merwe model [779]) a bend in the otherwise linear $K_{1,\mathrm{eff}} \cdot t_{\mathrm{Co}}(t_{\mathrm{Co}})$ behavior is theoretically expected when a transition from pseudomorphic to partially coherent, i.e., incoherent, stacking occurs [41]. For the incoherent stacking the strain ϵ is assumed to be partially accommodated via dislocations suchlike that ϵ is inversely proportional to the magnetic layer thickness. For Ni(111) sandwiched by Cu, where the mismatch between both lattice parameters is relatively small with about 2.5%, the observed bend in $K_{1,\mathrm{eff}} \cdot t_{\mathrm{Co}}(t_{\mathrm{Co}})$ at $t_{\mathrm{Ni}} = 3.2$ nm was attributed to such a coherent-incoherent transition [780, 41, 781]. For Co on Pt(111), due to the large lattice mismatch of 11% with respect to the lattice parameter of Co, a pseudomorphic growth can be excluded also for Co thicknesses in the monolayer range as particularly shown in this thesis (see section 5.3.1.1). Nevertheless, the Co was found to exhibit a strong tensile strain in the stacking direction at $t_{\mathrm{Co}} = 0.8$ nm, while strain relaxation somewhere in the range up to $t_{\mathrm{Co}} = 12$ nm occurs. This shows that the collapse as well as the bend at $t_{\mathrm{Co}} \approx 4$ nm in the $K_{1,\mathrm{eff}} \cdot t_{\mathrm{Co}}(t_{\mathrm{Co}})$ characteristic might be consequences of strain relaxation processes. According to current knowledge, the thickness range $t_{\mathrm{Co}} \geq 3$ nm was not investigated despite the large number of publications dealing with the evolution of the anisotropy of Co/Pt(111) with Co thickness. In particular, a bend in $K_{1,\mathrm{eff}} \cdot t_{\mathrm{Co}}(t_{\mathrm{Co}})$ above the spin reorientation transition was not observed so far.

In order to examine if the strain relaxation can be responsible for the deviations from the linear $K_{1,\mathrm{eff}} \cdot t_{\mathrm{Co}}(t_{\mathrm{Co}})$ behavior the associated magnetoelastic anisotropy constant K_{me} is estimated in the following. For isotropic in-plane strain $\epsilon_{11} = \epsilon_{22} = \epsilon_0$ and out-of-plane strain ϵ_3 the resulting uniaxial volume contributions to K_{me} for hcp(0001) and fcc(111) systems are given by [138]

$$K_{V,\mathrm{me}}^{\mathrm{hcp(0001)}} = (B_1^{\mathrm{hcp}} + 2B_3^{\mathrm{hcp}})\epsilon_0 + B_2^{\mathrm{hcp}}\epsilon_3 \quad , K_{V,\mathrm{me}}^{\mathrm{fcc(111)}} = B_2^{\mathrm{fcc}}(\epsilon_0 - \epsilon_3) \quad , \tag{5.67}$$

where B_i are the magnetoelastic coupling coefficients. For hcp bulk Co the coefficients are $B_1^{\mathrm{hcp}} = -8.1$ MJ/m^3, $B_2^{\mathrm{hcp}} = -29.0$ MJ/m^3, and $B_3^{\mathrm{hcp}} = +28.2$ MJ/m^3. For fcc Co the magnetoelastic constants were extrapolated in Refs. [141, 782] to $B_1^{\mathrm{fcc}} \approx -16$ MJ/m^3 and $B_2^{\mathrm{fcc}} \approx +26$ MJ/m^3 using the results of Refs. [783, 784].

Note, that even the smallest coefficient B_1^{hcp} is more than six times larger than the shape anisotropy of a Co film reflecting the strong impact of strain and its relaxation on magnetic anisotropy. Due to the lack of experimental values for the strain relaxation with Co thickness within this work, the magnetoelastic anisotropy was exemplarily calculated for the case of tensile in-plane strain relaxation of $\Delta\epsilon_0 = -1\%$ in order to get a qualitative impression. This value is within the span of values experimentally observed for Co/Pt layered structures as discussed in section 5.3.1.3. In the example case an out-of-plane relaxation was additionally considered as a consequence of the elastic response, which was calculated by using Eq. 5.66 to $\Delta\epsilon_3^{\mathrm{hcp}} = +0.58\%$ and $\Delta\epsilon_3^{\mathrm{fcc}} = +0.57\%$, respectively. According to Eq. 5.67 the corresponding changes in magnetoelastic anisotropy are $\Delta K_{\mathrm{me}}^{\mathrm{hcp}(0001)} = -0.65$ MJ/m^3 and $\Delta K_{\mathrm{me}}^{\mathrm{fcc}(111)} = -0.41$ MJ/m^3, respectively. This example shows that relaxations of the residual strain in the range of $\lesssim 1\%$ are sufficient to explain the differences between K_{1V} below and above $t_{\mathrm{Co}} \approx 4$ nm (see Tab. 5.3). Furthermore, such differences in residual strain can also account for the differences in K_{1V} obtained for the films grown on different substrates as well as for the collapse below $t_{\mathrm{Co}} \approx 1$ nm.
Regarding the magnetoelastic contributions of the interface atoms to the surface anisotropy constant, i.e., $K_{S,\mathrm{me}}$, theoretical *ab initio* studies showed that $K_{S,\mathrm{me}}$ basically depends linearly on the variation of isotropic in-plane strain ϵ_0 with a slope in the order of $\lesssim +100 \cdot \epsilon_0$ mJ/m^2 [785, 786]. The order of magnitude of the slope is in accordance with the experimental observations, when changes in strain at the interfaces of $|\Delta\epsilon_0| \lesssim 0.5\%$ are assumed (see Tab. 5.3). However, the actual value of $K_{S,\mathrm{me}}$ and of the slope are strongly correlated to the atomic species adjacent to the Co layer [787, 788], so that for a reasonable estimation of $K_{S,\mathrm{me}}$ the interdiffusion, roughness, and chemical order at the Co/Pt interfaces have to be taken into account [122].
Besides the relaxation of strain, another reason for the bend in $K_{1,\mathrm{eff}} \cdot t_{\mathrm{Co}}(t_{\mathrm{Co}})$ might be a transition from hcp to fcc Co stacking. Especially for the sandwiches grown on Si and Si_3N_4 the values of K_{1V} for $t_{\mathrm{Co}} < 4$ nm are close to the value expected for hcp bulk Co of $K_{1V}^{\mathrm{hcp}} \approx 0.5$ MJ/m^3 (see Tab. 5.3). Above $t_{\mathrm{Co}} \approx 4$ nm, however, K_{1V} is in the range of $K_{1V}^{\mathrm{fcc}} \approx 0.03 - 0.09$ MJ/m^3 [145, 86, 146] for both electric insulating substrates (see also inset of Fig. 5.30(a)). The assumption of a Co thickness driven transition from hcp to fcc Co is supported by the fact that a reversed transition, i.e., from fcc to hcp stacking, at about $t_{\mathrm{Co}} = 1.5$ nm was reported for Co/Pt layered structures as discussed in section 5.3.1.3 [766]. However, a strong argument against this interpretation is the fact, that the energetically more favorable phase of Co at room temperature is hcp, so that the Co is expected to grow further in hcp structure once initiated. Therefore, the changes in the slope of $K_{1,\mathrm{eff}} \cdot t_{\mathrm{Co}}$ at $t_{\mathrm{Co}} \approx 4$ nm are rather consequences of strain relaxation processes. As a thickness driven hcp-fcc transition is unlikely and as the structural analysis revealed that at large Co thicknesses the interior of the Co layer is basically relaxed and, therefore, magnetoelastic contributions in K_{1V} are negligibly small in this thickness regime, the K_{1V} values for $t_{\mathrm{Co}} \gtrsim 4$ nm give a strong indication that the Co layer exhibits fcc (111) stacking within the whole thickness range. It is recalled that in connection with Co/Pt(111) layered structure a stable (twinned) fcc Co(111) phase was frequently reported in literature (see section 5.3.1.3).

It is worth mentioning that the observed dependence of the degree of texture on the kind of substrate can be ruled out to be responsible for the differences in anisotropy constants as explained in the following. A crystallite, whose hcp $< 0001 >$ (or fcc $< 111 >$) axis includes a finite angle $\alpha \neq 0$ with the film normal exhibits an effective magnetocrystalline volume anisotropy along the film normal that is reduced by a factor of $(\cos^2\alpha - \cos^2(90^\circ - \alpha))$ compared to a crystallite with $\alpha = 0$. For the polycrystalline Co/Pt samples an upper bound for the mean value of the tilting of the crystallites $\overline{\alpha}$ can be estimated by $\overline{\alpha} < \sigma = b_\omega/(2\sqrt{2\ln 2})$, where σ and b_ω is the standard deviation and FWHM of the XRD rocking scans, respectively (see section 5.3.1.1). Using the b_ω values listed in Tab. 5.2 $\overline{\alpha}_{\mathrm{Si}} < 3^\circ$, $\overline{\alpha}_{\mathrm{Si_3N_4}} < 6^\circ$, and $\overline{\alpha}_{\mathrm{SiO_2}} < 10^\circ$ were determined. Therefore, the reduction in K_V compared to a perfectly textured film ($\overline{\alpha} = 0$) even for the films grown on SiO_2 substrate, which exhibit the least pronounced texture, is with a factor of less than $(\cos^2\overline{\alpha}_{\mathrm{SiO_2}} - \cos^2(90^\circ - \overline{\alpha}_{\mathrm{SiO_2}})) \approx 0.94$ negligibly small (of about 30 kJ/m^3 for hcp Co)[44].
For the sake of clarity it is mentioned that the made assumption of Co thickness-independent saturation magnetization of $M_{\mathrm{S}}^{\mathrm{bulk\ Co}}$ in the derivation of $K_{1,\mathrm{eff}}$ and K_2 is critically discussed in connection with the FMR results in the next section.
In conclusion, the discussion shows that the most probable explanation for the deviations from the linear $K_{1,\mathrm{eff}} \cdot t_{\mathrm{Co}}(t_{\mathrm{Co}})$ characteristic is connected with relaxation processes of residual strain, which affect the anisotropy via the magneto-elastic coupling. Slight differences in residual strain can also account for the dependence of K_S and K_{1V} on the kind of substrate. In the range of $t_{\mathrm{Co}} \gtrsim 5$ nm up to 50 nm for both electric insulating substrates the evolution of the anisotropy with thickness can be described by a single set of constants K_S and K_{1V} revealing that no drastic changes in the structural properties occur. Consequently, in accordance to the structural investigations that provide access to the properties of the Co material for $t_{\mathrm{Co}} \geq 12$ nm the increase of the Co layer thickness basically leads to an increase of the amount of Co "bulk" material within the interior of the layer. Moreover, the K_{1V} constants in this thickness regime suggest that the Co stacking is fcc. Further structural characterization as proposed in section 5.3.1.3 will help to correlate the structural and magnetic properties in a stricter manner.

Co/Pt multilayers: In this paragraph, at first the dependence of the anisotropy on the Pt interlayer thickness t_{Pt} is presented for the main series with a bilayer repetition of $n = 4$ ($t_{\mathrm{Co}} = 0.8$ nm). The anisotropy constants in second order approximation were determined from the respective hard axis curves as stated in the previous paragraph. Special features observed in the remagnetization for particular samples, which become noticeable in deviations from the fundamental behavior presented in connection with the sandwiches, are briefly addressed afterwards. All the multilayers can be magnetically saturated along any direction by a field of < 0.9 T, so that the performance of the MOKE setup was sufficient for the investigation. Therefore, this section is restricted to present results obtained by MOKE. More-

[44] As there is no preferential direction for the tilting of the crystallites within the film plane, a related action of an effective in-plane anisotropy does not exist.

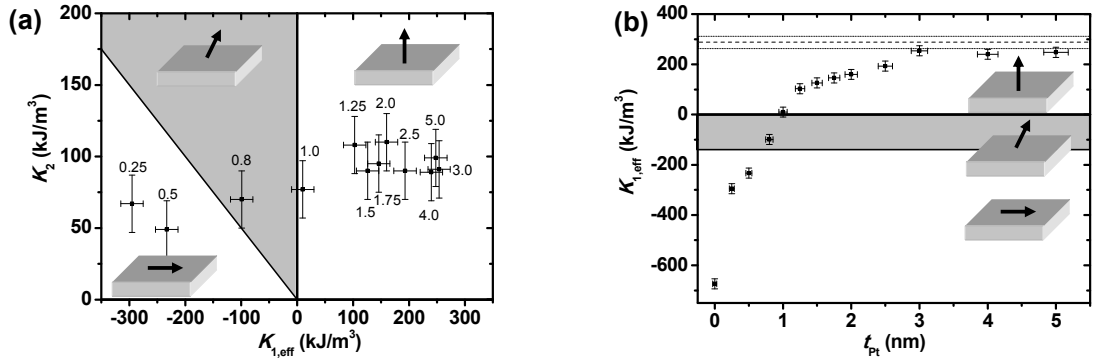

Figure 5.31: Anisotropy constants of 5 nm Pt/ (0.8 nm Co/ t_{Pt})$_3$/ 0.8 nm Co/ 3 nm Pt multilayers. (a) $K_{1,\mathrm{eff}}(K_2)$ phase diagram for different t_{Pt} (data points labeled by t_{Pt} in nanometers). (b) $K_{1,\mathrm{eff}}$ in dependence of t_{Pt}. The horizontal lines displays the $K_{1,\mathrm{eff}}$ value with the error margin of the Pt/Co/Pt sandwich with $t_{\mathrm{Co}} = 0.8$ nm. In the diagrams the sketches mark the different phases of easiest magnetizability, whereas the region of canted magnetization is additionally shaded in gray.

over, only the results for films grown on SiO_2 are presented, which were used only for the MR investigations (see section 5.7).
Fig. 5.31(a) displays the second order anisotropy constant K_2 in dependence of the effective first order anisotropy constant $K_{1,\mathrm{eff}}$. The respective t_{Pt} values label the data points. K_2 only shows a slight decrease with decreasing t_{Pt} within the error margins of the experiment and basically resembles the value found for the sandwiches ($K_2 = (70 \pm 30)$ kJ/m^3), while $K_{1,\mathrm{eff}}$ decreases from about +250 kJ/m^3 to −300 kJ/m^3. The evolution of $K_{1,\mathrm{eff}}$ with Pt interlayer thickness is displayed in Fig. 5.31(b). The value at $t_{\mathrm{Pt}} = 0$ nm belongs to the sandwich with $t_{\mathrm{Co}} = 3.2$ nm, which is also shown for comparison. The anisotropy constant strongly increases with increasing t_{Pt} in the range of $t_{\mathrm{Pt}} \lesssim 1$ nm, while at higher thicknesses the slope of the $K_{1,\mathrm{eff}}(t_{\mathrm{Pt}})$ characteristic gradually decreases, so that for $t_{\mathrm{Pt}} \gtrsim 3$ nm the anisotropy constant does not change with thickness. There, $K_{1,\mathrm{eff}}$ resembles the value found for the sandwich with the same individual Co layer thickness of $t_{\mathrm{Co}} = 0.8$ nm (see horizontal lines). For $t_{\mathrm{Pt}} \leq 0.5$ nm the samples show an easy plane behavior, while for $t_{\mathrm{Pt}} \geq 1$ nm they exhibit a perpendicular easy axis of magnetization. For the sample with $t_{\mathrm{Pt}} = 0.8$ nm a canted magnetization was found (see section 2.1.4.1). These findings reveal that besides the variation of the Co layer thickness the spin reorientation transition can also be initiated by a variation of the Pt interlayer thickness [103].
It is not possible to extract the contributions of K_S and $K_{1V,\mathrm{eff}}$ from the $K_{1,\mathrm{eff}}$ values as the Co thickness was not varied. However, as the nominal thickness of the Co layers is only about four monolayers ($t_{\mathrm{Co}} = 0.8$ nm) a differentiation between interface and volume anisotropy would be rather artificial anyway. In the following possible reasons for the $K_{1,\mathrm{eff}}(t_{\mathrm{Pt}})$ characteristic are discussed. An increasing anisotropy constant $K_{1,\mathrm{eff}}$ with increasing t_{Pt} was frequently reported in literature [675, 789, 95, 701, 109, 104, 704, 103]. In the studies, where t_{Pt} was systematically varied in such a way that more than two different interlayer thicknesses were used, a rather strong increase of $K_{1,\mathrm{eff}}$ with Pt interlayer thickness was observed

up to $t_{\mathrm{Pt}} \approx 1$ nm followed by a merging into a constant value [789, 701, 109, 103]. Obviously the depicted behavior is in qualitative accordance with the results of these studies. In the publications the dependence of $K_{1,\mathrm{eff}}$ on t_{Pt} was attributed to changes in strain [675, 95, 109, 104], roughness [103], or to the fact that pinholes in the Pt layer get erased [701, 704]. However, an accurate comparison between anisotropy and structural properties was not performed. In this work, the strong dependence of $K_{1,\mathrm{eff}}$ on t_{Pt} occurs in the thickness regime, where the nominal Pt interlayer thickness is below the thickness of the roughness and interdiffusion zone of $\sigma = (7 \pm 2)$ Å (see section 5.3.1.2), so that the interlayers are laterally discontinuous. Laterally discontinuous interlayers provide less interface regions, so that a reduced interface anisotropy is expected as discussed in section 2.1.5. For $t_{\mathrm{Pt}} \gtrsim \sigma$ the formation of laterally continuous interlayers is assumed to be basically completed. Obviously the size of σ fits with the change in the slope of the $K_{1,\mathrm{eff}}(t_{\mathrm{Pt}})$ curve at $t_{\mathrm{Pt}} \approx 1$ nm. Consequently, the strong increase of $K_{1,\mathrm{eff}}$ with t_{Pt} at low thicknesses can be related to the gradual formation of laterally continuous Pt interlayers. Certainly, the formation might be accompanied by significant changes in the strain within the Co material, so that the magnetoelastic contributions to the anisotropy terms are correspondingly affected. Above $t_{\mathrm{Pt}} \approx 1$ nm, where the Pt interlayers are laterally continuous and significant changes in roughness and interdiffusion can be ruled out, the slight residual increase of $K_{1,\mathrm{eff}}$ with thickness can be attributed to changes in the strain of the Co material. This is no contradiction to the XRD results, which indicate no detectable changes in the interplanar spacings for $t_{\mathrm{Pt}} \geq 1.5$ nm (see section 5.3.1.1): Already slight changes of the strain of only $\approx 0.3\%$, which is below the accuracy of the XRD investigations, can account for changes in $K_{1,\mathrm{eff}}$ in the range of about 100 kJ/m^3 as discussed in connection with the results for the sandwiches in the last paragraph. Thus, the slight increase of $K_{1,\mathrm{eff}}$ of only about 120 kJ/m^3 in the range of 1.5 nm $\leq t_{\mathrm{Pt}} \leq 3$ nm can be explained. This discussion again shows that the anisotropy is a rather sensitive probe that reflects small changes in the structural properties. Hence, the independence of the anisotropy constants on Pt interlayer thickness for $t_{\mathrm{Pt}} \gtrsim 3$ nm reveals that within this thickness regime no significant changes in the structural properties occur. Furthermore, as the anisotropy for large Pt thicknesses resembles the $K_{1,\mathrm{eff}}$ value found for the sandwich with the same Co layer thickness within the resolution of the experiment indicates that the properties of the individual Co layers in the stack are identical in a good approximation.

In the following, the remagnetization of selected multilayers is discussed, which deviate from the fundamental behavior presented in connection with the sandwiches (Fig. 5.29). Fig. 5.32(a) shows the in-plane and out-of-plane remagnetization curves of the canted sample with $t_{\mathrm{Pt}} = 0.8$ nm. For both field directions an open hysteresis was found and only a small field of about 100 mT is sufficient to fully saturate the magnetization along any field direction. It is recalled that a necessary prerequisite for the applied fitting procedure in order to determine the anisotropy constants from the coherent rotation of magnetization is, that the creation and annihilation of a multi-domain state is virtually invisible in the respective hard axis curve (see section 2.1.4.2). This is commonly fulfilled for samples with out-of-plane easy or hard axis behavior as for arbitrary field strengths in each domain the field includes the

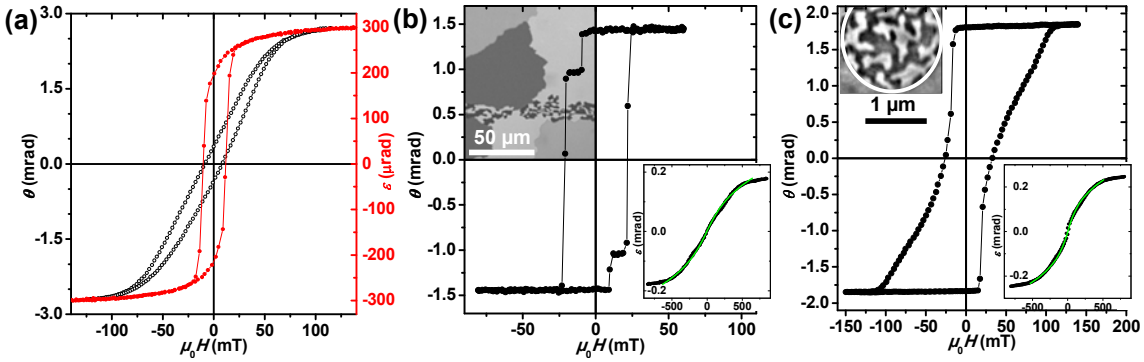

Figure 5.32: Kerr hysteresis loops of multilayers with (a) $t_{\mathrm{Pt}} = 0.8$ nm and Co/Pt bilayer repetition of $n = 4$, (b) $t_{\mathrm{Pt}} = 3$ nm, $n = 4$, and (c) $t_{\mathrm{Pt}} = 2$ nm, $n = 8$. The substrate is SiO_2. In (a) the longitudinal curve is given in red, while in (b) and (c) they are displayed as an inset in the lower right. The green lines in (b) and (c) are fits to the hard axis behavior. The insets in (b) and (c) in the upper left is a polar Kerr-microscopy and Fourier-transform holography (FTH) image, respectively, of the demagnetized state, where the black/white contrast color codes the perpendicular component of magnetization. For the latter image the substrate is Si_3N_4.

same angle with the magnetization. In the case of canting, however, during a domain decay the magnetization can populate two (field distorted) cones on the energy landscape. For instance, in polar geometry, starting from technical saturation, when reducing the field the magnetization can decompose into a multi-domain pattern, whose domains exhibit opposite vertical magnetization components in remanence. Thus, in this case the domain decay affects the $M_{\mathrm{p}}(H_{\mathrm{p}})$ signal, so that the mere contributions of coherent rotation is concealed. In order to determine canting angles (resolution of $\pm 2°$) and therefore the ratio of $K_{1,\mathrm{eff}}$ and K_2 accurately (see Eq. 2.20) a method was developed in our working group which utilizes the anisotropic interface magnetoresistance (AIMR) discovered within this thesis [E9]. For details about the method and about the canted phase in general the reader is referred to the publication Ref. [E9] and the references therein. Applying the method for the multilayer with $t_{\mathrm{Pt}} = 0.8$ nm the canting angle was determined to be $\Theta_{\mathrm{C}} = (57 \pm 2)°$, which yields to $K_{1,\mathrm{eff}} = (-99 \pm 5)$ kJ/m^3 via Eq. 2.20 under the condition of $K_2 = 70$ kJ/m^3 (fixed)[45].

Fig. 5.32(b) shows the remagnetization curves for $t_{\mathrm{Pt}} = 3$ nm. While the hard axis loop displays a typical remagnetization via coherent rotation in the easy axis curve plateaus separated by steep magnetization changes occur instead of a rectangular hysteresis. This qualitative behavior was found for all multilayers with $t_{\mathrm{Pt}} > 2.5$ nm. The steps between two plateaus can be attributed to the switching of individual Co layers, so that the magnetization orientation is not necessarily uniform along the stacking direction as it is always the case for $t_{\mathrm{Pt}} \leq 2.5$ nm at any lateral position [790]. This interpretation was confirmed by Kerr microscopy. The inset of Fig. 5.32(b) is a polar Kerr microscopy image of a part of the sample after demagnetization, which displays four different shades of gray. Each gray value represents

[45] Within this thesis further canted samples are the sandwiches that were grown on Si_3N_4 and naturally oxidized Si with $t_{\mathrm{Co}} = 1.5$ nm and $t_{\mathrm{Co}} = 2$ nm, respectively (see Fig. 5.30(b)).

a certain average magnetization M_p, thus revealing particularly the existence of antiparallel alignments of the magnetization of adjacent Co layers along the vertical direction for the regions of intermediate gray values. In the black and white regions the magnetization of all Co layers points down and up, respectively. The loss in ferromagnetic coupling between individual Co layers at similar Pt interlayer thicknesses is documented in a variety of investigations [791, 792, 793, 794, 795, 796, 152, 797, 798]. For more details about the (oscillatory) ferromagnetic interlayer exchange coupling in Co/Pt multilayers the reader is referred to these publications.
For multilayers with perpendicular easy axis besides increasing t_{Pt} an increasing number of bilayer repetition n yields deviations from a rectangular polar hysteresis curve as can be exemplarily seen in Fig. 5.32(c) for a sample with $t_{Pt} = 2$ nm and $n = 8$. The magnetization of the sample shows complete remanence and decays in a multi-domain state at an opposite field of about 20 mT. In contrast to a multilayer with smaller n the multi-domain state is stable over a relatively broad field range up to a field of about 110 mT. This indicates that the domain walls do not rush through the sample at the coercive field yielding an abrupt remagnetization. In contrast, the walls get pinned and are gradually shifted by increasing the magnetic field, so that the parallel-to-field-oriented domains grow at the expense of the domains that are oriented in an antiparallel manner. It is worth mentioning that, in general, the exact shape of the polar curve depends on the velocity of the ramp of the field sweep as the domain walls "creep" at constant field values on a time scale of seconds or minutes through the sample [799, 800, 801, 653, 802]. The inset of Fig. 5.32(c) is a Fourier-transform holography (FTH [803, 804, 805],[E5]) micrograph of the remanence state of a nominally identical sample grown on Si_3N_4 after the demagnetization in out-of-plane fields displaying a so-called maze or labyrinth pattern.
For the multilayers with perpendicular magnetic anisotropy and $n > 12$ a decay in domains is already observed before zero polar field so that in remanence a multi-domain state is always present. This decay in domains can be explained by the increase in stray field energy, which is connected with the increase of the Co material by increasing n [790], so that the single-domain remanence state is no longer a local energy minimum. For more details about recent research of the remagnetization and domain pattern of Co/Pt multilayers the reader is referred to Refs. [806, 795, 794, 807, 790, 808, 112, 809, 810, 103, 368, 153]. Besides the static behavior, it is nowadays possible to study the magnetization dynamics down to the picosecond time-scale with a temporal resolution in the femtosecond regime [811]. Such investigations for Co/Pt multilayers fabricated by our working group were recently performed in a successful cooperation by utilizing free-electron laser sources [812, 813],[E3, E8, E10, E12].

5.3.2.2 Saturation magnetization obtained via Ferromagnetic Resonance (FMR)

Ferromagnetic resonance measurements (FMR) at room temperature were performed for several Pt/Co/Pt sandwiches with $t_{Co} \geq 4$ nm in cooperation with F. Balhorn from the Institute of Applied Physics, University of Hamburg, in order to examine

the saturation magnetization. For thinner Co layer thicknesses and for the multilayers the signal to noise ratio was too low to obtain a FMR signal with the used setup.
The term FMR implies the resonant absorption of microwaves by the magnetic moments of the ferromagnet [814, 815, 816]. In the experiment the microwaves were coupled into the laterally homogeneous films by placing the samples upside down onto a coplanar waveguide. The frequency of the microwaves ν and the strength of a magnetic field $\mu_0 H$ oriented in a fixed in-plane direction were tuned from 10 MHz to 14 GHz and from -40 mT to $+40$ mT, respectively, while the transmission of the microwaves was measured by means of a vector network analyzer. More details about the setup and its functionality, see Ref. [817].
For a single-domain state, which is present for the samples with easy plane behavior above $\mu_0|H| \gtrsim 10$ mT (see inset of Fig. 5.29(b)), the precession of the magnetization (macrospin) around the effective field $\mathbf{H}_{\text{eff}}$ can be described by the Landau-Lifschitz-Gilbert equation (see Eq. 2.32). The resonance condition is then given by [818, 819, 820]

$$\nu_{\text{r}}(H) = \frac{\omega_{\text{r}}(H)}{2\pi} = \frac{\gamma\mu_0}{2\pi}\sqrt{H(H + M_{\text{eff}})} \quad , \tag{5.68}$$

where $\gamma = g\mu_{\text{B}}/\hbar = g \cdot 88.5$ GHz/T is the gyromagnetic ratio and g is the Landé-factor, which is for hcp and fcc bulk Co $g^{\text{hcp}}_{\text{Co, bulk}} = 2.18$ and $g^{\text{fcc}}_{\text{Co, bulk}} = 2.14$, respectively [821]. M_{eff} is the effective magnetization, which includes the saturation magnetization M_{S} and the anisotropy constants K_{1V} and K_S in first order approximation[46]:

$$\mu_0 M_{\text{eff}} = \mu_0 M_{\text{S}} - \frac{2K_{1V}}{M_{\text{S}}} - \frac{4K_S}{M_{\text{S}} \cdot t_{\text{Co}}} \tag{5.69}$$

Fig. 5.33(a) exemplarily displays the FMR spectrum, i.e., the relative transmission in dependence of microwave frequency ν and applied field $\mu_0 H$, of a sandwich with $t_{\text{Co}} = 15$ nm grown on SiO_2. Each frequency sweep at fixed $\mu_0 H$ shows a dip in the transmission revealing ν_{r} (see inset of Fig. 5.33(a)). From the position of the dips in the FMR spectrum $\nu_{\text{r}}(H)$ (see red squares in Fig. 5.33(a)) the saturation magnetization M_{S} of the films was determined. For that purpose, in the first step, the $\nu_{\text{r}}(H)$ dependence of the samples was fitted to Eq. 5.68 by using $g = 2.15$ (see blue dashed line in Fig. 5.33(a)) revealing $\mu_0 M_{\text{eff}}$. $\mu_0 M_{\text{eff}}$ in dependence of $1/t_{\text{Co}}$ can be seen as black symbols in Fig. 5.33(b). Second, utilizing $\mu_0 M_{\text{eff}}$ and the anisotropy constants determined in section 5.3.2.1 (K_{1V}, K_S, see Tab. 5.3) M_{S} was calculated via Eq. 5.69. $\mu_0 M_{\text{S}}$ in dependence of $1/t_{\text{Co}}$ is also displayed in Fig. 5.33(b). It is obvious that the saturation magnetization of the samples basically resembles the value of bulk Co of $\mu_0 M_{\text{S}}^{\text{bulk Co}} = 1.76$ T within the error margins of the experiment. The systematic deviation to lower values of about 10% compared to $\mu_0 M_{\text{S}}^{\text{bulk Co}}$ might partially be a consequence of a non-consideration of K_2. The apparently slight decrease of $\mu_0 M_{\text{S}}$ with decreasing t_{Co} is discussed below.
The thickness independence of M_{S} is in accordance with other studies concerning

[46] The non-consideration of K_2 is justified in a good approximation as $K_2 \ll K_{\text{d}}$. For more details about FMR the reader is referred to Refs. [814, 815, 820, 816].

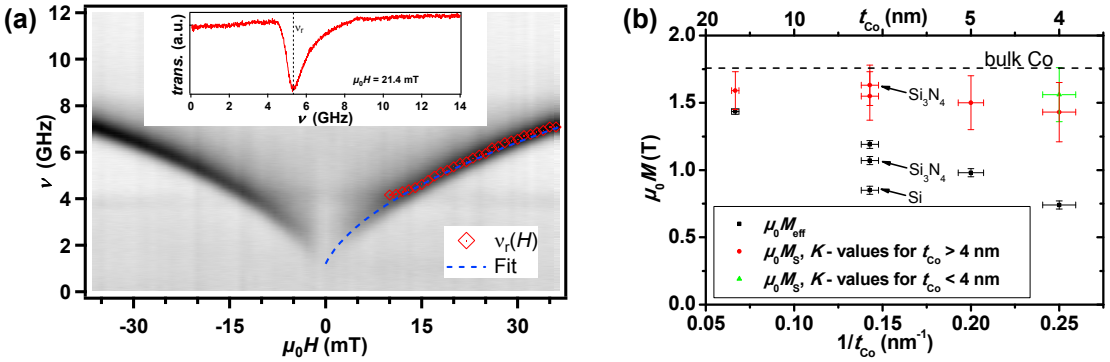

Figure 5.33: (a) FMR spectrum of the sandwich with $t_{\mathrm{Co}} = 15$ nm grown on SiO_2. The black-white contrast color codes the relative transmission of the microwave through the co-planar waveguide. Black (white) means strong (weak) absorption of the microwaves within the Co/Pt sample. The inset displays the frequency sweep for $\mu_0 H = 21.4$ mT revealing the resonance frequency $\nu_{\mathrm{r}}(21.4\ \mathrm{mT}) = 5.32$ GHz. The resonance frequency ν_{r} in dependence of applied magnetic field $\mu_0 H$ (red squares) shows a square-root behavior as indicated by the blue dashed line. (b) $\mu_0 M_{\mathrm{eff}}$ and $\mu_0 M_{\mathrm{S}}$ in dependence of $1/t_{\mathrm{Co}}$ for sandwiches grown on SiO_2. For $t_{\mathrm{Co}} = 4$ nm $\mu_0 M_{\mathrm{S}}$ was calculated by using the anisotropy constants determined for $t_{\mathrm{Co}} > 4$ nm (red squares) and $t_{\mathrm{Co}} < 4$ nm (green triangles), respectively. Samples with $t_{\mathrm{Co}} = 7$ nm grown on Si_3N_4 and naturally oxidized Si were also measured. Due to the lack of anisotropy constants for Si $\mu_0 M_{\mathrm{S}}$ could not be determined. Qualitatively, the lower value of $\mu_0 M_{\mathrm{eff}}$ indicates larger K_{1V} and K_S constants for Si as substrate similar to the findings for $t_{\mathrm{Co}} < 4$ nm presented in the previous section 5.3.2.1.

Co/Pt layered structures [105, 106, 778]. For instance, Shan et. al. found no significant change in M_{S} down to a nominal Co layer thickness of 0.3 nm at room temperature [105]. It is worth mentioning that at lower temperatures down to 5 K, however, in the thickness regime of $t_{\mathrm{Co}} \lesssim 1$ nm the saturation magnetization (effective magnetic moment per Co atom) was found to strongly increase with decreasing Co layer thickness and temperature exceeding the bulk value of Co [105, 107]. The apparent enhancement of M_{S} is connected with the magnetic moments of the interface atoms and is analogous to the findings for homogeneous CoPt alloys, where the resulting magnetization can be significantly larger than expected from the amount of Co material and the saturation magnetization of bulk Co (giant moment phenomenon) [822, 107]. For alloys and multilayers, the large effective moment per Co atom is caused by the polarization of the Pt atoms induced by adjacent Co atoms as well as by the enhancement of the orbital moments of the Co atoms located at the Co/Pt interfaces [822, 823, 824, 825, 826, 705][47]. The temperature dependence of the saturation magnetization even of dilute CoPt alloys with small Co concentrations [822, 832] as well as of the additional magnetic moments at the Co/Pt interfaces [833, 113, 549] basically obey Bloch's $T^{3/2}$ law (see Eq. 5.39), however, with a significantly enhanced constant B reflecting a much lower Curie temperature compared to bulk Co. For Co/Pt layered structures this implies that the higher the temperature the lower is the relative contribution of the Pt polar-

[47] For information about magnetic properties of Co ad-atoms and clusters on Pt substrates, see e.g. Refs. [827, 828, 755, 829, 830, 831].

ization and enhanced Co moment to the total magnetic moment. For instance, for (4 Å Co/9 – 23 Å Pt)$_{25}$ multilayers at room temperature a magnetic moment for the interfacial Pt atoms of $\mu_{\mathrm{Pt}} \approx 0.25\mu_{\mathrm{B}}$ was estimated from x-ray magnetic circular dichroism (XMCD) investigations at the Pt L_3 edge, while the moment was found to strongly decay in the Pt layers with increasing distance to the interface [823, 834, 106, 835]. The moments of the Pt atoms are much smaller than the moment of bulk Co atoms of $\mu_{\mathrm{Co}} = 1.72\mu_{\mathrm{B}}$ [834]. The enhanced orbital moment of Co was frequently found to be of similar size as μ_{Pt} [128, 826], e.g. Weller et al. measured an enhancement of $\Delta\mu_{\mathrm{Co,orbital}} \approx 0.07\mu_{\mathrm{B}}$ for (2 – 8.5 Å Co/10 Å Pt)$_{20}$ multilayers [824]. Hence, it can be concluded that at room temperature for Co layer thicknesses of $t_{\mathrm{Co}} \geq 0.8$ nm used in this work the relative additional contribution of the atoms at the Co/Pt interfaces (CoPt interdiffusion zone) to the total magnetic moment is rather small ($\lesssim 10\%$). For more details about the Pt polarization and enhanced orbital moments of Co the reader is referred to the given publications.
Concerning the apparently slight decrease of M_{S} with decreasing Co thickness it might be a consequence of a non-consideration of a possible thickness dependence of the Landé-factor, which is assumed to resemble the Co bulk value in the derivation of $\mu_0 M_{\mathrm{eff}}$ (see above). The Landé-factor might be increased due to the presence of the enhanced orbital moments of the Co atoms at the interface [836] or even reduced caused by an incomplete quenching of the orbital angular momentum at the interface [837]. For more details, see Refs. [836, 837] and references therein.
In conclusion, the FMR investigations reveal that the saturation magnetization of Co is thickness-independent for the investigated thickness range of $t_{\mathrm{Co}} \geq 4$ nm and resembles $M_{\mathrm{S}}^{\mathrm{bulk\ Co}}$. Moreover, down to the smallest Co layer thickness of $t_{\mathrm{Co}} = 0.8$ nm the relative contribution of the Pt polarization and enhanced orbital moment of Co at the interfaces to the total magnetic moment is estimated to be negligibly small, so that the assumption of $M_{\mathrm{S}}^{\mathrm{bulk\ Co}}$ is justified in the evaluation of the anisotropy constants performed in the previous section. Vice versa, as the anisotropy constants were used for the derivation of M_{S} from the FMR data the consistence of the FMR investigations with the MOKE and AHE results verifies the determined anisotropy constants.

In summary, the investigations of the magnetic properties indicate in particular that the structural properties of the Pt/Co/Pt sandwiches (multilayers) do not significantly change for $t_{\mathrm{Co}} \gtrsim 5$ nm ($t_{\mathrm{Pt}} \gtrsim 3$ nm).

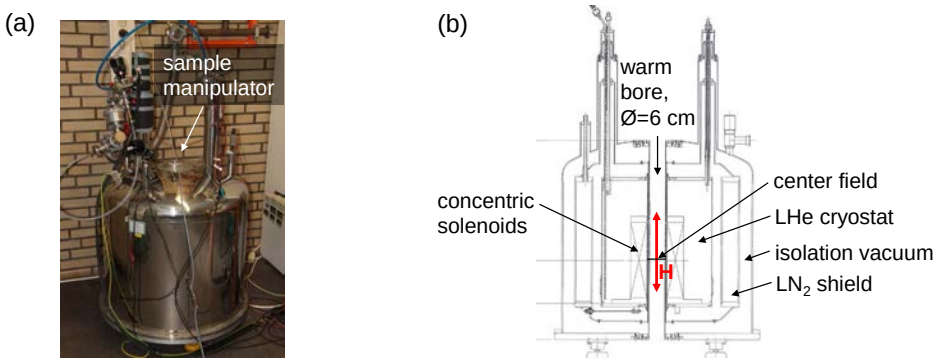

Figure 5.34: Warm-bore magnet. (a) Exterior view with the sample manipulator positioned at the bore. (b) Scheme of the cross-section, the main components are tagged.

5.4 Magnetoresistance measurements

5.4.1 MR measurement setup

The magnetoresistance measurements at room temperature[48] were performed by means of a superconducting magnet[49] providing fields of up to ±11 T, whose exterior view can be seen in Fig. 5.34(a). The magnet consists of a number of concentric solenoids, which are arranged horizontally in a liquid helium cryostat. The cryostat has a vertical warm bore with a diameter of 6 cm, which guarantees ambient conditions in the center of the solenoids (see Fig. 5.34(b)). The direction of the magnetic field within the bore is oriented in parallel to its axis. The field strength at the axial center field position in dependence of the current flowing through the solenoids was calibrated by means of a Hall probe[50]. A linear dependence was found with a slope of 107.14 mT/A, which is in accordance with the value stated in the manual. The relative deviation from the strength of the center field at an axial distance of 1 cm was specified from the manufacturer to be better than $5 \cdot 10^{-5}$, so that homogeneous field conditions for the MR investigations are guaranteed. To adjust the samples in the vicinity of the homogeneous center field the samples were mounted to a sample manipulator (see Fig. 5.35(a)). The sample manipulator, constructed in the framework of this thesis, enables the rotation of the samples in two ways: The sample can either be rotated so that the film normal is always oriented perpendicularly to the field direction (see Fig. 5.35(b)) or in such a manner that an arbitrary direction in the film plane is always oriented perpendicularly to the field direction (see Fig. 5.35(c)).

5.4.2 MR measurement scheme

The current in-plane MR of the samples was characterized by using two methods: In the case of the first method the magnitude of the applied magnetic field was

[48] For the MR investigations at lower temperatures another setup is used, which is briefly introduced in section 5.6.

[49] B-T environment of Oxford instruments, project number 37791.

[50] The magnet was operated using a *magnet power supply PS120-10*, Oxford instruments.

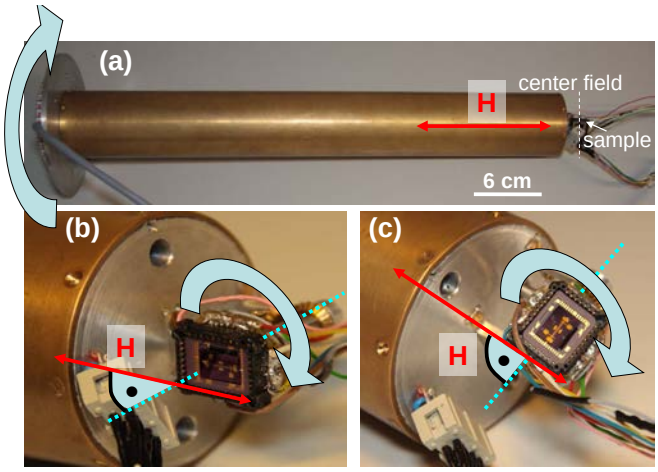

Figure 5.35: Sample manipulator. (a) The orientation of the sample with respect to the magnetic field can be manually tuned by a wheel from the top of the manipulator (see blue arrow). The sample can be mounted to the manipulator in order to reorientate the magnetic field within the film plane (b) or from out-of-plane to a particular in-plane direction (c). The mechanical transmission is provided by a pair of bevel gear wheels.

swept from −6 T to +6 T and then reversed, while the orientation of the film with respect to the direction of magnetic field was held constant (**H** field sweep measurements). The sweep rate was set to 0.2 T/min and the resistance was measured in steps of 10 mT (3 s). Generally, these field sweeps were performed for the three generic orientations between magnetic field and current direction. It is common use to denote the measurement geometries as longitudinal (||) and transverse (t) for applying the field in the film plane in parallel and perpendicularly to the current direction, respectively (see Fig. 5.36(a)). The polar (p) geometry denotes the case where the field is applied perpendicularly to the film plane. For the respective easy axes additional field sweeps were performed typically from −0.05 T to +0.05 T and then reversed by using a sweep rate of 0.01 T/min measuring the resistance in steps of 0.5 mT (3 s) in order to resolve the region of remagnetization in more detail.
The second method concerns the investigation of the angular dependence of the resistivity with respect to the orientation of the magnetization. For that purpose the samples were rotated in a constant field of $\mu_0|H| = 6$ T. This field strength was sufficient to align the magnetization with field along any direction in a good approximation. The samples were rotated in two ways: First, the samples were rotated so that the magnetic field was always oriented perpendicularly to the normal of the film in order to reveal the angular dependence of resistivity when **M** is varied in the film plane (see Fig. 5.35(b) and Fig. 5.36(b)). In the second way the samples were mounted to the sample manipulator in such a manner that the magnetization was rotated within the plane perpendicular to the current direction (see Fig. 5.35(c) and Fig. 5.36(b)). The investigated angular range amounted to $-95° \leq \theta, \varphi \leq 95°$.
The field sweep measurements in combination with the rotation of the samples in a saturation field reveal the complete information about the **M** and **H** dependence of the ρ_{xx} and ρ_{xy} terms of the resistivity tensor.
For the MR measurements a DC current of $I_x = 5$ mA was used and the resulting

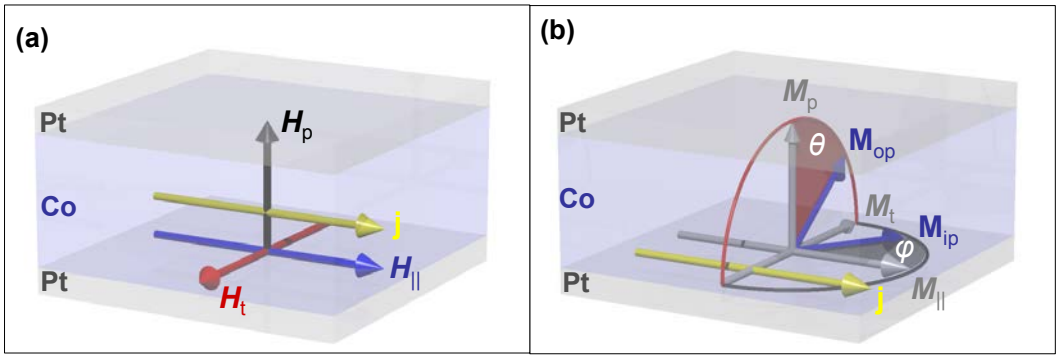

Figure 5.36: Sketches of a Pt/Co/Pt sandwich, where the current **j** flows in the plane. In (a) the three generic directions of the magnetic field **H** with respect to the current direction and layered structure are drawn, i.e., the so-called longitudinal (||), transverse (t), and polar (p) geometry. (b) shows the two generic rotation geometries. φ denotes the angle between the magnetization $\mathbf{M}_{\mathrm{ip}}$ and the current direction in the plane parallel to the surface, while θ denotes the angle between $\mathbf{M}_{\mathrm{op}}$ and the film normal in the plane perpendicular to the current direction.

DC voltages U_x and U_y were recorded by means of a nanovoltmeter[51]. Beforehand, it was examined that for this order of magnitude of the current a linear $I_x(U_x)$ characteristic exists. Quantitatively, within the current range of 1 mA $< |I_x| <$ 10 mA the resistivity change $\Delta R_{xx}/R_{xx}$ is within the measurement resolution of $1 \cdot 10^{-5}$. The fulfillment of Ohm's law reveals that the current does not cause any detectable heating of the samples.
It is worth mentioning that due to unavoidable deviations from the ideal sample geometry in the measured voltages U_x and U_y undesired contributions of U_y in U_x and vice versa always exist. Fortunately, these contributions can be quantified and eliminated as all terms in the diagonal component $R_{xx} = U_x/I_x$ are unaffected by reversing the field direction, while the leading terms in the off-diagonal component $R_{xy} = U_y/I_x$ change their sign (see Eq. 5.7). For the Co/Pt samples used in this study the undesired contributions of R_{xy} in R_{xx} arising from the Hall effects exhibit a maximum contribution of $< 0.02\ \Omega$, which is rather small compared with the actual size of the MR effects under investigation (see below). Similarly, the field dependent contributions of R_{xx} in R_{xy}, which are predominantly caused by the anisotropic (interface) MR, are also small with a maximum contribution of $< 0.05\ \Omega$. The actual size of the undesired contributions depend on the thickness of the individual layers. Prior to the quantitative analysis of the MR measurements and in all measurement curves shown in this chapter the undesired contributions were eliminated.
The $\rho_{xy}(\varphi, \theta)$ curves are not presented within this thesis as they provide no additional information for the quantitative analysis. The $\rho_{xy}(\varphi)$ curves behave according to Eq. 5.48 due to the presence of the planar Hall effect. In accordance with the expectation the size of the planar Hall effect (prefactor in Eq. 5.48) resembles the size of the AMR, i.e., $\Delta\rho_{\mathrm{AMR}}$. The $\rho_{xy}(\theta)$ curves display a $\cos\theta$ dependence as expected from Eq. 5.46, while the size is caused by a superposition of the normal and anomalous Hall effect.

[51] Keithley Model 6221 AC and DC current source; Keithley Model 2182A Nanovoltmeter.

5.5 Magnetoresistance of Pt/Co/Pt sandwiches - Anisotropic Interface Magnetoresistance (AIMR)

As stated in the introduction of this chapter, the starting point to systematically study the current in-plane (CIP) MR of Co/Pt layered structures was the observation obtained from preliminary investigations. These investigations unambiguously showed that the diagonal part of the resistivity tensor depends on the magnetization orientation within the plane perpendicular to the current direction in an unexpected manner: Contrary to the signature of the GSE (see section 5.1.4.3) the transverse resistivity ρ_{t} ($\mathbf{M}$ oriented in the film plane) is smaller than the polar resistivity ρ_{p} ($\mathbf{M}$ oriented perpendicularly to the film plane; see Fig. 5.1). In order to reveal the origin of this behavior in a first step the MR at room temperature of the simplest layered structure, i.e., Pt/Co/Pt sandwiches, was investigated. While the Pt cap and seed layers were kept constant the Co thickness t_{Co} was varied from 0.8 nm to 30 nm.
In section 5.5.1 the results of the MR investigations of the films grown on SiO_2 are presented and discussed. The results regarding the discovered $\rho_{\mathrm{t}} < \rho_{\mathrm{p}}$ behavior indicate that it is caused by the Co/Pt interfaces. Thus, this effect was named *Anisotropic Interface Magnetoresistance* (AIMR). In section 5.5.2 a phenomenological description of the resistivity $\rho_{xx}(\mathbf{M})$ in the framework of the Fuchs-Sondheimer model is given which in particular enables a quantification of the AIMR. Besides the AIMR further influences of the finite size on the magnetoresistance were found that are discussed in connection with section 5.5.1 and section 5.5.2. This section closes with a comparison of the AIMR for sandwiches grown on SiO_2 and Si_3N_4 (section 5.5.3).
The main results of this chapter regarding the AIMR effect were published in the Physical Review Letters [E6]. The letter can be found in the attachments.
In connection with this thesis a fully relativistic spin-polarized *ab initio* theoretical description regarding $\rho_{xx}(\mathbf{M})$ of Pt(111)/Co_n/Pt(111) sandwiches ($n \leq 90$ monolayers, $T = 0$ K) was performed by Prof. Dr. P. Weinberger, Center of Computational Nanoscience, Vienna (Austria), whose results are briefly presented and discussed in the context of section 5.5.2. The results of the theoretical study were published in the Philosophical Magazine [E7]. This paper is also given in the attachments.

5.5.1 Magnetoresistance of Pt/Co/Pt sandwiches grown on SiO_2

This section is divided into four parts: In the first one (section 5.5.1.1) the results of the field sweep measurements are presented. From these measurements the various MR effects are identified and disentangled. In the second section 5.5.1.2 the results of the sample rotation for ρ_{xx} at a fixed saturation field of 6 T are presented, which in particular reveal the angular dependence of the AIMR effect. The quantification and the obstacle in the description of the MR effects caused by the Co thickness-dependent current shunt through the Pt is discussed in section 5.5.1.3. The thickness

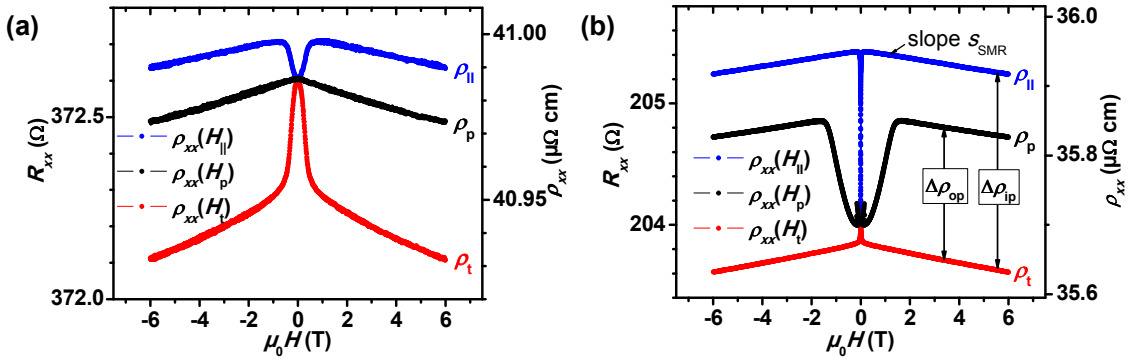

Figure 5.37: Resistance R_{xx}/ resistivity ρ_{xx} as a function of the applied field $\mu_0 H$ for the three principle directions of the field with respect to the current direction and stacking for (a) $t_{\mathrm{Co}} = 0.8$ nm and (b) $t_{\mathrm{Co}} = 6$ nm. The linear slopes s_{SMR} above technical saturation were determined by linear fits.

dependence of the various MR effects is presented and qualitatively discussed in section 5.5.1.4.

5.5.1.1 Dependence of resistivity on applied field

Diagonal element $\rho_{xx}(\mathbf{H})$: As presented in section 5.3.2.1 the sandwiches grown on SiO_2 exhibit a spin reorientation transition at a Co thickness of about 1.1 nm. Qualitatively, the shape of the field sweeps of each generic field orientation is similar for all films with perpendicular easy axis of magnetization and for all films with easy plane behavior, respectively. For both cases the measured curves are exemplarily shown in Fig. 5.37 ((a) $t_{\mathrm{Co}} = 0.8$ nm, (b) $t_{\mathrm{Co}} = 6$ nm)[52]. At first the curves obtained for the sandwich with the thinnest Co layer of $t_{\mathrm{Co}} = 0.8$ nm are discussed. Sweeping the magnetic field along the easy axis (polar geometry) results in a slight, almost linear decrease of the resistivity with increasing the absolute value of the field over the whole field range of ±6 T. In this geometry the simultaneously measured $\rho_{xy}(H_{\mathrm{p}})$ curve (see inset of Fig. 5.29(a) and Fig. 5.39(a) below) shows an almost rectangular hysteresis revealing that the remagnetization from one perpendicular magnetized single-domain state to the opposite is performed via domain wall movement at small opposite fields of $\lesssim 10$ mT. Hence, as within the whole field range the magnetization essentially changes its sign only, MR effects like the AMR or the GSE can be ruled out to be responsible for the linear dependence of $\rho_{xx}(H_{\mathrm{p}})$ on H_{p}. For the two hard axis curves (longitudinal and transverse geometry) parabolic behavior of the resistivity on field were found. As the magnetization rotates coherently (see Fig. 5.29(a)) this behavior is expected when MR effects dominate which depend quadratically on the orientation of magnetization, as e.g. the AMR, as particularly shown in the previous chapter (see Fig. 4.27). When the magnetization is aligned in parallel to the magnetic field at about ±0.6 T (see Fig. 5.29(a)) the parabolic behavior pass into a linear decrease, which is similar to the slope in the polar geometry. Note, that the

[52] As small variations in temperature slightly affect the resistivity the vertical positions of the three curves with respect to each other were corrected according to the data from the rotation of the samples at 6 T (see section 5.5.1.2).

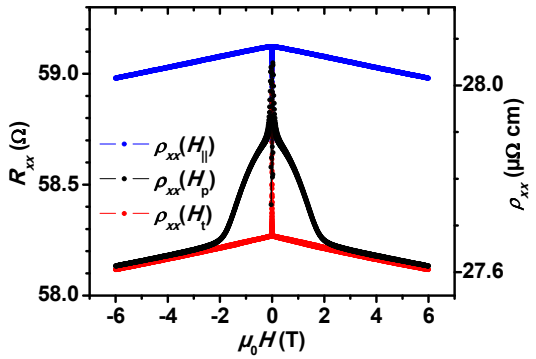

Figure 5.38: Resistance R_{xx}/ resistivity ρ_{xx} as a function of the applied field $\mu_0 H$ for the three principle directions of the field with respect to the current direction and stacking for $t_{\mathrm{Co}} = 30$ nm. The deviations from the parabolic shape of the polar curve can be related to a small misalignment of the magnetic field direction with respect to the normal of the film.

resistivity in remanence is almost the same in all three curves although for the polar geometry (in-plane geometries) the sample is in a single-domain state (multi-domain state). The influence of the magnetic microstructure on the resistivity for samples with perpendicular easy axis of magnetization is discussed in detail in section 5.7.
For the sample with $t_{\mathrm{Co}} = 6$ nm the easy plane behavior causes the magnetization to form domains in remanence (see e.g. inset of Fig. 5.29(b)). At small in plane fields ($\lesssim 20$ mT) the multiple domain state is erased by domain wall movement and the resistivity shows a steep increase (decrease) until a single-domain state is created along (perpendicularly oriented to) the current direction. Above technical saturation a linear decrease of the resistivity with the absolute value of field was found, whose slope is similar for both MR geometries. For the magnetic hard axis (polar geometry) the parabolic shape of the curve again indicates a coherent rotation of the magnetization that is completed at about 1.4 T, which is confirmed by the simultaneously measured $\rho_{xy}(H_{\mathrm{p}})$ curve (see Fig. 5.39(b) below). When the magnetization is field aligned the $\rho_{xx}(H_{\mathrm{p}})$ curve exhibits a linear decrease with similar slope as found for the two in-plane curves.
For the samples with easy plane behavior deviations from the parabolic shape of the polar curve were generally observed around zero field as can be seen in Fig. 5.37(b). Stronger deviations are exemplarily shown in Fig. 5.38, where the field sweeps for a sandwich with 30 nm Co thickness are displayed. The deviations can be explained by a small misalignment of the sample normal with respect to the magnetic field direction in the range of a few degrees [612], which is difficult to avoid experimentally. In remanence, the magnetization is in a multi-domain-state. Applying a field oriented perfectly in the polar direction results in a rotation of the magnetization within each domain into the polar direction. Even for rather small in-plane field components that are provided by the misalignment further remagnetization processes are likely to occur, like domain wall movement annihilating domains that are not oriented in parallel to the in-plane field component or in-plane rotation processes of the magnetization, hence, resulting in deviations from the parabolic shape.
From the characteristics of the curves in conjunction with symmetry considerations

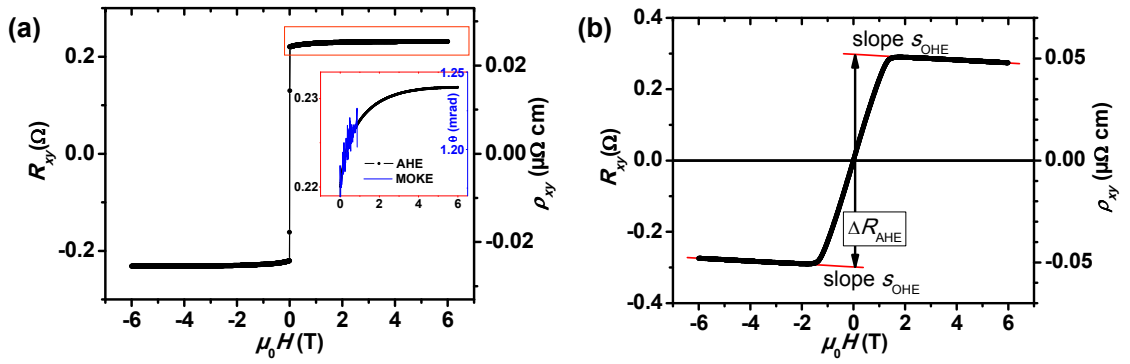

Figure 5.39: Resistance R_{xy}/ resistivity ρ_{xy} as a function of the polar field $\mu_0 H_\mathrm{p}$ for (a) $t_\mathrm{Co} = 0.8$ nm and (b) $t_\mathrm{Co} = 6$ nm. The inset in (a) highlights the characteristic above technical saturation and additionally shows the polar MOKE curve (blue line) by using for both curves the same relative scales of the ordinates with respect to the signal at 1 T. The red lines in (b) are linear fits used to determine the slope s_OHE and the difference ΔR_AHE.

the different MR effects can be disentangled. The quantification of the effects and their dependence on the Co thickness is given in the next sections. Here, the results are discussed qualitatively. Above technical saturation the resistivity decreases almost linearly and isotropically with increasing the absolute magnitude of the field (see Fig. 5.37 and Fig. 5.38). This behavior is caused by the spin-disorder MR and indicates that contributions of the anisotropic nature of the Lorentz MR are vanishingly small, which would yield parabolic-like upbending of the $\rho_{xx}(H_i)$ curves (see section 5.1.4.1). As a consequence the difference between the three curves remains almost constant in the saturation regime. The resistivity difference for $\mathbf{M}$ oriented in plane, $\Delta\rho_\mathrm{ip} = \rho_{||} - \rho_\mathrm{t}$, refers to the conventional AMR effect (see section 5.1.4.1) as for both orientations of the magnetization effects caused by the texture or the interfaces are identical because of symmetry considerations. As expected, for all samples in this work $\Delta\rho_\mathrm{ip} > 0$ was found. The resistivity difference in saturation for $\mathbf{M}$ oriented perpendicularly to the current $\Delta\rho_\mathrm{op} = \rho_\mathrm{p} - \rho_\mathrm{t}$ is nonzero, indicating an additive contribution to the resistivity that is similar to the signature of the GSE (see section 5.1.4.3). In contradiction to the GSE, however, it has a positive sign. The behavior $\rho_{||} > \rho_\mathrm{p} > \rho_\mathrm{t}$ was found for all samples with $t_\mathrm{Co} \leq 30$ nm as can be exemplarily seen in Fig. 5.37 and Fig. 5.38. As already mentioned above, this behavior was not found in polycrystalline films up to now.

Off-diagonal element $\rho_{xy}(H_\mathrm{p})$: In Fig. 5.39 the $\rho_{xy}(H_\mathrm{p})$ behavior for the samples with $t_\mathrm{Co} = 0.8$ nm (a) and $t_\mathrm{Co} = 6$ nm (b) are shown. As already stated in section 5.3.2.1, after subtracting the curve from $\rho_{xy}(H_\mathrm{p})$, which extrapolates the high-field behavior above technical saturation to zero field, the resulting curve reflects the polar remagnetization $M_\mathrm{p}(H_\mathrm{p})$. This contribution in $\rho_{xy}(H_\mathrm{p})$ refers to the anomalous Hall effect (AHE, see section 5.1.4.2). Regarding the behavior above technical saturation ($M_\mathrm{p}||H_\mathrm{p}$), for $t_\mathrm{Co} \gtrsim 2$ nm a linear decrease of ρ_{xy} with increasing the magnetic field was observed, which reveals the existence of another MR effect which is superimposed on the AHE. This characteristic is a consequence of

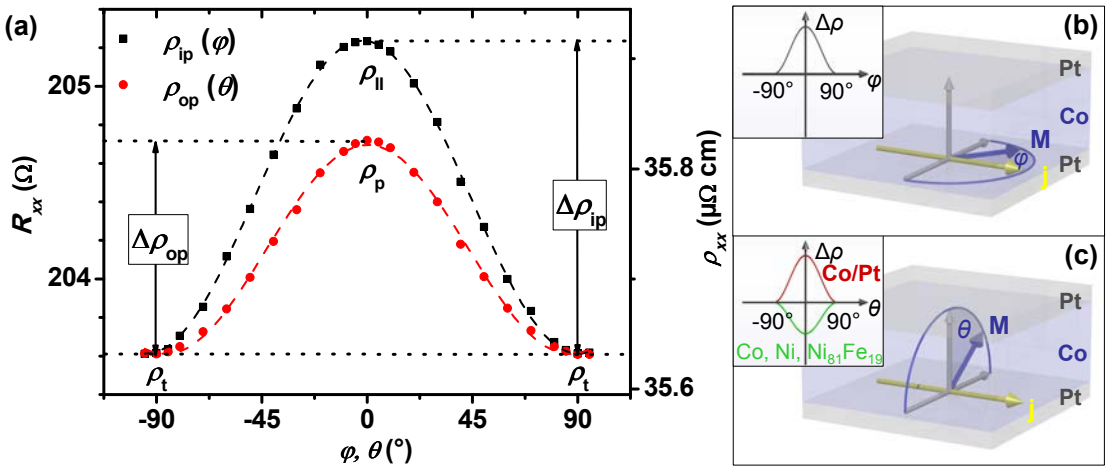

Figure 5.40: (a) Resistance R_{xx}/ resistivity ρ_{xx} as a function of the in-plane angle φ and out-of-plane angle θ for the sample with $t_{Co} = 6$ nm. The field strength was 6 T causing **M** to be field aligned. The dashed lines represent $\cos^2$ fits. The in-plane curve refers to the conventional AMR as schematically shown in the inset of (b), while the out-of-plane curve exhibits the same characteristic as the GSE but is of opposite sign (compare the green curve found for Co, Ni and permalloy films with the red curve in the inset of (c)).

the normal Hall effect (OHE, see also section 5.1.4.2). For thin Co layers $t_{Co} < 2$ nm deviations from a straight line were found as can be exemplarily seen in the inset of Fig. 5.39(a). The reason for this behavior is discussed in section 5.5.1.4.

5.5.1.2 Dependence of resistivity ρ_{xx} on magnetization orientation

Above technical saturation, the resistivity change with external field is isotropic. Thus, it is possible to reveal the dependence of the resistivity on magnetization orientation easily by rotating the samples in a sufficiently high field forcing **M** to be always aligned in parallel to **H**. In Fig. 5.40(a) the resistivity of the sample with $t_{Co} = 6$ nm is exemplarily displayed as a function of the orientation of the magnetization when **M** is rotated either in-plane (see Fig. 5.40(b)) or in the plane perpendicular to the current direction (see Fig. 5.40(c)). As already discussed above, possible influences of the texture and interfaces are the same in any in plane orientation of **M** because of symmetry reasons. Thus, the in plane curve reveals the angular dependence of the conventional AMR. As indicated by the fit (black dashed line) the functional shape of ρ_{ip} is $\rho_{ip} = \rho_t + \Delta\rho_{ip}\cos^2\varphi$, where φ is the angle between **M** and the current direction, as expected for the AMR (see Eq. 5.37 and inset of Fig. 5.40(b)). If θ denotes the angle between **M** and the film normal, then the same kind of angular dependence was found, namely,

$$\rho_{op} = \rho_t + \underbrace{(\rho_p - \rho_t)}_{\Delta\rho_{op}}\cos^2\theta \tag{5.70}$$

This angular dependence was also found by Chen and Marsocci for the GSE but with the opposite sign: $\Delta\rho_{op} < 0$ (see green curve in the inset of Fig. 5.40(c)) [611]. If arbitrary orientations of magnetization **M** are allowed besides the two sectional

planes considered only until now the resistivity contains in general a superposition of the AMR and of the AIMR (and/or the GSE) effect. Utilizing spherical coordinates, where θ' denotes the polar angle between $\mathbf{M}$ and the stacking direction and φ' is the azimuthal angle between $\mathbf{M}$ and the current direction, ρ_{xx} is given by:

$$\rho_{xx}(\varphi', \theta') = \rho_{\mathrm{t}} + \Delta\rho_{\mathrm{op}} \cos^2\theta' + \Delta\rho_{\mathrm{ip}} \sin^2\theta' \cos^2\varphi' \tag{5.71}$$

5.5.1.3 Quantification and description of magnetoresistance effects

For the quantitative analysis of the effects the three $R_{xx}(H_i)$ curves of every sample were fitted to linear slopes in the field ranges of 3 T $\leq \mu_0|H_i| \leq$ 6 T, where technical saturation is always ensured. The absolute value of the slopes $s_{\mathrm{SMR}} = -|\mathrm{d}R_{xx}/\mathrm{d}(\mu_0 H)|$ is a measure for the strength of the spin-disorder MR. The saturation resistances R_{t}, $R_{||}$, and R_{p} were determined by the extrapolation of the linear slopes to zero field. The corresponding ΔR_{ip} and ΔR_{op} values are nearly identical to the ones obtained from the rotation measurements due to the isotropic slope of $R_{xx}(H_i)$ curves above technical saturation. For the quantification of the normal and anomalous Hall effect the $R_{xy}(H_{\mathrm{p}})$ curve was fitted to straight lines above negative and positive saturation as well (3 T $\leq \mu_0|H_i| \leq$ 6 T). The slope $s_{\mathrm{OHE}} = \mathrm{d}R_{xy}/\mathrm{d}(\mu_0 H)$ and the difference between both straight lines (at zero field) ΔR_{AHE} is a measure for the strength of the normal and anomalous Hall effect, respectively (see Fig. 5.39(b)).
The determined quantities are extrinsic variables as they explicitly include the thickness t of the stack, whereas in the case of the MR effects in R_{xx} they additionally depend on the lateral dimensions of the macroscopic wire sample. In the following the approach to achieve reasonable intrinsic quantities is described. One obstacle in the description and quantification of the magnetoresistance effects arises from the facts that the thickness of the Pt and Co layers, that are connected in parallel, are in the same order of magnitude and that Pt and Co have similar bulk resistivities (see Fig. 5.5(a)). Consequently, with varying the Co layer thickness the associated changes in the resistance of the Co layer $R_{\mathrm{Co}}(t_{\mathrm{Co}}, \rho(t_{\mathrm{Co}}))$ drastically influences the relative fraction of the current that flows through the Co and Pt layers, respectively. This thickness-dependent current distribution within the stack is superimposed on and therefore masks the actual thickness dependence of the MR effects. The challenge is to define an intrinsic quantity which provides a simple access to the underlying physics. As the extraordinary effects (AHE, AMR, GSE, and SMR) basically originate in the ferromagnetic Co layer only for the sake of convenience it is justified to exclude the Pt thickness in the definition of the intrinsic variables. Accordingly, for the three MR quantities in R_{xx} the following definitions were used:

$$\Delta\widetilde{\rho}_{i,\mathrm{Co}} = \frac{\Delta R_i \cdot t_{\mathrm{Co}} \cdot w}{l},\ i = \mathrm{ip},\ \mathrm{op}, \quad \left|\frac{\mathrm{d}\widetilde{\rho}_{\mathrm{Co}}}{\mathrm{d}(\mu_0 H)}\right|_{\mathrm{SMR}} = \frac{s_{\mathrm{SMR}} \cdot t_{\mathrm{Co}} \cdot w}{l} \tag{5.72}$$

The Hall constants were calculated according to Eq. 5.46 by:

$$\widetilde{R}_{0,\mathrm{Co}} = s_{\mathrm{OHE}} \cdot t_{\mathrm{Co}}, \quad \widetilde{R}_{S,\mathrm{Co}} = \frac{\Delta R_{\mathrm{AHE}} \cdot t_{\mathrm{Co}}}{2\mu_0 M_{\mathrm{S}}} \tag{5.73}$$

For the normal Hall constant the same definition is used as for the extraordinary effects although a contribution to the normal Hall effect also arises from the Pt layers. The reason for this is that literature values indicate that R_0 for Co compared to Pt is one order of magnitude larger (see section 5.1.4.2), so that the Pt contribution to the normal Hall constant should be negligibly small. This was checked by additionally measuring $R_{xy}(H_\mathrm{p})$ of a 5 nm thick Pt film prepared by ECR technique. As expected, a purely linear dependence of R_{xy} on H_p was observed. From the negative slope $R_{0,\mathrm{Pt}} = -(1.4 \pm 0.1) \cdot 10^{-11}$ m^3/C was calculated according to Eq. 5.73. This value is in good agreement with the results of Ref. [601], so that in fact $R_{0,\mathrm{Pt}}$ is one order of magnitude lower than $R_{0,\mathrm{Co}}$ (see next section).
It is worth mentioning that the defined intrinsic quantities still include a thickness-dependent current shunt through the Pt seed and cap layers, which masks possible dependencies on Co thickness that might be caused by the particular nature of the MR effects or by structural variations. The reason for this is that in the evaluation of the resistance $R = U/I$, difference resistances $\Delta R_i = \Delta U_i/I$, etc. the total current $I = 5$ mA and not only the fraction that propagates through the Co material I_Co is used. Thus, the quantities defined in Eqs. 5.72, 5.73 underestimate the size of the MR effects in particular for low Co thicknesses, where most of the current flows trough the Pt material. Therefore, in section 5.5.2, where a phenomenological description of the sandwich resistivity is given, a further intrinsic quantity for the various MR effects is defined, which only considers I_Co.
In order to avoid misunderstandings it is explicitly noted that $t = t_\mathrm{Co} + t_{\mathrm{Pt,\,total}}$ is used in the derivation of ρ from R in the curves of Figs. 5.37−5.40, so that e.g. the corresponding difference resistivities $\Delta\rho_\mathrm{ip}$ are unequal to $\Delta\widetilde{\rho}_{\mathrm{ip,Co}}$. Nevertheless, the statements made in the previous sections are only of qualitative nature and, hence, valid for both definitions.
For the AMR and AIMR+GSE effects the magnetoresistance ratio $\frac{\Delta R_i}{R_\mathrm{t}} = \frac{\Delta\rho_i}{\rho_\mathrm{t}} = \frac{\Delta\widetilde{\rho}_{i,\mathrm{Co}}}{\widetilde{\rho}_{\mathrm{t,Co}}}$, which is the same in both definitions of difference resistivities $\Delta\rho$ as the thickness cancels out, is another reasonable intrinsic quantity and in the case of the AMR frequently used in literature as it provides a good comprehension about the strength of the effect. However, this intrinsic quantity has the same deficit as the ones defined in Eqs. 5.72, 5.73 since its value is also superimposed by the Co thickness-dependent Pt shunt.

5.5.1.4 Thickness dependence of magnetoresistance effects

In this section the thickness dependence of the various MR effects is discussed in a qualitative sense starting with the AMR and AIMR+GSE.

AMR and AIMR+GSE: In Fig. 5.41(a) the difference resistivities $\Delta\widetilde{\rho}_{\mathrm{ip,Co}}$ and $\Delta\widetilde{\rho}_{\mathrm{op,Co}}$ and in (b) the corresponding magnetoresistance ratios are plotted versus t_Co. Both descriptions show a similar dependence on Co thickness t_Co so that they are discussed simultaneously starting with the AMR curves. Up to a Co thickness of about 10 nm the AMR strongly increases with thickness, while at higher thicknesses the slope gradually decreases, so that for $t_\mathrm{Co} \gtrsim 25$ nm a limiting value of about $\Delta\widetilde{\rho}_{\mathrm{ip,Co\,bulk}} = 0.3\ \mu\Omega$cm ($(\Delta\rho_\mathrm{ip}/\rho_\mathrm{t})_\mathrm{bulk} = 1.5\%$) is approached. The apparent

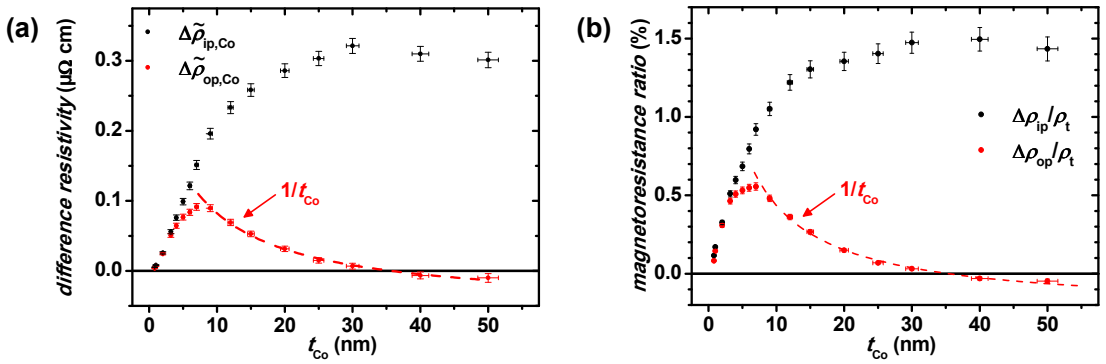

Figure 5.41: Dependence of AMR and AIMR on Co layer thickness t_{Co}. In (a) $\Delta\widetilde{\rho}_{\mathrm{ip,Co}}$ and $\Delta\widetilde{\rho}_{\mathrm{op,Co}}$ while in (b) $\Delta\rho_{\mathrm{ip}}/\rho_{\mathrm{t}}$ and $\Delta\rho_{\mathrm{op}}/\rho_{\mathrm{t}}$ are shown. The dashed lines are $1/t_{\mathrm{Co}}$ fits indicating that the AIMR originates at the Co/Pt interfaces.

increase of $\Delta\widetilde{\rho}_{\mathrm{ip,Co}}$ ($\Delta\rho_{\mathrm{ip}}/\rho_{\mathrm{t}}$) and its subsequent flattening out can be explained to a large extent by the monotonically decreasing current shunt through the Pt layers with increasing the Co layer thickness as explicitly shown in section 5.5.2. The bulk-like values of $\Delta\widetilde{\rho}_{\mathrm{ip,Co\ bulk}}$ and $(\Delta\rho_{\mathrm{ip}}/\rho_{\mathrm{t}})_{\mathrm{bulk}}$ attained for large Co thickness are within the span of values found for polycrystalline Co films [13, 838, 839, 840, 841, 553, 842]. Obviously $\Delta\widetilde{\rho}_{\mathrm{op,Co}}$ ($\Delta\rho_{\mathrm{op}}/\rho_{\mathrm{t}}$) shows a quite different behavior compared to the AMR. For small Co thicknesses $t_{\mathrm{Co}} \leq 7$ nm it increases continuously with thickness and is comparable to the AMR. For $t_{\mathrm{Co}} \geq 9$ nm, however, $\Delta\widetilde{\rho}_{\mathrm{op,Co}}$ ($\Delta\rho_{\mathrm{op}}/\rho_{\mathrm{t}}$) decreases proportionally to $1/t_{\mathrm{Co}}$ as indicated by the dashed red lines in Fig. 5.41, which are $1/t_{\mathrm{Co}}$-fits. In this thickness regime significant structural changes, which might influence the magnetoresistance can be excluded (see section 5.3). In particular, it was shown that the degree of the out-of-plane texture, which in addition to the interfaces perturbs the isotropy in the plane perpendicular to the current direction and enters $\Delta\widetilde{\rho}_{\mathrm{op}}$ via the GSE, is thickness-independent. Moreover, the leveling off of the AMR curve indicates that the thickness-dependent current shunt through the Pt has only minor influence on the actual size of the $\rho_{\mathrm{t}} < \rho_{\mathrm{p}}$ effect. Consequently, the $1/t_{\mathrm{Co}}$ behavior implies that the interior of the Co layer (bulk) does not contribute to this particular effect, which in turn means that it is essentially caused by the Co/Pt interface regions [461]. Therefore, it is appropriate to refer to this effect as anisotropic interface magnetoresistance (AIMR). To stress the point: The AIMR shows a completely different signature than any other MR effect found in polycrystalline films up to now. For $t_{\mathrm{Co}} > 35$ nm $\Delta\widetilde{\rho}_{\mathrm{op,Co}}$ becomes negative revealing the existence of another MR contribution that is superimposed on the AIMR. This effect exhibits also a $\cos^2\theta$ dependence while it is of opposite sign. These properties are typical for the GSE (see green curve in the inset of Fig. 5.40(c)) caused by the out-of-plane texture of the films. The increase of $\Delta\widetilde{\rho}_{\mathrm{op,Co}}(t_{\mathrm{Co}})$ at small thicknesses is partially caused by the increasing current that passes through the Co layer like in the AMR curve as shown in section 5.5.2. There, also the size of the GSE is discussed.
Before coming to the phenomenological description of the thickness dependence of $\rho_{xx}(\mathbf{M})$ the thickness dependence of the spin-disorder MR (SMR) and the normal and anomalous Hall constants ($\widetilde{R}_{0,\mathrm{Co}}$ and $\widetilde{R}_{S,\mathrm{Co}}$) is presented in the following.

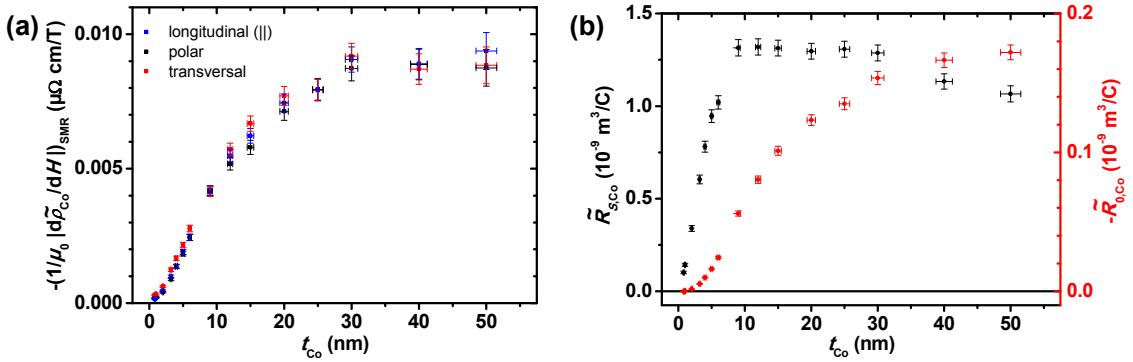

Figure 5.42: Dependence of (a) spin-disorder MR and of (b) normal and anomalous Hall constants on t_{Co}. For $t_{\mathrm{Co}} \leq 1$ nm the values for $\widetilde{R}_{0,\mathrm{Co}}$ are significantly superimposed by contributions of the AHE (see text).

SMR, OHE, and AHE: The thickness dependence of the slope $-|\mathrm{d}\widetilde{\rho}_{\mathrm{Co}}/\mathrm{d}(\mu_0 H)|_{\mathrm{SMR}}$ determined for the three generic orientations of the magnetic field is displayed in Fig. 5.42(a). It is obvious that the curves are similar for the three cases reflecting an isotropic resistance versus field behavior above technical saturation as already stated above. However, a closer look reveals that in the case of the transverse geometry the negative slope is systematically slightly larger at small Co thicknesses $t_{\mathrm{Co}} \lesssim 7$ nm. Qualitatively, the $|\mathrm{d}\widetilde{\rho}_{\mathrm{Co}}/\mathrm{d}(\mu_0 H)|_{\mathrm{SMR}}(t_{\mathrm{Co}})$ characteristic behaves like the thickness dependence of the AMR: Up to a Co thickness of about 10 nm the SMR strongly increases followed by a merging into a constant value, so that the SMR basically remains constant for $t_{\mathrm{Co}} \gtrsim 30$ nm. This behavior is partially caused by the thickness-dependent current shunt through the Pt material (see section 5.5.2 below). The bulk-like value obtained for large Co thicknesses of about $|\mathrm{d}\widetilde{\rho}_{\mathrm{Co}}/\mathrm{d}(\mu_0 H)|_{\mathrm{SMR,\,bulk}} = -(0.009 \pm 0.001)\ \mu\Omega\mathrm{cm/T}$ is similar to the literature values reported for polycrystalline Co films within the error margins of the experiment (see section 5.1.4.1 and Refs. [481, 553]).

In Fig. 5.42(b) the normal and the anomalous Hall constants versus Co thickness are shown. While the shape of the $\widetilde{R}_{0,\mathrm{Co}}(t_{\mathrm{Co}})$ curve is similar to the thickness dependence of the AMR and SMR, the $\widetilde{R}_{S,\mathrm{Co}}(t_{\mathrm{Co}})$ curve shows a stronger increase at small Co thicknesses $t_{\mathrm{Co}} \leq 9$ nm, then remains basically constant up to $t_{\mathrm{Co}} = 30$ nm, and significantly decreases at higher t_{Co}. In the two latter thickness regimes the values for the anomalous Hall constant are within the span of values reported for polycrystalline Co films (see section 5.1.4.2). The normal Hall constant obtained at high Co thicknesses of $\widetilde{R}_{0,\mathrm{Co\ bulk}} = -(1.7 \pm 0.1) \cdot 10^{-10}$ m^3/C is one order of magnitude larger than for Pt ($R_{0,\mathrm{Pt}} \approx 1.4 \cdot 10^{-11}$ m^3/C, see section 5.5.1.3) and slightly larger than the values reported for Co in literature.

Obviously the $\widetilde{R}_{S,\mathrm{Co}}(t_{\mathrm{Co}})$ curve, which even partially decreases, cannot be solely explained by a thickness-dependent current shunt through the Pt layers as the shunt monotonically decreases with increasing the Co layer thickness. Hence, this behavior clearly reveals a thickness-dependent $\widetilde{R}_{S,\mathrm{Co}}$ constant of the Co layer. Moreover, significant changes in the structural properties can be excluded in particular for $t_{\mathrm{Co}} \geq 9$ nm (see section 5.3), so that the $\widetilde{R}_{S,\mathrm{Co}}(t_{\mathrm{Co}})$ curve suggests that the Co

material closer to the Co/Pt interfaces exhibits a larger R_S compared to the interior of the Co layer. In the following, a brief overview of selected studies concerning the AHE in thin films and multilayers is given in order to classify this result. A decreasing R_S with increasing Co layer thickness was also reported by W. Gil and J. Kötzler for polycristalline Co films [580]. In the investigated thickness range of 10 nm to 188 nm they found a rather strong decrease of R_S by a factor of three, which they associated with the enhanced structural disorder in the thinner films, like larger surface roughness and increased density of grain boundaries and point defects [580]. A. Gerber et al. measured the AHE of Ni films in a similar thickness range as Kötzler and Gil ($t_{\mathrm{Ni}} = 5 - 100$ nm) and also found a strong increase of R_S with decreasing the thickness by a factor of five [843, 593, 844]. In contrast to Kötzler and Gil the authors argued that all the films of the series exhibit similar bulk properties as the difference in resistivity between room and LHe temperature is similar for all the films [843], so that the increase of R_S with shrinking t_{Ni} was attributed to the scattering of the electrons at the film surfaces. Gerber et al. separated the surface scattering contribution from the ρ_{xx}^0 term and from the AHE and found a linear relation between both surface contributions: $R_S^{\mathrm{surf}} \propto \rho_{xx}^{\mathrm{surf}}$ (see Eq. 5.47).
Besides thin films [843, 593, 844, 580, 845] significant interface contributions to the AHE were observed in Fe/Cr multilayers [846] and heterogeneous CoAg alloys [847] in connection with changes in the giant magnetoresistance (GMR) effect. Concerning Co/Pt multilayers, investigations of the AHE were performed in the ultrathin thickness regime with individual layer thicknesses $t_{\mathrm{Co}} < 2$ nm [848, 107, 12, 849]. By decreasing the Co layer thickness Canedy et al. observed a strong increase of R_S and therefore concluded that the AHE is dominated by Co/Pt interface scattering [107]. Zhang et. al. observed an oscillatory variation of R_S by varying the bilayer repetition, which they also attributed to the scattering at the Co/Pt interfaces [849]. For antiferromagnetically coupled $(\mathrm{Pt/Co})_5/\mathrm{Ru}/(\mathrm{Co/Pt})_5$ multilayers the enhancement of the AHE compared to pure Co/Pt multilayers was ascribed to the strong scattering at the Co/Ru interface [850]. Furthermore, a large enhancement of R_S was reported by capping Co/Pt multilayers with MgO [851].
The brief overview shows that significant surface and interface contributions to the AHE seem to be a more general phenomenon in thin films and multilayers, while the underlying scattering mechanisms are still under debate. The discussion of the Co thickness dependence of the AHE is continued in section 5.5.2, where strong indications for AHE contributions of the Co/Pt interfaces are presented.
Besides the above mentioned decrease of $\widetilde{R}_{S,\mathrm{Co}}$ with increasing Co thickness another feature that cannot be explained by a thickness-dependent current shunt through the Pt is that $\widetilde{R}_{0,\mathrm{Co}}$ is apparently positive for the smallest Co layer thickness of $t_{\mathrm{Co}} = 0.8$ nm (see Fig. 5.42(b)). This result is connected with the fact, already mentioned in section 5.5.1.1, that the $\rho_{xy}(H_{\mathrm{p}})$ curve clearly deviates from a straight line above technical saturation (see inset of Fig. 5.39(a)), which excludes the normal Hall effect as the reason for this behavior. However, the $\rho_{xy}(H_{\mathrm{p}})$ curve indicates a linear asymptotic behavior, whose slope might be even negative at sufficiently high fields $\gtrsim 10$ T due to the presence of the normal Hall effect. The deviation of $\rho_{xy}(H_{\mathrm{p}})$ from a linear decrease above technical saturation strongly declines with

Co layer thickness: For $t_{\mathrm{Co}} = 1$ nm the $\rho_{xy}(H_{\mathrm{p}})$ characteristic possesses a negative slope for $\mu_0|H_{\mathrm{p}}| \geq 4.5$ T, so that the effective value determined for $\widetilde{R}_{0,\mathrm{Co}}$ is already slightly negative (see Fig. 5.42(b)). Moreover, for $t_{\mathrm{Co}} = 2$ nm the complete high-field behavior ($\mu_0|H_{\mathrm{p}}| \geq 3$ T) of $\rho_{xy}(H_{\mathrm{p}})$ exhibits a negative decrease and the relative error of the linear fit is smaller than 0.5% revealing that the deviation from a straight line is negligibly small. The deviations from the linear slope above technical saturation might be interpreted in terms of a high-field susceptibility $\left(\frac{\mathrm{d}M_{\mathrm{S}}}{\mathrm{d}H_{\mathrm{p}}}\right)_{M_{\mathrm{S}}||H_{\mathrm{p}}}$ ("paraprocess" susceptibility), which enters the $\rho_{xy}(H_{\mathrm{p}})$ characteristic via the AHE effect [579]:

$$\left(\frac{\mathrm{d}\rho_{xy}}{\mu_0 \mathrm{d}H_{\mathrm{p}}}\right)_{M_{\mathrm{S}}||H_{\mathrm{p}}} = R_0 + R_S \left(\frac{\mathrm{d}M_{\mathrm{S}}}{\mathrm{d}H_{\mathrm{p}}}\right)_{M_{\mathrm{S}}||H_{\mathrm{p}}} \tag{5.74}$$

For room temperature regarding bulk Co the latter term is negligibly small compared to R_0 as $M_{\mathrm{S}}(T)$ resembles $M_{\mathrm{S}}(0)$ in a good approximation (see Bloch's $T^{3/2}$ law, Eq. 5.39). However, for Co/Pt layered structures the Curie temperature of the (interdiffused) Co/Pt interface regions is reduced compared to the interior of the Co layer, which exhibits M_{S} of bulk Co, as discussed in connection with the polarization of the Pt material in section 5.3.2.2. Consequently, at the interfaces the applied field can significantly enhance M_{S} over the spontaneous value at $H = 0$ and as $R_S \gg R_0$ applies the second term in Eq. 5.74 might dominate at small Co thicknesses. In order to examine if the high-field behavior of $\rho_{xy}(H_{\mathrm{p}})$ contains significant contributions caused by a non-vanishing high-field susceptibility the $\rho_{xy}(H_{\mathrm{p}})$ curves were compared with the polar MOKE curves. As can be seen in Fig. 5.39(a) for the thinnest Co layer thickness of $t_{\mathrm{Co}} = 0.8$ nm both curves are basically identical and display a relative increase of about 3% in the field range of $\mu_0|H_{\mathrm{p}}| = 0.1 - 0.9$ T, where the samples are by all means in a single-domain state. Hence, for this sample the $\rho_{xy}(H_{\mathrm{p}})$ curve is dominated by the second term in Eq. 5.74. For $t_{\mathrm{Co}} = 2$ nm, however, $\theta(H_{\mathrm{p}})$ resembles the curve, which is obtained after subtracting the curve from $\rho_{xy}(H_{\mathrm{p}})$, which linearly extrapolates its high-field behavior above technical saturation to zero field (see Fig. 5.29(b)). This finding clearly reveals the minor influence of the high-field susceptibility term compared to $\widetilde{R}_{0,\mathrm{Co}}$ for $t_{\mathrm{Co}} \geq 2$ nm.
In summary, for $t_{\mathrm{Co}} < 2$ nm significant contributions caused by the high field susceptibility of the Co/Pt interface regions are superimposed on the normal Hall effect. With increasing t_{Co} the relative contribution of the Co/Pt interface region to the total Hall signal and, thus, the influence of the high field susceptibility strongly decreases and the bulk-like material within the Co layer begins to dominate, so that for $t_{\mathrm{Co}} \geq 2$ nm the linear high-field characteristic of $\rho_{xy}(H_{\mathrm{p}})$ is solely determined by the normal Hall effect. The high field susceptibility can account for positive effective values of R_0 reported for multilayers [848, 107, 852, 851], alloys [853, 854], embedded clusters [593, 854], and thin films [855][53].
In the following section the discussion of the thickness dependence of the various

[53] Note, that a positive slope of $\rho_{xy}(H_{\mathrm{p}})$ above saturation does not necessarily indicate a significant contribution of the high-field susceptibility as e.g. Fe, FeCr alloys, and Fe/Cr multilayers exhibit a positive normal Hall constant R_0 [856, 589, 857, 855].

MR effects, which is not readily apparent without the elimination of the current shunt through the Pt, is continued (section 5.5.2.2).

5.5.2 Phenomenological description of sandwich resistance

In the first section 5.5.2.1, the developed model and its applicability to describe the sandwich resistance is presented. The model enables the determination of the Co thickness-dependent current shunt through the Pt, thus allowing its elimination in order to obtain the pure thickness dependence of the MR effects. This is shown in section 5.5.2.2, where, afterwards, also the thickness dependence of the various MR effects is presented and discussed. In the case of the AMR and AIMR the experimental curves are compared with the results of a fully relativistic spin-polarized *ab initio* theoretical description of $\rho_{xx}(\mathbf{M})$ for ideal Pt/Co$_n$/Pt sandwiches ($n \leq 90$ monolayers, $T = 0$ K), which was performed in connection with this thesis (see Ref. [E7] given in the attachments). Finally, the phenomenological model is applied in section 5.5.2.3 in order to quantify the magnetic scattering anisotropy at the Co/Pt interfaces caused by the presence of the AIMR effect.

5.5.2.1 Combination of parallel current model and Fuchs-Sondheimer model

The first integral part of the phenomenological model is the assumption that the resistance R of the Pt/Co/Pt sandwiches can be regarded as consisting of two resistors, one resistor R_{Co} for the Co layer and one resistor R_{Pt} for the Pt layers, which are connected in parallel:

$$I = I_{\mathrm{Co}} + I_{\mathrm{Pt}} \Leftrightarrow R(t_{\mathrm{Co}}, \mathbf{M}) = \left(\frac{1}{R_{\mathrm{Co}}(t_{\mathrm{Co}}, \mathbf{M})} + \frac{1}{R_{\mathrm{Pt}}} \right)^{-1} \tag{5.75}$$

The Pt is regarded to be fully unpolarized ($\mathbf{M} = 0$) and as the Pt thickness was held constant in the experiment R_{Pt} provides a constant contribution to the overall resistance R. The second integral part of the model is the implementation of the scattering at the two Co/Pt interfaces by utilizing the phenomenological Fuchs-Sondheimer model (see section 5.1.2). The interface scattering is incorporated by expressing the resistivity of the Co layer $\rho_{\mathrm{Co}}(t_{\mathrm{Co}}, \mathbf{M})$ of $R_{\mathrm{Co}}(t_{\mathrm{Co}}, \mathbf{M}) = \rho_{\mathrm{Co}}(t_{\mathrm{Co}}, \mathbf{M}) \cdot t_{\mathrm{Co}} w/l$ according to Eq. 5.25:

$$\begin{aligned} \sigma_{\mathrm{Co}}(t_{\mathrm{Co}}, p_m, \sigma_{m,\mathrm{bulk}}, \lambda_{\mathrm{m,bulk}}) &= \sigma_{m,\mathrm{bulk}} \times \\ \times \left(1 - \frac{3}{2} \frac{\lambda_{m,\mathrm{bulk}}}{t_{\mathrm{Co}}} (1 - p_m) \int_1^\infty \frac{\left(\frac{1}{x^3} - \frac{1}{x^5}\right) \left(1 - \exp(-\frac{t_{\mathrm{Co}}}{\lambda_{m,\mathrm{bulk}}} x)\right)}{1 - p_m \exp(-\frac{t_{\mathrm{Co}}}{\lambda_{m,\mathrm{bulk}}} x)} dx \right) \end{aligned} \tag{5.76}$$

The index m represents the dependence of the quantities on the magnetization orientation, namely $m = (t, ||, p)$ for the three generic orientation of $\mathbf{M}$ with respect to the current and stacking direction. Thereby, it has to be considered that the Co bulk resistivity $\rho_{m,\mathrm{bulk}} = 1/\sigma_{m,\mathrm{bulk}}$ and the (Co bulk) mean free path $\lambda_{m,\mathrm{bulk}}$ are functionally related to each other via the electron density (see Eq. 5.26). As the electrical transport in Co is dominated by the free-electron-like s electrons Eq. 5.26

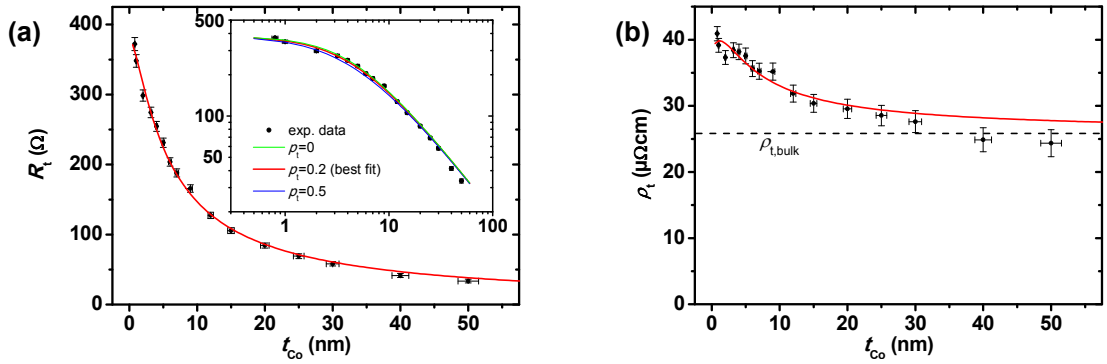

Figure 5.43: (a) Resistance R_t versus Co layer thickness. The red line is a fit according to the layer model (see text) yielding the values of the parameters given in Eq. 5.78. The inset displays $R_t(t_{Co})$ and the fit in double logarithmic scale. Besides, model curves for $p_t = 0$ and $p_t = 0.5$ are displayed for comparison. (b) displays the resistivity $\rho_t(t_{Co}) = R_t(t_{Co}) \cdot \frac{(t_{Co}+t_{Pt})w}{l}$ calculated from the curves shown in (a). The dashed line marks $\rho_{t,bulk}$.

may be utilized in a good approximation, which is the result for a quasi free electron gas [471, 580]. Using the electron density of $n^* = 3.7 \cdot 10^{28}$ m^{-3}, which was calculated according to Eq. 5.45 from the bulk-like normal Hall constant of Co ($\widetilde{R}_{0,\mathrm{Co\ bulk}} = (1.7 \pm 0.1) \cdot 10^{-10}$ m^3/C, see previous section), the number of independent variables in Eq. 5.76 was reduced by:

$$\lambda_{m,\mathrm{bulk}} \cdot \rho_{m,\mathrm{bulk}} = 1145 \cdot 10^{-18}\ \Omega\mathrm{m}^2 \tag{5.77}$$

It is worth mentioning that the scattering at the Pt/vacuum and SiO_2/Pt interfaces is included in the value of R_{Pt}. Furthermore, grain boundary scattering e.g. described by the model of Mayadas and Shatzkes (see Eq. 5.28) was not explicitly considered as the grain size remains constant within the whole thickness range (see section 5.3.1.1). Thus, grain boundary scattering only provides a thickness-independent scattering contribution in the parameters R_{Pt} and $\rho_{m,bulk}$.
In a first step the model was used to fit the thickness dependence of the overall resistance in order to examine its applicability for describing the electrical transport of the sandwich structure. Fig. 5.43(a) displays the transverse resistance R_t as a function of t_{Co}[54]. As can be seen the resistance monotonically decreases with thickness. The solid line represents the fit according to Eqs. 5.75−5.77. It is evident from the good accordance between experimental data and fit that the model describes the $R_t(t_{Co})$ curve quite well. From the fit the following values of the parameters were obtained:

$$R_{Pt} = (380 \pm 10)\ \Omega, \quad \rho_{t,bulk} = (26 \pm 2)\ \mu\Omega\ \mathrm{cm}, \quad p_t = (0.2 \pm 0.2) \tag{5.78}$$

According to Eq. 5.77 $\rho_{t,bulk}$ corresponds to a (bulk) mean free path of the electrons within the Co material of $\lambda_{t,bulk} = (4.4 \pm 0.4)$ nm. This value is about half the size of the lateral grain size of (11 ± 2) nm (see Tab. 5.2), so that the major scattering

[54]The specification of the magnetic state is only of minor importance as in this study the AIMR- and AMR-ratios are always $\leq 1.5\%$.

contributions seems to exist within the grains.
The inset of Fig. 5.43(a) shows the $R_\mathrm{t}(t_\mathrm{Co})$ curve in double logarithmic scale. The red line is the fit ($p_\mathrm{t} = 0.2$) and the two other lines are model curves with specularity parameters $p_\mathrm{t} = 0$ and $p_\mathrm{t} = 0.5$, respectively, whereas the other model parameters were held constant. Obviously the three model curves are nearly identical revealing the insensitivity of the curve on the choice of p_t especially for $t \gtrsim \lambda_\mathrm{t,bulk}$, where the relative contribution of interface scattering processes to the overall resistivity is small. However, a specularity parameter close to zero is reasonable according to Soffer's model (see Eq. 5.29) as the roughness of the Co/Pt interfaces of $\sigma_\mathrm{RMS} = (2 \pm 1)$ Å is similar to the Fermi wave length of $\lambda_\mathrm{F} \approx 6$ Å. The latter was deduced from $n^*/\ \widetilde{R}_{0,\mathrm{Co\ bulk}}$ according to Eq. 5.14 via $\lambda_\mathrm{F} = 2\pi/k_\mathrm{F}$ [443].
Fig. 5.43(b) displays the thickness dependence of the resistivity $\rho_\mathrm{t}(t_\mathrm{Co}) = R_\mathrm{t}(t_\mathrm{Co}) \cdot \frac{(t_\mathrm{Co}+t_\mathrm{Pt})w}{l}$ calculated from both the experimental data and the fit, again revealing a good correspondence of the model with the experiment within the whole thickness range down to 0.8 nm, where most of the Co material is interdiffused with the Pt. One reason why the simple layer model apparently applies even for ultrathin Co layer thicknesses is that most of the current runs through the Pt layers in this thickness regime, i.e., $R_\mathrm{Co} \gg R_\mathrm{Pt}$ applies. For instance, according to the results of the fitting, the fraction of the current through the Co layer is $I_\mathrm{Co}/I < 7\%$ for $t_\mathrm{Co} \leq 1$ nm (see Fig. 5.44 below), so that the overall sandwich resistance (resistivity) is very insensitive on changes in ρ_Co, which might be additionally caused by deviations from the perfect layer structure whose contributions to (the average) ρ_Co are relatively large in the ultrathin thickness regime.
Regarding the Co thickness-driven changes in the residual strain within the Co layer, which are significantly reflected in the anisotropy constants for $t_\mathrm{Co} \lesssim 5$ nm (see section 5.3.2.1), they are virtually invisible in the $R_\mathrm{t}(t_\mathrm{Co})$ (and $\rho_\mathrm{t}(t_\mathrm{Co})$) curve. An insensitivity of R_t caused by a too low current fraction through the Co layer (relatively high R_Co compared to R_Pt) can be ruled out to be the only reason for the invisibility as e.g. for $t_\mathrm{Co} = 4$ nm already $\approx 34\%$ of the current propagates through the Co (see Fig. 5.44 below). This observation can be rather comprehended as, in general, elastic deformations of the crystal lattice have only a small impact on the overall resistivity of metals [858]. Under hydrostatic pressure (compression of the crystal lattice) the resistance of most metals decreases, while the resistance mostly increases when the metals are elastically stretched (tension of the crystal lattice) [859, 860, 858]. For bulk Co the relative change in resistance is similar to the relative elastic deformation [858], so that for the expected changes in the residual strain in the range of 1% with increasing the Co layer thickness the corresponding changes in the resistance are negligibly small.
As shown in the next section 5.6 compared to the phonon and magnon contributions the scattering of the electrons at static defects dominates the resistance even at room temperature. Thus, the suitability of the model to describe the thickness dependence of the overall resistance indicates that the structural disorder (point defects, grain boundaries, surfaces/interfaces etc.), which provides the scattering centers for the electrons of static origin, is similar for all the samples of the series in accordance with the results of the structural investigations (see section 5.3.1).

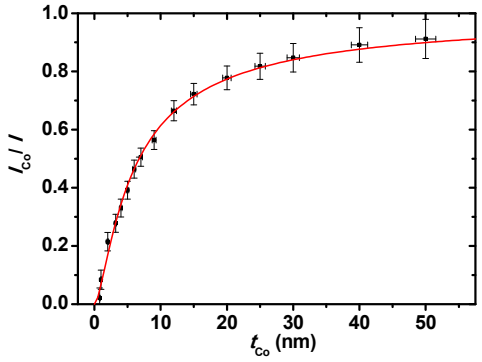

Figure 5.44: Fraction of the current I_{Co}/I that flows through the Co layer as a function of t_{Co} deduced from the experimental $R_{\mathrm{t}}(t_{\mathrm{Co}})$ curve and its fit (cycles and solid line, respectively).

5.5.2.2 Elimination of current shunt - pure thickness dependence of MR effects

For the description of the AIMR and the other MR effects it would be advantageous if the Pt shunt, which is superimposed on the actual thickness dependence of these effects, could be eliminated. In order to achieve this goal in the definitions of the intrinsic quantities of Eqs. 5.72, 5.73 the total current I has to be replaced by the part of the current I_{Co} that flows through the Co material as already discussed in section 5.5.1.3:

$$\Delta\rho_{i,\mathrm{Co}} = \frac{\Delta U_i \cdot t_{\mathrm{Co}} \cdot w}{I_{\mathrm{Co}} \cdot l} = \Delta\widetilde{\rho}_{i,\mathrm{Co}} / \frac{I_{\mathrm{Co}}}{I},\ i = \mathrm{ip},\ \mathrm{op},$$

$$-\left|\frac{\mathrm{d}\rho_{\mathrm{Co}}}{\mathrm{d}(\mu_0 H)}\right|_{\mathrm{SMR}} = -\left|\frac{\mathrm{d}\widetilde{\rho}_{\mathrm{Co}}}{\mathrm{d}(\mu_0 H)}\right|_{\mathrm{SMR}} / \frac{I_{\mathrm{Co}}}{I},\quad R_{k,\mathrm{Co}} = \widetilde{R}_{k,\mathrm{Co}} / \frac{I_{\mathrm{Co}}}{I},\ k = 0,\ S \qquad (5.79)$$

Within the framework of the parallel current model the scaling factor $I_{\mathrm{Co}}(t_{\mathrm{Co}})/I$ can be simply deduced from Eq. 5.75 to

$$\left(\frac{I_{\mathrm{Co}}(t_{\mathrm{Co}})}{I}\right)_m = \frac{R_{\mathrm{Pt}} - R_m(t_{\mathrm{Co}})}{R_{\mathrm{Pt}}}\quad , \qquad (5.80)$$

where R_{Pt} is the resistance of the Pt material obtained from the $R_{\mathrm{t}}(t_{\mathrm{Co}})$ fit (see Eq. 5.78). Actually $I_{\mathrm{Co}}/I(t_{\mathrm{Co}})$ depends on the orientation (and magnitude) of $\mathbf{M}$. However, the longitudinal MR effects alter the resistivity of the Co layer only by $\leq 1.5\%$, so that the variations in the current shunt due to changes in the orientation of $\mathbf{M}$ are small and can be neglected in particular in the definition of the intrinsic quantities in a good approximation. Within this study, $R_m = R_{\mathrm{t}}$ was used. Fig. 5.44 shows $I_{\mathrm{Co}}/I(t_{\mathrm{Co}})$ calculated from the experimental $R_{\mathrm{t}}(t_{\mathrm{Co}})$ curve and deduced from its fit. Obviously $I_{\mathrm{Co}}/I(t_{\mathrm{Co}})$ qualitatively resembles the shape of the thickness dependence of $\Delta\widetilde{\rho}_{\mathrm{ip,\ Co}}$ (AMR), $-|\mathrm{d}\widetilde{\rho}_{\mathrm{Co}}/\mathrm{d}(\mu_0 H)|_{\mathrm{SMR}}$, and $\widetilde{R}_{0,\mathrm{Co}}$ (see Figs. 5.41, 5.42), hence, revealing that at least a part of their thickness dependence can be explained by the Co thickness-dependent shunt through the Pt.
In the following the pure thickness dependence of the various MR effects corrected

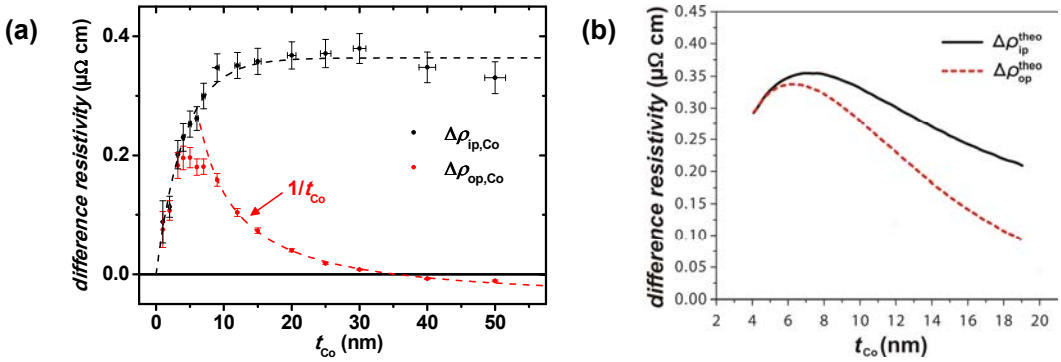

Figure 5.45: (a) AMR and AIMR corrected by the current shunt through the Pt, i.e., $\Delta\rho_{\mathrm{ip,Co}}$ and $\Delta\rho_{\mathrm{op,Co}}$, in dependence of t_{Co}. The black (red) dashed line is an exponential ($1/t_{\mathrm{Co}}$) fit to $\Delta\rho_{\mathrm{ip,Co}}$ ($\Delta\rho_{\mathrm{op,Co}}$ for $t_{\mathrm{Co}} \geq 9$ nm). (b) Results of the *ab initio* calculations [E7]: Difference resistivities $\Delta\rho_{\mathrm{ip,Co}}^{\mathrm{theo}}$ and $\Delta\rho_{\mathrm{op,Co}}^{\mathrm{theo}}$ as a function of t_{Co}.

by the current shunt is discussed, starting with the AMR and AIMR. Thereby, the results for $t_{\mathrm{Co}} = 0.8$ nm are omitted as the relatively large error in I_{Co}/I does not enable a reasonable determination.

AMR and AIMR+GSE: In Fig. 5.45(a) the difference resistivities $\Delta\rho_{\mathrm{ip,Co}}$ and $\Delta\rho_{\mathrm{op,Co}}$ are displayed versus Co layer thickness. At first, the pure thickness dependence of the AMR is discussed. For $t_{\mathrm{Co}} \geq 9$ nm the AMR remains constant within the error margins of the experiment with a value of $\Delta\rho_{\mathrm{ip,Co\ bulk}} \approx 0.36\ \mu\Omega$cm, while for smaller thicknesses a rather strong increase with t_{Co} occurs, so that for $t_{\mathrm{Co}} = 3.2$ nm the AMR is more than half the size as the bulk-like value attained for large Co thicknesses. In the whole thickness range the AMR can be phenomenologically described by an exponential law $\Delta\rho_{\mathrm{ip,Co}}(t_{\mathrm{Co}}) = \Delta\rho_{\mathrm{ip,Co\ bulk}}(1 - \exp(-t_{\mathrm{Co}}/\xi_{\mathrm{AMR}}))$ with a characteristic length of $\xi_{\mathrm{AMR}} = (4.2 \pm 0.3)$ nm as indicated by the black dashed line, which is the corresponding fit to the data. The characteristic length resembles the mean free path $\lambda_{\mathrm{t,bulk}} = (4.4 \pm 0.4)$ nm determined for the Co layer (see text in connection with Eq. 5.78). In the following the thickness dependence of the AMR is discussed. As already stated in section 5.1.4 it was frequently found for thin films that the resistivity difference caused by the AMR does not depend on film thickness. For instance, T. R. McGuire and R. I. Potter found no significant changes in $\Delta\rho_{\mathrm{ip}}$ for Ni based alloys down to film thicknesses of 5 nm [13]. This implies that for the scattering of the electrons at the surfaces anisotropic scattering contributions are zero, which is expected for varying the magnetization within the film plane because of symmetry reasons (see above). However, as the surface/interface atoms exhibit a different coordination chemistry compared to the atoms within the Co layer the spin-orbit coupling is affected, so that the scattering processes at the interfaces might provide a different $\Delta\rho_{\mathrm{ip}}$. Therefore, the overall $\Delta\rho_{\mathrm{ip}}$ might change with thickness even when the structural properties does not change. In conjunction with this thesis it was shown in terms of a fully relativistic spin-polarized ab initio-type approach that in ideal Pt(111)/Co_n/Pt(111) sandwiches ($20 \leq n \leq 90 \leftrightarrow 4.1$ nm $\leq t_{\mathrm{Co}} \leq 19$ nm) the Co/Pt interfaces act like extended area defects from a scattering point of view, which provide, besides a resistivity,

a conventional AMR according to Eq. 5.37 with $\rho_{||} > \rho_{\mathrm{t}}$ [E7][55]. Moreover, as can be seen in Fig. 5.45(b) the size of $\Delta\rho_{\mathrm{ip}}$ is comparable to the experimental findings. Up to $t_{\mathrm{Co}} \approx 6$ nm the AMR slightly increases and reaches a maximum value of $\Delta\rho^{\mathrm{theo}}_{\mathrm{ip,\,max}} = 0.36\ \mu\Omega$cm, while for higher thicknesses it decreases with $1/t_{\mathrm{Co}}$. The different asymptotic behavior compared to the experiment can be explained by the different sample quality. In the calculations a perfect crystal structure is assumed, so that the resistivity and thus the difference resistivity merge to zero in the limit of infinite Co thickness at $T = 0$ K. In the experiment, however, the static and dynamic deviations from the perfect crystal lattice provide AMR contributions within the interior of the Co layer. Thus, the apparently good agreement between theory and experiment concerning the size of $\Delta\rho_{\mathrm{ip}}$ at low Co thicknesses might be rather coincidental as interface contributions to the AMR are not readily apparent in the experimental curve of Fig. 5.45(a). In the "real" samples the theoretically proposed interface contributions are either masked by the bulk contributions or even suppressed as a consequence of deviations from atomically sharp Co/Pt interfaces. For details about the theoretical treatment the reader is referred to the attachments, where the corresponding publication can be found.

Even if the theoretically proposed AMR of the Co/Pt interfaces is absent in the experiment the CoPt interdiffusion regions might exhibit a different value for $\Delta\rho_{\mathrm{ip}}$ compared to the interior of the Co layer, which might contribute to the observed increase of $\Delta\rho_{\mathrm{ip}}$ at low Co thicknesses. Investigations of the AMR of (ferromagnetic) $\mathrm{Co}_{1-x}\mathrm{Pt}_x$ alloys at $T < 10$ K show that $\Delta\rho_{\mathrm{ip}} > 0$ applies for any composition x, while the actual value strongly depends on x [839, 861, 542]. The relative change in $\Delta\rho_{\mathrm{ip}}$ is similar to the relative change in the overall resistivity ρ with x, such that the AMR ratio $\Delta\rho_{\mathrm{ip}}/\rho$ only slightly depends on x ranging from about $0.3 - 1\%$. ρ basically describe an inverted parabola ($\rho(x) \propto x(1-x)$, Nordheim's rule [862, 397]) with a maximum value of $\rho \approx 40\ \mu\Omega$cm at about $x = 30 - 40$ at.% and a minimum value of $\rho \approx 2\ \mu\Omega$cm for $x = 0$ (pure Co). These findings show that the alloyed interface regions might provide a higher $\Delta\rho_{\mathrm{ip}}$ compared to the value within the interior of the Co layer, so that the increase of the overall $\Delta\rho_{\mathrm{ip}}$ observed for $t_{\mathrm{Co}} < 9$ nm cannot be explained by the decrease of the relative contribution of the CoPt interdiffusion zone to the AMR.

The characteristic length describing the increase of the AMR ($\xi_{\mathrm{AMR}} \approx 4 - 5$ nm) basically resembles the thickness up to where strong indications for strain relaxation processes within the Co material were found (see section 5.3.2). Investigations concerning the influence of elastic deformations (compression or unidirectional tension) on the AMR are rare in literature [528, 527, 863, 864]. Generally, these studies do not explicitly deal with the investigation of the influence of the strain on the size of $\Delta\rho_{\mathrm{ip}}$ [13]. They rather focus on the resistance versus pressure/ tension curves, which are governed by the AMR effect as remagnetization processes occur that are initiated by the deformation due to the magnetostriction of the samples ("elastoresistance"). However, it can be estimated from these investigations and it is explicitly shown in the case of several Fe alloys [865, 866, 867] that the AMR-ratio is basically unaffected

[55] This result is in accordance with the description of the AMR of thin films in the framework of extended Fuchs-Sondheimer models, where also an increase of $\Delta\rho_{\mathrm{ip}}$ with decreasing thickness is reported [613, 522].

by elastic deformations. As also the overall resistance is only slightly influenced by strain as stated in the previous section the same holds for $\Delta\rho_{\mathrm{ip}}$. These findings show that significant influences of the strain on AMR seem to be unlikely, so that the observed changes in residual strain cannot account for the rather strong increase of $\Delta\rho_{\mathrm{ip}}$ with increasing Co thickness. The reason for the increase of the AMR, which was also observed in the theoretical study (Ref. [E7]) as stated above, is unknown so far. However, as variations in the structural properties are unlikely to be the reason, which can be excluded anyway in the theoretical treatment, strong indications are given that the increase of the AMR might be an effect of finite size.
In the following the thickness dependence of $\Delta\rho_{\mathrm{op}}$ is discussed (see Fig. 5.45(a)). Obviously $\Delta\rho_{\mathrm{op}}$ is similar to the AMR at low Co thicknesses $t_{\mathrm{Co}} \leq 3.2$ nm, while for $3.2 \leq t_{\mathrm{Co}} \leq 7$ nm a plateau is reached, where it exhibits a maximum value of $\Delta\rho^{\mathrm{exp}}_{\mathrm{op,\,max}} \approx 0.2\ \mu\Omega$cm. In the thickness region $t_{\mathrm{Co}} \geq 9$ nm, where the AMR remains constant and significant structural changes can be ruled out, $\Delta\rho_{\mathrm{op}}$ decays with $1/t_{\mathrm{Co}}$ confirming that the $\Delta\rho_{\mathrm{op}} > 0$ effect is caused by the Co/Pt interface region. The merging into a constant value with $\Delta\rho_{\mathrm{op}} < 0$ in the limit of infinite Co layer thickness reveals the presence of the GSE, whose size is discussed in section 5.5.2.3. Coming back to the *ab initio* study, which deals with the resistivity of Pt(111)/Co$_n$/Pt(111) sandwiches [E7], the results of the calculations show that, besides a conventional AMR ($\Delta\rho_{\mathrm{ip}} > 0$), the ideal Co/Pt interfaces provide a resistivity anisotropy when the magnetization reorientates within the plane perpendicular to the current direction according to Eq. 5.70 with the same sign as found in the experiment, namely $\Delta\rho_{\mathrm{op}} > 0$ (see Fig. 5.45(b)). Furthermore, the size of the effect and the shape of the theoretical $\Delta\rho_{\mathrm{op}}(t_{\mathrm{Co}})$ curve are comparable to the experimental findings. Similar to the theoretical curve of the conventional AMR $\Delta\rho_{\mathrm{op}}(t_{\mathrm{Co}})$ was found to slightly increase up to $t_{\mathrm{Co}} \approx 6$ nm reaching a maximum value of $\Delta\rho^{\mathrm{theo}}_{\mathrm{op,\,max}} = 0.33\ \mu\Omega$cm, while for higher thicknesses it decreases with $1/t_{\mathrm{Co}}$. Just like for the AMR the reason for the observed increase of $\Delta\rho_{\mathrm{op}}(t_{\mathrm{Co}})$ is unknown so far. Despite the qualitative agreement between experiment and theory concerning $\Delta\rho_{\mathrm{op}}$ it has to be kept in mind that the different structural quality of the interfaces (interdiffusion and strain) as well as the finite temperature in the experiment might have significant impacts on the AIMR. However, it is shown in section 5.5.3 and section 5.6.4 that at least strain and temperature variations, respectively, have only minor influence on $\Delta\rho_{\mathrm{op}}$.
In the following, the thickness dependence of the SMR and of the Hall constants is briefly discussed.

SMR, OHE, and AHE: Fig. 5.46(a) displays $-|\mathrm{d}\rho_{\mathrm{Co}}/\mathrm{d}(\mu_0 H)|_{\mathrm{SMR}}$ versus Co thickness that is corrected by the Pt current shunt. As the spin-disorder MR is isotropic only the values obtained from the polar MR curves are shown here for the sake of convenience. Despite the elimination of the current shunt the SMR increases with thickness by a factor of five in the range of up to $t_{\mathrm{Co}} \approx 20$ nm, while for higher thicknesses it remains constant with $-|\mathrm{d}\rho_{\mathrm{Co,bulk}}/\mathrm{d}(\mu_0 H)|_{\mathrm{SMR}} = -(0.010 \pm 0.001)\ \mu\Omega$cm/T. Similar to the AMR the thickness dependence of the SMR can be phenomenologically described by an exponential law $-|\mathrm{d}\rho_{\mathrm{Co}}/\mathrm{d}(\mu_0 H)|_{\mathrm{SMR}}(t_{\mathrm{Co}}) = -|\mathrm{d}\rho_{\mathrm{Co,bulk}}/\mathrm{d}(\mu_0 H)|_{\mathrm{SMR}}(1 - \exp(-t_{\mathrm{Co}}/\xi_{\mathrm{SMR}}))$ yielding the characteristic length of $\xi_{\mathrm{SMR}} = (7.7 \pm 0.5)$ nm, which is larger than for the AMR. To current knowledge a

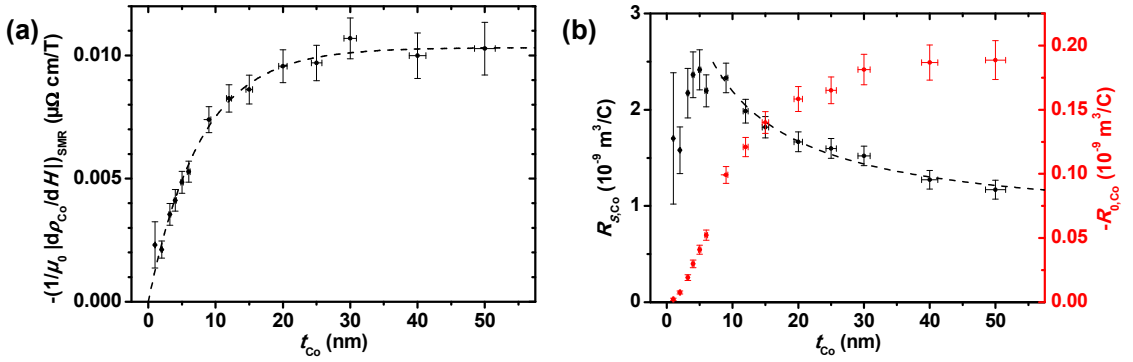

Figure 5.46: Dependence of (a) spin-disorder MR obtained from the polar MR curves and of (b) normal and anomalous Hall constants on t_{Co} corrected by the current shunt through the Pt. The black dashed line in (a) is an exponential fit, while in (b) it is a $1/t_{\mathrm{Co}}$ fit to the AHE data for $t_{\mathrm{Co}} \geq 9$ nm.

thickness dependence of the spin-disorder MR is unknown in literature, however, the known investigations are restricted to thicknesses $\gtrsim 7$ nm, where the SMR was found to be basically constant within this study. For instance, the elaborate investigations of Raquet et al. already presented in section 5.1.4.1 studied the thickness range from 1 μm down to 7 nm [481]. A possible explanation of the apparent thickness dependence of the SMR might be the presence of the linear positive magnetoresistance effect (LPMR) which can be superimposed on the SMR. Opposite to the SMR according to its name the LPMR causes an (isotropically) linear increase of the resistivity with increasing the absolute value of the applied magnetic field above technical saturation. The LPMR was recently discovered by A. Gerber et al. in thin films of Co, Fe, Ni, and their alloys for thicknesses in the range of $3-15$ nm for fields of up to 60 T [868]. A linear increase of the resistivity with field, i.e., a dominant LPMR, was only observed in the low temperature regime $T \leq T_{\mathrm{min}}$, $T_{\mathrm{min}} \lesssim 100$ K, while the actual value of T_{min} depends on the thickness and the kind of material. In this temperature regime significant contributions of the SMR can be ruled out as most of the magnons are frozen out. The LPMR was found to be temperature independent for $T \leq T_{\mathrm{min}}$ and the size of the LPMR was estimated from the $\rho_{xx}(H)$ curves given in Ref. [868] to be in the range of $0.001-0.005$ $\mu\Omega$cm/T. The thickness dependence of the size of the LPMR is not accessible from the publication, so that a comparison with the thickness dependence of the size of the slope displayed in Fig. 5.46(a) is not possible. However, the LPMR is unlikely to exist in the Co/Pt samples anyway as explained in the following. Significant contributions of the LPMR were not reported in Ref. [868] for $T > T_{\mathrm{min}}$ and the negative slope of the $\rho_{xx}(H)$ curve of a 10 nm thick Fe film measured at $T = 221$ K presented in the publication basically resembles the expected value for the SMR of Fe. More importantly, in the temperature regime $T \leq T_{\mathrm{min}}$, where the LPMR exists, the resistivity was found to increase logarithmically with decreasing temperature, while for $T > T_{\mathrm{min}}$ the resistivity monotonically increases with temperature. Thereby, the position of the absolute minimum of ρ_{xx} at T_{min} does not depend on the strength of the applied magnetic field. This behavior is typical for the electron-electron interaction in two-dimensional systems (see section 5.1.3.3), so that the authors argued that the

LPMR is a further consequence of this interaction due to the tight correlation between the logarithmic variation of $\rho_{xx}(T)$ and the existence of LPMR. In fact, they qualitatively showed that the $2D$ electron-electron interaction reproduces both the logarithmic decrease of $\rho_{xx}(T)$ and the LPMR. In contrast, the Co/Pt samples of this thesis exhibit a monotonically increasing $\rho_{xx}(T)$ behavior down to 2 K as shown in section 5.6.1, so that contributions of the $2D$ electron-electron interaction to the resistivity can be excluded in the whole temperature range. Therefore, the LPMR effect can be ruled out to be the reason for the observed thickness dependence of $-|\mathrm{d}\rho_{\mathrm{Co}}/\mathrm{d}(\mu_0 H)|_{\mathrm{SMR}}$, which in turn implies that the SMR effect depends on the Co layer thickness.
Structural changes can be ruled out as a possible reason for the thickness dependence of the SMR as structural variations might only have minor influences on the SMR as argued in Ref. [481], which can be excluded anyway for $t_{\mathrm{Co}} \gtrsim 5$ nm, while the SMR increases up to a thickness of $t_{\mathrm{Co}} \approx 20$ nm. In fact, the SMR was found to be basically the same for Co samples with a residual resistance ratio (RRR, see Eq. 5.19) of 27 and below two [481, 553]. Thus, the thickness dependence of the SMR indicates that either the field induced spin-wave damping or rather the electron-magnon scattering is suppressed at low Co thicknesses. The latter might be a consequence of a thickness-driven variation of the magnon-spectrum as frequently observed for thin films [869, 870, 871]. The discussion of the thickness dependence of the SMR is taken up in connection with the results of section 5.6.1.
Besides the AMR and SMR a decrease with decreasing thickness was also observed for the absolute value of $R_{0,\mathrm{Co}}$ as can be seen in Fig. 5.46(b). In the thickness regime $2\ \mathrm{nm} \leq t_{\mathrm{Co}} \leq 30\ \mathrm{nm}$, where significant influences of the high field susceptibility can be ruled out (see section 5.5.1.4), which might otherwise yield an underestimation of $R_{0,\mathrm{Co}}$, the absolute value of the normal Hall constant increases by more than a factor of 20. However, in contrast to the thickness dependence of the AMR and SMR the $R_{0,\mathrm{Co}}(t_{\mathrm{Co}})$ curve cannot be solely described by an exponential law, so that a corresponding fitting is omitted here. In the following, the thickness dependence of the normal Hall constant is briefly placed within the context of other studies. From a theoretical point of view Sondheimer described, besides the zero field resistivity $\rho^{(0)}$, the thickness dependence of the normal Hall constant by implementing a perpendicular magnetic field in the FS-model [872, 416]. This extended FS-model predicts an increase in the absolute value of the Hall constant with decreasing thickness, which is, although predicted to be less rapidly than the increase of $\rho^{(0)}$, in contradiction to the experimental finding of this study. However, it was frequently argued in literature that in Sondheimer's descriptions the confinement of the electron system in thin films and the corresponding discretization of energy and momentum is not considered [873, 874, 875, 876]. This might be important for $t \lesssim \pi\lambda$, where λ is the mean free path, so that quantum-size effect occurs [874]. D. Calecki solved the Boltzmann equation for thin films in the presence of perpendicular magnetic fields by considering a quantized momentum $k_\nu = \nu\pi/t$ along the direction of the film normal in the case that the electrons are elastically scattered at surfaces which exhibit a certain kind of roughness. One of his result is that the normal Hall constant is proportional to the film thickness t (for uncorrelated surface roughness) [875], which is qualitatively in accordance with the experimentally found $R_{0,Co}(t_{\mathrm{Co}})$ be-

havior. From an experimental point of view a decreasing absolute value of R_0 with decreasing thickness was observed by Munoz and co-workers for Au films at $T = 4$ K in the thickness range of $72 - 266$ nm, which is in the range of the mean free path of their films [877, 878]. However, the authors showed that Calecki's theory considerably failed to quantitatively describe the data. For polycrystalline Co films Kötzler and Gil found no thickness dependence of R_0 [580]. Instead they measured the bulk value of Co [571] in the thickness range from 188 nm down to 10 nm, where the latter thickness is comparable to the mean free path of their films, in contrast to the results of this thesis. To current knowledge besides the two works of Munoz et al. as well as of Kötzler and Gil there exist only a few older works dealing with the thickness dependence of R_0, which are even in qualitative contradiction to each other. For instance, regarding Cu films an increase [879, 880] or decrease [881] of the absolute value of R_0 with decreasing film thickness was observed. The brief overview shows that a thickness dependence of the normal Hall coefficient is frequently found for thin films, while the experimental results are at variance and the existing theories fail to describe the data.
The black curve in Fig. 5.46(b) displays the thickness dependence of the AHE also corrected by the current shunt through the Pt. Obviously, the shape of the curve is qualitatively the same as for $\Delta\rho_{\mathrm{op}}(t_{\mathrm{Co}})$, namely, it increases with thickness up to $t_{\mathrm{Co}} \approx 7$ nm, while it decays with $1/t_{\mathrm{Co}}$ at higher thicknesses as indicated by the black dashed line which is a $1/t_{\mathrm{Co}}$-fit. Adapting the argumentation given in connection with the AIMR the $1/t_{\mathrm{Co}}$ dependence reveals a contribution to the AHE that is essentially caused by Co/Pt interface region as for $t_{\mathrm{Co}} \geq 9$ nm structural changes which might influence the AHE can be ruled out. In contrast to $\Delta\rho_{\mathrm{op}}(t_{\mathrm{Co}})$, however, $R_{S,\mathrm{Co}}$ merges into a positive value at infinite Co layer thickness indicating that both the interface as well as the bulk contributions to the AHE provide a positive $R_{S,\mathrm{Co}}$ constant. The finding of an interface contribution to the AHE is placed within the context of other studies already in the previous section and is therefore not further discussed here. Similar to $\Delta\rho_{\mathrm{op}}$ and $\Delta\rho_{\mathrm{ip}}$ the reason for the increase of the AHE below $t_{\mathrm{Co}} < 9$ nm is unknown and not reported in literature so far. However, it is worth mentioning that the increase of the AHE occurs for $t_{\mathrm{Co}} \lesssim \lambda_{\mathrm{bulk}}$, which might give a strong indication that it is correlated with the reduced dimensionality.

In conclusion, despite the elimination of the current shunt through the Pt each of the various MR effects depend on the Co layer thickness. As significant influences of structural variations can be ruled out the Co thickness dependencies suggest the existence of finite size effects. In the case of the AMR, AIMR+GSE ($\Delta\rho_{\mathrm{op,Co}}$), and AHE an increase of the effects with increasing thickness was observed that is basically completed for $t_{\mathrm{Co}} \approx \lambda_{\mathrm{bulk}}$[56]. While the AMR remains constant at higher thicknesses, $\Delta\rho_{\mathrm{op,Co}}$ and $R_{S,\mathrm{Co}}$ decay with $1/t_{\mathrm{Co}}$ revealing the presence of the AIMR effect that is superimposed on the GSE and Co/Pt interface scattering contributions to the AHE, respectively. In the case of the SMR and OHE an increase of

[56] A disentangling of the GSE and of the AIMR at small thickness is not possible so far, so that it is unknown if both effects contribute to the increase of $\Delta\rho_{\mathrm{op}}$ or only one of them. To current knowledge a finite size effect in the GSE was not reported in literature, however, the known investigations concerning the GSE only cover the thickness regime $t \geq \lambda_{\mathrm{bulk}}$ [553].

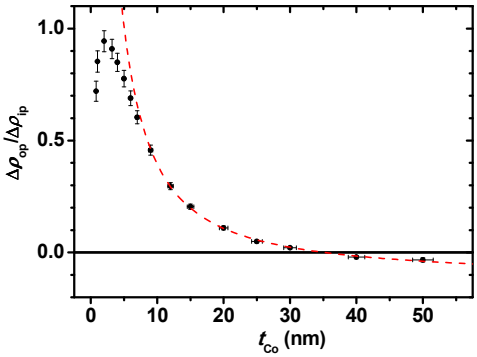

Figure 5.47: AIMR+GSE normalized by the AMR, i.e., $\Delta\rho_{\mathrm{op}}/\Delta\rho_{\mathrm{ip}}$, plotted versus Co layer thickness. The red dashed line is a fit for $t_{\mathrm{Co}} \geq 9$ nm according to the phenomenological model.

both effects with increasing thickness was observed as well. However, the increase is not completed until $t_{\mathrm{Co}} \approx 20$ nm and 30 nm, respectively, where the corresponding Co bulk values are attained. The increase of $R_{0,\mathrm{Co}}$ might be caused by a quantum size effect, while the increase of $-|\mathrm{d}\rho_{\mathrm{Co}}/\mathrm{d}(\mu_0 H)|_{\mathrm{SMR}}$ might be a consequence of a thickness-driven change in the magnon-spectrum.

5.5.2.3 Quantification of the magnetic scattering anisotropy at the Co/Pt interfaces and of the GSE

In this section the strength of the magnetic scattering anisotropy at the Co/Pt interfaces, which manifests in the existence of the AIMR, is quantified in terms of the phenomenological model. Furthermore, the size of the GSE is discussed. As the undesired current shunt through the Pt is eliminated in the quantity $\Delta\rho_{\mathrm{op,Co}}$ the scattering can be described in an effective single Co layer model, so that only Eq. 5.76 under consideration of Eq. 5.77 is needed. In the thickness range $t_{\mathrm{Co}} \geq 9$ nm, where $\Delta\rho_{\mathrm{op,Co}}(t_{\mathrm{Co}})$ obeys a $1/t_{\mathrm{Co}}$ decay, a simple alternative for the elimination of the Pt current shunt from the AIMR+GSE data is provided by the AMR effect as $\Delta\rho_{\mathrm{ip,Co}}(t_{\mathrm{Co}})$ remains constant there (see Fig. 5.45(a)). Hence, in this thickness regime the AMR effect is a suitable indicator for the fraction of the current I_{Co}/I that runs through the Co layer, so that the pure thickness dependence of the AIMR+GSE can be directly determined from the experimental data by using the AMR as normalization factor: $\Delta R_{\mathrm{op}}/\Delta R_{\mathrm{ip}} = \Delta\widetilde{\rho}_{\mathrm{op}}/\Delta\widetilde{\rho}_{\mathrm{ip}} = \Delta\rho_{\mathrm{op,Co}}/\Delta\rho_{\mathrm{ip,Co}} = \Delta\rho_{\mathrm{op}}/\Delta\rho_{\mathrm{ip}}$. Certainly, the ratio of the difference resistivities also resembles the quotient of both MR ratios, i.e., $\Delta\rho_{\mathrm{op}}/\rho_{\mathrm{t}}$ divided by $\Delta\rho_{\mathrm{ip}}/\rho_{\mathrm{t}}$. Furthermore, this description has the advantage that the strength of the AIMR+GSE is given in units of the AMR so that a good comparison between the MR effects is provided. A similar normalization as a measure for the size of the GSE was proposed by Gil et al. (see Eq. 5.50 and Ref. [553]). In Fig. 5.47 the ratio $\Delta\rho_{\mathrm{op}}/\Delta\rho_{\mathrm{ip}}$ is displayed versus Co thickness. At small thicknesses up to $t_{\mathrm{Co}} = 2$ nm the normalized AIMR+GSE increases and reaches a maximum value of $(94 \pm 4)\%$ of the size of the AMR, while for higher thicknesses it decreases. Certainly, for $t_{\mathrm{Co}} \geq 9$ nm the decrease is $1/t_{\mathrm{Co}}$-like. In order to quantify the scattering anisotropy at the Co/Pt interfaces the curve was

fitted for $t_{\mathrm{Co}} \geq 9$ nm according to

$$\frac{\Delta\rho_{\mathrm{op}}}{\Delta\rho_{\mathrm{ip}}}(t_{\mathrm{Co}}) = \frac{\rho_{\mathrm{Co}}(t_{\mathrm{Co}}, p_{\mathrm{p}}, \rho_{\mathrm{p,bulk}}) - \rho_{\mathrm{Co}}(t_{\mathrm{Co}}, p_{\mathrm{t}}, \rho_{\mathrm{t,bulk}})}{\rho_{\mathrm{Co}}(t_{\mathrm{Co}}, p_{||}, \rho_{||,\mathrm{bulk}}) - \rho_{\mathrm{Co}}(t_{\mathrm{Co}}, p_{\mathrm{t}}, \rho_{\mathrm{t,bulk}})} - k_{\mathrm{GSE}} \quad , \tag{5.81}$$

where the first and the second term individually describe the normalized AIMR and GSE, respectively, and the ρ_{Co} are given by Eq. 5.76 under consideration of Eq. 5.77. Thereby, for the AIMR part it was considered because of symmetry reasons that the scattering at the interfaces is the same for any in-plane direction, namely $p_{\mathrm{t}} = p_{||}$, and that the bulk resistivities in the plane perpendicular to the current direction is the same, $\rho_{\mathrm{t,bulk}} = \rho_{\mathrm{p,bulk}}$. For these four parameters the values obtained by the resistance R_{t} versus t_{Co} fitting procedure were used that are given in Eq. 5.78. Furthermore, $\rho_{||,\mathrm{bulk}}$ was determined via $\rho_{||,\mathrm{bulk}} = \Delta\rho_{\mathrm{ip,Co}} + \rho_{\mathrm{t,bulk}}$, where $\Delta\rho_{\mathrm{ip,Co}}$ was deduced from the exponential fit of the AMR curve of Fig. 5.45(a), so that besides k_{GSE} the specularity parameter p_{p} for $\mathbf{M}$ oriented in the polar direction is the only fitting parameter. k_{GSE} is an additive constant that resembles $\Delta\rho_{\mathrm{op}}/\Delta\rho_{\mathrm{ip}}$ at infinite Co thicknesses and is therefore a measure for the size of the GSE. The GSE was assumed to be independent of Co thickness as the degree of out-of-plane texture was found to be the same for any t_{Co} (see section 5.3.1.1). The dashed line in Fig. 5.47 displays the result of the fit, which reveals a very good agreement between the model and the experimental data. The following parameters were obtained by the fitting procedure:

$$\Delta p = p_{\mathrm{t}} - p_{\mathrm{p}} = 0.03 \pm 0.01, \quad k_{\mathrm{GSE}} = 0.12 \pm 0.02 \tag{5.82}$$

While the error in the determination of the specularity parameter p_{t} from the $R_{\mathrm{t}}(t_{\mathrm{Co}})$ curve is relatively high as shown in section 5.5.2.1 the fitting of $\Delta\rho_{\mathrm{op}}/\Delta\rho_{\mathrm{ip}}(t_{\mathrm{Co}})$ is very sensitive to the difference between both specularity parameters $\Delta p = p_{\mathrm{t}} - p_{\mathrm{p}}$ as it is the only parameter that determines the $1/t_{\mathrm{Co}}$ characteristic. The result of the fitting signifies that the specularity parameter changes by $\Delta p = 0.03 \pm 0.01$ when the magnetization orientation switches from polar to transverse direction. In other words, this result implies that the diffusive scattering probability of the electrons at the Co/Pt interfaces is enhanced by 3% when changing the magnetization from any desired in-plane to the out-of-plane direction giving rise to the AIMR effect.
In the following the size of the GSE is discussed. For $10 - 188$ nm thick polycrystalline Co films Gil et al. reported a GSE[57] $k_{\mathrm{GSE}} = \frac{\Delta\rho_{\mathrm{p}}}{\Delta\rho_{\mathrm{t}}} - 1$ in the range of $k_{\mathrm{GSE}} \approx 0.75 - 1.00$, which is significantly larger than the value of $k_{\mathrm{GSE}} = 0.12 \pm 0.02$ observed within this thesis [553]. The disagreement might be a consequence of differences in the crystalline stacking of the Co lattice planes. The authors stated that the Co films exhibit a hcp (0001) out-of-plane texture, while within this study strong indications were found that the Co layers have a fcc (111) texture (section 5.3.1.1). The symmetry of the hcp lattice is lower compared to the fcc lattice, so that for hcp a stronger anisotropy in the resistance can be expected when changing the magnetization orientation with respect to the texture axis, i.e., a stronger GSE might exist. It is worth mentioning that an inferior degree of texture of the Pt/Co/Pt sandwiches compared to the Co films of the study of Gil and co-workers can be ruled out to

[57] Definitions of $\Delta\rho_{\mathrm{p}}$ and $\Delta\rho_{\mathrm{t}}$, see Eq. 5.50 and Ref. [553].

be the reason for the large difference in the size of the GSE as explained in the following. Gil et al. did not report the degree of texture. However, as discussed in connection with the magnetocrystalline anisotropy in section 5.3.2.1 the texture of the films grown on SiO_2 is suchlike that the average tilting of the crystallite with respect to the film normal is $\overline{\alpha} < 10°$, so that a net MR anisotropy might act that is reduced by a factor of $> (\cos^2 \overline{\alpha}_{SiO_2} - \cos^2(90° - \overline{\alpha}_{SiO_2})) \approx 0.94$ compared to a film with perfect out-of-plane texture ($\overline{\alpha} = 0°$). Consequently, even in the case of a perfect texture for the Co films of Ref. [553] the much larger k_{GSE} value cannot be explained.
In conclusion, the phenomenological Fuchs-Sondheimer model describes the normalized $\Delta\rho_{op}/\Delta\rho_{ip}(t_{Co})$ curve quite well. The $1/t_{Co}$ characteristic, i.e., the AIMR contribution, can be reproduced by assuming that the specularity parameter $p(\mathbf{M})$ depends on the orientation of magnetization with respect to the film normal, so that the scattering anisotropy at the Co/Pt interfaces can be expressed in terms of changes in p. Quantitatively, the diffusive scattering probability of the electrons at the interfaces $(1-p)$ decreases by 0.03 when the magnetization orientation changes from out-of-plane to any in-plane direction. The thickness-independent negative offset k_{GSE} in $\Delta\rho_{op}/\Delta\rho_{ip}(t_{Co})$ can be attributed to the GSE as a consequence of the out-of-plane texture of the samples. However, the GSE is significantly reduced compared to hcp (0001) textured Co films. As differences in the degree of texture can be ruled out to be the reason the smaller GSE seems to reflect a higher crystalline symmetry/ smaller texture induced axial perturbation of the isotropy and therefore gives a further indication that the Co layers exhibit fcc stacking.
In the following section the MR results of the films grown on Si_3N_4 are briefly discussed.

5.5.3 Comparison of AMR and AIMR for Pt/Co/Pt sandwiches grown on SiO_2 and Si_3N_4

In this section the MR results for the samples grown on SiO_2 and Si_3N_4 are compared with each other. A presentation of the MR measurements for Si_3N_4 as substrate is omitted here as they qualitatively resemble the curves for SiO_2 presented in section 5.5.1. Furthermore, the results concerning the overall resistance R display no significant differences between nominally identical samples of both sample series, so that a presentation of the $R(t_{Co})$ curve for Si_3N_4 is omitted as well and this section instantaneously begins with the comparison of the thickness dependence of the MR effects. However, it should be explicitly stated beforehand that the independence of the resistance on the kind of substrate indicates that the samples of both series exhibit similar structural disorder (point defects, grain boundaries, surface/ interface etc.) in accordance with the structural results.
Fig. 5.48(a) displays the thickness dependence of the MR-ratios $\Delta\rho_{ip}/\rho_t$ and $\Delta\rho_{op}/\rho_t$ for both sample series. It is obvious that the thickness dependence of both MR-ratios is basically independent of the kind of substrate. Small differences between both series are only apparent at high Co thicknesses, namely, for Si_3N_4 as substrate the AMR-ratio is slightly smaller for Co layer thicknesses of $t_{Co} = 15$ nm and 30 nm as well as $\Delta\rho_{op}/\rho_t$ is smaller at $t_{Co} = 50$ nm. Furthermore, minor differences in the

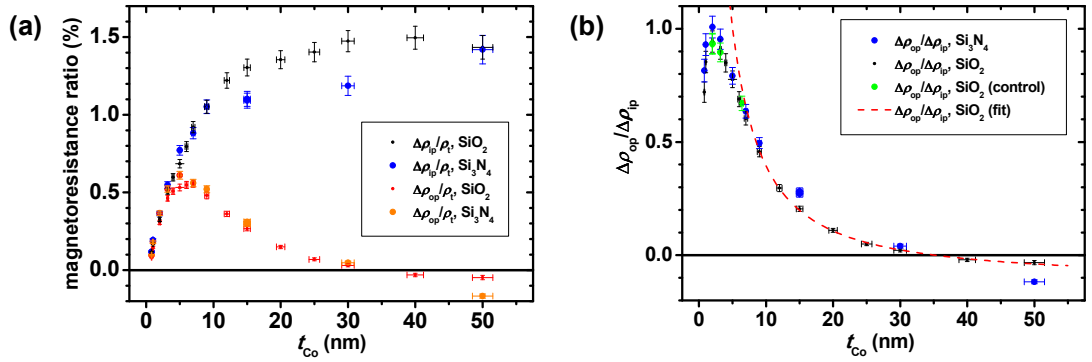

Figure 5.48: (a) $\Delta\rho_{ip}/\rho_t$ and $\Delta\rho_{op}/\rho_t$ as well as (b) AIMR+GSE normalized by the AMR, i.e., $\Delta\rho_{op}/\Delta\rho_{ip}$, plotted versus Co layer thickness for sandwiches grown on SiO_2 and Si_3N_4. The red dashed line in (b) is a fit to the SiO_2 data for $t_{Co} \geq 9$ nm according to the phenomenological model. The green data points are further results for sandwiches grown on SiO_2, which were prepared as a control during the time span of the preparation of the Si_3N_4 sample series.

MR between both series become obvious at low Co thicknesses when expressing the AIMR+GSE in units of the AMR as can be seen in Fig. 5.48(b), namely, $\Delta\rho_{op}/\Delta\rho_{ip}$ is systematically slightly larger for films grown on Si_3N_4. Thereby, it is worth mentioning that for $t_{Co} = 2$ nm, where the ratio of the difference resistivity for both series is at its maximum, $(\Delta\rho_{op}/\Delta\rho_{ip})_{Si_3N_4} = 1.01 \pm 0.04$ was observed. This means that in this particular case the size of the AIMR basically resembles the size of the AMR, which implies that $\rho_p \approx \rho_{||}$ is valid, i.e., the resistivity does not depend on the magnetization orientation in the plane that is spanned by the film normal and the current direction. Furthermore, this particular finding highlights the fact that, in general, the AIMR can be even larger than the conventional AMR for Co/Pt layered structures.

Due to the circumstance that the thickness dependence of the AMR and AIMR+GSE of both series are basically congruent the application of the phenomenological model to describe the $\Delta\rho_{op}/\Delta\rho_{ip}(t_{Co})$ for Si_3N_4 as substrate is redundant and omitted here as, anyway, only a few data points exist in the range of $t_{Co} \geq 9$ nm, where the characteristic is $1/t_{Co}$-like. However, the implications of the congruence as well as of the small deviations from it are briefly discussed under consideration of the two structural differences between both series that were observed so far, namely differences in texture and strain. First, the structural analysis revealed a more pronounced out-of-plane texture for the films grown on Si_3N_4 (see section 5.3.1.1). As a consequence it is reasonable to assume that a higher GSE exists for Si_3N_4 as substrate. However, the difference in the degree of texture is rather low and, according to the discussion about the GSE conducted in section 5.5.2.3, only a small effect can be expected. Probably, the slightly smaller value of $(\Delta\rho_{op}/\rho_t)_{Si_3N_4}$ at $t_{Co} = 50$ nm might indicate a smaller (more negative) $\Delta\rho_{op}/\rho_t$ at infinite Co thickness as a consequence of a larger GSE for the samples grown on Si_3N_4. Second, the difference between the anisotropy constants of both series indicates differences in the residual strain, in particular for $t_{Co} < 4$ nm (see Tab. 5.3). In this thickness regime the difference in the AMR-ratio between both series is rather small revealing that the differences

in residual strain have only minor impact on the AMR in accordance with studies, which showed that elastic deformations only slightly affect the AMR (see previous section). Furthermore, the ratio $\Delta\rho_{\mathrm{op}}/\rho_{\mathrm{t}}$ is basically unaffected by the strain variation as well, so that strain seems to have only minor influence on both the AIMR and the GSE. However, the differences in strain might be the reason why the ratio of the difference resistivities $\Delta\rho_{\mathrm{op}}/\Delta\rho_{\mathrm{ip}}$ is systematically slightly larger for Si_3N_4 as substrate in the thin film regime $t_{\mathrm{Co}} < 4$ nm.
Regarding the Co layer thickness dependence of the SMR, OHE, and AHE for films grown on Si_3N_4 only minor deviations to their counterparts for SiO_2 as substrate were observed, so that a presentation is omitted here for the sake of convenience.
In the following section the temperature dependence of the resistivity $\rho(\mathbf{M}, \mathbf{H})$ of selected sandwiches is discussed.

5.6 Temperature dependence of $\rho(\mathrm{M}, \mathrm{H})$ in Pt/Co/Pt sandwiches

The motivation for the investigation of the temperature dependence of $\rho(\mathbf{M})$ is given by the possibility to disentangle the different kinds of scattering processes to examine their contributions to the magnetoresistance effects. As discussed in connection with sections 5.1.1 and 5.1.3 by varying the temperature the probability of electron-phonon as well as the electron-magnon scattering processes is altered, whereas the scattering of the electrons at static defects is basically unaffected. Furthermore, electron-electron interactions could contribute to the resistivity at low temperatures $\lesssim 20$ K, which might also affect the magnetoresistance effects (section 5.1.3.3).
This section deals with the first results obtained so far in the ongoing research project of the temperature dependence of $\rho(\mathbf{M})$. The MR measurements were performed in cooperation with Matthias Schmidt and Stefan Knott at the Institute of Applied Physics, University of Hamburg, providing a superconducting split-pair magnet[58]. The term split-pair means that contrary to an ordinary solenoid, which is equipped in the warm-bore setup presented in section 5.4, a Helmholtz-pair is utilized providing magnetic fields that are oriented horizontally, i.e., perpendicularly oriented to the bore. This enables the manipulation of the field direction with respect to the sample orientation by rotating the whole sample holder without the need of a mechanical conversion. For the in-plane (out-of-plane) MR measurements the sample is mounted to the sample holder, so that during its rotation the film normal (current direction) is always oriented perpendicularly to the field direction. The sample chamber was evacuated permanently and the sample cooling was performed by means of a needle valve between the magnet chamber and the sample chamber providing liquid Helium. The setup enables stable temperatures with an accuracy of 0.1 K via a controllable heater in the range of 4.2 K to 200 K. At certain fixed temperatures the same kind of MR measurements as performed at room-temperature were carried out (field sweep measurements and sample rotation in saturation field of 6T, see section 5.4.2). The investigations were performed for Pt/Co/Pt sandwiches

[58] Oxford instruments, project number 40767.

grown on SiO_2 with Co layer thicknesses of $t_{Co} = 2$ nm, 6 nm, and 20 nm[59].
In addition to the MR investigations, the zero-field resistivities of the three samples were measured in great detail in the temperature range of 2 K $\leq T \leq$ 350 K. For that purpose the samples were mounted to the end of a cold-finger[60]. After evacuating the sample chamber the cold-finger was cooled via thermal contact by means of a liquid Helium conflux utilizing a scroll pump. The procedure was as follows: The samples were cooled down to $T = 2$ K. Then, the liquid Helium conflux was manually adjusted, so that the sample temperature gradually rose with small rates of ≤ 0.01 K/s in order to avoid significant temperature gradients between sample and cold-finger. At $T \approx 100$ K the liquid Helium conflux was terminated and the sample temperature was gradually enhanced by means of a heater and a PID controller with a rate of 0.01 K/s up to a temperature of $T = 350$ K. During the whole warm-up process the resistance and temperature were recorded every 5 s.
After the heat-treatment to 350 K (≈ 75°C) the MR of the samples was again measured at room temperature. Thereby, no changes in the MR properties were detected within the error margins of the experiment, which would otherwise have been indicated that the heat-treatment had caused irreversible changes in the structural properties of the samples (more details, see in the outlook, section 5.8).
In section 5.6.1 the temperature dependence of the zero-field resistivity and in section 5.6.4 the temperature dependence of the MR effects is discussed. Beforehand, in section 5.6.2 the results of the MR measurements obtained below room temperature are briefly presented while in section 5.6.3 the temperature dependence of the anisotropy is shown.

5.6.1 Temperature dependence of zero-field resistivity

In Fig. 5.49 the temperature dependence of the zero-field resistivity for the three sandwiches is displayed. The shape of the curves is similar for all three samples. The curves monotonically increase in the whole temperature range, in particular, a logarithmic decrease of $\rho(T)$ at low temperatures $\lesssim 20$ K was not observed, which would indicate a further contribution to the resistivity, e.g. the presence of electron-electron interactions in a two-dimensional system (see section 5.1.3.3). From the curves it is obvious that the residual resistance ratio (RRR, see Eq. 5.19) of the samples is rather low, namely $1.28 \leq RRR \leq 1.50$, which reveals that in the whole temperature range investigated the dominant scattering mechanism in the sandwiches is the scattering at static defects. The slight increase of RRR with thickness is partially a consequence of the decrease of the relative contribution of the electron-interface scattering to the overall resistivity as explicitly shown below. While the static scattering contributions can be disentangled from the dynamic contributions in a simple way as the former only provide a temperature independent offset to the resistivity a disentangling of the electron-phonon scattering from the electron-magnon scattering is more challenging. Furthermore, as it is dealt with a sandwich

[59] In near future further MR investigations in the temperature range of 4.2 K to 300 K utilizing fields of up to 7 T can be carried out by using the superconducting magnet (spectromag) system of Oxford instruments, project number 52398, purchased within the framework of this thesis.
[60] ST-400 Ultra High Vacuum (UHV) Cryostat of Janis Research Company.

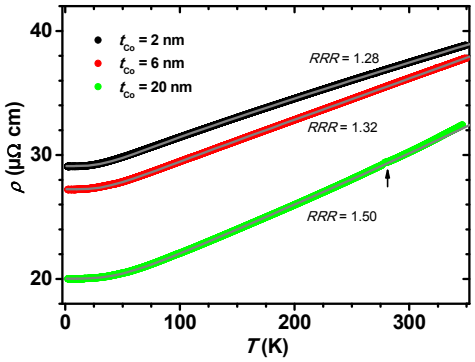

Figure 5.49: Temperature dependence of the resistivity for $t_{\mathrm{Co}} = 2$ nm, 6 nm, and 20 nm. The gray solid lines are fits to the data. For $t_{\mathrm{Co}} = 20$ nm only the temperature region up to 280 K is fitted (see black arrow) as for higher temperatures the heating rate was chosen to high yielding significant temperature gradients.

system it is appropriate to disentangle the resistivity contributions of the Co layer from the Pt layers as well in order to obtain a complete insight into the composition of the resistivity. For that purpose the parallel current model according to Eq. 5.75 was applied to quantitatively describe the $R(T)$ curves:

$$R(t_{\mathrm{Co}}, T) = \left(\frac{1}{R_{\mathrm{Co}}(t_{\mathrm{Co}}, T)} + \frac{1}{R_{\mathrm{Pt}}(T)} \right)^{-1} \tag{5.83}$$

According to Matthiessen's rule (see Eq. 5.17) the resistivities of the Co and Pt layers were assumed to be the sum of a static, a phonon, and a magnon contribution, the latter only in the case of Co[61]. By using the corresponding expressions given by Eqs. 5.18, 5.30, and 5.34 the layer resistances are[62]:

$$\begin{aligned} R_{\mathrm{Pt}}(T) &= R_{\mathrm{st,Pt}} + \underbrace{\widetilde{A}_{\text{el-ph,Pt}} \left(\frac{T}{\Theta_{\mathrm{D,Pt}}} \right)^{n_{\mathrm{Pt}}} \int_0^{\Theta_{\mathrm{D,Pt}}/T} \frac{x^{n_{\mathrm{Pt}}} dx}{(e^x - 1)(1 - e^{-x})}}_{R_{\mathrm{ph,Pt}}}, \quad n_{\mathrm{Pt}} = 3.7, \\ R_{\mathrm{Co}}(T) &= R_{\mathrm{st,Co}} + \underbrace{\widetilde{\alpha}_{\mathrm{Co}} T^2}_{R_{\mathrm{mag,Co}}(T)} + \\ &\quad + \underbrace{\widetilde{A}_{\text{el-ph,Co}} \left(\frac{T}{\Theta_{\mathrm{D,Co}}} \right)^{n_{\mathrm{Co}}} \int_0^{\Theta_{\mathrm{D,Co}}/T} \frac{x^{n_{\mathrm{Co}}} dx}{(e^x - 1)(1 - e^{-x})}}_{R_{\mathrm{ph,Co}}(T)}, \quad n_{\mathrm{Co}} = 3.3 \end{aligned} \tag{5.84}$$

In the case of the phonon terms $R_{\mathrm{ph},i}(T)$ for the exponents n_i whether the exponent of the Bloch-Grüneisen equation (s-s scattering, $n = 5$) nor the one of the Bloch-Wilson (s-d scattering, $n = 3$) equation was used. Instead, the exponents

[61] In paramagnetic materials like Pt the $s-d$ interaction provides a temperature independent term ρ_{PM} (see Eq. 5.33), which is virtually included here in the static term $\rho_{\mathrm{st,Pt}}$.

[62] For the sake of convenience the resistivity contribution that is caused by the magnon part of the s-d interaction is labeled as mag (=magnon) in the following.

t_{Co} (nm)	$\rho_{\mathrm{st,Pt}}$ ($\mu\Omega$cm)	$A_{\mathrm{el\text{-}ph,Pt}}$ ($\mu\Omega$cm)	$\rho_{\mathrm{st,Co}}$ ($\mu\Omega$cm)	$A_{\mathrm{el\text{-}ph,Co}}$ ($\mu\Omega$cm)	α_{Co} ($\mu\Omega$cm/K^2)
2	28 ± 2	21 ± 3	34 ± 2	2 ± 2	$(0.5 \pm 0.2) \cdot 10^{-5}$
6	27 ± 2	23 ± 3	27 ± 2	16 ± 3	$(1.3 \pm 0.3) \cdot 10^{-5}$
20	28 ± 2	22 ± 3	18 ± 2	24 ± 2	$(2.2 \pm 0.3) \cdot 10^{-5}$

Table 5.4: Parameters obtained by the fitting procedure of the $R(T)$ curves for the three Co layer thicknesses. The intrinsic quantities were calculated from the extrinsic parameters according to $\rho_{\mathrm{st},i} = R_{\mathrm{st},i} \cdot \frac{w \cdot t_i}{l}$, $A_{\mathrm{ph},i} = \widetilde{A}_{\mathrm{ph},i} \cdot \frac{w \cdot t_i}{l}$, and $\alpha_{\mathrm{Co}} = \widetilde{\alpha}_{\mathrm{Co}} \cdot \frac{w \cdot t_i}{l}$, where l and w are the dimensions of the macroscopic wire sample and t_i is the layer thickness.

experimentally found for bulk Co and Pt were utilized (see section 5.1.3.1). In addition, for the Debye temperatures of Co and Pt the bulk values $\Theta_{\mathrm{D,Co}} = 380$ K and $\Theta_{\mathrm{D,Co}} = 225$ K were applied. The curves were fitted to Eqs. 5.83 and 5.84 under the consideration of $R_{\mathrm{Pt}}(T = 295\ \mathrm{K}) = 380\ \Omega$, which was obtained from the fitting of the thickness dependence of the overall resistance presented in the previous section (see Eq. 5.78).
The gray solid lines in Fig. 5.49 display the results of the fitting procedure of the three curves. The good correspondence between the fits and the experimental data reveals that the applied model can describe the temperature dependence of the resistivity quite well. From the extrinsic parameters $R_{\mathrm{st},i}$, $\widetilde{A}_{\mathrm{el\text{-}ph},i}$, and $\widetilde{\alpha}_{\mathrm{Co}}$ obtained by the fitting procedure corresponding intrinsic parameters were calculated that are listed in Tab. 5.4. The parameters that describe the contributions of the Pt material to the resistivity are the same for the three samples within the error margins of the experiment, which was expected as the thickness of the Pt layers was held constant. Moreover, the temperature-dependent part of the resistivity is in very good agreement with the results obtained for bulk Pt as can be seen in Fig. 5.50(a), where experimental results for bulk Pt (gray dots) reported by White and Woods [468] are plotted together with the $\rho_{\mathrm{ph,Pt}}(T)$ model curve (gray line), which was calculated by using the fit parameter $A_{\mathrm{el\text{-}ph,Pt}} = 22\ \mu\Omega$cm.
In contrast to the results for the Pt material, the residual resistivity of the Co layer $\rho_{\mathrm{st,Co}}$ increases with decreasing t_{Co} reflecting the increase of the relative contribution of the interface scattering processes to the resistivity. Furthermore, $A_{\mathrm{el\text{-}ph,Co}}$ and α_{Co} strongly increase with Co layer thickness by a factor of twelve and four, respectively. In order to visualize the described trends for the temperature-dependent parts of the resistivity of the Co layer $\rho_{\mathrm{ph,Co}}(T)$ and $\rho_{\mathrm{mag,Co}}(T)$ are plotted in Fig. 5.50(a) and Fig. 5.50(b), respectively, which were calculated according to the fit parameters listed in Tab. 5.4. In the inset of Fig. 5.50(b) the sum of both temperature-dependent parts of the resistivity $\rho_T(T) = \rho_{\mathrm{ph,Co}}(T) + \rho_{\mathrm{mag,Co}}(T)$ of the sample with $t_{\mathrm{Co}} = 20$ nm is plotted (black solid line) together with the experimental behavior $\rho_T(T) = \rho(T) - \rho_{\mathrm{st}}$ of a thick Co film measured by Raquet et al. (black dots) [481]. Obviously both curves only slightly diverge from each other reflecting the fact that the thickest Co layer exhibits a $\rho_T(T)$ behavior that basically resembles bulk Co. Moreover, the magnon part $\rho_{\mathrm{mag,Co}}(T)$ also plotted in the inset (blue line) resembles the one calculated by Raquet et al. (blue dots) [481] revealing that even the relative fractions of $\rho_{\mathrm{ph,Co}}(T)$ and $\rho_{\mathrm{mag,Co}}(T)$ to $\rho_T(T)$ seem to be similar to bulk Co.

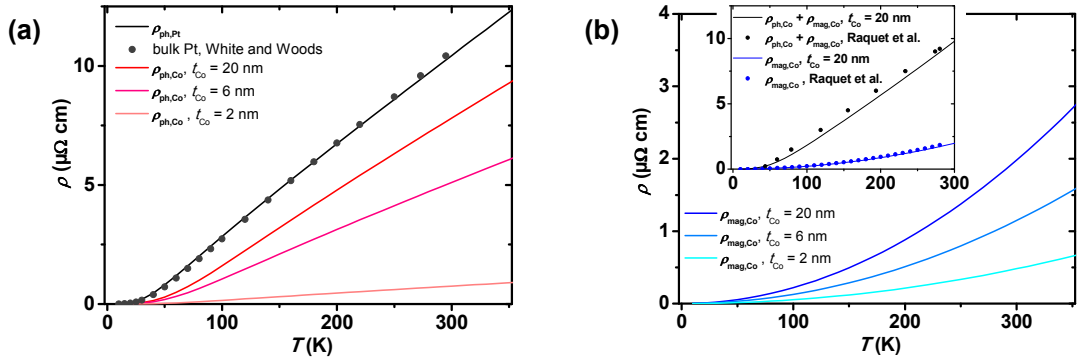

Figure 5.50: Temperature-dependent parts of the resistivity (a) $\rho_{\mathrm{ph},i}(T)$ and (b) $\rho_{\mathrm{mag,Co}}(T)$ calculated according to the terms of Eq. 5.84 by using the parameters of $A_{\text{el-ph},i}$ and α_{Co} obtained by the fitting procedure listed in Tab. 5.4. In (a) the experimental results of White and Woods [468] for bulk Pt are shown for comparison. The inset in (b) displays $\rho_{\mathrm{mag,Co}}(T)$ (blue) and the sum $\rho_{\mathrm{ph,Co}}(T) + \rho_{\mathrm{mag,Co}}(T)$ (black) for the sample with $t_{\mathrm{Co}} = 20$ nm together with the measured $\rho(T)$ curve and the calculated $\rho_{\mathrm{mag,Co}}(T)$ of Raquet et al. for bulk Co [481].

Quantitatively, at room temperature the fraction of the electron-magnon scattering to the temperature-dependent part of the resistivity is 20%, which is similar to the value of 18% determined by Raquet and co-workers (see section 5.1.3.2) [481]. While the thickest Co layer of $t_{\mathrm{Co}} = 20$ nm basically exhibits the temperature-dependent resistivity of bulk Co for the two thinner Co layers both components of $\rho_T(T)$ are significantly suppressed. Qualitatively, this fact is traceable directly from the measured $\rho(T)$ curves (see Fig. 5.49) as the overall resistivity increases by 10.0/ 8.8/ 8.2 $\mu\Omega$cm for the thickest/ intermediate/ smallest Co layer thickness in the temperature range from liquid Helium to room temperature. This implies that also the thickness dependence of $\rho_T(T)$ contributes to the decrease of RRR with decreasing t_{Co} besides the increase of the interface scattering that enhances $\rho_{\mathrm{st,Co}}$. In the following the observed thickness dependencies of $\rho_{\mathrm{ph,Co}}(T)$ and $\rho_{\mathrm{mag,Co}}(T)$ are discussed separately starting with the former term. A dependence of $\rho_{\mathrm{ph}}(T)$ on the sample dimensions was frequently observed in the case of thin films [882, 883, 441, 884], nanowires [883, 885, 489], multilayers [886], and nanoparticles [887, 888]. However, in all cases the Bloch-Grüneisen (or Bloch-Wilson) equation can be applied to describe the $\rho_{\mathrm{ph}}(T)$ behavior quite well as it is also the case within this work. Thereby, it was generally observed that the effective Debye temperature Θ_{D} decreases with decreasing film thickness t (wire diameter, particle size). For instance, G. Kästle et al. investigated epitaxial gold films in the thickness range of 2 nm $\leq t \leq$ 46 nm and found a decrease of Θ_{D} by about 50 K compared to the thickest films, which exhibits the bulk value of $\Theta_{\mathrm{D}}^{\text{Au bulk}} = 184$ K, while $A_{\text{el-ph}}$ was found to be nearly independent of film thickness. Only in a few investigations $A_{\text{el-ph}}$ was observed to vary with thickness, namely, an increase with decreasing t was found [886, 888] which is in contrast to the findings of this work for the Co layer. In order to examine whether a thickness dependence of the Debye temperature also exists for the sandwiches the Debye temperatures of Co and Pt were additionally used as fit parameters. However, as a result of the $R(T)$ fitting procedures in any

t_{Co} (nm)	α_{Co} ($\mu\Omega$cm/K^2)	$\alpha_{\mathrm{Co}}^{\mathrm{norm}}$	$-\lvert\mathrm{d}\rho_{\mathrm{Co}}/\mathrm{d}(\mu_0 H)\rvert_{\mathrm{SMR}}$ ($\mu\Omega$cm/T)	$-\lvert\mathrm{d}\rho_{\mathrm{Co}}/\mathrm{d}(\mu_0 H)\rvert_{\mathrm{SMR}}^{\mathrm{norm}}$
2	$(0.5 \pm 0.2) \cdot 10^{-5}$	(0.2 ± 0.1)	(0.0021 ± 0.0004)	(0.22 ± 0.05)
6	$(1.3 \pm 0.3) \cdot 10^{-5}$	(0.6 ± 0.2)	(0.0049 ± 0.0005)	(0.51 ± 0.07)
20	$(2.2 \pm 0.3) \cdot 10^{-5}$	1	(0.0096 ± 0.0007)	1

Table 5.5: α_{Co} and spin-disorder MR $-\lvert\mathrm{d}\rho_{\mathrm{Co}}/\mathrm{d}(\mu_0 H)\rvert_{\mathrm{SMR}}$ for the three Co layer thicknesses obtained by the fitting procedure and the polar MR curves at room temperature, respectively. The normalized values are calculated by $\alpha_{\mathrm{Co}}^{\mathrm{norm}} = \frac{\alpha_{\mathrm{Co}}(t_{\mathrm{Co}})}{\alpha_{\mathrm{Co}}(t_{\mathrm{Co}}=20\ \mathrm{nm})}$ and $-\lvert\mathrm{d}\rho_{\mathrm{Co}}/\mathrm{d}(\mu_0 H)\rvert_{\mathrm{SMR}}^{\mathrm{norm}} = \frac{-\lvert\mathrm{d}\rho_{\mathrm{Co}}/\mathrm{d}(\mu_0 H)\rvert_{\mathrm{SMR}}(t_{\mathrm{Co}})}{-\lvert\mathrm{d}\rho_{\mathrm{Co}}/\mathrm{d}(\mu_0 H)\rvert_{\mathrm{SMR}}(t_{\mathrm{Co}}=20\ \mathrm{nm})}$.

case both Θ_{D} values only differ by less than ± 20 K from the corresponding bulk values, while a systematic dependence on Co layer thickness was not found. Besides the mentioned results regarding $A_{\text{el-ph}}(t)$ reported in literature the observations of a decrease in the Debye temperature Θ_{D} with decreasing t implies the fact that the increase of the resistivity with temperature is the stronger the thinner the films are. This depicted dependence of $\rho_{\mathrm{ph}}(T)$ on t is in opposition to the calculated $\rho_{\mathrm{ph,Co}}(T)$ behavior shown in Fig. 5.50(a) (and to the experimental $\rho(T)$ curves, see Fig. 5.49). As a thickness dependence of Θ_{D} was not found within this thesis a deeper discussion is omitted here. For details about recent experimental results and possible explanations for the thickness dependence of Θ_{D} the reader is referred to Refs. [885, 489] and references therein. Concerning the thickness dependence of the electron-phonon coupling constant $A_{\text{el-ph}}$ S. Kim et al. explained the observed increase with decreasing film thickness with the presence of additional surface phonon modes decaying fast into the bulk material, so that for thin films the effective value of $A_{\text{el-ph}}$ is enhanced [886]. Adapting this argumentation the decrease of $A_{\text{el-ph,Co}}$ with decreasing Co layer thickness observed for the sandwiches indicates that at low t_{Co} the scattering of the electrons at the bulk phonon modes is suppressed within the Co layer. A possible reason for this finite size effect is unknown so far. A future explanation of this behavior also has to answer the question why in contrast to the Co layer the rather thin Pt seed and cap layers exhibit an electron-phonon scattering behavior that resembles bulk Pt.

In the following the thickness dependence of $\rho_{\mathrm{mag,Co}}(T)$ determined from the fitting procedure is discussed starting with a comparison of the parameter α_{Co} (see Tab. 5.5) with the size of the spin-disorder MR determined for the three samples at room temperature (see Fig. 5.46(a)). Remarkably, when normalizing both quantities to the corresponding value of the thickest sample, which basically resembles the bulk behavior, for each thickness the resulting ratios $\alpha_{\mathrm{Co}}^{\mathrm{norm}}$ and $-\lvert\mathrm{d}\rho_{\mathrm{Co}}/\mathrm{d}(\mu_0 H)\rvert_{\mathrm{SMR}}^{\mathrm{norm}}$ are similar within the error margins as can be seen in Tab. 5.5. This finding provides significant evidence that both size effects in $\rho_{\mathrm{mag,Co}}(T)$ and in the SMR are the consequence of the same physical reason revealing that, in fact, the thickness dependence of the SMR is a consequence of the suppression of the electron-magnon scattering with decreasing Co layer thickness as already assumed in section 5.5.2.2. There, it was also stated that the thickness dependence of the electron-magnon scattering might be a consequence of a thickness-driven variation of the magnon

spectrum as frequently observed for thin films [869, 870, 871]. To current knowledge in literature only one investigation reports on a size effect in α [489, 488]. M. V. Kamalakar and A. K. Raychaudhuri investigated the temperature dependence of the resistivity of arrays of Ni nanowires with diameters ranging from 13 nm to 55 nm and found a suppression of the electron-magnon scattering contribution by a factor of three for the thinnest wire compared to the thickest one whose α resembles the value for bulk Ni. However, the authors only investigated $\rho_{\mathrm{mag}}(T)$ for $T < 15$ K, which is traceable as for Ni complex deviations from a pure T^2 dependence are already expected beyond this temperature according to Raquet and co-workers [481]. It is recalled that in this low temperature regime ρ_{mag} is governed by *s*-*s* interband electron-magnon scattering processes in contrast to higher temperatures, where *s*-*d* intraband electron-magnon scattering dominates. Furthermore, it is worth mentioning that significant electron-electron scattering contributions might exist below $T \lesssim 20$ K that also generate a resistivity term ρ_{ee} that is proportional to T^2 in 3D (see section 5.1.3.3). Therefore, the decrease of α with decreasing the wire diameter might also be a consequence of a transition from a 3D to a reduced dimensionality behavior that affects the electron-electron scattering as frequently observed for thin films and nanowires. The results of this thesis suggest that the knowledge, whether a finite size effect in the SMR effect exists, provides the possibility to discriminate between a finite size effect in the electron-magnon or in the electron-electron scattering. As the authors did not measure the magnetoresistance it is not known if a size effect in the SMR of the Ni nanowires exists, which would confirm their interpretation of the data by means of electron-magnon scattering. However, as an explanation for the reduced electron-magnon scattering at low diameters the authors suggested that due to structural disorder at the surface of the nanowire the spins located there might not contribute to spin-waves with long wavelengths. As these magnons provide the electron-magnon scattering term ρ_{mag} the effective α is consequently reduced at low diameters.

The end of this section deals with the temperature-dependent current distribution within the sandwiches that is connected with the differences between the temperature dependence of R_{Co} and R_{Pt}. Within the framework of the parallel current model the fraction of the current that flows through the Co layer in dependence of the temperature, i.e., $I_{\mathrm{Co}}/I(T)$, can be calculated according to Eq. 5.80 by using the measured $R(T)$ curve and the resistance of the Pt material determined by the fits. Fig. 5.51 shows the calculated $I_{\mathrm{Co}}/I(T)$ curves for the three Co layer thicknesses. All three curves are almost horizontal lines, which is traceable as the RRR is relatively small, i.e., in the whole temperature range the scattering at static defects provides the dominant contribution to the overall resistance for both the Pt and Co layers, so that R_{Co} and R_{Pt} and therefore I_{Co}/I only vary slightly with temperature. In the low temperature range $T \lesssim 30$ K the $I_{\mathrm{Co}}/I(T)$ curves remain constant as magnons and phonons are basically frozen out, while in the range 30 K $\leq T \leq$ 295 K the $I_{\mathrm{Co}}/I(T)$ behavior varies by about +5%/ +3%/ -2% in the case of the thinnest/ intermediate/ thickest Co layer. This means that for $t_{\mathrm{Co}} = 20$ nm the fraction of the current that flows through the Co decreases with temperature, while for the two other samples it increases. The different behavior is a consequence of the finite size effect in $A_{\text{el-ph,Co}}$ and $\alpha_{\mathrm{mag,Co}}$ (see above). In conclusion, the fraction of the

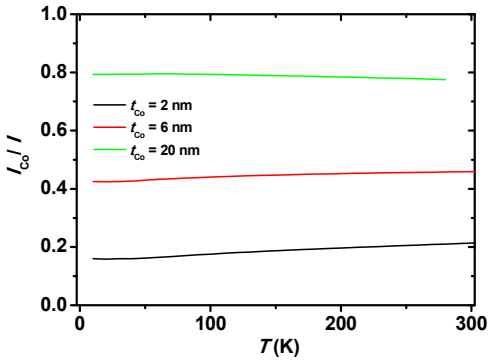

Figure 5.51: Fraction of the current I_{Co}/I that flows through the Co layer as a function of temperature deduced from the model curve $R_{\mathrm{Pt}}(T)$ and the experimental curve $R(T)$ for the three Co layer thicknesses.

current that flows through the Co layer only slightly depends on temperature, so that it should only have minor influence on the temperature dependencies of the MR effects.
The MR curves obtained at low temperatures are presented in the following section.

5.6.2 Dependence of resistivity on applied field and magnetization orientation below room temperature

In this section the results of the MR measurements obtained at low temperatures are presented and compared with the ones of the room temperature investigations. The three sandwiches ($t_{\mathrm{Co}} = 2$ nm, 6 nm, and 20 nm) exhibit an easy-plane behavior in the whole temperature range and, from a qualitative point of view, it was observed that at any temperature the shape of the resistivity versus field curves of each geometry is similar for all samples. Fig. 5.52(a) exemplarily shows the field dependence of the diagonal part of the resistivity tensor ρ_{xx} in dependence of the applied field for the three generic measurement geometries at a temperature of $T = 4.2$ K. In comparison to the room temperature counterparts (see Fig. 5.37(b)) it is obvious that below technical saturation ($M_{\mathrm{S}}||H$) the shape of the curves is basically unaffected by the reduction of temperature. Above $M_{\mathrm{S}}||H$, however, in contrast to a linear decrease of the resistivity with increasing the absolute value of the applied field, a slight bending up was found. For all three measurement geometries the magnitude of the bending up is the same reflecting an isotropic high field behavior of the resistivity. Such a behavior was expected at low temperatures as a consequence of the "residual" SMR according to Eq. 5.41 [481, 555]. It is worth mentioning that the isotropic high field behavior reveals that contributions of the Lorentz MR are negligibly small as the LMR would cause an anisotropic increase of the resistivity with field. A vanishingly small LMR was expected even for low temperatures (see section 5.1.4.1) as, at first, the RRR is rather low, so that the mean free path is only slightly enhanced compared to room temperature and therefore the size of the LMR does not significantly change with temperature. Secondly, even for Co films with $RRR = 27$ a vanishingly small LMR was detected below liquid He temperature [481].

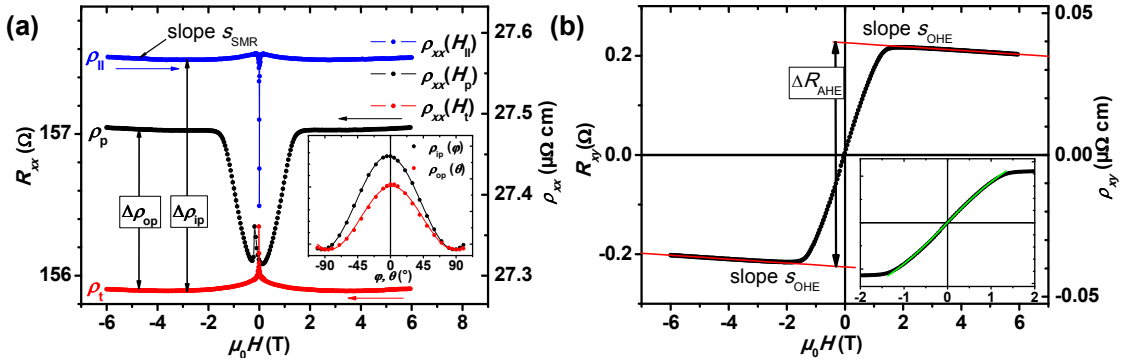

Figure 5.52: Magnetoresistance curves for $t_{Co} = 6$ nm at $T = 4.2$ K. (a) Resistance R_{xx}/ resistivity ρ_{xx} as a function of the applied field $\mu_0 H$ for the three principle directions of the field with respect to the current direction and stacking. The colored arrows show the corresponding sweep directions. The inset displays R_{xx}/ ρ_{xx} as a function of the in-plane angle φ (black) and out-of-plane angle θ (red) by using a saturation field of 6 T. The solid lines are $\cos^2$ fits. (b) Resistance R_{xy}/ resistivity ρ_{xy} as a function of the polar field $\mu_0 H_p$. The red lines are linear fits to the region $\mu_0|H_p| \geq 3$ T. The inset displays the region up to $\mu_0|H_p| = 2$ T after elimination of the OHE contributions. The green curve is a fit according to Eq. 2.23 in order to determine the anisotropy constants in second order approximation.

Below technical saturation for any desired temperature between liquid He temperature and room temperature the shape of each $\rho_{xx}(H_i)$ curve is unaffected by the temperature variation, while the slopes of the curves above saturation gradually change from a slight bending up to a linear decrease with increasing temperature indicating the increase of the SMR. At any temperature when the magnetization was field aligned the behavior $\rho_{||} > \rho_p > \rho_t$ was observed for all three Co thicknesses resembling the hierarchy found at room temperature. Therefore, this finding reveals the presence of the conventional AMR and particularly discloses the existence of the anisotropic interface magnetoresistance (AIMR) down to liquid He temperature. These facts can also be seen in the inset of Fig. 5.52(a), where the dependence of the resistivity with respect to the orientation of the magnetization is shown. The same as for room temperature the $\rho_{xx}(\varphi)$ and $\rho_{xx}(\theta)$ curves both follow a $\cos^2$ dependence as indicated by the solid lines.
In Fig. 5.52(b) the $\rho_{xy}(H_p)$ curve is shown that was simultaneously measured in polar geometry for the very same sample ($t_{Co} = 6$ nm) at $T = 4.2$ K. By comparison with Fig. 5.39(b) it is obvious that the measurement obtained at $T = 4.2$ K is connatural to the curve measured at room temperature revealing that $\rho_{xy}(H_p)$ is governed by the anomalous (normal) Hall effect below (above) technical saturation. This statement is valid for the three samples within the whole temperature range investigated within this thesis. The inset of Fig. 5.52(b) displays the resulting curve after the elimination of the OHE from the $\rho_{xy}(H_p)$ curve in order to determine the anisotropy constants. The temperature dependence of the anisotropy constants is presented in the following section.

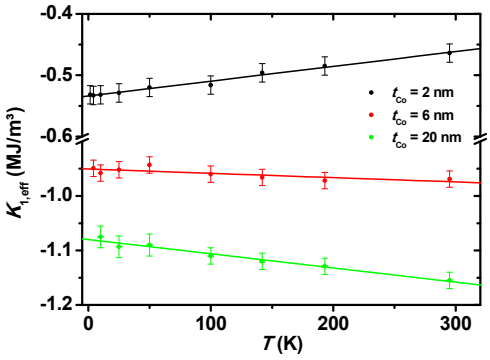

Figure 5.53: Effective first order uniaxial anisotropy constant $K_{1,\mathrm{eff}}$ in dependence of temperature for $t_{\mathrm{Co}} = 2$ nm, 6 nm, and 20 nm. The solid lines are linear fits to the data.

5.6.3 Temperature dependence of anisotropy constants

In order to determine the anisotropy constants in second order approximation the OHE contribution of the $\rho_{xy}(H_{\mathrm{p}})$ curves was eliminated as described in section 5.3.2.1 and the resulting AHE contribution was fitted according to Eq. 2.23[63]. As a result the second order uniaxial anisotropy constant K_2 does not change with temperature within the error margins of the experiment and basically resembles the value determined at room temperature for the sandwiches of $K_2 = (70 \pm 30)$ kJ/m^3. This finding is in accordance with the results for hcp bulk Co and Co/Pt layered structures, where K_2 was found to vary by less than 50 kJ/m^3 in the temperature range investigated within this work [85, 104, 109].

Fig. 5.53 shows the effective first order anisotropy constant $K_{1,\mathrm{eff}}$ in dependence of temperature for the three samples with Co layer thicknesses of $t_{\mathrm{Co}} = 2$ nm, 6 nm, and 20 nm. In contrast to K_2 it depends on temperature in such a manner that the $K_{1,\mathrm{eff}}(T)$ curves are straight lines as indicated by the solid lines in Fig. 5.53 that are linear fits of the data. For $t_{\mathrm{Co}} = 2$ nm the $K_{1,\mathrm{eff}}(T)$ behavior increases, while for $t_{\mathrm{Co}} = 6$ nm and $t_{\mathrm{Co}} = 20$ nm it decreases. The slopes are rather small, so that in the range investigated from liquid Helium to room temperature the anisotropy constant only increases by about 70 kJ/m^3 in the case of the smallest Co layer thickness, while it decreases by about 20 kJ/m^3 (80 kJ/m^3) for the intermediate (thickest) t_{Co}. The difference in the slopes indicates that the individual contributions to the effective anisotropy constant have a different temperature dependence: While at large Co layer thicknesses the anisotropy constant is governed by the effective volume anisotropy the interface anisotropy dominates at small t_{Co} (see Eq. 2.18). In the following the temperature dependence of the interface, shape, and magnetocrystalline volume anisotropy is briefly discussed starting with the latter term. At finite temperatures the thermal excitation of the magnetization (see Bloch's $T^{3/2}$ law, Eq. 5.39) is connected with a thermal distribution of the magneti-

[63] For the sample with $t_{\mathrm{Co}} = 2$ nm the field sweep measurements were only performed by using maximum fields of up to ± 2 T, so that the OHE contribution could not be determined and eliminated before performing the fitting procedure. The related systematic error was estimated from the room temperature measurement of $\rho_{xy}(H_{\mathrm{p}})$ to be smaller than 20 kJ/m^3 and is therefore negligibly small, which can be comprehended by the fact that the OHE is significantly suppressed at low Co layer thicknesses (see Fig. 5.46(b)).

zation over a small range on the energy landscape yielding a strong dependence of the anisotropy on temperature compared to the saturation magnetization itself (for details, see Refs. [889, 73]). Theoretically, $K_{iV}(T) \approx K_{iV}(0) \cdot \left(\frac{M_S(T)}{M_S(0)}\right)^{n_{iV}}$ is deduced for $T < T_C/2$, with $n_{1V,\mathrm{cub}} = 10$, $n_{2V,\mathrm{cub}} = 21$ and $n_{1V,\mathrm{uni}} = 3$ for cubic and uniaxial anisotropy, respectively. However, the power laws only apply qualitatively in the case of 3*d* transition metals [889, 73]. Experimentally, for hcp Co bulk it was found that the anisotropy constant $K_{1V,\mathrm{uni}}$ basically remains constant in the temperature range up to 100 K while it decreases by about 250 kJ/m^3 up to room temperature (see section 2.1.3.1) [85]. Regarding fcc Co T. Suzuki et al. measured the anisotropy constants $K_{1V,cub}$ and $K_{2V,\mathrm{cub}}$ of a 100 nm thick film in the temperature range of 77 K to 300 K and found out that the absolute value of both quantities linearly decreases with temperature from -72 kJ/m^3 to -62 kJ/m^3 and from $+20$ kJ/m^3 to ≈ 0 kJ/m^3, respectively [86]. According to this result, even when extrapolating the linear temperature dependence of both cubic anisotropy constants to zero temperature, for (111) textured polycrystalline Co films the expected temperature dependent decrease of the effectively acting uniaxial anisotropy constant up to room temperature is therefore with $\Delta K^{\mathrm{fcc}}_{1V,\mathrm{uni}} < \frac{1}{3}\Delta K_{1V,cub} + \frac{1}{27}\Delta K_{2V,cub} < 10$ kJ/m^3 negligibly small[64]. Consequently, the observed decrease of $K_{1,\mathrm{eff}}(T)$ by about 80 kJ/m^3 for the thickest Co layer, where the relative contribution of the interface anisotropy is negligibly small (see inset of Fig. 5.30(a)), does not fit with the results neither for hcp nor for fcc Co. However, the temperature dependence of the shape anisotropy has to be taken into account as well as the saturation magnetization varies with temperature according to Bloch's $T^{3/2}$ law from $M_S = 1.44$ MA/m at 4.2 K to $M_S = 1.40$ MA/m at room temperature [83]. Thus, the corresponding variation of the shape anisotropy $K_d = -\frac{\mu_0}{2}M_S^2$ of the Co layers is about 70 kJ/m^3, so that in the case of the thickest Co thickness according to Eq. 2.18 $K_{1V,\mathrm{uni}} = K_{1V,\mathrm{eff}} + \frac{\mu_0}{2}M_S^2$ decreases by about 150 kJ/m^3 up to room temperature. The difference to the expected change in $K_{1V,\mathrm{uni}}$ for hcp and fcc Co is in both cases about 100 kJ/m^3, so that the temperature dependence of $K_{1V,\mathrm{uni}}$ gives no further indication if the Co layers exhibit a fcc or hcp crystal lattice. The difference to one of the two bulk values can be explained by slight temperature-driven changes in the lattice strain in the order of $\lesssim 0.3\%$ (see Eq. 5.67).

In the following the investigations of the temperature dependence of the anisotropy of Co/Pt layered structures are briefly summarized always with regard to the temperature range investigated within this work (4.2 K $\leq T \leq$ 295 K) in order to comprehend the $K_{1,\mathrm{eff}}(T)$ curve of both samples with thinner Co layer thicknesses ($t_{\mathrm{Co}} = 2$ nm and $t_{\mathrm{Co}} = 6$ nm). T. Sugimoto et al. investigated the $K_{1,\mathrm{eff}}(T)$ behavior of (0.6 nm Co/1.8 nm Pt) multilayers and found a rise of the anisotropy constant with increasing temperature by about 100 kJ/m^3 including a temperature-driven spin-reorientation transition (SRT) to perpendicular easy axis at about 150 K [113]. In contrast to this finding Stamps et al. observed the opposite behavior for thicker Co layers by using (3.2 nm Co/2.0 nm Pt)$_6$ multilayers, namely a decrease of the

[64] For fcc Co the [111] direction is the easy axis, while the [110] direction is harder and the [100] direction is the hard axis [87, 86]. $\Delta(E/V) = \frac{1}{3}K_{1V,\mathrm{cub}} + \frac{1}{27}K_{2V,\mathrm{cub}}$ is the energy density difference between the hard and the easy axis used as an upper bound for the value of $\Delta K^{\mathrm{fcc}}_{1V,\mathrm{uni}}$.

anisotropy constant with increasing temperature by about 100 kJ/m^3 was found including a SRT to easy plane behavior at about 180 K [104, 109]. Similar to the results of this thesis the aforementioned investigations indicate that the $K_{1,\mathrm{eff}}(T)$ behavior changes from an increase to a decrease with increasing Co layer thickness. For the sake of completeness it is mentioned that for ultrathin nominal Co layer thicknesses below ≈ 0.6 nm, where the Co material is basically interdiffused with the Pt, it was observed that $K_{1,\mathrm{eff}}$ again monotonically increases with decreasing the temperature [890, 105]. In all the publications possible reasons for the temperature dependence of the anisotropy are discussed only from a qualitative point of view, namely it was suggested that the $K_{1,\mathrm{eff}}(T)$ behavior is a consequence of changes of the interfacial magnetism e.g. due to the temperature dependence of the Pt polarization (see section 5.3.2.2) [113, 105] or caused by changes in the lattice strain [890, 109, 104]. Therefore, it can only be stated that the temperature dependence observed for the sample with the thinnest Co layer thickness is within the span of other studies while the underlying mechanism affecting the anisotropy constant is unknown so far.
In conclusion, for thin/ thick Co layer thicknesses ($t_{\mathrm{Co}} = 2$ nm/ 20 nm) the effective first order anisotropy constant $K_{1,\mathrm{eff}}$ slightly increases/ decreases by about 70/ 80 kJ/m^3 with increasing the temperature from liquid He to room temperature, while for $t_{\mathrm{Co}} = 6$ nm it is nearly temperature-independent. This finding probably reveals a different temperature dependence of the effective volume anisotropy constant compared to the surface anisotropy constant. By comparison with bulk Co under consideration of temperature-driven changes of the shape anisotropy the temperature dependence of the volume anisotropy constant can only be explained by additionally assuming that the Co lattice strain slightly varies with temperature by $\lesssim 0.3\%$, which enters the magnetic ansiotropy via the magneto-elastic coupling. The temperature dependence of the surface anisotropy is probably connected with both changes of the lattice strain and of the magnetic moments at the Co/Pt interfaces. The temperature-driven changes in the strain of the Co lattice might originate from the difference of the thermal expansion coefficients between Co and Pt ($\alpha_{\mathrm{Co}} = 13 \cdot 10^{-6}$ K^{-1}, $\alpha_{\mathrm{Pt}} = 9 \cdot 10^{-6}$ K^{-1}) [549]. However, in any case the rather small dependencies of $K_{1,\mathrm{eff}}$ on temperature reveal that drastic structural changes can be ruled out that might have important impact on the magnetoresistance effects. The extent of how strong the magnetic properties of the magnetically active region at the interfaces varies with temperature is unknown so far.

5.6.4 Temperature dependence of magnetoresistance effects

In this section the temperature dependence of the various MR effects is presented and discussed for the three samples with Co layer thicknesses of $t_{\mathrm{Co}} = 2$ nm, 6 nm, and 20 nm starting with the AMR and AIMR+GSE. Thereby, an elimination of the current shunt is omitted as it only depends slightly on temperature (see Fig. 5.51) and the focus of this section is on the gross features of the temperature dependence of the MR effects. Thus, for their description the definitions of intrinsic variables given in section 5.5.1.3 are used (see Eqs. 5.72 and 5.73).

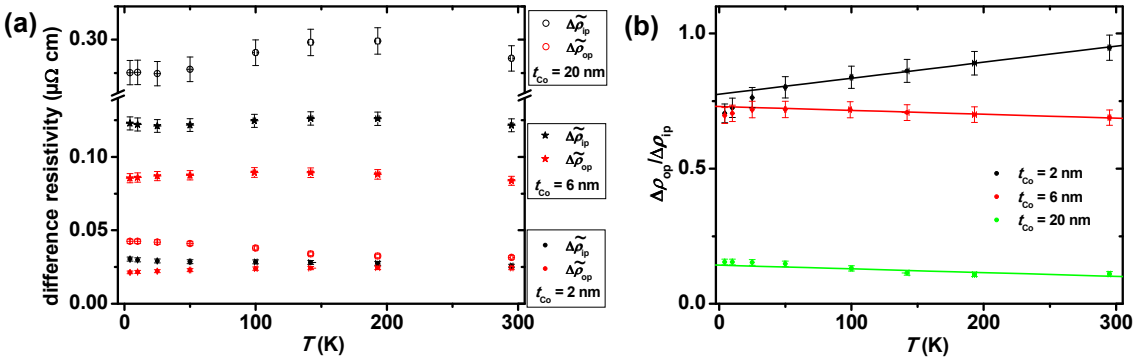

Figure 5.54: a) $\Delta\widetilde{\rho}_{ip}$ and $\Delta\widetilde{\rho}_{op}$ as well as (b) AIMR+GSE normalized by the AMR, i.e., $\Delta\rho_{op}/\Delta\rho_{ip}$, plotted versus temperature. The solid lines in (b) are linear fits to the data for $T \geq 50$ K.

AMR and AIMR+GSE: Fig. 5.54(a) shows the difference resistivities $\Delta\widetilde{\rho}_{ip,Co}$ and $\Delta\widetilde{\rho}_{op,Co}$ versus temperature. At first, the temperature dependence of the AMR is discussed. For all three Co layer thicknesses the $\Delta\widetilde{\rho}_{ip,Co}(T)$ behavior is roughly speaking a horizontal line revealing that the temperature variation only has minor influence on the magnitude of the AMR. Quantitatively, in the investigated temperature range of 4.2 K $\leq T \leq$ 295 K for the two thicker samples $\Delta\widetilde{\rho}_{ip,Co}(T)$ changes by less than 10% compared to the value at room temperature. For the thinnest sample the change is $\approx$ 15%. This finding in particular reveals that the scattering of the electrons at phonons and magnons only provides small contributions to the AMR as explained in the following. For the sample with the thickest Co layer a $RRR_{Co} = 1.5$ of the Co layer is calculated from the results of the fitting procedure of the $R(T)$ curve (see Tab. 5.4 and Fig. 5.50) meaning that about 1/3 of the scattering processes at room temperature is caused by phonons and magnons. Thus, if these processes exhibited the same scattering anisotropy as the scattering at static defects an increase of $\Delta\widetilde{\rho}_{ip,Co}$ to $\approx$ 0.4 $\mu\Omega$cm at room temperature would occur in contrast to the observed stagnation of the AMR with temperature. The rather small temperature dependence of the AMR can be comprehended from a theoretical point of view: The scattering at non-spherical potentials as in the case of the scattering at phonons and magnons yields a lower scattering anisotropy compared to the scattering at spherical defects (see section 5.1.4.1). Furthermore, the results are within the span of the results of other experimental studies concerning the AMR of Co films, where indications were found that the electron-phonon scattering only provides either small positive or even small negative AMR ($\rho_{||} < \rho_{\perp}$) contributions [523, 553]. Obviously similar to the AMR the difference resistivity $\Delta\widetilde{\rho}_{op,Co}$ only slightly varies with temperature revealing that, besides the AMR, both the AIMR and the GSE are basically governed by the scattering at static defects, i.e., the Co/Pt interfaces in the case of the AIMR. The temperature independence of the GSE is in accordance with the results of Gil et al. [553]. The insensitivity of $\Delta\widetilde{\rho}_{op,Co}$ on temperature variation implies that the related temperature-driven changes in the lattice strain have only minor influence on both the size of the AIMR and GSE in accordance with the results of section 5.5.3. Furthermore, regarding the AIMR the expected strong variation of the magnetic moments at the Co/Pt interfaces with temperature (see

section 5.3.2.2) seems to have only a minor impact on its magnitude.
Small differences in the temperature dependencies of the AMR and AIMR+GSE become obvious when normalizing $\Delta\widetilde{\rho}_{\mathrm{op,Co}}$ by $\Delta\widetilde{\rho}_{\mathrm{ip,Co}}$, i.e., $\Delta\rho_{\mathrm{op}}/\Delta\rho_{\mathrm{ip}}$, as can be seen in Fig. 5.54(b). While for the sample with the thicker Co layer thickness the $\Delta\rho_{\mathrm{op}}/\Delta\rho_{\mathrm{ip}}(T)$ curve is almost a horizontal line over the whole temperature range the curves for the two other samples deviate from a straight line below $T \approx 50$ K, namely a slight drop of $\Delta\rho_{\mathrm{op}}/\Delta\rho_{\mathrm{ip}}$ with decreasing temperature was found. The drop is a consequence of both a slight increase of the AMR and a slight decrease of the AIMR+GSE with decreasing temperature as can be seen in Fig. 5.54(a). In the following possible reasons for this feature are discussed. In the aforementioned low temperature regime most of the phonons and magnons are frozen out, so that the Co and Pt layer resistances do not change and therefore variations of the current distribution within the stack can be ruled out to be the reason for the drop (see Fig. 5.51). Furthermore, the temperature dependence of the magnetic moments at the interfaces should basically obey Bloch's $T^{3/2}$ law, so that their variation with temperature should be the less the lower the temperature is. Thus, possible influences on the AIMR are rather expected at higher temperatures. As only a small influence of changes in the magnetic moments at the interfaces on the AMR is expected, because the AMR effect should mostly originate from the interior of the Co layer, they cannot be the reason for the drop. A possible explanation for the drop in $\Delta\rho_{\mathrm{op}}/\Delta\rho_{\mathrm{ip}}$ might be connected with electron-electron scattering processes that are likely to contribute to the resistivity at low temperatures and that might differently affect the AMR and AIMR+GSE. However, such contributions were not detected in the measurements of the temperature dependence of the overall resistance (see section 5.6.1). A future explanation of the drop also has to answer why its magnitude apparently decreases with increasing the Co layer thickness, so that the drop do not appear for the sample with $t_{\mathrm{Co}} = 20$ nm.
A further distinctive feature in Fig. 5.54(b) is that in contrast to the $\Delta\rho_{\mathrm{op}}/\Delta\rho_{\mathrm{ip}}(T)$ behavior of the two thickest samples, which are basically horizontal lines (above $T = 50$ K), for $t_{\mathrm{Co}} = 2$ nm the curve linearly increases with a small slope of about $5.9 \cdot 10^{-4}$ K^{-1}. By extrapolating the straight line to higher temperatures a value of $\Delta\rho_{\mathrm{op}}/\Delta\rho_{\mathrm{ip}} = 1$ is obtained at about $T = 375$ K. This means that at this temperature the AIMR would be of the same size as the AMR, i.e., $\rho_{||} = \rho_{\mathrm{p}}$ applies, if the extrapolation is valid. Similar to the drop of $\Delta\rho_{\mathrm{op}}/\Delta\rho_{\mathrm{ip}}(T)$ at low temperatures the reason for its linear increase is unknown so far. Probably, a correlation with the observed linear increase of the anisotropy constant $K_{1,\mathrm{eff}}$ with temperature exists (see black curve in Fig. 5.53), so that both moderate increases might be at least partially caused by temperature-driven variations in the lattice strain.

SMR, AHE, and OHE: This paragraph deals with the temperature dependence of the SMR, AHE, and OHE. For the two high field effects (SMR and OHE) only the dependencies for the two samples with $t_{\mathrm{Co}} = 6$ nm and $t_{\mathrm{Co}} = 20$ nm were determined as for the sample with the thinnest Co layer thickness the field sweep measurements were only conducted up to ± 2 T. In Fig. 5.55(a) the temperature dependence of the spin-disorder MR is displayed that was obtained by fitting the isotropic high field behavior of the field sweep measurements of the polar MR geometry. Obviously

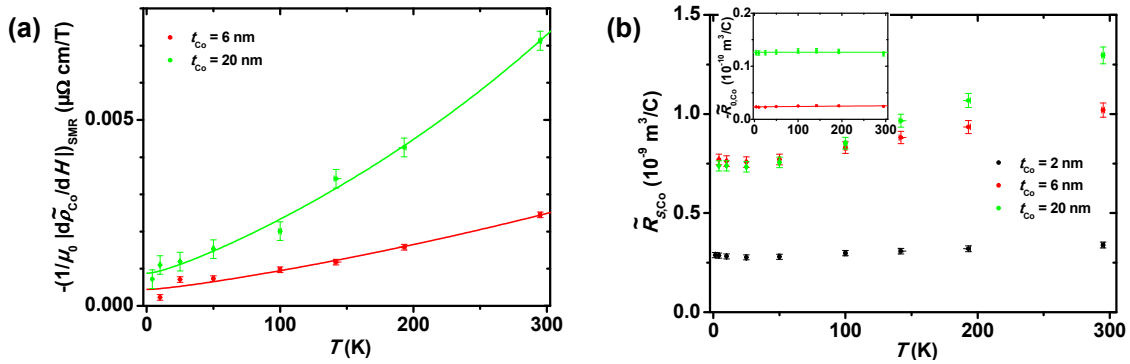

Figure 5.55: (a) Spin-disorder MR and (b) anomalous and normal Hall constants in dependence of temperature. The latter is given as inset in (b). The solid lines in (a) and in the inset of (b) are fits to the data.

$-|\mathrm{d}\widetilde{\rho}_{\mathrm{Co}}/\mathrm{d}(\mu_0 H)|_{\mathrm{SMR}}$ versus temperature shows a parabolic-like increase for both Co layer thicknesses. Quantitatively, the curves can be well-described by the theoretical model developed by Raquet et al. as indicated by the solid lines that are fits to the data according to Eq. 5.40:

$$-|\mathrm{d}\widetilde{\rho}_{\mathrm{Co}}/\mathrm{d}(\mu_0 H)|_{\mathrm{SMR}}(T) = A \cdot T(1 + 2d_1 T^2)\ln(T/T_0) \quad , \tag{5.85}$$

where A is a constant reflecting the strength of the *s*-*d* interaction [553]. During the fitting $T_0 = 1$ K was held constant, which is a reasonable value according to Refs. [553, 555]. For the sample with $t_{\mathrm{Co}} = 20$ nm, which exhibits an electron-magnon scattering contribution $\rho_{\mathrm{mag}}(T)$ that resembles bulk Co according to the results of section 5.6.1, the resulting fit parameters are $A = (3.1 \pm 0.4)$ pΩcm/(KT) and $d_1 = (1.2 \pm 0.8) \cdot 10^{-6}$ K^{-2}. The latter is the parameter that accounts for the magnon mass renormalization. The result for the prefactor A is a reasonable value, in particular when considering the current shunt through the Pt of about 20% (see Fig. 5.51), as it is in any case in the range of $3-4$ pΩcm/(KT) found experimentally for thick Co films [553]. Furthermore, within the error margins of the experiment the value obtained for d_1 is within the span of values reported in literature for Co of $1.5 - 3 \cdot 10^{-6}$ K^{-2} [481, 553]. Regarding the results of the fitting procedure for the sample with the thinner Co layer thickness of $t_{\mathrm{Co}} = 6$ nm a smaller prefactor $A = (1.1 \pm 0.3)$ pΩcm/(KT) was obtained, which can be explained by a combination of a more significant current shunt through the Pt material and the presence of the finite size effect observed for the electron-magnon scattering term of the resistivity (for the latter, see section 5.5.2.2 and 5.6.1). However, for the magnon mass renormalization, which defines the curvature, the obtained value $d_1 = (1 \pm 1) \cdot 10^{-6}$ K^{-2} is similar to the one of the thickest sample and therefore in good accordance with the values reported in literature.

In Fig. 5.55(b) the temperature dependence of the AHE is shown for the three samples. Obviously the shape of the curves is similar to the shape of the $R(T)$ behavior, namely they basically remain constant up to about 30 K and then they increase almost linearly. This finding is in qualitative accordance with the results reported in literature, where R_S was generally found to obey a ρ_{xx}^{ν} power law (see

section 5.1.4.2). It is worth explicitly mentioning that this finding implies that in contrast to the AMR and AIMR+GSE the scattering at phonons and magnons significantly contributes to the AHE. A quantification of ν is omitted here as its expressiveness is rather small in the case of thin films and multilayers due to the lack of adequate theories. The focus is rather on the gross feature that obviously the relative magnitude of the increase of the AHE with temperature strongly increases with Co layer thickness in particular yielding a crossing of the $R_S(T)$ curves for the two thickest samples. As R_S is tightly connected with $\rho_{xx,\mathrm{Co}}$ this result gives a direct indication that the RRR_{Co} of the Co layer strongly depends on Co layer thickness, which was found to be a consequence of both a stronger interface scattering contribution and a suppressed electron-magnon and electron-phonon scattering at low Co layer thicknesses (see section 5.6.1). For the sake of completeness it is mentioned that below $T = 50$ K a slight increase of the AHE with decreasing temperature was found that is similar to the bending up/ bending down found for the AMR/ AIMR+GSE (see Fig. 5.54). A deeper analysis of the $R_S(T)$ results would go beyond the scope of this thesis and is therefore omitted here.
In contrast to the AHE the normal Hall effect does not depend on temperature as indicated by the solid lines in the inset of Fig. 5.55(b) that are horizontal fits to the data. As the magnitude of the OHE is significantly suppressed at low Co layer thicknesses compared to bulk (see section 5.5.2) the $\widetilde{R}_0(T)$ behavior of the sample with $t_{\mathrm{Co}} = 6$ nm in particular reveals that the corresponding finite size effect does not vary with temperature. A temperature independence of the OHE is in accordance with the results found for thick Co films [580].

In conclusion, the temperature variation (4.2 K $\leq T \leq$ 295 K) reveals the existence of the AIMR down to liquid He temperature. Similar to the AMR the magnitude of the AIMR+GSE ($\Delta\widetilde{\rho}_{\mathrm{op}}$) only slightly depends on temperature. This finding reveals that electron-phonon scattering and electron-magnon scattering does not considerably contribute to these effects, so that they are basically governed by the scattering at static defects, i.e., the Co/Pt interface in the case of the AIMR. Furthermore, this result implies that temperature-driven changes in the strain and probably also in the magnetic moments of the atoms at the Co/Pt interfaces do not significantly alter these MR effects. Besides, the OHE does not depend on temperature. In contrast, the AHE increases with temperature revealing that the temperature dependent parts of the resistivity contribute to this particular effect. The parabolic-like increase of the SMR with temperature can be well-described by the model of Raquet and co-workers [481]. Concerning the finite size effects, i.e., the suppression of the various MR effects at small Co layer thicknesses $t_{\mathrm{Co}} \lesssim \lambda_{\mathrm{bulk\ Co}}$ (see section 5.5.2), a considerable temperature dependence of them can be ruled out in the case of the AMR, AIMR+GSE, SMR, and OHE. The temperature dependence of the overall resistivity reveals that the finite size effect in the SMR is a fingerprint of the suppression of the electron-magnon scattering at low Co layer thicknesses. Regarding the AHE a deeper analysis of the results for $R_S(T)$ will show how its interface and volume contributions are affected by the temperature variation and to what extent the finite size effects in the electron-magnon and electron-phonon scattering enter the AHE.

5.7 Anisotropic Interface Magnetoresistance (AIMR) of Co/Pt multilayers

In this section the results of the room temperature MR measurements concerning the AIMR[65] of Co/Pt multilayers are presented, where the Pt interlayer thickness was varied between $0.25 - 5$ nm and the Co thickness was held constant at 0.8 nm (see section 5.2.4). In this ultrathin layer-thickness regime, where the Co material is basically interdiffused with the Pt the application of the layer model would be rather artificial and is therefore omitted here. Furthermore, instead of a detailed presentation and description of the size of the various MR effects this section focuses on the important implications of the presence of the AIMR effect. As shown in section 5.5 in the thickness regime $t_{\mathrm{Co}} \leq 1$ nm, where the Pt/Co/Pt sandwiches exhibit an easy axis of magnetization, the AIMR is in the same order of magnitude as the AMR effect. In this section it is examined if this fact is generally valid for Co/Pt layered structures with perpendicular magnetic anisotropy (PMA), which would be of importance in particular for studying the intrinsic domain wall resistance (iDWR) in order to give a correct quantification of the iDWR contribution. In section 5.7.1 the $\rho(\mathbf{H})$ curves of Co/Pt multilayers with PMA are presented and discussed also with regard to the results of other studies, which particularly indicates that the lack of knowledge about the existence of the AIMR led to misinterpretations of the MR curves. Section 5.7.2 deals with the dependence of the AIMR and AMR on Pt interlayer thickness and number of bilayer repetition, where the AMR is used as a measure for the strength of the AIMR.

5.7.1 Influence of magnetic microstructure on resistivity & domain wall resistance

Fig. 5.56(a) exemplarily shows the diagonal part of the resistivity tensor ρ_{xx} of a multilayer with perpendicular magnetic anisotropy (PMA) in dependence of the applied field for the three generic measurement geometries. The Pt interlayer thickness and the bilayer repetition is $t_{\mathrm{Pt}} = 2$ nm and $n = 8$, respectively (MOKE measurements of the remagnetization of this sample, see Fig. 5.32(c)). From a qualitative point of view the measurements basically resemble the corresponding counterparts recorded for Pt/Co/Pt sandwiches, which can be comprehended by comparison with Fig. 5.37(a), where the MR curves for the sandwich with $t_{\mathrm{Co}} = 0.8$ nm are shown. In particular, $\rho_{||} > \rho_{\mathrm{p}} > \rho_{\mathrm{t}}$ applies above technical saturation revealing the existence of the AMR and AIMR effects[66]. However, a minor difference exists between both polar curves, namely, while for the sandwich the resistivity monotonically decreases with increasing the absolute value of the applied field (see Fig. 5.37(a)) in the $\rho_{xx}(H_{\mathrm{p}})$ curve of the multilayer peaks were observed. The peaks can best be seen

[65] Note that regarding the quantity $\Delta\rho_{\mathrm{op}}$ the term AIMR is frequently used throughout this chapter, although contributions of the GSE are likely to exist. However, the AIMR is the dominant contribution for all multilayers investigated in this thesis as $\Delta\rho_{\mathrm{op}} > 0$ always applies, so that the restriction to the AIMR is justified for the sake of convenience.

[66] $\rho_{xx}(\varphi)$ and $\rho_{xx}(\theta)$ both exhibit a $\cos^2$ dependence (not shown) as found for the sandwiches (see Fig. 5.40).

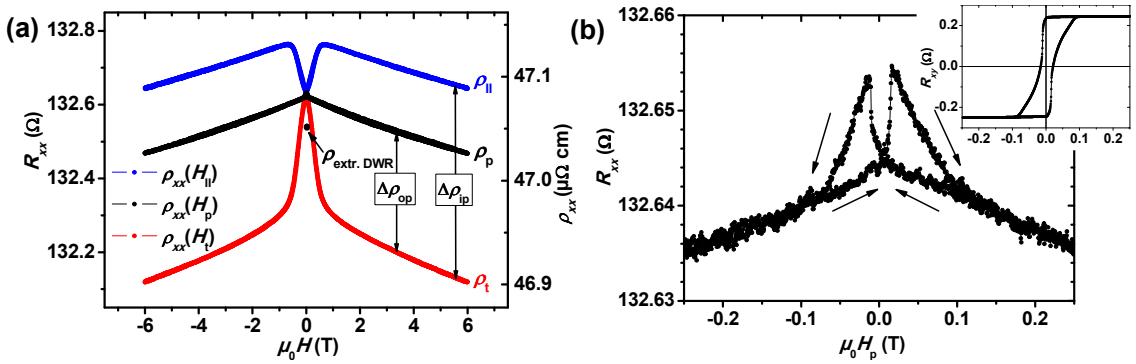

Figure 5.56: (a) Resistance R_{xx}/ resistivity ρ_{xx} as a function of the applied field $\mu_0 H$ for the three principle directions of the field with respect to the current direction and film orientation for a 5 nm Pt/(0.8 nm Co/2 nm Pt)$_8$/1 nm Pt multilayer. The black dot indicates the averaged extrinsic part of the resistivity of the domain walls $\rho_{\text{extr. DW}}$ (see text). (b) Zoom into the polar MR curve shown in (a). The inset shows the simultaneously measured $R_{xy}(H_\text{p})$ curve.

in Fig. 5.56(b), which is a zoom into the polar curve shown in Fig. 5.56(a). This difference in $\rho_{xx}(H_\text{p})$ between the multilayer and the sandwich can be attributed to a different remagnetization behavior. While the magnetization of the sandwich basically switches from one perpendicular magnetized single-domain state to the opposite at small opposite fields of about 10 mT (see inset of Fig. 5.29(a)) the magnetization of the multilayer decays into a multi-domain state at small opposite fields that, in contrast, is present over a relatively large field range of up to 90 mT. This can also be seen in the corresponding $R_{xy}(H_\text{p})$ curve (see inset of Fig. 5.56(b)) that is dominated by the anomalous Hall effect[67]. By comparing of $R_{xy}(H_\text{p})$ with $R_{xx}(H_\text{p})$ it is obvious that the occurrence of the peaks in the latter curve is correlated with the existence of a multi-domain state. In the following it is discussed why the creation of a multi-domain state yields a rather small but detectable increase of the resistivity. For that purpose the *extrinsic* effects on the resistivity are estimated that are connected with changes in the magnetic microstructure. In contrast to the domains, within the Bloch domain walls magnetization components exist that are oriented in the film plane, i.e., the magnetization exhibits different orientations with respect to the interfaces and texture, and, in addition, the magnetization is partially oriented along the current direction. Consequently, the resistivity locally varies within the domain walls due to the presence of the AIMR+GSE and AMR effects. While the superposition of the AIMR and GSE reduces the resistivity of the walls compared to the perpendicular magnetized domains according to both in-plane components of

[67] For the macroscopic wire sample the decay into a multi-domain state begins at a smaller field compared to the laterally homogeneous film (see Fig. 5.32(c)), which might be a consequence of a gradual reduction in the anisotropy at the wire edges due to shadowing effects caused by the mask technique during sample preparation (see section 5.3.2.1). In addition, for the wire-shaped sample the multi-domain state is erased at a lower field compared to the laterally homogeneous film sample (110 mT, see Fig. 5.32)(c)). It is checked that the lower sweep rate by about a factor of ten generally used for the former method, which might cause domain wall creeping processes contributing to the magnetization reversal, can be ruled out to be the reason for the difference, whose cause is unknown so far.

magnetization the AMR enhances the resistivity according to the longitudinal component $M_{||}$ (see Eq. 5.71). In polar measurement geometry no in-plane direction is outstanding in the energy landscape, so that on average the orientation of the walls should be arbitrary. In fact, as can be seen in the FTH micrograph given as inset in Fig. 5.32(c) after demagnetization in polar fields the magnetization of a nominally identical sample exhibits a maze pattern without a preferential direction for the orientation of the walls. Thus, on a macroscopic scale an average contribution of the walls to the resistance due to the AMR and AIMR+GSE is acting, so that the average resistivity of the center of the walls can be estimated by $\rho_{\text{extr. DW}} = \rho_{\text{t}} + \frac{\Delta\rho_{\text{ip}}}{2}$. Thereby, ρ_i is given by the extrapolation of the linear high field behavior of the corresponding curve to zero field. For the exemplary case considered here $\rho_{\text{extr. DW}} < \rho_{\text{p}}$ applies (see black dot in Fig. 5.56(a)). This means that a decrease of the resistance is expected when a maze pattern is created out of a single-domain state, which is in contradiction to the observed resistance increase. As will be shown in the next section 5.7.2 the condition $\rho_{\text{extr. DW}} < \rho_{\text{p}}$ ($\frac{\Delta\rho_{\text{op}}}{\Delta\rho_{\text{ip}}} > 0.5$) applies to all samples with PMA prepared within this thesis. Moreover, in the polar MR measurements not a single indication for a drop in resistance during remagnetization was found for any sample. These facts reveal the existence of a positive *intrinsic* domain wall resistance (iDWR) effect, meaning that the domain walls themselves are a source of resistivity, which overcompensates the extrinsic MR scattering contributions that are connected with the creation of the domain walls. However, resistance peaks during remagnetization were only detected for multilayers with bilayer repetitions of $n \geq 4$ when the individual Co layers are coupled ferromagnetically to each other (see section 5.3.2.1). All other samples, including the sandwiches with PMA, display no peaks in the resistivity in the vicinity of the coercive field, which might be a consequence of a rather low domain wall density as only a few domain walls rush through the sample providing the remagnetization. Thus, the resistance signal arising from the domain walls should be below the resolution of the experiment.
To summarize, the discussion reveals that the detected *positive* domain wall resistance cannot be a consequence of extrinsic contributions arising from the AMR and AIMR+GSE effects that are connected with the magnetic microstructure of the domain walls, which in turn reveals that an *intrinsic* DWR effect exists that overcompensates the extrinsic contributions. A positive intrinsic DWR is in accordance with other studies concerning iDWR of Co/Pt multilayers (see section 5.1.4.3). A quantification of the effect is omitted here as the evaluation of the microstructure with field is not known and it is restricted here to give a rough estimation of the strength of the extrinsic DWR contributions: The change in resistance that occurs when the maze domain pattern shown in the inset of Fig. 5.32(c) is created from a perpendicular single-domain state is given by $\Delta R_{\text{extr. DWR}} = 0.5 \cdot (R_{\text{p}} - (R_{\text{t}} + \frac{\Delta R_{\text{ip}}}{2})) \cdot A_{\text{DW}}$, where $A_{\text{DW}} \approx \frac{\delta}{D}$ is the area filling of the domain walls, D is the domain size[68], δ is the domain wall width, and the prefactor accounts for the gradual rotation of the magnetization within the walls. The domain size was determined from the FTH micrograph according to the method given in Ref. [891] to be $D \approx 150$ nm,

[68] More precisely, D is the average width of the branches of the labyrinth including the domain walls.

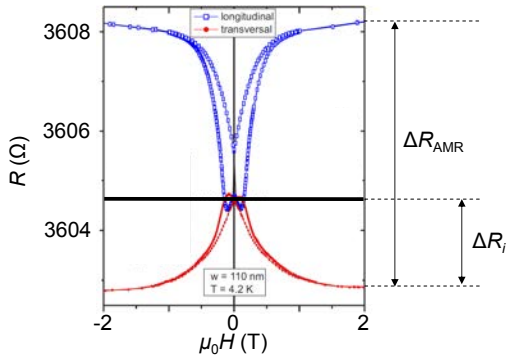

Figure 5.57: (a) Resistance R as a function of the applied field $\mu_0 H$ oriented in longitudinal and transverse direction for a 15 nm Pt/(0.3 nm Co/1 nm Pt)$_{10}$ multilayer nanowire with lateral dimensions of $w = 110$ nm and $l = 40$ μm. ΔR_i is rather a consequence of the AIMR effect, i.e., it resembles ΔR_{op}, than being caused by intrinsic domain wall scattering processes, see text. From Ref. [649].

and the domain wall width $\delta = 40$ nm was calculated via Eq. 2.29 by using the anisotropy constant $K_{1,\mathrm{eff}} = 160$ kJ/m^3 determined for the sample and the exchange stiffness $A_{\mathrm{Co}} = 31.4$ pJ/m of bulk Co [153]. As a result $\Delta R_{\mathrm{extr.\ DWR}} \approx -0.01\ \Omega$ was calculated, which is in the same order of magnitude but of opposite sign as the measured DWR $\Delta R_{\mathrm{meas.\ DWR}}$ highlighting that a knowledge about the extrinsic contributions is mandatory for a correct quantification of the intrinsic part $\Delta R_{\mathrm{iDWR}} = \Delta R_{\mathrm{meas.\ DWR}} - \Delta R_{\mathrm{extr.\ DWR}}$.
Generally, a slight asymmetry in the resistance peaks was observed, e.g. in the measurement shown in Fig. 5.56(b) the peak at negative fields is a little lower than the peak at positive fields. The asymmetry might be a consequence of contributions of the antisymmetric MR effect (see section 5.1.4.3), however, this topic was not further investigated.
Besides the contributions of the domain walls to the resistivity, which are rather small, namely within the order of magnitude of the resolution of the experiment of 10^{-5}, no further MR effects were observed that did not occur in the case of the sandwiches. In particular, it is worth mentioning that for samples with $t_{\mathrm{Pt}} \geq 3$ nm, where the individual Co layers are not necessarily coupled ferromagnetically (see section 5.3.2.1), no indications for the existence of contributions of the giant magnetoresistance effect were observed. This finding is in accordance with literature and can be comprehended as the Pt layer thickness is rather large and Pt is known to be a strong spin-flip scatterer [47].
In the following some implications of the existence of the AIMR on the results of the studies concerning intrinsic DWR are discussed. It is important to note that due to the lack of knowledge about the existence of the AIMR effect it was stated in literature that the measurement of the transverse MR curve of systems with PMA provides an easy access to determine the intrinsic domain wall resistance [648, 649]. Fig. 5.57 displays the longitudinal and transverse MR curves measured at $T = 4.2$ K of a 15 nm Pt/(0.3 nm Co/ 1 nm Pt)$_{10}$ nanowire that exhibits PMA (lateral dimensions: $w = 110$ nm and $l = 40$ μm) [649]. Obviously, both curves basically resemble the corresponding curves given in Fig. 5.56(a). G. Dumpich and co-workers ex-

plained the transverse MR curve as follows [648, 649]. Above technical saturation the magnetization is oriented perpendicularly to the current direction in the film plane. By reducing the field the magnetization rotates from in-plane to out-of-plane forming a multi-domain pattern with around 130 domains (domain size of $\approx$ 300 nm), while at the same time the resistance increases. The spins inside the domain walls are aligned along the transverse direction as long as the transverse field is non-zero due to energy minimization. Thus, with the exception around zero field, where the magnetization within the domain walls might exhibit components oriented along the current direction, the magnetization is always oriented perpendicularly to the current direction everywhere within the sample with and without domain walls. Consequently, the authors argued that in the transverse MR curve a change of the resistance due to changes in the AMR contribution can be excluded, which in turn means that the observed positive resistance difference ΔR_i between the saturated state and the multi-domain state solely arises from intrinsic domain wall scattering processes. This conclusion would be correct if further extrinsic MR effects like the AIMR and GSE were not present. Unfortunately, the authors did not examine these effects, i.e., they did not measure the polar MR curve, which would reveal whether there is a difference between R_p and R_t. However, the following argumentation shows that the interpretation of the transverse MR curve to be a consequence of preponderant intrinsic domain wall resistance is rather questionable. First, the transverse curve basically resembles the shape of the longitudinal MR curve when it is mirrored at the black horizontal line given in Fig. 5.57 that is governed by the AMR effect due to remagnetization processes within the domains. Thus, the transverse curve might also be a consequence of remagnetization processes within the domains, which enter the resistance due to the presence of the AIMR effect, rather than being caused by an increase of the domain wall width by increasing the absolute value of the transverse field that might decrease the intrinsic domain wall resistance as the authors argued. Second, a further indication against the interpretation of the transverse curve to be governed by intrinsic domain wall resistance is the size of the effect reported in the publication. The reported value of $\Delta\rho_\mathrm{iDWR}^\mathrm{cpw} = 0.23$ $\mu\Omega$cm calculated there from $\Delta R_i = 1.9$ Ω is within the span of values reported in literature (see below). However, the current shunt through the Pt, which might be mainly caused by the relatively thick Pt seed layer ($t_\mathrm{seed} = 15$ nm), is not considered in the estimation of $\Delta\rho_\mathrm{DWR}$ as it is otherwise the case. The current shunt can be roughly estimated from Fig. 5.44 and Refs. [652, 654] to be $\gtrsim 90\%$. Hence, after correction of the shunt the domain wall resistivity clearly exceeds the limits and it is reasonable to assume that resistance contributions of the domain walls are one order of magnitude lower than ΔR_i and therefore negligibly small in a first order approximation. This implies that the transverse curve should be basically a consequence of remagnetization processes within the domains due to the presence of a preponderant AIMR effect.

When domain wall contributions are negligibly small the size of the AIMR+GSE can be estimated by assuming that the polar curve is basically a straight horizontal line as the magnetization within the domains does not change its orientation with respect to the current and stacking direction within the whole field range and at liquid He temperature contributions of the SMR are negligibly small. Thereby, the

polar curve should virtually touch the transverse and longitudinal curves at zero field as the actual multi-domain state at remanence has only minor influence on the resistance as argued above (estimated polar MR curve, see black solid line in Fig. 5.57). This means that ΔR_i basically corresponds to the size of the AIMR+GSE, i.e., $\Delta R_i \approx \Delta R_{\mathrm{op}}$, instead of ΔR_{iDWR}. The size of the AIMR+GSE normalized to the AMR is $\Delta R_i/\Delta R_{\mathrm{AMR}} = 0.35$, which is rather low compared to the results of this thesis. However, the value is reasonable as the Co layer thickness is only $t_{\mathrm{Co}} = 0.3$ nm and a rather strong decrease of $\Delta\rho_{\mathrm{op}}/\Delta\rho_{\mathrm{ip}}$ with decreasing Co layer thickness was observed below $t_{\mathrm{Co}} = 2$ nm (see Fig. 5.48(b)).
In conclusion, the discussion of the results of Refs. [648, 649] reveals that a complete knowledge about the magnetoresistance effects of the samples is indispensable for a correct interpretation of the MR curves and shows that the existence of the AIMR+GSE can explain the data, so that intrinsic domain wall resistance might only play a minor role.
In the publications that deal with the quantification of iDWR from a well-defined number (< 10) of domain walls in Co/Pt multilayered nanowires positive domain wall resistivities of $\Delta\rho_{\mathrm{DWR}}^{\mathrm{cpw}} = 0.02-0.8$ $\mu\Omega$cm are reported for current perpendicular wall (cpw) geometry [652, 650, 654]. In these values the area filling of the domain walls and only the fraction of the current that flows through the Co is considered, so that they can be directly compared to $\Delta\rho_{\mathrm{op,Co}} \lesssim 0.1$ $\mu\Omega$cm determined for the sandwiches with PMA (see Fig. 5.45(a)). $\Delta\rho_{\mathrm{op,Co}}$ is in the same order of magnitude as $\Delta\rho_{\mathrm{DWR}}^{\mathrm{cpw}}$ revealing the fact that for a correct quantification of the intrinsic domain wall resistance it is mandatory to determine the AIMR+GSE of the samples. As the AIMR+GSE reduces the resistivity within the domain walls compared to the domains the intrinsic contribution is determined by $\Delta\rho_{\mathrm{iDWR}}^{\mathrm{cpw}} = \Delta\rho_{\mathrm{DWR}}^{\mathrm{cpw}} + \Delta\rho_{\mathrm{op,Co}}$. Thus, the recent studies should have underestimated $\Delta\rho_{\mathrm{iDWR}}^{\mathrm{cpw}}$ due to the presence of the AIMR effect. However, without exception $\Delta\rho_{\mathrm{DWR}}^{\mathrm{cpw}} > 0$ was reported revealing that the intrinsic scattering contributions within the walls generally overcompensates the extrinsic AIMR+GSE contributions connected with the microstructure of the walls.
In the following section 5.7.2 the quantification of the AIMR is given for the multilayers, where the Pt interlayer thickness and the bilayer repetition was varied.

5.7.2 Dependence of AIMR on Pt interlayer thickness and bilayer repetition

At first the dependence of the AIMR on Pt interlayer thickness t_{Pt} and thereafter its dependence on bilayer repetition n is discussed. Fig. 5.58(a) displays ΔR_{op} and ΔR_{ip} as a function of t_{Pt} for multilayers with $n = 4$, whereas the AMR (ΔR_{ip}) is shown for comparison. It is convenient to deal directly with the measured difference resistances as the amount of Co material is the same for all such samples. The values at $t_{\mathrm{Pt}} = 0$ nm belong to the sandwich with a Co thickness of $t_{\mathrm{Co}} = 3.2$ nm. At first the thickness dependence of the AMR is discussed. Obviously $\Delta R_{\mathrm{ip}}(t_{\mathrm{Pt}})$ monotonically decreases. For $t_{\mathrm{Pt}} \gtrsim 1$ nm, where the Pt interlayers can be regarded as laterally continuous and significant changes in the roughness and interdiffusion of the Co/Pt interfaces can be ruled out (see section 5.3.1.3), the decrease of $\Delta R_{\mathrm{ip}}(t_{\mathrm{Pt}})$ can be

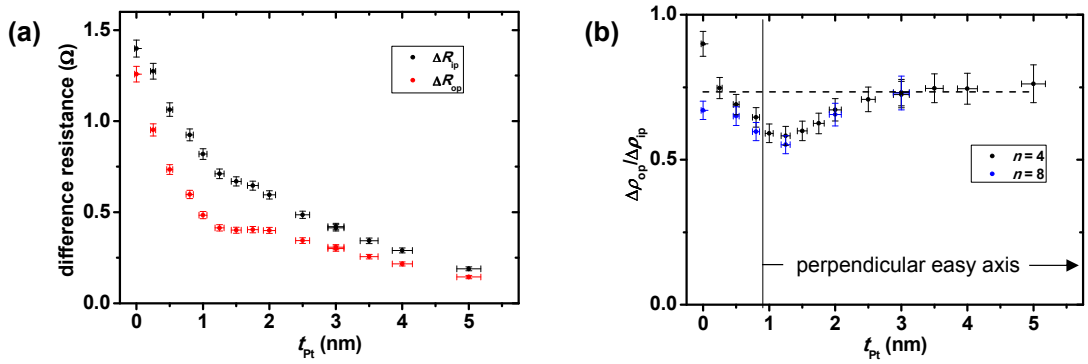

Figure 5.58: (a) Dependence of the difference resistances ΔR_{op} and ΔR_{ip} on Pt interlayer thickness for Co/Pt multilayers with bilayer repetition of $n = 4$. (b) Ratio of the two curves displayed in (a), i.e., $\Delta\rho_{\mathrm{op}}/\Delta\rho_{\mathrm{ip}}$, as a function of t_{Pt}. In addition, the results for multilayers with $n = 8$ are shown. The dashed line represents the value of the sandwich with the same individual Co layer thickness of $t_{\mathrm{Co}} = 0.8$ nm. The value at $t_{\mathrm{Pt}} = 0$ nm for $n = 4$ and $n = 8$ belongs to the sandwich with $t_{\mathrm{Co}} = 3.2$ nm and $t_{\mathrm{Co}} = 6.4$ nm, respectively.

primarily attributed to an increase of the current shunt through the Pt. Changes in the residual strain that result in changes of the anisotropy up to $t_{\mathrm{Pt}} = 3$ nm (see section 5.3.2.1) should only have minor influence on the size of the AMR as discussed in section 5.5.2. Below $t_{\mathrm{Pt}} \approx 1$ nm, where the Pt interlayers are no longer continuous and the Co layers are partially interconnected, a slightly stronger increase of the AMR with decreasing thickness was observed. In the regions, where the Co material of adjacent layers are in direct contact, a larger effective Co layer thickness exists. As for the sandwiches the difference resistivity $\Delta\rho_{\mathrm{ip,Co}}$ was found to increase with increasing the Co layer thickness (see Fig. 5.45(a)) $\Delta\rho_{\mathrm{ip,Co}}$ might be locally enhanced in these regions contributing to the stronger increase of the AMR with decreasing Pt interlayer thickness observed for $t_{\mathrm{Pt}} \lesssim 1$ nm. However, any profound interpretation of the evaluation of the AMR with t_{Pt} in this ultrathin-layer regime that is based on simple model concepts is rather dubious. The reason for this is that, for instance, complex effects on the local current density might act that are caused by the lateral inhomogeneity of the Pt material or significant thickness-driven variations of the atomic arrangement are likely to occur that might affect the AMR, so that the discussion of the AMR is restricted here to the given qualitative statements.

Obviously ΔR_{op} shows a similar dependence on t_{Pt} as ΔR_{ip} with the exceptions that it is systematically smaller and that it is basically constant in the thickness regime 1.25 nm $\leq t_{\mathrm{Pt}} \leq 2$ nm. The latter finding indicates that the increase of the current shunt with increasing t_{Pt} is compensated by a corresponding increase of the AIMR effect. Fig. 5.58(b) displays the AIMR normalized by the AMR, i.e., $\Delta R_{\mathrm{op}}/\Delta R_{\mathrm{ip}} = \Delta\rho_{\mathrm{op}}/\Delta\rho_{\mathrm{ip}}$, in dependence of Pt interlayer thickness for the multilayers with $n = 4$ and, in addition, for some multilayers with $n = 8$. The normalized depiction provides a good access to the strength of the *pure* AIMR effect that is corrected by the current shunt through the Pt for $t_{\mathrm{Pt}} \gtrsim 1$ nm as in this thickness regime changes in the strength of ΔR_{ip} should be basically determined by the current shunt

as stated above. It is worth mentioning that this assumption is in no contradiction to the results concerning the Pt/Co/Pt sandwiches. There, it was found that the AMR is independent of Co layer thickness for relatively thick samples with $t_{\mathrm{Co}} \geq 9$ nm, which was the initial motivation for using the AMR as normalization factor (see section 5.5.2.3), while for smaller Co layer thicknesses a finite size effect acts that significantly reduces the AMR compared to bulk. The reason why the AMR can be used, although the individual Co layer thickness is only $t_{\mathrm{Co}} = 0.8$ nm, is that t_{Co} was held constant for the multilayers, so that for all samples with laterally continuous Pt interlayers the AMR of the Co layers $\Delta\rho_{\mathrm{ip,Co}}$ should be basically the same.
As can be seen in Fig. 5.58(b) the normalized AIMR+GSE decreases with increasing Pt interlayer thickness up to the global minimum that is located at $t_{\mathrm{Pt}} = 1.25$ nm, then it increases up to $t_{\mathrm{Pt}} = 3$ nm, while for higher interlayer thicknesses it remains constant within the error margins of the experiment. In the following the evolution of the normalized AIMR with Pt interlayer thickness is discussed for $t_{\mathrm{Pt}} \geq 1$ nm, where the normalization by the AMR is legitimate in order to eliminate the current shunt and, therefore, the pure thickness dependence of the AIMR is obtained. Coincidentally, this thickness regime corresponds to the region where the Co/Pt multilayers exhibit a perpendicular easy axis of magnetization (see section 5.3.2.1). In contrast to the dependence of $\Delta\rho_{\mathrm{op}}/\Delta\rho_{\mathrm{ip}}$ on Co layer thickness investigated for the sandwiches (see section 5.5.2.3) this quantity only varies slightly with t_{Pt} by about 0.2. In order to find the reason for the small variation a comparison of the $\Delta\rho_{\mathrm{op}}/\Delta\rho_{\mathrm{ip}}(t_{\mathrm{Pt}})$ curve with the dependence of the effective first order anisotropy constant $K_{1,\mathrm{eff}}$ on t_{Pt} (see Fig. 5.31(b)) is useful. Obviously both quantities rise with increasing the interlayer thickness in the thickness range of up to $t_{\mathrm{Pt}} < 3$ nm, while for higher Pt interlayer thicknesses both quantities are basically constant. Importantly, above $t_{\mathrm{Pt}} = 3$ nm, similar to the findings for the anisotropy constant, $\Delta\rho_{\mathrm{op}}/\Delta\rho_{\mathrm{ip}}$ resembles the value determined for the sandwich with the same Co layer thickness of $t_{\mathrm{Co}} = 0.8$ nm (see dashed line in Fig. 5.58(b)) revealing that the AIMR of the individual Co/Pt interfaces within the stack are virtually identical. Due to the close relationship between the thickness dependence of the anisotropy constant $K_{1,\mathrm{eff}}$ and AIMR it is reasonable to assume that also for the latter quantity changes in the residual strain are the reason for the dependence on t_{Pt} as it is argued in the case of the anisotropy constant (see section 5.3.2.1). This interpretation is in accordance with the results obtained for the sandwiches grown on different substrates (see section 5.5.3). There, slight differences in $\Delta\rho_{\mathrm{op}}/\Delta\rho_{\mathrm{ip}}(t_{\mathrm{Co}})$ in the range of 0.1 for nominally identical samples grown on SiO_2 and Si_3N_4 in the Co layer thickness range $t_{\mathrm{Co}} < 4$ nm were found, which were also attributed to differences in residual strain that are likely to be the reason for the observed differences of the anisotropy constant between both sample series. The findings for the multilayers confirm the results found for the sandwiches, namely, that changes in the residual strain have only minor influence on both the AIMR and GSE.
Regarding the normalized AIMR of multilayers with $n = 8$ shown in Fig. 5.58(b) it is obvious that the values are basically congruent with the corresponding counterparts with $n = 4$. However, the values are systematically slightly smaller. This behavior can be comprehended by the fact that the Co/Pt interfaces to the Pt seed and cap layers do not exhibit necessarily the same properties as the interfaces of the

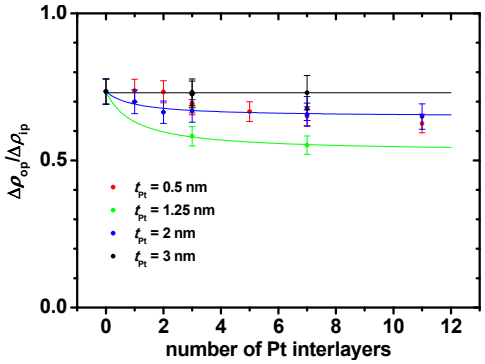

Figure 5.59: AIMR+GSE normalized by the AMR, i.e., $\Delta\rho_{op}/\Delta\rho_{ip}$, in dependence of number of Pt interlayers $n_{Pt} = n - 1$ (n: number of Co/Pt bilayers) for different Pt interlayer thicknesses. The value at $n_{Pt} = 0$ corresponds to the value of the sandwich with $t_{Co} = 0.8$ nm. The solid lines are fits according to a simple phenomenological model, see text. Certainly, only the values for natural numbers of n_{Pt} have a physical meaning.

Co/Pt bilayers since the Co to Pt ratio is different on a microscopic scale. Thus, the strain might locally vary in the stacking direction and as a consequence also the AIMR. For a multilayer with n_{Pt} Pt interlayers, where $n_{Pt} = (n - 1)$, the number of Co/Pt interfaces within the Co/Pt bilayers is $2n_{Pt} - 2$, while the number of the Pt seed/Co and Co/Pt cap interfaces is always two, so that the influence of the two latter interfaces on the overall AIMR should be less strong for $n = 8$ than for $n = 4$. By assuming that the two latter interfaces exhibit an AIMR that resembles the one for the sandwich $(\Delta\rho_{op}/\Delta\rho_{ip})_{sandwich}$ and that the AIMR at the interfaces of the bilayers $(\Delta\rho_{op}/\Delta\rho_{ip})_{bilayer} = (\Delta\rho_{op}/\Delta\rho_{ip})_{sandwich} - \Delta_{bilayer}$ is the same throughout the stack the dependence of the measured signal on the number of Pt interlayers n_{Pt} simply is[69]:

$$\frac{\Delta\rho_{op}}{\Delta\rho_{ip}}(n_{Pt}) = \left(\frac{\Delta\rho_{op}}{\Delta\rho_{ip}}\right)_{sandwich} - \Delta_{bilayer} \cdot \frac{2n_{Pt}}{2n_{Pt} + 2} \tag{5.86}$$

In order to examine whether this simple model can be applied to describe the AIMR in multilayers several samples with different n_{Pt} were investigated. Fig. 5.59 shows the normalized AIMR as a function of n_{Pt} for four different Pt interlayer thicknesses. The value for $n_{Pt} = 0$ corresponds to the value of the sandwich with $t_{Co} = 0.8$ nm. The solid lines are fits to the data under consideration of a fixed value of $(\Delta\rho_{op}/\Delta\rho_{ip})_{sandwich} = 0.73$ that was found for the addressed sandwich, so that $\Delta_{bilayer}$ was the only fitting parameter. In fact, the simple model describes the data quite well for the curves with $t_{Pt} \geq 1.25$ nm. In particular, for $t_{Pt} = 3$ nm the normalized AIMR does not depend on the number of Pt interlayers, i.e., $\Delta_{bilayer} \approx 0$. For $t_{Pt} = 1.25$ nm/ 2 nm $\Delta_{bilayer} \approx 0.2$/ 0.1 was found, which are much smaller than $(\Delta\rho_{op}/\Delta\rho_{ip})_{sandwich}$, again reflecting the finding for $n = 4$ that the AIMR only slightly depends on t_{Pt}. Furthermore, the dependence of the AIMR on n_{Pt} reveals that the results for $n = 4$ ($n_{Pt} = 3$) basically resemble the findings for any larger

[69] Certainly, the model is rather artificial as the strain and thus the AIMR might vary in a rather complex manner from bilayer to bilayer probably depending on the distance to the cap and seed layer and also the properties of the interfaces to the cap and the seed layer are likely to diverge from those of the sandwich.

n_{Pt} meaning that $(\Delta\rho_{\mathrm{op}}/\Delta\rho_{\mathrm{ip}})(n_{\mathrm{Pt}} = 3) \approx (\Delta\rho_{\mathrm{op}}/\Delta\rho_{\mathrm{ip}})_{\mathrm{bilayer}}$ is valid within the resolution of the experiment as, besides $\Delta_{\mathrm{bilayer}} \ll (\Delta\rho_{\mathrm{op}}/\Delta\rho_{\mathrm{ip}})_{\mathrm{sandwich}}$, in this case $2n_{\mathrm{Pt}}/(2n_{\mathrm{Pt}} + 2) = 0.75$ already applies.
In contrast to the results for $t_{\mathrm{Pt}} \geq 1.25$ nm, for $t_{\mathrm{Pt}} = 0.5$ nm the $\Delta\rho_{\mathrm{op}}/\Delta\rho_{\mathrm{ip}}(n_{\mathrm{Pt}})$ curve shows a more complex behavior, so that the curve cannot be described by the simple model according to Eq. 5.86. This behavior reveals that in the ultrathin thickness regime, where the Pt interlayers are laterally discontinuous, the AIMR+GSE normalized by the AMR has a rather complex physical meaning. This is traceable as both constituents (the AMR and AIMR+GSE) might be significantly altered in this thickness regime according to the argumentation given in connection with the discussion of the $\Delta R_{\mathrm{ip}}(t_{\mathrm{Pt}})$ curve.

In conclusion, the investigations of the AIMR of Co/Pt multilayers reveal that for any desired bilayer repetition and interlayer thickness (fixed $t_{\mathrm{Co}} = 0.8$ nm) the AIMR is of similar size as the conventional AMR effect, which was used to correct the current shunt through the Pt from the AIMR data for $t_{\mathrm{Pt}} \gtrsim 1$ nm. In this thickness regime the results of the AIMR+GSE normalized to the AMR are almost independent of the number of bilayers, especially for $n \geq 4$. Quantitatively, the dependence of the normalized AIMR on bilayer repetition can be phenomenologically described by assuming that the size of the AIMR of the Co/Pt interfaces within the bilayers can diverge from the AIMR of the interfaces to the Pt cap and seed layers. In the thickness regime 1 nm $\leq t_{\mathrm{Pt}} <$ 3 nm a small increase of the normalized AIMR+GSE with increasing t_{Pt} was found that can be most likely attributed to changes in the residual strain. For $t_{\mathrm{Pt}} \geq 3$ nm the normalized AIMR corresponds to the value found for the sandwich with the same nominal Co layer thickness of $t_{\mathrm{Co}} = 0.8$ nm reflecting the fact that for such samples the AIMR of all Co/Pt interfaces are identical within the stack. For $t_{\mathrm{Pt}} \lesssim 1$ nm both the AIMR and the AMR depends on t_{Pt} in a complex manner due to effects that might be correlated with the fall of the nominal thickness of the individual Pt interlayers below the interface roughness and interdiffusion zone. However, also in this ultrathin layer thickness regime, where the Co and Pt material is basically interdiffused so that a CoPt alloy with a heterogeneous depth profile exists, the AIMR is of similar size as the AMR. This finding shows that the AIMR has to be generally considered in Co/Pt layered structures. In particular, for Co/Pt samples with perpendicular magnetic anisotropy the AIMR ($\Delta\rho_{\mathrm{op,Co}} \approx 0.1$ $\mu\Omega$cm) is in the same order of magnitude as the *intrinsic* domain wall resistance reported in literature for current perpendicular wall geometry. This finding reveals that when studying the iDWR the AIMR has to be determined in order to give a reasonable interpretation of the MR data and therefore a correct quantification of the iDWR contribution as the AIMR is inherently included in the detected domain wall resistance as an extrinsic contribution. A positive iDWR contribution was found within this study in qualitative accordance with the results reported in literature concerning Co/Pt layered structures.
The rather slight dependence of the normalized AIMR on n and t_{Pt} enables an enhancement of the technologically relevant MR ratio of the AIMR as the ratio of "Co/Pt interfaces" to Co and Pt volume material can be enhanced by increasing n and/ or decreasing t_{Pt}, so that the current shunt is reduced. The multilayer with

$t_{\mathrm{Pt}} = 2$ nm and $n = 12$ exhibits the largest MR ratio $\Delta\rho_{\mathrm{op}}/\rho_{\mathrm{t}} = (0.28 \pm 0.03)\%$ of all multilayers with perpendicular magnetic anisotropy investigated within this thesis. Compared to the sandwich with the same nominal Co layer thickness ($t_{\mathrm{Co}} = 0.8$ nm) the MR ratio is about three times larger ($\Delta\rho_{\mathrm{op}}/\rho_{\mathrm{t}} = (0.10 \pm 0.04)\%$) and is therefore half the size of the largest value measured (at room temperature) within this thesis of $\Delta\rho_{\mathrm{op}}/\rho_{\mathrm{t}} = (0.56 \pm 0.03)\%$, which belongs to the sandwich with $t_{\mathrm{Co}} = 7$ nm. For the multilayer with $t_{\mathrm{Pt}} = 0.5$ nm and $n = 12$, which exhibits easy plane behavior, the largest MR ratio of all multilayers was found, namely $\Delta\rho_{\mathrm{op}}/\rho_{\mathrm{t}} = (0.41 \pm 0.03)\%$. This value is therefore comparable to the aforementioned largest value found within this thesis. However, from the asymptotic behavior of the $\Delta\rho_{\mathrm{op}}/\rho_{\mathrm{t}}(n)$ curve for any desired t_{Pt} it is obvious that for any higher bilayer repetition $n > 12$ only a negligibly small increase of the MR ratio can be expected, so that the reported values can be seen as the maximum that is possible for the respective Pt interlayer thicknesses. It is worth mentioning that in this study indications for an oscillatory behavior on n or t_{Pt} were found neither for the resistivity nor for any kind of the MR effects as it was otherwise observed for Co/Ni multilayers [892, 893, 19] and recently for Co/Pt layered structures [849].

5.8 Conclusion and outlook

The magnetoresistance of Co/Pt layered structures fabricated by means of sputtering techniques was investigated in current in-plane (CIP) geometry in the temperature range of 4.2 K $\leq T \leq$ 295 K utilizing magnetic fields of up to 6 T. The key result was the discovery that the resistivity ρ_{xx} depends on the magnetization orientation within the plane perpendicular to the current direction. Thereby, the fingerprint of the discovered MR effect is that ρ_{xx} shows a symmetry adapted $\cos^2$ dependence on the angle that the magnetization $\mathbf{M}$ includes with the surface normal and is largest for $\mathbf{M}$ oriented along the surface normal ($\Delta\rho_{\mathrm{op}} > 0$, section 5.5.1). By varying the Co layer thickness (0.8 nm $\leq t_{\mathrm{Co}} \leq$ 50 nm) of Pt/Co/Pt sandwiches a $1/t_{\mathrm{Co}}$ dependence of the effect was found for $t_{\mathrm{Co}} \geq 9$ nm providing strong evidence that it originates at the Co/Pt interfaces. Thus, the effect was named anisotropic interface magnetoresistance (AIMR) [E6].
The sandwich resistance $R_{xx}(t_{\mathrm{Co}})$ can be well-described under consideration of the phenomenological Fuchs-Sondheimer model in particular enabling a quantification of the magnetic scattering anisotropy at the Co/Pt interfaces that is caused by the AIMR effect (section 5.5.2). Its $1/t_{\mathrm{Co}}$ characteristic can be reproduced by only assuming that the specularity parameter p of the Fuchs-Sondheimer model depends on the orientation of the magnetization with respect to the surface normal. As a result, the diffusive scattering probability of the electrons at the Co/Pt interfaces $(1-p)$ is enhanced by 3% when changing the magnetization from any desired in-plane direction to the out-of-plane direction giving rise to the AIMR effect.
At large Co layer thicknesses $t_{\mathrm{Co}} > 30$ nm the AIMR is overcompensated by the texture induced geometrical size effect (GSE). This effect also provides a $\cos^2$ dependence of ρ_{xx} on the angle that $\mathbf{M}$ includes with the surface normal ([111] direction of the crystallites), but in contrast to the AIMR, the minimum in ρ_{xx} occurs for $\mathbf{M}$ aligned in parallel to the surface normal ($\Delta\rho_{\mathrm{op}} < 0$). At small Co layer thicknesses $t_{\mathrm{Co}} \leq 1$ nm, where a perpendicular magnetic anisotropy (PMA) exists, the magnitude of the AIMR+GSE ($\Delta\rho_{\mathrm{op}}$) is comparable to the conventional anisotropic MR (AMR). By investigating the MR of Co/Pt multilayers with different bilayer repetitions ($n = 2-12$) and Pt interlayer thicknesses (0.25 nm $\leq t_{\mathrm{Pt}} \leq$ 5 nm, $t_{\mathrm{Co}} = 0.8$ nm fixed) it was found out that this statement seems to be generally valid for Co/Pt layered structures (section 5.7). Moreover, the AIMR+GSE ($\Delta\rho_{\mathrm{op,Co}} \approx 0.1$ $\mu\Omega$cm, corrected by the current shunt through the Pt) is in the same order of magnitude as the *intrinsic* domain wall resistance (iDWR) reported in literature for Co/Pt layered structures with PMA. This finding is important in the light of recent efforts for studying the iDWR as the AIMR is inherently included in the detected domain wall resistance $\Delta\rho_{\mathrm{DWR}}$ as an extrinsic contribution. The AIMR reduces the resistivity within the domain walls compared to the domains, so that the iDWR contribution is determined by $\Delta\rho_{\mathrm{DWR}} = \Delta\rho_{\mathrm{iDWR}} - \Delta\rho_{\mathrm{op,Co}}$ (for current perpendicular wall geometry). However, without exception $\Delta\rho_{\mathrm{DWR}} > 0$ was reported in literature revealing that the intrinsic scattering contributions within the walls generally overcompensates the extrinsic AIMR contributions. In qualitative accordance with literature a positive iDWR contribution was observed within this study. A systematic investigation of the DWR under consideration of the AIMR effect will demonstrate to what

extent the iDWR contribution was underestimated in the recent studies.
In addition to the above mentioned quantification of the AIMR, the developed phenomenological model describing the thickness dependence of the sandwich resistance enables the elimination of the current shunt through the Pt material from the MR data, which masks the pure thickness dependence of the MR effects arising from the Co material or the Co/Pt interfaces (section 5.5.2). As a result, despite the elimination of the current shunt, the various MR effects depend on Co layer thickness revealing the presence of finite size effects. In the case of the AMR, AIMR+GSE ($\Delta\rho_{\mathrm{op,Co}}$), and anomalous Hall effect (AHE) an increase of the effects with increasing thickness was observed that is basically completed for $t_{\mathrm{Co}} \approx \lambda_{\mathrm{bulk}}$, where $\lambda_{\mathrm{bulk}} = (4.4 \pm 0.4)$ nm is the bulk mean free path of the electrons within the Co layer. While the AMR remains constant at higher thicknesses, besides $\Delta\rho_{\mathrm{op,Co}}$, also the AHE decays with $1/t_{\mathrm{Co}}$ revealing the existence of scattering processes at the Co/Pt interfaces that contribute to the AHE. In contrast to $\Delta\rho_{\mathrm{op,Co}}(t_{\mathrm{Co}})$, however, the AHE merges into a positive value at infinite Co layer thickness indicating that both the interface as well as the bulk contributions to the AHE provide a positive anomalous Hall constant. In the case of the spin-disorder MR (SMR) and normal Hall effect (OHE) their increases with increasing Co layer thickness is not completed until $t_{\mathrm{Co}} \approx 20$ nm and 30 nm, respectively, where the corresponding bulk values are attained. The increase of the OHE might be caused by a quantum size effect. The suppression of the OHE at low thicknesses $t_{\mathrm{Co}} \lesssim 1$ nm leads to the fact that the high field behavior of $\rho_{xy}(H_{\mathrm{p}})$ is dominated by the high field susceptibility that enters the curve via the AHE. The finite size effect in the SMR was found to be a fingerprint of the suppression of the electron-magnon scattering at low Co layer thicknesses, which might be caused by a thickness-driven change in the magnon spectrum. A suppression of the electron-magnon scattering as well as electron-phonon scattering within the Co layer at small Co layer thicknesses could be identified from the description of the temperature dependence of the sandwich resistance by means of the phenomenological layer model (section 5.6).
The temperature variation (4.2 K $\leq T \leq$ 295 K) further shows that the AMR and AIMR+GSE ($\Delta\rho_{\mathrm{op}}$) only slightly depend on temperature revealing that they are basically governed by the scattering of the electrons at static defects, i.e., the Co/Pt interfaces in the case of the AIMR. Furthermore, the investigation demonstrates that the OHE does not depend on temperature. The parabolic-like increase of the SMR with temperature can be well-described theoretically by the temperature dependence of the *s-d* interaction. The size of the AHE was found to depend on temperature revealing that the temperature dependent parts of the resistivity contribute to this particular effect. For the finite size effects, i.e., the suppression of the various MR effects at small Co layer thicknesses, a considerable temperature dependence can be ruled out in the case of the AMR, AIMR+GSE, SMR, and OHE. A deeper analysis of the results for the AHE will show how its interface and volume contributions are affected by the temperature variation and to what extent the finite size effects in the electron-magnon and electron-phonon scattering enter the AHE. A more elaborate study of the temperature dependence (4.2 K $\leq T \leq$ 295 K) of the AHE is

intended in the short term by using the new split-pair magnet[70] ordered within the framework of this thesis. Furthermore, a cooperation was initiated with the working group of Dr. Y. Mokrousov, Topological Nanoelectronics, Forschungszentrum Jülich (Germany), who started with *ab initio* calculations of the thickness dependence of the residual AHE ($T = 0$ K) of Pt/Co/Pt sandwiches. It will be interesting to see if the calculations show an inherent contribution of the Co/Pt interfaces to the AHE and to what extent the results match with the experimental findings of this study.
Concerning the AIMR, in connection with this thesis a fully relativistic spin-polarized *ab initio* theoretical description of $\rho_{xx}(\mathbf{M})$ for ideal Pt(111)/Co$_n$/Pt(111) sandwiches ($n \leq 90$ monolayers, $T = 0$ K) was performed by Prof. Dr. P. Weinberger, Center of Computational Nanoscience, Vienna (Austria) [E7]. The calculations reveal that the ideal Co/Pt interfaces provide a resistivity anisotropy with the same functional dependence as found in the experiment, namely a $\cos^2$ dependence, when the magnetization rotates within the plane perpendicular to the current direction, with the same sign ($\Delta\rho_{\mathrm{op}} > 0$). Furthermore, the magnitude of the effect and the shape of the theoretical $\Delta\rho_{\mathrm{op}}(t_{\mathrm{Co}})$ curve are comparable to the experimental findings. Despite the good agreement between experiment and theory it has to be considered that in the experiment the structural properties of the interfaces (finite interdiffusion and roughness) deviate from the ideal ones assumed in the theory, which might have significant impacts on the AIMR. This difference could also be the reason why the theoretically predicted interface contribution to the conventional AMR has not been detected experimentally so far.
The interpretation of the MR data as given above is based on a detailed investigation of the structural and magnetic properties of the samples (section 5.3). The structural investigations revealed that they exhibit a well-defined layered structure with an interface roughness in the range of one monolayer (ML) and an interdiffusion zone of about two to three MLs. The crystal structure of the samples is polycrystalline with a (111) out-of-plane texture and a lateral grain size of (11 ± 2) nm that was initiated during the growth of the Pt seed layer on the substrates. The rather large coherence lengths within the Co and Pt layers as well as the coherence between the Co and Pt layers obtained from x-ray diffraction (XRD) suggest single crystalline phases along the stacking direction. However, the loss in coherence observed at large Co layer thicknesses reveals a certain degree of structural disorder. The texture of the films is pronounced in such a manner that with respect to the film surface the orientation of the (111) lattice planes of the crystallites are normally distributed, whereas the degree of texture depends on the kind of substrate. However, even for the samples grown on SiO_2, which exhibit the less-pronounced texture, the average tilting of the crystallites with respect to the film normal is $< 10^\circ$, so that significant influences of the different kinds of texture on the magnetic and magnetogalvanic properties can be ruled out. The average spacing between the Pt(111) lattice planes is 0.7% larger than the bulk value. The limited experimental sensitivity for crystalline Co experienced at the standard x-ray tubes disables a statement about the interplanar Co-Co spacing for thin Co thicknesses t_{Co} in the case of the sandwiches. For $t_{\mathrm{Co}} \geq 12$ nm, where a Co peak can be observed, the properties of the Bragg peak

[70] Superconducting magnet (spectromag) system of Oxford instruments, project number 52398.

indicate that the Co material contributing to the peak is unstrained exhibiting the bulk lattice of Co. However, the findings for the multilayers reveal that for a thin Co thickness of $t_{\mathrm{Co}} = 0.8$ nm, where the Co material is basically interdiffused with the Pt, the Co is significantly tensely strained along the growth direction. In order to gain a more complete picture about the interatomic arrangement of the Co/Pt layered structures, i.e., lattice strain, Co stacking sequence (fcc (ABCABC...) or hcp (ABAB...)), and the chemically formation at the Co/Pt interfaces complementary investigations are planned. The high resolution TEM investigations recently initiated will be continued and improved by Dr. A. Chuvilin, CIC nanoGUNE, San Sebastian (Spain). Furthermore, it is planned to carry out resonant and high intensity diffraction studies as well as extended x-ray absorption fine structure (EXAFS) investigations at synchrotron sources (details, see section 5.3.1.3).
Concerning the open questions about the structural properties the results of the investigations of the magnetic anisotropy led to significant indications. The most probable explanation for the deviations from the linear characteristic of the effective first order anisotropy constant $K_{1,\mathrm{eff}} \cdot t_{\mathrm{Co}}(t_{\mathrm{Co}})$ found for the sandwiches is connected with relaxation processes of residual strain, which affect the anisotropy via the magneto-elastic coupling. Slight differences in residual strain can also account for the significant differences in the surface K_S and magnetocrystalline volume anisotropy constant K_{1V} between nominally identical samples grown on different kind of substrates. In the range of $t_{\mathrm{Co}} \gtrsim 5$ nm up to 50 nm for both electric insulating substrates (SiO_2 and Si_3N_4) the evolution of the anisotropy of the sandwiches with thickness can be described by a single set of constants K_S and K_{1V} revealing that no significant changes in the structural properties occur. Consequently, in accordance to the structural investigations that provide access to the properties of the Co material for $t_{\mathrm{Co}} \geq 12$ nm the increase of the Co layer thickness basically leads to an increase of the amount of Co "bulk" material within the interior of the layer. Moreover, the K_{1V} constant determined for this thickness regime gives a strong indication that the Co stacking is fcc. Besides the anisotropy constant K_{1V}, the magnitude of the GSE was found to be much smaller than reported for hcp Co. As differences in the degree of texture can be ruled out to be the reason the smaller GSE seems to reflect a higher crystalline symmetry/ smaller texture induced axial perturbation of the isotropy and therefore gives a further hint that the Co layers exhibit fcc stacking[71].
Besides the anisotropy investigated via AHE and magnetooptical Kerr effect (MOKE) ferromagnetic resonance (FMR) investigations of the samples were performed revealing that the saturation magnetization of Co is thickness-independent for the thickness range of $t_{\mathrm{Co}} \geq 4$ nm, which is experimentally accessible with the used setup, and resembles $M_{\mathrm{S}}^{\mathrm{bulk\ Co}}$. Moreover, down to the smallest Co layer thickness of $t_{\mathrm{Co}} = 0.8$ nm the relative contribution of the Pt polarization and of the enhanced orbital moment of Co at the interfaces to the total magnetic moment is estimated to be negligibly small at room temperature. It is intended to examine the correctness

[71] Very recently, XRD investigations (2θ scans) of sandwiches with $t_{\mathrm{Co}} = 50$ nm, where the plane of incidence included different angles with respect to the film normal in the range of $0 - 90°$, clearly reveal the Co fcc(200) Bragg peak for certain angles, while the Co hcp($10\bar{1}3$), ($20\bar{2}0$), and ($20\bar{2}1$) peaks are always missing. This finding gives a further strong indication that the Co lattice is fcc.

of this assumption and to determine the temperature dependence of the Pt polarization and the magnetic moment of Co by performing magnetic EXAFS (MEXAFS) and soft x-ray resonant magnetic reflectometry (XRMR) down to liquid He temperature. Both techniques add magnetic selectivity to the well-established EXAFS and XRR methods opening the door to the exploration of the local magnetic structure. Furthermore, x-ray magnetic circular dichroism (XMCD) measurements are intended. All proposed future structural investigations at synchrotron sources will be conducted in cooperation with the group of Prof. Dr. A. Schreyer, Helmholtz-Zentrum Geesthacht, Germany, under supervision of Dr. D. Lott.
In this thesis it is clearly demonstrated that the AIMR effect is caused by the Co/Pt interfaces. In order to get a deeper insight into the underlying physics and to understand which mechanism is responsible for the AIMR on a microscopic scale it is planned to vary the sample properties on purpose and study their influence on the effect. The reason for the suppression of the AIMR and various other MR effects at small Co thicknesses are further open questions that should also be addressed. The understanding of the underlying physics is essential for the enhancement of the magnitude of the AIMR to pave the way for possible technological applications.
Up to now, without placing the focus on a systematic optimization of the magnitude of the AIMR, a maximum value of the technologically relevant MR ratio of $\Delta\rho_{\mathrm{op}}/\rho_{\mathrm{t}} = (0.56 \pm 0.03)\%$ at room temperaure has been obtained for the sandwich with $t_{\mathrm{Co}} = 7$ nm. The rather slight dependence of the AIMR ($\Delta\rho_{\mathrm{op,Co}}$, corrected by the current shunt) on bilayer repetition n and Pt interlayer thickness t_{Pt} enables an enhancement of the AIMR ratio as the ratio of "Co/Pt interface regions" to Co and Pt volume material can be enhanced by increasing n and/ or decreasing t_{Pt}, so that the amount of current flowing through the interface regions is increased. Thus, compared to the sandwich with the same nominal Co layer thickness ($t_{\mathrm{Co}} = 0.8$ nm, $\Delta\rho_{\mathrm{op}}/\rho_{\mathrm{t}} = (0.10 \pm 0.04)\%$) the MR ratio is enhanced by about a factor of three to $\Delta\rho_{\mathrm{op}}/\rho_{\mathrm{t}} = (0.28 \pm 0.03)\%$ for the multilayer with $t_{\mathrm{Pt}} = 2$ nm and $n = 12$, so that the ratio is half the size of the aforementioned largest value found within this thesis. This is the largest AIMR ratio for a sample with PMA obtained so far. For the multilayer with $t_{\mathrm{Pt}} = 0.5$ nm and $n = 12$, which exhibits easy plane behavior, the largest MR ratio of all multilayers was found that is comparable to the aforementioned largest value, namely $\Delta\rho_{\mathrm{op}}/\rho_{\mathrm{t}} = (0.41 \pm 0.03)\%$. However, from the asymptotic behavior of the $\Delta\rho_{\mathrm{op}}/\rho_{\mathrm{t}}(n)$ curve for any desired t_{Pt} it is obvious that for any higher bilayer repetition $n > 12$ only a negligibly small increase of the MR ratio can be expected, so that the reported values can be seen as the maximum that is possible for the respective Pt interlayer thicknesses.
Concerning the influence of the structural properties on the AIMR the investigations conducted so far reveal that in contrast to the magnetic anisotropy slight differences in the residual strain in the range of $\lesssim 0.5\%$ seem to have only minor influence on the AIMR effect as summarized in the following. The first indication was provided by the almost identical magnetoresistance properties of nominally identical sandwiches grown on different electric insulating substrates (SiO_2 and Si_3N_4), which exhibit significant differences in the anisotropy constants that are most likely caused by differences in the residual strain. Furthermore, for the multilayers only a slight dependence of the AIMR on Pt interlayer thickness was found above $t_{\mathrm{Pt}} = 1$ nm. In

	$\Delta\rho_{ip}/\rho_t$ (%)	$\Delta\rho_{op}/\rho_t$ (%)	$\Delta\rho_{op}/\Delta\rho_{ip}$
Pt/ 2 nm Co/ Pt (common, Si_3N_4)	0.36 ± 0.02	0.37 ± 0.02	1.01 ± 0.04
Pt/ 2 nm Co/ Pt (common)	0.33 ± 0.02	0.31 ± 0.02	0.94 ± 0.04
Pt/ 2 nm Co/ Pt (all layers magnetron)	0.32 ± 0.02	0.30 ± 0.02	0.93 ± 0.04
Pt/ 2 nm Co/ Pt (all layers ECR)	0.41 ± 0.03	0.32 ± 0.02	0.77 ± 0.04
Pt/ 2 nm Co/ Pt (e-beam)	0.29 ± 0.02	0.20 ± 0.02	0.72 ± 0.03
Pt/ 6 nm Co/ Pt (e-beam)	0.65 ± 0.03	0.29 ± 0.02	0.45 ± 0.02
Pt/ 20 nm Co/ Pt (e-beam)	1.36 ± 0.05	0.10 ± 0.01	0.07 ± 0.01
Pt/ 50 nm Co/ Pt (e-beam)	1.76 ± 0.06	< 0.01	< 0.01

Table 5.6: Magnetoresistance ratios as well as AIMR+GSE normalized by the AMR, i.e., $\Delta\rho_{op}/\Delta\rho_{ip}$, of various 5 nm Pt/ 2 nm Co/ 3 nm Pt sandwiches fabricated with different preparation techniques and of 5 nm Pt/ t_{Co}/ 3 nm Pt sandwiches with different Co layer thicknesses fabricated by electron beam evaporation. "Common" stands for the general construction of the Co/Pt samples used within this thesis (see section 5.2.2). If not otherwise stated the substrate is thermally oxidized SiO_2.

this thickness regime laterally continuous Pt interlayers are established, so that the thickness dependence of the anisotropy constant observed up to $t_{Pt} = 3$ nm is probably caused by changes in the residual strain. A third indication for an insensitivity of the AIMR on strain variations is given by its considerably small dependence on temperature as according to the temperature dependence of the anisotropy constant the temperature variation is probably connected with changes in the elastic deformations of the crystal lattice.

Due to the origin of the AIMR at the Co/Pt interfaces a strong influence on its magnitude can be expected when their structural properties as roughness and interdiffusion are varied. In fact, first indications for such a strong dependence can be seen in Tab. 5.6, where the AMR and AIMR ratio as well as their ratio, i.e., $\Delta\rho_{op}/\Delta\rho_{ip}$, are listed for Pt/Co/Pt sandwiches that were prepared with different preparation techniques. In addition to the results obtained for the sandwiches of both main series (SiO_2 and Si_3N_4) with $t_{Co} = 2$ nm further preliminary results of samples with the same layer composition are shown that were solely prepared by DC magnetron and ECR sputtering, respectively, as well as by means of electron-beam evaporation. Further results for samples with different Co layer thicknesses that were prepared with the latter technique are also listed in the table. For the DC magnetron sputtered sample $\Delta\rho_{op}/\Delta\rho_{ip}$ resembles the values of the samples of the main series while for the sandwiches prepared by ECR sputtering and e-beam evaporation $\Delta\rho_{op}/\Delta\rho_{ip}$ is significantly smaller. In the case of the ECR sample the difference can be attributed to a stronger interdiffusion of the Co and Pt material at the interfaces as a consequence of the higher energies of the Ar^+ ions and sputtered atoms compared to the magnetron sputtering technique [368]. However, it has to be kept in mind that differences in the crystallinity (texture, layer stacking) are likely to occur that should also influence the magnetoresistance. Regarding the results for the electron-beam evaporated sample the relatively low value of $\Delta\rho_{op}/\Delta\rho_{ip}$ might be a consequence of rather rough Co/Pt interfaces, which should be caused by the low

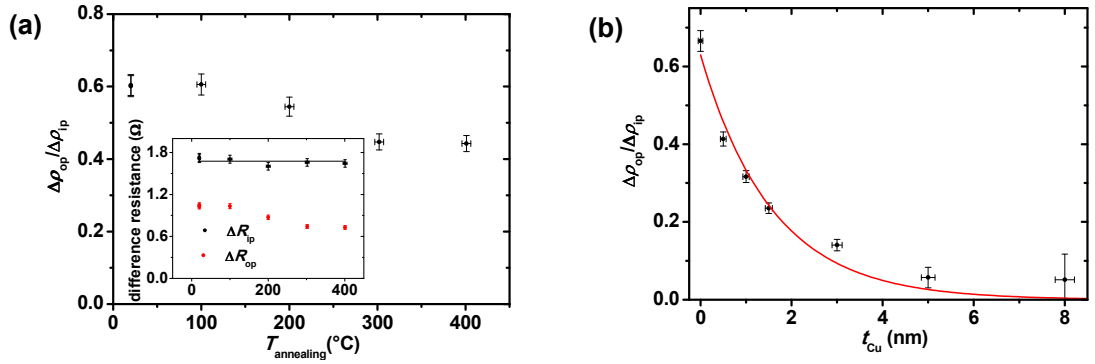

Figure 5.60: (a) $\Delta\rho_{\mathrm{op}}/\Delta\rho_{\mathrm{ip}}$ as a function of annealing temperature of the sandwich with $t_{\mathrm{Co}} = 7$ nm grown on SiO_2. The inset shows $\Delta R_{\mathrm{ip}}(T_{\mathrm{annealing}})$ and $\Delta R_{\mathrm{op}}(T_{\mathrm{annealing}})$. The solid line is a horizontal fit to the former curve. The values at 20°C belongs to the as grown state. (b) $\Delta\rho_{\mathrm{op}}/\Delta\rho_{\mathrm{ip}}$ in dependence of Cu layer thickness of 5 nm Pt/ t_{Cu}/ 6 nm Co/ t_{Cu}/ 3 nm Pt multilayers. The solid line is an exponential fit to the data.

mobility of the evaporated atoms during the deposition process as their kinetic energy is two orders of magnitude lower than in the case of sputtering techniques [674]. The thickness dependence of $\Delta\rho_{\mathrm{op}}/\Delta\rho_{\mathrm{ip}}$ of the sample series made by electron-beam evaporation shows a monotonically decrease as expected due to the AIMR effect and merges to zero at infinite Co layer thickness. The latter finding reveals that contributions of the GSE are zero, which indicates that the electron-beam evaporated samples exhibit no texture. This result shows that texture is not a necessary prerequisite for the existence of the AIMR effect. Altogether, the preliminary MR results for the samples made by different preparation techniques confirm that the AIMR is a general phenomenon that occurs in Co/Pt layered structures.

In addition to the change of deposition parameters and techniques it is planned to alter the quality of the Co/Pt interfaces by means of heat treatment, a method that is frequently applied in the case of Co/Pt layered structures (see e.g. Refs. [764, 735, 894, 895, 896]). Fig. 5.60(a) shows the preliminary result of the influence of the heat treatment on $\Delta\rho_{\mathrm{op}}/\Delta\rho_{\mathrm{ip}}$ for the sandwich with $t_{\mathrm{Co}} = 7$ nm grown on SiO_2. For each data point the sample was exposed to the annealing temperature $T_{\mathrm{annealing}}$ via thermal contact for 24 hours. The heat treatments were conducted under high vacuum conditions to avoid contaminations. The sample was gradually annealed starting in a first step at 100 °C raising the temperature up to 400°C. Between the individual annealing steps the MR measurements were conducted at room temperature. From the inset of Fig. 5.60(a) it is obvious that the decrease of $\Delta\rho_{\mathrm{op}}/\Delta\rho_{\mathrm{ip}}(T_{\mathrm{annealing}})$ starting at 200°C is caused by a decrease in $\Delta\rho_{\mathrm{op}}$, while the size of the AMR is basically unaffected by the heat treatment. The decrease of the AIMR is probably a consequence of heat induced alloying processes at the Co/Pt interfaces.

A further method to modify the properties of the Co/Pt samples on purpose is provided by the application of moderate ion doses of $\lesssim 1 \cdot 10^{14}$ Ga^+/cm^2 by means of focused ion beam (FIB) technique, where the impact of sputtering and implantation is rather small and the ion bombardment in particular leads to ion beam-induced mixing of the Co and Pt layers (more details, see section 4.4.2.1).

All presented approaches to modify the layer structure need very careful studies of

	$\Delta\rho_{\mathrm{ip}}/\rho$ (%)	$\Delta\rho_{\mathrm{op}}/\rho$ (%)	$\Delta\rho_{\mathrm{ip}}/\Delta\rho_{\mathrm{op}}$
Pt/ 6 nm Co/ Pt (common)	0.80 ± 0.03	0.55 ± 0.02	0.69 ± 0.03
Pt/ 6 nm Co/ Pt (e-beam)	0.65 ± 0.03	0.29 ± 0.02	0.45 ± 0.02
Pt/ 6 nm Fe/ Pt (e-beam)	0.31 ± 0.02	0.19 ± 0.02	0.61 ± 0.03
Pt/ 6 nm Ni/ Pt (e-beam)	0.48 ± 0.03	< 0.01	< 0.02
Pt/ 6 nm $Ni_{81}Fe_{19}$/ Pt (e-beam)	0.58 ± 0.03	0.16 ± 0.02	0.28 ± 0.02
Pt/ 6 nm $Co_{39}Fe_{54}Si_7$/ Pt (e-beam)	0.29 ± 0.02	0.17 ± 0.02	0.59 ± 0.03
Pt/ 6 nm $Co_{34}Pt_{68}$/ Pt (common)	0.29 ± 0.02	0.19 ± 0.02	0.67 ± 0.03
Pd/ 6 nm Co/ Pd (e-beam)	0.46 ± 0.03	0.07 ± 0.01	0.15 ± 0.02
Cu/ 6 nm Co/ Cu (e-beam)	0.46 ± 0.03	-0.05 ± 0.01	-0.10 ± 0.01
Au/ 6 nm Co/ Au (e-beam)	0.52 ± 0.03	-0.06 ± 0.01	-0.12 ± 0.01

Table 5.7: Magnetoresistance ratios as well as AIMR+GSE normalized by the AMR, i.e., $\Delta\rho_{\mathrm{op}}/\Delta\rho_{\mathrm{ip}}$ of various sandwiches. The samples were fabricated by electron-beam evaporation or by means of sputtering techniques ("common") according to the construction introduced in section 5.2.2. The substrate is always SiO_2 and the seed and the cap layer thickness is 5 nm and 3 nm, respectively. The layer of alloyed CoPt was prepared by co-sputtering of the Co and Pt targets while the sample surface included an angle of 45° with the surfaces of both sputtering targets.

the structural and magnetic properties, which will accompany future MR investigations in order to provide a reasonable interpretation of the data.
Another focus of the ongoing research to gain a deeper insight into the microscopic origin of the AIMR is to investigate the dependence of the effect on the involved materials, i.e., both the magnetic as well as the non-ferromagnetic interlayer material. For instance, the influence of the switching to materials that are isoelectronic but exhibit different nuclear charge Z or that exhibit different electronic states at the Fermi energy but have similar Z will help to find indications about the microscopic mechanism behind the effect. In Tab. 5.7 preliminary MR results for several sandwiches are listed. In some cases, namely for Fe/Pt and Co/Pd[72] layered structures as well as for the alloys permalloy ($Ni_{81}Fe_{19}$), $Co_{39}Fe_{54}Si_7$, and $Co_{34}Pt_{68}$ sandwiched by Pt the resistivity difference $\Delta\rho_{\mathrm{op}}$ was found to be larger than zero revealing the existence of the AIMR effect. These results already show that the AIMR is not only restricted to Co/Pt, so that the AIMR seems to be a more universal effect in layered systems. Regarding the size of the AIMR it is significantly smaller for Co/Pd compared to Co/Pt and Fe/Pt. This might be a consequence of a smaller Z for Pd giving further indication that the AIMR is of relativistic origin as the strength of the spin-orbit interaction varies with Z^4 [3, 898]. Interestingly, in the case of the stacking of isoelectronic Ni and Pt $\Delta\rho_{\mathrm{op}}$ is zero. This finding cannot be explained by the presence of the GSE that is superimposed on the AIMR. This is due to the fact that the electron-beam evaporated Pt grains are randomly oriented with respect to the sample surface (see above), so that the GSE is zero which consequently implies that the AIMR is absent. In the case of Au and Cu as seed and cap layer

[72] In the publication Ref. [897] from 1996, the resistance versus field sweeps measured for Co/Pd multilayers clearly reveals the signature of the AIMR effect.

$\Delta\rho_{\mathrm{op}}$ is slightly negative revealing that a small GSE exists indicating the presence of a certain degree of texture. Whether a rather small AIMR contribution exists in these stacks that is masked by the preponderant GSE has not been checked yet. The explanation for the strong suppression or even absence of the AIMR effect is probably connected with the fact that, in contrast to Pd and Pt, Cu and Au have completely filled d states.
Nowadays, in this working group the possibility exists to prepare multilayers by means of magnetron sputtering techniques that include more than two different materials. For that purpose a new UHV chamber was brought into operation, where in addition to the ECR gun five magnetron sputtering sources were equipped. Fig. 5.60(b) shows $\Delta\rho_{\mathrm{op}}/\Delta\rho_{\mathrm{ip}}$ as a function of Cu layer thickness that was deposited between the Co and Pt layers in the case of sandwiches with a Co layer thickness of $t_{\mathrm{Co}} = 6$ nm[73]. The idea behind this investigation was that the AIMR in Co/Cu was found to be at least rather small (see above). In fact, by implementing two Cu layers that separate the Co from the Pt layers $\Delta\rho_{\mathrm{op}}/\Delta\rho_{\mathrm{ip}}$ rapidly decreases with increasing Cu layer thickness giving a further clear evidence that the AIMR originates at the Co/Pt interfaces. Quantitatively, the decrease of $\Delta\rho_{\mathrm{op}}/\Delta\rho_{\mathrm{ip}}(t_{\mathrm{Cu}})$ can be described by an exponential decay as can be seen by the solid line in Fig. 5.60(b) which is a corresponding fit with a characteristic length of $\xi = (1.6 \pm 0.2)$ nm. Importantly, very recently it was found out that by only depositing Cu between the Co and Pt seed layer $\Delta\rho_{\mathrm{op}}/\Delta\rho_{\mathrm{ip}}$ merges at infinite Cu thickness into about 70% of the value found for $t_{\mathrm{Cu}} = 0$ nm and not into 50% as could be naively expected. Without going into detail also the results concerning the effective first order anisotropy constant indicates that the Co/Pt and Pt/Co interfaces exhibit different magnetic properties. An asymmetry in the surface aniostropy constant between Co/Pt and Pt/Co interfaces was recently reported for Co/Pt layered structures [778, 896] reflecting the existence of certain structural differences between both interfaces that are a consequence of differences in the growth of Co on Pt and vice versa (see section 5.3.1.3).
In addition to the preparation of metallic systems it is also possible to prepare insulators by means of radio frequency (RF) sputtering technique. Thereby, besides the information whether the AIMR occurs it will be interesting to see if some correlations to the tunneling anisotropic magnetoresistance (TAMR) [899, 900, 51, 901, 902] or to the very recently discovered Spin-Hall Magnetoresistance [903, 904] exist. In summary, the preliminary results concerning the variation of the involved materials are very promising to gain a deeper insight into the microscopic mechanism behind the AIMR.
A further project already planned is to perform current perpendicular plane (CPP) measurements. By means of the CIP geometry used until now two of the four components of the resistivity tensor can be measured (see section 5.1.1.1). In order to answer the question whether the AIMR exists in the ρ_{zz} component a CPP measurement geometry is needed. From an experimental point of view the impression of the current perpendicular to the film plane requires a more complicated sample preparation technique. The reason for this is that in CPP geometry the "length"

[73] According to the general construction of the Co/Pt samples (section 5.2.2) the first 4 nm of the Pt seed layer was prepared by ECR technique, while the other material was prepared by means of DC magnetron sputtering.

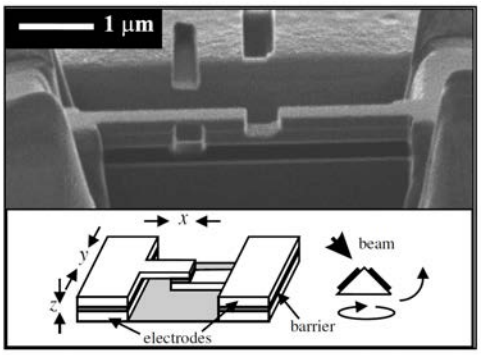

Figure 5.61: SEM micrograph of a current perpendicular to the plane (CPP) microcircuit device fabricated by ion milling utilizing a focused ion beam (FIB). The principle is sketched in the lower part. From Ref. [907].

of the resistor is only in the nanometer range (thickness of the stack). This implies that the cross-sectional area of the resistor has to be downscaled to get a significantly high signal [905] as e.g. a sample with 1 mm^2 cross section and 10 nm length would only exhibit a resistance of $R_{zz} = 10^{-10}$ Ω (for $\rho_{zz} = 10$ μΩcm). For typical currents of $I_z = 10$ mA only a voltage of $U_z = 1$ pV would be obtained. Since the discovery of giant MR (GMR) in the late 1980s, several preparation techniques were proposed to fabricate reduced cross-sectional areas fostered by the fact that the GMR and tunneling MR (TMR) ratios are generally larger in this current flow geometry [905, 906]. Moreover, the theoretical description of these effects is easier in CPP geometry as the individual layers (resistors) are connected in series and not in parallel as in CIP geometry. However, it is worth mentioning that the supply of a homogeneous current density within the cross-sectional area is challenging from an experimental point of view, which has to be guaranteed in order to obtain quantitative results. One method to prepare nanosized "pillars" is to utilize a focused ion beam (FIB) [907, 908, 909]. In future, the 3D FIB procedure introduced by C. Bell et al. should be used, which is as follows: In the first step the sample normal is oriented in parallel to the direction of the ion beam and an area of several microns down to the substrate has to be milled, excluding a track in the lateral middle with a typical width of about 500 nm (see Fig. 5.61). In the second step, the sample is tilted by about 80° with respect to the ion beam direction, so that the side planes of the track become accessible for the ion beam. Two cuts have to be made into the track, one removes the top and one the bottom of the stack, so that in between the cuts a pillar is created. By applying a voltage between the right and the left side of the track (electrodes) a current flow occurs that is oriented along the vertical direction within the pillar region.
The outlook closes with a presentation of a further project of ongoing research which was initiated very recently and deals with the investigation of magneto-thermoelectric phenomena of the layered structures. The generalization of Ohm's law (Eq. 5.2) under the presence of thermal gradients ∇T is [387, 910]

$$\mathbf{E} = \overleftrightarrow{\rho} \cdot \mathbf{j} - \overleftrightarrow{S} \cdot \nabla T \tag{5.87}$$

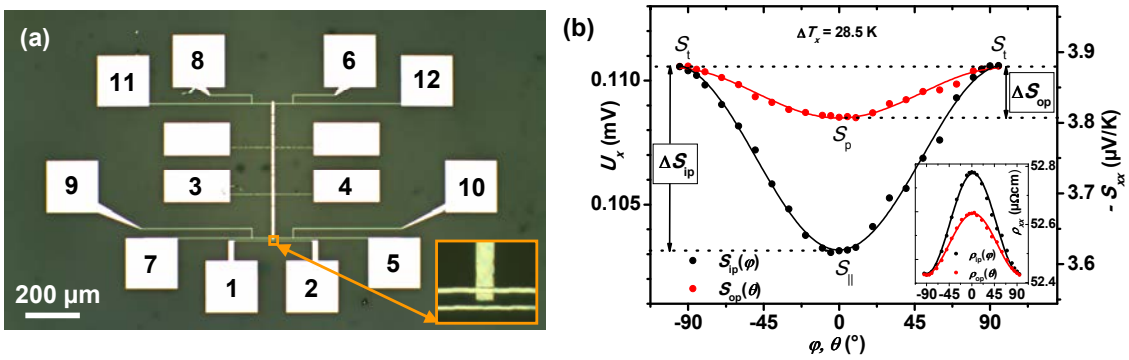

Figure 5.62: (a) Optical microscope image of the microcircuit for measuring the magneto-thermoelectric properties. The Pt heater (contacted via 1,2) supplies a thermal gradient along the 5 nm Pt/ (0.8 nm Co/ 1.4 nm Pt)$_{16}$/ 1.6 nm Pt multilayer wire that is vertically oriented (see inset). The Seebeck coefficient S_{xx} and the Nernst effects S_{xy} were measured via the Ti/Pt pads (5,6) and (3,4), respectively. The Ti/Pt contacts were also used to calibrate the temperature difference ΔT_x along the Co/Pt wire in four point geometry ((5,7), (9,10), and (6,8), (11,12), respectively). (b) Thermovoltage U_x for a temperature gradient of $\Delta T_x = 28.5$ K ($I_{\text{heat}} = 5$ mA)/ S_{xx} in dependence of the in-plane angle φ and out-of-plane angle θ. The field strength was 6 T causing **M** to be field aligned. The solid lines represent $\cos^2$ fits. The inset shows the corresponding MR measurements, which were performed by impressing a current of 0.5 mA via (5,6) and measuring the voltage drop via (7,8).

($U_i = R_{ij} \cdot I_j - S_{ik} \cdot \Delta T_k$), where $\overleftrightarrow{S}$ is the thermoelectric analogue of the resistivity tensor whose longitudinal component S_{xx} is the so-called Seebeck coefficient (or longitudinal thermoelectric power). According to Mott's law (see e.g. Refs. [911, 910, 912, 913]) S_{xx} is a function of the electrical resistivity, so that due to the existence of the various MR effects in ρ_{xx} the Seebeck coefficient implicitly depends on the magnetization and applied field. Fig. 5.62 shows a micro-circuit prepared by means of UV lithography used for the first magneto-Seebeck investigations (a) and some preliminary results (b) obtained for a 5 nm Pt/ (0.8 nm Co/ 1.4 nm Pt)$_{16}$/ 1.6 nm Pt multilayer grown on glass substrate (bad thermal conductor). At first the circuit layout is introduced. In a first lithography step the Co/Pt Hall-bar was prepared that can be seen in the middle of Fig. 5.62(a) consisting of the vertically oriented wire crossed by two horizontally oriented wires. The two latter wires enable the detection of the anomalous and normal Nernst effects, which are the thermoelectric counterparts of both Hall effects in S_{xy} (which also obey Mott's equation [914]). In a second lithography step leads and pads consisting of a 10 nm Ti/ 60 nm Pt bilayer were prepared for the electrical contacting of the Co/Pt bar. In addition, a Ti/Pt wire that is vertically oriented was prepared in front of one end of the Co/Pt wire at a distance of a few microns (see inset of Fig. 5.62(a)). This wire serves as a local heater providing a temperature gradient along the Co/Pt wire. For the magneto-thermoelectric (MTE) measurements a current of $I_{\text{heat}} = 5$ mA was driven (via the contact pads labeled as 1 and 2) through the heater and the corresponding Joule heating yields a temperature increase of

$\Delta T_x = 28.5$ K at the lower end of the Co/Pt wire[74]. The MTE measurements were performed by using the warm-bore magnet setup. To determine the MTE behavior the same kind of measurements as in the case of the MR investigations were performed, i.e., field sweep measurements and sample rotation in saturation field of 6 T (see section 5.4.2). The results of the first-mentioned method revealed the existence of the Nernst effects in the $S_{xy}(H_\mathrm{p})$ curve and the presence of the analogue of the AIMR, AMR, and SMR effects in the $S_{xx}(H_i)$ behavior (not shown). Fig. 5.62(b) displays the longitudinal thermovoltage (Seebeck coefficient) in dependence of the orientation of the magnetization $\mathbf{M}$ when $\mathbf{M}$ is rotated in the film plane $S_{xx}(\varphi)$ and in the plane perpendicular to the current direction $S_{xx}(\theta)$, respectively. Both curves show a $\cos^2$ dependence as indicated by the solid lines that are corresponding fits clearly revealing the analogue of the AMR and AIMR effect in the thermovoltage. Surprisingly, the ratio $\Delta S_\mathrm{op}/\Delta S_\mathrm{ip}$ is significantly smaller than $\Delta\rho_\mathrm{op}/\Delta\rho_\mathrm{ip}$ as can be seen by comparison with the inset, where $\rho_{xx}(\varphi)$ and $\rho_{xx}(\theta)$ are shown. The preliminary results demonstrate the feasibility of performing magneto-thermoelectric measurements and promise for the future further insights in the interplay of heat, charge, and spin currents to gain a more complete picture about the transport phenomena of layered structures, one focus of recent research in the field of magnetism of reduced dimensions. For an overview of the current state of research the reader is referred to Refs. [915, 916, 917, 918, 919, 32, 910, 920, 921, 922, 923] and references therein.

[74] The Ti/Pt wires crossing the Co/Pt wire at both ends were used as thermometers to calibrate $\Delta T_x(I_\mathrm{heat})$. For that purpose the resistance of both wires was measured in four-point probe geometry: For the Ti/Pt wire located nearer to the heater a (non-invasive) current was impressed through the contacts 5 and 7 and the resulting voltage drop $U_\mathrm{therm,1}$ was measured via 9 and 10 in dependence of different heating currents I_heat impressed via 1 and 2. The same procedure was performed for the top Ti/Pt wire (using the corresponding pads labeled as 6,8 and 11,12), while in this case no influence of I_heat on $U_\mathrm{therm,2}$ was measured. In a second step the whole sample was exposed to different temperatures up to $T = 50$°C and $R_\mathrm{therm,1}(T)$ was determined for $I_\mathrm{heat} = 0$ mA. The comparison of $R_\mathrm{therm,1}(T)$ with $R_\mathrm{therm,1}(I_\mathrm{heat})$ then provides the calibration of $\Delta T_x(I_\mathrm{heat})$.

Bibliography

[1] M. Faraday, "Experimental researches in electricity", *Philos. Trans. R. Soc. London* **122**, 125 (1832).

[2] J. C. Maxwell, "A dynamical theory of the electromagnetic field", *Philos. Trans. R. Soc. London* **155**, 459 (1865).

[3] J. D. Jackson, *Classical Electrodynamics*, (John Wiley & Sons, Inc., 1975).

[4] W. Thomson, "On the electro-dynamic qualities of metals: Effects of magnetization on the electric conductivity of nickel and of iron", *Proc. R. Soc.* **8**, 546 (1856).

[5] E. H. Hall, "On a new action of the magnet on electric currents", *Amer. J. Math.* **2**, 287 (1879).

[6] E. H. Hall, "XXIX. On a new action of the magnet on electric currents", *Philos. Mag. Ser. 5* **9**, 225 (1880).

[7] E. H. Hall, "XXXVIII. On the new action of magnetism on a permanent electric current", *Philos. Mag. Ser. 5* **10**, 301 (1880).

[8] E. H. Hall, "XVIII. On the "rotational coefficient" in nickel and cobalt", *Philos. Mag. Ser. 5* **12**, 157 (1881).

[9] E. Ramsden, *Hall-Effect Sensors: Theory and Application*, (Elsevier Inc., 2006).

[10] A. Gerber, "Towards Hall effect spintronics", *J. Magn. Magn. Mater.* **310**, 2749 (2007).

[11] A. Gerber and O. Riss, "Perspective of spintronics applications based on the extraordinary Hall effect", *J. Nanoelectron. Optoelectron.* **3**, 35 (2008).

[12] J. Moritz, B. Rodmacq, S. Auffret, and B. Dieny, "Extraordinary Hall effect in thin magnetic films and its potential for sensors, memories and magnetic logic applications", *J. Phys. D: Appl. Phys.* **41**, 135001 (2008).

[13] T. R. McGuire and R. I. Potter, "Anisotropic magnetoresistance in ferromagnetic 3d alloys", *IEEE Trans. Magn.* **11**, 1018 (1975).

[14] C. Chappert, A. Fert, and F. Nguyen Van Dau, "The emergence of spin electronics in data storage", *Nat. Mater.* **6**, 813 (2007).

[15] M. N. Baibich, J. M. Broto, A. Fert, F. Nguyen Van Dau, F. Petroff, P. Eitenne, G. Creuzet, A. Friederich, and J. Chazelas, "Giant magnetoresistance of (001)Fe/(001)Cr magnetic superlattices", *Phys. Rev. Lett.* **61**, 2472 (1988).

[16] G. Binasch, P. Grünberg, F. Saurenbach, and W. Zinn, "Enhanced magnetoresistance in layered magnetic-structures with antiferromagnetic interlayer exchange", *Phys. Rev. B* **39**, 4828 (1989).

[17] A. Fert, "Nobel lecture: Origin, development, and future of spintronics", *Rev. Mod. Phys.* **80**, 1517 (2008).

[18] P. A. Grünberg, "Nobel lecture: From spin waves to giant magnetoresistance and beyond", *Rev. Mod. Phys.* **80**, 1531 (2008).

[19] I. K. Schuller, S. Kim, and C. Leighton, "Magnetic superlattices and multilayers", *J. Magn. Magn. Mater.* **200**, 571 (1999).

[20] B. Dieny, *Magnetic Thin Films and Multilayers - Magnetism: Materials and Applications*, (Springer Verlag, 2005).

[21] G. A. Prinz, "Device physics - magnetoelectronics", *Science* **282**, 1660 (1998).

[22] A. Barthelemy, A. Fert, J.-P. Contour, M. Bowen, V. Cros, J. De Teresa, A. Hamzic, J. Faini, J. George, J. Grollier, F. Montaigne, F. Pailloux, F. Petroff, and C. Vouille, "Magnetoresistance and spin electronics", *J. Magn. Magn. Mater.* **242-245**, 68 (2002).

[23] J. F. Gregg, I. Petej, E. Jouguelet, and C. Dennis, "Spin electronics - a review", *J. Phys. D: Appl. Phys.* **35**, R121 (2002).

[24] C. L. Dennis, R. P. Borges, L. D. Buda, U. Ebels, J. F. Gregg, M. Hehn, E. Jouguelet, K. Ounadjela, I. Petej, I. L. Prejbeanu, and M. J. Thornton, "The defining length scales of mesomagnetism: A review", *J. Phys.: Condens. Matter* **14**, R1175 (2002).

[25] I. Zutic, J. Fabian, and S. Das Sarma, "Spintronics: Fundamentals and applications", *Rev. Mod. Phys.* **76**, 323 (2004).

[26] C. H. Marrows, "Spin-polarised currents and magnetic domain walls", *Adv. Phys.* **54**, 585 (2005).

[27] B. Dieny, R. Sousa, and L. Prejbeanu, "Spin electronics - preface", *J. Phys.: Condens. Matter* **19**, 160301 (2007).

[28] H. Zabel, "Progress in spintronics", *Superlattices Microstruct.* **46**, 541 (2009).

[29] S. D. Bader and S. S. P. Parkin, "Spintronics", *Annu. Rev. Cond. Mat. Phys.* **1**, 71 (2010).

[30] C. H. Marrows and B. J. Hickey, "New directions in spintronics: Introduction", *Phil. Trans. R. Soc. A* **369**, 3027 (2011).

[31] P. Gambardella and I. M. Miron, "Current-induced spin-orbit torques", *Phil. Trans. R. Soc. A* **369**, 3175 (2011).

[32] J. Sinova and I. Zutic, "New moves of the spintronics tango", *Nat. Mater.* **11**, 368 (2012).

[33] J. S. Moodera, L. R. Kinder, T. M. Wong, and R. Meservey, "Large magnetoresistance at room-temperature in ferromagnetic thin-film tunnel-junctions", *Phys. Rev. Lett.* **74**, 3273 (1995).

[34] B. Dieny, R. C. Sousa, J. Hérault, C. Papusoi, G. Prenat, U. Ebels, D. Houssameddine, B. Rodmacq, S. Auffret, L. D. Buda-Prejbeanu, M. C. Cyrille, B. Delaet, O. Redon, C. Ducruet, J. P. Nozières, and I. L. Prejbeanu, "Spin-transfer effect and its use in spintronic components", *Int. J. Nanotechnol.* **7**, 591 (2010).

[35] S. Parkin, X. Jiang, C. Kaiser, A. Panchula, K. Roche, and M. Samant, "Magnetically engineered spintronic sensors and memory", *Proc. IEEE* **91**, 661 (2003).

[36] R. C. Sousa and I. L. Prejbeanu, "Non-volatile magnetic random access memories (MRAM)", *C. R. Phys.* **6**, 1013 (2005).

[37] I. L. Prejbeanu, M. Kerekes, R. C. Sousa, H. Sibuet, O. Redon, B. Dieny, and J. P. Nozières, "Thermally assisted MRAM", *J. Phys.: Condens. Matter* **19**, 165218 (2007).

[38] B. Dieny, R. C. Sousa, J. Hérault, C. Papusoi, G. Prenat, U. Ebels, D. Houssameddine, B. Rodmacq, S. Auffret, L. Prejbeanu-Buda, M. C. Cyrille, B. Delaet, O. Redon, C. Ducruet, J. P. Nozières, and L. Prejbeanu, *Spintronic Devices for Memory and Logic Applications - Handbook of Magnetic Materials Vol. 19*, (North Holland, Elsevier, 2011).

[39] B. Carvello, C. Ducruet, B. Rodmacq, S. Auffret, E. Gautier, G. Gaudin, and B. Dieny, "Sizable room-temperature magnetoresistance in cobalt based magnetic tunnel junctions with out-of-plane anisotropy", *Appl. Phys. Lett.* **92**, 102508 (2008).

[40] "Perpendicular magnetic recording technology, Whitepaper Nov. 2007", (2007), http://www.hgst.com.

[41] M. T. Johnson, P. J. H. Bloemen, F. J. A. den Broeder, and J. J. de Vries, "Magnetic anisotropy in metallic multilayers", *Rep. Prog. Phys.* **59**, 1409 (1996).

[42] C. Ducruet, B. Carvello, B. Rodmacq, S. Auffret, G. Gaudin, and B. Dieny, "Magnetoresistance in Co/Pt based magnetic tunnel junctions with out-of-plane magnetization", *J. Appl. Phys.* **103**, 07A918 (2008).

[43] J.-H. Park, C. Park, T. Jeong, M. T. Moneck, N. T. Nufer, and J.-G. Zhu, "Co/Pt multilayer based magnetic tunnel junctions using perpendicular magnetic anisotropy", *J. Appl. Phys.* **103**, 07A917 (2008).

[44] Y. Wang, W. X. Wang, H. X. Wei, B. S. Zhang, W. S. Zhan, and X. F. Han, "Effect of annealing on the magnetic tunnel junction with Co/Pt perpendicular anisotropy ferromagnetic multilayers", *J. Appl. Phys.* **107**, 09C711 (2010).

[45] Z. Kugler, J.-P. Grote, V. Drewello, O. Schebaum, G. Reiss, and A. Thomas, "Co/Pt multilayer-based magnetic tunnel junctions with perpendicular magnetic anisotropy", *J. Appl. Phys.* **111**, 07C703 (2012).

[46] F. Garcia, J. Moritz, F. Ernult, S. Auffret, B. Rodmacq, B. Dieny, J. Camarero, Y. Pennec, S. Pizzini, and J. Vogel, "Exchange bias with perpendicular anisotropy in (Pt-Co)$_n$-FeMn multilayers", *IEEE Trans. Magn.* **38**, 2730 (2002).

[47] F. Garcia, F. Fettar, S. Auffret, B. Rodmacq, and B. Dieny, "Exchange-biased spin valves with perpendicular magnetic anisotropy based on (Co/Pt) multilayers", *J. Appl. Phys.* **93**, 8397 (2003).

[48] J. Sort, B. Dieny, M. Fraune, C. Koenig, F. Lunnebach, B. Beschoten, and G. Güntherodt, "Perpendicular exchange bias in antiferromagnetic-ferromagnetic nanostructures", *Appl. Phys. Lett.* **84**, 3696 (2004).

[49] J. Sort, V. Baltz, F. Garcia, B. Rodmacq, and B. Dieny, "Tailoring perpendicular exchange bias in [Pt/Co]-IrMn multilayers", *Phys. Rev. B* **71**, 054411 (2005).

[50] A. Bollero, V. Baltz, L. D. Buda-Prejbeanu, B. Rodmacq, and B. Dieny, "Origin and control of exchange-bias-like phenomenon in coupled ferromagnetic [Pt/Co]/NiFe bilayers", *Phys. Rev. B* **84**, 094423 (2011).

[51] B. G. Park, J. Wunderlich, D. A. Williams, S. J. Joo, K. Y. Jung, K. H. Shin, K. Olejnik, A. B. Shick, and T. Jungwirth, "Tunneling anisotropic magnetoresistance in multilayer-(Co/Pt)/AlOx/Pt structures", *Phys. Rev. Lett.* **100**, 087204 (2008).

[52] I. M. Miron, K. Garello, G. Gaudin, P.-J. Zermatten, M. V. Costache, S. Auffret, S. Bandiera, B. Rodmacq, A. Schuhl, and P. Gambardella, "Perpendicular switching of a single ferromagnetic layer induced by in-plane current injection", *Nature* **476**, 189 (2011).

[53] C. O. Avci, K. Garello, I. M. Miron, G. Gaudin, S. Auffret, O. Boulle, and P. Gambardella, "Magnetization switching of an MgO/Co/Pt layer by in-plane current injection", *Appl. Phys. Lett.* **100**, 212404 (2012).

[54] R. P. Cowburn, "Property variation with shape in magnetic nanoelements", *J. Phys. D: Appl. Phys.* **33**, R1 (2000).

[55] A. Thiaville and Y. Nakatani, *Domain-Wall Dynamics in Nanowires and Nanostrips - Spin Dynamics in Confined Magnetic Structures III, Topics Appl. Physics 101*, (Springer-Verlag, 2006).

[56] J. C. Slonczewski, "Current-driven excitation of magnetic multilayers", *J. Magn. Magn. Mater.* **159**, L1 (1996).

[57] L. Berger, "Emission of spin waves by a magnetic multilayer traversed by a current", *Phys. Rev. B* **54**, 9353 (1996).

[58] M. D. Stiles and J. Miltat, *Spin-Transfer Torque and Dynamics - Spin Dynamics in Confined Magnetic Structures III, Topics Appl. Physics 101*, (Springer-Verlag, 2006).

[59] M. Tsoi, A. G. M. Jansen, J. Bass, W. C. Chiang, M. Seck, V. Tsoi, and P. Wyder, "Excitation of a magnetic multilayer by an electric current", *Phys. Rev. Lett.* **80**, 4281 (1998).

[60] A. Yamaguchi, T. Ono, S. Nasu, K. Miyake, K. Mibu, and T. Shinjo, "Real-space observation of current-driven domain wall motion in submicron magnetic wires", *Phys. Rev. Lett.* **92**, 077205 (2004).

[61] S. S. P. Parkin, M. Hayashi, and L. Thomas, "Magnetic domain-wall racetrack memory", *Science* **320**, 190 (2008).

[62] D. A. Allwood, G. Xiong, C. C. Faulkner, D. Atkinson, D. Petit, and R. P. Cowburn, "Magnetic domain-wall logic", *Science* **309**, 1688 (2005).

[63] D. Atkinson, C. C. Faulkner, D. A. Allwood, and R. P. Cowburn, *Domain-Wall Dynamics in Magnetic Logic Devices - Spin Dynamics in Confined Magnetic structures III, Topics Appl. Physics 101*, (Springer-Verlag, 2006).

[64] R. P. Cowburn, "Spintronics - change of direction", *Nat. Mater.* **6**, 255 (2007).

[65] S. Bohlens, B. Krüger, A. Drews, M. Bolte, G. Meier, and D. Pfannkuche, "Current controlled random-access memory based on magnetic vortex handedness", *Appl. Phys. Lett.* **93**, 142508 (2008).

[66] R. P. Cowburn and M. E. Welland, "Room temperature magnetic quantum cellular automata", *Science* **287**, 1466 (2000).

[67] B. D. Terris and T. Thomson, "Nanofabricated and self-assembled magnetic structures as data storage media", *J. Phys. D: Appl. Phys.* **38**, R199 (2005).

[68] R. Hertel, *Micromagnetism - Lecture Notes of the 40th spring school 2009: Spintronics - From GMR to Quantum Information*, (Forschungszentrum Jülich GmbH, Institut für Festkörperforschung, 2009).

[69] P. Hohenberg and W. Kohn, "Inhomogeneous electron gas", *Phys. Rev.* **136**, B864 (1964).

[70] W. Kohn and L. J. Sham, "Self-consistent equations including exchange and correlation effects", *Phys. Rev.* **140**, 1133 (1965).

[71] J. B. Staunton, "The electronic-structure of magnetic transition metallic materials", *Rep. Prog. Phys.* **57**, 1289 (1994).

[72] S. Blundell, *Magnetism in Condensed Matter - Oxford Master Series in Condensed Matter Physics*, (Oxford University Press, 2001).

[73] R. O'Handley, *Modern Magnetic Materials: Principles and Applications*, (John Wiley & Sons, Inc., 2000).

[74] W. Rave and A. Hubert, "Magnetic ground state of a thin-film element", *IEEE Trans. Magn.* **36**, 3886 (2000).

[75] S. Blügel, *Magnetische Anisotropie und Magnetostriktion (Theorie) - 30. IFF-Ferienkurs 1999: Magnetische Schichtsysteme*, (Forschungszentrum Jülich GmbH, Institut für Festkörperforschung, 1999).

[76] A. Hubert and R. Schäfer, *Magnetic Domains: The Analysis of Magnetic Microstructures*, (Springer Verlag, 1998).

[77] A. Aharoni, *Introduction to the Theory of Ferromagnetism - International Series of Monographs on Physics 109*, (Oxford University Press, 1996).

[78] J. A. Osborn, "Demagnetizing factors of the general ellipsoid", *Phys. Rev.* **67**, 351 (1945).

[79] B. B. Pant, "Effect of interstrip gap on the sensitivity of high sensitivity magnetoresistive transducers", *J. Appl. Phys.* **79**, 6123 (1996).

[80] A. O. Adeyeye, J. A. C. Bland, C. Daboo, J. Lee, U. Ebels, and H. Ahmed, "Size dependence of the magnetoresistance in submicron FeNi wires", *J. Appl. Phys.* **79**, 6120 (1996).

[81] A. O. Adeyeye, J. A. C. Bland, C. Daboo, and D. G. Hasko, "Magnetostatic interactions and magnetization reversal in ferromagnetic wires", *Phys. Rev. B* **56**, 3265 (1997).

[82] A. Aharoni, "Demagnetizing factors for rectangular ferromagnetic prisms", *J. Appl. Phys.* **83**, 3432 (1998).

[83] C. Kittel, *Einführung in die Festkörperphysik*, (Oldenbourg Verlag, 1996).

[84] H. Ibach, *Physics of Surfaces and Interfaces*, (Springer-Verlag, 2006).

[85] M. B. Stearns, *Landolt-Börnstein - Group III Condensed Matter, Numerical Data and Functional Relationships in Science and Technology*, Volume 19a, (Springer-Verlag, 1986).

[86] T. Suzuki, D. Weller, C. A. Chang, R. Savoy, T. Huang, B. A. Gurney, and V. Speriosu, "Magnetic and magnetooptic properties of thick face-centered-cubic Co single-crystal films", *Appl. Phys. Lett.* **64**, 2736 (1994).

[87] D. S. Rodbell, "Temperature dependence of magnetocrystalline anisotropy of face-centered cubic cobalt", *J. Phys. Soc. Jpn.* **17**, 313 (1962).

[88] L. Néel, "Anisotropie magnétique superficielle et surstructures d'orientation", *J. Phys. Radium* **15**, 225 (1954).

[89] L. Néel, *Surface magnetic anisotropy and orientational superlattices (english translation of Ref. 87) - Selected Works of Louis Néel*, (Gordon and Breach Science Publishers, 1988).

[90] U. Gradmann and J. Müller, "Flat ferromagnetic epitaxial 48Ni/52Fe(111) films of few atomic layers", *Phys. Status Solidi* **27**, 313 (1968).

[91] M. T. Johnson, R. Jungblut, P. J. Kelly, and F. J. A. den Broeder, "Perpendicular magnetic-anisotropy of multilayers - recent insights", *J. Magn. Magn. Mater.* **148**, 118 (1995).

[92] O. Fruchart and A. Thiaville, "Magnetism in reduced dimensions", *C. R. Phys.* **6**, 921 (2005).

[93] P. F. Carcia, A. D. Meinhaldt, and A. Suna, "Perpendicular magnetic-anisotropy in Pd/Co thin-film layered structures", *Appl. Phys. Lett.* **47**, 178 (1985).

[94] P. F. Carcia, "Perpendicular magnetic-anisotropy in Pd/Co and Pt/Co thin-film layered structures", *J. Appl. Phys.* **63**, 5066 (1988).

[95] F. J. A. den Broeder, W. Hoving, and P. J. H. Bloemen, "Magnetic-anisotropy of multilayers", *J. Magn. Magn. Mater.* **93**, 562 (1991).

[96] T. Kingetsu, "Molecular-beam-epitaxial growth and magnetic-properties of (111)Pt/Co/Ag, Pt/Co, and Ag/Co/Pt superlattices", *J. Appl. Phys.* **76**, 4267 (1994).

[97] J. M. MacLaren and R. H. Victora, "Theoretical predictions for magnetic interface anisotropy", *IEEE Trans. Magn.* **29**, 3034 (1993).

[98] R. H. Victora and J. M. MacLaren, "Theory of anisotropy in strained superlattices", *J. Appl. Phys.* **73**, 6415 (1993).

[99] P. Weinberger and L. Szunyogh, "Perpendicular magnetism in magnetic multilayer systems", *Comput. Mater. Sci.* **17**, 414 (2000).

[100] O. Sipr, S. Bornemann, J. Minar, and H. Ebert, "Magnetic anisotropy of Fe and Co adatoms and monolayers: Need for a proper treatment of the substrate", *Phys. Rev. B* **82**, 174414 (2010).

[101] Y. Millev and J. Kirschner, "Reorientation transitions in ultrathin ferromagnetic films by thickness- and temperature-driven anisotropy flows", *Phys. Rev. B* **54**, 4137 (1996).

[102] M. Kisielewski, A. Maziewski, M. Tekielak, J. Ferré, S. Lemerle, V. Mathet, and C. Chappert, "Magnetic anisotropy and magnetization reversal processes in Pt/Co/Pt films", *J. Magn. Magn. Mater.* **260**, 231 (2003).

[103] H. Stillrich, C. Menk, R. Frömter, and H. P. Oepen, "Magnetic anisotropy and the cone state in Co/Pt multilayer films", *J. Appl. Phys.* **105**, 07C308 (2009).

[104] R. L. Stamps, L. Louail, M. Hehn, M. Gester, and K. Ounadjela, "Anisotropies, cone states, and stripe domains in Co/Pt multilayers", *J. Appl. Phys.* **81**, 4751 (1997).

[105] Z. S. Shan, J. X. Shen, R. D. Kirby, D. J. Sellmyer, and Y. J. Wang, "Temperature-dependent interface magnetism and magnetization reversal In Co/Pt multilayers", *J. Appl. Phys.* **75**, 6418 (1994).

[106] R. T. Heap and S. J. Greaves, "The magnetic-structure of platinum cobalt multilayers", *J. Phys. D: Appl. Phys.* **27**, 1343 (1994).

[107] C. L. Canedy, X. W. Li, and G. Xiao, "Large magnetic moment enhancement and extraordinary Hall effect in Co/Pt superlattices", *Phys. Rev. B* **62**, 508 (2000).

[108] E. Y. Vedmedenko, H. P. Oepen, and J. Kirschner, "Microstructure of the spin reorientation transition in second-order approximation of magnetic anisotropy", *Phys. Rev. B* **66**, 214401 (2002).

[109] L. Louail, K. Ounadjela, and R. L. Stamps, "Temperature-dependent thin-film cone states in epitaxial Co/Pt multilayers", *J. Magn. Magn. Mater.* **167**, L189 (1997).

[110] P. J. Jensen and K. H. Bennemann, "Magnetic structure of films: Dependence on anisotropy and atomic morphology", *Surf. Sci. Rep.* **61**, 129 (2006).

[111] R. Frömter, C. Menk, H. Stillrich, and H. P. Oepen, "Imaging the domain pattern of the canted magnetization state in Co/Pt multilayer films", *Vacuum* **82**, 395 (2007).

[112] R. Frömter, H. Stillrich, C. Menk, and H. P. Oepen, "Imaging the cone state of the spin reorientation transition", *Phys. Rev. Lett.* **100**, 207202 (2008).

[113] T. Sugimoto, T. Katayama, Y. Suzuki, M. Hashimoto, Y. Nishihara, A. Itoh, and K. Kawanishi, "Temperature-dependence of perpendicular magnetic-anisotropy In Co/Au and Co/Pt multilayers", *J. Magn. Magn. Mater.* **104**, 1845 (1992).

[114] E. Y. Vedmedenko, H. P. Oepen, and J. Kirschner, "Magnetic microstructure of the spin reorientation transition", *J. Appl. Phys.* **89**, 7145 (2001).

[115] H. P. Oepen, M. Speckmann, Y. Millev, and J. Kirschner, "Unified approach to thickness-driven magnetic reorientation transitions", *Phys. Rev. B* **55**, 2752 (1997).

[116] H. P. Oepen, Y. T. Millev, and J. Kirschner, "The reorientation transition in Co/Au(111)", *J. Appl. Phys.* **81**, 5044 (1997).

[117] H. F. Ding, S. Pütter, H. P. Oepen, and J. Kirschner, "Spin-reorientation transition in thin films studied by the component-resolved Kerr effect", *Phys. Rev. B* **63**, 134425 (2001).

[118] H. Brune, "Microscopic view of epitaxial metal growth: Nucleation and aggregation", *Surf. Sci. Rep.* **31**, 121 (1998).

[119] P. Bruno, "Magnetic surface anisotropy of cobalt and surface roughness effects within Néel's model", *J. Phys. F: Met. Phys.* **18**, 1291 (1988).

[120] P. Bruno, "Dipolar magnetic surface anisotropy in ferromagnetic thin films with interfacial roughness", *J. Appl. Phys.* **64**, 3153 (1988).

[121] H. J. G. Draaisma, F. J. A. den Broeder, and W. J. M. de Jonge, "Perpendicular anisotropy In Pd/Co Multilayers", *J. Appl. Phys.* **63**, 3479 (1988).

[122] J. M. MacLaren and R. H. Victora, "Theoretical predictions of interface anisotropy in the presence of interdiffusion (invited)", *J. Appl. Phys.* **76**, 6069 (1994).

[123] D. Weller, H. Brändle, and C. Chappert, "Relationship between Kerr effect and perpendicular magnetic-anisotropy In $Co_{1-x}Pt_x$ and $Co_{1-x}Pd_x$ alloys", *J. Magn. Magn. Mater.* **121**, 461 (1993).

[124] O. Robach, C. Quiros, P. Steadman, K. F. Peters, E. Lundgren, J. Alvarez, H. Isern, and S. Ferrer, "Magnetic anisotropy of ultrathin cobalt films on Pt(111) investigated with x-ray diffraction: Effect of atomic mixing at the interface", *Phys. Rev. B* **65**, 054423 (2002).

[125] C. H. Su, S. C. Lo, J. van Lierop, K. W. Lin, and H. Ouyang, "The intermixing induced perpendicular magnetic anisotropy in ultrathin Co/Pt multilayers", *J. Appl. Phys.* **105**, 07C316 (2009).

[126] D. Treves, J. T. Jacobs, and E. Sawatzky, "Platinum-cobalt films for digital magneto-optic recording", *J. Appl. Phys.* **46**, 2760 (1975).

[127] C. J. Lin and G. L. Gorman, "Evaporated CoPt alloy-films with strong perpendicular magnetic-anisotropy", *Appl. Phys. Lett.* **61**, 1600 (1992).

[128] W. Grange, M. Maret, J. P. Kappler, J. Vogel, A. Fontaine, F. Petroff, G. Krill, A. Rogalev, J. Goulon, M. Finazzi, and N. B. Brookes, "Magnetocrystalline anisotropy in (111) $CoPt_3$ thin films probed by x-ray magnetic circular dichroism", *Phys. Rev. B* **58**, 6298 (1998).

[129] D. Weller, H. Brändle, G. Gorman, C. J. Lin, and H. Notarys, "Magnetic and magnetooptical properties of cobalt-platinum alloys with perpendicular magnetic-anisotropy", *Appl. Phys. Lett.* **61**, 2726 (1992).

[130] S. E. Park, P. Y. Jung, and K. B. Kim, "Magnetic-properties and microstructural analysis of sputter-deposited and annealed co-pt alloys", *J. Appl. Phys.* **77**, 2641 (1995).

[131] T. A. Tyson, S. D. Conradson, R. F. C. Farrow, and B. A. Jones, "Observation of internal interfaces in Pt_xCo_{1-x} (x approximate to 0.7) alloy films: A likely cause of perpendicular magnetic anisotropy", *Phys. Rev. B* **54**, R3702 (1996).

[132] C. Meneghini, M. Maret, V. Parasote, M. C. Cadeville, J. L. Hazemann, R. Cortes, and S. Colonna, "Structural origin of magnetic anisotropy in Co-Pt alloy films probed by polarized XAFS", *Eur. Phys. J. B* **7**, 347 (1999).

[133] U. Pustogowa, J. Zabloudil, C. Uiberacker, C. Blaas, P. Weinberger, L. Szunyogh, and C. Sommers, "Magnetic properties of thin films of Co and of (CoPt) superstructures on Pt(100) and Pt(111)", *Phys. Rev. B* **60**, 414 (1999).

[134] L. Szunyogh, P. Weinberger, and C. Sommers, "Disorder, ordering, and superstructures of (FePt) and (CoPt) on Pt substrates", *Phys. Rev. B* **60**, 11910 (1999).

[135] M. De Santis, R. Baudoing-Savois, P. Dolle, and M. C. Saint-Lager, "Chemical ordering in the first stages of Co-Pt film growth on Pt(111)", *Phys. Rev. B* **66**, 085412 (2002).

[136] D. Makarov, F. Klimenta, S. Fischer, F. Liscio, S. Schulze, M. Hietschold, M. Maret, and M. Albrecht, "Nonepitaxially grown nanopatterned Co-Pt alloys with out-of-plane magnetic anisotropy", *J. Appl. Phys.* **106**, 114322 (2009).

[137] T. Kingetsu, Y. Kamada, and M. Yamamoto, "Epitaxial growth of binary and ternary metallic strained superlattices and their magnetic properties", *Sci. Technol. Adv. Mater.* **2**, 331 (2001).

[138] D. Sander, "The magnetic anisotropy and spin reorientation of nanostructures and nanoscale films", *J. Phys.: Condens. Matter* **16**, R603 (2004).

[139] G. Andersson and B. Hjorvarsson, "Effects of strain on magnetic anisotropy in Fe- and Co-based heterostructures", *Phase Transitions* **81**, 679 (2008).

[140] D. Sander, A. Enders, and J. Kirschner, "Stress and magnetic properties of surfaces and ultrathin films", *J. Magn. Magn. Mater.* **200**, 439 (1999).

[141] D. Sander, "The correlation between mechanical stress and magnetic anisotropy in ultrathin films", *Rep. Prog. Phys.* **62**, 809 (1999).

[142] C. Chappert and P. Bruno, "Magnetic-anisotropy in metallic ultrathin films and related experiments on cobalt films", *J. Appl. Phys.* **64**, 5736 (1988).

[143] C. R. Chang, "Influence of roughness on magnetic surface anisotropy in ultrathin films", *J. Appl. Phys.* **72**, 596 (1992).

[144] J. S. Yang and C. R. Chang, "The statistical roughness and magnetic surface anisotropy", *IEEE Trans. Magn.* **31**, 1825 (1995).

[145] S. J. Greaves, A. K. Petford-Long, Y. H. Kim, R. J. Pollard, P. J. Grundy, and J. P. Jakubovics, "A magnetic and high-resolution structural investigation of Pt/Co multilayers", *J. Magn. Magn. Mater.* **113**, 63 (1992).

[146] D. Weller, A. Carl, R. Savoy, T. C. Huang, M. F. Toney, and C. Chappert, "Structural transitions and magnetic-anisotropy in ultrathin Co wedges on Pt(111) investigated with the magnetooptical Kerr-effect", *J. Phys. Chem. Solids* **56**, 1563 (1995).

[147] B. Heinrich and J. F. Cochran, "Ultrathin metallic magnetic-films - magnetic anisotropies and exchange interactions", *Adv. Phys.* **42**, 523 (1993).

[148] K. M. Krishnan, "Magnetism and microstructure: The role of interfaces", *Acta Mater.* **47**, 4233 (1999).

[149] C. Kittel, "Physical theory of ferromagnetic domains", *Rev. Mod. Phys.* **21**, 541 (1949).

[150] B. Kaplan and G. Gehring, "The domain structure in ultrathin magnetic films", *J. Magn. Magn. Mater.* **128**, 111 (1993).

[151] M. Speckmann, H. P. Oepen, and H. Ibach, "Magnetic domain-structures in ultrathin Co/Au(111) - on the influence of film morphology", *Phys. Rev. Lett.* **75**, 2035 (1995).

[152] V. Baltz, A. Marty, B. Rodmacq, and B. Dieny, "Magnetic domain replication in interacting bilayers with out-of-plane anisotropy: Application to Co/Pt multilayers", *Phys. Rev. B* **75**, 014406 (2007).

[153] D. Stickler, R. Frömter, H. Stillrich, C. Menk, H. P. Oepen, C. Gutt, S. Streit-Nierobisch, L. M. Stadler, G. Grübel, C. Tieg, and F. Yakhou-Harris, "Domain size in systems with canted magnetization", *Phys. Rev. B* **84**, 104412 (2011).

[154] M. R. Scheinfein, J. Unguris, R. J. Celotta, and D. T. Pierce, "Influence of the surface on magnetic domain-wall microstructure", *Phys. Rev. Lett.* **63**, 668 (1989).

[155] H. P. Oepen and J. Kirschner, "Magnetization distribution of 180-degrees domain-walls a Fe(100) single-crystal surfaces", *Phys. Rev. Lett.* **62**, 819 (1989).

[156] F. Bloch, "Zur Theorie des Austauschproblems und der Remanenzerscheinung der Ferromagnetika", *Z. Phys. A: At. Nucl.* **74**, 295 (1932).

[157] L. Néel, "Energie des parois de Bloch dans les couches minces", *C. R. Acad. Sci.* **241**, 533 (1955).

[158] L. Néel, *Bloch wall energy in thin films (english translation of Ref. 156) - Selected Works of Louis Néel*, (Gordon and Breach Science Publishers, 1988).

[159] D. J. Craik and R. S. Tebble, "Magnetic domains", *Rep. Prog. Phys.* **24**, 116 (1961).

[160] E. E. Huber, D. O. Smith, and J. B. Goodenough, "Domain-wall structure in permalloy films", *J. Appl. Phys.* **29**, 294 (1958).

[161] S. Middelhoek, "Domain walls in thin Ni-Fe films", *J. Appl. Phys.* **34**, 1054 (1963).

[162] H. P. Oepen, G. Steierl, and J. Kirschner, "Scanning electron microscope with polarization analysis: Micromagnetic structures in ultrathin films", *J. Vac. Sci. Technol. B* **20**, 2535 (2002).

[163] A. Berger and H. P. Oepen, "Magnetic domain-walls in ultrathin fcc cobalt films", *Phys. Rev. B* **45**, 12596 (1992).

[164] S. Chikazumi, *Physics of Ferromagnetism - International Series of Monographs on Physics 94*, (Oxford University Press, 1997).

[165] A. Aharoni, "Domain walls and micromagnetics", *J. Phys. Colloques* **32**, 966 (1971).

[166] W. F. Brown, *Micromagnetics - Interscience Tracts on Physics and Astronomy 18*, (Interscience Publishers, a division of John Wiley & Sons, 1963).

[167] J. Stöhr and H. C. Siegmann, *Magnetism: From Fundamentals to Nanoscale Dynamics - Springer Series in Solid-State Sciences*, (Springer-Verlag, 2006).

[168] M. Donahue and D. Porter, OOMMF User's Guide, Version 1.0, National Institue of Standards and Technology, Interagency Report NISTIR 6376, National Institute of Standards and Technology, Gaithersburg, MD (Sept 1999).

[169] R. D. McMichael and M. J. Donahue, "Head to head domain wall structures in thin magnetic strips", *IEEE Trans. Magn.* **33**, 4167 (1997).

[170] A. Thiaville, J. M. Garcia, R. Dittrich, J. Miltat, and T. Schrefl, "Micromagnetic study of Bloch-point-mediated vortex core reversal", *Phys. Rev. B* **67**, 094410 (2003).

[171] G. W. Chern, H. Youk, and O. Tchernyshyov, "Topological defects in flat nanomagnets: The magnetostatic limit", *J. Appl. Phys.* **99**, 08Q505 (2006).

[172] P. Fischer, M. Y. Im, S. Kasai, K. Yamada, T. Ono, and A. Thiaville, "X-ray imaging of vortex cores in confined magnetic structures", *Phys. Rev. B* **83**, 212402 (2011).

[173] J. Fidler and T. Schrefl, "Micromagnetic modelling - the current state of the art", *J. Phys. D: Appl. Phys.* **33**, R135 (2000).

[174] A. Aharoni, "Micromagnetics: Past, present and future", *Physica B* **306**, 1 (2001).

[175] M. Kruzik and A. Prohl, "Recent developments in the modeling, analysis, and numerics of ferromagnetism", *SIAM Rev.* **48**, 439 (2006).

[176] H. P. Oepen and J. Kirschner, "Nanomagnetic structures at surfaces", *Curr. Opin. Solid State Mater. Sci.* **4**, 217 (1999).

[177] C. A. Ross, S. Haratani, F. J. Castano, Y. Hao, M. Hwang, M. Shima, J. Y. Cheng, B. Vogeli, M. Farhoud, M. Walsh, and H. I. Smith, "Magnetic behavior of lithographically patterned particle arrays (invited)", *J. Appl. Phys.* **91**, 6848 (2002).

[178] M. Kläui, C. A. F. Vaz, L. Lopez-Diaz, and J. A. C. Bland, "Vortex formation in narrow ferromagnetic rings", *J. Phys.: Condens. Matter* **15**, R985 (2003).

[179] J. I. Martin, J. Nogués, K. Liu, J. L. Vicent, and I. K. Schuller, "Ordered magnetic nanostructures: Fabrication and properties", *J. Magn. Magn. Mater.* **256**, 449 (2003).

[180] A. O. Adeyeye and N. Singh, "Large area patterned magnetic nanostructures", *J. Phys. D: Appl. Phys.* **41**, 153001 (2008).

[181] J. W. Lau and J. M. Shaw, "Magnetic nanostructures for advanced technologies: Fabrication, metrology and challenges", *J. Phys. D: Appl. Phys.* **44**, 303001 (2011).

[182] H. Youk, G. W. Chern, K. Merit, B. Oppenheimer, and O. Tchernyshyov, "Composite domain walls in flat nanomagnets: The magnetostatic limit", *J. Appl. Phys.* **99**, 08B101 (2006).

[183] W. C. Uhlig and J. Unguris, "Size-dependent transition from shape to exchange dominated magnetic nanostructure", *J. Appl. Phys.* **99**, 08G302 (2006).

[184] M. Kläui, "Head-to-head domain walls in magnetic nanostructures", *J. Phys.: Condens. Matter* **20**, 313001 (2008).

[185] T. Ono, H. Miyajima, K. Shigeto, K. Mibu, N. Hosoito, and T. Shinjo, "Propagation of the magnetic domain wall in submicron magnetic wire investigated by using giant magnetoresistance effect", *J. Appl. Phys.* **85**, 6181 (1999).

[186] T. Ono, H. Miyajima, K. Shigeto, K. Mibu, N. Hosoito, and T. Shinjo, "Propagation of a magnetic domain wall in a submicrometer magnetic wire", *Science* **284**, 468 (1999).

[187] M. Hayashi, L. Thomas, C. Rettner, R. Moriya, and S. S. P. Parkin, "Direct observation of the coherent precession of magnetic domain walls propagating along permalloy nanowires", *Nat. Phys.* **3**, 21 (2007).

[188] J. A. Katine, F. J. Albert, R. A. Buhrman, E. B. Myers, and D. C. Ralph, "Current-driven magnetization reversal and spin-wave excitations in Co/Cu/Co pillars", *Phys. Rev. Lett.* **84**, 3149 (2000).

[189] G. Beach, M. Tsoi, and J. Erskine, "Current-induced domain wall motion", *J. Magn. Magn. Mater.* **320**, 1272 (2008).

[190] L. Bocklage, B. Krüger, T. Matsuyama, M. Bolte, U. Merkt, D. Pfannkuche, and G. Meier, "Dependence of magnetic domain-wall motion on a fast changing current", *Phys. Rev. Lett.* **103**, 197204 (2009).

[191] L. Thomas, R. Moriya, C. Rettner, and S. S. P. Parkin, "Dynamics of magnetic domain walls under their own inertia", *Science* **330**, 1810 (2010).

[192] O. Boulle, G. Malinowski, and M. Kläui, "Current-induced domain wall motion in nanoscale ferromagnetic elements", *Mater. Sci. Eng. R Rep.* **72**, 3 (2011).

[193] C. H. Marrows and G. Meier, "Domain wall dynamics in nanostructures", *J. Phys.: Condens. Matter* **24**, 020301 (2012).

[194] M. Kläui, C. A. F. Vaz, J. Rothman, J. A. C. Bland, W. Wernsdorfer, G. Faini, and E. Cambril, "Domain wall pinning in narrow ferromagnetic ring structures probed by magnetoresistance measurements", *Phys. Rev. Lett.* **90**, 097202 (2003).

[195] L. K. Bogart and D. Atkinson, "Domain wall anisotropic magnetoresistance in planar nanowires", *Appl. Phys. Lett.* **94**, 042511 (2009).

[196] J. Jaworowicz, N. Vernier, J. Ferré, A. Maziewski, D. Stanescu, D. Ravelosona, A. S. Jacqueline, C. Chappert, B. Rodmacq, and B. Dieny, "Magnetic logic using nanowires with perpendicular anisotropy", *Nanotechnology* **20**, 215401 (2009).

[197] L. O'Brien, D. E. Read, H. T. Zeng, E. R. Lewis, D. Petit, and R. P. Cowburn, "Bidirectional magnetic nanowire shift register", *Appl. Phys. Lett.* **95**, 232502 (2009).

[198] H. T. Zeng, D. Read, L. O'Brien, J. Sampaio, E. R. Lewis, D. Petit, and R. P. Cowburn, "Asymmetric magnetic not gate and shift registers for high density data storage", *Appl. Phys. Lett.* **96**, 262510 (2010).

[199] M. Kläui, C. A. F. Vaz, J. A. C. Bland, W. Wernsdorfer, G. Faini, and E. Cambril, "Controlled magnetic switching in single narrow rings probed by magnetoresistance measurements", *Appl. Phys. Lett.* **81**, 108 (2002).

[200] M. Hayashi, L. Thomas, C. Rettner, R. Moriya, X. Jiang, and S. S. P. Parkin, "Dependence of current and field driven depinning of domain walls on their structure and chirality in permalloy nanowires", *Phys. Rev. Lett.* **97**, 207205 (2006).

[201] C. W. Sandweg, N. Wiese, D. McGrouther, S. J. Hermsdoerfer, H. Schultheiss, B. Leven, S. McVitie, B. Hillebrands, and J. N. Chapman, "Direct observation of domain wall structures in curved permalloy wires containing an antinotch", *J. Appl. Phys.* **103**, 093906 (2008).

[202] K. He, D. J. Smith, and M. R. McCartney, "Observation of asymmetrical pinning of domain walls in notched permalloy nanowires using electron holography", *Appl. Phys. Lett.* **95**, 182507 (2009).

[203] M. Y. Im, L. Bocklage, P. Fischer, and G. Meier, "Direct observation of stochastic domain-wall depinning in magnetic nanowires", *Phys. Rev. Lett.* **102**, 147204 (2009).

[204] L. K. Bogart, D. Atkinson, K. O'Shea, D. McGrouther, and S. McVitie, "Dependence of domain wall pinning potential landscapes on domain wall chirality and pinning site geometry in planar nanowires", *Phys. Rev. B* **79**, 054414 (2009).

[205] T. Taniyama, I. Nakatani, T. Namikawa, and Y. Yamazaki, "Resistivity due to domain walls in Co zigzag wires", *Phys. Rev. Lett.* **82**, 2780 (1999).

[206] T. Taniyama, I. Nakatani, T. Yakabe, and Y. Yamazaki, "Control of domain structures and magnetotransport properties in patterned ferromagnetic wires", *Appl. Phys. Lett.* **76**, 613 (2000).

[207] J. L. Tsai, S. F. Lee, Y. D. Yao, C. Yu, and S. H. Liou, "Magnetoresistance study in thin zig zag NiFe wires", *J. Appl. Phys.* **91**, 7983 (2002).

[208] M. Tanase, D. M. Silevitch, C. L. Chien, and D. H. Reich, "Magnetotransport properties of bent ferromagnetic nanowires", *J. Appl. Phys.* **93**, 7616 (2003).

[209] M. Kläui, P. O. Jubert, R. Allenspach, A. Bischof, J. A. C. Bland, G. Faini, U. Rüdiger, C. A. F. Vaz, L. Vila, and C. Vouille, "Direct observation of domain-wall configurations transformed by spin currents", *Phys. Rev. Lett.* **95**, 026601 (2005).

[210] C. Brownlie, S. McVitie, J. N. Chapman, and C. D. W. Wilkinson, "Lorentz microscopy studies of domain wall trap structures", *J. Appl. Phys.* **100**, 033902 (2006).

[211] P. O. Jubert, M. Kläui, A. Bischof, U. Rüdiger, and R. Allenspach, "Velocity of vortex walls moved by current", *J. Appl. Phys.* **99**, 08G523 (2006).

[212] L. Heyne, M. Kläui, D. Backes, P. Möhrke, T. A. Moore, J. G. Kimling, O. Boulle, U. Rüdiger, L. J. Heyderman, A. F. Rodriguez, F. Nolting, K. Kirsch, and R. Mattheis, "Direct imaging of current-induced domain wall motion in CoFeB structures", *J. Appl. Phys.* **103**, 07D928 (2008).

[213] L. Heyne, M. Kläui, D. Backes, T. A. Moore, S. Krzyk, U. Rüdiger, L. J. Heyderman, A. F. Rodriguez, F. Nolting, T. O. Mentes, M. A. Nino, A. Locatelli, K. Kirsch, and R. Mattheis, "Relationship between nonadiabaticity and damping in permalloy studied by current induced spin structure transformations", *Phys. Rev. Lett.* **100**, 066603 (2008).

[214] A. Vanhaverbeke, A. Bischof, and R. Allenspach, "Control of domain wall polarity by current pulses", *Phys. Rev. Lett.* **101**, 107202 (2008).

[215] M. Donolato, M. Gobbi, P. Vavassori, M. Leone, M. Cantoni, V. Metlushko, B. Ilic, M. L. Zhang, S. X. Wang, and R. Bertacco, "Nanosized corners for trapping and detecting magnetic nanoparticles", *Nanotechnology* **20**, 385501 (2009).

[216] T. Manago, K. Kanazawa, and T. Kera, "Magneto-resistance of NiFe nanowire with zigzag shape", *J. Magn. Magn. Mater.* **321**, 2327 (2009).

[217] E. S. Wilhelm, D. McGrouther, L. Heyne, A. Bisig, and M. Kläui, "Vortex domain wall chirality rectification due to the interaction with end domain spin structures in permalloy nanowires", *Appl. Phys. Lett.* **95**, 252501 (2009).

[218] M. Donolato, P. Vavassori, M. Gobbi, M. Deryabina, M. F. Hansen, V. Metlushko, B. Ilic, M. Cantoni, D. Petti, S. Brivio, and R. Bertacco, "On-chip manipulation of protein-coated magnetic beads via domain-wall conduits", *Adv. Mater.* **22**, 2706 (2010).

[219] M. Donolato, F. Lofink, S. Hankemeier, J. M. Porro, H. P. Oepen, and P. Vavassori, "Characterization of domain wall-based traps for magnetic beads separation", *J. Appl. Phys.* **111**, 07B336 (2012).

[220] J. Y. Lee, K. S. Lee, S. Choi, K. Y. Guslienko, and S. K. Kim, "Dynamic transformations of the internal structure of a moving domain wall in magnetic nanostripes", *Phys. Rev. B* **76**, 184408 (2007).

[221] E. R. Lewis, D. Petit, L. Thevenard, A. V. Jausovec, L. O'Brien, D. E. Read, and R. P. Cowburn, "Magnetic domain wall pinning by a curved conduit", *Appl. Phys. Lett.* **95**, 152505 (2009).

[222] Y. Nakatani, A. Thiaville, and J. Miltat, "Head-to-head domain walls in soft nano-strips: A refined phase diagram", *J. Magn. Magn. Mater.* **290**, 750 (2005).

[223] R. Frömter, S. Hankemeier, H. P. Oepen, and J. Kirschner, "Optimizing a low-energy electron diffraction spin-polarization analyzer for imaging of magnetic surface structures", *Rev. Sci. Instrum.* **82**, 033704 (2011).

[224] F. Lofink, S. Hankemeier, R. Frömter, J. Kirschner, and H. P. Oepen, "Long-time stability of a low-energy electron diffraction spin polarization analyzer for magnetic imaging", *Rev. Sci. Instrum.* **83**, 023708 (2012).

[225] H. Hopster and H. P. Oepen (Eds.) *Magnetic Microscopy of Nanostructures*, (Springer-Verlag, 2005).

[226] H. P. Oepen and R. Frömter, *Scanning Electron Microscopy with Polarisation Analysis - The Handbook of Magnetism and Advanced Magnetic Materials Vol. 3*, (John Wiley & Sons, Inc., 2007).

[227] J. Unguris, A. Seiler, R. J. Celotta, D. T. Pierce, P. D. Johnson, and N. V. Smith, "Spin-polarized inverse photo-electron spectroscopy of solid-surfaces - Ni(110)", *Phys. Rev. Lett.* **49**, 1047 (1982).

[228] H. Hopster, R. Raue, E. Kisker, G. Güntherodt, and M. Campagna, "Evidence for spin-dependent electron-hole-pair excitations in spin-polarized secondary-electron emission from Ni(110)", *Phys. Rev. Lett.* **50**, 70 (1983).

[229] J. Kirschner, "Direct and exchange contributions in inelastic scattering of spin-polarized electrons from iron", *Phys. Rev. Lett.* **55**, 973 (1985).

[230] D. L. Abraham and H. Hopster, "Magnetic probing depth in spin-polarized secondary-electron spectroscopy", *Phys. Rev. Lett.* **58**, 1352 (1987).

[231] T. van Zandt and R. Browning, "Determination of spin-polarized secondary-electron escape depth through oxidation of iron", *J. Appl. Phys.* **68**, 5835 (1990).

[232] J. A. C. Bland and B. Heinrich (Eds.) *Ultrathin Magnetic Structures I: An Introduction to the Electronic, Magnetic and Structural Properties*, (Springer-Verlag, 2005).

[233] M. Donath, D. Scholl, H. C. Siegmann, and E. Kay, "Probing depth of the low-energy cascade electrons from a transition-metal", *Appl. Phys. A Mater. Sci. Process.* **52**, 206 (1991).

[234] T. van Zandt, R. Browning, and M. Landolt, "Iron overlayer polarization enhancement technique for spin-polarized electron-microscopy", *J. Appl. Phys.* **69**, 1564 (1991).

[235] O. Paul, S. Toscano, K. Totland, and M. Landolt, "The spatial origin of the spin-polarization of secondary-electron emission from Fe", *Surf. Sci.* **251**, 27 (1991).

[236] R. Wiesendanger, *Scanning Probe Microscopy and Spectroscopy: Methods and Applications*, (Cambridge University Press, 1994).

[237] R. Allenspach, "Ultrathin films - magnetism on the microscopic scale", *J. Magn. Magn. Mater.* **129**, 160 (1994).

[238] A. Yang, H. Imrane, J. Lou, J. Kirkland, C. Vittoria, N. Sun, and V. G. Harris, "Effects of boron addition to the atomic structure and soft magnetic properties of FeCoB films", *J. Appl. Phys.* **103**, 07E736 (2008).

[239] S. Hankemeier, *The magnetic fine structure of thin-film elements*, Ph.D. thesis, Universität Hamburg (2010).

[240] L. Reimer, *Scanning Electron Microscopy: Physics of Image Formation and Microanalysis, Springer Series in Optical Sciences Vol. 45*, (Springer-Verlag, 1998).

[241] E. Feldtkeller, "Ripple hysteresis in thin magnetic films", *J. Appl. Phys.* **34**, 2646 (1963).

[242] H. B. Callen, R. L. Coren, and W. D. Doyle, "Magnetization ripple and arctic foxes", *J. Appl. Phys.* **36**, 1064 (1965).

[243] K. J. Harte, "Theory of magnetization ripple in ferromagnetic films", *J. Appl. Phys.* **39**, 1503 (1968).

[244] X. Liu, R. Sooryakumar, C. J. Gutierrez, and G. A. Prinz, "Exchange stiffness and magnetic anisotropies in bcc $Fe_{1-x}Co_x$ alloys", *J. Appl. Phys.* **75**, 7021 (1994).

[245] O. Tchernyshyov and G. W. Chern, "Fractional vortices and composite domain walls in flat nanomagnets", *Phys. Rev. Lett.* **95**, 197204 (2005).

[246] P. M. Chaikin and L. T.C., *Principles of condensed matter physics*, (Cambrigde University Press, 1995).

[247] M. Bode, O. Pietzsch, A. Kubetzka, W. Wulfhekel, D. McGrouther, S. McVitie, and J. N. Chapman, "Comment on 'Three-dimensional, spin-resolved structure of magnetic vortex and antivortex states in patterned Co films using scanning ion microscopy with polarization analysis'", *Phys. Rev. Lett.* **100**, 029703 (2008).

[248] A. Thiaville, Y. Nakatani, F. Piechon, J. Miltat, and T. Ono, "Transient domain wall displacement under spin-polarized current pulses", *Eur. Phys. J. B* **60**, 15 (2007).

[249] W. C. Uhlig, M. J. Donahue, D. T. Pierce, and J. Unguris, "Direct imaging of current-driven domain walls in ferromagnetic nanostripes", *J. Appl. Phys.* **105**, 103902 (2009).

[250] D. McGrouther, S. McVitie, J. N. Chapman, and A. Gentils, "Controlled domain wall injection into ferromagnetic nanowires from an optimized pad geometry", *Appl. Phys. Lett.* **91**, 022506 (2007).

[251] K. J. O'Shea, S. McVitie, J. N. Chapman, and J. M. R. Weaver, "Direct observation of changes to domain wall structures in magnetic nanowires of varying width", *Appl. Phys. Lett.* **93**, 202505 (2008).

[252] D. Backes, C. Schieback, M. Kläui, F. Junginger, H. Ehrke, P. Nielaba, U. Rüdiger, L. J. Heyderman, C. S. Chen, T. Kasama, R. E. Dunin-Borkowski, C. A. F. Vaz, and J. A. C. Bland, "Transverse domain walls in nanoconstrictions", *Appl. Phys. Lett.* **91**, 112502 (2007).

[253] M. Kläui, C. A. F. Vaz, J. A. C. Bland, L. J. Heyderman, F. Nolting, A. Pavlovska, E. Bauer, S. Cherifi, S. Heun, and A. Locatelli, "Head-to-head domain-wall phase diagram in mesoscopic ring magnets", *Appl. Phys. Lett.* **85**, 5637 (2004).

[254] M. Konoto, T. Yamada, K. Koike, H. Akoh, T. Arima, and Y. Tokura, "Formation and control of magnetic vortex chirality in patterned micromagnet arrays", *J. Appl. Phys.* **103**, 023904 (2008).

[255] J. E. Wegrowe, S. E. Gilbert, D. Kelly, B. Doudin, and J. P. Ansermet, "Anisotropic magnetoresistance as a probe of magnetization reversal in individual nano-sized nickel wires.", *IEEE Trans. Magn.* **34**, 903 (1998).

[256] J. E. Wegrowe, D. Kelly, A. Franck, S. E. Gilbert, and J. P. Ansermet, "Magnetoresistance of ferromagnetic nanowires", *Phys. Rev. Lett.* **82**, 3681 (1999).

[257] L. Vila, L. Piraux, J. M. George, and G. Faini, "Multiprobe magnetoresistance measurements on isolated magnetic nanowires", *Appl. Phys. Lett.* **80**, 3805 (2002).

[258] M. Steiner, C. Pels, and G. Meier, "Reversible and irreversible magnetoresistance of quasisingle domain permalloy microstructures", *J. Appl. Phys.* **95**, 6759 (2004).

[259] M. Brands and G. Dumpich, "Experimental determination of anisotropy and demagnetizing factors of single Co nanowires by magnetoresistance measurements", *J. Appl. Phys.* **98**, 014309 (2005).

[260] M. Brands, C. Hassel, A. Carl, and G. Dumpich, "Electron-electron interaction in quasi-one-dimensional cobalt nanowires capped with platinum: Low-temperature magnetoresistance measurements", *Phys. Rev. B* **74**, 033406 (2006).

[261] T. Haug, A. Vogl, J. Zweck, and C. H. Back, "In situ measurements of magnetoresistive effects in ferromagnetic microstructures by Lorentz microscopy", *Appl. Phys. Lett.* **88**, 082506 (2006).

[262] A. B. Oliveira, S. M. Rezende, and A. Azevedo, "Magnetization reversal in permalloy ferromagnetic nanowires investigated with magnetoresistance measurements", *Phys. Rev. B* **78**, 4423 (2008).

[263] R. Silva, "Magnetoreistance and magnetization reversal of single Co nanowires", *Phys. Rev. B* (2009).

[264] W. Wulfhekel and J. Kirschner, "Spin-polarized scanning tunneling microscopy of magnetic structures and antiferromagnetic thin films", *Annu. Rev. Mater. Res.* **37**, 69 (2007).

[265] G. Rodary, S. Wedekind, D. Sander, and J. Kirschner, "Magnetic hysteresis loop of single Co nano-islands", *Jpn. J. Appl. Phys.* **47**, 9013 (2008).

[266] R. Wiesendanger, "Spin mapping at the nanoscale and atomic scale", *Rev. Mod. Phys.* **81**, 1495 (2009).

[267] R. Wiesendanger, "Single-atom magnetometry", *Curr. Opin. Solid State Mater. Sci.* **15**, 1 (2011).

[268] D. Sander, H. Oka, M. Corbetta, V. Stepanyuk, and J. Kirschner, "New insights into nano-magnetism by spin-polarized scanning tunneling microscopy", *J. Electron Spectrosc. Relat. Phenom.*, in press (2012).

[269] J. Aumentado and V. Chandrasekhar, "Magnetoresistance of single-domain ferromagnetic particles", *Appl. Phys. Lett.* **74**, 1898 (1999).

[270] P. Vavassori, M. Grimsditch, V. Metlushko, N. Zaluzec, and B. Ilic, "Magnetoresistance of single magnetic vortices", *Appl. Phys. Lett.* **86**, 072507 (2005).

[271] D. Ruzmetov and V. Chandrasekhar, "The dynamics of magnetic vortex states in a single permalloy nanoparticle", *J. Magn. Magn. Mater.* **320**, 47 (2008).

[272] F. Cheynis, A. Masseboeuf, O. Fruchart, N. Rougemaille, J. C. Toussaint, R. Belkhou, P. Bayle-Guillemaud, and A. Marty, "Controlled switching of Néel caps in flux-closure magnetic dots", *Phys. Rev. Lett.* **102**, 107201 (2009).

[273] R. P. Cowburn and M. E. Welland, "Micromagnetics of the single-domain state of square ferromagnetic nanostructures", *Phys. Rev. B* **58**, 9217 (1998).

[274] J. Shi, S. Tehrani, and M. R. Scheinfein, "Geometry dependence of magnetization vortices in patterned submicron NiFe elements", *Appl. Phys. Lett.* **76**, 2588 (2000).

[275] J. Y. Cheng, W. Jung, and C. A. Ross, "Magnetic nanostructures from block copolymer lithography: Hysteresis, thermal stability, and magnetoresistance", *Phys. Rev. B* **70**, 064417 (2004).

[276] M. Pardavi-Horvath, C. A. Ross, and R. D. McMichael, "Shape effects in the ferromagnetic resonance of nanosize rectangular permalloy arrays", *IEEE Trans. Magn.* **41**, 3601 (2005).

[277] T. Y. Chung and S. Y. Hsu, "Detection of the domain structure change using magnetotransport for a series of circular permalloy dots", *J. Appl. Phys.* **99**, 08B707 (2006).

[278] A. V. Jausovec, G. Xiong, and R. P. Cowburn, "Stability of magnetization states in submicron permalloy disks", *J. Appl. Phys.* **99**, 08B103 (2006).

[279] W. Wernsdorfer, K. Hasselbach, D. Mailly, B. Barbara, A. Benoit, L. Thomas, and G. Suran, "DC-SQUID magnetization measurements of single magnetic particles", *J. Magn. Magn. Mater.* **145**, 33 (1995).

[280] W. Wernsdorfer, K. Hasselbach, A. Benoit, G. Cernicchiaro, D. Mailly, B. Barbara, and L. Thomas, "Measurement of the dynamics of the magnetization reversal individual single-domain co particles", *J. Magn. Magn. Mater.* **151**, 38 (1995).

[281] C. Thirion, W. Wernsdorfer, M. Kläui, C. A. F. Vaz, P. Lewis, H. Ahmed, J. A. C. Bland, and D. Mailly, "Anisotropy engineering in Co nanodiscs fabricated using prepatterned silicon pillars", *Nanotechnology* **17**, 1960 (2006).

[282] W. Wernsdorfer, K. Hasselbach, A. Benoit, B. Barbara, B. Doudin, J. Meier, J. P. Ansermet, and D. Mailly, "Measurements of magnetization switching in individual nickel nanowires", *Phys. Rev. B* **55**, 11552 (1997).

[283] J. Wang, A. O. Adeyeye, and N. Singh, "Magnetostatic interactions in mesoscopic $Ni_{80}Fe_{20}$ ring arrays", *Appl. Phys. Lett.* **87**, 262508 (2005).

[284] Micromagnetic Modeling Activity Group, National Institute of Standard and Technology, http://www.ctcms.nist.gov/∼rdm/mumag.html.

[285] D. R. Fredkin and T. R. Koehler, "Numerical micromagnetics by the finite-element method", *IEEE Trans. Magn.* **23**, 3385 (1987).

[286] R. Hertel, "Computational micromagnetism of magnetization processes in nickel nanowires", *J. Magn. Magn. Mater.* **249**, 251 (2002).

[287] K. X. Xie, X. P. Zhang, W. W. Lin, P. Zhang, and H. Sang, "Magnetization splitting in Landau and diamond-domain structures: Dependence on exchange interaction, anisotropy, and size", *Phys. Rev. B* **84**, 054460 (2011).

[288] R. D. Gomez, T. V. Luu, A. O. Pak, K. J. Kirk, and J. N. Chapman, "Domain configurations of nanostructured permalloy elements", *J. Appl. Phys.* **85**, 6163 (1999).

[289] M. Barthelmess, C. Pels, A. Thieme, and G. Meier, "Stray fields of domains in permalloy microstructures - measurements and simulations", *J. Appl. Phys.* **95**, 5641 (2004).

[290] M. Bolte, M. Steiner, C. Pels, M. Barthelmess, J. Kruse, U. Merkt, G. Meier, M. Holz, and D. Pfannkuche, "Magnetotransport through magnetic domain patterns in permalloy rectangles", *Phys. Rev. B* **72**, 224436 (2005).

[291] S. Cherifi, R. Hertel, J. Kirschner, H. Wang, R. Belkhou, A. Locatelli, S. Heun, A. Pavlovska, and E. Bauer, "Virgin domain structures in mesoscopic Co patterns: Comparison between simulation and experiment", *J. Appl. Phys.* **98**, 043901 (2005).

[292] S. Hankemeier, R. Frömter, N. Mikuszeit, D. Stickler, H. Stillrich, S. Pütter, E. Y. Vedmedenko, and H. P. Oepen, "Magnetic ground state of single and coupled permalloy rectangles", *Phys. Rev. Lett.* **103**, 147204 (2009).

[293] H. A. M. van den Berg, "Self-consistent domain theory in soft ferromagnetic media. i. solenoidal distributions in elliptical thin-film elements", *J. Appl. Phys.* **57**, 2168 (1985).

[294] H. A. M. van den Berg, "Self-consistent domain theory in soft-ferromagnetic media. ii. basic domain-structures in thin-film objects", *J. Appl. Phys.* **60**, 1104 (1986).

[295] H. A. M. van den Berg, "Domain-structures in soft-ferromagnetic thin-film objects", *J. Appl. Phys.* **61**, 4194 (1987).

[296] S. Pütter, N. Mikuszeit, E. Y. Vedmedenko, and H. P. Oepen, "The effect of tilted edges on the shape anisotropy and stray field coupling of uniformly magnetized rectangular elements", *J. Appl. Phys.* **106**, 043916 (2009).

[297] J. Orloff, *Handbook of charged particle optics*, (CRC Press, 1997).

[298] J. Orloff, M. Utlaut, and L. Swanson, *High Resolution Focused Ion Beams: FIB and its Applications*, (Springer-Verlag, 2002).

[299] L. A. Giannuzzi and F. A. Stevie (Eds.) *Introduction to Focused Ion Beams: Instrumentation, Theory, Techniques and Practice*, (Springer Science+Business Media LLC, 2005).

[300] I. C. Lo, J. C. Wu, L. Horng, Z. H. Wei, M. F. Lai, and C. R. Chang, "Probing the local magnetization reversal through magnetoresistance measurement", *J. Appl. Phys.* **97**, 10M102 (2005).

[301] N. Kuhlmann, A. Vogel, and G. Meier, "Magnetization dynamics and cone angle precession in permalloy rectangles", *Phys. Rev. B* **85**, 014410 (2012).

[302] C. A. Volkert and A. M. Minor, "Focused ion beam microscopy and micromachining", *MRS Bull.* (2007).

[303] J. Ziegler, J. Biersack, and U. Littmark, "The stopping and range of ions in solids", New York: Pergamon (1985), SRIM code: http://www.srim.org.

[304] G. Carter, I. Katardjiev, and M. J. Nobes, *High Fluence Ion Irradiation: An Overview - Materials Modification by High-fluence Ion Beams, NATO ASI Series*, (Kluwer Academic Publishers, 1989).

[305] J. Fassbender, A. Mücklich, K. Potzger, and W. Möller, "Mixing and subsequent amorphization of ultrathin $Ni_{81}Fe_{19}$/Ta bilayers by 30 keV Ni implantation", *Nucl. Instrum. Methods Phys. Res. Sect. B* **248**, 343 (2006).

[306] C. M. Park and J. A. Bain, "Local degradation of magnetic properties in magnetic thin films irradiated by Ga^+ focused-ion-beams", *IEEE Trans. Magn.* **38**, 2237 (2002).

[307] P. Warin, R. Hyndman, J. Glerak, J. N. Chapman, J. Ferré, J. P. Jamet, V. Mathet, and C. Chappert, "Modification of Co/Pt multilayers by gallium irradiation - Part 2: The effect of patterning using a highly focused ion beam", *J. Appl. Phys.* **90**, 3850 (2001).

[308] J. Jaworowicz, A. Maziewski, P. Mazalski, M. Kisielewski, I. Sveklo, M. Tekielak, V. Zablotskii, J. Ferré, N. Vernier, A. Mougin, A. Henschke, and J. Fassbender, "Spin reorientation transitions in Pt/Co/Pt films under low dose Ga^+ ion irradiation", *Appl. Phys. Lett.* **95**, 022502 (2009).

[309] T. Devolder and H. Bernas, *Magnetic Properties and Ion Beams: Why and How - Materials Science with Ion Beams, Topics Appl. Physics 116*, (Springer-Verlag, 2010).

[310] Z. B. Guo, D. You, J. J. Qiu, K. B. Li, and Y. H. Wu, "Influence of Ga^+ ion irradiation on magnetoresistance and exchange bias of IrMn/CoFe/Cu/CoFe/NiFe spin valve", *Solid State Commun.* **120**, 459 (2001).

[311] E. Kerr, S. van Dijken, R. M. Langford, and J. M. D. Coey, "Effects of Ga^+ ion implantation on the magneto resistive properties of spin valves", *J. Magn. Magn. Mater.* **290**, 124 (2005).

[312] C. Chappert, H. Bernas, J. Ferré, V. Kottler, J. P. Jamet, Y. Chen, E. Cambril, T. Devolder, F. Rousseaux, V. Mathet, and H. Launois, "Planar patterned magnetic media obtained by ion irradiation", *Science* **280**, 1919 (1998).

[313] J. Fassbender, D. Ravelosona, and Y. Samson, "Tailoring magnetism by light-ion irradiation", *J. Phys. D: Appl. Phys.* **37**, R179 (2004).

[314] J. Fassbender and J. McCord, "Magnetic patterning by means of ion irradiation and implantation", *J. Magn. Magn. Mater.* **320**, 579 (2008).

[315] D. Ozkaya, R. M. Langford, W. L. Chan, and A. K. Petford-Long, "Effect of Ga implantation on the magnetic properties of permalloy thin films", *J. Appl. Phys.* **91**, 9937 (2002).

[316] C. M. Park, J. A. Bain, T. W. Clinton, P. A. A. van der Heijden, and T. J. Klemmer, "Measurement of Ga implantation profiles in the sidewall and bottom of focused-ion-beam-etched structures", *Appl. Phys. Lett.* **84**, 3331 (2004).

[317] W. Y. Lee, M. F. Toney, P. Tameerug, E. Allen, and D. Mauri, "High magnetoresistance permalloy films deposited on a thin NiFeCr or NiCr underlayer", *J. Appl. Phys.* **87**, 6992 (2000).

[318] T. Miyazaki and T. Ajima, "Impurity effect on the anisotropic magnetoresistivity of 82Ni-Fe alloy film", *J. Magn. Magn. Mater.* **81**, 91 (1989).

[319] J. Fassbender, J. von Borany, A. Mücklich, K. Potzger, W. Möller, J. McCord, L. Schultz, and R. Mattheis, "Structural and magnetic modifications of Cr-implanted permalloy", *Phys. Rev. B* **73**, 184410 (2006).

[320] H. Nagura, K. Saito, K. Takanashi, and H. Fujimori, "Influence of third elements on the anisotropic magnetoresistance in permalloy films", *J. Magn. Magn. Mater.* **212**, 53 (2000).

[321] W. L. Johnson, *Ion-irradiation induced phase changes in metallic systems - Materials Modification by High-fluence Ion Beams, NATO ASI Series*, (Kluwer Academic Publishers, 1989).

[322] A. Perin, R. Gupta, G. Principi, C. Tosello, L. M. Gratton, E. Kuzmann, and Z. Klencsar, "Thermal stability of ion-beam mixed and laser-irradiated FeNiCr multilayers", *Surf. Coat. Technol.* **104**, 93 (1998).

[323] W. M. Kaminsky, G. A. C. Jones, N. K. Patel, W. E. Booij, M. G. Blamire, S. M. Gardiner, Y. B. Xu, and J. A. C. Bland, "Patterning ferromagnetism in $Ni_{80}Fe_{20}$ films via Ga^+ ion irradiation", *Appl. Phys. Lett.* **78**, 1589 (2001).

[324] T. Last, S. Hacia, S. F. Fischer, and U. Kunze, "Aging phenomena in single nanopatterned permalloy wires", *Physica B* **384**, 9 (2006).

[325] R. E. Parra and J. W. Cable, "Magnetic-Moment Distribution In Ni-Pt Alloys", *J. Appl. Phys.* **50**, 7522 (1979).

[326] M. C. Cadeville and J. L. Moran-Lopez, "Magnetism and spatial order in transition-metal alloys - experimental and theoretical aspects", *Phys. Rep.* **153**, 331 (1987).

[327] T. Golod, A. Rydh, and V. M. Krasnov, "Anomalous Hall effect in NiPt thin films", *J. Appl. Phys.* **110**, 033909 (2011).

[328] R. L. Kubena and J. W. Ward, "Current-density profiles for a Ga^+ ion microprobe and their lithographic implications", *Appl. Phys. Lett.* **51**, 1960 (1987).

[329] J. Clarke and A. I. Braginski (Eds.) *The SQUID Handbook, Vol. I: Fundamentals and Technology of SQUIDs and SQUID Systems*, (John Wiley & Sons, Inc., 2004).

[330] W. Pamler, K. Wangemann, S. Kampermann, and W. Hösler, "Depth resolution in Auger depth profile analysis of aluminum metallization in microelectronics - the effect of crystalline texture", *Nucl. Instrum. Methods Phys. Res. Sect. B* **51**, 34 (1990).

[331] T. Wöhner, G. Ecke, H. Rössler, and S. Hofmann, "Sputtering-induced surface roughness of polycrystalline Al films and its influence on AES depth profiles", *Surf. Interface Anal.* **26**, 1 (1998).

[332] Y. Stark, R. Frömter, D. Stickler, and H. P. Oepen, "Sputter yields of single- and polycrystalline metals for application in focused ion beam technology", *J. Appl. Phys.* **105**, 013542 (2009).

[333] G. S. Was, "Ion-beam modification of metals - compositional and microstructural changes", *Prog. Surf. Sci.* **32**, 211 (1989).

[334] J. M. Garcia, A. Thiaville, J. Miltat, K. J. Kirk, and J. N. Chapman, "MFM imaging of patterned permalloy elements under an external applied field", *J. Magn. Magn. Mater.* **242**, 1267 (2002).

[335] L. V. Dzemiantsova, M. Karolak, F. Lofink, A. Kubetzka, B. Sachs, K. von Bergmann, S. Hankemeier, T. O. Wehling, R. Frömter, H. P. Oepen, A. I. Lichtenstein, and R. Wiesendanger, "Multiscale magnetic study of Ni(111) and graphene on Ni(111)", *Phys. Rev. B* **84**, 205431 (2011).

[336] A. Aharoni, "'Local' demagnetization in a rectangular ferromagnetic prism", *Phys. Status Solidi B* **229**, 1413 (2002).

[337] R. P. Cowburn, D. K. Koltsov, A. O. Adeyeye, and M. E. Welland, "Lateral interface anisotropy in nanomagnets", *J. Appl. Phys.* **87**, 7067 (2000).

[338] M. T. Bryan, D. Atkinson, and R. P. Cowburn, "Experimental study of the influence of edge roughness on magnetization switching in permalloy nanostructures", *Appl. Phys. Lett.* **85**, 3510 (2004).

[339] E. Y. Vedmedenko, N. Mikuszeit, H. P. Oepen, and R. Wiesendanger, "Multipolar ordering and magnetization reversal in two-dimensional nanomagnet arrays", *Phys. Rev. Lett.* **95**, 207202 (2005).

[340] A. Imre, G. Csaba, L. Ji, A. Orlov, G. H. Bernstein, and W. Porod, "Majority logic gate for magnetic quantum-dot cellular automata", *Science* **311**, 205 (2006).

[341] D. B. Carlton, N. C. Emley, E. Tuchfeld, and J. Bokor, "Simulation studies of nanomagnet-based logic architecture", *Nano Lett.* **8**, 4173 (2008).

[342] S. Jain and A. O. Adeyeye, "Giant magnetoresistance behavior of pseudo spin valve rings with magnetostatically coupled elements", *Europhys. Lett.* **84**, 17002 (2008).

[343] M. Pardavi-Horvath, P. E. Si, C. A. Ross, F. J. Castano, B. G. Ng, and S. Moralejo, "Configurational stability of patterned magnetic nanosystems", *J. Appl. Phys.* **103**, 07D516 (2008).

[344] A. Remhof, A. Schumann, A. Westphalen, H. Zabel, N. Mikuszeit, E. Y. Vedmedenko, T. Last, and U. Kunze, "Magnetostatic interactions on a square lattice", *Phys. Rev. B* **77**, 134409 (2008).

[345] S. Jain, Y. Ren, A. O. Adeyeye, and N. Singh, "Configurational anisotropy and control of magnetic vortex chirality in arrays of circular $Ni_{80}Fe_{20}$ nanoscale dots", *Phys. Rev. B* **80**, 132401 (2009).

[346] S. Bandyopadhyay and M. Cahay, "Electron spin for classical information processing: A brief survey of spin-based logic devices, gates and circuits", *Nanotechnology* **20**, 412001 (2009).

[347] S. A. Wolf, J. W. Lu, M. R. Stan, E. Chen, and D. M. Treger, "The promise of nanomagnetics and spintronics for future logic and universal memory", *Proc. IEEE* **98**, 2155 (2010).

[348] S. Jain and A. O. Adeyeye, "Anisotropic magnetostatic interactions in arrays of ellipsoidal shaped $Ni_{80}Fe_{20}$ magnets", *J. Appl. Phys.* **108**, 113915 (2010).

[349] J. Seo, T. H. Kim, S. H. Chung, Y. Oh, J. H. Choi, and Y. Kuk, "Tuning magnetostatic interaction in single-crystalline nanodot arrays with in-plane easy axes", *Appl. Phys. Lett.* **96**, 073106 (2010).

[350] A. Vogel, A. Drews, T. Kamionka, M. Bolte, and G. Meier, "Influence of dipolar interaction on vortex dynamics in arrays of ferromagnetic disks", *Phys. Rev. Lett.* **105**, 037201 (2010).

[351] J. P. Morgan, A. Stein, S. Langridge, and C. H. Marrows, "Magnetic reversal of an artificial square ice: Dipolar correlation and charge ordering", *New J. Phys.* **13**, 105002 (2011).

[352] S. Kurtz, E. Varga, M. J. Siddiq, M. Niemier, W. Porod, X. S. Hu, and G. H. Bernstein, "Non-majority magnetic logic gates: A review of experiments and future prospects for 'shape-based' logic", *J. Phys.: Condens. Matter* **23**, 053202 (2011).

[353] S. Jain, M. Kostylev, and A. O. Adeyeye, "Coupled oscillations in non-collinear microscale rectangular magnets", *Phys. Rev. B* **82**, 214422 (2010).

[354] S. Jain, A. O. Adeyeye, and N. Singh, "Spin re-orientation in magnetostatically coupled $Ni_{80}Fe_{20}$ ellipsoidal nanomagnets", *Nanotechnology* **21**, 285702 (2010).

[355] J. Ding, S. Jain, and A. O. Adeyeye, "Static and dynamic properties of one-dimensional linear chain of nanomagnets", *J. Appl. Phys.* **109**, 07D301 (2011).

[356] A. O. Adeyeye and S. Jain, "Coupled periodic magnetic nanostructures (invited)", *J. Appl. Phys.* **109**, 07B903 (2011).

[357] R. Zivieri, F. Montoncello, L. Giovannini, F. Nizzoli, S. Tacchi, M. Madami, G. Gubbiotti, G. Carlotti, and A. Adeyeye, "Effect of interdot separation on collective magnonic modes in chains of rectangular dots", *IEEE Trans. Magn.* **47**, 1563 (2011).

[358] A. Vogel, M. Martens, M. Weigand, and G. Meier, "Signal transfer in a chain of stray-field coupled ferromagnetic squares", *Appl. Phys. Lett.* **99**, 042506 (2011).

[359] K. M. Lebecki, M. J. Donahue, and M. W. Gutowski, "Periodic boundary conditions for demagnetization interactions in micromagnetic simulations", *J. Phys. D: Appl. Phys.* **41**, 175005 (2008).

[360] B. Beyersdorff, S. Hankemeier, S. Rössler, Y. Stark, G. Hoffmann, R. Frömter, H. P. Oepen, and B. Krüger, "Thermal effects in spin-torque assisted domain wall depinning", *Phys. Rev. B* **86**, 184427 (2012).

[361] A. Segal and A. Gerber, "Core contribution to magnetotransport of ferromagnetic dots in vortex state", *J. Appl. Phys.* **111**, 073902 (2012).

[362] B. Dieny, V. S. Speriosu, S. S. P. Parkin, B. A. Gurney, D. R. Wilhoit, and D. Mauri, "Giant magnetoresistance in soft ferromagnetic multilayers", *Phys. Rev. B* **43**, 1297 (1991).

[363] B. Dieny, V. S. Speriosu, S. Metin, S. S. P. Parkin, B. A. Gurney, P. Baumgart, and D. R. Wilhoit, "Magnetotransport properties of magnetically soft spin-valve structures", *J. Appl. Phys.* **69**, 4774 (1991).

[364] V. Cros, S. F. Lee, G. Faini, A. Cornette, A. Hamzic, and A. Fert, "Detection of the magnetization reversal in submicron Co particles by GMR measurements", *J. Magn. Magn. Mater.* **165**, 512 (1997).

[365] F. J. Castano, D. Morecroft, and C. A. Ross, "Low-field giant magnetoresistance in layered magnetic rings", *Phys. Rev. B* **74**, 224401 (2006).

[366] A. S. Demiray, M. Kohda, T. Miyawaki, Y. Watanabe, K. Saito, S. Mitani, K. Takanashi, and J. Nitta, "Electrical determination of relative chirality direction in a Co/Cu/Co ferromagnetic ring", *Appl. Phys. Lett.* **101**, 062409 (2012).

[367] M. Wellhöfer, M. Weissenborn, R. Anton, S. Pütter, and H. P. Oepen, "Morphology and magnetic properties of ECR ion beam sputtered Co/Pt films", *J. Magn. Magn. Mater.* **292**, 345 (2005).

[368] H. Stillrich, C. Menk, R. Frömter, and H. P. Oepen, "Magnetic anisotropy and spin reorientation in Co/Pt multilayers: Influence of preparation", *J. Magn. Magn. Mater.* **322**, 1353 (2010).

[369] N. Mikuszeit, S. Pütter, R. Frömter, and H. P. Oepen, "Magneto-optic Kerr effect: Incorporating the nonlinearities of the analyzer into static photometric ellipsometry analysis", *J. Appl. Phys.* **97**, 103107 (2005).

[370] S. Fiedler, H. Stillrich, and H. P. Oepen, "Magneto-optic properties of electron cyclotron resonance ion beam sputtered and magnetron sputtered Co/Pt multilayers", *J. Appl. Phys.* **102**, 083906 (2007).

[371] A. Frömsdorf, A. Kornowski, S. Pütter, H. Stillrich, and L.-T. Lee, "Highly ordered nanostructured surfaces obtained with silica-filled diblock-copolymer micelles as templates", *Small* **3**, 880 (2007).

[372] H. Stillrich, A. Frömsdorf, S. Pütter, S. Forster, and H. P. Oepen, "Sub-20 nm magnetic dots with perpendicular magnetic anisotropy", *Adv. Funct. Mater.* **18**, 76 (2008).

[373] A. Neumann, N. Franz, G. Hoffmann, A. Meyer, and H. P. Oepen, "Fabrication of magnetic Co/Pt nanodots utilizing filled diblock copolymers", *Open Surf. Sci. J.* **4**, 55 (2012).

[374] A. Gerber, A. Milner, J. Tuaillon-Combes, M. Negrier, O. Boisron, P. Melinon, and A. Perez, "Probing planar arrays of magnetic nano-particles by the extraordinary Hall effect", *J. Magn. Magn. Mater.* **241**, 340 (2002).

[375] N. Kikuchi, S. Okamoto, O. Kitakami, Y. Shimada, and K. Fukamichi, "Sensitive detection of irreversible switching in a single FePt nanosized dot", *Appl. Phys. Lett.* **82**, 4313 (2003).

[376] N. Kikuchi, T. Kato, S. Okamoto, O. Kitakami, N. Tezuka, and S. Sugimoto, "Magnetization reversal process and bistability of Co/Pt multilayer dot", *J. Appl. Phys.* **103**, 07C510 (2008).

[377] J. B. C. Engelen, M. Delalande, A. J. le Fèbre, T. Bolhuis, T. Shimatsu, N. Kikuchi, L. Abelmann, and J. C. Lodder, "Thermally induced switching field distribution of a single CoPt dot in a large array", *Nanotechnology* **21**, 035703 (2010).

[378] M. Alexandrou, P. W. Nutter, M. Delalande, J. de Vries, E. W. Hill, F. Schedin, L. Abelmann, and T. Thomson, "Spatial sensitivity mapping of Hall crosses using patterned magnetic nanostructures", *J. Appl. Phys.* **108**, 043920 (2010).

[379] M. Delalande, J. de Vries, L. Abelmann, and J. C. Lodder, "Measurement of the nucleation and domain depinning field in a single Co/Pt multilayer dot by anomalous Hall effect", *J. Magn. Magn. Mater.* **324**, 1277 (2012).

[380] J. P. Jan, *Galvanomagnetic and Thermomagnetic Effects in Metals - Solid State Physics Vol. 5*, (Academic Press Inc., 1957).

[381] C. M. Hurd, "Galvanomagnetic effects in anisotropic metals", *Adv. Phys.* **23**, 315 (1974).

[382] H. J. Juretschke, "Symmetry of galvanomagnetic effects in antimony", *Acta Crystallographica* **8**, 716 (1955).

[383] L. Onsager, "Reciprocal relations in irreversible processes. I.", *Phys. Rev.* **37**, 405 (1931).

[384] L. Onsager, "Reciprocal relations in irreversible processes. II.", *Phys. Rev.* **38**, 2265 (1931).

[385] J. F. Nye, *Physical properties of crystals: Their representation by tensors and matrices*, (Oxford University Press, 1957).

[386] W. Döring, "Die Abhängigkeit des Widerstandes von Nickelkristallen von der Richtung der spontanen Magnetisierung", *Ann. Phys.* **424**, 259 (1938).

[387] H. Ibach and H. Lüth, *Festkörperphysik: Einführung in die Grundlagen*, (Springer Verlag, 2002).

[388] K. Kopitzki and P. Herzog, *Einführung in die Festkörperphysik*, (Teubner Verlag, 2007).

[389] A. B. Pippard, *Magnetoresistance in Metals - Cambridge Studies in Low Temperature Physics*, (Cambridge University Press, 1989).

[390] F. Bloch, "Über die Quantenmechanik der Elektronen in Kristallgittern", *Z. Phys. A: At. Nucl.* **52**, 555 (1929).

[391] I. Mertig, "Transport properties of dilute alloys", *Rep. Prog. Phys.* **62**, 237 (1999).

[392] C. Lehmann, S. Sinning, P. Zahn, H. Wonn, and I. Mertig (1996-1998), Fermi Surface Explorer, www.phy.tu-dresden.de/∼fermisur.

[393] J. S. Dugdale, *The Electrical Properties of Metals and Alloys - The Structures and Properties of Solids 5*, (Edward Arnold (Publishers) Limited, 1977).

[394] F. Schwabl, *Quantenmechanik (QM I)*, (Springer-Verlag, 2007).

[395] P. Drude, "Zur Elektronentheorie der Metalle", *Ann. Phys.* **306**, 566 (1900).

[396] H. Masumoto, H. Saito, and M. Kikuchi, "On the magetoresistance and the electrical resistivity of Co single crystals", *J.J. Inst. Met.* **30**, 885 (1966).

[397] J. M. Ziman, *Electrons and Photons, The Theory of Transport Phenomena in Solids - The International Series of Monographs on Physics*, (Oxford University Press, 1960).

[398] A. Matthiessen and M. Holzmann, "On the effect of the presence of metals and metalloids upon the electric conducting power of pure copper", *Philos. Trans. R. Soc. London* **150**, 85 (1860).

[399] A. Matthiessen, "On the electric conducting power of alloys", *Philos. Trans. R. Soc. London* **150**, 161 (1860).

[400] A. Matthiessen and M. von Bose, "On the influence of temperature on the electric conducting power of metals", *Philos. Trans. R. Soc. London* **152**, 1 (1862).

[401] A. Matthiessen and C. Vogt, "On the influence of temperature on the electric conducting-power of alloys", *Philos. Trans. R. Soc. London* **154**, 167 (1864).

[402] S. Hankemeier, K. Sachse, Y. Stark, R. Frömter, and H. P. Oepen, "Ultrahigh current densities in permalloy nanowires on diamond", *Appl. Phys. Lett.* **92**, 242503 (2008).

[403] T. Sun, B. Yao, A. P. Warren, K. Barmak, M. F. Toney, R. E. Peale, and K. R. Coffey, "Surface and grain-boundary scattering in nanometric Cu films", *Phys. Rev. B* **81**, 155454 (2010).

[404] W. Meissner, *Handbuch der Experimentalphysik, Band 11, Teil 2: Elektronenleitung, galvanomagnetische, thermoelektrische und verwandte Effekte*, (Akademische Verlagsgesellschaft, Leipzig, 1935).

[405] J. S. Dugdale and Z. S. Basinski, "Mathiessen's rule and anisotropic relaxation times", *Phys. Rev.* **157**, 552 (1967).

[406] J. Bass, "Deviations from Matthiessen's rule", *Adv. Phys.* **21**, 431 (1972).

[407] N. Wiser, "The electrical resistivity of the simple metals", *Contemp. Phys.* **25**, 211 (1984).

[408] B. J. Hickey, G. J. Morgan, and M. A. Howson, *Basic Electron Transport - Spin Electronics - Lecture Notes in Physics 569*, (Springer-Verlag, 2001).

[409] F. Bloch, "Zum elektrischen Widerstandsgesetz bei tiefen Temperaturen", *Z. Phys. A At. Nucl.* **59**, 208 (1930).

[410] E. Grüneisen, "Die Abhängigkeit des elektrischen Widerstandes reiner Metalle von der Temperatur", *Ann. Phys.* **408**, 530 (1933).

[411] I. Stone, "On the electrical resistance of thin films", *Phys. Rev.* **6**, 1 (1898).

[412] J. J. Thomson, "On the theory of electric conduction through thin metallic films", *Proc. Cambridge Phil. Soc.* **11**, 118 (1901).

[413] J. M. Purswani and D. Gall, "Electron scattering at single crystal Cu surfaces", *Thin Solid Films* **516**, 465 (2007).

[414] K. Fuchs, "The conductivity of thin metallic films according to the electron theory of metals", *Math. Proc. Cambridge Philos. Soc.* **34**, 100 (1938).

[415] E. H. Sondheimer, "The mean free path of electrons in metals", *Adv. Phys.* **1**, 1 (1952).

[416] E. H. Sondheimer, "The mean free path of electrons in metals", *Adv. Phys.* **50**, 499 (2001).

[417] G. Fischer, H. Hoffmann, and J. Vancea, "Mean free-path and density of conductance electrons in platinum determined by the size effect in extremely thin-films", *Phys. Rev. B* **22**, 6065 (1980).

[418] M. A. Angadi, "Some transport-properties of transition-metal films", *J. Mater. Sci.* **20**, 761 (1985).

[419] D. K. C. MacDonald and K. Sarginson, "Size effect variation of the electrical conductivity of metals", *Proc. R. Soc. A* **203**, 223 (1950).

[420] R. G. Chambers, "The conductivity of thin wires in a magnetic field", *Proc. R. Soc. A* **202**, 378 (1950).

[421] R. B. Dingle, "The electrical conductivity of thin wires", *Proc. R. Soc. A* **201**, 545 (1950).

[422] C. Durkan and M. E. Welland, "Size effects in the electrical resistivity of polycrystalline nanowires", *Phys. Rev. B* **61**, 14215 (2000).

[423] W. Steinhögl, G. Schindler, G. Steinlesberger, and M. Engelhardt, "Size-dependent resistivity of metallic wires in the mesoscopic range", *Phys. Rev. B* **66**, 075414 (2002).

[424] W. Steinhögl, G. Schindler, G. Steinlesberger, M. Traving, and M. Engelhardt, "Comprehensive study of the resistivity of copper wires with lateral dimensions of 100 nm and smaller", *J. Appl. Phys.* **97**, 023706 (2005).

[425] Q. J. Huang, C. M. Lilley, M. Bode, and R. Divan, "Surface and size effects on the electrical properties of Cu nanowires", *J. Appl. Phys.* **104**, 023709 (2008).

[426] Q. J. Huang, C. M. Lilley, and M. Bode, "Surface scattering effect on the electrical resistivity of single crystalline silver nanowires self-assembled on vicinal Si (001)", *Appl. Phys. Lett.* **95**, 103112 (2009).

[427] D. Josell, S. H. Brongersma, and Z. Tokei, "Size-dependent resistivity in nanoscale interconnects", *Annu. Rev. Mater. Res.* **39**, 231 (2009).

[428] R. L. Graham, G. B. Alers, T. Mountsier, N. Shamma, S. Dhuey, S. Cabrini, R. H. Geiss, D. T. Read, and S. Peddeti, "Resistivity dominated by surface scattering in sub-50 nm Cu wires", *Appl. Phys. Lett.* **96**, 042116 (2010).

[429] J. S. Chawla, F. Gstrein, K. P. O'Brien, J. S. Clarke, and D. Gall, "Electron scattering at surfaces and grain boundaries in Cu thin films and wires", *Phys. Rev. B* **84**, 235423 (2011).

[430] A. F. Mayadas, M. Shatzkes, and J. F. Janak, "Electrical resistivity model for polycrystalline films - case of specular reflection at external surfaces", *Appl. Phys. Lett.* **14**, 345 (1969).

[431] A. F. Mayadas and M. Shatzkes, "Electrical-resistivity model for polycrystalline films - case of arbitrary reflection at external surfaces", *Phys. Rev. B* **1**, 1382 (1970).

[432] Y. Kitaoka, T. Tono, S. Yoshimoto, T. Hirahara, S. Hasegawa, and T. Ohba, "Direct detection of grain boundary scattering in damascene Cu wires by nanoscale four-point probe resistance measurements", *Appl. Phys. Lett.* **95**, 052110 (2009).

[433] T. H. Kim, X. G. Zhang, D. M. Nicholson, B. M. Evans, N. S. Kulkarni, B. Radhakrishnan, E. A. Kenik, and A. P. Li, "Large discrete resistance jump at grain boundary in copper nanowire", *Nano Lett.* **10**, 3096 (2010).

[434] E. E. Mola, J. Borrajo, and J. M. Heras, "Electrical resistivity of evaporated thin cobalt films - an approach based on the Mayadas-Shatzkes model", *Surf. Sci.* **34**, 561 (1973).

[435] R. Suri, A. P. Thakoor, and K. L. Chopra, "Electron-transport properties of thin copper-films. I.", *J. Appl. Phys.* **46**, 2574 (1975).

[436] T. G. S. M. Rijks, R. L. H. Sour, D. G. Neerinck, A. E. M. Deveirman, R. Coehoorn, J. C. S. Kools, M. F. Gillies, and W. J. M. de Jonge, "Influence of grain-size on the transport-properties of $Ni_{80}Fe_{20}$ and Cu thin-films", *IEEE Trans. Magn.* **31**, 3865 (1995).

[437] W. Zhang, S. H. Brongersma, O. Richard, B. Brijs, R. Palmans, L. Froyen, and K. Maex, "Influence of the electron mean free path on the resistivity of thin metal films", *Microelectron. Eng.* **76**, 146 (2004).

[438] J. M. Camacho and A. Oliva, "Surface and grain boundary contributions in the electrical resistivity of metallic nanofilms", *Thin Solid Films* **515**, 1881 (2006).

[439] R. Henriquez, S. Cancino, A. Espinosa, M. Flores, T. Hoffmann, G. Kremer, J. G. Lisoni, L. Moraga, R. Morales, S. Oyarzun, M. A. Suarez, A. Zuniga, and R. C. Munoz, "Electron grain boundary scattering and the resistivity of nanometric metallic structures", *Phys. Rev. B* **82**, 113409 (2010).

[440] S. B. Soffer, "Statistical model for size effect in electrical conduction", *J. Appl. Phys.* **38**, 1710 (1967).

[441] G. Kästle, H. G. Boyen, A. Schröder, A. Plettl, and P. Ziemann, "Size effect of the resistivity of thin epitaxial gold films", *Phys. Rev. B* **70**, 165414 (2004).

[442] H. Marom and M. Eizenberg, "The effect of surface roughness on the resistivity increase in nanometric dimensions", *J. Appl. Phys.* **99**, 123705 (2006).

[443] H. Hoffmann and J. Vancea, "Critical-assessment of thickness-dependent conductivity of thin metal-films", *Thin Solid Films* **85**, 147 (1981).

[444] K. C. Elsom and J. R. Sambles, "Macroscopic surface-roughness and the resistivity of thin metal-films", *J. Phys. F: Met. Phys.* **11**, 647 (1981).

[445] H. D. Liu, Y. P. Zhao, G. Ramanath, S. P. Murarka, and G. C. Wang, "Thickness dependent electrical resistivity of ultrathin (< 40 nm) Cu films", *Thin Solid Films* **384**, 151 (2001).

[446] Y. Namba, "Electrical conduction of thin metallic films with rough surface", *J. Appl. Phys.* **39**, 6117 (1968).

[447] Y. Namba, "Resistivity and temperature coefficient of thin metal films with rough surface", *Jpn. J. Appl. Phys.* **9**, 1326 (1970).

[448] M. S. P. Lucas, "Electrical conductivity of thin metallic films with unlike surfaces", *J. Appl. Phys.* **36**, 1632 (1965).

[449] J. S. Chawla and D. Gall, "Specular electron scattering at single-crystal Cu(001) surfaces", *Appl. Phys. Lett.* **94**, 252101 (2009).

[450] R. C. Munoz, M. A. Suarez, S. Oyarzun, R. Henriquez, A. Espinosa, G. Kremer, L. Moraga, S. Cancino, and R. Morales, "Longitudinal magnetoresistance of thin gold films deposited on mica arising from electron-surface scattering", *Phys. Rev. B* **81**, 165408 (2010).

[451] P. F. Carcia and A. Suna, "Properties of Pd/Au thin-film layered structures", *J. Appl. Phys.* **54**, 2000 (1983).

[452] R. E. Camley and J. Barnas, "Theory of giant magnetoresistance effects in magnetic layered structures with antiferromagnetic coupling", *Phys. Rev. Lett.* **63**, 664 (1989).

[453] X. G. Zhang and W. H. Butler, "Conductivity of metallic-films and multilayers", *Phys. Rev. B* **51**, 10085 (1995).

[454] S. P. Chen and C. R. Chang, "Analytic solutions of the linear Boltzmann transport equation for multilayered systems", *Phys. Rev. B* **72**, 064445 (2005).

[455] J. Barnas, A. Fuss, R. E. Camley, P. Grünberg, and W. Zinn, "Novel magnetoresistance effect in layered magnetic-structures - theory and experiment", *Phys. Rev. B* **42**, 8110 (1990).

[456] R. Q. Hood and L. M. Falicov, "Boltzmann-equation approach to the negative magnetoresistance of ferromagnetic - normal-metal multilayers", *Phys. Rev. B* **46**, 8287 (1992).

[457] B. Dieny, "Classical-theory of giant magnetoresistance in spin-valve multilayers - influence of thicknesses, number of periods, bulk and interfacial spin-dependent scattering", *J. Phys.: Condens. Matter* **4**, 8009 (1992).

[458] W. H. Butler, X. G. Zhang, and J. M. MacLaren, "Semiclassical theory of spin-dependent transport in magnetic multilayers", *J. Supercond.* **13**, 221 (2000).

[459] S. M. Thompson, "The discovery, development and future of GMR: The Nobel Prize 2007", *J. Phys. D: Appl. Phys.* **41**, 093001 (2008).

[460] J. R. Sambles, "The resistivity of thin metal-films - some critical remarks", *Thin Solid Films* **106**, 321 (1983).

[461] M. A. M. Gijs and G. E. W. Bauer, "Perpendicular giant magnetoresistance of magnetic multilayers", *Adv. Phys.* **46**, 285 (1997).

[462] P. Weinberger, "Ab initio theories of electric transport in solid systems with reduced dimensions", *Phys. Rep.* **377**, 281 (2003).

[463] J. W. F. Dorleijn, "Electrical-conduction in ferromagnetic metals", *Philips Res. Repts.* **31**, 287 (1976).

[464] N. F. Mott, "A discussion of the transition metals on the basis of quantum mechanics", *Proc. Phys. Soc.* **47**, 571 (1935).

[465] N. F. Mott, "The electrical conductivity of transition metals", *Proc. R. Soc. A* **153**, 699 (1936).

[466] N. F. Mott, "Electrons in transition metals", *Adv. Phys.* **13**, 325 (1964).

[467] I. A. Campbell and A. Fert, *Transport Properties of Ferromagnets - Ferromagnetic Materials Vol. 3*, (North Holland Publishing Company, 1982).

[468] G. K. White and S. B. Woods, "Electrical and thermal resistivity of the transition elements at low temperatures", *Philos. Trans. R. Soc. London Ser. A* **251**, 273 (1959).

[469] A. H. Wilson, "The electrical conductivity of the transition metals", *Proc. R. Soc. A* **167**, 580 (1938).

[470] D. A. Goodings, "Eletrical resistivity of ferromagnetic metals at low temperatures", *Phys. Rev.* **132**, 542 (1963).

[471] B. A. Gurney, V. S. Speriosu, J. P. Nozières, H. Lefakis, D. R. Wilhoit, and O. U. Need, "Direct measurement of spin-dependent conduction-electron mean free paths in ferromagnetic metals", *Phys. Rev. Lett.* **71**, 4023 (1993).

[472] J. G. G. Conybeare, "The resistance of palladium and palladium-gold alloys", *Proc. Phys. Soc.* **49**, 29 (1937).

[473] H. H. Potter, "The electrical resistance of ferromagnetics", *Proc. Phys. Soc.* **49**, 671 (1937).

[474] H. Bittel and W. Gerlach, "Ferromagnetismus und elektrische Eigenschaften, IX. Mitteilung: Curiepunkt und elektrischer Widerstand", *Ann. Phys.* **425**, 661 (1938).

[475] B. R. Coles, "Spin-disorder effects in the electrical resistivities of metals and alloys", *Adv. Phys.* **7**, 40 (1958).

[476] W. Kierspe, R. Kohlhaas, and H. Gonska, "On specific electric resistance of cobalt compared to iron and nickel", *Z. Angew. Phys.* **24**, 28 (1967).

[477] M. J. Laubitz and T. Matsumura, "Transport properties of ferromagnetic metals. I. Cobalt", *Can. J. Phys.* **51**, 1247 (1973).

[478] K. Ikeda, "Electrical-resistivity of nickel, cobalt and their alloys", *Trans. Jpn. Inst. Met.* **29**, 183 (1988).

[479] W. de Haas and J. de Boer, "The electrical resistance of platinum at low temperatures", *Physica* **1**, 609 (1934).

[480] A. Fert and I. A. Campbell, "Electrical-resistivity of ferromagnetic nickel and iron based alloys", *J. Phys. F: Met. Phys.* **6**, 849 (1976).

[481] B. Raquet, M. Viret, E. Sondergard, O. Cespedes, and R. Mamy, "Electron-magnon scattering and magnetic resistivity in 3d ferromagnets", *Phys. Rev. B* **66**, 024433 (2002).

[482] N. F. Mott and K. W. H. Stevens, "The band structure of the transition metals", *Philos. Mag.* **2**, 1364 (1957).

[483] T. Kasuya, "Electrical resistance of ferromagnetic metals", *Prog. Theor. Phys.* **16**, 58 (1956).

[484] I. Mannari, "Electrical resistance of ferromagnetic metals", *Prog. Theor. Phys.* **22**, 335 (1959).

[485] T. Kasuya, "Effects of s-d interaction on transport phenomena", *Prog. Theor. Phys.* **22**, 227 (1959).

[486] R. S. Patel, A. K. Majumdar, A. F. Hebard, and D. Temple, "Magnetic scattering in Fe-Cr multilayers in the ferromagnetic state at low temperatures", *J. Appl. Phys.* **93**, 7684 (2003).

[487] C. Christides and T. Speliotis, "Polarity of anomalous Hall effect hysteresis loops in $[Pt/Co]_{15}/AF/[Co/Pt]_{15}$ (AF=FeMn, NiO) multilayers with perpendicular anisotropy", *J. Appl. Phys.* **97**, 013901 (2005).

[488] M. V. Kamalakar, A. K. Raychaudhuri, X. Y. Wei, J. Teng, and P. D. Prewett, "Temperature dependent electrical resistivity of a single strand of ferromagnetic single crystalline nanowire", *Appl. Phys. Lett.* **95**, 013112 (2009).

[489] M. V. Kamalakar and A. K. Raychaudhuri, "Low temperature electrical transport in ferromagnetic Ni nanowires", *Phys. Rev. B* **79**, 205417 (2009).

[490] X. P. Feng, W. B. Mi, and H. L. Bai, "Polycrystalline iron nitride films fabricated by reactive facing-target sputtering: Structure, magnetic and electrical transport properties", *J. Appl. Phys.* **110**, 053911 (2011).

[491] A. Buruzs, L. Szunyogh, and P. Weinberger, "Ab-initio theory of temperature-dependent magneto-resistivities", *Philos. Mag.* **88**, 2615 (2008).

[492] W. G. Baber, "The contribution to the electrical resistance of metals from collisions between electrons", *Proc. R. Soc. A* **158**, 383 (1937).

[493] P. Radhakrishna and M. Nielsen, "Transport properties of cobalt at low temperatures", *Phys. Status Solidi* **11**, 111 (1965).

[494] J. Yamashita, S. Wakoh, and S. Asano, "Electrical-resistivity of transition-metals. II", *J. Phys. Soc. Jpn.* **39**, 344 (1975).

[495] R. H. Freeman, F. J. Blatt, and J. Bass, "Resistivity of fine platinum wires", *Phys. kondens. Materie* **9**, 271 (1969).

[496] R. A. Matula, "Electrical-resistivity of copper, gold, palladium, and silver", *J. Phys. Chem. Ref. Data* **8**, 1147 (1979).

[497] D. B. Poker and C. E. Klabunde, "Temperature-dependence of electrical-resistivity of vanadium, platinum, and copper", *Phys. Rev. B* **26**, 7012 (1982).

[498] M. Isshiki, Y. Fukuda, and K. Igaki, "Temperature-dependence of the electrical-resistivity of pure cobalt at low-temperatures", *J. Phys. F: Met. Phys.* **14**, 3007 (1984).

[499] M. Kaveh and N. Wiser, "Electron electron-scattering in conducting materials", *Adv. Phys.* **33**, 257 (1984).

[500] M. Rubinstein, F. J. Rachford, W. W. Fuller, and G. A. Prinz, "Electrical transport-properties of thin epitaxially grown iron films", *Phys. Rev. B* **37**, 8689 (1988).

[501] F. G. Aliev, E. Kunnen, K. Temst, K. Mae, G. Verbanck, J. Barnas, V. V. Moshchalkov, and Y. Bruynseraede, "Periodic enhancement of the electron-electron interactions and the magnetoresistance in magnetic Co/(Cr/Ag)/Co multilayers", *Phys. Rev. Lett.* **78**, 134 (1997).

[502] M. Brands, A. Carl, and G. Dumpich, "Absence of weak electron localization in $(Co/Pt)_n$-multilayer-nanowires with perpendicular anisotropy", *Ann. Phys.* **14**, 745 (2005).

[503] T. Ono, Y. Ooka, S. Kasai, H. Miyajima, N. Nakatani, N. Hayashi, K. Shigeto, K. Mibu, and T. Shinjo, "Magnetization reversal and electric transport in ferromagnetic nanowires", *Mater. Sci. Eng. B* **84**, 126 (2001).

[504] M. Brands, A. Carl, O. Posth, and G. Dumpich, "Electron-electron interaction in carbon-coated ferromagnetic nanowires", *Phys. Rev. B* **72**, 085457 (2005).

[505] J. Appel, "Effect of electron-electron scattering on electrical and thermal conductivity of metals", *Philos. Mag.* **8**, 1071 (1963).

[506] M. J. Rice, "Electron-electron scattering in transition metals", *Phys. Rev. Lett.* **20**, 1439 (1968).

[507] N. V. Volkenshtein, V. P. Dyakina, and V. E. Startsev, "Scattering mechanisms of conduction electrons in transition-metals at low-temperatures", *Phys. Status Solidi B* **57**, 9 (1973).

[508] G. Bergmann, "Weak localization in thin-films - a time-of-flight experiment with conduction electrons", *Phys. Rep.* **107**, 1 (1984).

[509] P. A. Lee and T. V. Ramakrishnan, "Disordered electronic systems", *Rev. Mod. Phys.* **57**, 287 (1985).

[510] A. Carl, G. Dumpich, and D. Hallfarth, "Antilocalization and electron-electron interaction in thin granular palladium-carbon mixture films", *Phys. Rev. B* **39**, 3015 (1989).

[511] W. Meissner and B. Voigt, "Messungen mit Hilfe von flüssigem Helium, XI. Widerstand der reinen Metalle in tiefen Temperaturen", *Ann. Phys.* **399**, 761 (1930).

[512] J. Kondo, "Resistance minimum in dilute magnetic alloys", *Prog. Theor. Phys.* **32**, 37 (1964).

[513] L. M. Fabietti, J. Ferreyra, M. Villafuerte, S. E. Urreta, and S. P. Heluani, "Kondo-like effect in magnetoresistive CuCo alloys", *Phys. Rev. B* **82**, 172410 (2010).

[514] B. Dieny, "Giant magnetoresistance in spin-valve multilayers", *J. Magn. Magn. Mater.* **136**, 335 (1994).

[515] A. Fert, "The present and the future of spintronics", *Thin Solid Films* **517**, 2 (2008).

[516] G. X. Miao, M. Münzenberg, and J. S. Moodera, "Tunneling path toward spintronics", *Rep. Prog. Phys.* **74**, 036501 (2011).

[517] L. F. Bates, "The magneto-resistance of high coercivity alloys", *Proc. Phys. Soc.* **58**, 153 (1946).

[518] J. Smit, "Magnetoresistance of ferromagnetic metals and alloys at low temperatures", *Physica* **17**, 612 (1951).

[519] S. Kokado, M. Tsunoda, K. Harigaya, and A. Sakuma, "Anisotropic magnetoresistance effects in Fe, Co, Ni, Fe_4N, and half-metallic ferromagnet: A systematic analysis", *J. Phys. Soc. Jpn.* **81**, 024705 (2012).

[520] E. N. Mitchell, H. D. Bale, H. B. Haukaas, and J. B. Streeper, "Compositional and thickness dependence of ferromagnetic anisotropy in resistance of iron-nickel films", *J. Appl. Phys.* **35**, 2604 (1964).

[521] T. Miyazaki, T. Ajima, and F. Sato, "Dependence of magnetoresistance on thickness and substrate-temperature for 82Ni-Fe alloy film", *J. Magn. Magn. Mater.* **81**, 86 (1989).

[522] B. Dieny, M. Li, S. H. Liao, C. Horng, and K. Ju, "Effect of interfacial specular electron reflection on the anisotropic magnetoresistance of magnetic thin films", *J. Appl. Phys.* **88**, 4140 (2000).

[523] P. P. Freitas, A. A. Gomes, T. R. McGuire, and T. S. Plaskett, "Anisotropic magnetoresistance in Co films", *J. Magn. Magn. Mater.* **83**, 113 (1990).

[524] E. Englert, "Ferromagnetismus und elektrische Eigenschaften, VI. Mitteilung: Longitudinale und transversale ferromagnetische Widerstandsänderung", *Ann. Phys.* **406**, 589 (1932).

[525] S. N. Kaul, "Spontaneous resistivity anistropy in nickel-copper alloys", *J. Phys. F: Met. Phys.* **7**, 2091 (1977).

[526] J. Kondo, "Anomalous Hall effect and magnetoresistance of ferromagnetic metals", *Prog. Theor. Phys.* **27**, 772 (1962).

[527] R. M. Bozorth, "Magneto-resistance and domain theory", *Phys. Rev.* **70**, 106 (1946).

[528] L. W. McKeehan, "Electrical resistance of nickel and permalloy wires as affected by longitudinal magnetization and tension", *Phys. Rev.* **36**, 948 (1930).

[529] J. L. Snoek, "The Weiss-Heisenberg theory of ferromagnetism and a new rule concerning magnetostriction and magnetoresistance", *Nature* **163**, 837 (1949).

[530] I. A. Campbell, A. Fert, and O. Jaoul, "Spontaneous resistivity anisotropy in Ni-based alloys", *J. Phys. C: Solid State Phys.* **3**, S95 (1970).

[531] O. Jaoul, I. A. Campbell, and A. Fert, "Spontaneous resistivity anisotropy in Ni-alloys", *J. Magn. Magn. Mater.* **5**, 23 (1977).

[532] L. Berger, "Influence of spin-orbit interaction on transport processes in ferromagnetic nickel alloys in presence of degeneracy of 3d band", *Physica* **30**, 1141 (1964).

[533] R. I. Potter, "Magnetoresistance anisotropy in ferromagnetic NiCu alloys", *Phys. Rev. B* **10**, 4626 (1974).

[534] H. C. van Elst, "The anisotropy in the magneto-resistance of some nickel alloys", *Physica* **25**, 708 (1959).

[535] T. McGuire, J. Aboaf, and E. Klokholm, "Negative anisotropic magnetoresistance in 3d metals and alloys containing iridium", *IEEE Trans. Magn.* **20**, 972 (1984).

[536] H. Ebert, D. Ködderitzsch, and J. Minar, "Calculating condensed matter properties using the KKR-Green's function method-recent developments and applications", *Rep. Prog. Phys.* **74**, 096501 (2011).

[537] J. Banhart, A. Vernes, and H. Ebert, "Spin-orbit interaction and spontaneous galvanomagnetic effects in ferromagnetic alloys", *Solid State Commun.* **98**, 129 (1996).

[538] J. Banhart and H. Ebert, "First-principles theory of spontaneous-resistance anisotropy and spontaneous Hall-effect In disordered ferromagnetic-alloys", *Europhys. Lett.* **32**, 517 (1995).

[539] S. Khmelevskyi, K. Palotas, L. Szunyogh, and P. Weinberger, "*Ab initio* calculation of the anisotropic magnetoresistance in $Ni_{1-c}Fe_c$ bulk alloys", *Phys. Rev. B* **68**, 012402 (2003).

[540] A. A. Starikov, P. J. Kelly, A. Brataas, Y. Tserkovnyak, and G. E. W. Bauer, "Unified first-principles study of Gilbert damping, spin-flip diffusion, and resistivity in transition metal alloys", *Phys. Rev. Lett.* **105**, 236601 (2010).

[541] I. Turek, J. Kudrnovsky, and V. Drchal, "Ab initio theory of galvanomagnetic phenomena in ferromagnetic metals and disordered alloys", *Phys. Rev. B* **86**, 014405 (2012).

[542] H. Ebert, A. Vernes, and J. Banhart, "Anisotropic electrical resistivity of ferromagnetic Co-Pd and Co-Pt alloys", *Phys. Rev. B* **54**, 8479 (1996).

[543] J. Banhart, H. Ebert, and A. Vernes, "Applicability of the two-current model for systems with strongly spin-dependent disorder", *Phys. Rev. B* **56**, 10165 (1997).

[544] R. Gans and J. v. Harlem, "Widerstandsänderung ferromagnetischer Kristalle", *Ann. Phys.* **407**, 516 (1932).

[545] L. Berger and S. A. Friedberg, "Magnetoresistance of a permalloy single crystal and effect of 3d orbital degeneracies", *Phys. Rev.* **165**, 670 (1968).

[546] J. C. A. Huang, Y. Liou, Y. D. Yao, W. T. Yang, C. P. Chang, S. Y. Liao, and Y. M. Hu, "Large crystalline-induced magnetic-anisotropy and field-direction-dependent magnetoresistance in Co($1\bar{1}00$)/Cr(211) superlattices", *Phys. Rev. B* **52**, 13110 (1995).

[547] R. P. van Gorkom, J. Caro, T. M. Klapwijk, and S. Radelaar, "Temperature and angular dependence of the anisotropic magnetoresistance in epitaxial Fe films", *Phys. Rev. B* **63**, 134432 (2001).

[548] F. Bloch, "Zur Theorie des Ferromagnetismus", *Z. Phys. A At. Nucl.* **61**, 206 (1930).

[549] L. F. Liu, W. Y. Zhou, S. S. Xie, O. Albrecht, and K. Nielsch, "Microstructure and temperature-dependent magnetic properties of Co/Pt multilayered nanowires", *Chem. Phys. Lett.* **466**, 165 (2008).

[550] P. Kapitza, "The change of electrical conductivity in strong magnetic fields. Part I. Experimental results", *Proc. R. Soc. A* **123**, 292 (1929).

[551] B. Raquet, M. Viret, P. Warin, E. Sondergard, and R. Mamy, "Negative high field magnetoresistance in 3d ferromagnets", *Physica B* **294**, 102 (2001).

[552] B. Raquet, M. Viret, J. M. Broto, E. Sondergard, O. Cespedes, and R. Mamy, "Magnetic resistivity and electron-magnon scattering in 3d ferromagnets", *J. Appl. Phys.* **91**, 8129 (2002).

[553] W. Gil, D. Görlitz, M. Horisberger, and J. Kötzler, "Magnetoresistance anisotropy of polycrystalline cobalt films: Geometrical-size and domain effects", *Phys. Rev. B* **72**, 134401 (2005).

[554] J. Mathon and E. P. Wohlfarth, "Temperature dependence of spin wave energy in itinerant electron model of ferromagnetism", *Proc. R. Soc. A* **302**, 409 (1968).

[555] A. P. Mihai, J. P. Attané, A. Marty, P. Warin, and Y. Samson, "Electron-magnon diffusion and magnetization reversal detection in FePt thin films", *Phys. Rev. B* **77**, 060401 (2008).

[556] V. D. Nguyen, L. Vila, P. Laczkowski, A. Marty, T. Faivre, and J. P. Attané, "Detection of domain-wall position and magnetization reversal in nanostructures using the magnon contribution to the resistivity", *Phys. Rev. Lett.* **107**, 136605 (2011).

[557] V. D. Nguyen, C. Naylor, L. Vila, A. Marty, P. Laczkowski, C. Beigné, L. Notin, Z. Ishaque, and J. P. Attané, "Magnon magnetoresistance of NiFe nanowires: Size dependence and domain wall detection", *Appl. Phys. Lett.* **99**, 262504 (2011).

[558] R. A. Hajjar, M. Mansuripur, and H. P. D. Shieh, "Measurements of the anomalous magnetoresistance effect in Co/Pt and Co/Pd multilayer films for magnetooptical data-storage applications", *J. Appl. Phys.* **69**, 4686 (1991).

[559] R. A. Hajjar, T. H. Wu, and M. Mansuripur, "Magnetoresistance of Co/Pd and Co/Pt multilayer films for magnetooptical data-storage applications", *J. Appl. Phys.* **70**, 6041 (1991).

[560] R. A. Hajjar, M. Mansuripur, and H. P. D. Shieh, "Measurements of magnetoresistance in magnetooptical recording media", *J. Appl. Phys.* **69**, 7067 (1991).

[561] R. A. Hajjar and M. Mansuripur, "Magnetoresistance peaks in the neighborhood of coercivity in magnetooptical recording media", *J. Appl. Phys.* **72**, 1528 (1992).

[562] J. L. Olsen, *Electron Transport in Metals - Interscience Tracts on Physics and Astronomy 12*, (Interscience Publishers, a division of John Wiley & Sons, 1962).

[563] M. Kohler, "Zur magnetischen Widerstandsänderung reiner Metalle", *Ann. Phys.* **424**, 211 (1938).

[564] R. Peierls, "Zur Theorie der magnetischen Widerstandsänderung", *Ann. Phys.* **402**, 97 (1931).

[565] M. Springford, "Anisotropy of conduction electron scattering in noble metals", *Adv. Phys.* **20**, 493 (1971).

[566] H. K. Pal and D. L. Maslov, "Necessary and sufficient condition for longitudinal magnetoresistance", *Phys. Rev. B* **81**, 214438 (2010).

[567] B. Leven and G. Dumpich, "Resistance behavior and magnetization reversal analysis of individual Co nanowires", *Phys. Rev. B* **71**, 064411 (2005).

[568] A. Parsons, V. T. Petrashov, and I. A. Sosnin, "Anomalies in quantum and classical magnetoresistance of semi-metallic nanowires", *Physica B* **284**, 1744 (2000).

[569] R. C. Munoz, R. Henriquez, J. Garcia, A. M. Moncada, A. Espinosa, M. Robles, G. Kremer, L. Moraga, S. Cancino, J. R. Morales, A. Ramirez, S. Oyarzun, M. A. Suarez, D. Chen, E. Zumelzu, and C. Lizama, "Size effects under a strong magnetic field: Transverse magnetoresistance of thin gold films deposited on mica", *J. Phys.: Condens. Matter* **18**, 3401 (2006).

[570] R. V. Coleman, R. C. Morris, and D. J. Sellmyer, "Magnetoresistance in iron and cobalt to 150 kOe", *Phys. Rev. B* **8**, 317 (1973).

[571] E. N. Kondorski, O. S. Galinka, V. I. Ivanoskii, A. V. Cheremushkina, and U. T. Usarov, "Anisotropy of galvanomagnetic effects in single-crystal cobalt", *Sov. Phys. - JETP* **38**, 977 (1974).

[572] P. L. Rossiter and J. Bass, *Electronic and Magnetic Properties of Metals and Ceramics - Electronic Transport Properties of Normal Metals*, (John Wiley & Sons, Inc., 1992).

[573] A. B. Pippard, "Experimental analysis of the electronic structure of metals", *Rep. Prog. Phys.* **23**, 176 (1960).

[574] A. V. Gold, "Fermi surfaces of ferromagnetic transition-metals", *J. Low Temp. Phys.* **16**, 3 (1974).

[575] F. Batallan, I. Rosenman, and C. B. Sommers, "Band-structure and fermi-surface of hcp ferromagnetic cobalt", *Phys. Rev. B* **11**, 545 (1975).

[576] L. Schubnikow and W. J. de Haas, "A new phenomenon in the change of resistance in a magnetic field of single crystals of bismuth", *Nature* **126**, 500 (1930).

[577] G. Brandli and J. L. Olsen, "Size effects in electron transport in metals", *Mater. Sci. Eng.* **4**, 61 (1969).

[578] O. A. Panchenko, P. P. Lutsishin, and S. V. Sologub, "Galvanomagnetic size studies of metallic surface processes", *Prog. Surf. Sci.* **69**, 193 (2002).

[579] C. M. Hurd, *The Hall Effect in Metals and Alloys - The International Cryogenics Monograph Series*, (Plenum Press, 1972).

[580] J. Kötzler and W. Gil, "Anomalous Hall resistivity of cobalt films: Evidence for the intrinsic spin-orbit effect", *Phys. Rev. B* **72**, 060412 (2005).

[581] E. M. Pugh, "Hall effect and the magnetic properties of some ferromagnetic materials", *Phys. Rev.* **36**, 1503 (1930).

[582] N. Nagaosa, J. Sinova, S. Onoda, A. H. MacDonald, and N. P. Ong, "Anomalous Hall effect", *Rev. Mod. Phys.* **82**, 1539 (2010).

[583] R. Karplus and J. M. Luttinger, "Hall effect in ferromagnetics", *Phys. Rev.* **95**, 1154 (1954).

[584] J. Smit, "The spontaneous Hall effect in ferromagnetics. I.", *Physica* **21**, 877 (1955).

[585] L. Berger, "Side-jump mechanism for the Hall effect of ferromagnets", *Phys. Rev. B* **2**, 4559 (1970).

[586] T. Jungwirth, Q. Niu, and A. H. MacDonald, "Anomalous Hall effect in ferromagnetic semiconductors", *Phys. Rev. Lett.* **88**, 207208 (2002).

[587] K. M. Seemann, Y. Mokrousov, A. Aziz, J. Miguel, F. Kronast, W. Kuch, M. G. Blamire, A. T. Hindmarch, B. J. Hickey, I. Souza, and C. H. Marrows, "Spin-orbit strength driven crossover between intrinsic and extrinsic mechanisms of the anomalous Hall effect in the epitaxial $L1_0$-ordered ferromagnets FePd and FePt", *Phys. Rev. Lett.* **104**, 076402 (2010).

[588] Y. Tian, L. Ye, and X. F. Jin, "Proper scaling of the anomalous hall effect", *Phys. Rev. Lett.* **103**, 087206 (2009).

[589] S. N. Song, C. Sellers, and J. B. Ketterson, "Anomalous Hall-effect in (110)Fe/(110)Cr multilayers", *Appl. Phys. Lett.* **59**, 479 (1991).

[590] S. Zhang, "Extraordinary Hall effect in magnetic multilayers", *Phys. Rev. B* **51**, 3632 (1995).

[591] Z. B. Guo, W. B. Mi, R. O. Aboljadayel, B. Zhang, Q. Zhang, P. G. Barba, A. Manchon, and X. X. Zhang, "Effects of surface and interface scattering on anomalous Hall effect in Co/Pd multilayers", *Phys. Rev. B* **86**, 104433 (2012).

[592] S. P. McAlister and C. M. Hurd, "Hall-effect in 3d-transition metals and alloys", *J. Appl. Phys.* **50**, 7526 (1979).

[593] A. Gerber, A. Milner, M. Karpovsky, B. Lemke, H. U. Habermeier, J. Tuaillon-Combes, M. Negrier, O. Boisron, P. Melinon, and A. Perez, "Extraordinary Hall effect in magnetic films", *J. Magn. Magn. Mater.* **242**, 90 (2002).

[594] N. A. Sinitsyn, "Semiclassical theories of the anomalous Hall effect", *J. Phys.: Condens. Matter* **20**, 023201 (2008).

[595] S. Foner and E. M. Pugh, "Hall effects of the cobalt nickel alloys and of Armco iron", *Phys. Rev.* **91**, 20 (1953).

[596] R. Jaggi and F. Hulliger, *Landolt-Börnstein - Band II Elektrische Eigenschaften I*, Volume 19a, (Springer-Verlag, 1965).

[597] W. Betteridge, "Properties of metallic cobalt", *Prog. Mater Sci.* **24**, 51 (1979).

[598] F. P. Beitel and E. M. Pugh, "Two Hall effects of iron-cobalt alloys", *Phys. Rev.* **112**, 1516 (1958).

[599] G. J. van Gurp, "Electromigration and Hall-effect in cobalt films", *J. Phys. Chem. Solids* **38**, 627 (1977).

[600] E. Roman, Y. Mokrousov, and I. Souza, "Orientation dependence of the intrinsic anomalous Hall effect in hcp cobalt", *Phys. Rev. Lett.* **103**, 097203 (2009).

[601] O. A. Panchenko, P. P. Lutsishin, and Y. G. Ptushinskii, "Galvanomagnetic effects in thin films of some transition metals", *Sov. Phys. - JETP* **29**, 76 (1969).

[602] C. Goldberg and R. E. Davis, "New galvanomagnetic effect", *Phys. Rev.* **94**, 1121 (1954).

[603] K. M. Koch, "Zum Problem der galvanomagnetischen Effekte in Ferromagneticis", *Z. Naturforsch. A Phys. Sci.* **10**, 496 (1955).

[604] M. Yu and J. Chang, "The temperature dependence of the planar Hall effect in iron, cobalt and nickel", *J. Phys. Chem. Solids* **31**, 1997 (1970).

[605] K. L. Yau and J. T. H. Chang, "The planar Hall effect in thin foils of Ni-Fe alloy", *J. Phys. F: Met. Phys.* **1**, 38 (1971).

[606] G. H. Li, Z. Q. Lu, C. L. Chai, H. W. Jiang, and W. Y. Lai, "Pseudo-Hall effect in spin-valve multilayers", *Appl. Phys. Lett.* **74**, 747 (1999).

[607] S. T. B. Goennenwein, R. S. Keizer, S. W. Schink, I. Van Dijk, T. M. Klapwijk, and G. X. Miao, "Planar Hall effect and magnetic anisotropy in epitaxially strained chromium dioxide thin films", *Appl. Phys. Lett.* **90**, 142509 (2007).

[608] N. T. Thanh, L. T. Tu, N. D. Ha, C. O. Kim, C. Kim, K. H. Shin, and B. P. Rao, "Thickness dependence of parallel and perpendicular anisotropic resistivity in Ta/NiFe/IrMn/Ta multilayer studied by anisotropic magnetoresistance and planar Hall effect", *J. Appl. Phys.* **101**, 053702 (2007).

[609] K. M. Seemann, F. Freimuth, H. Zhang, S. Blügel, Y. Mokrousov, D. E. Bürgler, and C. M. Schneider, "Origin of the planar Hall effect in nanocrystalline $Co_{60}Fe_{20}B_{20}$", *Phys. Rev. Lett.* **107**, 086603 (2011).

[610] M. Donolato, B. T. Dalslet, C. D. Damsgaard, K. Gunnarsson, C. S. Jacobsen, P. Svedlindh, and M. F. Hansen, "Size-dependent effects in exchange-biased planar Hall effect sensor crosses", *J. Appl. Phys.* **109**, 064511 (2011).

[611] T. T. Chen and V. A. Marsocci, "Transverse magnetoresistivity anisotropy measurements and geometrical size effect in nickel thin films", *J. Appl. Phys.* **43**, 1554 (1972).

[612] T. G. S. M. Rijks, S. K. J. Lenczowski, R. Coehoorn, and W. J. M. de Jonge, "In-plane and out-of-plane anisotropic magnetoresistance in $Ni_{80}Fe_{20}$ thin films", *Phys. Rev. B* **56**, 362 (1997).

[613] T. G. S. M. Rijks, R. Coehoorn, M. J. M. de Jong, and W. J. M. de Jonge, "Semiclassical calculations of the anisotropic magnetoresistance of NiFe-based thin-films, wires, and multilayers", *Phys. Rev. B* **51**, 283 (1995).

[614] G. R. Taylor, A. Isin, and R. V. Coleman, "Resistivity of iron as a function of temperature and magnetization", *Phys. Rev.* **165**, 621 (1968).

[615] P. W. Shumate, R. V. Coleman, and R. C. Fivaz, "Resistivity of iron as a function of magnetization and stress", *Phys. Rev. B* **1**, 394 (1970).

[616] G. G. Cabrera and L. M. Falicov, "Theory of residual resistivity of Bloch walls, I. Paramagnetic effects", *Phys. Status Solidi B* **61**, 539 (1974).

[617] G. G. Cabrera and L. M. Falicov, "Theory of residual resistivity of Bloch walls, II. Inclusion of diamagnetic effects", *Phys. Status Solidi B* **62**, 217 (1974).

[618] L. Berger, "Low-field magnetoresistance and domain drag in ferromagnets", *J. Appl. Phys.* **49**, 2156 (1978).

[619] P. M. Levy and S. F. Zhang, "Resistivity due to domain wall scattering", *Phys. Rev. Lett.* **79**, 5110 (1997).

[620] J. F. Gregg, W. Allen, K. Ounadjela, M. Viret, M. Hehn, S. M. Thompson, and J. M. D. Coey, "Giant magnetoresistive effects in a single element magnetic thin film", *Phys. Rev. Lett.* **77**, 1580 (1996).

[621] D. Ravelosona, A. Cebollada, F. Briones, C. Diaz-Paniagua, M. A. Hidalgo, and F. Batallan, "Domain-wall scattering in epitaxial FePd ordered alloy films with perpendicular magnetic anisotropy", *Phys. Rev. B* **59**, 4322 (1999).

[622] M. Viret, Y. Samson, P. Warin, A. Marty, F. Ott, E. Sondergard, O. Klein, and C. Fermon, "Anisotropy of domain wall resistance", *Phys. Rev. Lett.* **85**, 3962 (2000).

[623] J. E. Wegrowe, A. Comment, Y. Jaccard, J. P. Ansermet, N. M. Dempsey, and J. P. Nozières, "Spin-dependent scattering of a domain wall of controlled size", *Phys. Rev. B* **61**, 12216 (2000).

[624] U. Ebels, A. Radulescu, Y. Henry, L. Piraux, and K. Ounadjela, "Spin accumulation and domain wall magnetoresistance in 35 nm Co wires", *Phys. Rev. Lett.* **84**, 983 (2000).

[625] R. Danneau, P. Warin, J. P. Attané, I. Petej, C. Beigné, C. Fermon, O. Klein, A. Marty, F. Ott, Y. Samson, and M. Viret, "Individual domain wall resistance in submicron ferromagnetic structures", *Phys. Rev. Lett.* **88**, 157201 (2002).

[626] S. Lepadatu and Y. B. Xu, "Direct observation of domain wall scattering in patterned $Ni_{80}Fe_{20}$ and Ni nanowires by current-voltage measurements", *Phys. Rev. Lett.* **92**, 127201 (2004).

[627] D. Buntinx, S. Brems, A. Volodin, K. Temst, and C. van Haesendonck, "Positive domain wall resistance of 180 degrees Néel walls in Co thin films", *Phys. Rev. Lett.* **94**, 017204 (2005).

[628] W. L. Lee, F. Q. Zhu, and C. L. Chien, "Determination of domain wall resistance in a cobalt thin film by thickness modulation", *Appl. Phys. Lett.* **88**, 122503 (2006).

[629] C. Hassel, S. Stienen, F. M. Römer, R. Meckenstock, G. Dumpich, and J. Lindner, "Resistance of domain walls created by means of a magnetic force microscope in transversally magnetized epitaxial Fe wires", *Appl. Phys. Lett.* **95**, 032504 (2009).

[630] S. Vandezande, C. van Haesendonck, and K. Temst, "The intrinsic domain wall resistance of Fe films with a periodic domain pattern", *Appl. Phys. Lett.* **94**, 192501 (2009).

[631] K. M. Seemann, M. C. Hickey, V. Baltz, B. J. Hickey, and C. H. Marrows, "Spin-dependent scattering and the spin polarization of a diffusive current in partly disordered $L1_0$ epitaxial FePd", *New J. Phys.* **12**, 033033 (2010).

[632] M. Viret, D. Vignoles, D. Cole, J. M. D. Coey, W. Allen, D. S. Daniel, and J. F. Gregg, "Spin scattering in ferromagnetic thin films", *Phys. Rev. B* **53**, 8464 (1996).

[633] E. Simanek, "Spin accumulation and resistance due to a domain wall", *Phys. Rev. B* **63**, 224412 (2001).

[634] C. H. Marrows and B. C. Dalton, "Spin mixing and spin-current asymmetry measured by domain wall magnetoresistance", *Phys. Rev. Lett.* **92**, 097206 (2004).

[635] L. Berger, "Relation between damping, current-induced torques, and wall resistance for domain walls in magnetic nanowires", *Phys. Rev. B* **75**, 174401 (2007).

[636] H. C. Herper and P. Entel, "Influence of domain wall scattering on the magnetoresistance of Co and $Co_{80}Pt_{20}$ film systems", *Phys. Rev. B* **77**, 174406 (2008).

[637] C. Wickles and W. Belzig, "Electronic transport in ferromagnetic conductors with inhomogeneous magnetic order parameter and domain-wall resistance", *Phys. Rev. B* **80**, 104435 (2009).

[638] G. Tatara and H. Fukuyama, "Resistivity due to a domain wall in ferromagnetic metal", *Phys. Rev. Lett.* **78**, 3773 (1997).

[639] R. P. van Gorkom, A. Brataas, and G. E. W. Bauer, "Negative domain wall resistance in ferromagnets", *Phys. Rev. Lett.* **83**, 4401 (1999).

[640] K. M. Hong and N. Giordano, "Resistance of a domain wall in a thin ferromagnetic wire", *J. Phys.: Condens. Matter* **10**, L401 (1998).

[641] U. Ruediger, J. Yu, S. Zhang, A. D. Kent, and S. S. P. Parkin, "Negative domain wall contribution to the resistivity of microfabricated Fe wires", *Phys. Rev. Lett.* **80**, 5639 (1998).

[642] A. D. Kent, J. Yu, U. Rüdiger, and S. S. P. Parkin, "Domain wall resistivity in epitaxial thin film microstructures", *J. Phys.: Condens. Matter* **13**, R461 (2001).

[643] H. X. Tang, S. Masmanidis, R. K. Kawakami, D. D. Awschalom, and M. L. Roukes, "Negative intrinsic resistivity of an individual domain wall in epitaxial (Ga,Mn)As microdevices", *Nature* **431**, 52 (2004).

[644] D. Elefant and R. Schäfer, "Giant negative domain wall resistance in iron", *Phys. Rev. B* **82**, 134438 (2010).

[645] A. Ben Hamida, O. Rousseau, S. Petit-Watelot, and M. Viret, "Positive domain wall resistance in atomic-sized constrictions", *Europhys. Lett.* **94**, 27002 (2011).

[646] U. Rüdiger, J. Yu, L. Thomas, S. S. P. Parkin, and A. D. Kent, "Magnetoresistance, micromagnetism, and domain-wall scattering in epitaxial hcp Co films", *Phys. Rev. B* **59**, 11914 (1999).

[647] I. Knittel and U. Hartmann, "Interplay between domain-wall resistance and surface scattering in ferromagnetic thin films", *Appl. Phys. A Mater. Sci. Process.* **78**, 359 (2004).

[648] G. Dumpich, B. Leven, and M. Brands, "Electron transport in magnetic nanostructures", *Phys. Status Solidi A* **201**, 3237 (2004).

[649] B. Leven, U. Nowak, and G. Dumpich, "Domain wall resistance in $(Co/Pt)_{10}$-nanowires", *Europhys. Lett.* **70**, 803 (2005).

[650] C. Hassel, M. Brands, F. Y. Lo, A. D. Wieck, and G. Dumpich, "Resistance of a single domain wall in $(Co/Pt)_7$ multilayer nanowires", *Phys. Rev. Lett.* **97**, 226805 (2006).

[651] A. Aziz, S. J. Bending, H. Roberts, S. Crampin, P. J. Heard, and C. H. Marrows, "Investigation of artificial domains realized by local gallium focused ion-beam modification of Pt/Co/Pt trilayer structures", *J. Appl. Phys.* **99**, 08C504 (2006).

[652] A. Aziz, S. J. Bending, H. G. Roberts, S. Crampin, P. J. Heard, and C. H. Marrows, "Angular dependence of domain wall resistivity in artificial magnetic domain structures", *Phys. Rev. Lett.* **97**, 206602 (2006).

[653] L. S. E. Alvarez, K. Y. Wang, S. Lepadatu, S. Landi, S. J. Bending, and C. H. Marrows, "Spin-transfer-torque-assisted domain-wall creep in a Co/Pt multilayer wire", *Phys. Rev. Lett.* **104**, 137205 (2010).

[654] J. H. Franken, M. Hoeijmakers, H. J. M. Swagten, and B. Koopmans, "Tunable resistivity of individual magnetic domain walls", *Phys. Rev. Lett.* **108**, 037205 (2012).

[655] J. C. Wu, C. S. Wu, T. H. Wu, B. M. Chen, and H. P. D. Shieh, "Magnetoresistance anomaly in DyFeCo thin films", *J. Appl. Phys.* **89**, 7209 (2001).

[656] H. X. Tang and M. L. Roukes, "Electrical transport across an individual magnetic domain wall in (Ga,Mn)As microdevices", *Phys. Rev. B* **70**, 205213 (2004).

[657] X. M. Cheng, S. Urazhdin, O. Tchernyshyov, C. L. Chien, V. I. Nikitenko, A. J. Shapiro, and R. D. Shull, "Antisymmetric magnetoresistance in magnetic multilayers with perpendicular anisotropy", *Phys. Rev. Lett.* **94**, 017203 (2005).

[658] A. Segal, O. Shaya, M. Karpovski, and A. Gerber, "Asymmetric field dependence of magnetoresistance in magnetic films", *Phys. Rev. B* **79**, 144434 (2009).

[659] G. Xiang, A. W. Holleitner, B. L. Sheu, F. M. Mendoza, O. Maksimov, M. B. Stone, P. Schiffer, D. D. Awschalom, and N. Samarth, "Magnetoresistance anomalies in (Ga,Mn)As epilayers with perpendicular magnetic anisotropy", *Phys. Rev. B* **71**, 241307 (2005).

[660] G. Rodriguez-Rodriguez, J. L. Menendez, A. Hierro-Rodriguez, A. Perez-Junquera, N. Montenegro, D. Ravelosona, J. M. Alameda, and M. Velez, "Interplay between collective pinning and artificial defects on domain wall propagation in Co/Pt multilayers", *J. Phys. D: Appl. Phys.* **43**, 305002 (2010).

[661] G. Xiang and N. Samarth, "Theoretical analysis of the influence of magnetic domain walls on longitudinal and transverse magnetoresistance in tensile strained (Ga,Mn)As epilayers", *Phys. Rev. B* **76**, 054440 (2007).

[662] B. Doudin and M. Viret, "Ballistic magnetoresistance?", *J. Phys.: Condens. Matter* **20**, 083201 (2008).

[663] O. Boulle, J. Kimling, P. Warnicke, M. Kläui, U. Rüdiger, G. Malinowski, H. J. M. Swagten, B. Koopmans, C. Ulysse, and G. Faini, "Nonadiabatic spin transfer torque in high anisotropy magnetic nanowires with narrow domain walls", *Phys. Rev. Lett.* **101**, 216601 (2008).

[664] J. H. Park, M. T. Moneck, C. Park, and J. G. Zhu, "Spin-transfer induced switching in nanomagnetoresistive devices composed of Co/Pt multilayers with perpendicular magnetic anisotropy", *J. Appl. Phys.* **105**, 07D129 (2009).

[665] J. Heinen, O. Boulle, K. Rousseau, G. Malinowski, M. Kläui, H. J. M. Swagten, B. Koopmans, C. Ulysse, and G. Faini, "Current-induced domain wall motion in Co/Pt nanowires: Separating spin torque and Oersted-field effects", *Appl. Phys. Lett.* **96**, 202510 (2010).

[666] K. J. Kim, J. C. Lee, S. J. Yun, G. H. Gim, K. S. Lee, S. B. Choe, and K. H. Shin, "Electric control of multiple domain walls in Pt/Co/Pt nanotracks with perpendicular magnetic anisotropy", *Appl. Phys. Express* **3**, 083001 (2010).

[667] M. Cormier, A. Mougin, J. Ferré, A. Thiaville, N. Charpentier, F. Piechon, R. Weil, V. Baltz, and B. Rodmacq, "Effect of electrical current pulses on domain walls in Pt/Co/Pt nanotracks with out-of-plane anisotropy: Spin transfer torque versus Joule heating", *Phys. Rev. B* **81**, 024407 (2010).

[668] M. Cormier, A. Mougin, J. Ferré, J. P. Jamet, R. Weil, J. Fassbender, V. Baltz, and B. Rodmacq, "Fast propagation of weakly pinned domain walls and current-assisted magnetization reversal in He^+-irradiated Pt/Co/Pt nanotracks", *J. Phys. D: Appl. Phys.* **44**, 215002 (2011).

[669] G. Tatara and H. Kohno, "Theory of current-driven domain wall motion: Spin transfer versus momentum transfer", *Phys. Rev. Lett.* **92**, 086601 (2004).

[670] D. C. Ralph and M. D. Stiles, "Spin transfer torques", *J. Magn. Magn. Mater.* **320**, 1190 (2008).

[671] H. Stillrich, *Magnetische Nanostrukturen basierend auf Co/Pt-Multilagen, hergestellt mittels selbstorganisierter Masken aus Blockcopolymer-Micellen*, Ph.D. thesis, Universität Hamburg (2008).

[672] R. Anton, T. Wiegner, W. Naumann, M. Liebmann, C. Klein, and C. Bradley, "Design and performance of a versatile, cost-effective microwave electron cyclotron resonance plasma source for surface and thin film processing", *Rev. Sci. Instrum.* **71**, 1177 (2000).

[673] E. D. McClanahan and N. Laegreid, *Production of thin films by controlled deposition of sputtered material - Sputtering By Particle Bombardment III, Topics Appl. Physics 64*, (Springer-Verlag, 1991).

[674] W. Schweika, *Schichtpräparation mit Sputterverfahren - 30. IFF-Ferienkurs 1999: Magnetische Schichtsysteme*, (Forschungszentrum Jülich GmbH, Institut für Festkörperforschung, 1999).

[675] S. Hashimoto, Y. Ochiai, and K. Aso, "Perpendicular magnetic-anisotropy and magnetostriction of sputtered Co/Pd and Co/Pt multilayered films", *J. Appl. Phys.* **66**, 4909 (1989).

[676] Z. G. Li and P. F. Carcia, "Microstructural dependence of magnetic properties of Pt/Co multilayer thin films", *J. Appl. Phys.* **71**, 842 (1992).

[677] P. F. Carcia, Z. G. Li, and W. B. Zeper, "Effect of sputter-deposition processes on the microstructure and magnetic properties of Pt/Co multilayers", *J. Magn. Magn. Mater.* **121**, 452 (1993).

[678] G. A. Bertero and R. Sinclair, "Structure-property correlations in Pt/Co multilayers for magnetooptic recording", *J. Magn. Magn. Mater.* **134**, 173 (1994).

[679] G. A. Bertero, R. Sinclair, C. H. Park, and Z. X. Shen, "Interface structure and perpendicular magnetic-anisotropy in Pt/Co multilayers", *J. Appl. Phys.* **77**, 3953 (1995).

[680] J. H. Kim and S. C. Shin, "Interface roughness effects on the surface anisotropy in Co/Pt multilayer films", *J. Appl. Phys.* **80**, 3121 (1996).

[681] J. H. Kim and S. C. Shin, "Logarithmic dependence of the surface anisotropy on the low-angle x-ray diffraction intensity in Co-based multilayers", *Thin Solid Films* **301**, 249 (1997).

[682] L. Reimer and K. Kohl, *Transmisson Electron Microscopy: Physics of Image Formation, Springer Series in Optical Sciences Vol. 36*, (Springer-Verlag, 1989).

[683] T. C. Schulthess, W. H. Butler, X. G. Zhang, D. M. C. Nicholson, and J. M. MacLaren, "Calculation of conductivity in the presence of structural defects: Application to spin dependence of conductivity in cobalt", *Phys. Rev. B* **56**, 8970 (1997).

[684] M. Erbudak, E. Wetli, M. Hochstrasser, D. Pescia, and D. D. Vvedensky, "Surface phase transitions during martensitic transformations of single-crystal Co", *Phys. Rev. Lett.* **79**, 1893 (1997).

[685] B. D. Cullity, *Elements of X-Ray Diffraction - Addison-Wesley Series in Metallurgy and Materials*, (Addison-Wesley Publishing Company, Inc., 1978).

[686] B. E. Warren, *X-ray diffraction*, (Dover Publications, Inc., 1990).

[687] C. H. MacGillavry, G. D. Rieck, and K. Lonsdale (Eds.) *International Tables for X-Ray Crystallography, Vol. III Physical and Chemical Tables*, (The Kynoch Press, 1968).

[688] A. I. Ibers and W. C. Hamilton (Eds.) *International Tables for X-Ray Crystallography, Vol. IV Revised and Supplementary Tables to Vol. II and III*, (Kluwer Academic Publishers, 1989).

[689] P. Scherrer, "Bestimmung der Größe und der inneren Struktur von Kolloidteilchen mittels Röntgenstrahlen", *Nachr. Ges. Wiss. Göttingen, Math.-Phys. Kl.* p. 98 (1918).

[690] I. K. Schuller, "New class of layered materials", *Phys. Rev. Lett.* **44**, 1597 (1980).

[691] P. J. Mohr, B. N. Taylor, and D. B. Newell, "CODATA recommended values of the fundamental physical constants: 2006", *Rev. Mod. Phys.* **80**, 633 (2008).

[692] R. A. Young and D. B. Wiles, "Profile shape functions in Rietveld refinements", *J. Appl. Crystallogr.* **15**, 430 (1982).

[693] J. I. Langford and D. Louer, "Powder diffraction", *Rep. Prog. Phys.* **59**, 131 (1996).

[694] A. Segmüller and A. E. Blakeslee, "X-ray diffraction from one-dimensional superlattices in $GaAs_{1-x}P_x$ crystals", *J. Appl. Crystallogr.* **6**, 19 (1973).

[695] N. Sato, "Crystallographic structure and magnetism of Co-Pd and Co-Pt films with an artificially layered structure", *J. Appl. Phys.* **64**, 6424 (1988).

[696] E. E. Fullerton, I. K. Schuller, H. Vanderstraeten, and Y. Bruynseraede, "Structural refinement of superlattices from x-ray-diffraction", *Phys. Rev. B* **45**, 9292 (1992).

[697] D. Ariosa, O. Fischer, M. G. Karkut, and J.-M. Triscone, "Elastic model for the partially coherent growth of metallic superlattices. I. Interdiffusion, strain, and misfit dislocations", *Phys. Rev. B* **37**, 2415 (1988).

[698] J. P. Locquet, D. Neerinck, L. Stockman, Y. Bruynseraede, and I. K. Schuller, "Discrete and continuous disorder in superlattices", *Phys. Rev. B* **39**, 13338 (1989).

[699] D. Neerinck, J.-P. Locquet, L. Stockman, Y. Bruynseraede, and I. K. Schuller, "Lattice mismatch and interfacial disorder in superlattices", *Phys. Scr.* **39**, 346 (1989).

[700] D. Lott, private communication.

[701] C. J. Lin, G. L. Gorman, C. H. Lee, R. F. C. Farrow, E. E. Marinero, H. V. Do, H. Notarys, and C. J. Chien, "Magnetic and structural-properties of Co/Pt multilayers", *J. Magn. Magn. Mater.* **93**, 194 (1991).

[702] D. Weller, L. Folks, M. Best, E. E. Fullerton, B. D. Terris, G. J. Kusinski, K. M. Krishnan, and G. Thomas, "Growth, structural, and magnetic properties of high coercivity Co/Pt multilayers", *J. Appl. Phys.* **89**, 7525 (2001).

[703] R. Shan, T. R. Gao, S. M. Zhou, X. S. Wu, Y. K. Fang, and B. S. Han, "Co/Pt multilayers with large coercivity and small grains", *J. Appl. Phys.* **99**, 063907 (2006).

[704] V. W. Guo, B. Lu, X. W. Wu, G. P. Ju, B. Valcu, and D. Weller, "A survey of anisotropy measurement techniques and study of thickness effect on interfacial and volume anisotropies in Co/Pt multilayer media", *J. Appl. Phys.* **99**, 08E918 (2006).

[705] M. Angelakeris, E. T. Papaioannou, P. Poulopoulos, A. Vlachos, G. Natsiopoulos, F. Wilhelm, A. Rogalev, and N. K. Flevaris, "Pt-Co multilayers: Interface effects at the monolayer limit", *Phys. Status Solidi A* **205**, 2302 (2008).

[706] A. Markou, K. G. Beltsios, I. Panagiotopoulos, M. E. Vlachopoulou, A. Tserepi, V. Alexandrakis, T. Bakas, and T. Dimopoulos, "Magnetic properties of Co films and Co/Pt multilayers deposited on PDMS nanostructures", *J. Magn. Magn. Mater.* **321**, 2582 (2009).

[707] C. H. Lee, R. F. C. Farrow, C. J. Lin, E. E. Marinero, and C. J. Chien, "Molecular-beam-epitaxial growth and magnetic-properties of Co-Pt superlattices oriented along the [001], [110], and [111] axes of Pt", *Phys. Rev. B* **42**, 11384 (1990).

[708] W. B. Zeper, F. J. A. M. Greidanus, P. F. Carcia, and C. R. Fincher, "Perpendicular magnetic-anisotropy and magneto-optical Kerr effect of vapor-deposited Co/Pt-layered structures", *J. Appl. Phys.* **65**, 4971 (1989).

[709] B. J. Lee, Y. P. Lee, J. I. Jeong, and Y. M. Koo, "Effects of the structural parameters including surface roughness, on the properties of Co/Pt multilayered films", *J. Korean Phys. Soc.* **36**, 54 (2000).

[710] N. Nakamura, H. Ogi, T. Ono, M. Hirao, and M. Nishiyama, "Elastic constants and magnetic anisotropy of Co/Pt superlattice: Resonance-ultrasound-spectroscopy method", *Jpn. J. Appl. Phys.* **44**, 4427 (2005).

[711] N. Nakamura, H. Ogi, M. Hirao, and T. Ono, "Determination of anisotropic elastic constants of superlattice thin films by resonant-ultrasound spectroscopy", *J. Appl. Phys.* **97**, 013532 (2005).

[712] Y. An, L. Duan, T. Liu, Z. Wu, and J. Liu, "Structural and magnetic properties of Pt in Co/Pt multilayers", *Appl. Surf. Sci.* **257**, 7427 (2011).

[713] K. K. M. Pandey, J. S. Chen, T. Liu, C. J. Sun, and G. M. Chow, "Crystallographic origin of perpendicular magnetic anisotropy in CoPt film: Polarized x-ray absorption study", *J. Phys. D: Appl. Phys.* **42**, 185007 (2009).

[714] J. Daillant and A. Gibaud (Eds.) *X-Ray and Neutron Reflectivity: Principles and Applications - Lect. Notes Phys. 770*, (Springer Verlag, 2009).

[715] C. Braun, "Parrat32", HMI Berlin.

[716] J. Als-Nielsen and D. McMorrow, *Elements of Modern X-ray Physics*, (John Wiley & Sons, Inc., 2008).

[717] H. Kiessig, "Interferenz von röntgenstrahlen an dünnen schichten", *Ann. Phys.* **402**, 769 (1931).

[718] L. G. Parratt, "Surface studies of solids by total reflection of x-rays", *Phys. Rev.* **95**, 359 (1954).

[719] S. K. Sinha, E. B. Sirota, S. Garoff, and H. B. Stanley, "X-ray and neutron-scattering from rough surfaces", *Phys. Rev. B* **38**, 2297 (1988).

[720] Y. Yoneda, "Anomalous surface reflection of x rays", *Phys. Rev.* **131**, 2010 (1963).

[721] C. J. Chien, R. F. C. Farrow, C. H. Lee, C. J. Lin, and E. E. Marinero, "High-resolution transmission electron-microscopy studies of seeded epitaxial Co/Pt superlattices", *J. Magn. Magn. Mater.* **93**, 47 (1991).

[722] B. D. Hermsmeier, R. F. C. Farrow, C. H. Lee, E. E. Marinero, C. J. Lin, R. F. Marks, and C. J. Chien, "Magnetic-anisotropy and structural characterization of Co/Pt superlattices grown along selected orientations by molecular-beam epitaxy", *J. Appl. Phys.* **69**, 5646 (1991).

[723] N. H. Cho, K. M. Krishnan, C. A. Lucas, and R. F. C. Farrow, "Microstructure and magnetic-anisotropy of ultrathin Co/Pt multilayers grown on GaAs ($\overline{111}$) by molecular-beam epitaxy", *J. Appl. Phys.* **72**, 5799 (1992).

[724] B. Zhang, K. M. Krishnan, and R. F. C. Farrow, "Crystallography of Co/Pt multilayers and nanostructures", *Ultramicroscopy* **51**, 298 (1993).

[725] J. F. Ankner, J. A. Borchers, R. F. C. Farrow, and R. F. Marks, "Combined low-angle and high-angle x-ray structural refinement of a Co/Pt(111) multilayer exhibiting perpendicular magnetic-anisotropy", *J. Appl. Phys.* **73**, 6427 (1993).

[726] B. D. Fulthorpe, D. E. Joyce, T. P. A. Hase, A. S. H. Rozatian, B. K. Tanner, and P. J. Grundy, "The progression of interface structure through sputtered Co/Cu and Co/Pt multilayer films", *J. Phys.: Condens. Matter* **11**, 8477 (1999).

[727] I. B. Chung, Y. M. Koo, and J. M. Lee, "Interface structure and magnetic anisotropy of a Co/Pt multilayer", *J. Appl. Phys.* **87**, 4205 (2000).

[728] A. S. H. Rozatian, B. D. Fulthorpe, T. P. A. Hase, D. E. Read, G. Ashcroft, D. E. Joyce, P. J. Grundy, J. Amighian, and B. K. Tanner, "Anisotropy and interface structure in sputtered Co/Pt multilayers on Si", *J. Magn. Magn. Mater.* **256**, 365 (2003).

[729] C. Schug, H. Grimm, R. Berger, A. Dietzel, and M. Wormington, "Specular and off-specular x-ray reflectivity study of ion irradiated Co/Pt multilayers", *Surf. Interface Anal.* **36**, 908 (2004).

[730] M. Björck, G. Andersson, B. Sanyal, M. Hedlund, and A. Wildes, "Segregation and interdiffusion in (Fe,Co)/Pt superlattices", *Phys. Rev. B* **79**, 085428 (2009).

[731] W. B. Zeper, H. W. van Kesteren, B. A. J. Jacobs, J. H. M. Spruit, and P. F. Carcia, "Hysteresis, microstructure, and magnetooptical recording in Co/Pt and Co/Pd multilayers", *J. Appl. Phys.* **70**, 2264 (1991).

[732] Z. G. Li, P. F. Carcia, and Y. Cheng, "Co thickness dependence of the microstructure of Pt/Co multilayers", *J. Appl. Phys.* **73**, 2433 (1993).

[733] G. N. Phillips, K. O'Grady, and J. C. Lodder, "Magnetization reversal at elevated temperatures in Co/Pt multilayer thin films", *J. Phys. D: Appl. Phys.* **34**, 2960 (2001).

[734] J. S. Agustsson, U. B. Arnalds, A. S. Ingason, K. B. Gylfason, K. Johnsen, S. Olafsson, and J. T. Gudmundsson, "Growth, coalescence, and electrical resistivity of thin Pt films grown by dc magnetron sputtering on SiO_2", *Appl. Surf. Sci.* **254**, 7356 (2008).

[735] S. Sumi, Y. Kusumoto, Y. Teragaki, K. Torazawa, S. Tsunashima, and S. Uchiyama, "Thermal-stability of Pt/Co multilayered films", *J. Appl. Phys.* **73**, 6835 (1993).

[736] H. Windischmann, "Intrinsic stress in sputter-deposited thin-films", *Crit. Rev. Solid State Mater. Sci.* **17**, 547 (1992).

[737] B. Zhang, K. M. Krishnan, C. H. Lee, and R. F. C. Farrow, "Magnetic-anisotropy and lattice strain in Co/Pt multilayers", *J. Appl. Phys.* **73**, 6198 (1993).

[738] J. Birch, J. E. Sundgren, and P. F. Fewster, "Measurement of the lattice-parameters in the individual layers of single-crystal superlattices", *J. Appl. Phys.* **78**, 6562 (1995).

[739] N. Nakamura, H. Ogi, M. Hirao, and T. Ono, "Elastic constants and magnetic anisotropy of Co/Pt superlattice thin films", *Appl. Phys. Lett.* **86**, 111918 (2005).

[740] H. Tanei, N. Nakamura, Y. Kake, H. Ogi, K. Kusakabe, and M. Hirao, "Elastic constants of Co/Pt superlattice studied by acoustic measurements and ab initio calculations", *Jpn. J. Appl. Phys.* **47**, 3847 (2008).

[741] L. Vegard, "Die Konstitution der Mischkristalle und die Raumfüllung der Atome", *Z. Phys. A At. Nucl.* **5**, 17 (1921).

[742] N. W. E. McGee, M. T. Johnson, J. J. de Vries, and J. aan de Stegge, "Localized Kerr study of the magnetic-properties of an ultrathin epitaxial Co wedge grown on Pt(111)", *J. Appl. Phys.* **73**, 3418 (1993).

[743] M. Galeotti, A. Atrei, U. Bardi, B. Cortigiani, G. Rovida, and M. Torrini, "Epitaxy and alloying at the Co-Pt(111) interface - a study by x-ray photoelectron diffraction", *Surf. Sci.* **297**, 202 (1993).

[744] J. Thiele, N. T. Barrett, R. Belkhou, C. Guillot, and H. Koundi, "An experimental-study of the growth of Co/Pt(111) by core-level photoemission spectroscopy, low-energy-electron diffraction and Auger-electron spectroscopy", *J. Phys.: Condens. Matter* **6**, 5025 (1994).

[745] P. Grütter and U. T. Dürig, "Scanning-tunneling-microscopy of Co on Pt(111)", *J. Vac. Sci. Technol. B* **12**, 1768 (1994).

[746] J. Thiele, R. Belkhou, H. Bulou, O. Heckmann, H. Magnan, P. Le Fèvre, D. Chandesris, and C. Guillot, "EXAFS study of the crystallographic structure of cobalt thin films on Pt(111)", *Surf. Sci.* **384**, 120 (1997).

[747] J. S. Tsay and C. S. Shern, "Structure evolution for annealing Co ultrathin films on Pt(111)", *Surf. Sci.* **396**, 313 (1998).

[748] R. Baudoing-Savois, P. Dolle, Y. Gauthier, M. C. Saint-Lager, M. De Santis, and V. Jahns, "Co ultra-thin films on Pt(111) and Co-Pt alloying: A LEED, Auger and synchrotron x-ray diffraction study", *J. Phys.: Condens. Matter* **11**, 8355 (1999).

[749] E. Lundgren, B. Stanka, M. Schmid, and P. Varga, "Thin films of Co on Pt(111): Strain relaxation and growth", *Phys. Rev. B* **62**, 2843 (2000).

[750] P. Varga, E. Lundgren, J. Redinger, and M. Schmid, "Ultrathin films of Co on Pt(111): An STM view", *Phys. Status Solidi A* **187**, 97 (2001).

[751] J. Kim, J. W. Lee, J. R. Jeong, S. C. Shin, Y. H. Ha, Y. Park, and D. W. Moon, "Ultrathin Co films on Pt(111) and the Co-Pt interface investigated by surface magneto-optical Kerr effect and medium-energy ion scattering spectroscopy", *Phys. Rev. B* **65**, 104428 (2002).

[752] E. Lundgren, G. Leonardelli, M. Schmid, and P. Varga, "A misfit structure in the Co/Pt(111) system studied by scanning tunnelling microscopy and embedded atom method calculations", *Surf. Sci.* **498**, 257 (2002).

[753] C. Quiros, S. M. Valvidares, O. Robach, and S. Ferrer, "Low-temperature growth favours hcp structure, flatness and perpendicular magnetic anisotropy of thin (1-5 nm) Co films on Pt(111)", *J. Phys.: Condens. Matter* **17**, 5551 (2005).

[754] F. Meier, K. von Bergmann, P. Ferriani, J. Wiebe, M. Bode, K. Hashimoto, S. Heinze, and R. Wiesendanger, "Spin-dependent electronic and magnetic properties of Co nanostructures on Pt(111) studied by spin-resolved scanning tunneling spectroscopy", *Phys. Rev. B* **74**, 195411 (2006).

[755] F. Meier, K. von Bergmann, J. Wiebe, M. Bode, and R. Wiesendanger, "Co double-layer nanostructures on Pt(111) studied by spin-polarized scanning tunnelling microscopy", *J. Phys. D: Appl. Phys.* **40**, 1306 (2007).

[756] W. Weber, D. A. Wesner, D. Hartmann, and G. Güntherodt, "Spin-polarized interface states at the Pd(111)/Fe(110), Pd(111)/Co(0001), and Pt(111)/Co(0001) interfaces", *Phys. Rev. B* **46**, 6199 (1992).

[757] A. Barbier, B. Carrière, and J. P. Deville, "Growth and structure of Pt on Co(11$\bar{2}$0) versus Pt on Co(10$\bar{1}$0) and Pt on Co(0001)", *Surf. Sci.* **344**, 33 (1995).

[758] H. Bulou, A. Barbier, R. Belkhou, C. Guillot, B. Carrière, and J. P. Deville, "Chemical structure of the Pt/Co(0001) interface", *Surf. Sci.* **352**, 828 (1996).

[759] G. F. Cabeza, P. Legare, A. Sadki, and N. J. Castellani, "Growth and structure of thin platinum films deposited on Co(0001) studied by low-energy electron diffraction, x-ray photoelectron spectroscopy, ultraviolet photoelectron spectroscopy and scanning tunneling microscopy", *Surf. Sci.* **457**, 121 (2000).

[760] P. Legare, N. J. Castellani, and G. F. Cabeza, "Adhesion of metal on metal. The Pt on Co case", *Surf. Sci.* **496**, L51 (2002).

[761] C. Goyhenex and G. Treglia, "Theoretical determination of two critical sizes for strain relaxation during Co/Pt(111) heteroepitaxy", *Surf. Sci.* **446**, 272 (2000).

[762] C. Goyhenex, H. Bulou, J. P. Deville, and G. Treglia, "Compressive strain versus tensile strain - a theoretical study of Pt/Co(0001) and Co/Pt(111) heteroepitaxy", *Appl. Surf. Sci.* **177**, 238 (2001).

[763] K. Nishikawa, T. Kingetsu, K. Sakai, T. Kurumizawa, and M. Yamamoto, "Structure and properties of MBE-grown Pt/Co multilayer, Pt/Cu doublelayer, Co/Cu doublelayer, Pt film and Cu film on Si(111)-(7 x 7) substrate", *J. Magn. Magn. Mater.* **126**, 153 (1993).

[764] K. Spörl and D. Weller, "Interface anisotropy and chemistry of magnetic multilayers - Au/Co, Pt/Co and Pd/Co", *J. Magn. Magn. Mater.* **93**, 379 (1991).

[765] M. C. Saint-Lager, R. Baudoing-Savois, M. De Santis, P. Dolle, and Y. Gauthier, "Thickness effect on alloying of ultrathin Co films on Pt(111): A real time and in situ UHV study with synchrotron x-ray diffraction", *Surf. Sci.* **418**, 485 (1998).

[766] N. Nakajima, T. Koide, T. Shidara, H. Miyauchi, I. Fukutani, A. Fujimori, K. Iio, T. Katayama, M. Nyvlt, and Y. Suzuki, "Perpendicular magnetic anisotropy caused by interfacial hybridization via enhanced orbital moment in Co/Pt multilayers: Magnetic circular x-ray dichroism study", *Phys. Rev. Lett.* **81**, 5229 (1998).

[767] S. Ferrer, J. Alvarez, E. Lundgren, X. Torrelles, P. Fajardo, and F. Boscherini, "Surface x-ray diffraction from Co/Pt(111) ultrathin films and alloys: Structure and magnetism", *Phys. Rev. B* **56**, 9848 (1997).

[768] A. Gutakovskii, A. Chuvilin, and S. Song, "Application of high-resolution electron microscopy for visualization and quantitative analysis of strain fields in heterostructures", *Bull. Russ. Acad. Sci. Phys.* **71**, 1426 (2007).

[769] I. K. Robinson, "Crystal truncation rods and surface roughness", *Phys. Rev. B* **33**, 3830 (1986).

[770] D. E. Sayers, E. A. Stern, and F. W. Lytle, "New technique for investigating noncrystalline structures: Fourier analysis of the extended x-ray-absorption fine structure", *Phys. Rev. Lett.* **27**, 1204 (1971).

[771] R. Vollmer, *Lineare und nichtlineare Magnetoptik an ultradünnen ferromagnetischen Schichten und Vielfachschichten - 30. IFF-Ferienkurs 1999: Magnetische Schichtsysteme*, (Forschungszentrum Jülich GmbH, Institut für Festkörperforschung, 1999).

[772] H. F. Ding, S. Pütter, H. P. Oepen, and J. Kirschner, "Experimental method for separating longitudinal and polar Kerr signals", *J. Magn. Magn. Mater.* **212**, L5 (2000).

[773] J. W. Lee, J. R. Jeong, S. C. Shin, J. Kim, and S. K. Kim, "Spin-reorientation transitions in ultrathin Co films on Pt(111) and Pd(111) single-crystal substrates", *Phys. Rev. B* **66**, 172409 (2002).

[774] W. B. Zeper, F. J. A. M. Greidanus, and P. F. Carcia, "Evaporated Co/Pt layered structures for magneto-optical recording", *IEEE Trans. Magn.* **25**, 3764 (1989).

[775] W. Andra, H. Danan, L. Fritzsch, R. Mattheis, B. Solcher, and F. Thrum, "Magnetic-behavior of Pt/Co/Pt layered films - experiments and micromagnetic modeling", *J. Magn. Magn. Mater.* **113**, 155 (1992).

[776] D. Weller, R. F. C. Farrow, R. F. Marks, H. Notarys, and G. Gorman, "Interface and volume anisotropy of MBE-grown Co/Pt(111),

(110) and (001) and sputtered Co/Pt multilayers", *Mat. Res. Soc. Symp. Proc.* **313**, 791 (1993).

[777] S. J. Greaves, P. J. Grundy, and R. J. Pollard, "Magnetic properties of cobalt layers and Co/Pt multilayers", *J. Magn. Magn. Mater.* **121**, 532 (1993).

[778] S. Bandiera, R. Sousa, B. Rodmacq, and B. Dieny, "Asymmetric interfacial perpendicular magnetic anisotropy in Pt/Co/Pt trilayers", *IEEE Magn. Lett.* **2**, 3000504 (2011).

[779] J. H. van der Merwe, "Crystal interfaces. Part II. Finite overgrowths", *J. Appl. Phys.* **34**, 123 (1963).

[780] R. Jungblut, M. T. Johnson, J. aan de Stegge, A. Reinders, and F. J. A. den Broeder, "Orientational and structural dependence of magnetic-anisotropy of Cu/Ni/Cu sandwiches - misfit interface anisotropy", *J. Appl. Phys.* **75**, 6424 (1994).

[781] C. Uiberacker, J. Zabloudil, P. Weinberger, L. Szunyogh, and C. Sommers, "Lattice relaxation driven reorientation transition in Ni_n/Cu(100)", *Phys. Rev. Lett.* **82**, 1289 (1999).

[782] K. Chen, R. Frömter, S. Rössler, N. Mikuszeit, and H. P. Oepen, "Uniaxial magnetic anisotropy of cobalt films deposited on sputtered MgO(001) substrates", *Phys. Rev. B* **86**, 064432 (2012).

[783] H. Fujiwara, H. Kadomatsu, and T. Tokunaga, "Magnetocrystalline anisotropy and magnetostriction of Pd-Co alloys", *J. Magn. Magn. Mater.* **31-34**, 809 (1983).

[784] H. Takahashi, S. Tsunashima, S. Iwata, and S. Uchiyama, "Measurement of magnetostriction constants in polycrystalline alloy and multilayer films of PdCo and PtCo", *J. Magn. Magn. Mater.* **126**, 282 (1993).

[785] K. Kyuno, R. Yamamoto, and S. Asano, "Theoretical-study on the magnetocrystalline anisotropy of X/Co (X = Pd, Pt, Cu, Ag, Au) multilayers", *J. Phys. Soc. Jpn.* **61**, 2099 (1992).

[786] K. Kyuno, J. G. Ha, R. Yamamoto, and S. Asano, "Theoretical study on the strain dependence of the magnetic anisotropy of X/Co (X=Pt, Cu, Ag, and Au) metallic multilayers", *J. Appl. Phys.* **79**, 7084 (1996).

[787] K. Kyuno, J. G. Ha, R. Yamamoto, and S. Asano, "Magnetoelastic contribution to the interface anisotropy of Pd/Co metallic multilayers", *Phys. Rev. B* **54**, 1092 (1996).

[788] A. B. Shick, D. L. Novikov, and A. J. Freeman, "Relativistic spin-polarized theory of magnetoelastic coupling and magnetic anisotropy strain dependence: Application to Co/Cu(001)", *Phys. Rev. B* **56**, 14259 (1997).

[789] Z. Zhang, P. E. Wigen, and S. S. P. Parkin, "Pt layer thickness dependence of magnetic properties in Co/Pt multilayers", *J. Appl. Phys.* **69**, 5649 (1991).

[790] O. Hellwig, A. Berger, J. B. Kortright, and E. E. Fullerton, "Domain structure and magnetization reversal of antiferromagnetically coupled perpendicular anisotropy films", *J. Magn. Magn. Mater.* **319**, 13 (2007).

[791] J. Moritz, F. Garcia, J. C. Toussaint, B. Dieny, and J. P. Nozières, "Orange peel coupling in multilayers with perpendicular magnetic anisotropy: Application to (Co/Pt)-based exchange-biased spin-valves", *Europhys. Lett.* **65**, 123 (2004).

[792] J. W. Knepper and F. Y. Yang, "Oscillatory interlayer coupling in Co/Pt multilayers with perpendicular anisotropy", *Phys. Rev. B* **71**, 224403 (2005).

[793] Z. Y. Liu, G. H. Yu, G. Han, and Z. C. Wang, "Investigation of ferromagnetic coupling between Co layers in a Co/Pt multilayer with perpendicular anisotropy", *J. Magn. Magn. Mater.* **299**, 120 (2006).

[794] M. Robinson, Y. Au, J. W. Knepper, F. Y. Yang, and R. Sooryakumar, "Magnetic imaging of layer-by-layer reversal in Co/Pt multilayers with perpendicular anisotropy", *Phys. Rev. B* **73**, 224422 (2006).

[795] S. Wiebel, J. P. Jamet, N. Vernier, A. Mougin, J. Ferré, V. Baltz, B. Rodmacq, and B. Dieny, "Magnetic domain structure and dynamics in interacting ferromagnetic stacks with perpendicular anisotropy", *J. Appl. Phys.* **100**, 043912 (2006).

[796] Z. Y. Liu, F. Zhang, H. L. Chen, B. Xu, D. L. Yu, J. L. He, and Y. J. Tian, "Antiferromagnetic interlayer coupling in Pt/Co multilayers with perpendicular anisotropy", *Phys. Rev. B* **79**, 024427 (2009).

[797] Z. Y. Liu, F. Zhang, N. Li, B. Xu, J. L. He, D. L. Yu, and Y. J. Tian, "Oscillatory antiferromagnetic interlayer coupling in Co(4 Å)/Pt(t(Pt) Å)/[Co(4 Å)/Pt(6 Å)/Co(4 Å)]/NiO(20 Å) multilayers with perpendicular anisotropy", *Phys. Rev. B* **77**, 012409 (2008).

[798] F. Zhang, F. S. Wen, L. Li, N. Wang, Y. F. Lu, Z. Y. Liu, B. Xu, D. L. Yu, J. L. He, and Y. J. Tian, "Investigations on the interlayer coupling in Co/Pt multilayers with perpendicular anisotropy via the extraordinary Hall effect", *Thin Solid Films* **519**, 1980 (2011).

[799] F. Cayssol, D. Ravelosona, C. Chappert, J. Ferré, and J. P. Jamet, "Domain wall creep in magnetic wires", *Phys. Rev. Lett.* **92**, 107202 (2004).

[800] J. Ferré, V. Repain, J. P. Jamet, A. Mougin, V. Mathet, C. Chappert, and H. Bernas, "Magnetisation reversal dynamics in an ultrathin

magnetic film and the creep phenomenon", *Phys. Status Solidi A* **201**, 1386 (2004).

[801] P. J. Metaxas, J. P. Jamet, A. Mougin, M. Cormier, J. Ferré, V. Baltz, B. Rodmacq, B. Dieny, and R. L. Stamps, "Creep and flow regimes of magnetic domain-wall motion in ultrathin Pt/Co/Pt films with perpendicular anisotropy", *Phys. Rev. Lett.* **99**, 217208 (2007).

[802] L. S. Alvarez, K. Y. Wang, and C. H. Marrows, "Field-driven creep motion of a composite domain wall in a Pt/Co/Pt/Co/Pt multilayer wire", *J. Magn. Magn. Mater.* **322**, 2529 (2010).

[803] S. Eisebitt, J. Lüning, W. F. Schlotter, M. Lorgen, O. Hellwig, W. Eberhardt, and J. Stöhr, "Lensless imaging of magnetic nanostructures by x-ray spectro-holography", *Nature* **432**, 885 (2004).

[804] D. Stickler, R. Frömter, H. Stillrich, C. Menk, C. Tieg, S. Streit-Nierobisch, M. Sprung, C. Gutt, L. M. Stadler, O. Leupold, G. Grübel, and H. P. Oepen, "Soft x-ray holographic microscopy", *Appl. Phys. Lett.* **96**, 042501 (2010).

[805] J. Camarero, E. Jimenez, J. Vogel, C. Tieg, P. Perna, A. Bollero, F. Yakhou-Harris, C. Arm, B. Rodmacq, E. Gautier, S. Auffret, B. Delaup, G. Gaudin, B. Dieny, and R. Miranda, "Exploring the limits of soft x-ray magnetic holography: Imaging magnetization reversal of buried interfaces (invited)", *J. Appl. Phys.* **109**, 07D357 (2011).

[806] J. E. Davies, O. Hellwig, E. E. Fullerton, G. Denbeaux, J. B. Kortright, and K. Liu, "Magnetization reversal of Co/Pt multilayers: Microscopic origin of high-field magnetic irreversibility", *Phys. Rev. B* **70**, 224434 (2004).

[807] X. M. Cheng, V. I. Nikitenko, A. J. Shapiro, R. D. Shull, and C. L. Chien, "Unusual magnetization reversal in $[Co/Pt]_4$ multilayers with perpendicular anisotropy", *J. Appl. Phys.* **99**, 08C905 (2006).

[808] Y. L. Iunin, Y. P. Kabanov, V. I. Nikitenko, X. M. Cheng, D. Clarke, O. A. Tretiakov, O. Tchernyshyov, A. J. Shapiro, R. D. Shull, and C. L. Chien, "Asymmetric domain nucleation and unusual magnetization reversal in ultrathin Co films with perpendicular anisotropy", *Phys. Rev. Lett.* **98**, 117204 (2007).

[809] J. E. Davies, O. Hellwig, E. E. Fullerton, M. Winklhofer, R. D. Shull, and K. Liu, "Frustration driven stripe domain formation in Co/Pt multilayer films", *Appl. Phys. Lett.* **95**, 022505 (2009), journal article.

[810] S. Streit-Nierobisch, D. Stickler, C. Gutt, L.-M. Stadler, H. Stillrich, C. Menk, R. Frömter, C. Tieg, O. Leupold, H. P. Oepen, and G. Grübel, "Magnetic soft x-ray holography study of focused ion beam-patterned Co/Pt multilayers", *J. Appl. Phys.* **106**, 083909 (2009).

[811] E. Beaurepaire, J.-C. Merle, A. Daunois, and J.-Y. Bigot, "Ultrafast spin dynamics in ferromagnetic nickel", *Phys. Rev. Lett.* **76**, 4250 (1996).

[812] C. Gutt, L. M. Stadler, S. Streit-Nierobisch, A. P. Mancuso, A. Schropp, B. Pfau, C. M. Günther, R. Könnecke, J. Gulden, B. Reime, J. Feldhaus, E. Weckert, I. A. Vartanyants, O. Hellwig, F. Staier, R. Barth, M. Grunze, A. Rosenhahn, D. Stickler, H. Stillrich, R. Frömter, H. P. Oepen, M. Martins, T. Nisius, T. Wilhein, B. Faatz, N. Guerassimova, K. Honkavaara, V. Kocharyan, R. Treusch, E. Saldin, S. Schreiber, E. A. Schneidmiller, M. V. Yurkov, S. Eisebitt, and G. Grübel, "Resonant magnetic scattering with soft x-ray pulses from a free-electron laser operating at 1.59 nm", *Phys. Rev. B* **79**, 212406 (2009).

[813] B. W. J. McNeil and N. R. Thompson, "X-ray free-electron lasers", *Nat. Photon.* **4**, 814 (2010).

[814] C. Kittel, "Interpretation of anomalous Larmor frequencies in ferromagnetic resonance experiment", *Phys. Rev.* **71**, 270 (1947).

[815] C. Kittel, "On the theory of ferromagnetic resonance absorption", *Phys. Rev.* **73**, 155 (1948).

[816] M. Farle, "Ferromagnetic resonance of ultrathin metallic layers", *Rep. Prog. Phys.* **61**, 755 (1998).

[817] F. Balhorn, *Spin-Wave Interference in Rolled-Up Ferromagnetic Microtubes*, Diploma thesis, University of Hamburg, Germany (2009).

[818] M. Farle, B. Mirwald-Schulz, A. N. Anisimov, W. Platow, and K. Baberschke, "Higher-order magnetic anisotropies and the nature of the spin-reorientation transition in face-centered-tetragonal Ni(001)/Cu(001)", *Phys. Rev. B* **55**, 3708 (1997).

[819] W. Platow, A. N. Anisimov, G. L. Dunifer, M. Farle, and K. Baberschke, "Correlations between ferromagnetic-resonance linewidths and sample quality in the study of metallic ultrathin films", *Phys. Rev. B* **58**, 5611 (1998).

[820] S. V. Vonsovskii (Ed.) *Ferromagnetic Resonance: The Phenomenon of Resonance Absorption of the HF Electromagnetic Field Energy in Ferromagnetic Materials*, (Israel Program for Scientific Translations Ltd., 1964).

[821] U. Wiedwald, M. Spasova, M. Farle, M. Hilgendorff, and M. Giersig, "Ferromagnetic resonance of monodisperse Co particles", *J. Vac. Sci. Technol. A* **19**, 1773 (2001).

[822] J. Crangle and W. R. Scott, "Dilute ferromagnetic alloys", *J. Appl. Phys.* **36**, 921 (1965).

[823] G. Schütz, R. Wienke, W. Wilhelm, W. B. Zeper, H. Ebert, and K. Spörl, "Spin-dependent x-ray absorption in Co/Pt multilayers and $Co_{50}Pt_{50}$ alloy", *J. Appl. Phys.* **67**, 4456 (1990).

[824] D. Weller, Y. Wu, J. Stöhr, M. G. Samant, B. D. Hermsmeier, and C. Chappert, "Orbital magnetic moments of Co in multilayers with perpendicular magnetic anisotropy", *Phys. Rev. B* **49**, 12888 (1994).

[825] J. Thiele, C. Boeglin, K. Hricovini, and F. Chevrier, "Magnetic circular x-ray-dichroism study of Co/Pt(111)", *Phys. Rev. B* **53**, 11934 (1996).

[826] P. Poulopoulos, M. Angelakeris, E. T. Papaioannou, N. K. Flevaris, D. Niarchos, M. Nyvlt, V. Prosser, S. Visnovsky, C. Mueller, P. Fumagalli, F. Wilhelm, and A. Rogalev, "Structural, magnetic, and spectroscopic magneto-optical properties aspects of Pt-Co multilayers with intentionally alloyed layers", *J. Appl. Phys.* **94**, 7662 (2003).

[827] P. Gambardella, S. Rusponi, M. Veronese, S. S. Dhesi, C. Grazioli, A. Dallmeyer, C. I, R. Zeller, P. H. Dederichs, K. Kern, C. Carbone, and H. Brune, "Giant magnetic anisotropy of single cobalt atoms and nanoparticles", *Science* **300**, 1130 (2003).

[828] P. Gambardella, S. Rusponi, T. Cren, N. Weiss, and H. Brune, "Magnetic anisotropy from single atoms to large monodomain islands of Co/Pt(111)", *C. R. Phys.* **6**, 75 (2005).

[829] C. Etz, J. Zabloudil, P. Weinberger, and E. Y. Vedmedenko, "Magnetic properties of single atoms of Fe and Co on Ir(111) and Pt(111)", *Phys. Rev. B* **77**, 184425 (2008).

[830] G. Moulas, A. Lehnert, S. Rusponi, J. Zabloudil, C. Etz, S. Ouazi, M. Etzkorn, P. Bencok, P. Gambardella, P. Weinberger, and H. Brune, "High magnetic moments and anisotropies for Fe_xCo_{1-x} monolayers on Pt(111)", *Phys. Rev. B* **78**, 214424 (2008).

[831] F. Meier, S. Lounis, J. Wiebe, L. Zhou, S. Heers, P. Mavropoulos, P. H. Dederichs, S. Blügel, and R. Wiesendanger, "Spin polarization of platinum (111) induced by the proximity to cobalt nanostripes", *Phys. Rev. B* **83**, 075407 (2011).

[832] R. A. Lopez and R. E. Parra, "Magnetization and temperature dependence of polarization clouds in PtCo dilute alloys", *J. Magn. Magn. Mater.* **79**, 373 (1989).

[833] P. J. H. Bloemen, W. J. M. de Jonge, and F. J. A. den Broeder, "The temperature dependence of the magnetization of magnetic multilayers", *J. Magn. Magn. Mater.* **93**, 105 (1991).

[834] H. Ebert, S. Ruegg, G. Schütz, R. Wienke, and W. B. Zeper, "Magnetic-properties of Co/Pt-multilayers", *J. Magn. Magn. Mater.* **93**, 601 (1991).

[835] E. Goering, J. Will, J. Geissler, M. Justen, F. Weigand, and G. Schuetz, "X-ray magnetic circular dichroism - a universal tool for magnetic investigations", *J. Alloys Compd.* **328**, 14 (2001).

[836] F. Schreiber, Z. Frait, T. Zeidler, N. Metoki, W. Donner, H. Zabel, and J. Pelzl, "Strong anisotropies in MBE-grown Co/Cr(001) - ferromagnetic-resonance and magnetooptical Kerr-effect studies", *Phys. Rev. B* **51**, 2920 (1995).

[837] J. P. Nibarger, R. Lopusnik, Z. Celinski, and T. J. Silva, "Variation of magnetization and the Landé g factor with thickness in Ni-Fe films", *Appl. Phys. Lett.* **83**, 93 (2003).

[838] T. R. McGuire, J. Aboaf, and E. Klokholm, "Co-Sn thin-films: Magnetic and transport properties", *J. Appl. Phys.* **53**, 8219 (1982).

[839] T. R. McGuire, J. A. Aboaf, and E. Klokholm, "Magnetic and transport properties of Co-Pt thin films", *J. Appl. Phys.* **55**, 1951 (1984).

[840] P. P. Freitas, L. Berger, and J. F. Silvain, "Anisotropic magnetoresistance of Co-Fe thin-films", *J. Appl. Phys.* **61**, 4385 (1987).

[841] M. Knobel, J. C. Denardin, H. B. de Carvalho, M. J. S. P. Brasil, A. B. Pakhomov, and F. P. Missell, "Magnetic and magnetotransport properties of Co thin films on Si", *Phys. Status Solidi A* **187**, 177 (2001).

[842] A. Fernandez-Pacheco, J. M. De Teresa, R. Cordoba, and M. R. Ibarra, "Magnetotransport properties of high-quality cobalt nanowires grown by focused-electron-beam-induced deposition", *J. Phys. D: Appl. Phys.* **42**, 055005 (2009).

[843] A. Gerber, A. Milner, L. Goldshmit, M. Karpovski, B. Lemke, H. U. Habermeier, and A. Sulpice, "Effect of surface scattering on the extraordinary Hall coefficient in ferromagnetic films", *Phys. Rev. B* **65**, 054426 (2002).

[844] A. Gerber, A. Milner, A. Finkler, M. Karpovski, L. Goldsmith, J. Tuaillon-Combes, O. Boisron, P. Melinon, and A. Perez, "Correlation between the extraordinary Hall effect and resistivity", *Phys. Rev. B* **69**, 224403 (2004).

[845] Z. B. Guo, W. B. Mi, Q. Zhang, B. Zhang, R. O. Aboljadayel, and X. X. Zhang, "Anomalous Hall effect in polycrystalline Ni films", *Solid State Commun.* **152**, 220 (2012).

[846] H. Sato, T. Kumano, Y. Aoki, T. Kaneko, and R. Yamamoto, "Anomalous field dependence of Hall resistivity in Fe/Cr multilayers", *J. Phys. Soc. Jpn.* **62**, 416 (1993).

[847] J. Q. Wang and G. Xiao, "Large finite-size effect of giant magnetoresistance in magnetic granular thin-films", *Phys. Rev. B* **51**, 5863 (1995).

[848] C. L. Canedy, X. W. Li, and G. Xiao, "Extraordinary Hall effect in (111) and (100)-orientated Co/Pt superlattices", *J. Appl. Phys.* **81**, 5367 (1997).

[849] F. Zhang, F. S. Wen, Y. F. Lu, W. Li, Y. F. Lu, Z. Y. Liu, B. Xu, D. L. Yu, J. L. He, and Y. J. Tian, "Proper scaling of the anomalous Hall effect in the Co/Pt multilayers", *J. Appl. Phys.* **110**, 033921 (2011).

[850] J. Zhao, Y. J. Wang, X. F. Han, S. Zhang, and X. H. Ma, "Large extraordinary Hall effect in $[Pt/Co]_5/Ru/[Co/Pt]_5$ multilayers", *Phys. Rev. B* **81**, 172404 (2010).

[851] S. L. Zhang, J. Teng, J. Y. Zhang, Y. Liu, J. W. Li, G. H. Yu, and S. G. Wang, "Large enhancement of the anomalous Hall effect in Co/Pt multilayers sandwiched by MgO layers", *Appl. Phys. Lett.* **97**, 222504 (2010).

[852] S. Das, H. Yoshikawa, and S. Nakagawa, "Simultaneous detection of perpendicular and in-plane magnetization component in a $[Co/Pd]_n$ perpendicular magnetic recording media", *J. Appl. Phys.* **93**, 8098 (2003).

[853] C. L. Canedy, G. Q. Gong, J. Q. Wang, and G. Xiao, "Large magnetic Hall effect in ferromagnetic Fe_xPt_{100-x}thin films", *J. Appl. Phys.* **79**, 6126 (1996).

[854] A. Gerber, A. Milner, M. Karpovski, A. Tsukernik, A. Sulpice, J. Tuaillon-Combes, P. Melinon, and A. Perez, "Anomalous magnetization of nanoscale ferromagnet/normal-metal systems: Possible evidence of the electronic spin polarization", *Phys. Rev. B* **69**, 134422 (2004).

[855] S. Sangiao, L. Morellon, G. Simon, J. M. De Teresa, J. A. Pardo, J. Arbiol, and M. R. Ibarra, "Anomalous Hall effect in Fe (001) epitaxial thin films over a wide range in conductivity", *Phys. Rev. B* **79**, 014431 (2009).

[856] G. C. Carter and E. M. Pugh, "Hall effect and transverse magnetoresistance in some ferromagnetic iron-chromium alloys", *Phys. Rev.* **152**, 498 (1966).

[857] V. Korenivski, K. V. Rao, J. Colino, and I. K. Schuller, "Extraordinary Hall effect in giant magnetoresistive Fe/Cr multilayers: The role of interface scattering", *Phys. Rev. B* **53**, 11938 (1996).

[858] W. Meissner, F. Schmeissner, and R. Doll, *Landolt-Börnstein - Band II Elektrische Eigenschaften I*, Volume 19a, (Springer-Verlag, 1965).

[859] P. W. Brigdman, "The effect of tension on the electrical resistance of certain abnormal metals", *Proc. Amer. Acad. Arts Sci.* **57**, 41 (1922).

[860] G. C. Kuczynski, "Effect of elastic strain on the electrical resistance of metals", *Phys. Rev.* **94**, 61 (1954).

[861] S. U. Jen, T. P. Chen, and B. L. Chao, "Saturation moment, specific-heat, and transport properties of disordered $Co_{100-x}Pt_x$ alloys", *Phys. Rev. B* **48**, 12789 (1993).

[862] L. Nordheim, "Zur Elektronentheorie der Metalle. I", *Ann. Phys.* **401**, 607 (1931).

[863] M. Sonehara, T. Shinohara, T. Sato, K. Yamasawa, and Y. Miura, "Strain sensor using stress-magnetoresistance effect of Ni-Fe/Mn-Ir exchange-coupled magnetic film", *J. Appl. Phys.* **107**, 09E718 (2010).

[864] A. Bartok, L. Daniel, and A. Razek, "Micro-macro modelling of stress-dependent anisotropic magnetoresistance", *J. Phys. D: Appl. Phys.* **44**, 135001 (2011).

[865] R. Aidun, S. Arajs, E. K. Dokyi, and M. C. Martin, "Electrical-conduction in some glassy metal-alloys in the presence of magnetic-fields and tensile stresses", *J. Appl. Phys.* **53**, 8243 (1982).

[866] A. Raoufi and S. Arajs, "Effects of magnetic-field and tensile-stress on the electrical-resistivity of some amorphous ferromagnets", *Phys. Status Solidi A* **95**, 193 (1986).

[867] A. Raoufi and S. Arajs, "Stress dependence of magnetoresistance in crystalline and amorphous ferromagnets", *Phys. Status Solidi A* **108**, 369 (1988).

[868] A. Gerber, I. Kishon, I. Y. Korenblit, O. Riss, A. Segal, M. Karpovski, and B. Raquet, "Linear positive magnetoresistance and quantum interference in ferromagnetic metals", *Phys. Rev. Lett.* **99**, 027201 (2007).

[869] M. Plihal, D. L. Mills, and J. Kirschner, "Spin wave signature in the spin polarized electron energy loss spectrum of ultrathin Fe films: Theory and experiment", *Phys. Rev. Lett.* **82**, 2579 (1999).

[870] R. Vollmer, M. Etzkorn, P. S. A. Kumar, H. Ibach, and J. Kirschner, "Spin-polarized electron energy loss spectroscopy of high energy, large wave vector spin waves in ultrathin fcc Co films on Cu(001)", *Phys. Rev. Lett.* **91**, 147201 (2003).

[871] A. Taroni, A. Bergman, L. Bergqvist, J. Hellsvik, and O. Eriksson, "Suppression of standing spin waves in low-dimensional ferromagnets", *Phys. Rev. Lett.* **107**, 037202 (2011).

[872] E. H. Sondheimer, "The influence of a transverse magnetic field on the conductivity of thin metallic films", *Phys. Rev.* **80**, 401 (1950).

[873] Z. Tesanovic, M. V. Jaric, and S. Maekawa, "Quantum transport and surface scattering", *Phys. Rev. Lett.* **57**, 2760 (1986).

[874] N. Trivedi and N. W. Ashcroft, "Quantum size effects in transport-properties of metallic-films", *Phys. Rev. B* **38**, 12298 (1988).

[875] D. Calecki, "Galvanomagnetic phenomena and surface-roughness in thin metallic-films", *Phys. Rev. B* **42**, 6906 (1990).

[876] A. E. Meyerovich and I. V. Ponomarev, "Surface roughness and size effects in quantized films", *Phys. Rev. B* **65**, 155413 (2002).

[877] R. C. Munoz, J. P. Garcia, R. Henriquez, A. M. Moncada, A. Espinosa, M. Robles, G. Kremer, L. Moraga, S. Cancino, J. R. Morales, A. Ramirez, S. Oyarzun, M. A. Suarez, D. Chen, E. Zumelzu, and C. Lizama, "Size effects under a strong magnetic field: Hall effect induced by electron-surface scattering on thin gold films deposited onto mica substrates under high vacuum", *Phys. Rev. Lett.* **96**, 206803 (2006).

[878] R. Henriquez, S. Oyarzun, M. Flores, M. A. Suarez, L. Moraga, G. Kremer, C. A. Gonzalez-Fuentes, M. Robles, and R. C. Munoz, "Size effects on the Hall constant in thin gold films", *J. Appl. Phys.* **108**, 123704 (2010).

[879] K. L. Chopra and S. K. Bahl, "Hall effect in thin metal films", *J. Appl. Phys.* **38**, 3607 (1967).

[880] G. Wedler and W. Wiebauer, "Resistivity and Hall-effect of copper-films before and after adsorption of carbon-monoxide", *Thin Solid Films* **28**, 65 (1975).

[881] J. Gogl, J. Vancea, and H. Hoffmann, "Hall-coefficient and resistivity of thin polycrystalline Cu films - contributions of band-structure", *J. Phys.: Condens. Matter* **2**, 1795 (1990).

[882] P. M. T. M. van Attekum, P. H. Woerlee, G. C. Verkade, and A. A. M. Hoeben, "Influence of grain-boundaries and surface Debye temperature on the electrical-resistance of thin gold-films", *Phys. Rev. B* **29**, 645 (1984).

[883] W. Wu, S. H. Brongersma, M. van Hove, and K. Maex, "Influence of surface and grain-boundary scattering on the resistivity of copper in reduced dimensions", *Appl. Phys. Lett.* **84**, 2838 (2004).

[884] W. G. Ma, X. Zhang, and K. Takahashi, "Electrical properties and reduced Debye temperature of polycrystalline thin gold films", *J. Phys. D: Appl. Phys.* **43**, 465301 (2010).

[885] A. Bid, A. Bora, and A. K. Raychaudhuri, "Temperature dependence of the resistance of metallic nanowires of diameter $\geq$ 15 nm: Applicability of Bloch-Grüneisen theorem", *Phys. Rev. B* **74**, 035426 (2006).

[886] S. Kim, H. Suhl, and I. K. Schuller, "Surface phonon scattering in the electrical resistivity on Co/Ni superlattices", *Phys. Rev. Lett.* **78**, 322 (1997).

[887] M. X. Gu, C. Q. Sun, Z. Chen, T. C. A. Yeung, S. Li, C. M. Tan, and V. Nosik, "Size, temperature, and bond nature dependence of elasticity and its derivatives on extensibility, Debye temperature, and heat capacity of nanostructures", *Phys. Rev. B* **75**, 125403 (2007).

[888] G. S. Okram and N. Kaurav, "Size-dependent resistivity and thermopower of nanocrystalline copper", *J. Appl. Phys.* **110**, 023713 (2011).

[889] H. B. Callen and E. Callen, "Present status of temperature dependence of magnetocrystalline anisotropy and $l(l+1)/2$ power law", *J. Phys. Chem. Solids* **27**, 1271 (1966).

[890] H. Y. Zhang, Y. J. Wang, G. G. Zheng, J. X. Shen, Z. S. Shan, and D. J. Sellmyer, "The temperature dependence of perpendicular anisotropy in Co/Pt and Co/Au multilayer films", *IEEE Trans. Magn.* **29**, 3376 (1993).

[891] R. Bodenberger and A. Hubert, "Determination of Bloch wall energy of uniaxial ferromagnets", *Phys. Status Solidi A* **44**, K7 (1977).

[892] J. M. Gallego, D. Lederman, S. Kim, and I. K. Schuller, "Oscillatory behavior of the transport properties in Ni/Co multilayers - a superlattice effect", *Phys. Rev. Lett.* **74**, 4515 (1995).

[893] S. H. Kim and I. K. Schuller, "Oscillatory behavior in the electrical resistivity of transition-metal superlattices", *Phys. Rev. B* **58**, 2240 (1998).

[894] P. C. McIntyre, D. T. Wu, and M. Nastasi, "Interdiffusion in epitaxial Co/Pt multilayers", *J. Appl. Phys.* **81**, 637 (1997).

[895] B. Rodmacq, A. Manchon, C. Ducruet, S. Auffret, and B. Dieny, "Influence of thermal annealing on the perpendicular magnetic anisotropy of Pt/Co/AlOx trilayers", *Phys. Rev. B* **79**, 024423 (2009).

[896] S. Bandiera, R. C. Sousa, B. Rodmacq, and B. Dieny, "Enhancement of perpendicular magnetic anisotropy through reduction of Co-Pt interdiffusion in (Co/Pt) multilayers", *Appl. Phys. Lett.* **100**, 142410 (2012).

[897] Y. Aoki, K. Honda, H. Sato, Y. Kobayashi, S. Hashimoto, T. Yokoyama, and T. Hanyu, "The extraordinary Hall effect of Pd/Co multilayers", *J. Magn. Magn. Mater.* **162**, 1 (1996).

[898] K. Schroeder, *Magnetism in Atoms - 36. Spring School of the Institute of Solid State Research 2005: Magnetism goes Nano*, (Forschungszentrum Jülich GmbH, Institut für Festkörperforschung, 2005).

[899] M. Bode, S. Heinze, A. Kubetzka, O. Pietzsch, X. Nie, G. Bihlmayer, S. Blügel, and R. Wiesendanger, "Magnetization-direction-dependent local electronic structure probed by scanning tunneling spectroscopy", *Phys. Rev. Lett.* **89**, 237205 (2002).

[900] C. Gould, C. Ruster, T. Jungwirth, E. Girgis, G. M. Schott, R. Giraud, K. Brunner, G. Schmidt, and L. W. Molenkamp, "Tunneling anisotropic magnetoresistance: A spin-valve-like tunnel magnetoresistance using a single magnetic layer", *Phys. Rev. Lett.* **93**, 117203 (2004).

[901] A. Matos-Abiague and J. Fabian, "Anisotropic tunneling magnetoresistance and tunneling anisotropic magnetoresistance: Spin-orbit coupling in magnetic tunnel junctions", *Phys. Rev. B* **79**, 155303 (2009).

[902] K. von Bergmann, M. Menzel, D. Serrate, Y. Yoshida, S. Schröder, P. Ferriani, A. Kubetzka, R. Wiesendanger, and S. Heinze, "Tunneling anisotropic magnetoresistance on the atomic scale", *Phys. Rev. B* **86**, 134422 (2012).

[903] S. Y. Huang, X. Fan, D. Qu, Y. P. Chen, W. G. Wang, J. Wu, T. Y. Chen, J. Q. Xiao, and C. L. Chien, "Transport magnetic proximity effects in platinum", *Phys. Rev. Lett.* **109**, 107204 (2012).

[904] H. Nakayama, M. Althammer, Y.-T. Chen, K. Uchida, Y. Kajiwara, D. Kikuchi, T. Ohtani, S. Geprägs, M. Opel, S. Takahashi, R. Gross, G. E. W. Bauer, S. T. B. Goennenwein, and E. Saitoh, "Spin Hall magnetoresistance induced by a non-equilibrium proximity effect", *arXiv:1211.0098* (2012).

[905] W. P. Pratt, S. F. Lee, J. M. Slaughter, R. Loloee, P. A. Schroeder, and J. Bass, "Perpendicular giant magnetoresistances of Ag/Co multilayers", *Phys. Rev. Lett.* **66**, 3060 (1991).

[906] J. Bass and W. P. Pratt, "Current-perpendicular (CPP) magnetoresistance in magnetic metallic multilayers", *J. Magn. Magn. Mater.* **200**, 274 (1999).

[907] C. Bell, G. Burnell, D. J. Kang, R. H. Hadfield, M. J. Kappers, and M. G. Blamire, "Fabrication of nanoscale heterostructure devices with a focused ion beam microscope", *Nanotechnology* **14**, 630 (2003).

[908] C. W. Leung, C. Bell, G. Burnell, and M. G. Blamire, "In situ fabrication of a cross-bridge Kelvin resistor structure by focused ion beam microscopy", *Nanotechnology* **15**, 786 (2004).

[909] M. C. Wu, A. Aziz, J. D. S. Witt, M. C. Hickey, M. Ali, C. H. Marrows, B. J. Hickey, and M. G. Blamire, "Structural and functional analysis of nanopillar spin electronic devices fabricated by 3D focused ion beam lithography", *Nanotechnology* **19**, 485305 (2008).

[910] G. E. W. Bauer, E. Saitoh, and B. J. van Wees, "Spin caloritronics", *Nat. Mater.* **11**, 391 (2012).

[911] M. Jonson and G. D. Mahan, "Mott's formula for the thermopower and the Wiedemann-Franz law", *Phys. Rev. B* **21**, 4223 (1980).

[912] R. Mitdank, M. Handwerg, C. Steinweg, W. Tollner, M. Daub, K. Nielsch, and S. F. Fischer, "Enhanced magneto-thermoelectric power factor of a 70 nm Ni-nanowire", *J. Appl. Phys.* **111**, 104320 (2012).

[913] A. D. Avery, M. R. Pufall, and B. L. Zink, "Determining the planar Nernst effect from magnetic-field-dependent thermopower and resistance in nickel and permalloy thin films", *Phys. Rev. B* **86**, 184408 (2012).

[914] T. Miyasato, N. Abe, T. Fujii, A. Asamitsu, S. Onoda, Y. Onose, N. Nagaosa, and Y. Tokura, "Crossover behavior of the anomalous Hall effect and anomalous Nernst effect in itinerant ferromagnets", *Phys. Rev. Lett.* **99**, 086602 (2007).

[915] K. Uchida, S. Takahashi, K. Harii, J. Ieda, W. Koshibae, K. Ando, S. Maekawa, and E. Saitoh, "Observation of the spin Seebeck effect", *Nature* **455**, 778 (2008).

[916] G. E. W. Bauer, A. H. MacDonald, and S. Maekawa, "Spin caloritronics", *Solid State Commun.* **150**, 459 (2010).

[917] H. Yu, S. Granville, D. P. Yu, and J.-P. Ansermet, "Evidence for thermal spin-transfer torque", *Phys. Rev. Lett.* **104**, 146601 (2010).

[918] S. Y. Huang, W. G. Wang, S. F. Lee, J. Kwo, and C. L. Chien, "Intrinsic spin-dependent thermal transport", *Phys. Rev. Lett.* **107**, 216604 (2011).

[919] M. Walter, J. Walowski, V. Zbarsky, M. Münzenberg, M. Schäfers, D. Ebke, G. Reiss, A. Thomas, P. Peretzki, M. Seibt, J. S. Moodera, M. Czerner, M. Bachmann, and C. Heiliger, "Seebeck effect in magnetic tunnel junctions", *Nat. Mater.* **10**, 742 (2011).

[920] S. T. B. Goennenwein and G. E. W. Bauer, "Spin caloritronics - electron spins blow hot and cold", *Nat. Nanotechnol.* **7**, 145 (2012).

[921] J. Flipse, F. L. Bakker, A. Slachter, F. K. Dejene, and B. J. van Wees, "Direct observation of the spin-dependent Peltier effect", *Nat. Nanotechnol.* **7**, 166 (2012).

[922] W. W. Lin, M. Hehn, L. Chaput, B. Negulescu, S. Andrieu, F. Montaigne, and S. Mangin, "Giant spin-dependent thermoelectric effect in magnetic tunnel junctions", *Nat. Commun.* **3**, 744 (2012).

[923] M. V. Costache, G. Bridoux, I. Neumann, and S. O. Valenzuela, "Magnon-drag thermopile", *Nat. Mater.* **11**, 199 (2012).

Publications

Publication List and Conference Contributions

Publication List

published

[E12] L. Müller, C. Gutt, B. Pfau, S. Schaffert, J. Geilhufe, F. Büttner, J. Mohanty, S. Flewett, , R. Treusch, S. Düsterer, H. Redlin, A. Al-Shemmary, M. Hille, A. Kobs, R. Frömter, H. P. Oepen, B. Ziaja, N. Medvedev, S.-K. Son, R. Thiele, R. Santra, W. Schlotter, B. Vodungbo, J. Lüning, S. Eisebitt, and G. Grübel,
Breakdown of the X-ray resonant magnetic scattering signal during intense XUV FEL irradiation
Phys. Rev. Lett. **110**, 234801 (2013).

[E11] Judith Kimling, Theo Gerhardt, André Kobs, Andreas Vogel, Sebastian Wintz, Mi-Young Im, Peter Fischer, Hans Peter Oepen, Ulrich Merkt, and Guido Meier,
Tuning of the nucleation field in nanowires with perpendicular magnetic anisotropy
J. Appl. Phys. **113**, 163902 (2013).

[E10] L. Müller, C. Gutt, S. Streit-Nierobisch, M. Walther, S. Schaffert, B. Pfau, J. Geilhufe, F. Büttner, S. Flewett, C. M. Günther, S. Eisebitt, A. Kobs, M. Hille, D. Stickler, R. Frömter, H. P. Oepen, J. Lüning, and G. Grübel,
Endstation for ultrafast magnetic scattering experiments at free-electron laser in Hamburg
Rev. Sci. Instr. **84**, 013906 (2013).

[E9] M. Hille, A. Frauen, B. Beyersdorff, A. Kobs, S. Heße, R. Frömter, and H. P. Oepen,
Direct method for measuring the canting angle of magnetization
J. Appl. Phys. **113**, 023902 (2013).

[E8] B. Pfau, S. Schaffert, L. Müller, C. Gutt, A. Al-Shemmary, F. Büttner, R. Delaunay, S. Düsterer, S. Flewett, R. Frömter, J. Geilhufe, E. Guehrs, C. M. Günther, R. Hawaldar, M. Hille, N. Jaouen, A. Kobs, K. Li, J. Mohanty, H. Redlin, W. F. Schlotter, D. Stickler, R. Treusch, B. Vodungbo, M. Kläui, H. P. Oepen, J. Lüning, G. Grübel, and S. Eisebitt,
Ultrafast Optical Demagnetization manipulates Nanoscale Spin Structure in Domain Walls
Nature Comm. **3**, 1100 (2012).

[E7] A. Kobs, S. Heße, H. P. Oepen, and P. Weinberger,
Anisotropic Interface Magnetoresistances in Pt(111)/Co_n/Pt(111)
Philos. Mag. **92**, 2835 (2012).

[E6] A. Kobs, S. Heße, W. Kreuzpaintner, G. Winkler, D. Lott, P. Weinberger, A. Schreyer, H. P. Oepen,
Anisotropic Interface Magnetoresistance in Pt/Co/Pt Sandwiches
Phys. Rev. Lett. **106**, 217207 (2011).

[E5] C. Tieg, R. Frömter, D. Stickler, S. Hankemeier, A. Kobs, S. Streit-Nierobisch, C. Gutt, G. Grübel, and H. P Oepen,
Imaging the in-plane magnetization in a Co microstructure by Fourier transform holography
Opt. Express **18**, 27251 (2010).

[E4] S. Hankemeier, A. Kobs, R. Frömter, and H. P. Oepen,
Controlling the properties of vortex domain walls via magnetic seeding fields
Phys. Rev. B **82**, 064414 (2010).

[E3] C. Gutt, S. Streit-Nierobisch, L. M. Stadler, B. Pfau, C. M. Günther, R. Könnecke, R. Frömter, A. Kobs, D. Stickler, H. P. Oepen, R. R. Fäustlin, R. Treusch, J. Feldhaus, E. Weckert, I. A. Vartanyants, M. Grunze, A. Rosenhahn, T. Wilhein, S. Eisebitt, and G. Grubel,
Single-pulse resonant magnetic scattering using a soft x-ray free-electron laser
Phys. Rev. B **81**, 100401 (2010).

[E2] André Kobs, Hendrik Spahr, Daniel Stickler, Sebastian Hankemeier, Robert Frömter, and Hans Peter Oepen,
Magnetic energies of single submicron permalloy rectangles determined via magnetotransport
Phys. Rev. B **80**, 134415 (2009).

[E1] D. Stickler, R. Frömter, W. Li, A. Kobs, and H. P. Oepen,
Integrated setup for the fabrication and measurement of magnetoresistive nanoconstrictions in ultrahigh vacuum
Rev. Sci. Instr. **79**, 103901 (2008).

in preparation

[E13] A. Kobs, F. Lofink, S. Hankemeier, G. Hoffmann, R. Frömter, and H. P. Oepen,
Domain walls in bent nanowires.

[E14] M. R. Rahbar Azad, A. Kobs, B. Beyersdorff, H. Spahr, R. Frömter, and H. P. Oepen,
Magnetostatic interaction of single submicron permalloy rectangles determined via magnetotransport.

[E15] Mi-Young Im, Peter Fischer, Judith Kimling, André Kobs, Hans Peter Oepen, and Guido Meier,
Stochastic Nature of Switching Fields in a Single Co/Pt Multilayer Disk.

Conference Contributions

M. R. Rahbar Azad, A. Kobs, B. Beyersdorff, P. Staeck, H. Spahr, R. Frömter, and H. P. Oepen,
Magneto-static interaction of single NiFe nanostructures
Talk at 58th Annual Conference on MMM 2013, Denver (USA).

A. Frauen, T. Böhnert, A. Kobs, A. Burgardt, G. Winkler, K Nielsch, and H. P. Oepen,
Anisotropic magnetothermopower and magnetotransport effects in Pt/Co/Pt layered structures
Poster at 58th Annual Conference on MMM 2013, Denver (USA).

C. Weier, R. Adam, D. Rudolf, P. Crychtol, A. Kobs, G. Winkler, R. Frömter, H. P. Oepen, M. M. Murnane, H. C. Kapteyn, and C. M. Schneider,
Resonant magnetic scattering at magnetic domains in Co/Pt multilayers using laser-generated XUV light
Talk at Spring-meeting of the German Physical Society 2013, Regensburg.

A. Kobs, S. Heße, W. Kreuzpaintner, G. Winkler, D. Lott, P. Weinberger, A. Schreyer, and H. P. Oepen,
Interface contributions to the magnetoresistance and anomalous Hall effect in Co/Pt layered structures
Poster at 520. WE-Heraeus-Seminar 2012, Bad Honnef,
Poster Price Award.

A. Kobs, S. Heße, W. Kreuzpaintner, G. Winkler, D. Lott, P. Weinberger, A. Schreyer, and H. P. Oepen,
Anisotropic Interface Magnetoresistance in Pt/Co/Pt
Talk at Spring-meeting of Materials Research Society (MRS) 2012, San Francisco (USA).

F. Lofink, S. Hankemeier, A. Kobs, R. Frömter, and H. P. Oepen,
Domain Walls in V-shaped Nanowires
Poster at Spring-meeting of Materials Research Society (MRS) 2012, San Francisco (USA).

P. Staeck, M. R. Rahbar Azad, A. Kobs, D. Stickler, B. Beyersdorff, H. Spahr, R. Frömter, and H. P. Oepen,
Magneto-static interaction of single NiFe nanostructures
Talk at Spring-meeting of the German Physical Society 2012, Berlin.

M. Hille, A. Frauen, B. Beyersdorff, A. Kobs, S. Heße, R. Frömter, and H. P. Oepen,
Determining the canting angle of magnetization via magnetoresistance measurements
Talk at Spring-meeting of the German Physical Society 2012, Berlin.

C. Weier, D. Rudolf, R. Adam, C. M. Schneider, A. Kobs, G. Winkler, R. Frömter, H. P. Oepen, M. M. Murane, and H. C. Kapteyn,

Magnetic resonant scattering with Laser generated higher harmonic radiation
Poster at Spring-meeting of the German Physical Society 2012, Berlin.

L. Müller, C. Gutt, S. Schaffert, B. Pfau, J. Geilhufe, F. Büttner, S. Felewett, J. Mohanty, S. Eisebitt, A. Kobs, M. Hille, D. Stickler, R. Frömter, H. P. Oepen, B. Vodungbo, J. Lüning, W. Schlotter, and G. Grübel,
Spatially resolved ultrafast magnetization dynamics tracked via resonant magnetic scattering at the free-electron laser FLASH
Poster at 56th Annual conference on Magnetism and Magnetic Materials (MMM) 2011, Scottsdale, Arizona (USA).

A. Kobs, S. Hesse, W. Kreuzpaintner, G. Winkler, D. Lott, P. Weinberger, A. Schreyer, and H. P. Oepen,
Anisotropic Interface Magnetoresistance in Pt/Co/Pt
Poster at Recent Trends in Nanomagnetism, Spintronics and their Applications (RTNSA) 2011, Ordizia (Spain).

S. Hankemeier, A. Kobs, R. Frömter, and H. P. Oepen,
Domain walls in bent nanowires
Talk at Recent Trends in Nanomagnetism, Spintronics and their Applications (RTNSA) 2011, Ordizia (Spain).

André Kobs, Simon Heße, Wolfgang Kreuzpaintner, Gerrit Winkler, Dieter Lott, Andreas Schreyer, and Hans Peter Oepen,
Anisotropic interface magnetoresistance in Co/Pt
Talk at Spring-meeting of the German Physical Society 2011, Dresden.

Mahmut Caylioglu, Andreas Rathjen, Alexander Neumann, André Kobs, Andreas Meyer, Robert Frömter, and Hans Peter Oepen,
Fabrication of ferromagnetic Co/Pt nanodots on NaCl-crystals
Talk at Spring-meeting of the German Physical Society 2011, Dresden.

Judith Kimling, Andreas Vogel, André Kobs, Lars Bocklage, Sebastian Wintz, Jürgen Fassbender, Mi-Young Im, Peter Fischer, Ulrich Merkt, Hans Peter Oepen, and Guido Meier
Preparation of domain walls in Co/Pt multilayer wires
Poster at Spring-meeting of the German Physical Society 2011, Dresden.

Mahmoud Reza Rahbar Azad, André Kobs, Hendrik Spahr, Björn Beyersdorff, Daniel Stickler, Robert Frömter, and Hans Peter Oepen,
Magnetostatic interaction of single NiFe nanostructures
Talk at Spring-meeting of the German Physical Society 2011, Dresden.

Gerrit Winkler, André Kobs, Wolfgang Kreuzpaintner, Simon Hesse, Dieter Lott, Andreas Schreyer, and Hans Peter Oepen,
Structure and magnetic anisotropy of Co/Pt thin film
Talk at Spring-meeting of the German Physical Society 2011, Dresden.

André Kobs, Sebastian Hankemeier, Robert Frömter, and Hans Peter Oepen,
Domain walls in bent nanowires
Talk at Spring-meeting of the German Physical Society 2010, Regensburg.

Simon Heße, Matthias Jacobi, André Kobs, Daniel Stickler, Holger Stillrich, Alexander Neumann, Andreas Meyer, and Hans Peter Oepen,
Determining the magnetic properties of small assemblies of nanodots Talk at Spring-meeting of the German Physical Society 2010, Regensburg.

Carsten Tieg, Robert Frömter, Daniel Stickler, Sebastian Hankemeier, André Kobs, Hans Peter Oepen, Simone Streit-Nierobisch, Christian Gutt, and Gerhard Grübel,
Imaging the in-plane magnetisation of Co microstructures by soft x-ray holography
Talk at Spring-meeting of the German Physical Society 2010, Regensburg.

Matthias Hille, Daniel Stickler, André Kobs, Robert Frömter, and Hans Peter Oepen,
Effect of the iron overlayer thickness on the first and second order anisotropy constants of a $(Co/Pt)_8$ multilayer film
Talk at Spring-meeting of the German Physical Society 2010, Regensburg.

Alexander Neumann, Simon Hesse, André Kobs, Andreas Frömsdorf, and Hans Peter Oepen,
Superparamagnetism of Co/Pt nanodots with perpendicular anisotropy
Talk at Spring-meeting of the German Physical Society 2010, Regensburg.

Theo Gerhardt, Judith Moser, Andreas Vogel, Andre Kobs, Guido Meier, and Markus Bolte,
Domain-wall types and switching fields in magnetic nanowires with perpendicular magnetic anisotropy determined by micromagnetic simulations
Poster at Spring-meeting of the German Physical Society 2010, Regensburg.

Judith Moser, André Kobs, Andreas Vogel, Theo Gerhardt, Markus Bolte, Mi-Young Im, Peter Fischer, Sebastian Wintz, Ulrich Merkt, Hans Peter Oepen, and Guido Meier
Controlled decrease of the nucleation field in Co/Pt multilayer wires
Poster at Spring-meeting of the German Physical Society 2010, Regensburg.

André Kobs, Simon Heße, and H. P. Oepen,
Magnetoresistance effects of Co/Pt layered structures,
Talk at Spring-meeting of the German Physical Society 2009, Dresden.

Hendrik Spahr, André Kobs, Daniel Stickler, Sebastian Hankemeier, and Hans Peter Oepen,
Magnetization reversal of single submicron NiFe rectangles
Talk at Spring-meeting of the German Physical Society 2009, Dresden.

Matthias Jacobi, Daniel Stickler, André Kobs, Simon Hesse, Holger Stillrich, Andreas Frömsdorf, and Hans Peter Oepen,
Magnetization behaviour of perpendicular magnetized particles and nanostructures Talk at Spring-meeting of the German Physical Society 2009, Dresden.

André Kobs, Daniel Stickler, Robert Frömter, and Hans Peter Oepen,
In situ magnetoresistance (MR) of FIB-milled permalloy-structures
Poster at International FIB-workshop 2008, Luzern (Swiss).

André Kobs, Daniel Stickler, Matthias Scholz, Germar Hoffmann, and Hans Peter Oepen,
Effects of Ga^+ irradiation on the magnetotransport in NiFe
Talk at Spring-meeting of the German Physical Society 2008, Berlin.

Daniel Stickler, André Kobs, Genhua Pan, and Hans Peter Oepen,
In situ magnetoresistance measurements of FIB-milled nanoconstrictions
Talk at Spring-meeting of the German Physical Society 2008, Berlin.

Publication related to chapter 3

S. Hankemeier, A. Kobs, R. Frömter, and H. P. Oepen,
Controlling the properties of vortex domain walls via magnetic seeding fields
Phys. Rev. B **82**, 064414 (2010).
http://link.aps.org/doi/10.1103/PhysRevB.82.064414

Publication related to chapter 4

André Kobs, Hendrik Spahr, Daniel Stickler, Sebastian Hankemeier, Robert Frömter, and Hans Peter Oepen,
Magnetic energies of single submicron permalloy rectangles determined via magnetotransport
Phys. Rev. B **80**, 134415 (2009).
`http://link.aps.org/abstract/PRB/v80/e134415`

Publications related to chapter 5

A. Kobs, S. Heße, W. Kreuzpaintner, G. Winkler, D. Lott, P. Weinberger, A. Schreyer, H. P. Oepen,
Anisotropic Interface Magnetoresistance in Pt/Co/Pt Sandwiches
Phys. Rev. Lett. **106**, 217207 (2011).
http://prl.aps.org/abstract/PRL/v106/i21/e217207

A. Kobs, S. Heße, H. P. Oepen, and P. Weinberger,
Anisotropic Interface Magnetoresistances in Pt(111)/Co_n/Pt(111)
Philos. Mag. **92**, 2835 (2012).
http://dx.doi.org/10.1080/14786435.2012.676213

Acknowledgement

My thesis is the result of a fruitful cooperation with many people, all of whom I would like to thank very sincerely at this point! I would like to acknowledge

first of all, Prof. Dr. Hans Peter Oepen for his great supervision, intensive pursuing discussions, his patience and guidance in the hard times of writing, and for the shared publications about the main results of my thesis.

Prof. Dr. Bernard Dieny for refereeing this thesis as second assessor. It is a great honor for me.

Simon Heße for the successful joint working on the MISA aka AIMR project, for the proofreading of this thesis, and apart from the work, for nice hours of playing Backgammon, DOKO, and Junta.

Dr. Daniel Stickler for inspiring me to join the group for performing my diploma thesis making this dissertation possible, for his great collegiality and spirit, and for the joint working in the FIB lab (das waren noch Zeiten!) and in connection with FLASH.

Dr. Sebastian Hankemeier for the great teamwork particularly concerning the "side-project" bend wires, his support in providing SEMPA images, which rather simplified the understanding about the MR curves of the rectangles, and for playing soccer on many sundays, even when the landscape was deeply covered with snow.

Hendrik Spahr, Mahmoud Reza Rahbar Azad, and Björn Beyersdorff for fruitful cooperation in the *in situ* MR project and the two latter guys also for the great road-trip across California! Remember the infinite loop: "We are young..."

Fabian Lofink for joining and promoting the project V-shaped wires.

Dr. Holger Stillrich for training me in MOKE and preparation of Co/Pt samples by means of sputter techniques.

Gerrit Winkler and the (former) GKSS team, namely, Dr. Wolfgang Kreuzpaintner, Dr. Dieter Lott, and Prof. Dr. Andreas Schreyer for elaborate x-ray structure investigations of the Co/Pt samples and ongoing research planned at PETRA III and BESSY.

Matthias Hille for cooperation in the AIMR/canting project and many crazy and hil(le)arious moments.

Stefan Rößler for performing additional SEMPA measurements.

Alexander Neumann for providing the cold-finger setup.

Wolfgang Pfützner for support concerning the e-beam preparation chamber.

All team members of Gruppe G for cooperativeness and nice working atmosphere.

Prof. Dr. Peter Weinberger for theoretical support and two joint publications, in particular for vaporizing the PRL manuscript down to four pages.

Dr. Matthias Schmidt and Dr. Stefan Knott for supplying the split-pair superconducting magnet enabling low temperature measurements of the AIMR.

Felix Balhorn, Dr. Jesco Topp, and Dr. Ole Albrecht for conducting FMR and SQUID measurements, respectively.

Dr. Andriy Chuvilin for preliminary results concerning HRTEM of Co/Pt and ongoing research.

Axel Frauen, Artur Burgardt, Tim Böhnert, and Prof. Dr. Kornelius Nielsch for cooperation concerning the ongoing research on spin-dependent Seebeck effect in Co/Pt layered structures.

Dr. Hongbin Zhang and Dr. Yuriy Mokrousov for inviting me to the Forschungszentrum Jülich and for future theoretical support concerning the understanding of the AHE in Co/Pt layered structures.

Judith Kimling for cooperation at the investigations regarding the magnetization reversal of perpendicular magnetized Co/Pt nanostructures.

The fine mechanic and electronic workshops for their labour, and the members of the library for providing me any article I needed.

Anja Wetzlaugk for great (1+) spelling corrections.

Besides the working life, I have to thank my family and friends for unlimited support! I would like to dedicate this thesis to my closest family circle, namely my parents Petra & Klaus, my sister Sandra, my grandparents Magda & Harry Jürs, and especially my lovely girlfriend Lena Philippi.